NEW MODALITIES OF STRAIN-BASED ENGINEERING OF FERROELECTRICS: DOMAIN STRUCTURE AND PROPERTIES OF $PbZr_{1-X}Ti_XO_3$ THIN FILMS

BY

JOSHUA C. AGAR

DISSERTATION

Submitted in partial fulfillment of the requirements
for the degree of Doctor of Philosophy in Materials Science and Engineering
in the Graduate College of the
University of Illinois at Urbana-Champaign, 2015

Urbana, Illinois

Doctoral Committee:

Professor Lane W. Martin, Chair
Professor Paul V. Braun
Professor Jian-Min Zuo
Professor Daniel P. Shoemaker

Abstract

Epitaxial strain has been widely used to modify the crystal and domain structure, and ultimately the dielectric, ferroelectric, and pyroelectric responses of ferroelectric thin-films for a wide variety of applications including memories, transducers, energy harvesters, sensors, and many more. Traditionally, the ability to engineer materials using epitaxial strain has been confined to a limited range of materials systems which are closely lattice matched to commercially available substrates. In turn, considering the $PbZr_{1-x}Ti_xO_3$ system, a model ferroelectric, study of strain effects has been primarily limited to the Ti-rich variants where a wealth of closely lattice matched substrates (~±1%) exists, enabling nearly-coherently-strained films to be obtained. While these studies have generated a wealth of knowledge on the basic effects of epitaxial strain and have demonstrated the ability to enhance ferroelectric susceptibilities, these improvements have only been incremental. In the present work, we seek to expand the bounds of epitaxial strain engineering through the use of chemistry, controlled epitaxial strain (and relaxation), and compositional and strain gradients with the directive of generating phase competition and high-energy ferroelastic domain structures to enhance ferroelectric susceptibilities. We, for the first time, grow epitaxial thin films of $PbZr_{1-x}Ti_xO_3$ across the compositional phase diagram, and show that the rate of strain relaxation is significantly enhanced at the morphotropic phase boundary ($PbZr_{0.52}Ti_{0.48}O_3$), as the result of the high adaptability of the crystal and domain structure. Despite the appearance of nearly "relaxed" crystal structures, $PbZr_{0.52}Ti_{0.48}O_3$ thin films were shown to exhibit significantly different dielectric responses when grown on various substrates. Highlighting the more nuanced effects of partial strain relaxation in tuning ferroelectric susceptibilities. We then proceed to extend the bounds of epitaxial strain by growing compositionally-graded heterostructures which facilitates the retention of strains in excess of 3.5%, large strain gradients (~4.35×10^{-5} m^{-1}), and has the ability to stabilize the tetragonal crystal and domain structure, in $PbZr_{1-x}Ti_xO_3$ solid solutions that are rhombohedral in the bulk. Furthermore, we show that by varying the compositional-gradient form (in terms of the nature of the compositional gradient and heterostructure thickness) that it is possible to generate large built-in potentials, which significantly suppresses the dielectric response, but has minimal detrimental impact on the ferroelectric and pyroelectric susceptibilities, giving rise to dramatically enhanced pyroelectric figures of merit. Additionally, we show that the magnitude of the built-in potential does not follow predictions based on the magnitude of the strain gradient alone, and instead, is enhanced by local strain gradients which occur when traversing chemistries associated with structural phase boundaries (where there are abrupt changes in the lattice parameter) and at/near ferroelastic domain boundaries. Finally, we explore the nanoscale response of these ferroelastic domains in compositionally-graded heterostructures using a combination of transmission electron microscopy-based nanobeam diffraction strain mapping and multi-dimensional band-excitation switching spectroscopy. We observe that the presence of compositional and strain gradients can preferentially stabilize highly-energetic, needle-like domains, which under electrical excitation are highly labile in the out-of-plane direction (while remaining spatially fixed in the plane). These labile domain walls act like domain wall springs (enhancing the magnitude of the built-in potential), transferring elastic energy between the *a* and *c* domains (depending on the direction of the applied bias), and giving rise to locally enhanced piezoresponse at the *a* domains, as the result of a switching mechanism where the *a* domains expand towards the free surface or are nearly excluded from the film (once again, depending on the direction of applied bias). These studies demonstrate the efficacy of compositional and strain gradients as a new modality of strain engineering capable of significantly altering the crystal and domain structure, and ferroelectric susceptibilities of ferroelectric thin films inconceivable in the absence of compositional/strain gradients.

Acknowledgments

Completion of a Ph.D. is a difficult journey full of diversion, dead-ends and unexpected forks in the road. Without the help, guidance and support of a team of people who all believed in me, my journey would have never been completed. While this section is too short to thank everyone who contributed to my success I would like to thank some of the most influential people here.

First and foremost I would like to thank my Advisor Lane Martin. His constant drive for excellence, efficiency, and dedication to his trade has shaped who I am as a researcher today. The skills that he has taught and instilled in me will be useful in all aspects of life and for this I will be forever indebted. How you advise, manage our group, and conduct research provides such an exemplary role model as to what a researcher and advisor should be, and what I will strive to achieve in the years to come.

Additionally, I would like to give a special thanks to Sergei Kalinin, Nina Balke, Stephen Jesse, Rama K. Vasudevan and Baris Okatan for their guidance and willingness to collaborate on the band-excitation-based scanning probe measurements.

I would also like to thank my committee members Professor Jim Zuo, Professor Daniel Shoemaker whose advice has been invaluable. I would also like to particularly thank Professor Paul Braun, who first introduced me to the world of material science more than 10 years ago and has been a valued mentor ever since.

I would also like to thank the various funding sources which supported the work presented in this thesis including: Department of Defense, Office of Naval Research, Department of Energy, and the Department of Materials Science and Engineering at the University of Illinois. I would also like to particularly thank Oak Ridge National Lab and the Center for Nanophase Materials for providing unbridled access to their lab and resources.

Throughout my Ph.D. I have had the privilege of working and collaborating with many exceptional staff members, graduate students, post-docs, undergrads and colleagues including: Scott, Mauro, Karthik, Vengadesh, Sungki, Brent, Eric, Anoop, Ruijuan, Zach, Justin, Liv, Gabe, Jay, Spencer, Jialan, Shishir, Ran, Sahar, James, Yeonbae, and many more.

I would also like to thank Cassie for always being there to support me, helping me find balance, providing perspective, and moving half-way across the country (in the wrong direction) to be there for me.

Finally, I owe this thesis to my family which without their unwaivering and multifaceted love and support this thesis would have never been possible.

Table of Contents

Table of Figures

List of Abbreviations

ac	Alternating current
AFM	Atomic force microscopy
BE	Band-excitation
BE-PFM	Band-excitation piezoresponse force microscopy
BE-SS	Band-excitation switching spectroscopy
DUT	Device under test
dc	Direct current
dpi	Dots per inch
DART	Dual ac resonance tracking
FeRAM	Ferroelectric Random Access Memory
GPA	Geometric phase analysis
GLD	Ginzburg-Landau Devonshire
HAADF-STEM	High angle annular dark field scanning transmission electron microscopy
HR-TEM	High resolution transmission electron microscopy
LCR	Inductance capacitance resistance
MOCVD	Metal-organic chemical vapor deposition
MBE	Molecular beam epitaxy
MPB	Morphotropic phase boundary
NBED	Nanobeam electron diffraction
PR	Photoresist
PFM	Piezoresponse force microscopy
KDP	potassium dihydrogen phosphate
PLD	Pulsed-laser deposition
RF	Radio frequency
RSM	Reciprocal space maps
rms	Root-mean-square
SHO	Simple harmonic oscillator
TEM	Transmission electron microscopy
XRD	X-ray diffraction

List of Symbols

A	Electrical, Pyroelectric – Area
A	BE-PFM – Amplitude
A_0	BE-PFM – Resonance amplitude
$a_{1\text{-}2}$	Conventional fitting – Saturation amplitude
$a_{1\text{-}6}$	Multi-transition loop fitting – Amplitude plateaus
a_3	Conventional fitting – Linear contribution
a_7	Multi-transition loop fitting – Loop tilts
a_b	Epitaxial strain –bulk in-plane lattice parameter
a_f	Epitaxial strain – Film in-plane lattice parameter
$A_{l1\text{-}3}$	Multi-transition loop fitting – Lower branch coercive bias
a_{pc}	General – Pseudocubic in-plane lattice parameter for an orthorhombic substrate
Aq_x	X-ray diffraction – Logarithmically-scaled weighted mean peak position in q_x space
Aq_y	X-ray diffraction – Logarithmically-scaled weighted mean peak position in q_y space
a_s	Epitaxial strain – Substrate in-plane lattice parameter
$A_{U1\text{-}3}$	Multi-transition loop fitting – Upper branch coercive bias
$b_{1\text{-}12}$	Multi-transition loop fitting – Loop corner curvature
$b_{1\text{-}4}$	Conventional fitting – Loop sharpness
$b_{5\text{-}6}$	Conventional fitting – Loop transition parameter
$B_{6\text{-}7}$	Conventional fitting – Transition midpoint
C	Electrical – Capacitance
c	Epitaxial strain – Out-of-plane lattice parameter
c	Piezoelectricity – Stiffness
$C_{1\text{-}6}$	Multi-transition loop fitting – Inflection point between loop corners
C_E	Electrocaloric, Pyroelectricity – Heat capacity
d	X-ray diffraction – Interplanar spacing
D	X-ray diffraction – Coherence length perpendicular to the film
$D_{1\text{-}6}$	Multi-transition loop fitting – Rate of transition between b parameters
D_{ij}	Piezoelectricity – Electrical displacement
d_{ijk}	Piezoelectricity – Piezoelectric tensor
d_{ijk}	Piezoelectricity – Piezoelectric coefficient
E	General – Electric field
E_c	Ferroelectricity – Coercive Field
$E_c^{+,-}$	Conventional fitting – Coercive bias
E_F	Flexoelectricity – Flexoelectric coefficient
$\mathrm{FOM_{EM}}$	Piezoelectricity – Electromechanical figure of merit
$\mathrm{FOM_{IR}}$	Pyroelectricity – Figure of merit infrared sensing and electron emission
$\mathrm{FOM_{PEC}}$	Pyroelectricity – Figure of merit pyroelectric energy conversion
F_R	X-ray diffraction – Fraction relaxed
F_S	X-ray diffraction – Fraction strained
g_i	NBED – Diffraction vector
g_i^{ref}	NBED – Reference spot diffraction vector
H	X-ray diffraction – Height of triangle
i	Ferroelectric – Current
I	General – Current

I	X-ray diffraction – Intensity in counts
i_{cur}	Pyroelectric – Total measurement current
i_p	Pyroelectric – Pyroelectric current
i_s	Pyroelectric – Thermally stimulated current
i_{so}	Pyroelectric – Room temperature thermally stimulated current
K	X-ray diffraction – Williamson-Hall constant
n	X-ray diffraction – Diffraction order
P	Ferroelectricity – Polarization
P_3	Epitaxial strain – Out-of-plane polarization
P_{rem}	Ferroelectricity – Remanent polarization
P_s	Ferroelectricity - Spontaneous Polarization
Q	BE-PFM – Quality factor
q_x	X-ray diffraction – In-plane reciprocal lattice vector
Q_{xx}	Epitaxial strain – Electrostrictive coefficients
q_y	X-ray diffraction – out-of-plane reciprocal lattice vector
R	NBED – Rotation matrix
Rq_x	X-ray diffraction – Relaxed peak position in q_x space
Rq_y	X-ray diffraction – Relaxed peak position in q_y space
R_x	Goldschmidt tolerance factor – atomic radius of atom X
S	General, Electrocaloric – Entropy
S_{ij}	Piezoelectricity – Strain tensor
Sq_x	X-ray diffraction – Strained peak position in q_x space
Sq_y	X-ray diffraction – Strained peak position in q_y space
S_{xx}	Epitaxial strain – Elastic compliance
T	General, Pyroelectric – Temperature
t	Goldschmidt tolerance factor - Goldschmidt tolerance factor
t	Electrical – Thickness
t	Ferroelectric, Pyroelectric – Time
T	NBED – Transformation matrix
T_0	Pyroelectric – Temperature amplitude
T_c	Ferroelectricity - Curie temperature
U	NBED- Strain matrix
V	General – Voltage
V_{ac}	BE-PFM – Applied ac sense voltage
V_{dc}	BE-PFM, Single-Loop fitting – dc voltage
$V_{Top/bot}$	Multi-transition loop fitting – Voltage of top/bottom branches
x_i	Flexoelectricity - Distance
α_{ex}	High Bias Dielectric – Extrinsic tunabilitiy
α_f	High Bias Dielectric – Frequency dependent slope
α_{in}	High Bias Dielectric – Intrinsic tunabilitiy
α_{irr}	Rayleigh – Irreversible Rayleigh coefficient
β	X-ray diffraction – Peak breadth
ε	Epitaxial strain – Strain
ε_0	General – Permittivity of free space
ε_{ex}	High Bias Dielectric – Zero-field extrinsic permittivity
ε_i	High Bias Dielectric – Permittivity intercept

ε_{ij}	General – Dielectric susceptibility
ε_{ij}	Flexoelectricity – Strain
ε_{in}	High bias dielectric – Zero-field intrinsic permittivity
$\varepsilon_{\mathrm{inh}}$	X-ray diffraction – Inhomogeneous strain
ε_{m}	Epitaxial strain – Lattice mismatch
$\varepsilon_{\mathrm{rev}}$	Rayleigh – Reversible Rayleigh coefficient
ε_{xx}	NBED – In-plane strain
ε_{xy}	NBED – Shear strain
ε_{yy}	NBED - Out-of-plane strain
η	X-ray diffraction – Percent relaxation
η_{33}	Flexoelectricity – Average intrinsic dielectric permittivity
θ	X-ray diffraction – Theta angle
θ	Pyroelectric – Phase offset
θ_{ave}	X-ray diffraction – Logarithmically-scaled weighted mean θ angle
κ_{b}	General – Boltzmann constant
λ	X-ray diffraction – Wavelength
λ_{Therm}	Pyroelectric – Trap state energy coefficient
μ_{ikjl}	Flexoelectricity – Flexoelectric coefficient
π	Pyroelectricity – Pyroelectric coefficient
σ	Piezoelectricity - Stress
φ	X-ray diffraction – Phi angle
φ	BE-PFM – Phase
ω	X-ray diffraction – Omega angle
ω	Pyroelectric – Angular frequency of oscillation
ω	BE-PFM – Frequency
ω_{ave}	X-ray diffraction – Logarithmically-scaled weighted mean ω angle
ω_0	BE-PFM – Resonance Frequency

Chapter 1

Ferroelectricity: Materials, Structures and Properties

In this chapter, we provide a review of the history and basic concepts of ferroelectricity providing a general overview of the practical importance of these materials. We then briefly discuss the symmetry requirements and fundamental origins of ferroelectricity in bulk materials. This is followed by a discussion of the basic nature of ferroelectric response and the various electrical, mechanical and thermal susceptibilities which these materials exhibit. Armed with this knowledge, we explore the various routes that have been commonly employed to tune these materials, highlighting the effects of chemical pressure and epitaxial strain which are used extensively throughout this thesis. This naturally leads to a discussion of techniques used to fabricate, and the current capabilities and limitations of thin-film epitaxy. Finally, we discuss the basic implications of epitaxial strain and strain gradients on the crystal and domain structure, and ultimately the dielectric, ferroelectric, and pyroelectric responses of ferroelectric materials. The chapter concludes with a summary of the organization of the remainder of the thesis.

1.1 Introduction to Ferroelectrics

The observance of unique electromechanical responses including piezoelectric response[1, 2] and anomalous dielectric response[3] in Rochelle salts in the late 1800's, sparked mankind's interest in ferroic materials. Based on the early work on piezoelectricity, Peter Debye proposed that "certain interesting classes of molecules can carry a permanent electric dipole moment" analogous to a ferromagnet.[4] This theory eventually lead to the development of a critical temperature analogous to the so-called Curie Temperature (T_c) in magnets, explaining the observed anomalous dielectric response in these materials.[4] This strong perceived analogy between magnets and the nature of the electrical moment observed in Rochelle salt led Schördinger to coin a term "ferroelektrish" or ferroelectric for these materials,[5] choosing to emphasize this analogy (through the inclusion of the prefix ferro- meaning iron) despite Rochelle salt (and most ferroelectric known to date) being free of iron. Even though coining the term ferroelectricity, these early experiment never actually proved ferroelectricity instead they only showed: 1) That a spontaneous polarization exists, 2) that this spontaneous polarization is temperature dependent (i.e., pyroelectric), going to zero at the T_c, 3) that this transition at the T_c results in a dielectric anomaly, and 4) that the strain and the electrical polarization are linearly coupled (i.e., piezoelectric).

The near stagnate early development of ferroelectric materials changed drastically following World War I, once it was realized that these materials had the potential to dramatically outperform quartz as piezoelectric transducers for underwater submarine detection. In turn, immediately following World War I, many seminal works on ferroelectricity were published. This work included the first studies which unequivocally proved ferroelectricity by demonstrating ferroelectric hysteresis with switchable polarization that is stable under zero bias, in Rochelle salt.[6-8] Even with this interest in ferroelectricity, both practically and scientifically, it was not until the 1935 that a second ferroelectric material potassium dihydrogen phosphate (KDP) was discovered.[9, 10] In actual devices, however, ferroelectricity was mostly a scientific curiosity as both Rochelle salt and KDP are hygroscopic and water soluble limiting their implementation. The major turning point came in the 1940 with the discovery of ferroelectricity in $BaTiO_3$, a robust, stable ceramic material with a relatively simple perovskite structure.[11] This discovery of a perovskite ferroelectric naturally motivated the examination and study of other perovskite compounds leading to the discovery of a wide variety of perovskite ferroelectrics with a range of useful properties.[12-15] To date, these developments in

ferroelectrics and in particular perovskite ferroelectric have been implemented in a many functional devices including: ultrasonic transducers,[16] highly-tunable dielectrics,[17, 18] piezoelectric actuators,[19-21] positive temperature coefficient resistors,[22, 23] *etc.*,. Looking forward the future for ferroelectrics is bright. Integration of these materials into functional devices has started, and likely will continue to follow trends set by the semiconductor industry seeking routes to create miniaturized functional devices for pyroelectric[24-27] and piezoelectric sensors/energy harvesters,[28-32] surface acoustic wave devices,[33-35] micro actuators,[28, 36, 37] logic devices,[38-41] and non-volatile random access memory,[42-44] and among others. In this regard, there is a significant need and interest to understand how to manipulate and control the structure, properties, and modes of response in these materials.

1.2 Crystal Structure and Classes

For ferroelectricity to exist it is a prerequisite that it belongs to the ferroelectric crystal class of materials. Of the 32 crystal classes that exist, 11 of these crystal classes have a center of symmetry (Figure 1.1a). Of the remaining 21 crystal classes, all but one possesses a polar axis and therefore are piezoelectric (Figure 1.1b). Piezoelectricity is characterized by two analogous effects. The direct piezoelectric effect which is the linear coupling of a stress to the polarization and the converse piezoelectric effect which is the linear coupling of an applied field to the strain (Figure 1.1c). Of the class of piezoelectric materials only a very small subset of these materials exhibit piezoelectric responses of measurable magnitudes.[45] Of these 20 remaining crystal classes, only 10 of these crystal classes have a unique polar axis meaning they have the necessary conditions to be pyroelectric; and therefore, if they have a spontaneous polarization along a unique polar axes they will exhibit temperature dependent changes in the spontaneous polarization (Figure 1.1d). Finally, within the pyroelectric crystal class a small subset of these materials have an energy landscape with two (or more) symmetric and stable spontaneous polarization states below the T_c, which can be switched between these two states by the application of an electric field and therefore are ferroelectric (Figure 1.1e).

1.3 Origins of Ferroelectricity

From a phenomenological perspective ferroelectricity occurs when two key requirements are met. First, the material must undergo a structural distortion from the prototypical paraelectric phase (in perovskites the cubic phase) at T_c. Secondly, there must exist two or more equivalent

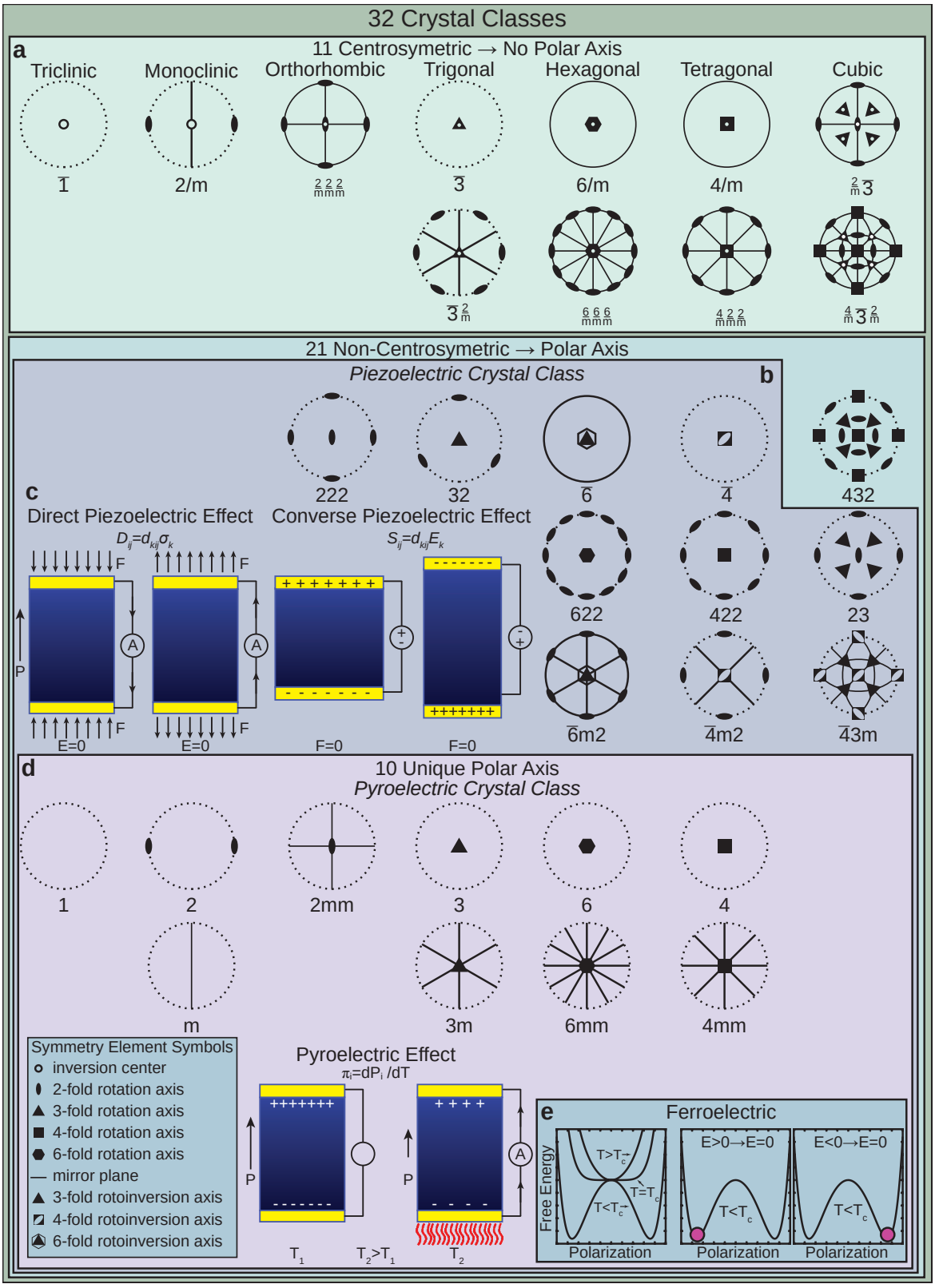

Figure 1.1. Diagram showing materials hierarchy of the crystallographic classes. Diagram indicates the crystallographic classes whose symmetry can permit piezoelectricity, pyroelectricity and ferroelectricity. Included in this figure are schematic diagrams indicating the basic modes of response for the direct and converse piezoelectric effects and pyroelectricity.

structural distortions which the material can be switched between by the application of an electric field. These ferroelectric distortions are accompanied by a spontaneous strain (at the unit cell level) which generates charge asymmetry typically discussed of in terms of a spontaneous polarization (P_s).

Perovskite ferroelectrics of the form ABX_3 can be represented structurally by 8 corner sharing *A*-site cations with six, face-sharing oxygen atoms and a central *B*-site cation inside an oxygen octahedron (Figure 1.2a). When the material is above its T_c the structure is cubic (Figure 2a); however, upon transitioning through the T_c the material undergoes a distortion producing a spontaneous polarization (Figure 1.2b). Here, we show a representative tetragonal distortion where the *B*-site cation displaces within the oxygen octahedra towards one of the oxygen atoms, producing a

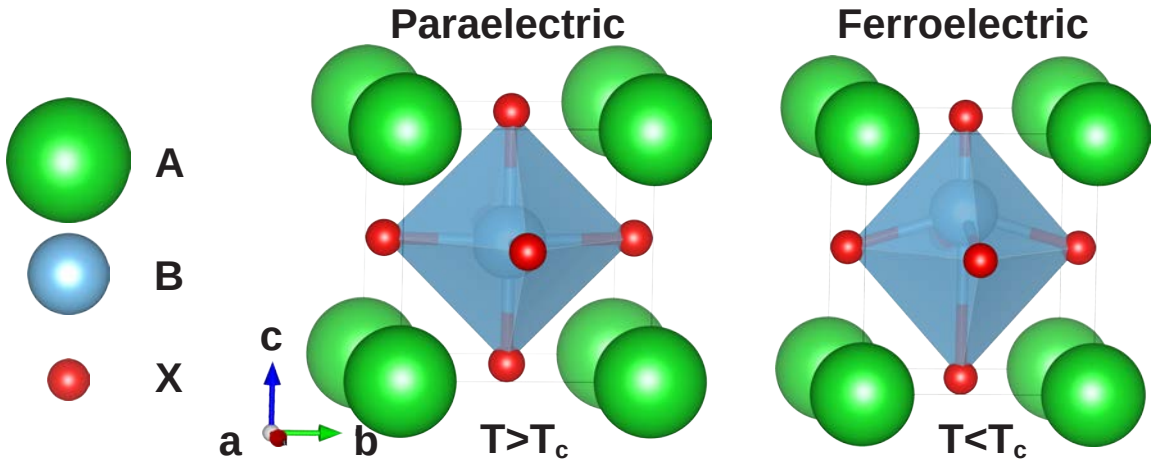

Figure 1.2. Schematic drawing of the (a) perovskite cubic parent phase above the Curie temperature. (b) Perovskite unit-cell exhibiting a typically tetragonal distortion occurring below the Curie temperature.

tetragonal distortion in the unit cell. This is just an example of one type of ferroelectric distortion and many other distortions are possible. The perovskite structure is extremely flexible enabling the inclusion of a wide variety of *A*- and *B*- site cations with various valence states (*i.e.*, $A^{+1}B^{+5}O_3$, $A^{+2}B^{+4}O_3$ and $A^{+3}B^{+3}O_3$) and defect chemistries of up to a few percent.[14] To highlight this flexibility we include a periodic table illustrating the elements which can be incorporated into the perovskite structure and which sites these elements can occupy (Figure 1.3).

Considering the atomic structure (under a hard atomic sphere model) all perovskite structures are centrosymmetric and therefore are incompatible with ferroelectricity. To explain this seeming contradiction requires the consideration of the atomic orbitals and their associated interactions. While nearly every element of the periodic table can be included in the perovskite structure only a very select few exhibit ferroelectricity. To begin with the perovskite phase is susceptible

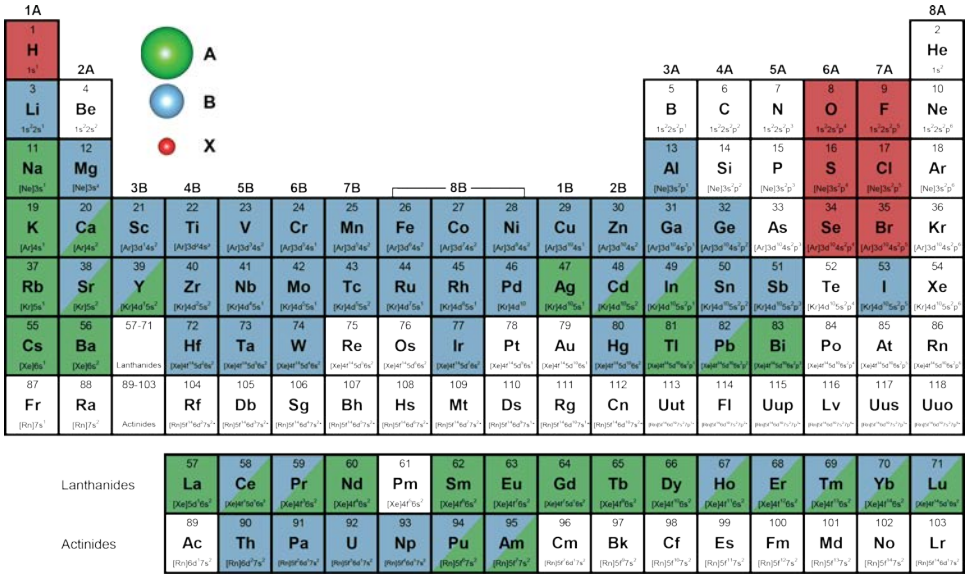

Figure 1.3. Periodic table showing the elements which can be incorporated into the perovskite structure and the various sites which they can be located within the structure.

to octahedral rotations depending on the atomic radius of the *A*- and *B*- site cations. The resulting structure (including these octahedral rotations) can be predicted by calculating the Goldschmidt tolerance factor (equation 1.1) where R_o, R_a and R_b are the atomic radius of the oxygen, *A*-site and *B*-site cations respectively.[46]

$$t = \frac{R_0 + R_a}{\sqrt{2}\left(R_0 + R_b\right)} \tag{1.1}$$

Based on the calculation of the tolerance factor, if $t > 1$ the structure is hexagonal, if $0.9 < t < 1$ the structure is cubic or tetragonal, and if $0.7 < t < 0.9$ the structure undergoes octahedral rotations and is rhombohedral. While in some systems these octahedral rotations can give rise to ferroelectricity; in general, the weak coordination environment of the *A*-site cation in low tolerance factors perovskites results in *A*-site distortions which suppress ferroelectricity.[47] Hence, most perovskites with low tolerance factors are not ferroelectric or are weakly ferroelectric.

A second stronger form of ferroelectric distortions can occur as the result of a symmetry breaking distortion of the *B*-site cation within the oxygen octahedra. *B*-site driven ferroelectricity results from an effect known as the second order Jahn-Teller effect which occurs when mixing between the *d* orbitals of the *B*-site cation and oxygen 2*p* orbitals is geometrically allowed and results in the mixing of a non-degenerate ground state with a low lying excited state.[48-50] This mixing of the atomic orbitals generates a distortion in the position of the *B*-site cation, ultimately giving rise to ferroelectricity. Hence, because of these spatial and orbital requirements *B*-site driven

ferroelectricity exists nearly exclusively in perovskites which have *B*-site cations with d^0 formal charge, as the *d*-orbitals can readily mix with the oxygen 2*p* orbitals and the empty *d* shell results in a smaller atomic radius, minimizing coulombic repulsion as the *B*-site cation moves around within the oxygen octahedron. $BaTiO_3$ is the prototypical example of *B*-site driven ferroelectricity as the Ti 3*d* orbital hybridizes with the O 2*p* orbital while the Ba 5*p* orbital remains stereochemically inactive.[51] While $BaTiO_3$ is ferroelectric, it is only weakly ferroelectric having a T_c of ~120°C.[52] On the other hand, $PbZr_{1-x}Ti_xO_3$ is a more robust ferroelectric with T_c ranging between 235-490°C depending on the Zr:Ti ratio.[53] This difference is the result of a secondary, and typically stronger *A*-site driven ferroelectric distortion,[51, 54] where the Pb 6*s* orbital lone-pair electrons become localized by hybridizing with the O 2*p* orbitals, increasing the tetragonality of the unit cell and in turn, the distortion of the *B*-site cation. This unusually robust ferroelectricity observed in $PbZr_{1-x}Ti_xO_3$ as a result of the contribution from the Pb 6*s* lone pair electrons is one of the contributing factors that has made $PbZr_{1-x}Ti_xO_3$ one of the most widely studied prototypical ferroelectric systems.

1.4 Ferroelectric Switching

Since the ferroelectric distortion which produces ferroelectricity can exist in two, or more, equivalent states the energy landscape can be viewed as a multi-well potential which can be switched between states by application of an electric field. Experimentally proving ferroelectricity typically involves measuring a ferroelectric hysteresis loop (*i.e.,* the polarization vs. electric field), providing insight into the switching process. Starting with a material, in its idealized equilibrium state with zero net macroscopic polarization (Figure 1.4a) application of positive bias (to the bottom electrode) results in switching to the up-poled saturation state (as long as the applied bias surpasses the coercive field (E_c), defined as the field upon which 50% of the film has switched polarization states (Figure 1.4b). Upon removing the bias a constant non-zero spontaneous polarization remains which is called the remanent polarization (P_{rem}, Figure 1.4c).

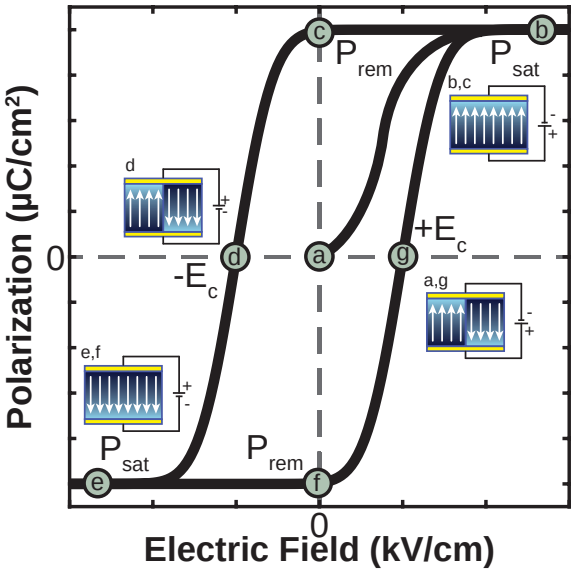

Figure 1.4. Representative polarization electric field ferroelectric hysteresis loop indicating the location of the coercive fields (E_c), remanent polarization (P_{rem}) and saturation polarization (P_{sat}). Included in this image are schematic drawings indicating the polarization at each stage during the switching process.

Moving around to loop in the counter-clockwise direction, the application of negative bias (once again to the bottom electrode) results in ferroelectric switching to the down-poled state, so long as the applied bias surpasses the negative coercive field (Figure 1.4d). As the magnitude of the negative bias increases the polarization again saturates to its saturation polarization (P_{sat}, Figure 1.4e). This processes of using an electric field to switch the direction of spontaneous polarization is called "ferroelectric switching". From this final, down-poled state, ferroelectric switching to the up-poled state occurs in an identical manner but with opposite sense (Figure 1.4e-f-a). Since ferroelectric materials can intrinsically exist in two identical but distinguishable states, these states can be used to store information, and in turn, these materials have been used as active materials in ferroelectric random access memories (FeRAM) where data bits are stored in the form of a polarization direction in ferroelectric capacitors.[42, 55] In this regard, there has been dedicated effort to produce materials with enhanced P_{rem} and reduced E_c to facilitate the read/write steps in these devices while reducing power consumption.[42, 55]

1.5 Ferroelectric Susceptibilities

In addition to ferroelectric switching the spontaneous polarization can be perturbed by electric fields, stress, and temperature giving rise to electromechanical and thermal susceptibilities which result from a change in the polarization, strain, and/or entropy. In turn, ferroelectric materials can have large dielectric, thermoelastic, electromechanical and thermoelectric responses not possible, or much larger than observed in other classes of materials. Understanding of the various susceptibilities in ferroelectrics can be aided by representing the susceptibility to field, stress and temperature graphically (Figure 1.5a).[56] Using this diagram it is easy to describe, for instance, the well-known piezoelectric effect (*i.e.,* the linear coupling of a strain to a polarization). In addition, this diagram also reveals some less commonly discussed susceptibilities such as the electrocaloric effect which describes the coupling between an electric field and entropy.[57-60] All told, what is important to take away from this diagram is that the highly-coupled susceptibilities in ferroelectric materials allow for the conversion of a material response to field, temperature or stress to a measurable response or to perform a function involving a change in polarization, strain or entropy. These large susceptibilities are the primary reason for the overwhelming interest in these materials for a range of applications.

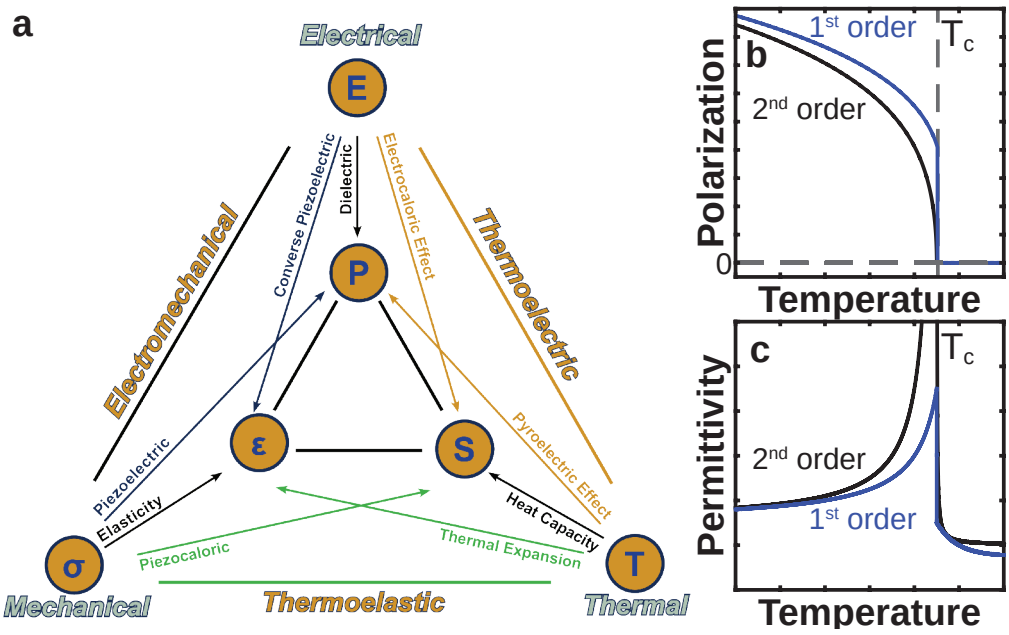

Figure 1.5. (a) Diagram indicating the various susceptibilities of ferroelectric materials. Schematic plots of (b) polarization and (c) dielectric permittivity evolution with temperature for ferroelectric exhibiting 1st and 2nd order transitions.

Since these ferroelectric susceptibilities are primarily attributed to changes in the polarization, the susceptibility of a material tends to be maximized at structural instabilities (such as at the T_c and/or near structural and chemical phase boundaries), where large changes in the polarization can be easily driven (Figure 1.5b). For example, if we consider the dielectric susceptibility $\left(\varepsilon_{ij} = \frac{\partial P}{\partial E}\right)$ the permittivity is maximized at the T_c (Figure 1.5c). In this light, much of the research interests in engineering ferroelectric materials has focused on designing ferroelectric materials with structures, composition, or phases near structural or thermal phase boundaries such that electrical, mechanical, and/or thermal perturbations can drive structural transformations to generate large responses.

1.6 Bulk Ferroelectrics

Historically, the study of ferroelectric materials has mainly focused on bulk, sintered ceramic materials with dimensions typically on the order of millimeters. Bulk ferroelectric materials are generally polycrystalline with grain sizes on the order of 1-10 μm. While many functional devices have been developed and designed based on polycrystalline ferroelectric their polycrystalline nature pose significant challenges for modern devices where the design constraints on magnitude, specificity, and consistency of the responses is paramount. For example, polycrystalline ferroelectrics typically require frequent poling to maintain a primary orientation of the domains, the

presence of grain boundaries can adversely affect ferroelectric properties, the large dimensionality requires that massive external voltages (> 1kV) are needed to surpass the coercive field, and their size is prohibitive for use as functional elements in microelectronic devices.[61] Similarly, from a fundamental research perspective it is also challenging to understand the physics of the responses in macroscopic polycrystalline ferroelectrics as: 1) the response of the grain boundaries can contribute or even dominate the observed response and 2) it is difficult to accurately define the orientation of the polarization making it difficult to deconvolute the field- and polarization- direction dependence of the response. While single crystal of ferroelectric materials have been fabricated they are difficult to grow as it is exceedingly challenging to control the orientation, avoid forming voids, and chemical defects in materials with such complex and adaptable chemistries.[62]

1.7 Ferroelectric Thin Films

By constraining one of the dimensions of bulk ferroelectrics to form a thin film (thickness <1000 μm) it is possible to create a convenient form factor to control the structure and properties of ferroelectrics to a degree not achievable in the bulk. Ferroelectric thin films have many advantages compared to their bulk counterparts: 1) it is fairly easy to achieve a strong degree of texturing (preferred grain orientation), 2) voltages to reach the coercive fields are intrinsically lower, and 3) these materials can be readily integrated into microelectronic devices. In addition to textured polycrystalline thin films, it is also possible to grow ferroelectric thin films epitaxially on closely lattice matched substrates. Epitaxy not only enables the precise control of crystallographic orientation, but also provides a flexible route (in addition to chemical pressure) to strain materials to a degree significantly larger than is possible in the bulk. For instance bulk ceramics fail structurally under modest strains (typically <0.1% both compressive and tensile),[63] well before interesting structural changes have occurred. While on the contrary, in thin films large strains of ±3% are commonly achievable with massive strains of 6% being reported in $BiFeO_3$ on $YAlO_3$ (110).[64-66] These large strains are capable of causing significant changes to the film on the unit-cell level (in terms of crystal structure), and in the nanoscale and mesoscale domain structures. In turn, thin-film versions of ferroelectric materials (and in particular those grown epitaxially) represent a convenient platform, upon which an expansive range of model systems can be grown, controllably oriented, strained, and probed to discover new physics difficult to access in the bulk.

1.8 Growth of Ferroelectric Thin Films

The growth of high quality films (in terms of composition, epitaxy, *etc.*) requires that the ferroelectric be deposited in a thermodynamic and kinetically controlled environment. This has been successfully achieved using a wide variety of deposition techniques including sol-gel,[67, 68] sputtering,[69-71] metal-organic chemical vapor deposition (MOCVD),[61, 72, 73] molecular beam epitaxy (MBE)[74-76] and pulsed-laser deposition (PLD).[77-79] Although all of these deposition techniques have their advantages and drawbacks here we focus solely on PLD as it was the growth technique used for all films studied in this work.

Conceptually, PLD is a very simple. The basic infrastructure consists of a laser (in our case 248 nm) which is fired at a target (typically set to rotate and raster) inside a vacuum chamber (commonly in a slightly oxidizing atmosphere). The basic PLD setup is shown (Figure 1.6a). The fluence (energy/area) of the laser spot can be easily controlled by changing the power input to the laser or by changing the external focusing optics. In PLD the fluence (usually between 1-5 J/cm^2) is typically well above the ablation threshold; therefore, as long as the material absorbs the laser energy a small amount of material is ejected from the target, forming a plasma plume. Since the ablation process occurs inside a vacuum system at low pressure (1-500 mTorr) this plasma plume is forward-accelerated towards the substrate, being physically deposited on the surface of a heated substrate. PLD provides many easily tunable parameters which can be used to control the growth process including: laser fluence, spot size, frequency, chamber pressure, temperature, *etc.*,. PLD has some key advantages compared to other deposition techniques, of which, the most important are: 1) thin films of complex stoichiometry can be produced (as long as the right deposition conditions

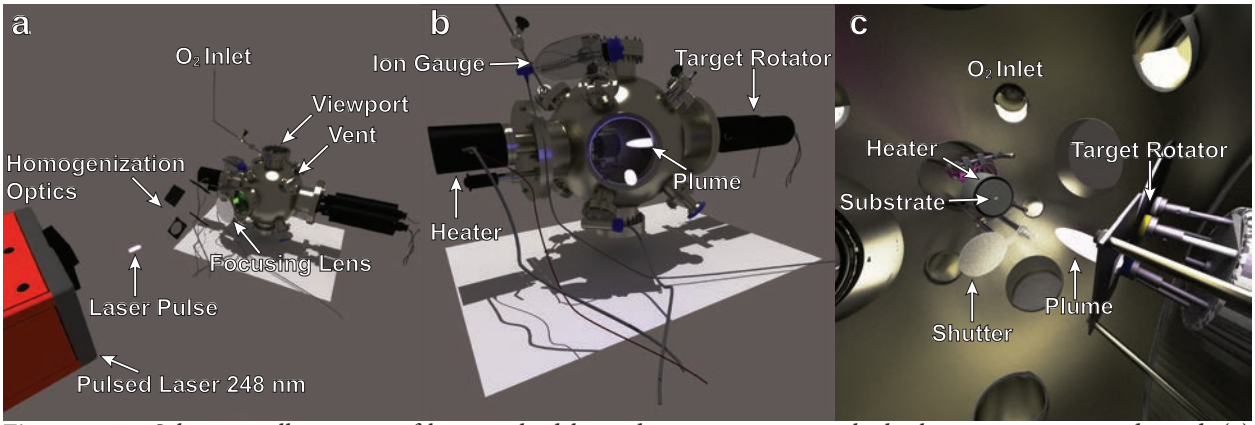

Figure 1.6. Schematic illustration of basic pulsed laser deposition setup with the key components indicated. (a) highlights the laser and optics setup. (b) shows the key functional components on the vacuum chamber and (c) Shows the heater, targets rotator and substrate (mounted on the heater) during a deposition.

are chosen) from targets of similar stoichiometry, 2) the ions deposited during the growth are highly energetic (orders of magnitude higher than thermally deposited species) allowing sufficient surface mobility for the adatoms to diffuse along the surface, and 3) growth kinetics can easily be easily controlled by changes to chamber pressure, laser fluence, frequency, *etc.*,. While PLD is limited in its ability to deposit over large areas and with high throughput necessary for commercial implementation, at a research level PLD provides the most flexible platform to grow high quality (in terms of crystal structure, chemical composition, and epitaxy) ferroelectric thin films with unit-cell level control. More details of the history, mechanisms and growth modes of PLD are provided in Appendix A.

1.9 Strain Engineering in Ferroelectric Thin Films

While chemistry is the most common method to control material properties, when growing epitaxial thin films of ferroelectrics researchers have an additional strain knob to turn that provides further control over the structure and properties of these materials. In such work, careful care needs to be taken in designing heterostructures. Strain engineering cannot persist to limitless bounds, and when the magnitude of the strain (or lattice mismatch) is too large, materials seek routes such as defect,[80] dislocations and domain formation[81-84] to accommodate or relax the strain. Fortunately, this interest has motivated the development and commercialization of a vast array of isostructural perovskite substrates (primarily made using either floating zone growth or Czochralski method) with reasonable quality and having a wide range of suitable lattice parameters capable of imposing various degrees of epitaxial strain (Figure 1.7, bottom panel).[85-95] Typically, to fully utilize these materials in devices requires a bottom electrode which is lattice matched to the film/substrate. To meet these requirements, a range of conductive perovskite-based electrode materials have been developed and employed in epitaxial heterostructures (Figure 1.7, middle panel). Comparing the lattice parameters of the available substrates and bottom electrodes[96, 97] to a selected subset of known ferroelectric materials (Figure 1.7, top panel), [98-110] there are many suitable substrates and electrode materials to provided flexibility in designing heterostructures; however, there are some problem areas. Particularly, there are a limited number of suitable substrate and electrode materials with lattice parameters between 4.05-4.2Å. The scarcity of materials within this range is not a fundamental limit, but rather a limitation of availability and demand.

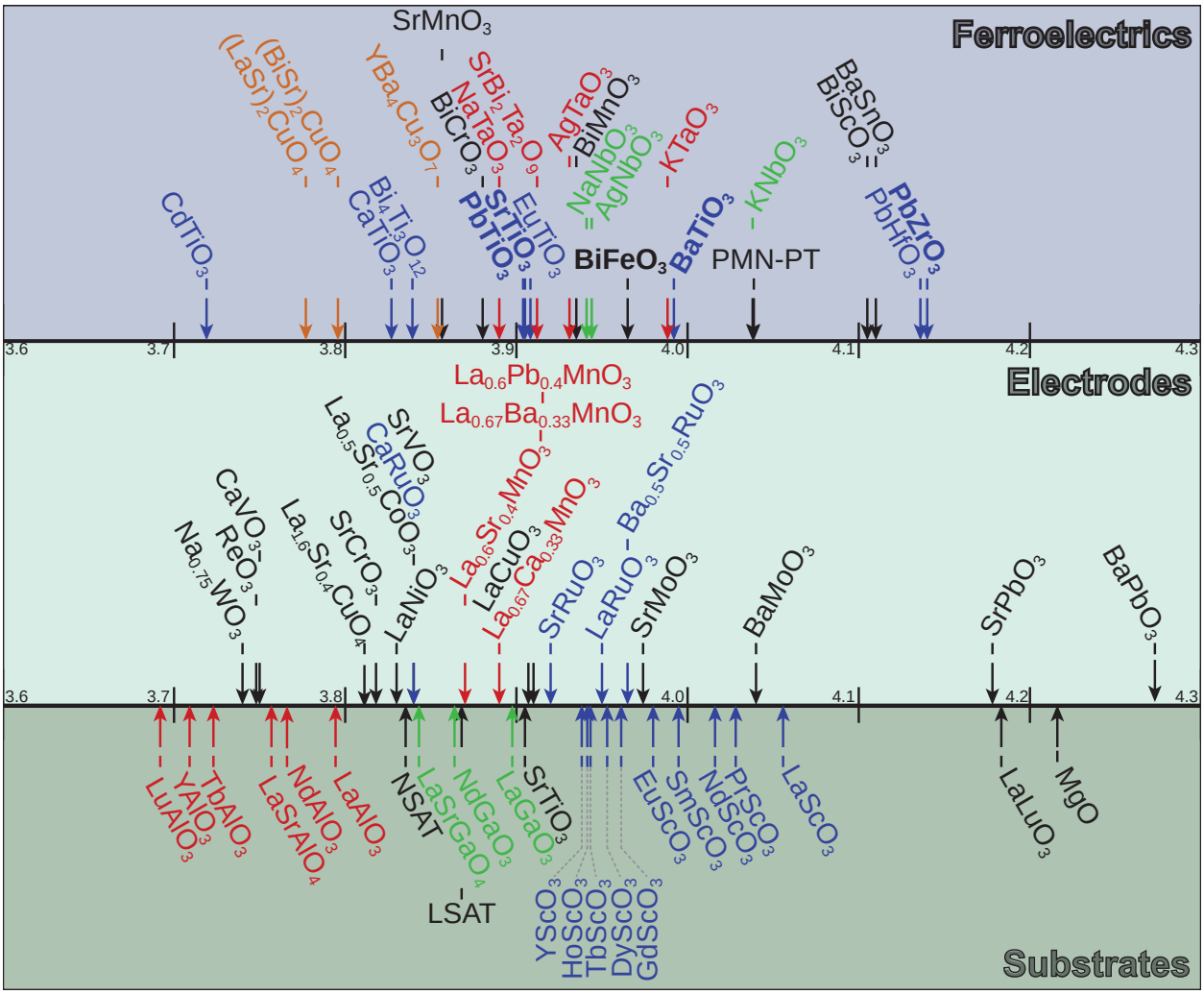

Figure 1.7. Figure indicating the lattice parameters of commercially available substrate materials (bottom section), a select list of perovskite electrode materials and ferroelectric, incipient ferroelectrics and anti-ferroelectric materials.

When it is possible to find a suitable substrate and/or electrode strain tuning of ferroelectric thin films can produce structures and properties vastly different from what is observed in the bulk. For instance, it has been shown that epitaxial strain can be used: to shift the T_c of $BaTiO_3$ by more than 500°C and increase the remanent polarization by 250%[111] (similar results have been observed in other systems),[112-115] induce ferroelectricity in $SrTiO_3$ (which is typically paraelectric),[116] produce new phases[115, 117-119] and phase competition,[64, 120] modify ferroelectric domain structures,[81-83, 121-130] and generate new forms of polar order in ferroelectrics.[131-142] While the successes of strain engineering of ferroelectric thin films have been great, we have only scratched the surface of what is possible. In this regard, recently, there has been dedicated efforts to invent new forms of strain engineering through the use of: thermal mismatch strain effects,[143-146] anisotropic strain,[147-149] controlled defect engineering,[80, 150-157] orientation control,[158-162] superlattice structures,[131-137, 141, 142, 163

strain gradient,[151, 152, 164-173] and many more. These new forms of strain engineering are exciting as they expand the capabilities and possibilities of structures and properties which can be achieved in ferroelectric materials.

1.10 Domain Formation in Ferroelectric Thin Films

When ferroelectrics undergo a transition from the paraelectric to ferroelectric state they seek routes to minimize the sum of the electrostatic and elastic energies. While it is possible to form a material with a single polarization direction (monodomain, Figure 1.8a) under the right conditions films break down into domains to minimize the sum of the various energies (primarily the electrostatic, elastic, and domain wall energies). For simplicity if we consider a Ti-rich variant in the $PbZr_{1-x}Ti_xO_3$ family $PbZr_{0.2}Ti_{0.8}O_3$, with lattice constants $a = b = 3.94$ Å and $c = 4.12$ Å the polar axis can exist in two degenerate states along one of three directions (*i.e.* [100], [010], or [001]) when grown epitaxial on (00*l*)-oriented substrates, and forms fractions of each of these domain variants to minimize the energy.

First, considering the electrostatic energy, if the ferroelectric thin film is grown on a closely lattice matched insulating substrate without a bottom electrode there exists strong depolarization fields which drives the formation of anti-parallel, out-of-plane oriented c^+ and c^- domains, in an attempt to minimize the depolarization fields/energies (Figure 1.8b). The boundary between neighboring domains is typically described by the angular difference of the polarization direction on adjacent sides of the domain wall which, in the case of anti-polar domains, is 180°. Therefore these domain wall are called 180° domain walls. Since the origin of these domains is purely electrostatic in nature, 180° domain walls are typically referred to as ferroelectric domains walls. In many cases ferroelectric thin films are grown on top of bottom electrodes which can easily screen the depolarization fields. Therefore, when ferroelectrics are grown with bottom electrodes the polarization can

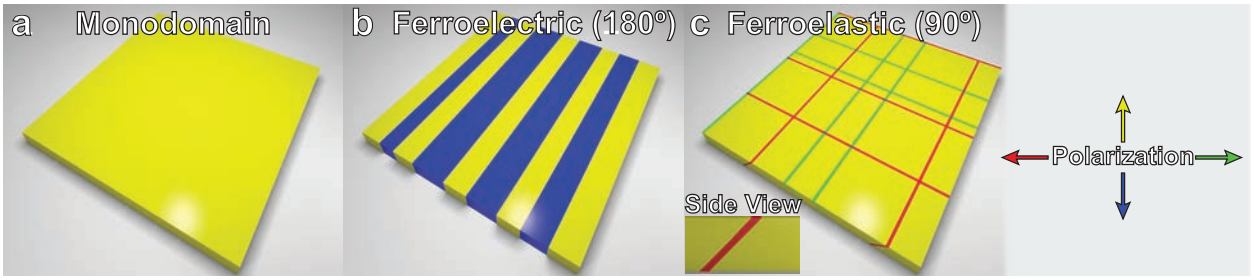

Figure 1.8. Schematic of common ferroelastic domain structures (a) a monodomain structure where the polarization points in a single direction. (b) ferroelectric 180° domain walls where the polarization between domains points anti-parallel to one another. (c) ferroelastic 90° domain walls where the polarization points perpendicular to one another. Inset shows side view of the domain structure. The Polarization direction is indicated by the color of the region.

have a preferred orientation and 180° domains walls are typically not observed.

In addition to electrostatic driving forces for domain formation, the elastic boundary conditions can significantly influence the domain structure. In the presence of substrate imposed epitaxial strain 90° domain walls consisting of a boundary between an out-of-plane oriented *c* domains and in-plane oriented *a* domain can form (Figure 1.8c). Since the origins of these domains are elastic in nature they are typically referred to as ferroelastic domain. When these domains form they must conform to the constraints imposed by the electrical boundary conditions. Therefore, these walls must form at 45° angle (in reference to the *c* domain polar axis) along the {101} family of planes. The polarization must also be oriented such that the polarization directions do not point towards (or away) from each other (*i.e.,* head-to-head or tail-to-tail), in order to avoid forming a charged domain wall. Since these domains form to accommodate the elastic strain energy their presence and density is highly dependent on the substrate imposed biaxial strain. For instance, returning to $PbZr_{0.2}Ti_{0.8}O_3$ as an example, under compressive strain there is minimal to no driving force for ferroelastic domain formation, as the average in-plane lattice parameters is universally smaller than the in-plane lattice parameter of the parent phase. In turn, this strain condition favors forming a monodomain structure with a single polarization direction (excluding electrostatic effects). In the case of tensile strain, however, the average in-plane lattice parameter of the film is larger than the in-plane lattice parameter of the parent phase and, therefore, the film can reduce the overall elastic energy by forming some fraction of in-plane oriented *a* domains (as long as the reduction in elastic energy is greater than the domain wall energy typically ~35 mJ/m^2 in $PbTiO_3$).[174] The scenario mentioned above is just an example and in actuality ferroelastic domain formation has been shown to depend on a wide variety of factors including: the epitaxial strain, film composition, film thickness, cooling rate, thermal expansion mismatch, *etc.*.

To complement experimental work there has been considerable studies focusing on developing phenomenological models based on Ginzburg-Landau-Devonshire (GLD) theory of ferroelectricity which are capable of accurately predicting the strain-evolution of domain structures.[175-180] Guided by these theories and understanding of the forces driving domain formation researchers have the ability to produce a wide variety of domain structures with fecundity including: *c/a/c/a* domain structures in tetragonal ferroelectric,[82, 181, 182] 180°, 71°, and 109° domains rhombohedral ferroelectrics,[183, 184] nanodomain structures near morphotropic phase boundaries,[128, 185, 186]

mixed-phase domain structures,[64, 119, 187, 188] and many more, with the occasional possibility of inventing a new domain structure.

Ferroelastic domains have a profound effect on the switchable polarization and the ferroelectric susceptibilities. Understanding the effect on the switchable polarization is rather simple. Considering, for instance, a *c*/*a*/*c*/*a* domain structure, as the density of in-plane oriented *a* domains increases the switchable out-of-plane polarization (defined by the density of out-of-plane polarized *c* domains) correspondingly decreases. On the other hand, understanding the effect of the domain structure on ferroelectric susceptibility is much more complex. Typically, when a perturbation (electrical, mechanical, thermal) is applied to a material not only does the magnitude of the polarization in both the *c* and *a* domains change but also the fraction of the domain variants changes. This change in the density of the domain variants causes movement of the domain walls. While it has been known for a long time that 180° domain walls can be moved easily and should significantly enhance both piezoelectric and dielectric susceptibilities,[189-191] ferroelastic 90° domain walls in thin films were only thought to contribute to the piezoelectric susceptibilities.[192, 193] Recently, however, it has been proven that the reversible motion of 90° ferroelastic domain walls can provide a significant extrinsic contribution (up to 50% of the total response) to the dielectric and pyroelectric response.[125, 194] This discovery changed how we perceive the influence of ferroelastic domain wall contributions to ferroelectric susceptibilities. A large majority of this thesis will focus on the influences of various types of ferroelastic domains on the susceptibilities and modes of response in ferroelectric thin films.

1.11 Strain Gradients in Ferroelectrics

Typically when straining ferroelectrics thin films it is assumed (primarily for simplicity) that strain manifests in a uniform manner, however, in actually epitaxial strain commonly seeks routes to relax strain. While initially such strain relaxation might seem detrimental to the materials properties the strain gradients can be large (commonly on the order of 10^5 m^{-1}), and researchers have looked to leverage the ability to deterministically create inhomogeneous strains to gain further control of materials.[151, 152, 172, 195-197] The presence of strain gradients are particularly interesting in ferroelectrics because of the potential for strong so-called flexoelectric effects.[198] Flexoelectricity refers to the linear coupling of a strain gradient $\left(\partial\varepsilon_{ij}/\partial x_k\right)$ and the polarization (P_i) of a material,

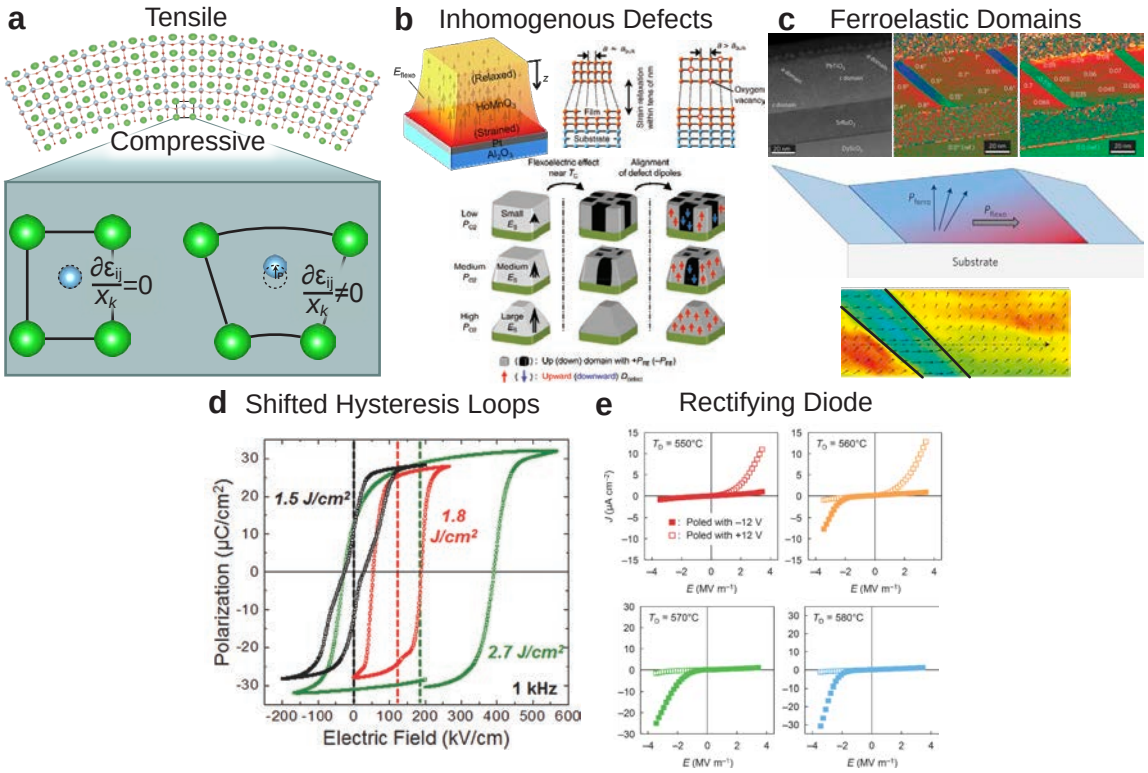

Figure 1.9. (a) Schematic illustration indicating fundamental principles of flexoelectricity (images made using VESTA). (b) Illustration of methodologies of generating strain gradients through controlled defects. Top shows a diagram indicating strain relaxation caused by the lack of oxygen vacancies in $HoMnO_3$. Bottom, indicates how growth pressure can be used to tune the magnitude of strain relaxation and flexoelectric effects (c) Top HAADF-STEM imaging and geometric phase analysis of a typical ferroelastic c/a/c/a domain structure in $PbTiO_3$. Middle schematic drawing indicating the flexoelectric polarization and its influence on the rotation of the polarization direction. Bottom Out-of-plane strain (color) and polarization maps (vectors) near a ferroelastic domains observing a difference in polarization rotation between the acute and obtuse corners caused by flexoelectric effects. (d) Ferroelectric hysteresis loops in $BaTiO_3$ grown with controlled defect densities by modulating the laser fluence. Hysteresis loops show large horizontal shifts (particularly when grown at high laser fluence) due to flexoelectric effects. (e) Growth temperature dependent non-switchable and switchable rectifying diode behavior in $BeFeO_3$.

mediated by the fourth-rank flexoelectric tensor (μ_{ikjl}). The fourth-rank nature of the flexoelectric tensor necessitates that it exists in all classes of materials regardless of symmetry. Flexoelectricity can be imagined by considering the convex bending of a thin film causing the top of the film to be under tension while the bottom side is under compression, thereby generating a strain gradient (Figure 1.9a). Upon bending the *B*-site cation (whose distortion defines the polarization) moves within the unit-cell like a pea in a pea pod, generating a polarization in centrosymmetric materials, or modifying the polarization in ferroelectric materials. These flexoelectric effects (or effects that mimic those arising from flexoelectricity) can alter the ferroic response of materials,[166, 167] allow for mechanically-induced ferroelectric switching,[43, 199, 200] drive horizontal shifts of ferroelectric hysteresis loops,[172, 173, 195, 201, 202] and allow for independent tuning of typically coupled ferroelectric suscep-

tibilities.[195, 196]

At first pass, one might assume that flexoelectricity could be easily studied by applying an external inhomogeneous strain to a material, and initially, researchers took this approach.[43, 203-211] While capable of determining a value of the flexoelectric coefficient these experiments were imprecise, with even the best experimental designs having limited control and ability to measure the strain and electric field gradients necessary to accurately predict flexoelectric effects.[205, 206] As a results, these measurements commonly resulted in values for flexoelectric coefficients which varied by more than an order of magnitude between measurements.[210, 211] Further complicating this discussion, experimentally measured values for flexoelectric coefficients are typically orders of magnitude larger[204, 212-214] than theoretically predicted values.[212, 215, 216] While there has been many hypotheses as to the origin of this discrepancy including: polar clusters/nanoregions,[217-220] inhomogenously distributed electronic/ionic defects,[221, 222] polarization gradients (in the presence of screening charges which minimize depolarization fields),[171] surface piezoelectricity,[167, 223, 224] dynamic piezoelectricity,[225-228] and other forms of macroscopic symmetry breaking,[229] there is still no way to truly reconcile this discrepancy.[216, 230]

Once again, constraining one of the bulk dimension (forming a thin film) provides a convenient platform to probe these flexoelectric effects. For instance, crystallographic orientation can be easily define by the nature of the epitaxy and it is possible to generate large strains gradients that would cause even the strongest of bulk materials to fail; however, the challenge comes in devising routes to-, and ways to measure the strain gradient in these materials. To engineer strain gradients in ferroelectric thin films one of the most developed approaches involves creating a defect gradient which through an effective "chemical pressure" generates a strain gradient (as graphically depicted in Figure 1.9b). This approach has been successfully employed to produced strain gradients on the order of 10^5 m^{-1} in $HmMnO_3$ by varying the oxygen partial pressure during growth,[151, 152] $BiFeO_3$ by varying film thickness and temperature,[165, 231] and $BaTiO_3$ by varying the laser fluence.[150] Recently, detailed high angle annular dark field scanning transmission electron microscopy (HAADF-STEM) and geometric phase analysis (GPA) has revealed that polarization rotation and large strain gradients (once again on the order of 10^5) can exist at ferroelastic domains walls (Figure 1.9c),[140, 166] demonstrating the possibility that domain structure engineering could be employed to produce large flexoelectric effects. Once these strain gradients are formed, it is exceedingly difficult

to directly measure the strain gradients, as X-ray based approaches which generally measures the average structural properties of materials struggle analyzing local variations in materials properties[151, 165, 197, 232] and conventional transmission electron microscopy (TEM)-based GPA can only image over small length scales not suitable for complete strain gradient analysis.[233] In this thesis we will present two novel approaches to quantify and measure strain gradients and relaxation in ferroelectric thin films.

Despite these prior challenges quantifying the full nature of the flexoelectric effects in these strain gradient engineered thin-films the manifestations of the flexoelectric effects are obvious and meritorious of study. The most pronounced effect of the flexoelectric effect is visualized by observing shifted hysteresis loops. These shifts were first recognized as shifts along the polarization axis,[202, 234] but were later proven to be the results of the measurement circuit (*i.e.* the reference capacitor of the Sawyer-Tower circuit and the applied voltage),[235, 236] and instead the shifts actually lie along the voltage (or field axis).[237] The shift (along the horizontal axis), the so-called built-in potential is typically quantified in terms of the midpoint of the coercive fields and has been reported to be as large as 30 kV/cm (0.75 V) in $BiFeO_3$,[165] 50 kV/cm (1.75 V) in $HmMnO_3$,[152] and 100 kV/cm (1.5 V) in $BaTiO_3$ (Figure 1.9d).[150] It is worth emphasizing that these built-in potentials are intrinsic to the material (in its current strain state) and are different in nature from extrinsic effects such as asymmetric electrodes which typically give rise to imprint,[238, 239] which if careful care is taken can be completely neglected.[240] the presence of these built-in potentials can act similar to an externally applied voltage, acting to suppress the dielectric susceptibility while having minimal impact on the polarization,[196, 241] enabling the decoupling of typically coupled ferroelectric susceptibilities. Finally, if the origins of the strain gradient arise from a localized defect layer at one of the interfaces, the material can give rise to non-switchable rectifying diode behavior (shown in Figure 1.9e),[165] where switchable rectifying diode behavior is caused by the V_o-rich layer at the interface.[242]

1.12 Organization of Thesis

The remainder of this thesis will consist of six additional chapters and ten appendixes followed by a reference section.

In Chapter 2, we will introduce the basic operation principles, capabilities, and limitations of the various experimental techniques used to probe the materials studied in this thesis.

In Chapter 3, we explore the effect of chemical composition on the crystal and domain structure in compositionally-homogeneous $PbZr_{1-x}Ti_xO_3$ heterostructures. We evaluate how the strain state, electrical, dielectric, and ferroelectric response evolve in these various heterostructures.

In Chapter 4, we take an in-depth look at the strain evolution in morphotropic phase boundary $PbZr_{0.52}Ti_{0.48}O_3$ thin films. We explore how the presence of phase competition can skirt classical assumptions of epitaxial strain; and determine how this new form of strain engineering effects the electrical, dielectric, and pyroelectric responses of these materials.

In Chapter 5, we present the growth, crystal and domain structure, and properties of compositionally-graded $PbZr_{1-x}Ti_xO_3$ heterostructures. We will focus on how strain (and potentially chemical) gradients can be used to generate large built-in potentials and evaluate their influence on the dielectric and pyroelectric responses, and figures of merit. We explore the chemical and thickness dependence of the built-in potential and demonstrate that the magnitude of the built-in potential does not follow trends based on the maximum theoretical strain gradient alone and instead, is dominated by the presence of transitions through the MPB and/or the presence of ferroelastic domain structures.

In Chapter 6, we conduct detailed local probes of ferroelectricity in homogeneous and compositionally-graded heterostructures using multi-dimensional, band-excitation based piezoresponse force microscopy. Coupled with detailed nanobeam diffraction strain mapping studies we observe how the presence of a strain gradient can modify the nature and response of ferroelastic domains. Specifically, we show that ferroelastic domains can be manipulated to be needle-like in nature by the presence of a strain gradient. We observe using local piezoelectric probes that these needle-like ferroelastic domains act like domain wall springs which are much more labile (in the out-of-plane direction) than typical ferroelastic domains (under applied electric fields) producing locally enhanced piezoresponse.

In Chapter 7, we present preliminary multidimensional, band-excitation piezoresponse force microscopy studies of strain-induced mixed-phase $PbTiO_3$ and $PbZr_{0.2}Ti_{0.8}O_3$ heterostructures. These studies reveal a hierarchical mixed phase domain structure which permits field induced structural phase transitions and has evidence of multi-stage switching events. In this section we derive new routes to start to understand the switching processes in these mixed-phase systems.

We conclude this chapter with suggestions for future work.

The main text is supplemented by ten appendixes which include: history, mechanisms and growth modes of pulsed-laser deposition, measurement and quantification of laser fluence, additional studies of $PbZr_{0.2}Ti_{0.8}O_3$ heterostructures, additional band-excitation switching spectroscopy images of $PbZr_{0.2}Ti_{0.8}O_3$ heterostructures, additional band-excitation switching spectroscopy images of (20,80) compositionally-graded heterostructures, additional loop shape parameters for homogeneous $PbZr_{0.2}Ti_{0.8}O_3$ and compositionally-graded (20,80) heterostructures, additional band-excitation switching spectroscopy images of mixed-phase $PbTiO_3$ heterostructures, band-excitation switching spectroscopy, multi-step loop fitting, loop shape parameters of mixed-phase $PbTiO_3$ heterostructures, additional band-excitation switching spectroscopy images of mixed-phase $PbZr_{0.2}Ti_{0.8}O_3$ heterostructures, and band-excitation switching spectroscopy loop shape parameters of mixed-phase $PbZr_{0.2}Ti_{0.8}O_3$ heterostructures.

This thesis is also supplemented by movies (available online) of the switching spectroscopy in homogeneous $PbZr_{0.2}Ti_{0.8}O_3$, compositionally-graded (20,80), mixed phase $PbTiO_3$ and mixed-phase $PbZr_{0.2}Ti_{0.8}O_3$ heterostructures.

Chapter 2

Characterization of Ferroelectric Thin Films

In this chapter, we describe the techniques and methodologies used to characterize the complex oxide ferroelectric thin films studied in this work. We start this discussion with basic crystallographic and domain structure metrological techniques (X-ray diffraction, Atomic Force Microscopy, and Piezoresponse Force Microscopy). Following that description, we move on to discuss the fabrication process used to fabricate parallel plate capacitor structures with symmetric epitaxial electrodes using an MgO hard mask process. We then describe the experiments needed to characterize ferroelectric and dielectric susceptibilities with a particular interest on illuminating the domain wall contributions. In the second section of this chapter, we describe the background information for the advance metrology and data analysis which have been developed specifically for, or implemented in new ways, to address scientific challenges presented in this work. This section includes a description of: a high dc bias permittivity measurement capable of measuring intrinsic contributions to the dielectric permittivity, a phase-sensitive pyroelectric measurement methodology that can isolate pyroelectric current and thermally stimulated current, band-excitation piezoresponse force microscopy and switching spectroscopy capable of excluding topographical crosstalk and measuring local piezoelectric hysteresis loops, the methodology and methods used to fit and extract data from local piezoelectric hysteresis loops, and a transmission electron microscopy technique based on nanobeam diffraction capable of measuring local strain maps. Together, this collection of techniques provides the tools needed to understand the structure, properties, and modes of responses in these complex ferroelectric materials.

2.1 Basic Crystal Structure Characterization

2.1.1 X-ray Diffraction (XRD) of Ferroelectric Thin films

In ferroelectric thin films the form and function is defined on the atomic scale by the crystal structure which can be studied by X-ray diffraction-based techniques. To conduct these measurements an incident beam of X-rays is focused towards a sample of interest causing some of these X-rays to be elastically scattered by the electrons of the atoms (Thompson Scattering). Since all crystalline materials have long-range atomic order when the incident beam, sample, and detector geometrically satisfies the Bragg condition the elastically scattered X-rays constructively interfere, having an intensity much greater than the background noise. The angular location of this diffraction peak can easily be used to calculate the interplanar lattice spacing using $n\lambda=2d\sin(\theta)$ as long as the order of the diffraction condition (n), incident wavelength (λ), and the angle which the diffraction peak occurs (θ) is known.[243]

Experimentally, initial crystal structure characterization of thin films is commonly accomplished by conducting a $2\theta/\omega$ scan, to quantify the position, shape and intensity of the Bragg reflections. To do this, the sample reference frame is established by aligning the incident X-ray, sample and detector to the substrate diffraction condition of interest. Throughout the measurement both the angle between the sample, X-ray source, and detector are moved such that 2θ and ω angles are equivalent and the path length is unchanged (Figure 2.1a-b). It is worth noting that if the quality of the epitaxy is in doubt a φ scan along an asymmetric diffraction condition for the film and substrate can be used to verify the quality of the epitaxy. In most cases high-quality epitaxy is relatively easy to achieve (as long as a suitable substrate is chosen) over a wide range of growth conditions. If all other film characteristics fit prior expectations it is fairly safe to assume epitaxy without measuring each time. When films are grown epitaxially on lattice matched substrates scans near the diffraction

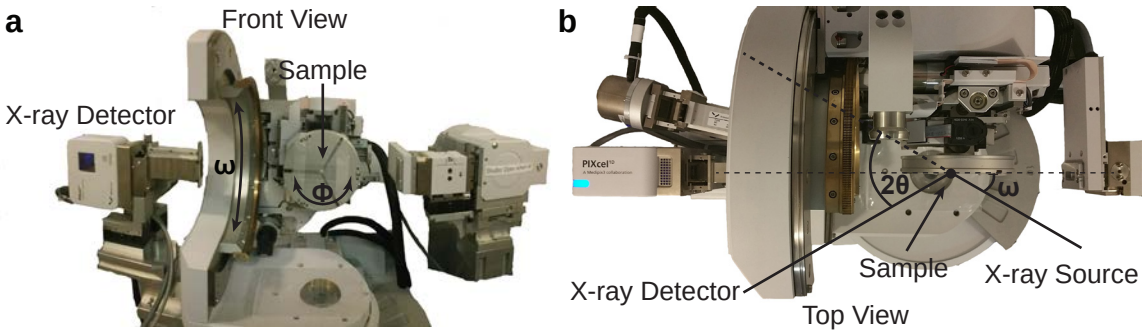

Figure 2.1. (a) Front and (b) top view of X-ray diffractometer indicating the positions of the X-ray source, X-ray detector, and sample. Rotations axes of the goniometer are indicated.

condition of the substrate can capture the diffraction of the film, providing a wealth of information including: structure and lattice parameter from the diffraction position, film thickness, the presence of possible secondary phases, and crystal quality in the normal direction (in terms of strain and defect density). For instance, if the crystalline quality of the film is sufficiently good the diffraction condition can have Laue fringes (from the $2\theta/\omega$ scan), which can be used to calculate film thickness.[244, 245] Alternatively, the thickness of a film can be quantified by conducting X-ray reflectivity measurements where differences in electron density between layers result in some X-rays being reflected by the interface (in accordance with Fresnel's equations); which upon interfering generate Kiessig fringes. While the quality of Laue fringes are primarily determined by the crystalline quality, the quality of Kiessig fringes are determined primarily by the quality of the interface (in terms of roughness) between layers.[246] If additional information about the in-plane crystal quality is required, rocking curves about ω at the diffraction condition for the substrate and the films can be acquired.

2.1.2 Multi-Dimensional X-ray Diffraction of Ferroelectric Thin Films

While these one-dimensional X-ray diffraction techniques provide the insight needed to visualize films when the in-plane lattice parameters and crystallographic tilts are equivalent to the substrate, when differences exist a single line scan is insufficient to fully visualize the structure. To gain more insight into the structure requires the ability to measure on two-axes creating a reciprocal space map in 2θ and ω space. Experimentally, these scans are typically accomplished by aligning the X-ray to the diffraction conditions of the substrate, defining a 2θ and ω space, and conducting a series of 2θ scans at various ω values. These scans can then be combined to create a two-dimensional map of the diffraction intensity. If the scan is centered around a symmetric diffraction condition [(00l) for an (00l) oriented substrate] the resulting image provides insight into the crystalline quality and crystallographic tilts of the film (or variants within the film). On the other hand, if a scan is conducted near an asymmetric diffraction condition [(hkl) ≠ (00l) for an (00l)-oriented substrate] the resulting diffraction peaks provide insight into the average in-plane and out-of-plane lattice parameter of the film, in addition to information about the crystallographic tilts. Typically, after data collection, these plots are converted into q_x and q_y space using $q_x = \frac{1}{\lambda}\left(\cos\omega - \cos\left(2\theta - \omega\right)\right)$ and $q_y = \frac{1}{\lambda}\left(\sin\omega - \sin\left(2\theta - \omega\right)\right)$, such that the diffraction peak is represented in units of (1/Å). Using this convenient representation, it is easy to classify whether a film is relaxed (q_x-value of film varies

from substrate) or coherently strained (q_x-value of film is identical to substrate) to the substrate.

X-ray diffraction is a proven, powerful technique capable of exploring the average crystal structure of thin films. At times, it is also desirable to measure the inhomogeneous strain or strain relaxation in thin films. If the diffraction peak of interest can be modeled as a single material with a known lattice parameter strain relaxation can be quantified using the Williamson-Hall approach.[232] To do this, it is necessary to separate out the broadening (due to the finite thickness of the film) and strain relaxation of the diffraction peak using the Willliamson-Hall relation $\beta\cos\theta = K\frac{\lambda}{D} + 4\varepsilon_{inh}\sin\theta$; where D is the coherence length perpendicular to the film thickness (approximately the film thickness), β is the breadth of the peak (which can be approximated by the full width half max), λ is the X-ray wavelength, θ is the diffraction angle, K is a constant close to unity and ε_{inh} is the inhomogeneous strain. By measuring the breadth of the diffraction peak of various orders it is possible to make a Williamson-Hall plot $\beta\cos\theta$ vs $\sin\theta$ where the linear fit of this plot provides a quantification of strain relaxation. This approach has been employed to measure strain relaxation in a wide variety of ferroelectric thin films;[151, 165, 197] however, it is important to re-emphasize that this approach can only provide a measure of average strain relaxation, and is unable to predict the origins and/or how strain relaxation evolves throughout the thickness of a film.

2.1.3 Surface Topography Imaging of Ferroelectric Thin Films

When growing thin films using PLD it is ideal to grow films layer-by-layer, however, this growth mode can only occur under optimal conditions (see Appendix A for discussion of common growth modes in PLD). In turn, the topographical structure provides critical feedback regarding growth indicating potential defects (such as particles, second phases, or holes). The features which define the surface topography are typically on the order of Å-nm. To probe such features atomic force microscopy (AFM) is the most suitable metrology technique. AFM operates by taking an ultra-sharp cantilever (with a tip radius typically on the order of 5-10 nm, but are commercially available as low as 1 nm) which is brought into contact (or near contact)

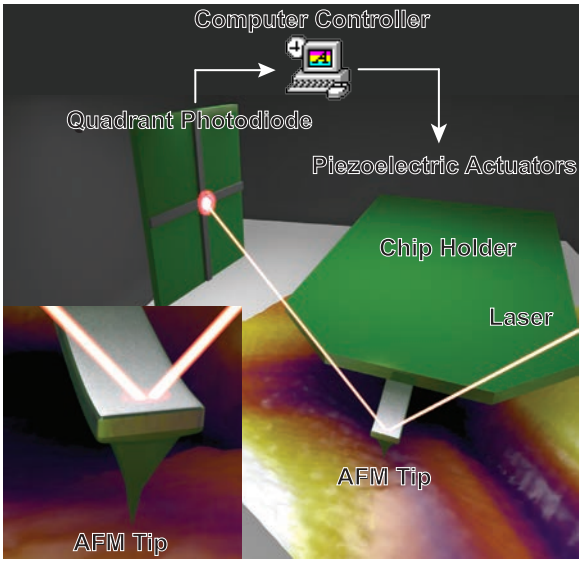

Figure 2.2. Schematic drawing indicating the basic operation of an atomic force microscope.

with a surface. This tip is then scanned across the surface of the sample (using piezoelectric actuators) while simultaneously measuring the deflection of the cantilever by reflecting a laser off the back of the cantilever and measuring its location using a quadrant photodiode (Figure 2.2). The measured deflection is used to establish a feedback loop with the height of the cantilever enabling a constant set point (of the photodiode) to be maintained (by adjusting the z-piezo). As the tip scans across the surface the deflection of the cantilever is sampled allowing the construction of an image. By bouncing the laser off the cantilever it is possible to amplify the deflection signal and using this approach it is quite common to achieve vertical resolution on the order of 0.2Å (well below the diffraction limit); while the lateral resolution is limited by the radius of curvature of the tip. Since what is actual being imaged is a convolution of the tip and sample surface (imaging the less sharp feature) any damage to the tip will distort the image. To avoid such damage, it is common to image in tapping mode, where instead of being in direct contact with the sample surface the tip images the topography by measuring a change in the resonance response of the cantilever as a result of changes in the short-range repulsive coulombic forces and long-range attractive forces. While there are many details of this technique which help imaging difficult samples they are beyond the scope of this thesis.[247-249] In general, many of the challenges barring the acquisition of a good image using AFM have been automated in commercially available instruments making it fairly easy to obtain high-resolution topographical images.

2.1.4 Imaging Domain Structures in Ferroelectric Thin Films

Imaging is just the most basic function of AFM and once a cantilever is in intimate contact or interacting with a surface it is possible to measure other properties of the surface. Using the AFM tip as an atomic probe a wide variety of modes capable of characterizing material properties on the nanoscale have been developed including: single-molecule spectroscopy,[250, 251] nano-mechanical microscopy,[252, 253] electrostatic force microscopy,[254, 255] magnetic force microscopy,[256-258] nanolithography,[259, 260] scanning microwave impedance spectroscopy,[261, 262] nano-Raman,[263, 264] and many more. Specifically, in the context of ferroelectric materials the conductive cantilever can be used to electrically perturb a material generating a measurable piezoresponse (Figure 2.3a-b). Since the magnitude of the piezoresponse depends on the domain type and the phase depends on the polarization direction (Figure 2.3c), it is possible to use piezoresponse force microscopy (PFM) to construct an image of the domain structure. To do this, a cantilever is brought into contact with the

surface and a small ac voltage is applied between the tip and the sample while measuring the deflection using a lock-in amplifier. While any frequency can be chosen for the ac excitation it is important to consider the magnitude of the piezoelectric displacement of the cantilever in reference to the noise floor of the instrument. In a clamped thin films piezoelectric coefficients are 100-300 pm/V at best,[265] meaning the maximum sub-coercive displacement is on the order of 1-10 Å. To increase the deflection it is possible to leverage the cantilever ability to amplify this response by exciting the cantilever at its contact resonance frequency, generating orders of magnitude enhancement in the cantilever deflection. While single-frequency PFM is powerful for imaging highly-responsive materials with large domain features its limitations become obvious even when considering the simplest, idealized model of the cantilever resonance in the form of a simple harmonic oscillator (SHO). In this case, the response of the cantilever is primarily determined by the resonance frequency (defined by the tip-surface spring constant), amplitude (a measure of the piezoresponse

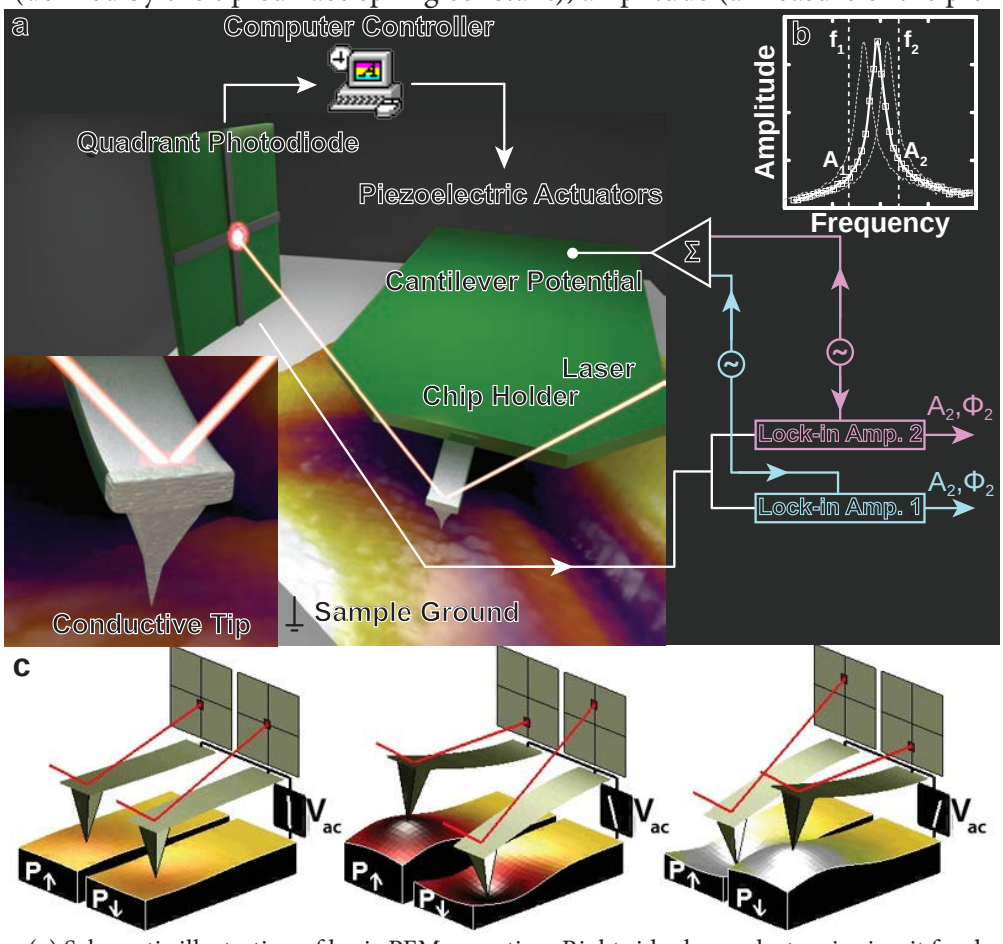

Figure 2.3. (a) Schematic illustration of basic PFM operation. Right side shows electronic circuit for dual frequency PFM (DART). (b) Illustration of conventional PFM cantilever resonance indicating the ideal frequencies for excitation using DART. Dashed lines indicate the potential for resonance hopping based on the tip-surface contact resonance. (c) image showing the sign dependence of sample strain. When domains are poled up and negative bias is applied, domains expand and vice versa, resulting in a polarization dependent phase shift between the applied bias and piezoresponse.

response), and Q-factor (defined by the tip-surface dissipation), all of which are intimately linked to the tip-surface interaction. In real measurements, due to changing topography, the tip surface interaction is constantly changing resulting in cantilever resonance frequency hopping (Figure 2.3b), which is difficult to deconvolute. While more advanced approaches based on phase-locked loops (which use external circuitry to try to maintain the system at resonance) or dual-frequency resonance tracking (DART, which excites, measures, and then tracks the resonance using two frequencies) provide a more accurate measure of piezoresponse,[266] they still only provide incremental improvements applicable under the strictest of assumptions.[266, 267]

2.2 Basic Macroscopic Electrical Characterization

2.2.1 Fabrication of Symmetric Epitaxial Top Contacts

When conducting electrical measurements of ferroelectric materials the choice of electrode material is of paramount importance. As an electrode material with poor chemical compatibility or finite screening length can result in "so-called" dead layers.[268-273] These dead layers can give rise to problems with fatigue, retention, and imprint.[274-276] It has been shown both theoretically, and experimentally that these detrimental effects can be mitigated by using structurally- and chemically-compatible oxide metals ($SrRuO_3$, *etc.*).[274, 276-278] This choice of electrodes material becomes particularly important when measuring at elevated temperatures where leakage is increased, there is diminished chemical stability, and electrodes are more likely to delaminate from the surface.[279] When designing capacitor structures the ideal structure would be an epitaxial stack where both the bottom and top layers are the same chemical composition, similar in chemistry to the active layer, and epitaxial in nature. In this thesis to achieve such a structure we grew patterned epitaxial $SrRuO_3$ top electrodes using an MgO hard mask process. To create this capacitor structure

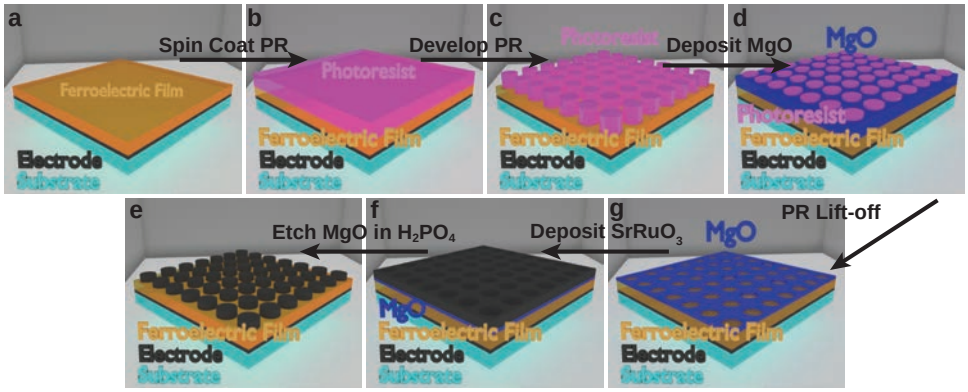

Figure 2.4. (a-g) Schematic illustration of processing steps for the growth of epitaxial top electrodes for parallel-plate capacitor structures used for electrical characterization.

photoresist (PR) is spin coated onto a ferroelectric/$SrRuO_3$/substrate heterostructure (Figure 2.4a-b). The PR is then exposed and developed generating an inverse mask of the device structure to be fabricated (Figure 2.4c). A hard mask of MgO is then deposited on the surface using either electron-beam evaporation or PLD (Figure 2.4d), and the PR is lifted off in acetone (Figure 2.4e). Following lift off the sample is descumed using a plasma cleaner, and high-temperature (550 °C) top $SrRuO_3$ is grown using PLD (Figure 2.4f). During this process care is taken to minimize the time that the sample is at high temperatures and low pressure in order to minimize any potential Pb loss from the film. Following $SrRuO_3$ growth the hard mask is etched using phosphoric acid revealing the patterned $SrRuO_3$ contacts (Figure 2.4g). Capacitor structures fabricated using this approach have been shown to give excellent symmetric leakage performance, improved fatigue, high retention, and excellent thermal stability.[240]

2.2.2 Low-Field Permittivity Measurements of Ferroelectric Thin Films

One of the most basic properties of any dielectric material is its ability to become polarized in the presence of an electric field (dielectric susceptibility) and this material property is crucial for many high-performance applications. For instance, materials with large dielectric constants (high-k) are needed as gate electrode materials,[280-282] low dielectric materials are needed to insulate conductive components in microelectronic devices,[283, 284] and highly-field tunable dielectrics are needed for tunable radio frequency (RF)-devices.[17, 18, 285] In turn, there has been significant research interest in how to control the dielectric properties of materials.[31, 125, 186, 286-288] Moreover, from a fundamental perspective the dielectric response of a material can provide insight into the physical nature of the field dependent responses as the relative contributions to the dielectric response can be altered by changing the magnitude/frequency of the excitation voltage allowing the dielectric nonlinearity to be assesed.[12, 289, 290] To quantify dielectric nonlinearity in ferroelectric materials the so-called Rayleigh law has been evoked. This concept was originally developed by Lord Rayleigh in 1887 in response to an empirical observation that the magnetic permeability is linearly dependent on the applied magnetic field (over an intermediate field range).[291] Based on this observation, a mechanism was derived involving the motion of a domain wall within a potential well which can be driven to overcome the energy barrier of this well (by the application of an external field).[292, 293] More recently, this approach has been applied to ferroelectrics to explain the observation of dielectric non-linearity. Typically dielectric responses are categorize into *intrinsic responses* associated

with the average response of all domain variants within the lattice and *extrinsic responses* (consisting of reversible and irreversible contributions) primarily associated with a field induced change in volume fraction of domain variants.[289, 294, 295] When domain walls are excited to move around (by changing their volume fraction) they randomly encounter defects that are both electronic and ionic in nature. These randomly distributed defects act as pinning sites creating a barrier for domain wall motion.[294, 296] Therefore, it is possible to conceptualize the energy landscape for a domain wall as existing in a varying potential determined by the type and density of pinning defects (Figure 2.5a).[294, 297, 298] When the domain wall is perturbed with a small packet of energy it can move around within its current potential well, resulting in a reversible extrinsic domain wall contribution. On the other hand, if the packet of energy is greater than the barrier height the domain wall can hop between local potential wells, undergoing irreversible domain wall motion and generating an irreversible domain wall contribution to the dielectric permittivity.

To experimentally measure and extract importance of each of these contributions detailed dielectric measurements must be undertaken. Throughout this thesis the dielectric susceptibility (defined as $\varepsilon_{ij} = \frac{\partial P_i}{\partial E_j}$) was measured by applying a small ac voltage using an inductance, capacitance, resistance (LCR) meter to a parallel plate capacitor, generating a field along the out-of-plane direction (*i.e.*, the [00*l*]), enabling the measure of capacitance (*C*) and loss. From these measurements it is possible to calculate the dielectric permittivity (ε_{33}) from $C=\varepsilon_0 \varepsilon_{33} A/t$ where *A* is the area, *t* is the thickness. Typically, when first analyzing the dielectric response of a ferroelectric material it is important to determine the appropriate small-signal ac excitation to exclude dielectric non-linearity (*i.e.*, the irreversible extrinsic contributions). To determine this voltage so-called Rayleigh studies can be conducted where the permittivity is measured over a range of ac excitations voltages at a given frequency (typically 1-10 kHz). In conducting these measurements there are three clear regions of response (Figure 2.5b).[286] Region I, where the response is nearly invariant with increasing excitation

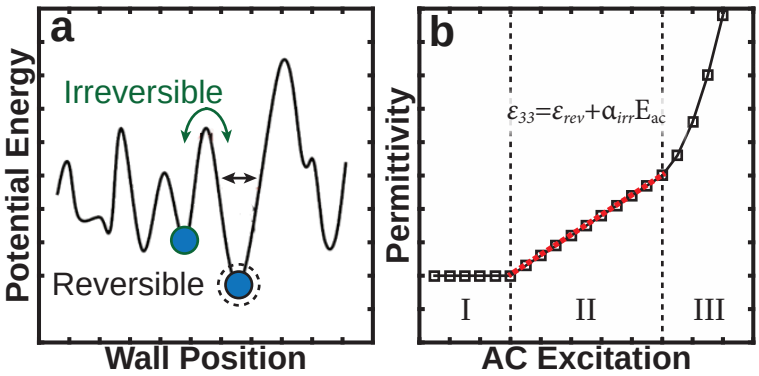

Figure 2.5. (a) Schematic illustration of position dependent domain wall energy. (b) Typically dielectric permittivity measurement as a function of ac excitation showing the three regimes defined by Rayleigh's Law.

(representative of intrinsic and reversible extrinsic contributions). Region II, also called the Rayleigh region, where the permittivity increases linearly with increasing ac excitation. And, Region III, where the onset of ferroelectric switching has occurred. From these measurements, Region II, can be fit using the Rayleigh law $\varepsilon_{33} = \varepsilon_{rev} + \alpha_{irr} E_{ac}$ where ε_{rev} and α_{irr} are the reversible and irreversible Rayleigh coefficients, which are representative of the reversible and irreversible domain wall contributions.[286, 294] Using such measurements, it is possible to choose an ac excitation below the threshold field where irreversible contributions to the permittivity become active, allowing subsequent measurements of permittivity (as a function of frequency, dc voltage, *etc.*).

2.2.3 Measurement of Ferroelectric Hysteresis

Beyond measuring the dielectric response, it is also useful to measure ferroelectric hysteresis loops which provides insight into the switching process (*see* section 1.4). Typically, to measure ferroelectric hysteresis loops an external bi-polar triangular waveform is applied to a ferroelectric capacitor structure. If the combined energy of the triangular waveform (in terms of voltage and frequency) exceeds the coercive field the polarization switches, necessitating a change in the compensating charge carriers at the electrode interface. This movement of compensating charge carriers generates a measurable current. If no current flows through the capacitor, the polarization can be measured using $P = \int i dt - \varepsilon_0 E$ where i is the current and t is the time. Classically ferroelectric hysteresis loops have been measured using a Sawyer-Tower circuit which operates by connecting the device under test (DUT) and a reference capacitor in series (so that the charge flow is the same) and measuring the voltage across the shunt capacitor (as a bias is externally applied).[265, 299] It is important that the reference capacitor have extremely low loss and that its capacitance is such that it generates a measurable voltage without causing significant errors in the voltage seen by a DUT. Due to these complications and availability of high-quality electronics capable of easily measuring currents in the fA range it is possible to directly measure the switching current eliminating common sources of error.[265] With this new accessibility of "black box" electronics capable of measuring ferroelectric hysteresis comes new challenges associated with improper implementation and analysis of results. Recently, this problem highlighted in a satirical way by making the implication that researchers are commonly confusing bananas with a ferroelectric material $Ba_2NaNb_5O_{15}$ (nicknamed "Bananas") by showing that charge vs. voltage loops (identical to those published as evidence of ferroelectricity) can be obtained from a skin of a banana; which is obvious not ferroelectric.[300]

2.3 Advanced Electrical Characterization of Ferroelectric Thin Films

Throughout this thesis we employ cutting-edge characterization techniques which are in the proof-of-concept stage or were developed specifically to observe phenomenon predicted in some of the unique materials studied in this thesis. The following section will outline the various operating principals of these techniques and the methodology used for analysis.

2.3.1 High-Field Permittivity Measurements of Ferroelectric Thin Films

While we have previously shown how low-field permittivity measurements can effectively separate out the reversible and irreversible extrinsic contributions to the dielectric permittivity this measurement is unable to isolate the intrinsic and extrinsic contributions. Classically, measurement of intrinsic permittivity of ferroelectric materials has been achieved in one of three ways: 1) By growing monodomain films without domain walls,[301] 2) By measuring the dielectric response at high frequencies (in the gigahertz regime) where the domain walls no longer respond,[302-305] and 3) By measuring the dielectric response at temperatures (approaching absolute zero) where domain wall motion is assumed to be frozen.[186, 306-308] The major drawbacks of these methods are: 1) Inability to measure intrinsic response of polydomain films and inability to grow some structures in monodomain form, 2) Difficulty designing and implementing high-frequency measurements on ferroelectric thin films, 3) The high cost and limited availability of cryogenic systems. In this thesis we took a simple and inexpensive alternative approach to measure the intrinsic permittivity by measuring the dielectric permittivity under high dc biases, where the dc bias acts to pin domain wall motion, suppressing its response.[241, 287, 309] To do these measurements, the samples were pre-poled in the direction of applied background dc bias. Capacitance vs. frequency measurements (from 1–100 kHz) were measured over a range of applied background dc electric fields (Figure 2.6a). The resulting curves were fit to the equation $\varepsilon_{33}=\varepsilon_i-\alpha_f \log f$ extracting the field-dependence of the permittivity intercept (ε_i) and slope (α_f). We

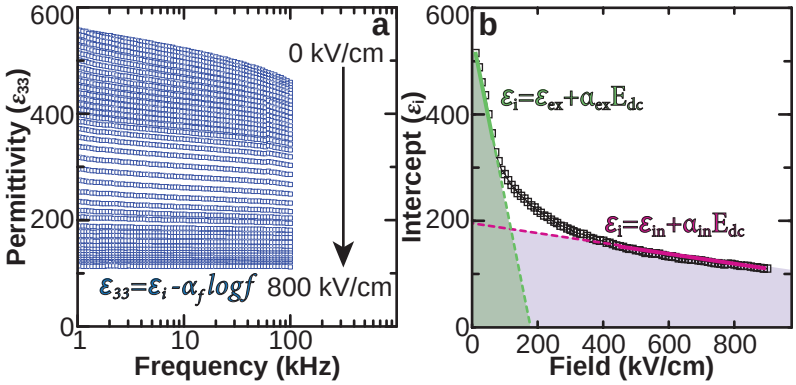

Figure 2.6. Demonstration of methodology used for extraction of intrinsic and extrinsic contributions to the dielectric permittivity using high-bias fields (a) shows typical measurement of capacitance vs. frequency with increasing dc bias fields. (b) extracted fits to the high- and low- field regimes indicating the extrinsic (green) and intrinsic (purple) response.

then plot ε_i as a function of the background dc electric field (Figure 2.6b). These plots typically show two regimes, a low-field regime (where the response consists of both intrinsic and extrinsic contributions, shown in green) and a high-field regime (where the response is thought to be reflective of only the intrinsic response, shown in purple). The slope and intercepts of linear fits in the low-field regime correspond to the extrinsic tunability (α_{ex}, which describes how the applied dc electric field suppresses the extrinsic response) and the zero-field extrinsic permittivity (ε_{ex}), respectively. The slope and intercepts of linear fits in the high-field regime correspond to the intrinsic tunabilitiy (α_{in}, which describes how the external dc electric field suppresses the intrinsic response) and the zero-field intrinsic permittivity (ε_{in}), respectively. It has been demonstrated that this technique is capable of extracting intrinsic permittivity values similar to those obtained using the aforementioned approaches; however, prior to this work, this method has yet to be broadly applied to the study of ferroelectric thin films.[241]

2.3.2 Pyroelectric Measurements of Ferroelectric Thin Films

From a device standpoint there is significant interest in using ferroelectric thin films for nanoscale pyroelectric energy harvesting and sensing components capable of being integrated into microelectronic devices. Measuring pyroelectric response in thin films is difficult leading some to call it "one of the least-known properties of solid materials".[310] While there are adequate techniques to measure pyroelectric response in the bulk materials, including extraction of remanent polarization from temperature dependent hysteresis loops,[59, 311, 312] laser-induced sample heating,[313] and linear resistive heating methods;[314] these techniques lack the temperature stability and are unable to

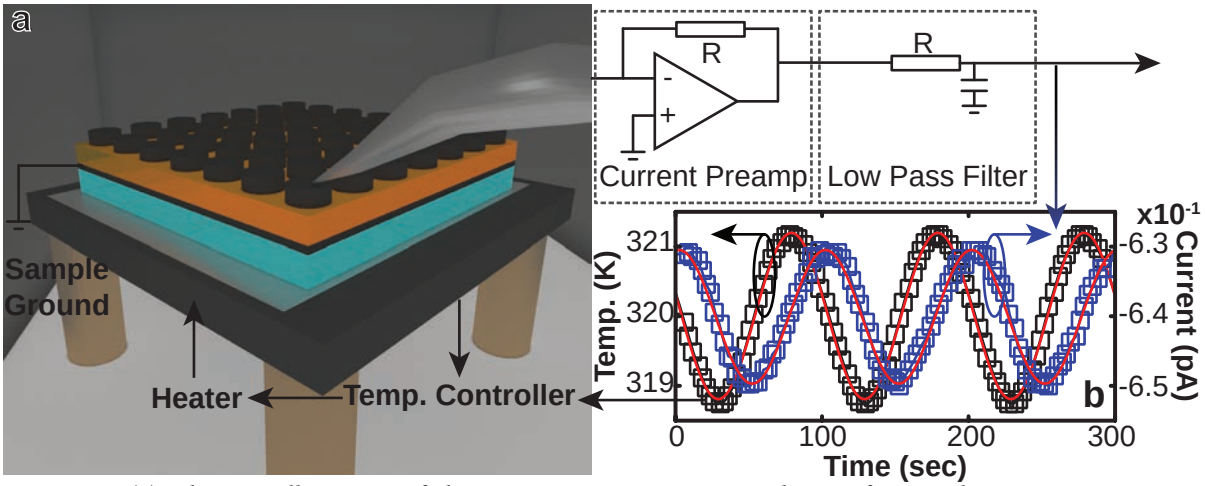

Figure 2.7. (a) Schematic illustration of phase-sensitive measurement technique for pyroelectric measurements using a sinusoidal temperature oscillation. (b) shows a typical measurement results for pyroelectric current measurements on a 200 μm diameter $PbZr_{0.2}Ti_{0.8}O_3$ capacitor.

properly exclude thermally stimulated currents, complicating their implementation in thin films.[315] Nevertheless, these approaches have still been applied to thin films.[59, 311, 312, 316-318] In this thesis, we utilize a phase-sensitive pyroelectric measurement approach which can overcome some of these challenges (Figure 2.7a).[319, 320] To conduct these measurements epitaxial $SrRuO_3$ heterostructures were fabricated, as previously described, and mounted onto a heater using silver paint. The heater was set to sinusoidally oscillate the temperature at a frequency of 0.05-0.2 Hz (Figure 2.7b, black curve), controlled *via* a computer controlled feedback loop between the heater power and sample surface temperature (measured on top of a reference substrate). The pyroelectric current generated (i_p) depends on the rate of temperature change $\left(\frac{dT}{dt}\right)$ as $i_p = \pi A\left(\frac{dT}{dt}\right)$, where π is the pyroelectric coefficient and A is the area of the capacitor. Additionally, the temperature change results in a change in thermally stimulated current (i_s), which is linearly dependent on the temperature, $i_s = i_{so}+\lambda_{Therm}T$, where i_{so} is the thermally stimulated current at room temperature and λ_{Therm} is a constant associated with the average trap state energy. In turn, the sinusoidal temperature change generates thermally stimulated current in-phase with- and pyroelectric current out-of-phase with the temperature change. The sum of these currents can be measured using a current to voltage converter (mounted in close proximity to the DUT). It is worth noting that the experimentally measured currents are extremely small, typically on the order of ~100 fA for dT/dt = 1-10 K/min for a 200 μm capacitor. Due to the extreme sensitivity of this measurement it necessitates that the films are extremely insulating and that high-quality epitaxial electrodes are used.

To extract the pyroelectric current from these measurements the temperature curve is fit using $T=T_0\sin(\omega t)$ where T_0 is the amplitude of the temperature oscillation and ω is the angular frequency of oscillation. Using a similar approach, the extracted current can be fit using $i_{cur}=i_0\sin(\omega t+\theta)$ where θ is the phase offset between the temperature and current. Once fit the pyroelectric coefficient (π) can be obtained (Equation 2.1). It is worth noting that in literature it is common to convert pyroelectric coefficients through a Maxwell conversion $\left(\frac{\partial P}{\partial T}\right)=\left(\frac{\partial S}{\partial E}\right)$ to extract electrocaloric temperature change (Equation 2.2), where C_E is the heat capacity.[24, 57, 59, 60, 311, 321-323] However,

$$\pi = \frac{i_0 \sin\left(\omega t+\theta\right)}{AT_0\omega} \tag{2.1}$$

$$\Delta T\left(T,E\right) = -\int_{E_a}^{E_b}\frac{T}{C_E\left(T,E\right)}\left[\frac{\partial P\left(T,E\right)}{\partial T}\right]_E \tag{2.2}$$

there is evidence that this approach might not be applicable in thin films where secondary mechanical contributions (or elastocaloric effects) can be significant.[324, 325] During the time of this work two additional high-frequency pyroelectric measurement approaches based on the 2ω method,[326, 327] and a laser intensity modulated method[325, 327] have been developed. While these techniques require significantly more investment in terms of fabrication and infrastructure they are able to access pyroelectric responses at more practically relevant frequencies (kHz-MHz) and under the application of electric field. In turn, these approaches enable for the first time the accurate direct measurements of pyroelectric and electrocaloric effects in ferroelectric thin films.[324, 3]

2.4 Advanced Structural Characterization of Ferroelectric Thin Films

2.4.1 Band-Excitation Piezoresponse Force Microscopy Imaging

From our previous discussion of single- and dual-frequency PFM the challenges associated with changing contact resonances was emphasized. It is critical to remove these bandwidth limitations to measure the piezoresponse without artifacts imposed by changing cantilever dynamics. To do this, we applied band-excitation piezoresponse force microscopy (BE-PFM),[267, 328] which uses a computer generated waveform (Figure 2.8a-b) spanning a band of frequencies near the cantilever resonance to electrically perturb the sample (Figure 2.8c). The response of the cantilever can then be measured with a high-speed data acquisition system and Fourier transformed (Figure 2.8d) into frequency domain. Since, at each point along a scan, the measurement collects the amplitude (A) and phase (φ), at each coordinate in space (x,y), and frequency (ω), the data takes the form of two $\{A, \varphi\}$, 3D matrices (x, y, ω). Following data collection, assuming that the tip-sample interaction is weak, the amplitude and phase can be fit to a SHO model (equation 2.3-4, Figure 2.8d, red curve).[267]

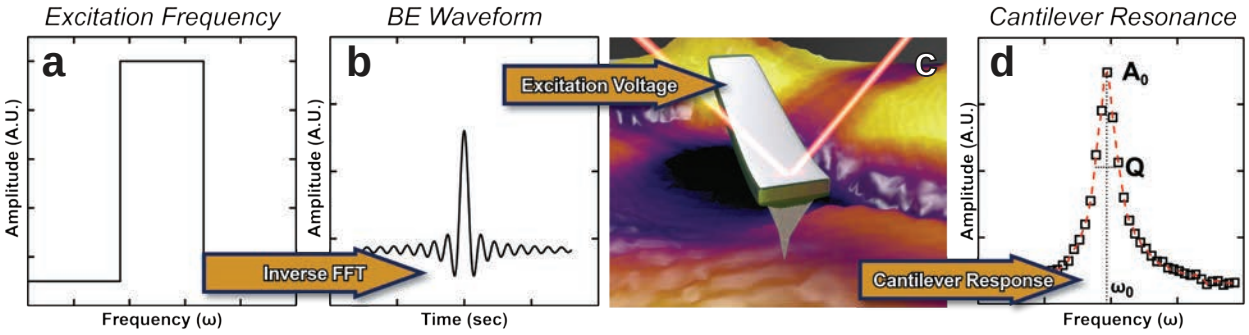

Figure 2.8. Schematic illustration of work flow for band-excitation piezoresponse force microscopy imaging. (a) Typical frequency domain plot of band-excitation signal chosen to excite the cantilever near the cantilever resonance. (b) Example band-excitation (BE) sinc waveform in time domain used to excite the tip at a range of frequencies. (c) Schematic drawing of AFM cantilever in contact with surface. (d) Typical cantilever resonance response shown in frequency domain. Red dashed line shows the fit, based on equations 2.3-4. Characteristic variables which define the cantilever/material response are indicated.

$$A(\omega) = \frac{A_0 \omega_0^2}{\sqrt{\left(\omega^2 - \omega_0^2\right)^2 + \left(\frac{\omega\omega_0}{Q}\right)^2}} \tag{2.3}$$

$$\tan\left[\varphi(\omega)\right] = \frac{\omega\omega_0 / Q}{\omega^2 - \omega_0^2} \tag{2.4}$$

Following fitting, the error of the fits can be evaluated (*i.e.*, the quality of the deconvolution), and if good, the data yields (*x*,*y*) maps of resonance amplitude (A_0), resonance frequency (ω_0), and Q-factor or dissipation (Q) as well as the phase (φ) of the response. Therefore, with the proper care, the application of BE-PFM enables the exclusion of cross-talk (associated with position dependent changes in the cantilever resonance) minimizing the contribution from the tip-surface interaction.[267, 328]

2.4.2 *Band-Excitation Piezoresponse Force Microscopy Switching Spectroscopy*

Building off the added accuracy of BE-PFM imaging it is possible to add additional dimensionality to the measurements, providing deeper insight into the response of the material.

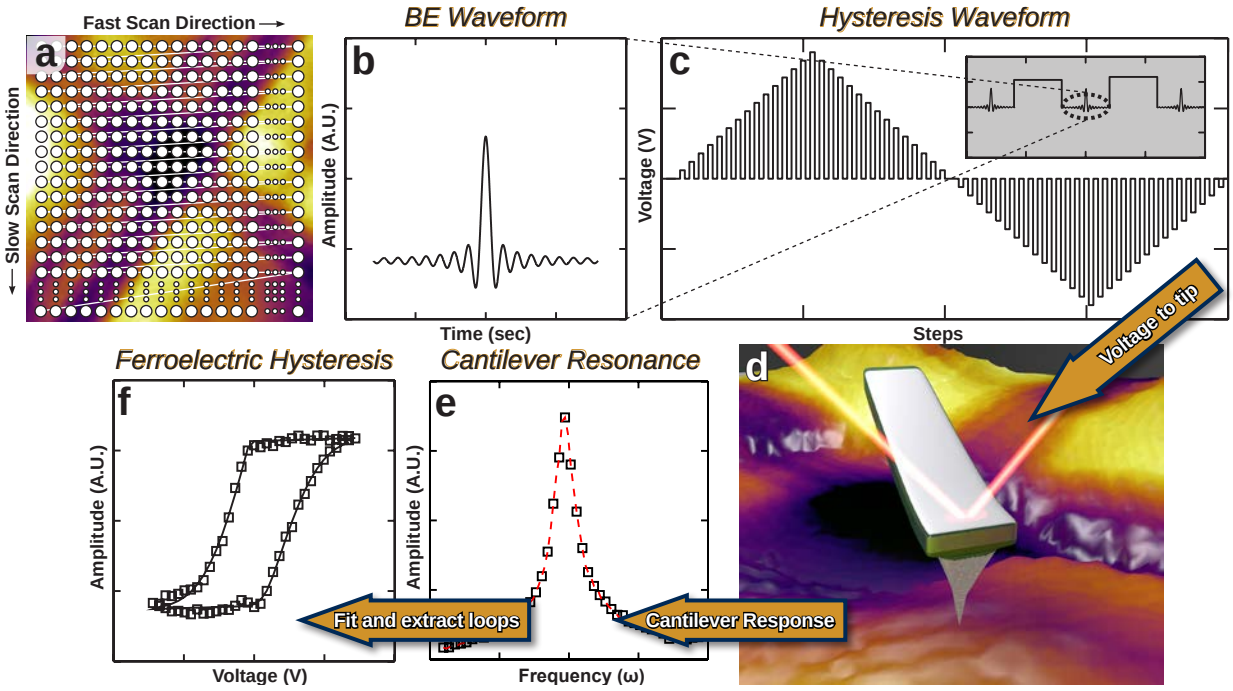

Figure 2.9. Schematic illustration of work flow for band-excitation piezoresponse force microscopy switching spectroscopy measurements. (a) Schematic of the sampling, and fast and slow scan direction used for imaging. (b) Example BE excitation sinc waveform in time domain used to excite the tip at a range of frequencies. (c) Triangular switching waveform used to locally switch the film. Inset highlights where the sinc function is applied, note the magnitude of the sinc function is magnified for visual purposes. (d) Schematic drawing of AFM cantilever in contact with surface. (e) Typical cantilever resonance response shown in frequency domain. Red dashed line shows the fit, based on equations 2.3-2.4 (f) Typical piezoelectric hysteresis loop obtained from BE-SS.

Specifically, instead of just measuring $\{A, \varphi\}(x, y, \omega)$ we can add an additional dc-voltage dimensionality to the measurement [*i.e.*, $\{A, \varphi\}(x, y, \omega, V_{dc})$] enabling local piezoelectric hysteresis loops to be measured while taking advantage of the enhanced measurement precision provided by band-excitation (BE) in a technique called band-excitation switching spectroscopy (BE-SS).[267, 328-331] To do this, we superimposed a n x n grid ($n > 50$) on a previously scanned region of interest (Figure 2.9a), with a horizontal fast scan and vertical slow scan direction. At each point, a full bipolar triangular switching waveform is applied to the cantilever (Figure 2.9b-d). Readout of the piezoresponse is conducted in the off-state (remanent state) by superimposing a BE-waveform (sense pulse). This whole process happens rapidly (total elapsed time < 5 ms). Following acquisitions the data is fit using SHO model as previously described (Figure 2.9e), yielding data of the form $\{A_0, \omega_0, Q, \varphi\}(x, y, V_{dc})$. By optimizing the rotation angle of the phase (φ) to maximize the real component of the mixed-signal hysteresis loop ($A_0\cos\varphi$) it is possible to generate local piezoelectric hysteresis loops of the same general form as typical macroscopic ferroelectric hysteresis loops (Figure 2.9f).

2.4.3 Fitting of Conventional Piezoelectric Hysteresis Loops

Once BE-SS is completed, it is useful to extract and fit the piezoelectric hysteresis loops to aid in the visualization process. To begin the fitting process, piezoelectric hysteresis loops need to be obtained from conventional piezoresponse butterfly loops (Figure 2.10a) and phase loops (Figure 2.10b). To do this, the optimum rotation angle is determined by shifting the phase (φ) to maximize the real component of the hysteresis loop [$A_0\cos(\varphi)$] while minimizing the imaginary component [$A_0\sin(\varphi)$]. Once the piezoresponse hysteresis loops are obtained, the top and bottom branches of the hysteresis loop are isolated and fit (equation 2.5-8, Figure 2.10c-d).

$$\sigma_1 = \left(\frac{b_1 + b_2}{2}\right) + \left(\frac{b_2 - b_1}{2}\right) erf\left(\frac{V_{dc} - b_7}{b_5}\right) \tag{2.5}$$

$$\sigma_2 = \left(\frac{b_4 + b_3}{2}\right) + \left(\frac{b_3 - b_4}{2}\right) erf\left(\frac{V_{dc} - b_8}{b_6}\right) \tag{2.6}$$

Upper Branch

$$\Gamma_1 = \left(\frac{a_1 + a_2}{2}\right) + \left(\frac{a_2 - a_1}{2}\right) erf\left(\frac{V_{dc} - E_c^-}{\sigma_1}\right) + a_3 V \tag{2.7}$$

Lower Branch

$$\Gamma_2 = \left(\frac{a_1 + a_2}{2}\right) + \left(\frac{a_2 - a_1}{2}\right) erf\left(\frac{V_{dc} - E_c^+}{\sigma_2}\right) + a_3 V_{dc} \tag{2.8}$$

where, V_{dc} is the dc voltage, b_1-b_4 control the sharpness of the loop corners (as $b_x \rightarrow 0$ corner approaches 90°), $b_{5\text{-}6}$ control the rate of transition from b_1 to b_2, and b_3 to b_4, respectively, $b_{6\text{-}7}$ locate the midpoint of the transition from b_1 to b_2 and b_3 to b_4, respectively, a_1 and a_2 represent the bottom and top saturation amplitudes, a_3 represents the linear contribution, $E_c^{-,+}$ represents the negative and positive coercive bias, respectively. All these parameters are depicted schematically (Figure 2.10e). This set of empirical equations was derived because it represents the loop shape well and has empirical parameters which can be correlated to common loop shape features. To demonstrate the quality of the fits, we show an example piezoresponse hysteresis loop fit using these empirical equations (Figure 2.10d, solid black line). From this fitting it is evident that these empirical equations fit the hysteresis loops well and accounts for all features of the ferroelectric hysteresis loop.

Once fit, it is possible to calculate a wide variety of loop shape features which provide insight into the switching process. For instance, one can calculate the local: loop height, loop width, coercive fields, nucleation bias (defined as the bias where a 3% change in the loop height has been

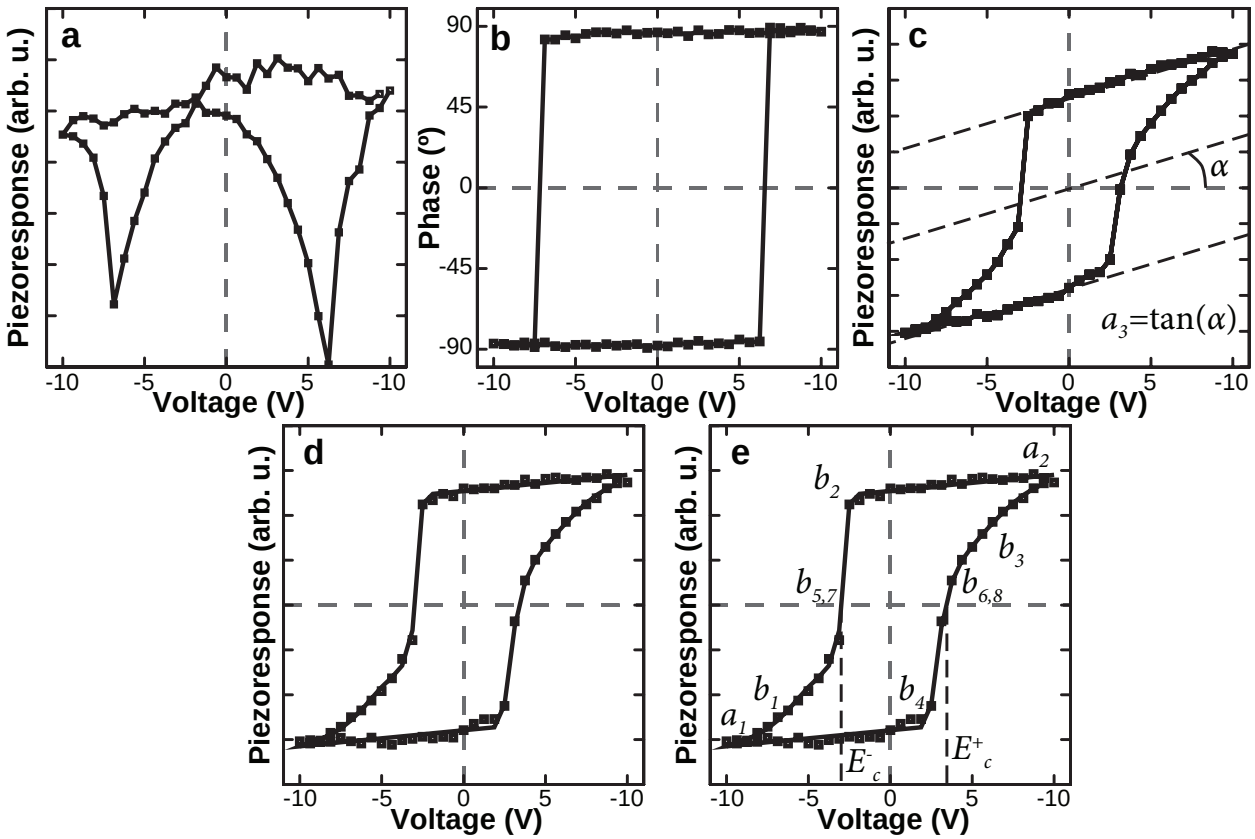

Figure 2.10. (a) Typical piezoelectric butterfly loop and (b) phase loop extracted from band-excitation switching spectroscopy. (c) Typical piezoelectric hysteresis loop extracted after phase optimization of $A\cos(\varphi)$. (c) Example piezoelectric hysteresis loop showing correction for the linear contribution. (d) Example final piezoelectric hysteresis loop, black line indicates a typical loop fit based on equation (2.5-8). (e) Piezoelectric hysteresis loop showing the location of the primary fitting parameters.

reached), the voltage and amplitude centroids (from the raw and fitted data), work of switching (the loop area, once again calculated from the raw and fitted data), *etc.*,. All of these parameters can be plotted as images allowing visualization of the local variance in response which can be correlated to the domain structure. Since these measurements generate "big data" they are ideal candidates to be interpreted using statistical methods. At the most basic level it is possible to create thresholds to partition the data to isolate the response in a domain variant. At a higher level, techniques like principal component analysis can be used to identify regions of variance[332, 333] and k-means clustering can be used to statistically group data amongst a multi-dimensional space.[334] In this work, all instrumentation, instrumentation control, and basic computational processing of conventional piezoelectric hysteresis loops were completed using software and graphical user interfaces designed in Labview™ and Matlab™ designed and provided by Oak Ridge National Laboratory.

2.4.4 Nanobeam Diffraction Strain Mapping

As previously mentioned, typically in literature it is assumed (due to measurement difficulties) that films are either nearly coherently strained or are fully relaxed; however, in actuality, films commonly seek routes to accommodate strain (giving rise to inhomogeneous strains). To fully understand the strain state in the film it is crucial to be able to quantify inhomogeneous strains on an appropriate length scale. Classically, inhomogeneous strain has been quantified using X-ray diffraction; however, this approach is not suitable as it can only measure the average inhomogeneous strain. More recently, high resolution transmission electron microscopy (HR-TEM) geometric phase analysis (GPA) has been employed to locally image inhomogeneous strains in ferroelectric thin films.[166, 335, 336] Once again, this approach is imperfect, as it is unable to accurately resolve strain in highly defective regions (*i.e.* locations with large unit cell rotations) and has a limited field of view.[337, 338] To overcome these limitations we employed a new technique (for the first time in ferroelectrics) based on nanobeam electron diffraction (NBED) that calculates elastic strains and rigid-body crystal rotations directly from nanobeam diffraction patterns.[338] In the TEM, a nanobeam probe is formed and diffraction patterns are collected in a grid pattern while the

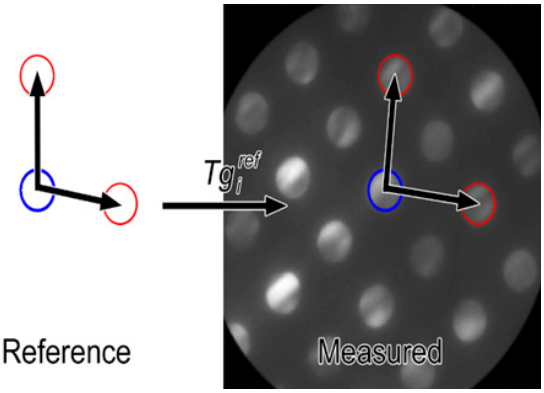

Figure 2.11. Reference mask compared to location of diffraction spots in a measured pattern. Shifts of the diffraction spots between the reference and measured patterns are mapped onto each other using the transformation matrix T.

beam is rastered across the sample. Each diffraction pattern contains information on the crystal orientation and elastic strain which can be calculated from the spacing and angles of the diffraction spots. To do this, the position of the centroids of the diffractions spots are calculated and compared to the positions of the diffractions spots of the unstrained pattern (Figure 2.11). A convolution mask is then constructed in the shape of a NBED disk with the intensity near the edge of the disk being weighted more heavily. This weighting helps avoid dynamic diffraction effects in the disk interiors. A sub-pixel resolution cross-correlation algorithm is then applied to the convolution mask and the individual diffraction patterns to detect the centroids of the NBED disks. A reference spot was selected in the scan and designated as g_i^{ref}. Subsequently, for each diffraction pattern of the transformation matrix T was computed from the diffraction vectors g_i using $g_i = T\, g_i^{ref}$. Polar deconvolution was used to separate the transformation matrix T into a rotation matrix R and a symmetric strain matrix U. In-plane and out-of-plane strains were computed by $\varepsilon_{xx} = 1\text{-}U_{00}$ and $\varepsilon_{yy} = 1\text{-}U_{11}$ and the shear and rotation can be computed using $\varepsilon_{xy} = 1\text{-}R_{01}$ and $\theta = cos^{-1}R_{00}$. Unlike GPA, NBED has few restraints in terms of sample, scan geometry and map area making it the ideal candidate to image inhomogeneous strains in ferroelectric thin films. For example, NBED has been used to map out elastic strains in a GaAs/GaAsP multilayer device over a 1x1 μm region containing significant internal crystal rotations while still maintaining an elastic strain resolution of 0.1%,[338] something that would not be possible using the more restrictive GPA approach.[233]

Chapter 3

Growth and Structural Studies of Single-Layer $PbZr_{1-x}Ti_xO_3$ Thin Films

In this chapter, we explore how composition and strain can be used to tune the crystal and domain structure, and ultimately the dielectric and ferroelectric responses of $PbZr_{1-x}Ti_xO_3$ thin films. We begin with a discussion of how epitaxial strain can be used to modify the crystal and domain structure in $PbZr_{0.2}Ti_{0.8}O_3$ thin films, a model tetragonal ferroelectric. We demonstrate that large strains (~1% tensile strains) can be achieved due to strain accommodation *via* ferroelastic domain formation; however, similar magnitudes of compressive strain cannot be achieved. We observe that these films form classical *c/a/c/a* domain structures whose *a* domain fraction increases with increasing tensile strain. We explore how the presence of strain and the density of ferroelastic domain structures influences the ferroelectric hysteresis and dielectric permittivity (in terms of the reversible and irreversible domain wall contributions) in these heterostructures. In the second section of this chapter, we investigate how composition and strain influences the crystal, domain structure, and ultimately the dielectric and ferroelectric responses of $PbZr_{1-x}Ti_xO_3$ thin films. We observe that $PbZr_{0.52}Ti_{0.48}O_3$ and $PbZr_{0.8}Ti_{0.2}O_3$ form dense (possibly nanoscale) mosaic domain structures. These heterostructures as a result of their dense ferroelastic domain structure give rise to highly tilted ferroelectric hysteresis loops and large dielectric responses. We show that these enhanced dielectric responses (which are maximized in $PbZr_{0.52}Ti_{0.48}O_3$ heterostructures) are primarily attributed to large extrinsic contributions to the dielectric permittivity and the possibility of polarization rotation (in $PbZr_{0.52}Ti_{0.48}O_3$ heterostructures). This chapter while providing some new insight is included primarily to set a foundation for our discussion in the chapters which follow.

3.5 Design of Epitaxial $PbZr_{0.2}Ti_{0.8}O_3$ Thin Films

When designing heterostructures for a specific application it is important to consider the crystal and domain structure, lattice mismatch, crystallographic orientation, chemistry, electrode material and configuration, and much more, as they can all significantly affect the susceptibilities of the ferroelectric layer. In this thesis, we limit the scope of our discussion to ferroelectric layers within the $PbZr_{1-x}Ti_xO_3$ family. $PbZr_{1-x}Ti_xO_3$ is a good prototypical ferroelectric systems to study as it possesses large susceptibilities (*i.e.* dielectric, piezoelectric, pyroelectric, *etc.*), has a large polarization, low coercive fields, and high Curie temperatures.[61] Additionally, the $PbZr_{1-x}Ti_xO_3$ family offers useful structural flexibility through the application of chemical pressure (by varying Zr/Ti ratios) creating competition between tetragonal (Ti-rich) and rhombohedral (Zr-rich) phases (Figure 3.1a).[339] Between these phases exists a nearly temperature-independent phase boundary called the morphotropic phase boundary (MPB, occurring at x = 0.48).[53, 340, 341] In addition to the structural changes that can occur, the bulk lattice parameters also evolves with composition. Specifically, the lattice parameter evolution is nearly linear throughout the entire compositional range, with the exception of at the MPB where there is a discontinuous change in lattice parameter and slope of the lattice parameter evolution (Figure 3.1b).

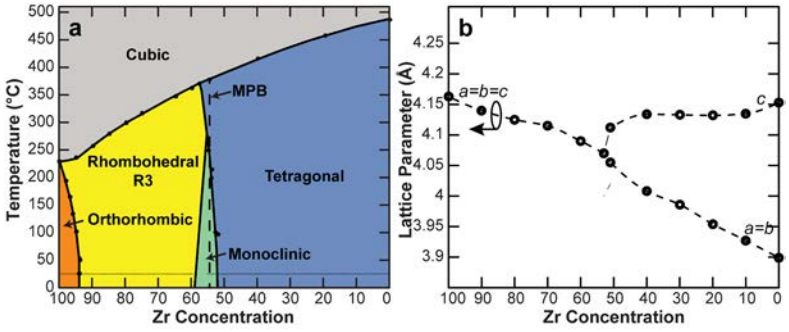

Figure 3.1. (a) Phase diagram of the $PbZr_{1-x}Ti_xO_3$ system. (b) Lattice parameter evolution with increasing chemical compositions.

Beyond chemical pressure, epitaxial thin-film strain can be utilized to further alter the structure and, in turn, the response of ferroelectric layer.[13] For instance, much work has been focused on Ti-rich $PbZr_{1-x}Ti_xO_3$ variants, which in general, has shown that lattice mismatch $\left(\varepsilon_m = \frac{a_s - a_b}{a_b} x100\%\right)$ with the substrate acts *via* the Poisson relationship (assuming that the Poisson ratio is ~0.3 for most ferroelectric materials)[53, 265] to exert a change in the out-of-plane lattice parameter. If the elastic compliances (S_{xx}) and electrostrictive coefficients (Q_{xx}) of the film are known, a more precise prediction of the out-of-plane lattice parameter is possible (equation 3.1).[111]

$$c = a_c\left\{1+\left[\frac{2S_{12}\varepsilon_m}{S_{11}+S_{12}} + P_3^2\left(Q_{11} - \frac{2S_{12}Q_{12}}{S_{11}+S_{12}}\right)\right]\right\} \tag{3.1}$$

At a critical point, however, the strain can no longer persist and the material accommodates the growing strain energy by forming defects or, if possible, domain structures.[84, 342] It has been well established that strain and the presence of domains can dramatically influence the magnitude of the spontaneous polarization, T_c, dielectric, piezoelectric, and pyroelectric susceptibilities, and much more.[125, 182, 301] Despite these observations, the limited availability of closely lattice match substrates and electrodes (up until recently) has relegated the study of strain-engineering in ferroelectrics thin films primarily to the Ti-rich $PbZr_{1-x}Ti_xO_3$ variants which are closely lattice matched to the most common commercially available perovskite substrates and electrode materials. In the first part of this chapter, we demonstrate the effects of epitaxial strain in $PbZr_{0.2}Ti_{0.8}O_3$, a prototypical tetragonal ferroelectric, to explore how strain can influence crystal and domain structure, and ultimately how these strain-engineered structures impacts the electrical, dielectric, and ferroelectric responses. In the second part of this chapter we expand our treatment to include compositions across the $PbZr_{1-x}Ti_xO_3$ compositional spectrum to, once again, determine the effect of composition, crystal and domain structure on the ferroic susceptibilities.

3.6 Growth of Epitaxial $PbZr_{1-x}Ti_xO_3$ Thin Films

All heterostructures used in this treatment were grown using pulsed-laser deposition. All films were supported on a thin layer (15-30 nm) of $SrRuO_3$ grown at 635-700 °C at a pressure of 100 mTorr of oxygen, at a laser fluence of 1-1.7 J/cm^2 (see Appendix B for the methodology used to calculate laser fluence). A laser repetition rate of 10-16 Hz was used to grow $SrRuO_3$. Following $SrRuO_3$ growth, the $PbZr_{1-x}Ti_xO_3$ layer was grown at 635-680 °C in 100-250 mTorr of oxygen. For $PbZr_{1-x}Ti_xO_3$ growth, the laser fluence was between 1.2-2 J/cm^2 at a repetition rate of 1-10 Hz. $PbZr_{1-x}Ti_xO_3$ was grown from targets which are 10% Pb excess to compensate for any potential Pb loss. For all growths the target-heater spacing was fixed at a distance of 6.5 cm producing growth rates of 7-9 nm/min and 3.5-50 nm/min for the $SrRuO_3$ and $PbZr_{1-x}Ti_xO_3$ layers, respectively. Following growth all films were cooled to room temperature at a rate of 5 °C/min in 760 Torr of oxygen.

3.7 Crystal and Domain Structure, and Ferroic Responses of $PbZr_{0.2}Ti_{0.8}O_3$ Heterostructures

3.7.1 X-ray Diffraction Studies (XRD) of $PbZr_{0.2}Ti_{0.8}O_3$ Heterostructures

To provide a foundation for our explorations of $PbZr_{1-x}Ti_xO_3$ thin films with various chemistries it is worth discussing in brevity the effects of misfit strain on the crystal, domains structure and ferroic susceptibilities in $PbZr_{0.2}Ti_{0.8}O_3$. The results presented in this chapter are consistent with recently published results.[125, 194] $PbZr_{0.2}Ti_{0.8}O_3$ is a prototypical ferroelectric of the tetragonal $PbZr_{1-x}Ti_xO_3$ family with lattice constants (at 300 K) of a = 3.94 Å and c = 4.12 Å.[316, 343] This composition of $PbZr_{1-x}Ti_xO_3$ has been used and studied extensively due to its simple structure, relative high T_c (~420 °C), and robust spontaneous polarization (P_s ~65-70 μC/cm²). $PbZr_{0.2}Ti_{0.8}O_3$ is particularly attractive to study in thin film form as there are many commercially available substrates capable of producing 00*l* oriented films with misfit strains of ~±1%.[301] To study the effects of strain on the crystal and domain structures we grew 100 nm $PbZr_{0.2}Ti_{0.8}O_3$/15 nm $SrRuO_3$/heterostructures on $SrTiO_3$ (001), $DyScO_3$ (110), $TbScO_3$ (110), and $GdScO_3$ (110) single crystal substrates (Crystec GmbH, Berlin). These substrates were chosen as they provide a lattice mismatch with the $PbZr_{0.2}Ti_{0.8}O_3$ of -0.8%, 0.3%, 0.7%, and 0.9%, respectively.

Detailed XRD 2θ-ω scans of the heterostructures reveal that all heterostructures are single phase (00*l*)-oriented (Appendix C). High-resolution scans about the 002-diffraction condition reveal that the out-of-plane lattice parameter of the $PbZr_{1-x}Ti_xO_3$ layer increases (decreases) with increasing compressive (tensile) strain. As the tensile strain increases, the necessary fraction of *a* domains is expected to, and has been previously shown to increase.[81-83, 125, 194] These *a* domains, due to geometric reasons are tilted away from the substrate normal,[81-83] and therefore, a 2θ-ω scan along the substrate diffraction condition does not satisfies the diffraction condition. To observe these *a* domains, we conducted XRD reciprocal space maps (RSM) which measures a series of 2θ-ω scans, at various ω values, about the 002-diffraction condition of $PbZr_{1-x}Ti_xO_3$. These RSM show no

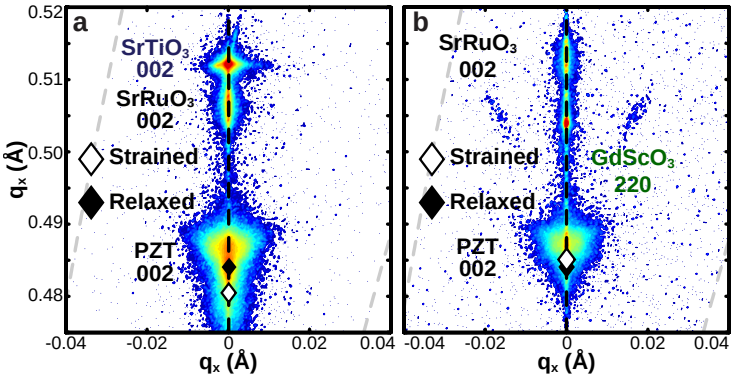

Figure 3.2. Symmetric reciprocal space maps about the 002-diffraction condition for $PbZr_{0.2}Ti_{0.8}O_3$ for films grown on substrates with increasing tensile strain (a) SrTiO3 (001) and (b) $GdScO_3$ (110).

evidence of *a* domains in the compressively strained heterostructure on $SrTiO_3$ (Figure 3.2a), however, as the tensile strain increases, as is the case for the heterostructures on $GdScO_3$ (Figure 3.2b), a peak from the in-plane oriented *a* domains emerges. The intensity of this peak is found to increase with increasing tensile strain an indication that the volume fraction of in-plane oriented *a* domains increases with tensile strain (Appendix C). To further characterize the strain state detailed asymmetric RSM about the 103-diffraction condition for the $PbZr_{1-x}Ti_xO_3$ were measured (Appendix C). It was found that all heterostructures were coherently strained to the substrates, with the exception of those heterostructures grown on $SrTiO_3$ which show indication of relaxation.

3.7.2 Piezoresponse Force Microscopy Studies of $PbZr_{0.2}Ti_{0.8}O_3$ Heterostructures

From the XRD studies we observed diffraction peaks corresponding to in-plane oriented *a* domains. To directly image and determine the density and spatial dependence of these domain structures, high-resolution tapping mode height images (Figure 3.3a-d) and piezoresponse force microscopy images of the domain structures were obtained (Figure 3.3e-h). The presence of *a* domains can be seen by looking for bands along the $[100]_{c/pc}$ or $[010]_{c/pc}$ directions which have crystallographic tilts at the surface, a reduction (enhancement) in local piezoresponse in the out-of-plane (in-plane) direction, and a change in phase of the measured piezoresponse. Starting with the heterostructures grown on $SrTiO_3$ (Figure 3.3a,e), which imposes a 0.8% compressive strain on the

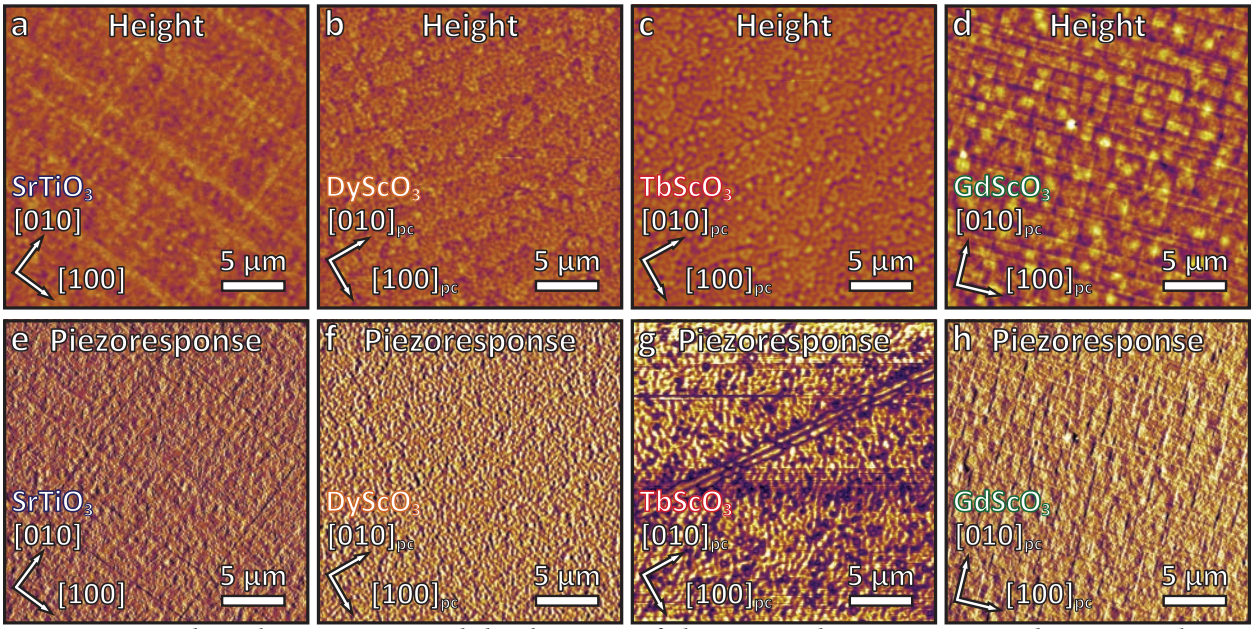

Figure 3.3. High resolution tapping mode height images of $PbZr_{0.2}Ti_{0.8}O_3$ heterostructures under various substrate imposed misfit strains on (a) $SrTiO_3$ (001), (b) $DyScO_3$ (110), (c) $TbScO_3$ (110), and (d) $GdScO_3$ (110). Piezoresponse amplitude images of $PbZr_{0.2}Ti_{0.8}O_3$ heterostructures on (e) $SrTiO_3$ (110), (f) $DyScO_3$ (110). (g) $TbScO_3$ (110), and (h) $GdScO_3$ (110).

$PbZr_{1-x}Ti_xO_3$ layer we notice a clearly defined cross-hatched pattern which would commonly be interpreted as *a* domains. This observation is a somewhat surprising considering the XRD studies do not show any indication of *a* domains. This seeming discrepancy might be an indication that these topographic structures are not actually *a* domain, but instead, surface ripples, which result from changes in surface diffusion and crystal growth, caused by strain fields from misfit dislocations that form as the film relaxes.[344] Now focusing on the heterostructures grown on $DyScO_3$ (Figure 3.3b,f) which imposes a small tensile misfit strain of 0.3%, there is a single, narrow *a* domain visible, an expected result considering the small tensile misfit strain. Moving on to the heterostructures grown on substrates with increasing tensile strain, we observe, as expected, that the density and volume fraction of *a* domains increases slightly and significantly in the heterostructures grown on $TbScO_3$ (Figure 3.3c,g) and $GdScO_3$ (Figure 3.3d,h), respectively.

3.7.3 Dielectric and Ferroelectric Responses of $PbZr_{0.2}Ti_{0.8}O_3$ *Heterostructures*

To explore how the evolution of crystal and domain structure influences the ferroelectric response parallel plate capacitors were fabricated using the MgO hard mask process (as described in section 2.2.1) ferroelectric hysteresis loops were measured at various frequencies from 1-100 kHz. Here, we show ferroelectric hysteresis loops measured at 10 kHz for all heterostructures studied in this treatment (Figure 3.4a). Due to the high quality of the heterostructures measurements of ferroelectric hysteresis reveal square hysteresis loops, with near closure, large saturation, and remanent polarization on all substrates. Additionally, due to the symmetric nature of the electrodes (see Appendix C for *I-V* measurements) there is negligible electrode induced imprint which commonly results in voltage shifted hysteresis loops. From these hysteresis loop measurements the coercive fields were found to be nearly invariant on all substrates. While P_{sat} and P_{rem} was found to increase (from 60 to 100 μC/cm²) with increasing compressive strain (from $GdScO_3$ to $SrTiO_3$). This observation can be attributed to two factors: 1) as the compressive strain increases the tetragonality of the unit cell also increases, causing the polarization to increase, and 2) as the tensile strain increases the volume

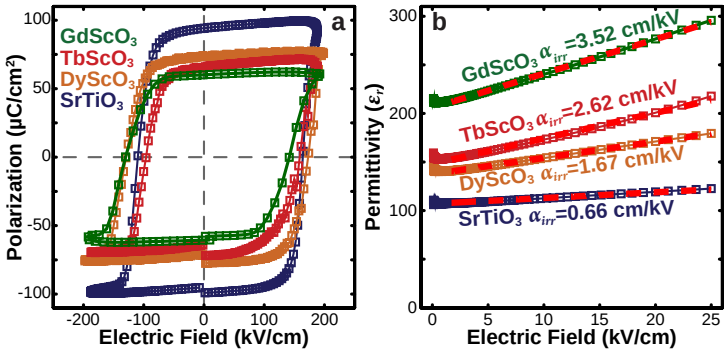

Figure 3.4. Room temperature (a) ferroelectric hysteresis loops (b) Dielectric permittivity as a function of low-field biases (Rayleigh studies) of $PbZr_{0.2}Ti_{0.8}O_3$ heterostructures on various substrates.

fraction of *a* domains increases, and since these *a* domains are in-plane polarized they do not contribute to the out-of-plane polarization.

It has been well established that the presence of domains can contribute to the dielectric response.[289, 294, 295] To understand how the domain structure influences the dielectric susceptibility in this model system detailed Rayleigh studies were undertaken (as described in section 2.2.2, Figure 3.4b). By looking at the dielectric permittivity in region I (the low-field regime), which measures the intrinsic and reversible domain wall contributions, it is evident that the dielectric permittivity scales with the tensile strain, and in turn, the domain density. It is worth noting that the low dielectric response observed in the $SrTiO_3$ heterostructures is again an indication that the observed topological features (from the PFM studies) are not actually *a* domains, and instead are of a different origin (such as surface ripples). Now, focusing on region II (the Rayleigh regime), the slope in this region, once again, increases monotonically with increasing tensile strain/*a* domain density, as expected. By fitting the linear portion of the response in region II, α_{irr} a measure of the irreversible domain wall contribution can be extracted. α_{irr}, once again, as expected, is found to increase with increasing tensile strain/*a* domain density.

3.8 Design and Growth of Epitaxial $PbZr_{1-x}Ti_xO_3$ Heterostructures

Armed with this information we can expand our treatment to look at the influence of composition on the crystal and domain structure of $PbZr_{1-x}Ti_xO_3$ heterostructures with various chemistries. To do this, we grew a series of heterostructures using the same methods and conditions as previously described. For this study we focus on three compositions $PbZr_{0.2}Ti_{0.8}O_3$, $PbZr_{0.52}Ti_{0.48}O_3$, and $PbZr_{0.8}Ti_{0.2}O_3$. All heterostructures in this study were supported on 15-20 nm of $SrRuO_3$ bottom electrodes and the thickness of the $PbZr_{1-x}Ti_xO_3$ layer was fixed at ~100 nm thick. When increasing the Zr concentration the bulk lattice parameter increases and the phase evolves from tetragonal to rhombohedral. These changes in the crystal structure and limited availability of commercially available substrate and electrode materials makes it impossible apply a similar degree of strain across this compositional range. Instead, for this study we chose to grow all heterostructures on $GdScO_3$ (110) a_{pc}=3.973 Å. We chose $GdScO_3$ as it has one of the largest in-plane lattice parameters of the commonly available substrates upon which high-quality, single-phase, smooth, and epitaxially strained $SrRuO_3$ bottom electrodes can be grown. In turn, as we vary the composition across

the $PbZr_{1-x}Ti_xO_3$ spectrum the lattice mismatch evolves from 0.8% tensile for $PbZr_{0.2}Ti_{0.8}O_3$, to 1.9% compressive for $PbZr_{0.52}Ti_{0.48}O_3$, to 3.5% compressive for $PbZr_{0.8}Ti_{0.2}O_3$.

3.8.1 X-ray Diffraction Studies of $PbZr_{1-x}Ti_xO_3$ Heterostructures

Asymmetric RSM about the 332 diffraction condition of the substrate, 103 diffraction condition of the $PbZr_{1-x}Ti_xO_3$ film are provided (Figure 3.5a-c). Starting with the $PbZr_{0.2}Ti_{0.8}O_3$ heterostructure (Figure 3.5a). We notice that the $PbZr_{0.2}Ti_{0.8}O_3$ layer is coherently strained having nearly the same in-plane lattice parameter (q_x value) as the substrate. Moving on to the $PbZr_{0.52}Ti_{0.48}O_3$ heterostructures (Figure 3.5b), there is almost no spectral weight located near the expected strained peak position, indicating that the film is completely relaxed. The minimal spectral weight located near the strained peak position indicates the strain relaxation happens exceedingly fast. Now focusing on the $PbZr_{0.8}Ti_{0.2}O_3$ heterostructure (Figure 3.5c), we again notice that the film is completely relaxed. Taking a closer look however, there is significant more spectral weight located near the theoretically strained peak position, indicating that strain relaxation happens more gradually eventually reaching complete relaxation at some finite thickness. This result is somewhat surprising when considering that the $PbZr_{0.52}Ti_{0.48}O_3$ heterostructures relaxed much more rapidly despite having a smaller misfit strain (1.9% compared to 3.5%). This difference in the rate of strain relaxation is likely related to the multiplicity of energetically equivalent phases and domain variants which can exist in $PbZr_{1-x}Ti_xO_3$ compositionally close to the MPB, which could allow for the relaxation of strain in ways not possible in $PbZr_{0.8}Ti_{0.2}O_3$.[345-347]

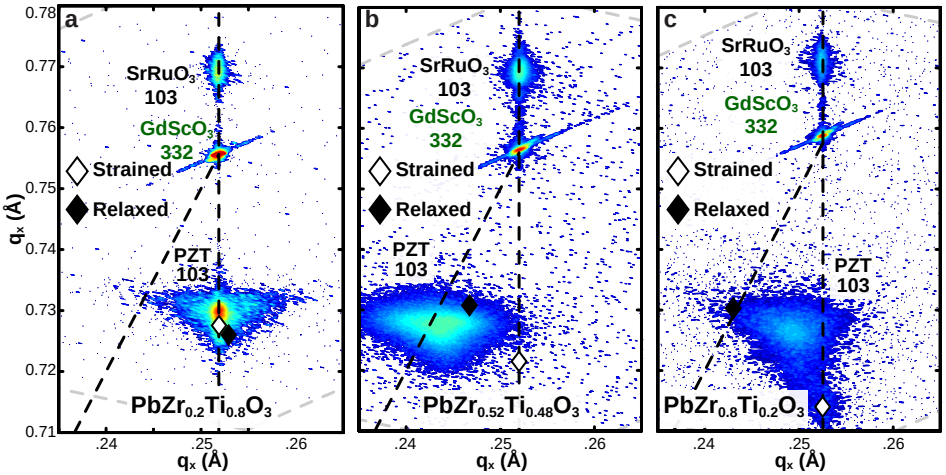

Figure 3.5. Asymmetric reciprocal space maps about the 103-diffraction condition for (a) $PbZr_{0.2}Ti_{0.8}O_3$ (b) $PbZr_{0.52}Ti_{0.48}O_3$ (c) $PbZr_{0.8}Ti_{0.2}O_3$ grown on $SrRuO_3$ (15 nm)/$GdScO_3$ (110).

3.8.2 *Piezoresponse Force Microscopy Studies of $PbZr_{1-x}Ti_xO_3$ Heterostructures*

In addition to X-ray diffraction studies the domain structure of these heterostructures can be imaged using PFM. We show height, piezoresponse and phase images for all heterostructures studied (figure 3.6a-i). Starting again with the $PbZr_{0.2}Ti_{0.8}O_3$ heterostructures (Figure 3.6a-c) we observe a typical *c*/*a*/c/*a* domain structure consisting of out-of-plane polarized *c* domains interspersed with a high density of in-plane oriented *a* domains. As previously mentioned, this is the expected domain structure as the tensile epitaxial strain drives the formation of *a* domains to accommodate the strain. Now focusing on the PFM of the $PbZr_{0.52}Ti_{0.48}O_3$ heterostructures (Figure 3.6d-f), we observe very smooth films [root-mean-square (rms) surface roughness <0.5 nm]. The PFM images (both phase and amplitude) reveals some contrast; however, the structure is mosaic in nature having no crystallographic order. The observed domain structure has features which are exceedingly small and are likely well below the lateral resolution limitation of PFM ~20-50 nm. Such a domain structure with nanometer scale domain features is expected in $PbZr_{0.52}Ti_{0.48}O_3$, as it

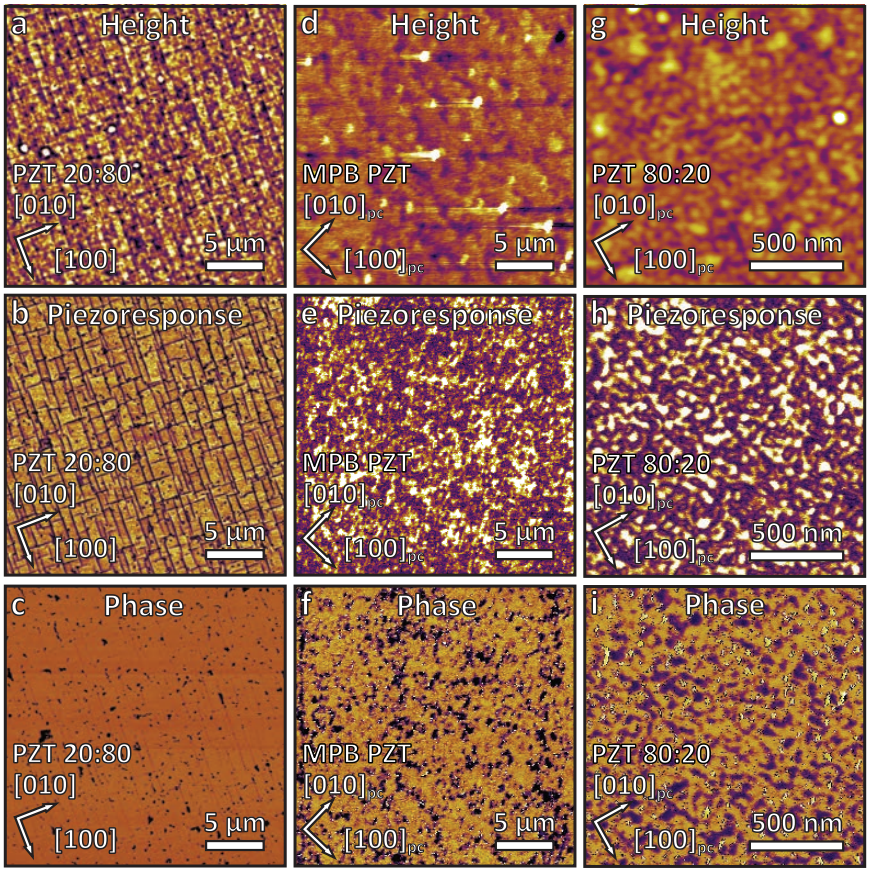

Figure 3.6. Images of topography, and piezoresponse amplitude and phase of (a-c) $PbZr_{0.2}Ti_{0.8}O_3$ (d-f) $PbZr_{0.52}Ti_{0.48}O_3$ (g-i) $PbZr_{0.8}Ti_{0.2}O_3$ grown on $SrRuO_3$ (15 nm)/$GdScO_3$ (110). Vertical height and phase scales are normalized to 4 nm and 180° respectively.

has been predicted that at the MPB the flat energy landscape facilitates the formation of nanoscale, or nano-twinned domains.[163, 348] Finally, in the $PbZr_{0.8}Ti_{0.2}O_3$ heterostructures (Figure 3.6g-i), we again observe very smooth films (rms surface roughness <0.5 nm) and similar mosaic domain structures with minimal crystallographic order. Similar to the $PbZr_{0.52}Ti_{0.48}O_3$ heterostructures, the domain structure in the $PbZr_{0.8}Ti_{0.2}O_3$ heterostructures is exceedingly fine, once again possibly below the resolution limitation of PFM. This result indicates that relaxed heterostructures on the Zr-rich side of the phase diagram form a high density of ferroelectric/ferroelastic domains which should result in large extrinsic contributions to the ferroelectric susceptibilities.

3.8.3 Dielectric and Ferroelectric Responses of $PbZr_{1-x}Ti_xO_3$ Heterostructures

To study the influence of the composition, crystal and domain structure of the 100 nm $PbZr_{1-x}Ti_xO_3$ heterostructures on the dielectric and ferroelectric responses symmetric $SrRuO_3$ top contacts were fabricated as previously described. To begin our discussion, we start by studying the ferroelectric hysteresis loops of these heterostructures. Ferroelectric hysteresis loops were measured for all samples at frequencies of 1-100 kHz. Here, for brevity we show just the ferroelectric hysteresis loops measured at 10 kHz (Figure 3.7a). All hysteresis loops show clear ferroelectric hysteresis with well-defined saturation and remanent polarization. All loops show minimal evidence of leakage and have near closure, an indication of the high quality of the heterostructures. Starting with the $PbZr_{0.2}Ti_{0.8}O_3$ heterostructures (shown in blue) the hysteresis loops have a square shape and large saturation polarization (~63 μC/cm²). The hysteresis loops show a large remanent polarization which is nearly identical in magnitude to the saturation polarization. As mentioned previously, the saturation and remanent polarization measured in the $PbZr_{0.2}Ti_{0.8}O_3$ heterostructures on $GdScO_3$ are significantly lower than observed in bulk as a result of the tensile strain and large volume fraction of in-plane oriented *a* domains. Now focusing on the hysteresis loops of the $PbZr_{0.8}Ti_{0.2}O_3$ heterostructures (red curve), we notice that both the magnitude of the saturation polarization (coercive field) is slightly (significantly) lower than observed in the $PbZr_{0.2}Ti_{0.8}O_3$ heterostructures. This slight

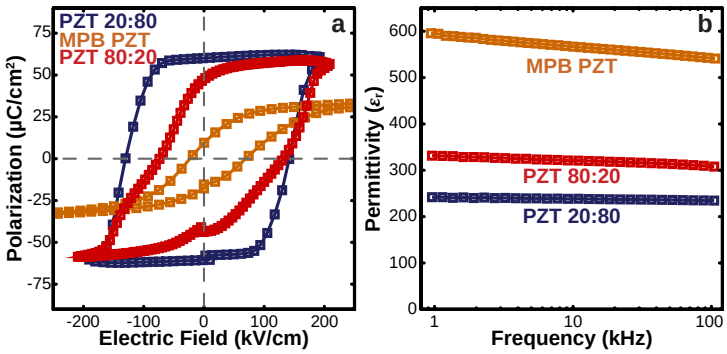

Figure 3.7. (a) ferroelectric hysteresis loops measured at 10 kHz and (b) dielectric permittivity as a function of frequency for $PbZr_{1-x}Ti_xO_3$ of various compositions.

reduction in saturation polarization is expected as the $PbZr_{0.8}Ti_{0.2}O_3$ heterostructures are rhombohedral, having a polarization oriented along the <111> slightly misaligned with the measurement direction (i.e., [001]). The remanent polarization in the $PbZr_{0.8}Ti_{0.2}O_3$ heterostructure, while still large, is significantly lower than the saturation polarization, an indication that the film might be elastically driven to back switch (at least partially) from its poled state. The hysteresis loops are also significantly less square being highly tilted away from the polarization axis. This difference in loop shape implies that the heterostructures switch more gradually than in the $PbZr_{0.2}Ti_{0.8}O_3$ heterostructures. The highly-tilted hysteresis loops observed could be an indication that switching occurs in a multifaceted manner, where certain domain variants switch at different coercive biases, or where switching includes intermediate metastable states. Finally, looking at the $PbZr_{0.52}Ti_{0.48}O_3$ heterostructures (green curve), we notice a significant reduction in both the coercive field, saturation and remanent polarization, an observation consistent with previous studies on textured polycrystalline thin films.[349, 350] Additionally, the hysteresis loops in the $PbZr_{0.52}Ti_{0.48}O_3$ are tilted to a greater extent than the $PbZr_{0.8}Ti_{0.2}O_3$ heterostructures. The tilted nature of the loops could possibly be related to a more continuous nature of ferroelectric switching involving the possibility of polarization rotation towards the field axis (as the structure transitions from rhombohedral to tetragonal) through a bridging monoclinic phase which has been theorized,[351, 352] and experimentally observed,[353-356] in ferroelectrics near MPB. All told, these studies of the ferroelectric hysteresis of epitaxial heterostructures across the $PbZr_{1-x}Ti_xO_3$ compositional spectrum reveal the saturation and remanent polarization, coercive fields, and general loop shape are highly dependent on the composition, strain state, and domain structure. It is observed that heterostructures which are predominately polarized along the out-of-plane direction (i.e., $PbZr_{0.2}Ti_{0.8}O_3$) have square hysteresis loops with large saturation polarization, while heterostructures with a high density of domains (*i.e.*, $PbZr_{0.52}Ti_{0.48}O_3$ and $PbZr_{0.8}Ti_{0.2}O_3$) have reduced coercive fields and highly tilted ferroelectric hysteresis loops where the remanent polarization is significantly reduced compared to the saturation polarization.

Beyond influencing the ferroelectric hysteresis, the chemical composition and domain structure has a significant influence on the dielectric susceptibility. For all heterostructures studied we measured the dielectric permittivity as a function of frequency (between 1-100 kHz) with an ac excitation voltage of 8 mV (Figure 3.7b). Prior to these measurement Rayleigh studies (at 1

kHz) were completed to ensure the measured dielectric response was entirely reversible in nature. When analyzing the frequency dependent dielectric response there are two key attributes to consider. First, since the intrinsic dielectric response across the $PbZr_{1-x}Ti_xO_3$ spectrum is known to be nearly invariant with composition,[357] all significant differences in the dielectric permittivity can be attributed to differences in the reversible extrinsic domain wall contributions to the dielectric permittivity. Secondly, by analyzing the frequency dispersion (or quenching of the dielectric response) from the slope of the frequency dependent dielectric response the relative significance of extrinsic ferroelastic domain wall contribution can be assessed.[297, 358-360]

Looking first at the magnitude of the dielectric permittivity we notice that the dielectric permittivity is lowest in the $PbZr_{0.2}Ti_{0.8}O_3$ (~235), intermediate in the $PbZr_{0.8}Ti_{0.2}O_3$ (~340) and maximum in the $PbZr_{0.52}Ti_{0.48}O_3$ heterostructures (~590). This trend makes sense when considering the domain structure. First, considering the $PbZr_{0.2}Ti_{0.8}O_3$ heterostructures, which have a high density of ferroelastic *a* domains, the dielectric permittivity was found to be significantly higher than the intrinsic permittivity, which for $PbZr_{1-x}Ti_xO_3$ is ~90.[301] This result indicates that a large fraction of the response can be attributed to extrinsic domain wall contributions to the dielectric permittivity, a result consistent with prior reports.[125, 194] Moving on to the $PbZr_{0.8}Ti_{0.2}O_3$ heterostructures, which once again have a dense mosaic domain structure, we observe, as expected, an increase in the dielectric permittivity to ~340. Once again this large permittivity can be primarily attributed to extrinsic domain wall contributions to the permittivity. Finally, in the $PbZr_{0.52}Ti_{0.48}O_3$ heterostructures we observe a significant increase in dielectric permittivity (compared to the $PbZr_{0.2}Ti_{0.8}O_3$ and $PbZr_{0.8}Ti_{0.2}O_3$ heterostructures) to ~590, implying that extrinsic domain wall contributions dramatically enhance the dielectric response at the MPB. While there is no visual evidence of an increased domain fraction in the $PbZr_{0.52}Ti_{0.48}O_3$ heterostructures, compared to the $PbZr_{0.8}Ti_{0.2}O_3$ heterostructures (due to instrumental limitations), the large dielectric response observed provides credence to the theoretical predictions which predict a nanodomain and/or nanotwinned domain structures. [351-356] Finally, focusing on the frequency dispersion in dielectric response, we observe the same trend, where the magnitude is minimum in the $PbZr_{0.2}Ti_{0.8}O_3$, intermediate in the $PbZr_{0.8}Ti_{0.2}O_3$, and maximum in $PbZr_{0.52}Ti_{0.48}O_3$. This once again indicates that the large dielectric response observed in these heterostructures is primarily the result of a high density of ferroelastic domains and their extrinsic contributions to the dielectric permittivity

3.9 Conclusions

In conclusion, we have grown a series of high-quality $PbZr_{1-x}Ti_xO_3$ heterostructure of various compositions and strain states. We demonstrate that large strains up to ~1% can be stabilized and evaluate the influence of strain and chemistry on the crystal and domain structure, and ultimately the dielectric and ferroelectric responses of $PbZr_{1-x}Ti_xO_3$ heterostructures. We show in a model tetragonal ferroelectric, $PbZr_{0.2}Ti_{0.8}O_3$, that the density of ferroelastic *a* domains can be tuned using epitaxial strain and that the presence of these domains can significantly enhance the dielectric responses, a result consistent with prior reports. Using this foundational knowledge, we explore the crystal and domain structure, dielectric, and ferroelectric responses of $PbZr_{1-x}Ti_xO_3$ heterostructures of various chemical compositions. Specifically, we observe that strain relaxation does not follow trends based on misfit strain alone, and instead, occurs more rapidly at the MPB where a multiplicity of structural variants are thermodynamically stable. Both the $PbZr_{0.52}Ti_{0.48}O_3$ and $PbZr_{0.8}Ti_{0.2}O_3$ heterostructures are found to have dense mosaic (potentially nanoscale) domain structure, highly tilted ferroelectric hysteresis loops, and large extrinsic dielectric responses (all of which are maximized in $PbZr_{0.52}Ti_{0.48}O_3$). We posit that the enhanced responses at the MPB are likely attributed the presence of a nanodomain and/or nanotwined domain structures, and the possibility of field induced polarization rotation.

Chapter 4

Tuning Susceptibility *via* Misfit Strain in "Relaxed" Morphotropic Phase Boundary $PbZr_{1-x}Ti_xO_3$ Epitaxial Thin Films

In the previous chapter, we showed how epitaxial strain can be used as a powerful tool to manipulate the properties of ferroelectric materials. But despite extensive work in this regard, few studies have explored the effect of epitaxial strain in $PbZr_{0.52}Ti_{0.48}O_3$. Here, we explore how epitaxial strain impacts the structure and properties of 75 nm thick heterostructures of $PbZr_{0.52}Ti_{0.48}O_3$. We grow and show that single-phase, fully-epitaxial films possess "relaxed" or nearly "relaxed" structures despite growth on a range of substrates. Subsequent studies of the dielectric and ferroelectric properties reveal films with exceedingly low leakage currents which facilitates the measurement of low-loss hysteresis loops at frequencies as low as 30 mHz and dielectric response at background dc bias fields as large as 850 kV/cm. Despite a seeming insensitivity of the crystal structure to the epitaxial strain, the polarization and switching characteristics are found to vary with substrate. The elastic constraint from the substrate produces residual strains that dramatically alter the electric-field response including quenching domain wall contributions to the dielectric permittivity and suppressing field-induced structural reorientation. These results demonstrate that substrate mediated epitaxial strain in $PbZr_{0.52}Ti_{0.48}O_3$ heterostructures is more nuanced than in conventional ferroelectrics with discretely defined phases, yet can have a marked effect on the material properties and its responses.

4.1 Introduction: The Morphotropic Phase Boundary in $PbZr_{1-x}Ti_xO_3$

In Chapter 3, we showed how chemistry and epitaxial strain can be used to engineer the crystal and domain structure, and ferroic responses in $PbZr_{1-x}Ti_xO_3$ across the compositionally spectrum. While there have been many studies focusing on the effects of epitaxial strain in Ti-rich $PbZr_{1-x}Ti_xO_3$ variants,[125, 194] considerably less work, however, has focused on using epitaxial strain to manipulate $PbZr_{0.52}Ti_{0.48}O_3$ and, considering the relatively flat energy landscape near the MPB which eliminates the discrete nature of structural variants, the effects of such strain on the evolution of the structure and properties are expected to be less intuitive.[345-347] What little work that does exist in this regard, focuses on the structural evolution of relatively thick films (>200 nm) with minimal emphasis on how the structure or potential strain influences the properties.[57, 350, 361]

4.2 Design of Epitaxial $PbZr_{0.52}Ti_{0.48}O_3$ Heterostructures

75 nm $PbZr_{0.52}Ti_{0.48}O_3$/25 nm $SrRuO_3$/$SrTiO_3$ (001) (a = 3.905 Å), $DyScO_3$ (110) (pseudocubic a_{pc} = 3.944 Å), and $NdScO_3$ (110) (pseudocubic a_{pc} = 4.013 Å) heterostructures were grown using PLD. For all heterostructures, an on-axis geometry with a target-to-substrate spacing of 6.35 cm was used. The $SrRuO_3$ bottom electrode was deposited from a stoichiometric target at 645 °C, in a 100 mTorr pressure of oxygen, at a laser fluence of 1.2 J cm^{-2}, with a laser repetition rate of 14 Hz. The $PbZr_{0.52}Ti_{0.48}O_3$ layer was deposited from a $Pb_{1.1}Zr_{0.52}Ti_{0.48}O_3$ target, at 625 °C, in a 200 mTorr pressure of oxygen, at a laser fluence of 1.3 J cm^{-2}, at a laser repetition of 2 Hz. Following growth samples were cooled in 700 mTorr of oxygen at a rate of 5 °C/min. On the various substrates the compressive lattice mismatch between the tetragonal- (rhombohedral-) versions of $PbZr_{0.52}Ti_{0.48}O_3$ and $SrTiO_3$, $DyScO_3$, and $NdScO_3$ are 3.58% (4.05%), 2.62% (3.10%), and 0.91% (1.40%), respectively.

4.3 Surface and Domain Structure of $PbZr_{0.52}Ti_{0.48}O_3$ Heterostructures

Atomic force microscopy (AFM) images reveal smooth, atomically-terraced surfaces with rms surface roughness of <0.5 nm on all samples. For brevity we show a characteristic topography image obtained from a heterostructure grown on a $SrTiO_3$ (001) substrate (Figure 4.1a). The domain structures of the heterostructures were probed using vertical band-excitation piezoresponse force microscopy (BE-PFM). All BE-PFM images were acquired using a Budget Sensors Multi75-G, Cr/Pt coated cantilevers. Images were acquired using a waveform of total sinc character with a

peak-to-peak amplitude of 1 V and a bandwidth of 60 kHz centered on the cantilever contact resonance frequency. At each point the band-excitation sense pulse was repeated 4 times and the average response was fit. Typical BE-PFM amplitude images for all heterostructures are displayed (Figure 4.1b–d). There are very few published PFM images of the domain structure of epitaxial $PbZr_{0.52}Ti_{0.48}O_3$ and the application of BE-PFM imaging provides potentially the best opportunity to image this fine-scale and highly-susceptible domain structure.[328] From our imaging, all films exhibit similar mosaic domain structures with features on the order of 25-200 nm. The scale of these features is at, or near, the lateral resolution limit of PFM determined by the finite tip radius

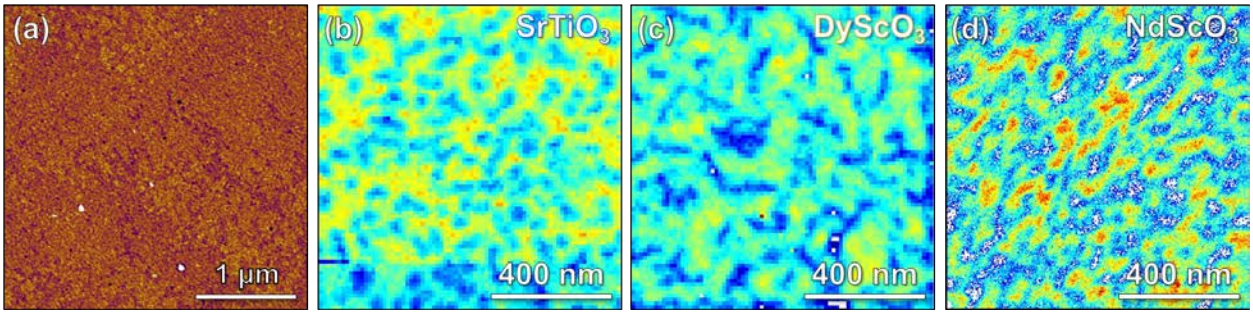

Figure 4.1. (a) Atomic force microscopy topography image of a typical 75 nm $PbZr_{0.52}Ti_{0.48}O_3$/25 nm $SrRuO_3$/$SrTiO_3$ (001) heterostructure. Representative vertical band-excitation piezoresponse force microscopy amplitude images of 75 nm $PbZr_{0.52}Ti_{0.48}O_3$/25 nm $SrRuO_3$ heterostructures grown on (b) $SrTiO_3$ (001), (c) $DyScO_3$ (110), and (d) $NdScO_3$ (110) substrates.

and therefore, it is possible that there are smaller-scale nanodomains which we are unable to resolve (note that such domains have been observed in transmission electron microscopy studies).[185, 186, 348, 362] In turn, although the BE-PFM images provide some indication of disorder and the nature of the domain structure at a length scale >20 nm, it does not provide an exact visual representation of the differences between the films. We also note that there was no observable phase contrast in these images, consistent with films that are fully downward poled due to the electrical boundary conditions imposed by the bottom electrode.

4.4 Crystal Structure of $PbZr_{0.52}Ti_{0.48}O_3$ Heterostructures

To gather additional insight into the structural differences of these heterostructures the samples were probed using XRD. All heterostructures were found to be fully 00*l*-oriented with no evidence of secondary phases (Figure 4.2). Subsequent asymmetric XRD RSM studies about the 103-diffraction condition of the $PbZr_{0.52}Ti_{0.48}O_3$ (Figure 4.3a–c) indicates that the $PbZr_{0.52}Ti_{0.48}O_3$ films possess considerably broadened diffraction

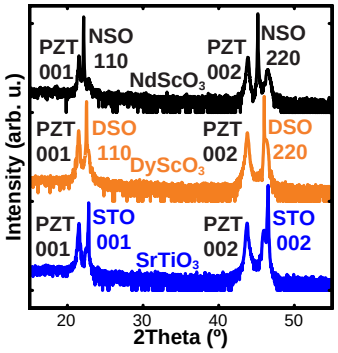

Figure 4.2. Full range 2θ-ω scans about the (00l)-diffraction conditions of $PbZr_{0.52}Ti_{04.8}O_3$ on various substrates.

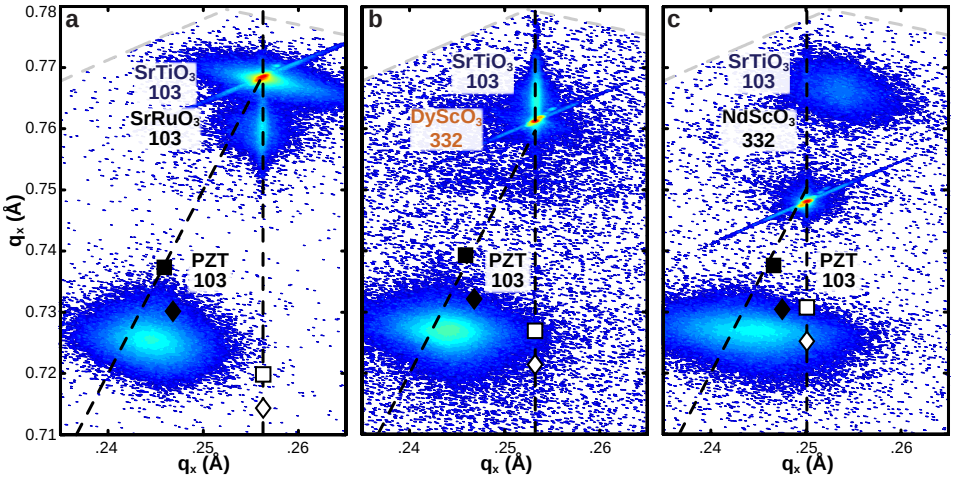

Figure 4.3. Asymmetric reciprocal space maps about the 103-diffraction condition for $PbZr_{0.52}Ti_{0.48}O_3$/25 nm $SrRuO_3$ heterostructures grown on (a) $SrTiO_3$ (001), (b) $DyScO_3$ (110), and (c) $NdScO_3$ (110) substrates.

peaks (with smearing towards the cubic line) and, regardless of substrate, a nearly relaxed structure. We note that the broadened diffraction peaks makes accurate determination of the lattice parameter and phase distribution difficult. The broadened diffraction peaks are likely the consequence of a number of features. First, it is known that anomalous diffraction, caused by coherent scattering from nanotwinned domains,[163, 348] can result in broaden diffraction peaks. Second, the presence of inhomogeneous strain in the films could also give rise to broaden diffraction peaks. Close inspection of the diffraction peaks reveals slight differences between the films. As the misfit strain decreases (*i.e.*, moving from $SrTiO_3$ to $NdScO_3$) the diffraction peaks are observed to broaden towards larger q_x-values (this would be commensurate with an increase substrate coherency) while the q_y-values remain relatively unchanged between the heterostructures. This subtle change in the diffraction peak shape suggests that even though the films are not perfectly, coherently strained, some level of residual strain from the lattice mismatch persists, to an increasing degree as the lattice mismatch is reduced. To attempt to quantify the degree of relaxation in these heterostructures we use the methods described in section 2.1.1. From this analysis it is found that the heterostructures on average are ~84% (~52%) relaxed on $SrTiO_3$, ~75% (~32%) relaxed on $DyScO_3$, and ~69% (~9%) relaxed on $NdScO_3$ assuming the tetragonal (rhombohedral) bulk lattice parameters, matching the visual trends. This difference in the strain state is a bit surprising, but can potentially explained by the fact that large lattice mismatches can be readily accommodated by relaxation *via* structural variation, domain formation, *etc.*, which occurs to an increasing degree as the misfit strain increases. In turn, only the heterostructures on $NdScO_3$ exhibits a significant amount of residual compressive strain, and as a result, the structure is driven towards increased

tetragonality. These observations differ dramatically from similar studies of, for instance, $PbZr_{0.2}Ti_{0.8}O_3$ where changing the substrate (even in thicker films) commonly results in coherently strained, out-of-plane oriented, *c* domains that are punctuated by varying densities of in-plane oriented *a* domains to accommodate the overall strain state.[125] For $PbZr_{0.52}Ti_{0.48}O_3$, however, even in only 75 nm thick films the presence of a number of structural degrees of freedom appears to result in rapid accommodation of the strain and an inability to apply epitaxial strains in the same regard. Thus, in the end, only films with small lattice mismatches exhibit any strain effects, and all others appear fully relaxed.

4.5 Electrical Response of $PbZr_{0.52}Ti_{0.48}O_3$ Heterostructures

4.5.1 Leakage Studies of $PbZr_{0.52}Ti_{0.48}O_3$ Heterostructures

Even though the structural and domain characterization suggests minimal differences between the heterostructures, subsequent studies of the electrical, dielectric, and ferroelectric properties reveal intriguing differences. These studies were conducted at room temperature using circular capacitor structures (25-100 μm in diameter) with symmetric $SrRuO_3$ electrodes fabricated using the MgO hardmask process (described in section 2.2.1).[240] Leakage measurements show highly symmetric response (implying minimal electrode induced imprint in the films) with low leakage currents (Figure 4.4), which are orders of magnitude lower than similarly processed 150 nm $PbZr_{0.2}Ti_{0.8}O_3$ heterostructures, as expected.[363] Overall, the high quality of these films is evident and enables non-traditional studies of ultra-slow ferroelectric hysteresis loops and dielectric measurements at high bias fields.

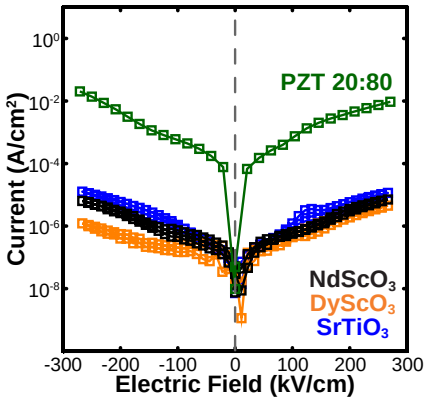

Figure 4.4. Current-voltage measurements of 75 nm $PbZr_{0.52}Ti_{0.48}O_3$/25 nm $SrRuO_3$ heterostructures on various substrates (including, for comparison, 150 nm $PbZr_{0.2}Ti_{0.8}O_3$/25 nm $SrRuO_3$/$GdScO_3$ (110) heterostructures).

4.5.2 Ferroelectric Responses of $PbZr_{0.52}Ti_{0.48}O_3$ Heterostructures

The ferroelectric properties of the various $PbZr_{0.52}Ti_{0.48}O_3$ heterostructures were probed as a function of frequency between 30mHz–100 kHz. All heterostructures underwent ferroelectric switching without significant losses even at the lowest frequencies. Characteristic hysteresis loops for all heterostructures measured at 1 kHz are provided (Figure 4.5a). All loops are well-saturated,

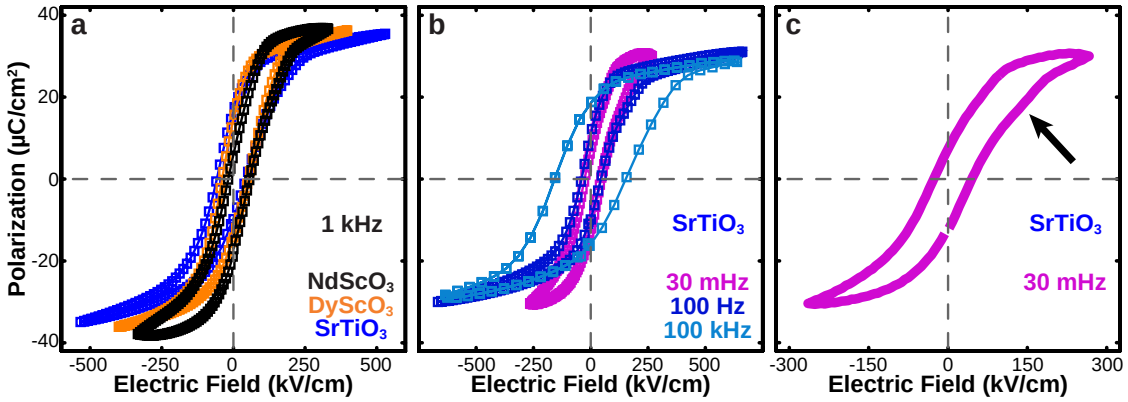

Figure 4.5. (a) Ferroelectric hysteresis loops measured at 1 kHz of 75 nm $PbZr_{0.52}Ti_{0.48}O_3$/25 nm $SrRuO_3$ heterostructures on various substrates. (b) Ferroelectric hysteresis loops for $PbZr_{0.52}Ti_{0.48}O_3/SrRuO_3/SrTiO_3$ (001) heterostructures measured at various frequencies. (c) Ferroelectric hysteresis loops for $PbZr_{0.52}Ti_{0.48}O_3/SrRuO_3/SrTiO_3$ (001) heterostructures measured at 30 mHz highlighting the transition region observed in ferroelectric hysteresis loops (indicated by the black arrow).

with $P_S \sim$ 35-38 μC/cm² which increases (slightly) with decreasing lattice mismatch between film and substrate – consistent with the structural studies which suggest a similar trend in increasing residual strain. A similar trend persists in the horizontal offset of the hysteresis loops which increases from 6.5 kV/cm to 18.5 kV/cm for heterostructures grown on $SrTiO_3$ and $NdScO_3$ substrates, respectively, and is indicative of flexoelectric fields, caused by the presence of strain gradients, which result from the residual inhomogeneous strain.[152, 172, 237]

Frequency-dependent ferroelectric hysteresis loop studies, spanning eight decades of frequency, were completed and representative hysteresis loops for heterostructures grown on $SrTiO_3$ substrates are provided (Figure 4.5b). These studies reveal the presence of features which could potentially be related to a field-induced structural transition. As the frequency of measurement was decreased there is evidence of a transition near ~150 kV/cm resulting in a change in slope of the hysteresis loop (Figure 4.5c). This transition is not observed in the films with increased residual strain (*i.e.*, those on $DyScO_3$ to $NdScO_3$) where the strain acts to promote increased tetragonality.

4.5.3 Local Studies of Ferroelectric Switching of $PbZr_{0.52}Ti_{0.48}O_3$ Heterostructures

The role of this residual strain can be locally probed by measuring the differences in switched area following local single point switching. Single point BE-SS within a pre-poled region, was conducted in a 10 × 10 grid. At each point, local piezoresponse and phase loops were extracted using the SHO fitting and loop unfolding methodologies (described in section 2.4.2). At each point PFM phase loops indicated that the film underwent ferroelectric switching to saturation. Following switching, BE-PFM images of the switched region were acquired, which after SHO fitting produce

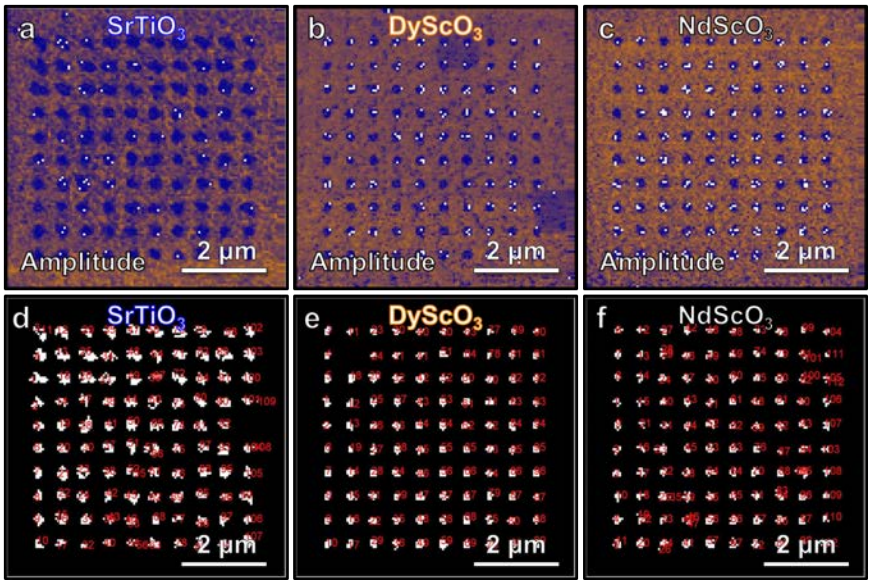

Figure 4.6. Band-excitation amplitude image of following single point switching spectroscopy in a sparsely populated 10 x 10 grid on 75 nm $PbZr_{0.52}Ti_{0.48}O_3$/25 nm $SrRuO_3$ heterostructures supported on (a) $SrTiO_3$ (001), (b) $DyScO_3$ (110), (c) $NdScO_3$ (110). Matlab™ extracted area of heterostructures grown on (g) $SrTiO_3$ (001), (h) $DyScO_3$ (110), and (i) $NdScO_3$ (110).

amplitude, phase, resonance frequency and loss images of the switched regions (amplitude images on various films after switching are provided in Figure 4.6a-c). From these images it is visually apparent that the switched area is significantly larger in the heterostructures grown on $SrTiO_3$ than $DyScO_3$ or $NdScO_3$ (which are visually indistinguishable), despite keeping all other factors constant (i.e., switching waveform, PFM tip, contact set-point, *etc.*). To quantify the switched area, we calculated the number of pixels which exhibited phase inversion from the pre-poled state (at each of the switched locations) from the corresponding phase image. The Matlab™ image processing toolbox was used to isolate independent regions where phase inversion occurred. A binary (black and white) representation of the phase images with each independent switched region marked, for all heterostructures variants, is provided (Figure 4.6d-f). Following correction for anomalous phase inversion and regions where a single switched region was unintentionally split the pixels were counted and represented as a histogram (Figure 4.7). The histogram of this data confirms the visual observations that the switched area is reduced in films with increased

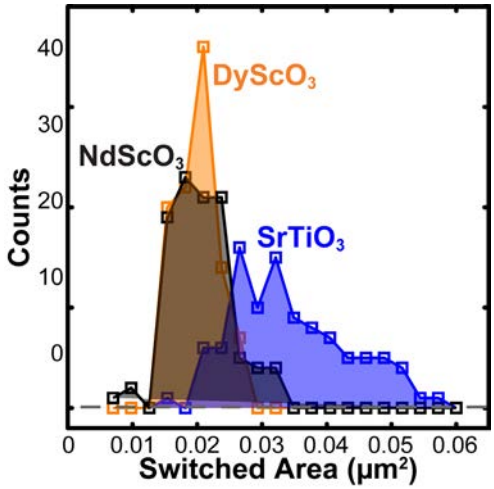

Figure 4.7. Average switched area extracted from the band excitation piezoresponse force microscopy phase image represented as a histogram – indicating on average larger switched domains in heterostructures on $SrTiO_3$, as compared to the heterostructures on $DyScO_3$ and $NdScO_3$ substrates.

residual strain (i.e., $DyScO_3$ to $NdScO_3$). This observation is likely related to the increased elastic constraints from the substrate and the presence of a built-in potential, in those heterostructures with increased residual strain, which could promote back switching following a switching pulse. In the end, the presence of an elastic constraint (in the form of a residual epitaxial strain) dramatically impacts the nature of switching and, in general, the electric-field dependence of the films.

4.5.4 Low-field Dielectric Response of $PbZr_{0.52}Ti_{0.48}O_3$ Heterostructures

The data thus far has illustrated how the elastic constraints from residual epitaxial strain can impact the high-field response of $PbZr_{0.52}Ti_{0.48}O_3$ thin films. Here, we move on to probe the implications of the residual strain on the low-field response – in particular the dielectric permittivity, with a special focus on how the elastic constraints impact the extrinsic domain wall contributions. We completed two measurements: 1) Rayleigh studies with increasing ac excitation field and 2) frequency-dependent permittivity measurements at increasing background dc bias; to extract the domain wall contributions to the permittivity. For the Rayleigh studies, we report both the dielectric permittivity (Figure 4.8a) and loss tangent (Figure 4.8b) as a function of increasing ac

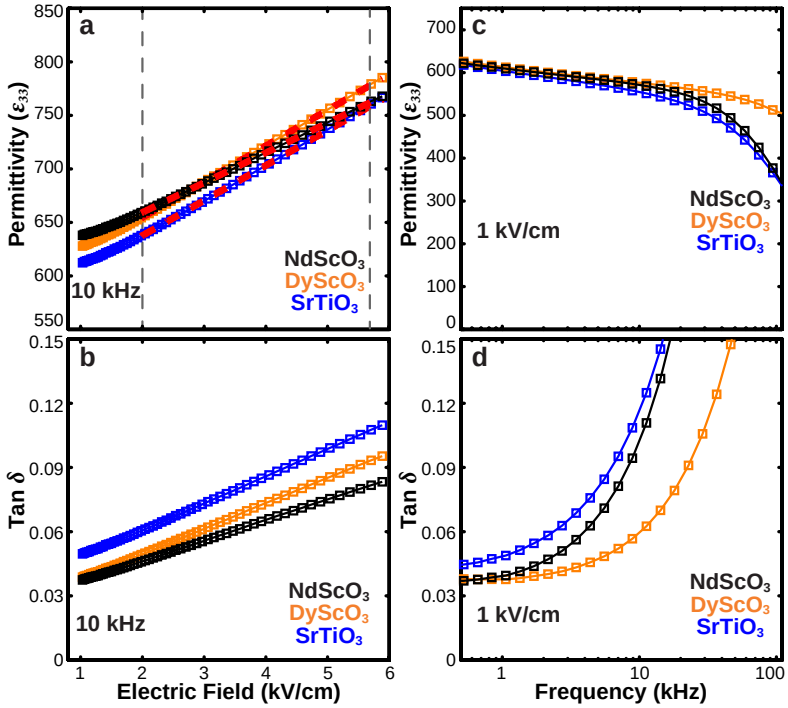

e

	ε_{rev}	α_{irr} (cm/kv)
$SrTiO_3$	573.1 ± 0.3	33.4 ± 0.1
$DyScO_3$	588 ± 0.2	33.3 ± 0.08
$NdScO_3$	603 ± 0.1	29.9 ± 0.03

Figure 4.8. (a) Dielectric permittivity and (b) loss tangent for all heterostructure variants displayed as a function of ac excitation bias represented as field. Frequency dependence of the (c) dielectric permittivity and (d) loss tangent for all heterostructure variants. (e) linear fit results from within the Rayleigh regime [marked by the black dashed lines and red dashed lines (linear fits) in (a)] which reveal values of ε_{rev} and α_{irr}.

excitation bias. Reversible domain wall contributions are found to persist up to ~1.33 kV/cm and below this point the dielectric permittivity of all heterostructures is similar (611–640). This measured dielectric permittivity is at the low end of previously published values for $PbZr_{0.52}Ti_{0.48}O_3$ films (values vary from 600–1300 depending on thickness, processing, and preferred orientation for polycrystalline films).[132, 349, 364] This slightly diminished response is likely the result of the elastic constraints imposed by the substrate which tends to suppress domain wall and structural contributions.[290, 365, 366] Corresponding frequency-dependent studies of the dielectric permittivity and loss tangent (using an excitation bias of 1 kV/cm, within the reversible regime) were also completed (Figure 4.8c-d). It is worth noting that the dielectric loss increases drastically upon increasing the measurement frequency above 1–10 kHz; a feature not observed in thin films of other compositions of $PbZr_{1-x}Ti_xO_3$ synthesized and probed in a similar fashion. We correlate this to the potential freezing out of sluggish domain wall contributions or contributions from collective responses only possible in $PbZr_{0.52}Ti_{0.48}O_3$.[367, 368] The loss tangent is also found to increase within the frequency regime where the change in slope of the hysteresis loop stops being observable, which we previously hypothesized is related to a possible structural phase transition near ~150 kV/cm. This observation could be an indication that the quenching of this response could be the cause of the increased loss observed within this frequency regime.

Returning now to focus on the ac field dependent Rayleigh studies, within the Rayleigh regime (demarcated by the dashed lines, Figure 4.8a) the ac field dependence of the permittivity was fitted to the Rayleigh law $\varepsilon_{33} = \varepsilon_{rev} + \alpha_{irr} E_{ac}$ ($r^2 > 0.98$) where ε_{33} is the out-of-plane permittivity, E_{ac} is the amplitude of the ac electric field (sense pulse), and ε_{rev} and α_{irr} are the reversible and irreversible domain wall contributions to the dielectric permittivity, respectively (Figure 4.8e, as described in section 2.2.2).[286, 297] We start by focusing on the α_{irr} values (29.9–33.4 cm/kV) which are an order of magnitude larger than values extracted from $PbZr_{0.2}Ti_{0.8}O_3$ (1.4 cm/kV) and $PbZr_{0.8}Ti_{0.2}O_3$ (2.08 cm/kV) heterostructures prepared and probed in a similar fashion,[172] significantly lower than those reported for bulk $PbZr_{0.52}Ti_{0.48}O_3$ samples, yet comparable to values reported for polycrystalline $PbZr_{0.52}Ti_{0.48}O_3$ films.[369, 370] Although the range observed for our heterostructures is somewhat narrow, the films possessing the most residual strain (*i.e.*, those grown on $NdScO_3$ substrates) are found to possess reduced α_{irr}, suggesting that the elastic constraints impact the domain wall contributions to response in these heterostructures.

4.5.5 *High-field Dielectric Response of $PbZr_{0.52}Ti_{0.48}O_3$ Heterostructures*

The Rayleigh studies are further supported by applied background dc electric field studies, which use a dc bias to suppress the extrinsic (domain wall) contributions, allowing for a quantitative measure of the intrinsic response (as described in section 2.3.1).[241] In brief, this is achieved by fitting the frequency dependence of the permittivity (from 1–100 kHz) at each applied background dc electric field (from 0 to -850 kV/cm) to the equation $\varepsilon_{33} = \varepsilon_i - \alpha_f \log f$ and extracting the field-dependence of the permittivity intercept (ε_i) and slope (α_f). Using this approach, the field at which extrinsic contributions are suppressed and the zero-field intrinsic permittivity of a material can be extracted. Such background dc electric field measurements have been applied to all $PbZr_{0.52}Ti_{0.48}O_3$ heterostructures studied in this treatment, as well as similarly prepared 100 nm $PbZr_{0.2}Ti_{0.8}O_3$ and $PbZr_{0.8}Ti_{0.2}O_3$ heterostructures. We represent a small portion of the acquired permittivity curves for each of the films measured in this treatment (Figure 4.9a-e). This figure shows that both the measured permittivity and frequency dispersion (represented by the slope of the curves) decreases as the dc background field is increased. This change in the dielectric response is the result of freezing out the extrinsic contributions to the response under high fields.[195, 287] In turn, the measured permittivity is closely related to the intrinsic permittivity of the material.[359] We then plot the field-dependence of the intercept (ε_i) as a function of the background dc electric field for all heterostructure variants (Figure 4.10a-e). These plots show two regimes, a low-field regime (where the response consists of both intrinsic and extrinsic contributions, shown in purple) and a high-field regime (where the response is thought to be reflective of only the intrinsic response, shown in green). The slope and intercepts of the linear fits in the low-field regime correspond to the extrinsic tunability (α_{ex}, which describes how the applied dc electric field suppresses the extrinsic response) and the zero-field extrinsic permittivity (ε_{ex}), respectively. The slope and intercepts of linear fits in

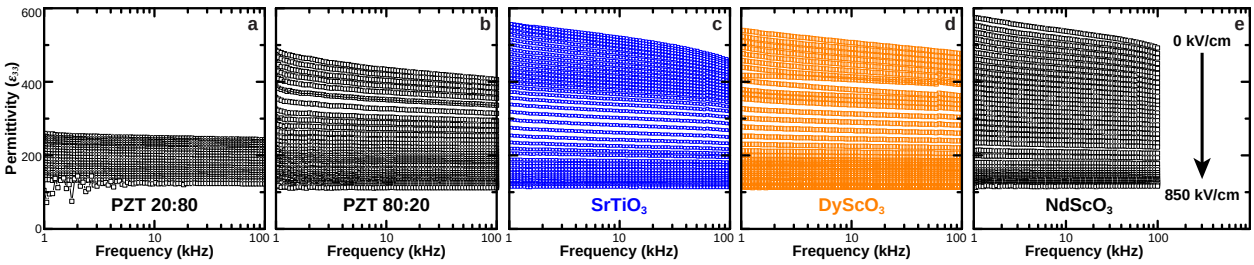

Figure 4.9. Dielectric permittivity curves as a function of frequency with increasing dc background bias measured with an ac excitation bias of 8 mV for 100 nm (a) $PbZr_{0.2}Ti_{0.8}O_3$ and (b) $PbZr_{0.8}Ti_{0.2}O_3$ heterostructures on $GdScO_3$ (110) and for 75 nm $PbZr_{0.52}Ti_{0.48}O_3$ heterostructure supported on (c) $SrTiO_3$ (001), (d) $DyScO_3$ (110), and (e) $NdScO_3$ (110). *n.b.* to aid in visualization only a small subset of the measured data is shown.

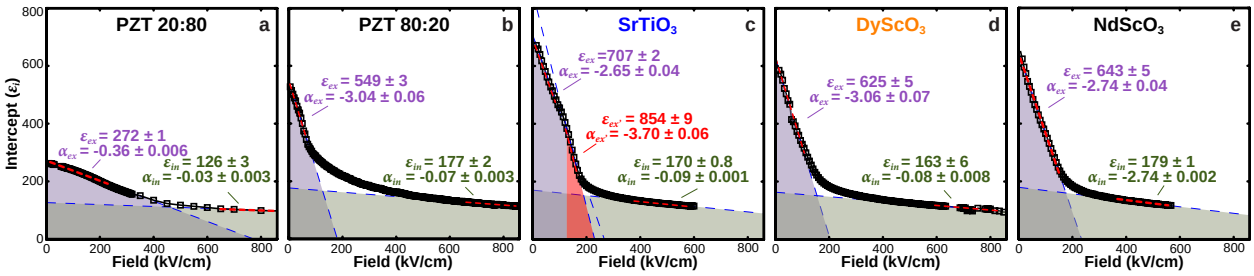

Figure 4.10. Extracted zero frequency permittivity as a function of increasing background fields for (a) $PbZr_{0.2}Ti_{0.8}O_3$, (b) $PbZr_{0.8}Ti_{0.2}O_3$, heterostructures supported on $GdScO_3$ (110) and $PbZr_{0.52}Ti_{0.48}O_3$ heterostructures grown on (c) $SrTiO_3$ (001), (d) $DyScO_3$ (110), and (e) $GdScO_3$ (110) substrates. Regions where linear fits were computed are shown as red dashed lines. The regions representing the intrinsic, intermediate, and extrinsic regimes are colored green, red, and purple, respectively.

the high-field regime correspond to the intrinsic tunability (α_{in}, which describes how the external dc electric field suppresses the intrinsic response) and the zero-field intrinsic permittivity (ε_{in}), respectively.

In the low-field regime the $PbZr_{0.52}Ti_{0.48}O_3$ films have nearly identical ε_{ex} (625-700) which are considerably larger than those for $PbZr_{0.2}Ti_{0.8}O_3$ (272) and somewhat larger than that for $PbZr_{0.8}Ti_{0.2}O_3$ (549). Furthermore, the α_{ex} values of the $PbZr_{0.52}Ti_{0.48}O_3$ heterostructures are similar indicating that the extrinsic tunabilities are comparable (-2.65 to -3.06 cm/kV) and similar to that for $PbZr_{0.8}Ti_{0.2}O_3$ (-3.04 cm/kV), but much larger than that for $PbZr_{0.2}Ti_{0.8}O_3$ (-0.36 cm/kV). Upon application of higher fields, we again see a difference between the $PbZr_{0.52}Ti_{0.48}O_3$ (and $PbZr_{0.8}Ti_{0.2}O_3$) heterostructures which undergo the transition to the high-field regime (where extrinsic contributions are quenched) at fields of magnitude 100-200 kV/cm and the $PbZr_{0.2}Ti_{0.8}O_3$ heterostructures which do not transition until fields of magnitude 400 kV/cm. Finally, in the high-field regime, $PbZr_{0.52}Ti_{0.48}O_3$ and $PbZr_{0.8}Ti_{0.2}O_3$ heterostructures exhibit comparable α_{in} (-0.07 to -0.11 cm/kV) and ε_{in} (163-179) while the $PbZr_{0.2}Ti_{0.8}O_3$ heterostructures have reduced α_{in} (-0.03 cm/kV) and ε_{in} (126) (consistent with prior reports).[195, 241]

There are a number of features worth highlighting from this analysis. Overall the $PbZr_{0.52}Ti_{0.48}O_3$ and $PbZr_{0.8}Ti_{0.2}O_3$ heterostructures show markedly different response from the $PbZr_{0.2}Ti_{0.8}O_3$ heterostructures which can be understood in the context of their domain structures and elastic coupling with the substrate. First, ε_{in} increases as we move to compositions possessing more Zr. This can be readily understood by the fact that as the Zr-content increases the excitation field is applied increasingly along non-polar directions, exciting additional intrinsic contributions to the permittivity. Second, α_{in} values are the largest in the $PbZr_{0.52}Ti_{0.48}O_3$ heterostructures,

intermediate for the $PbZr_{0.8}Ti_{0.2}O_3$, and smallest for $PbZr_{0.2}Ti_{0.8}O_3$ suggesting that the intrinsic instabilities of $PbZr_{0.52}Ti_{0.48}O_3$ enhances the tunability. Third, ε_{ex} is larger for both the $PbZr_{0.52}Ti_{0.48}O_3$ and $PbZr_{0.8}Ti_{0.2}O_3$ than for $PbZr_{0.2}Ti_{0.8}O_3$ which is likely due to the higher density of domain walls, which gives rise to a greatly enhanced extrinsic contribution to the permittivity. Finally, the α_{ex} values for $PbZr_{0.52}Ti_{0.48}O_3$ and $PbZr_{0.8}Ti_{0.2}O_3$ are similar and nearly an order of magnitude larger than that of $PbZr_{0.2}Ti_{0.8}O_3$. This is likely the result of a combination of effects including the adaptability of the domain structure and the elastic interactions, which can occur within the film and/or between the film and substrate. In these measurements, we pre-pole the sample and then measure with increasing fields applied along that same direction. This quenches or minimizes domain wall contributions from ferroelectric (*i.e.*, 180°) domain walls, limiting the extrinsic response to just ferroelastic (*i.e.*, non-180°) domain walls. The large α_{ex} for the $PbZr_{0.52}Ti_{0.48}O_3$ heterostructures likely results from the adaptive nature of the structure and the nearly flat energy landscape which allows for large susceptibilities. Additionally, because of this adaptability the system can readily adjust the volume surrounding an excited area to accommodate the additional strain energy that forms, thereby reducing the clamping effect of the film and substrate (as evidenced by the insensitivity of the material to the changing lattice mismatch from the substrates). On the other hand, in $PbZr_{0.2}Ti_{0.8}O_3$, the domain structure that forms (*i.e.*, *c/a/c/a*) is the result of the elastic boundary conditions of the substrate. Thus, it is extraordinarily difficult to adjust the domain structure as the domains are strongly coupled to the total strain state of the film. In turn, not only does this reduce α_{ex}, but it also increases the critical field required to suppress the stiffened domain wall contributions.

The final feature to highlight is found in the $PbZr_{0.52}Ti_{0.48}O_3$ heterostructures grown on $SrTiO_3$ substrates. A regime of enhanced susceptibility (occurring between 100-200 kV/cm) is observed (red area, Figure 4.10c) in which there is a change in the slope of field-dependence of the permittivity. This regime matches the location of the feature observed in the ferroelectric hysteresis loops (Figure 4.5d). Within this region of enhanced susceptibility $\varepsilon_{ex} \sim 850$ and $\alpha_{ex} \sim -3.7$ cm/kV are both considerably larger than observed in low-field regimes for all other samples studied. It is possible that this enhanced response arises in the $PbZr_{0.52}Ti_{0.48}O_3$ samples possessing the least residual strain as a result of a field-induced structural transformation towards the applied electric field. Such a structural transition could potentially be suppressed in those heterostructures that possess larger amounts of residual strain (*i.e.*, $DyScO_3$ to $NdScO_3$).

4.6 Pyroelectric Response of $PbZr_{0.52}Ti_{0.48}O_3$ Heterostructures

4.6.1 Pyroelectric Response Measured by Temperature Dependent Ferroelectric Hysteresis-Loops of $PbZr_{0.52}Ti_{0.48}O_3$ Heterostructures

Due to the high quality of the $PbZr_{0.52}Ti_{0.48}O_3$ heterostructures studied in this work, it was possible to measure the pyroelectric response over a wide temperature range. This is not typically possible due to large leakage and thermally stimulated currents which are significant in most thin films at elevated temperatures. Some had suggested that the pyroelectric response should be maximized at the MPB due to the possibility of undergoing thermally induced structural transformation, which can give rise to large changes in polarization and thus have the potential for large pyroelectric responses.[371-373] For this study we focus our attention on the 75 nm thick $PbZr_{0.52}Ti_{0.48}O_3$ heterostructures on $SrTiO_3$ (001). To measure the pyroelectric response of these heterostructures we measured temperature-dependent hysteresis loops from 300-460 K at 20 K temperature intervals. The heterostructures were heated at a constant ramp rate of 5°C/min. and allowed to equilibrate at each temperature for 15 minutes prior to measurement. At each temperature, hysteresis loops were measured on 10 or more capacitors and the average remanent polarization was noted. We show a small subset of example hysteresis loops obtained from these measurements (Figure 4.11a). All hysteresis loops were well saturated with minimal evidence of leakage even at the highest measurement temperatures. The remanent polarization from these loops were extracted and plotted as a function of temperature (Figure 4.11b). The remanent polarization as a function of temperature shows a clear linear trend which can be fit to extract a measure of the pyroelectric coefficient. Using this approach, the pyroelectric coefficient (π) was found to be -751 μC/m²K. While this approach to measure pyroelectric coefficient has been extensively used in literature,[59, 311, 312] this approach is known to significantly overestimate the pyroelectric response as it is unable to exclude dc leakage and thermally stimulated currents.[319, 320]

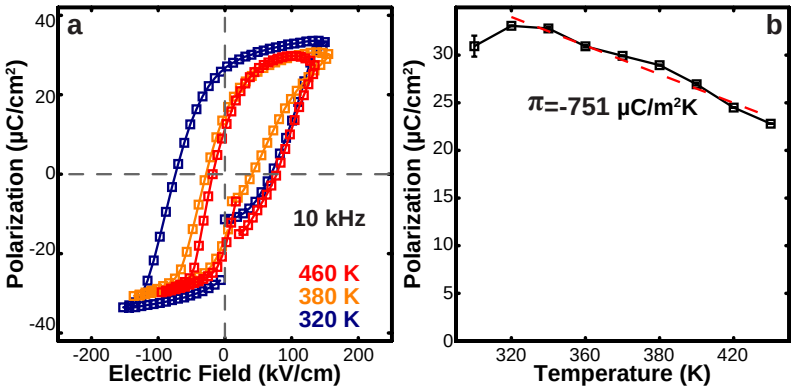

Figure 4.11. Pyroelectric measurements conducted on $PbZr_{0.52}Ti_{0.48}O_3$ (75 nm)/$SrRuO_3$ (25 nm)/$SrTiO_3$ (001) heterostructures. (a) Selection of temperature dependent hysteresis loops used to extract remanent polarization for calculation of pyroelectric response. (b) Remanent polarization as a function of temperature used to approximate pyroelectric response

4.6.2 *Phase Sensitive Pyroelectric Measurement of $PbZr_{0.52}Ti_{0.48}O_3$ Heterostructures*

To more precisely measure the temperature-dependent pyroelectric response, we conducted phase sensitive pyroelectric measurements as described in section 2.3.2. To conduct these measurements, the heterostructures were heated and allowed to equilibrate at the desired set point temperature (between 300-360 K). Once equilibrated the heater was set to oscillate the temperature sinusoidally with a temperature amplitude of 1.25 K at a frequency of 0.02 Hz, while simultaneously measuring the current generated at the top electrode. Following data collections, fits of the temperature and current response allows for the calculation of the pyroelectric coefficient and phase shifts (a measure of the fraction of the current which is pyroelectric in nature, Figure 4.12a). The fits of the temperature-dependent pyroelectric response and phase (Figure 4.12b) reveals that the measured response is predominantly pyroelectric (phase offset >60) and the pyroelectric coefficient is ~-200 μC/m²K, decreasing slightly as the temperature increases. This value for the pyroelectric response is significantly lower than found from the temperature dependent hysteresis-loop-based method (-751 μC/m²K). This measurement dependent interpretation of the pyroelectric response highlights some of the difficulties in measuring and interpreting reported values for pyroelectric response in thin films. Comparing the pyroelectric coefficient extracted from the phase sensitive pyroelectric measurements, to those obtained on $PbZr_{0.2}Ti_{0.8}O_3$ heterostructures (See Ref. 374), contrary to the theoretical prediction, the $PbZr_{0.52}Ti_{0.48}O_3$ heterostructures were found to have a pyroelectric responses significantly lower than $PbZr_{0.2}Ti_{0.8}O_3$ heterostructures. This unexpected outcome could be attributed to not being located close enough to the phase boundary to invoke thermally-induced structural transformations, the slight misorientation between the polarization

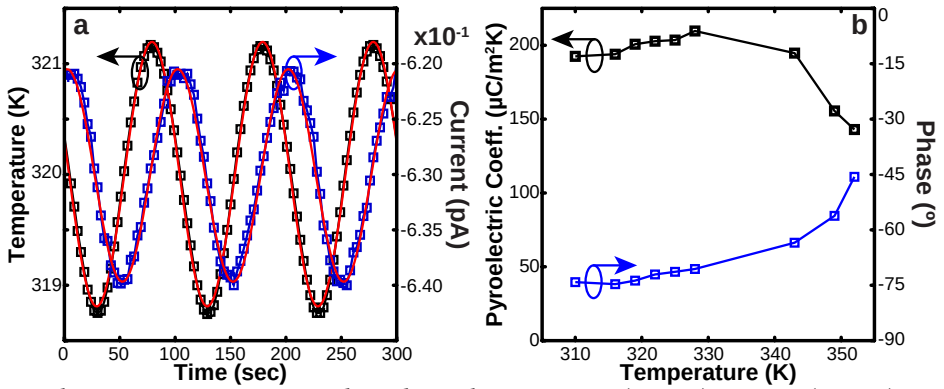

Figure 4.12. Pyroelectric measurements conducted on $PbZr_{0.52}Ti_{0.48}O_3$ (75 nm)/$SrRuO_3$ (15 nm)/$SrTiO_3$ (001) heterostructures. (a) Characteristic temperature and current response achieved during phase sensitive pyroelectric measurement. Note that both curves are sinusoidal in nature and phase shifted by nearly 90° (b) Extracted pyroelectric coefficient and phase from phase sensitive pyroelectric measurements as a function of temperature.

direction <111> and the measurement direction [001], and/or the possibility of oppositely poled domains which generate pyroelectric responses of opposite senses. All told, what is most important to take away from this study is the paramount importance of the methods and methodologies used to predict and interpret pyroelectric response in ferroelectric thin films.

4.7 Conclusions

In this chapter, we take an in-depth look at how epitaxial strain in the form of lattice mismatch can impact the evolution of crystal and domain structure, and ultimately the properties of $PbZr_{0.52}Ti_{0.48}O_3$ thin films. In general, this work highlights the complexity of strain evolution in the highly-adaptable $PbZr_{0.52}Ti_{0.48}O_3$ material and how the innate flat energy landscape can skirt classical assumptions of epitaxial thin-film strain. In the end, high-quality, single-phase films of $PbZr_{0.52}Ti_{0.48}O_3$ were shown to exhibit significantly different field induced dielectric responses when grown on various substrates despite the appearance of a "relaxed" crystal structure. Local probes of switching in these heterostructures reveal distinct differences in the average switched area of the heterostructures which depend on the lattice mismatch with the substrate, as a result of changes to the corresponding elastic boundary conditions of the film. Subsequent dielectric and ferroelectric studies reveal transitions in ferroelectric switching at ultra-low frequencies and in the dielectric response at high dc fields that suggest that reduced residual strain promotes full adaptability of the structure under applied fields and, as a result, enhanced electric field susceptibility and tunability. Moreover, we demonstrate the importance of the measurement approach in obtaining an accurate measure of pyroelectric response and show surprisingly that the pyroelectric response is slightly suppressed in epitaxial thin films near the morphotropic phase boundary (compared to tetragonal $PbZr_{1-x}Ti_xO_3$ variants). Overall, $PbZr_{0.52}Ti_{0.48}O_3$ – and other systems with highly-adaptable structures – may not be beholden to the classic effects of epitaxial strain in the same manner as more conventional materials. Nonetheless, the role of strain or residual strains in materials possessing elastic order is something that must not be overlooked as it can lead to non-intuitive and useful observations, and can alter ferroic susceptibilities and response.

Chapter 5

Complex Evolution of Built-in Potential and Responses in Compositionally-Graded $PbZr_{1-x}Ti_xO_3$

In the previous chapter we explored the effects of epitaxial strain on the crystal and domain structure, and the resulting electrical, dielectric and ferroic responses in heterostructures with compositions spanning the $PbZr_{1-x}Ti_xO_3$ phase diagram. Throughout these studies due to the limited availability of well latticed matched substrates and electrode materials we ran into limitations in the magnitude of epitaxial strain which we could impose. Here, we explore how compositionally-graded heterostructure can be used to skirt some of the limitations of strain engineering allowing large strains to be achieved. To do this, we grew a series compositionally-graded heterostructures where we vary chemical composition and film thickness to demonstrate how these structures can be used to achieve strain, crystal and domain structures not possible in heterostructures of a single composition. Specifically, we observe that large epitaxial strains can be achieved in compositionally-graded heterostructures if large local changes in lattice mismatch are avoided and that the domain structures take a form highly influenced by the domain structure of the $PbZr_{1-x}Ti_xO_3$ composition at the substrate interface. Using this approach, we demonstrate that it is possible to achieve large strain gradients, and in turn, large flexoelectric effects and fields (*i.e.*, built-in potentials) which give rise to horizontally-shifted hysteresis loops, highly-suppressed dielectric permittivity, and improved pyroelectric figures of merit. In our study of this phenomenon, we observe a non-intuitive evolution of the built-in potential, which does not scale directly with the magnitude of the strain gradient as would be expected. Instead, large built-in potentials are observed in compositionally-graded heterostructures that contain: 1) compositional gradients that traverse chemistries associated with structural phase boundaries (such as the morphotropic phase boundary), and 2) ferroelastic domain structures. In turn, the built-in potential is observed to be dependent on a combination of flexoelectric effects (*i.e.*, polarization–strain gradient coupling), chemical-gradient effects (*i.e.*, polarization–chemical potential gradient coupling), and local inhomogeneities (in structure or chemistry) that enhance strain (and/or chemical potential) gradients such as areas with nonlinear lattice parameter variation with chemistry or near ferroelastic domain boundaries.

5.1 Introduction to Compositionally-Graded Heterostructures

Historically, due to the inherent complexity of perovskite ferroelectrics, research has focused primarily on ferroelectric heterostructures of a single composition. This constraint can limit creativity in designing novel crystal and domain structures with potentially exciting properties unachievable in compositionally-homogeneous ferroelectrics. Recently, there has been growing interest in using advance growth techniques capable of producing complex bilayer[172, 331, 375-377] and superlattice structures[131-137, 139, 141, 142, 163, 378] with at least one ferroelectric layer, and have shown using these approaches that it is possible to produce remarkable domain structures and properties. For instance, in $PbZr_{1-x}Ti_xO_3$, it has been shown that design of bilayer heterostructures can give rise to enhanced dielectric and piezoelectric responses,[375] and that superlattice structures can be utilized to deterministically control the spontaneous polarization, dielectric constant, Curie temperatures, and even produce vortex polarization states.[135, 136, 139, 379]

In an alternative approach, compositionally-graded heterostructures, formed from smoothly varying solid solutions have shown considerable promise in extending our capability to control epitaxial strain. Such compositional gradients have been implemented in semiconductor epitaxy (*e.g.*, Si_xGe_{1-x} and $In_{1-x}Ga_xAs$) to engineer strain to form dislocation-free epilayers and for bandgap control.[380-382] In ferroelectrics, compositionally-graded heterostructures are less studied; however, the few prior works on compositionally-graded ferroelectric (in systems including $PbZr_{1-x}Ti_xO_3$ and $Ba_{1-x}Sr_xTiO_3$) have focused on relatively thick heterostructures (>300 nm), where effects of epitaxial strain are nearly non-existent. Nevertheless, these studies revealed a range of novel phenomena such as the presence of built-in electric fields,[234, 237] shifted hysteresis loops,[202, 234, 237, 383] and large susceptibilities.[384]

In addition, recently, it has been recognized that strain need not be homogeneous and researchers have worked to develop routes to deterministically create inhomogeneous strains to further control materials.[151, 152, 172, 195-197] The presence of strain gradients are particularly interesting in ferroelectrics because of the potential for strong so-called flexoelectric effects. Flexoelectricity refers to the linear coupling of a strain gradient ($\partial\varepsilon_{ij}/\partial x_k$) to the polarization ($P_i$) of a material which is mediated by a fourth-rank flexoelectric tensor (μ_{ijkl}). While large strain gradients, on the order of 10^5 m^{-1}, are possible in thin films through the use of mechanical stress,[43, 199, 200] and defect and

domain engineering,[151, 152, 165, 166] control of these strain gradients is difficult, complicating any theoretical studies of flexoelectric effects whose contributions and magnitude is still highly contested.[216, 230] Despite the open theoretical questions, these large strain gradients produce large flexoelectric effects (or effects that mimic those arising from flexoelectricity) that can alter the ferroic response of materials,[167, 212] allow for mechanically induced ferroelectric switching,[43, 199, 200] drive horizontal shifts of ferroelectric hysteresis loops,[201, 202, 234] and allow for independent tuning of typically coupled ferroelectric susceptibilities.[196]

Compositionally-graded heterostructures represent a model system capable of generating large strain gradients which can easily be controlled by the chemical composition (bulk lattice parameter) and thickness, as long as the heterostructure remains coherently strained to the underlying substrate. In this chapter, we explore deterministic routes to control the strain state and gradients, crystal and domain structure, and the dielectric, ferroelectric and pyroelectric responses of these materials by designing compositionally-graded $PbZr_{1-x}Ti_xO_3$ heterostructures with controlled chemistry and thickness.

5.1.1 Introduction to Compositional Gradients in $PbZr_{1-x}Ti_xO_3$

As previously mentioned, looking at the composition-phase diagram of the $PbZr_{1-x}Ti_xO_3$ system (Figure 5.1a) there is a structural competition between tetragonal and rhombohedral symmetry on the Ti- and Zr-rich sides, respectively, which is separated by the morphotropic phase boundary where phase competition between these two phases exists. Likewise, the room-temperature lattice parameter-composition evolution (Figure 5.1b) reveals that the lattice parameters do not vary linearly with composition and instead changes rapidly near the morphotropic phase boundary (MPB, x = 0.48). On the basis of this information, we focused on compositionally-graded heterostructures $PbZr_{1-y}Ti_yO_3 \Leftrightarrow PbZr_{1-x}Ti_xO_3$/30 nm

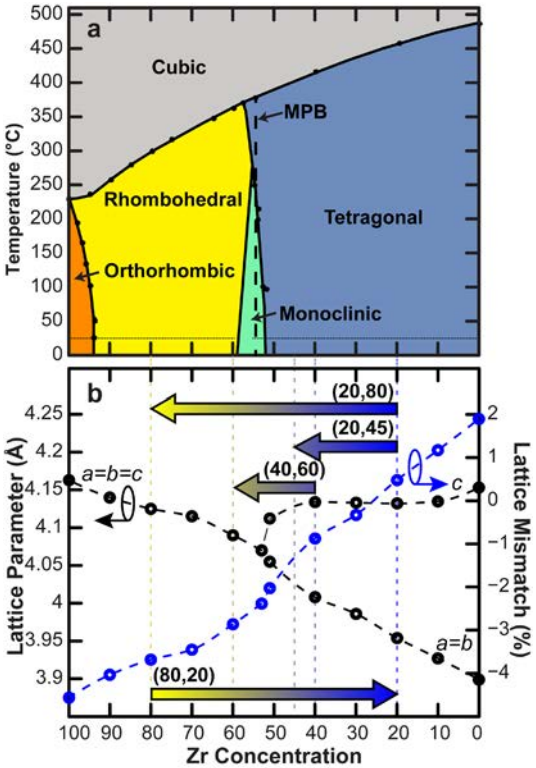

Figure 5.1. (a) $PbZr_{1-x}Ti_xO_3$ phase diagram, adapted from B. Jaffe *et al.*[53, 340] (b) Bulk lattice parameter (black) and calculated misfit strain with $GdScO_3$ (110) (blue) spanning across the $PbZr_{1-x}Ti_xO_3$ phase diagram.

$SrRuO_3$/ $GdScO_3$ (110) (a = 5.45 Å, b = 5.75 Å, c = 7.93 Å, pseudocubic a_{pc} = 3.96 Å). Growth on $GdScO_3$ substrates provides lattice mismatches between −4.6 to 2% as one transitions from $PbZrO_3$ to $PbTiO_3$ (Figure 5.1b, right axis). All heterostructures are named on the basis of the variation of the Zr-content upon transitioning from the substrate interface (x) to the free surface of the film (y) in the form (x,y). In all cases, the composition of the bottom-most $PbZr_{1-x}Ti_xO_3$ layer is chosen to be the composition with the least lattice mismatch to the substrate [with the exception of the (80,20) heterostructures] and all compositional gradients are controlled to be linear in nature.

5.2 Growth of Compositionally-Graded $PbZr_{1-x}Ti_xO_3$ Heterostructures

All films were grown using pulsed-laser deposition with an on-axis geometry (target-to-substrate spacing of 6.35 cm). The $SrRuO_3$ bottom electrode was deposited from a stoichiometric target at 645 °C, in 100 mTorr pressure of oxygen, at a laser fluence of 1.8 J cm^{-2}, and a laser repetition rate of 13 Hz. The $PbZr_{1-x}Ti_xO_3$ layers were grown at a temperature of 560-600 °C, at a pressure of 200 mTorr of oxygen, a laser fluence of 1.9 J cm^{-2}, and a laser repetition rate of 3 Hz. Compositionally-graded heterostructures were synthesized by continuously varying the composition from $PbZr_{1-x}Ti_xO_3$ to $PbZr_{1-y}Ti_yO_3$ by controlling the number of pulses between two end-member targets of $Pb_{1.1}Zr_{0.2}Ti_{0.8}O_3$ and $Pb_{1.1}Zr_{0.8}Ti_{0.2}O_3$ using a programmable target rotator (Neocera, LLC) synced with an excimer laser. Mixing of the targets was done such that each semi-discrete level (defined programmatically) deposited a sub-unit cell layer. Following growth samples were cooled in 760 mTorr of oxygen at a rate of 5 °C/min.

5.3 Design of Compositionally-Graded $PbZr_{1-x}Ti_xO_3$ Heterostructures

In this work, we studied seven compositionally-graded-heterostructure variants, which are separated into two groups. First is a series probing the effects of film thickness variation wherein we probe 50, 75, 100, and 150 nm thick (20,80) compositionally-graded heterostructures (Figure 5.2a). These thicknesses were selected because they permit a large variation in the magnitude of the maximum theoretical average strain gradient (from 8.7 × 10^5 m^{-1} to 2.9 × 10^5 m^{-1} for the 50 and 150 nm

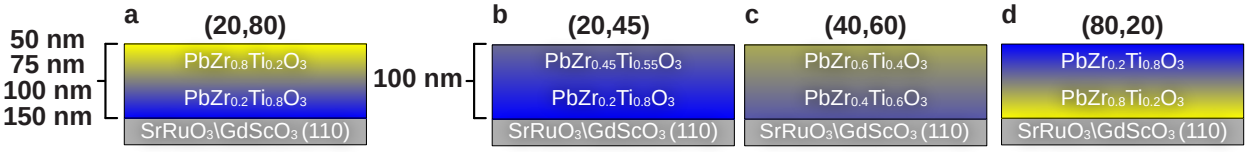

Figure 5.2. Schematic illustrations of compositionally-graded heterostructures studied in this work (a) (20,80) compositionally-graded heterostructures of various thickness, (b) (20,45), (c) (40,60), and (d) (80,20) compositionally-graded heterostructures.

thick heterostructures, respectively). Note that the theoretical strain gradients can be obtained by taking the difference in the misfit strain between the substrate and the bulk lattice parameter of the parent phases at the substrate–film interface and the free surface, and dividing by the film thickness [values for lattice parameters are provided (Figure 5.1b)]. In addition to the strain gradient effects, variation of thickness is a well-established pathway to alter the form and density of the ferroelastic domain structure.[81-83, 385]

The second series of heterostructures focusing on 100 nm thick (20,45), (40,60), (20,80) and (80,20) heterostructures was chosen to probe the effects of varying the nature of the compositional gradient (Figure 5.2b-c). This series of compositionally-graded heterostructures was selected for three primary reasons: 1) the (20,80) heterostructures (4.3×10^5 m^{-1}) have approximately double the strain gradient of the (20,45) (*i.e.*, 2.2×10^5 m^{-1}) and (40,60) (*i.e.*, 2.5×10^5 m^{-1}) heterostructures which allows us to probe the effect of varying strain gradient magnitude, 2) the (20,80) and (40,60) heterostructures include the MPB composition, while the (20,45) heterostructures do not, allowing the role of the nonlinear lattice parameter evolution near the MPB in this system to be probed, and 3) the (20,80) and (80,20) heterostructures are chemically equivalent yet inverted, allowing the influence of the layer at the substrate film interface and sense of the chemical gradient (and potentially strain gradient) to be investigated

5.4 Crystal Structure of Compositionally-graded Heterostructures

X-ray diffraction (XRD) θ-2θ and reciprocal space mapping (RSM) studies found all heterostructure variants to be single-phase, fully epitaxial, and (00*l*)-oriented regardless of thickness or gradient design. The crystal structure and strain state of the compositionally-graded heterostructures was studied using XRD RSM about the 103 and 332 diffraction conditions for the film and substrates, respectively. The positions of the bulk and strained peaks for the parent phases are provided for reference. Focusing first on the 100 nm thick compositionally-graded heterostructures with different gradient forms [*i.e.*, (20,45) (Figure 5.3a), (40,60) (Figure 5.3b), (20,80) (Figure 5.3c) and (80,20) (Figure 5.3d)]. Looking at the general form of these RSM the heterostructures whose compositions at the substrate interface is more Ti-rich (*i.e.*, the (20,45), (40,60), and (20,80) heterostructures) have q_y-values which span continuously between the between the theoretical strained-peak positions of the parent phases, indicating they are strained (to some extent) to the substrate.

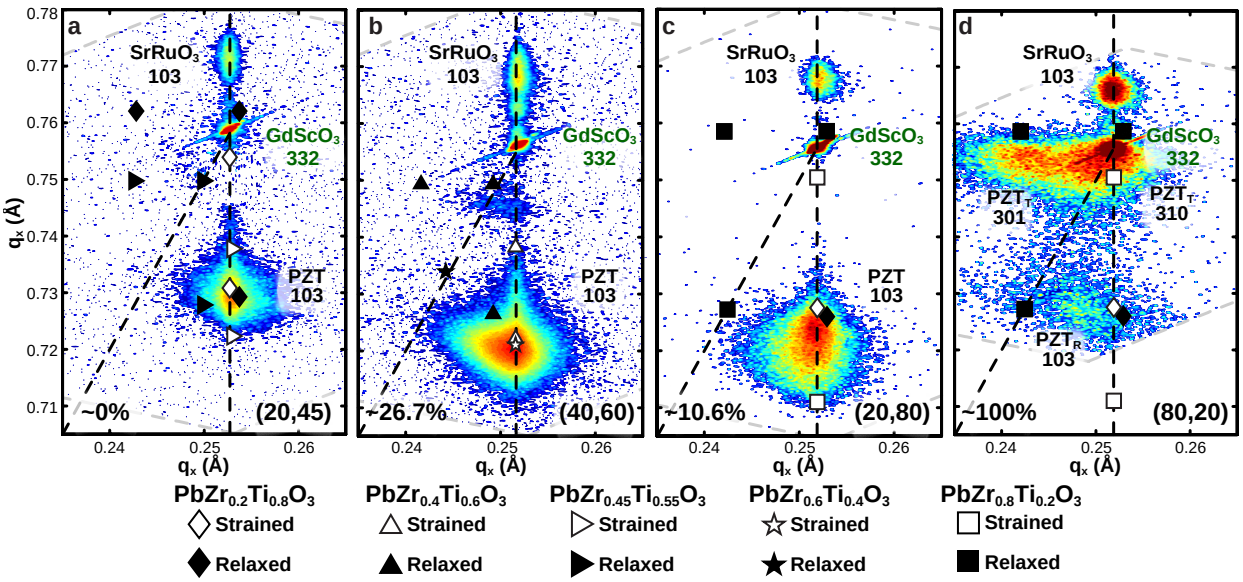

Figure 5.3. Reciprocal space mapping about the 103-diffraction conditions for 100 nm $PbZr_yTi_{1-y}O_3$ ↔ $PbZr_xTi_{1-x}O_3$/$SrRuO_3$/$GdScO_3$ (110) heterostructures (sample name: (*x*,*y*)) (a) (20,45), (b) (40,60), (c) (20,80), and (d) (80,20). Dashed lines represent the coherently strain (vertical) and cubic (angled) lattice parameters. The expected peak positions for bulk (solid) and strained (empty) versions of the parent phases are labeled in each graph. The percentage of strain relaxation is also noted.

On the other hand, the (80,20) heterostructures possess peaks for both the rhombohedral ($PbZr_{0.8}Ti_{0.2}O_3$, referred to as PZT_R, Figure 5.3d) and tetragonal in-plane oriented *a* domains ($PbZr_{0.2}Ti_{0.8}O_3$, referred to as PZT_T, Figure 5.3d); an indication of complete strain relaxation.

The asymmetry in the strain relaxation and observed crystal structures is fairly straightforward to understand by considering the 100 nm (20,80) and (80,20) heterostructures. Recall that the lattice mismatch between $PbZr_{0.2}Ti_{0.8}O_3$ and the substrate (0.8% tensile) is considerably smaller than the lattice mismatch between the $PbZr_{0.8}Ti_{0.2}O_3$ and the substrate (3.5% compressive). As a result, $PbZr_{0.8}Ti_{0.2}O_3$ are more susceptible to strain relaxation as compared to $PbZr_{0.2}Ti_{0.8}O_3$ films of similar thickness. Therefore, the (80,20) heterostructures are expected to undergo rapid strain relaxation and present the subsequent Ti-rich phase with an effectively larger in-plane lattice parameter than the $GdScO_3$ substrate. The subsequently deposited Ti-rich (tetragonal) material will, in turn, accommodate the large tensile strain by forming *a* domains, as seen in the RSM. On the other hand, when the Ti-rich material is grown at the substrate interface, as is the case in the (20,80) heterostructures, the small lattice mismatch with the substrate is easily accommodated and the subsequent Zr-rich material is presented with in-plane lattice parameters that are more favorable for generating a compressively-strained film.

With this in mind, now considering the thickness series of (20,80) heterostructures (Figure

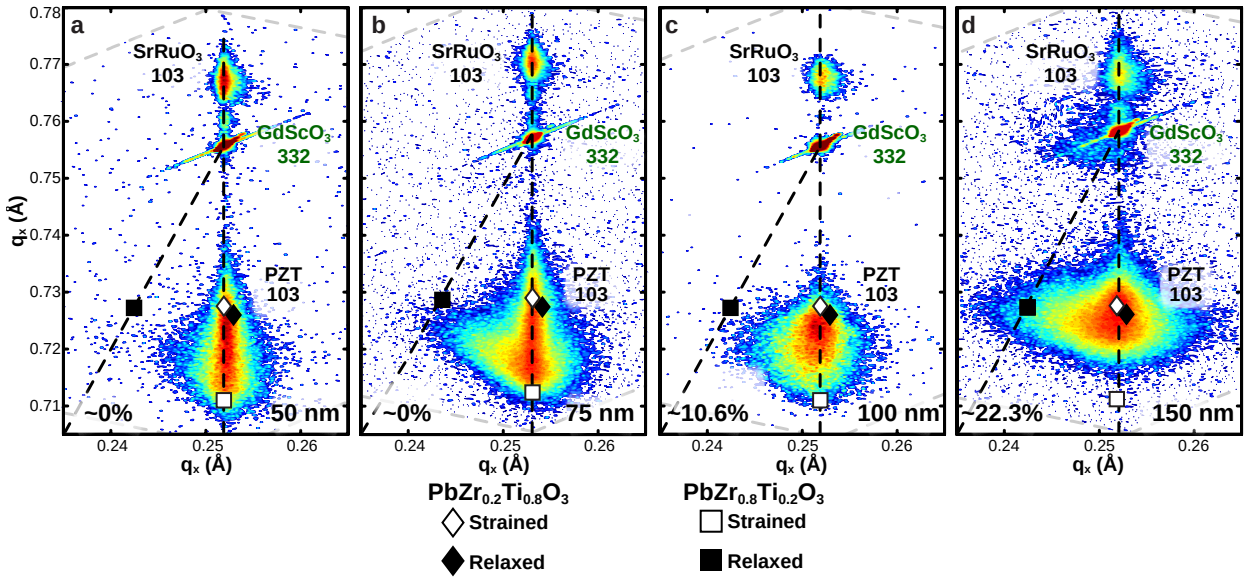

Figure 5.4. Reciprocal space mapping about the 103-diffraction conditions for $PbZr_{0.8}Ti_{0.2}O_3$ ↔ $PbZr_{0.2}Ti_{0.8}O_3$/$SrRuO_3$/$GdScO_3$ (110) heterostructures of various thickness (a) 50 nm, (b) 75 nm, (c) 100 nm, and (d) 150 nm. Dashed lines represent the coherently strain (vertical) and cubic (angled) lattice parameters. The expected peak positions for bulk (solid) and strained (empty) versions of the parent phases are labeled in each graph. The percentage of strain relaxation is also noted.

5.4a-d) we find, as expected, the q_y-values spans continuously between the theoretical strained peak positions of the parent phase. On closer inspection however, it is evident that as the thickness of the heterostructures increases there is a slight increase in spectral weight toward lower q_x-values and a slight decrease in spectral weight near the expected lattice parameter for strained $PbZr_{0.8}Ti_{0.2}O_3$ an indication that the heterostructures might be partially relaxed.

5.4.1 Quantification of Strain Relaxation in Graded Heterostructures

From the XRD studies it is evident that the compositionally-graded heterostructures are not coherently strain to the substrate, and in actuality they are partially relaxed. In general, extracting a quantitative measure of strain relaxation from homogeneous, single-composition heterostructures is based on analyzing the breadth of the diffraction peak of the film relative to that of the substrate. For instance, one commonly-used approach is to apply something akin to the Williamson-Hall method,[232] which has been used in a number of recent publications.[151, 165, 197] This approach requires that the film of interest can be modeled as a single diffraction peak whose peak width is reflective of the degree of relaxation.

In the case of the compositionally-graded heterostructures studied herein, however, the simultaneous change of composition, relaxation, and possibly phase makes the assumption of a single, clearly-defined diffraction peak untenable. In turn, no established approaches for inhomogeneous,

compositionally-graded thin films are available to quantify strain relaxation. Thus we developed a unique approach to provide a quantitative assessment of relaxation in compositionally-graded heterostructures.

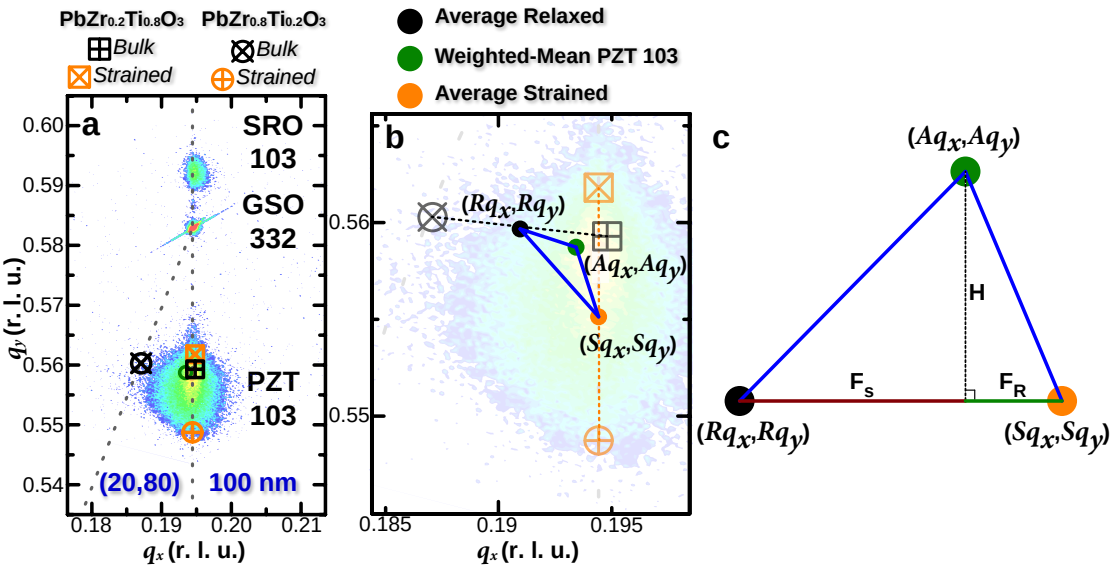

Figure 5.5. Figure demonstrating methodology used to calculate residual strain from RSM studies of compositionally-graded heterostructures. (a) Representative RSM of 100 nm thick (20,80) compositionally-graded heterostructure about the 332 and 103 diffraction condition for the substrate and film, respectively. Coherently strained and relaxed peak positions are indicated. (b) Close-up of the 103 diffraction peak for $PbZr_{1-x}Ti_xO_3$ indicating the calculated weighted-mean peak position, average strained, and relaxed peak position. (c) Diagram showing the geometry used to calculate the residual strain.

To quantify the strain relaxation in the compositionally-graded heterostructures, we initially extracted the logarithmically-scaled, weighted-mean diffraction peak position (weighted by the peak intensity *I*) from the reciprocal space maps about the 103-diffraction condition for $PbZr_{1-x}Ti_xO_3$ (*e.g.*, Figure 5.5a) (equation 5.1-2) as indicated in (Figure 5.5b, green marker).

$$2\theta_{ave} = \frac{\sum_{i=1}^{n} 2\theta \log I}{\sum_{i=1}^{n} \log I} \tag{5.1}$$

$$2\omega_{ave} = \frac{\sum_{i=1}^{n} 2\omega \log I}{\sum_{i=1}^{n} \log I} \tag{5.2}$$

Similarly, the average-relaxed (Figure 5.5b, black marker) and average-strained (Figure 5.5b, orange marker) peak positions were defined from the midpoint of the line between the relaxed and strained peaks of the end-member compositions, as depicted graphically (dashed lines, Figure 5.5b). The percentage of the film relaxed is then calculated by computing the relative distance of the projection of the weighted-mean peak position on the line defined by the average relaxed and strained peak position (Figure 5.5c, equations 5.3-5.6). Using this methodology the percentage of

relaxation in the heterostructures (η) was calculated (as shown in the bottom left hand corner of the RSM, Figure 5.3-5.4).

$$H = \frac{\left|\left(Sq_y - Rq_y\right)Aq_x - \left(Sq_x - Rq_x\right)Aq_y + Sq_xRq_y - Sq_yRq_x\right|}{\sqrt{\left(Sq_y - Rq_y\right)^2 + \left(Sq_x - Rq_x\right)^2}} \tag{5.3}$$

$$F_s = \sqrt{\sqrt{\left(Rq_x - Aq_x\right)^2 + \left(Rq_y - Aq_y\right)^2}} - \tag{5.4}$$

$$F_R = \sqrt{\sqrt{\left(Sq_x - Aq_x\right)^2 + \left(Sq_y - Aq_y\right)^2}} - \tag{5.5}$$

$$\eta = \frac{F_R}{F_R + F_S} x100\% \tag{5.6}$$

5.4.2 Description of Crystal Structure and Strain State in Compositionally-Graded $PbZr_{1-x}Ti_xO_3$ Heterostructures

To begin our discussion of the crystal structure and strain state in the compositionally-graded heterostructures we start with the (20,80) heterostructures of various thicknesses, as understanding the trends in this sample set is less complicated. Based on the analysis of strain relaxation, both the 50 and 75 nm thick (20,80) heterostructures (Figure 5.4a-b) are found to be coherently strained to the substrate (within experimental resolution limits). As the thickness of the (20,80) heterostructure is increased to 100 nm (Figure 5.4c) and 150 nm (Figure 5.4d), the relaxation from the theoretical strained peak position increases to ~10.6% and ~22.3%, respectively. All told, these observations imply that strain relaxation increases with film thickness as would typically be expected.[81]

Similar analyses on the 100 nm thick compositionally-graded heterostructures with different gradient forms [*i.e.*, (20,45) (Figure 5.3a), (40,60) (Figure 5.3b), (20,80) (Figure 5.3c), and (80,20) (Figure 5.3d)] reveal that the (20,45) heterostructures are coherently strained to the substrate (within the experimental resolution limits), but that the (40,60) heterostructures and the (80,20) heterostructures undergo significantly relaxation (~26.7% and nearly 100% from the theoretical strained peak position, respectively). The minimal (or negligible) strain relaxation in the (20,45) heterostructures can be readily understood since the films possess uniform bulk tetragonal structure and smaller lattice parameter variation across the thickness of the heterostructure. On the other hand, the (40,60) heterostructures possess more than double the amount of strain relaxation

than the 100 nm (20,80) heterostructures despite having approximately half the maximum theoretical strain gradient. This discrepancy can be understood by considering the lattice mismatch between the substrate and the bottom-layer $PbZr_{1-x}Ti_xO_3$, which in the (20,80) heterostructures is only 0.15% tensile as compared to −1.2% compressive in the (40,60) heterostructures. Thus, the larger lattice mismatch at the substrate–film interface likely begets more pronounced and rapid strain relaxation. This same rational can be used to explain the near complete relaxation observed in the (80,20) heterostructure, as the mismatch at the substrate film interface is significantly larger (-3.5% compressive) than all other heterostructure in this treatment.

The key insight from these analyses is that regardless of the heterostructure thickness and the nature of the compositional gradient the heterostructures retain a large majority (if not all) of the epitaxial strain imparted by the substrate, as long as the misfit strain at the substrate film interface is small. This stands in contrast to what is typically observed in homogeneous films of the various parent materials, *i.e.*, 100 nm thick $PbZr_{0.2}Ti_{0.8}O_3$, $PbZr_{0.52}Ti_{0.48}O_3$, and $PbZr_{0.8}Ti_{0.2}O_3$ heterostructures grown on $GdScO_3$ substrates, which reveal ~0%, ~84.0%, and 45.3% strain relaxation using the same methodology, respectively, (see sections 3.3.1 and 4.4). Thus, consistent with what has been observed in group IV and III–V semiconductor systems, these results demonstrate that the presence of the compositional gradient (and in particular, those with minimal lattice mismatch at the film–substrate interface) provides a pathway to retain large residual strains and strain gradients not possible in homogeneous heterostructures.[380-382]

5.5 Domain Structure of Compositionally-Graded $PbZr_{1-x}Ti_xO_3$ Heterostructures

Not only does changing the nature of the compositional gradient and heterostructure thickness impact the crystal structure and strain state of the heterostructures, but it also can give rise to and vary both the density and nature of ferroelastic domains.[81-83, 385] To image these nanoscale ferroelastic domains we conducted out-of-plane piezoresponse force microscopy (PFM) studies. Focusing first on the thickness series of (20,80) heterostructures, the 50 nm thick heterostructures are observed to exhibit a monodomain structure (Figure 5.6a), consistent with expectations for a (00*l*)-oriented, highly compressively strained tetragonal ferroelectric (such as Ti-rich $PbZr_{1-x}Ti_xO_3$). Upon increasing the thickness of the heterostructures to 75 and 100 nm, *c*/*a*/*c*/*a* domain structures (consisting of out-of-plane polarized *c* domains and in-plane polarized *a* domains) emerge, with a

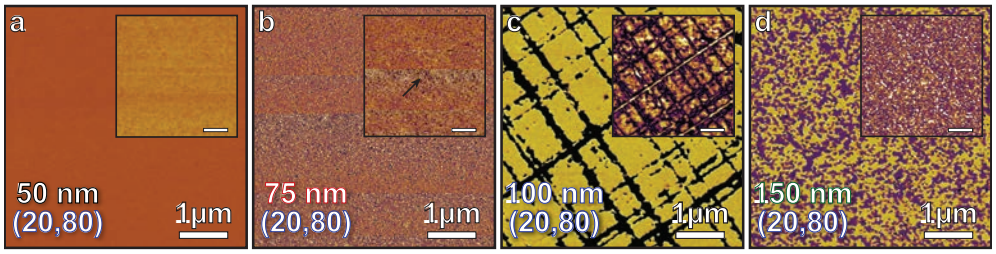

Figure 5.6. Vertical phase piezoresponse force microscopy images of $PbZr_{0.8}Ti_{0.2}O_3$ ↔ $PbZr_{0.2}Ti_{0.8}O_3$/$SrRuO_3$/$GdScO_3$ (110) heterostructures with $PbZr_{1-x}Ti_xO_3$ layers (a) 50 nm, (b) 100 nm, (c) 75 nm, and (d) 150 nm thick. Vertical amplitude piezoresponse force microscopy images are provided as an inset in each of the figures. Arrow in (b) indicates the lone *a* domain visible in the scanned region of the 75 nm (20,80) heterostructure.

density and domain width which increases significantly with heterostructure thickness (Figure 5.6b-c). Again, such a domain structure is typically observed only in tetragonal ferroelectrics (see section 3.4.2).[81, 125, 194] Finally, for the 150 nm thick heterostructures, a complex mosaic-like domain structure is observed (Figure 5.6d), indicating that, at least at the surface, the tetragonal-like domain structure is no longer stabilized. Instead the domain structure is consistent with what is observed in typical rhombohedral $PbZr_{1-x}Ti_xO_3$ heterostructures (see Figure 3.6g-i). These observations can be understood by considering the driving forces for ferroelastic domain formation and the observed crystal structures. In the thinnest films, coherency with the substrate is maintained and the large compressive strain drives the manifestation of a tetragonal-like crystal and monodomain structure. At intermediate thicknesses, the growing strain energy results in slight strain accommodation (*via* domain formation), but the residual epitaxial strain is enough still to stabilize the tetragonal crystal and domain structure. The presence of classical monodomain *c*-like and *c*/*a*/*c*/*a*-like domain structures in compositionally-graded heterostructures where the top 50% of the heterostructures is made up of Zr-rich $PbZr_{1-x}Ti_xO_3$ (with a bulk rhombohedral phases) demonstrate the efficacy of compositional gradients at retaining large residual compressive strains, and its ability to stabilize the tetragonal phase and domain structures. Finally, in the thickest heterostructures, the more significant relaxation (especially at the free surface) results in loss of coherency to the substrate and relaxation (at least at the surface) to the parent rhombohedral phase (and domain structure).

We have also probed the effect of changing the nature of the compositional gradient on the domain structure evolution. First comparing the 100 nm (20,80) (Figure 5.7a) and (80,20) heterostructures (vertical piezoresponse images Figure 5.7b, lateral piezoresponse images Figure 5.8c) we observe contrasting domain structures. As previously described in the 100 nm (20,80)

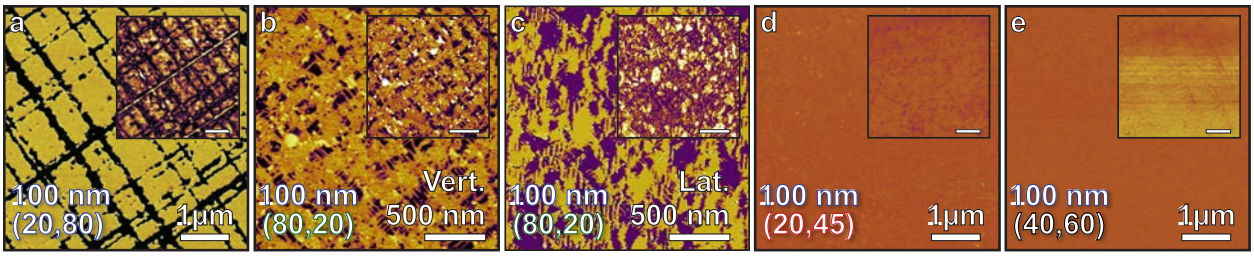

Figure 5.7. Piezoresponse force microscopy images of 100 nm thick $PbZr_yTi_{1-y}O_3$ ↔ $PbZr_xTi_{1-x}O_3/SrRuO_3/GdScO_3$ (110) heterostructures of various chemical compositions (sample name: (*x*,*y*)) (a) vertical phase image of a (20,80) heterostructure, (b) vertical phase image of a (80,20) heterostructure, (c) lateral phase image of a (80,20) heterostructure, (d) vertical phase image of a (20,45) heterostructure, and (e) vertical phase image of a (40,60) heterostructure. Amplitude piezoresponse force microscopy images are provided as an inset in each of the figures.

heterostructures we observe a classical *c*/*a*/*c*/*a*-like domain structure. On the other hand, the (80,20) compositionally-graded heterostructures exhibit domain structures which look remarkably similar to the domain structures observed in highly tensile-strained, mixed-phase tetragonal $PbZr_{1-x}Ti_xO_3$, having a mixture of dense c/a/c/a domains (which could be rhombohedrally distorted) and in-plane oriented $a_1/a_2/a_1/a_2$ domains (more details about this structure are included in section 7.2.1).[119] While these simple studies are not capable of quantifying all features of such a complex domain structure what is evident that the strain (imposed by the bottom Zr-rich $PbZr_{1-x}Ti_xO_3$ layer) is accommodated by forming a high density of ferroelastic domains. This domain structure is consistent with the RSM studies which showed a high density of in-plane oriented, Ti-rich (tetragonal) phases (Figure 5.3d). Moving on to the PFM studies the 100 nm thick (20,45) (Figure 5.7e) and (40,60) (Figure 5.7e) heterostructures both reveal a monodomain structure; once again, similar to, those observed in highly compressively strained tetragonal ferroelectrics. Such a monodomain structure in the (20,45) heterostructures is unsurprising since the film is entirely on the tetragonal side of the phase diagram, where compressive strains act to stabilize the *c* phase. Conversely, the presence of a monodomain structure in the (40,60) heterostructures is unexpected as these heterostructures have many attributes which should drive the formation of a polydomain structure. First, the (40,60) heterostructures have a considerably larger average misfit strain and subsequent relaxation (as compared to the (20,45) heterostructures). Second, they possess a large fraction of the heterostructure compositionally near the MPB where the flattened energy landscape between the structural variants facilitates ferroelastic domain formation[386] and nanodomain structures.[128, 348] Third, the top ~50% of the film is compositionally such that it should have rhombohedral structure. It is likely, the presence of the continually increasing compressive strain state in these heterostructures, which transitions from −1.2% compressive at the film–substrate interface to −3.2%

compressive at the free surface, enables the retention of considerably more strain than is achievable in homogeneous films, thereby stabilizing the tetragonal-like crystal and domain structure.

5.6 Dielectric and Ferroelectric response of Compositionally-Graded $PbZr_{1-x}Ti_xO_3$ Heterostructures

Armed with this knowledge of how the nature of the compositional gradient and the heterostructure thickness can be manipulated to engineer the strain gradient and domain structure in these materials, we set out to explore how the structure influences the dielectric and ferroelectric responses of these heterostructures. To conduct these electrical measurement parallel plate capacitor structures were fabricated using the MgO hardmask processes (as described in section 2.2.1).

Before discussing the more nuanced effects of changing the nature of the compositional gradient and film thickness on the dielectric and ferroelectric responses of these heterostructures we want to first highlight the more general features of heterostructures with compositional and strain gradients. To do this, we focus on the 100 nm thick (20,80) and (80,20) compositionally-graded heterostructures and compare their responses to single-layer heterostructures of their parent end members $PbZr_{0.2}Ti_{0.8}O_3$ and $PbZr_{0.8}Ti_{0.2}O_3$. These heterostructures were chosen as they have the largest chemical and strain gradient and have the most variance in the crystal and domains structures characteristic of the entire set of compositionally-graded heterostructures studied.

5.6.1 *Ferroelectric Response of Single-Layer and Compositionally-Graded $PbZr_{1-x}Ti_xO_3$ Heterostructures*

We begin our discussion with the ferroelectric hysteresis loops of these heterostructures. The hysteresis loops for all four heterostructures were measured at a range of frequencies, but for brevity, only the hysteresis loops measured at 1 kHz are provided (Figure 5.8). Looking at the general form of the hysteresis loops, the (20,80) and (80,20) heterostructures have distinct behaviors which are different from the single-layer heterostructures. Beginning with the (80,20) heterostructure (Figure 5.8, green curve) we observe a voltage-symmetric hysteresis loops with greatly diminished remnant and

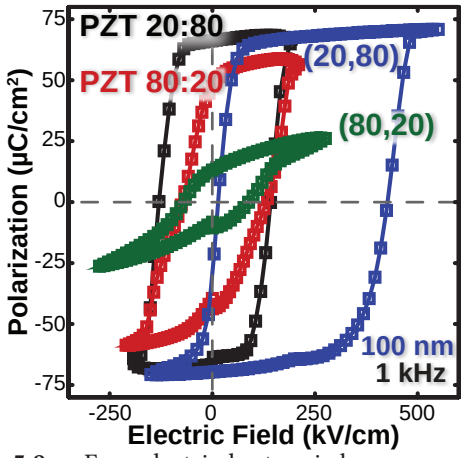

Figure 5.8. Ferroelectric hysteresis loops measured at 1 kHz for 100 nm thick single-layer $PbZr_{0.2}Ti_{0.8}O_3$ and $PbZr_{0.8}Ti_{0.2}O_3$ heterostructures, and compositionally-graded (20,80) and (80,20) heterostructures.

saturation polarization compared to single-layer $PbZr_{0.2}Ti_{0.8}O_3$ and $PbZr_{0.8}Ti_{0.2}O_3$ heterostructures (Figure 5.8, black and red curves, respectively). This response could be attributed to the fact that (80,20) heterostructures have a large fraction of in-plane polarized *a* domains (which cannot be switched in the out-of-plane direction) and thus nearly half of the film is essentially ferroelectrically inactive in this device geometry. The 100 nm (20,80) heterostructures, on the other hand, show very different behavior (Figure 5.8, blue curve) having a large saturation and remnant polarization (commensurate with that measured in the single-layer films). The large saturation polarization in these heterostructures can be easily explained as the stabilization of tetragonal-like phases and domain structures means the entire thickness of the film has a switchable polarization.

More interestingly, the (20,80) heterostructures show large horizontal shifts of the hysteresis loops (along the electric field axis) of up to ~200 kV/cm. The shift observed in the hysteresis loops is not a result of measurement artifact as the response changes direction when changing the electrode geometry. Although reminiscent of an imprint,[12] which can occur due to a variety of extrinsic factors such as space charge accumulation due to asymmetric electrodes or the presence of defect dipoles within the ferroelectric,[239, 387] the observed shifts of the hysteresis loop are indeed intrinsic to the sample. Classic imprint can be easily eliminated with symmetric capacitor structures and oxide electrodes (such as the $SrRuO_3$ electrodes used here) and the fact that only the (20,80) heterostructures show shifted hysteresis loops imply that the shift is intrinsic to the heterostructure. Such shifts are correlated to symmetry breaking within the material caused by some combination of chemical, strain, and/or structural gradients within the material. As previously mentioned prior work on single-layer thin films has highlighted the role of strain gradient induced flexoelectric effects, a possible mechanism capable of forming built-in electric fields.[196, 197, 388] Considering our structural studies which revealed significant retention of compressive strain, resulting in strain gradients as large as 4.3×10^5 m^{-1} (corresponding to a 4.3% strain gradient over a 100 nm thick film), it is likely that flexoelectric effects contribute significantly to the observed built-in potential. The following sub-sections will provide more insight into the nature of the contributions to the built-in potential, however, what is most important to take away from this result is that the presence of a chemical and strain gradient (not possible in coherently-strained, single-layer heterostructures) represent a route to achieve large symmetry breaking in ferroelectric heterostructures and in turn, large built-in potentials.

5.6.2 *Low-Field Dielectric Response of Single-Layer and Compositionally-Graded $PbZr_{1-x}Ti_xO_3$ Heterostructures*

The observed built-in electric fields also have a large effect on the small signal dielectric permittivity (ε_{33}) of the heterostructures. Detailed Rayleigh studies (Figure 5.9a-c) were completed (as described in section 2.2.2). All heterostructures showed low loss (tan $\delta < 0.1$) throughout the entire measurement range. The dielectric permittivity was found to fall into three distinct regimes. The single-layer $PbZr_{0.8}Ti_{0.2}O_3$ and (80,20) compositionally-graded heterostructures exhibit permittivity values in excess of 300 within the reversible regimes. This is consistent with what is expected for samples possessing polydomain structures and large extrinsic domain wall contributions to the permittivity.[125] Consistent with prior studies, the single-layer $PbZr_{0.2}Ti_{0.8}O_3$ heterostructures have an intermediate permittivity with a value around 240 (measured within the reversible regime). Finally, the 100 nm (20,80) compositionally-graded heterostructures exhibit considerably reduced permittivity of ~85, comparable to the intrinsic dielectric permittivity of monodomain, tetragonal $PbZr_{0.2}Ti_{0.8}O_3$ (~90).[301] It has been shown previously that inhomogeneous strain or strain gradients and the resulting built-in electric fields can lead to significant reduction in dielectric permittivity.[196, 197, 388] Our studies lead to precisely the same conclusion as the 100 nm (20,80) heterostructures with the large strain gradients (and built-in potentials) have a dielectric permittivity below that of intrinsic monodomain $PbZr_{0.2}Ti_{0.8}O_3$ despite having a high density of ferroelastic domains. These prior studies, however, do not

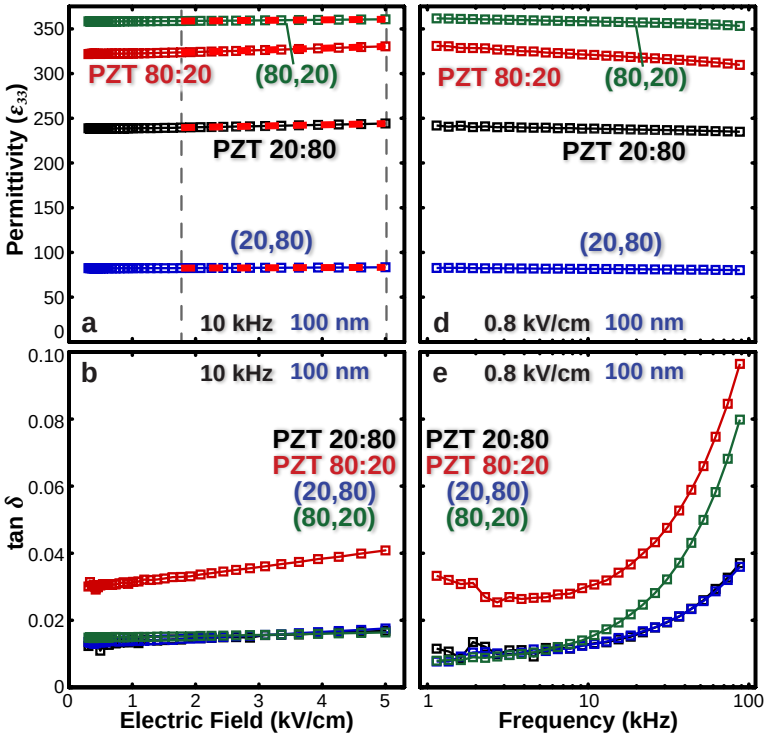

c

	ε_{rev}	α_{irr} (cm/kv)
PZT 20:80	237 ± 0.9	1.4 ± 0.4
PZT 80:20	320 ± 0.5	2.1 ± 0.3
100 nm (20,80)	82 ± 0.2	0.28 ± 0.08
100 nm (80,20)	384 ± 0.6	0.6 ± 0.2

Figure 5.9. (a) Dielectric permittivity and (b) loss tangent for all heterostructure variants displayed as a function of ac excitation bias represented as field. (c) ε_{rev} and α_{irr} obtained from linear fit within the Rayleigh regime [marked by the black dashed lines and red dashed lines (linear fits) in (a)]. Frequency dependence of the (d) dielectric permittivity and (e) loss tangent for all heterostructure variants.

comment on the microscopic mechanism giving rise to reduced dielectric response. We contend that the presence of built-in fields, in a similar fashion to externally applied electric field, can reduce the extrinsic contributions from domain walls by effectively stiffening or pinning the domain walls, due to the increased stability of a single polarization variant at zero bias. In other words, the presence of a built-in potential pointing parallel to the *c* domains in these heterostructures could potentially skew the energy landscape such that the small signal susceptibility is greatly diminished.

To support this hypothesis, we extract the irreversible Rayleigh coefficient (Figure 5.9c), a quantitative measurement of the irreversible domain wall contribution to the permittivity for all heterostructures studied. We observe, as predicted, large Rayleigh coefficients for single-layer $PbZr_{0.8}Ti_{0.2}O_3$ (~2.1 cm/kV), intermediate Rayleigh coefficients for the $PbZr_{0.2}Ti_{0.8}O_3$ heterostructures (~1.4 cm/kV), and greatly diminished Rayleigh coefficients in the 100 nm (20,80) heterostructures (~0.28 cm/kV). Surprisingly, the 100 nm (80,20) heterostructures which have a high density of ferroelastic domains show a rather low irreversible Rayleigh coefficient (~0.6 cm/kV). We contest that due to the in-plane orientation and high density of ferroelastic domains that these domains are elastically pinned by one another, suppressing their irreversible domain wall contributions to the dielectric response, while not significantly impacting their reversible domain wall contributions. All told, these results corroborates our initial hypothesis that the presence of a built-in potential in the 100 nm (20,80) heterostructures acts to pin domain wall responses in a manner similar to an applied electric field, resulting in greatly diminished dielectric permittivities.

Following these Rayleigh studies, frequency-dependent dielectric permittivity measurements using an ac excitation of 8 mV (within the reversible regime) were undertaken (Figure 5.9d-e). Throughout the entire frequency range all samples showed low losses ($\tan \delta < 0.1$). The measured dielectric permittivity of all heterostructures are consistent with the Rayleigh studies which show enhanced dielectric permittivity the in single-layer $PbZr_{0.8}Ti_{0.2}O_3$ and (80,20) compositionally-graded heterostructures, intermediate permittivity in the single-layer $PbZr_{0.2}Ti_{0.8}O_3$, and significantly reduced permittivity in the 100 nm (20,80) compositionally-graded heterostructures. Furthermore, the dispersions (the slope of the frequency dependent dielectric permittivity) while small in all cases is found to follow the same trends as the irreversible Rayleigh coefficients, once again an indication of enhanced extrinsic domain wall contributions in the single-layer $PbZr_{0.8}Ti_{0.2}O_3$ with large density of ferroelastic domains, intermediate extrinsic domain wall contributions in the

single-layer $PbZr_{0.2}Ti_{0.8}O_3$ and (80,20) compositionally-graded heterostructures, and significantly reduced extrinsic domain wall contributions in the 100 nm (20,80) compositionally-graded heterostructures, due to the significant domain wall pinning as a result of the large built-in potential.

5.6.3 *High-Field Dielectric Response of Single-Layer and Compositionally-Graded $PbZr_{1-x}Ti_xO_3$ Heterostructures*

Beyond our studies of the low-field permittivity we have explored permittivity (or capacitance)–voltage butterfly loops for all heterostructure variants. Interesting differences were observed between 100 nm (20,80) compositionally-graded heterostructures that have large built-in potentials and the other heterostructures which do not. Specifically, the 100 nm (20,80) heterostructures (Figure 5.10a) exhibits two distinct small-signal permittivity values and asymmetric butterfly loop shape; whereas, as an example, the (80,20) heterostructures (Figure 5.10b) exhibit only a single value of small-signal permittivity at zero bias and a symmetric loop shape. To explore this anomalous response in more detail the 100 nm (20,80) heterostructure was sequentially poled, up and down using a 1 ms, 2 V pulse. After each poling cycle the heterostructure capacitance was probed using a small sense pulse (0.8 kV/cm at 10 kHz) as it was allowed to relax over 30 minutes. From this measurement (Figure 5.10c) the capacitance has two values depending on the polarization direction. When the heterostructures were poled up (towards the as grown state and the built-in potential) the capacitance increased, on the other hand, when the heterostructures were poled down (away from the as grown state and self-poling direction) the capacitance decreased. After initial poling the capacitance in both the up- and down-poled states reduced slightly; however, during the 30 minute relaxation period the capacitance of the up- and down-poled states never overlapped. This interesting polarization direction dependent capacitance has potential as a

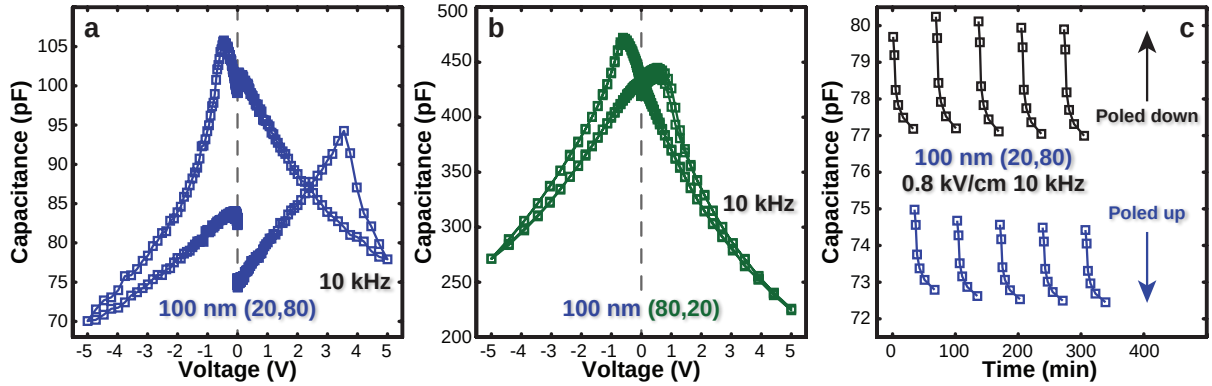

Figure 5.10. Capacitance as a function of voltage for 100 nm compositionally-graded (a) (20,80) and (b) (80,20) heterostructures. (c) Capacitance relaxation following sequential poling measured over the course of 30 minutes. For all measurements the sense pulse was 0.8 kV/cm at a frequency of 10 kHz.

possible new mode of operation for non-volatile, low-power memories. Unlike traditional ferroelectric memories which require multiple capacitors to store a single data bit and destructive read/write operations, a new mode of operation based on the zero-bias capacitance would offer smaller feature size and non-destructive read operations.

Finally, to better understand the importance of built-in potentials in suppressing the dielectric permittivity, we carried out capacitance measurement as a function of frequency between 1 and 200 kHz at different applied background dc electric fields as previously described (section 2.3.1, Figure 5.11a-b). Here, we report such background dc electric field for 100 nm (20,80) compositionally-graded heterostructures (which once again exhibit *c*/*a*/*c*/*a*-like domain structures and a large built-in potential, Figure 5.11b) and compared its response to the single-layer $PbZr_{0.2}Ti_{0.8}O_3$ heterostructures (which has similar *c*/*a*/*c*/*a* domain structures yet, no built-in potential, Figure 5.11a). The data for the $PbZr_{0.2}Ti_{0.8}O_3$ heterostructures reveal two clear regimes (a low- and high-field regime) with a change in the trend around 400–500 kV/cm, regardless of the poling/field direction. Moving on to the 100 nm (20,80) compositionally-graded heterostructures, we once again, observe field and polarization direction dependent responses. Upon poling and measuring the response under the application of negative bias to the top electrode (*i.e.* the up-poled and self-poling direction) the permittivity is found to decrease linearly without changes in the mode of response evident. On the other hand, under the application of positive bias (opposing the built-in potential) a different response is observed. Under low positive biases the dielectric permittivity is found to increase slightly until reaching a critical field (~400 kV/cm) where the permittivity decreases.

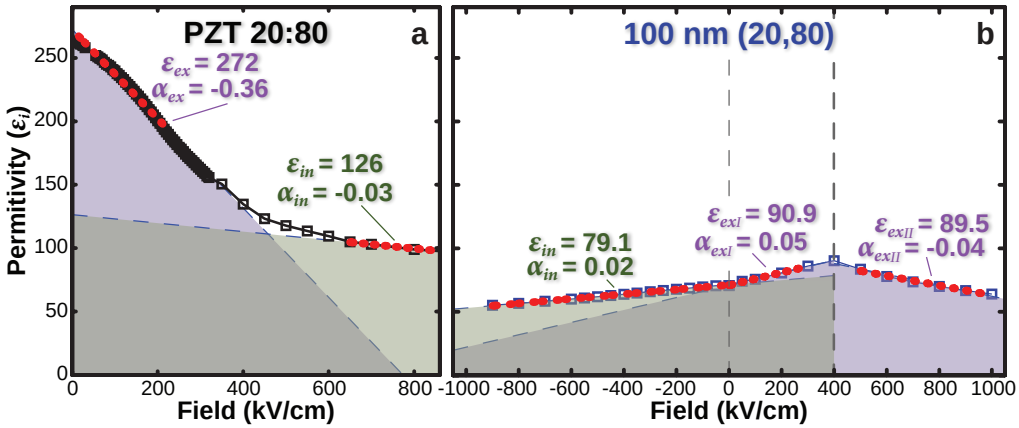

Figure 5.11. Zero-frequency permittivity (ε_i) obtained from a linear logarithmic fit of the dielectric permittivity–frequency data at different applied background dc electric fields is plotted as a function of the applied background dc electric fields for (a) single-layer $PbZr_{0.2}Ti_{0.8}O_3$ and (b) 100 nm (20,80) compositionally-graded heterostructures. Zero-field intrinsic/extrinsic permittivity (ε_{in}/ε_{ex}) and tunabilitiy (α_{in}/ α_{ex}) are obtained from linear fits within each of the regions (red dashed line). Regions of extrinsic (intrinsic) like response are shaded purple (green).

To analyze this response further, we can fit the response within each of these regions to extract values of zero-field intrinsic/extrinsic permittivity ($\varepsilon_{in}/\varepsilon_{ex}$) and tunability ($\alpha_{ex}/\alpha_{in}$) as a function of applied background dc electric field. The low-field regime is generally thought to include information about both the intrinsic and extrinsic contributions to the permittivity, and the high-field regime is thought to be indicative of just the intrinsic response, where the extrinsic contributions to permittivity are suppressed. Linear fits to the low-field regime provide information about how the applied background dc electric field suppresses the extrinsic response (extrinsic tunabilitiy, α_{ex}) and zero-field intrinsic–extrinsic permittivity (ε_{ex}). Linear fits to the high-field regime provide information about how the applied background dc electric field suppresses the intrinsic response (intrinsic tunabilitiy α_{in}) and the zero-field intrinsic permittivity (ε_{in}). In the case of the single-layer $PbZr_{0.2}Ti_{0.8}O_3$ there is an order of magnitude decrease in tunabilitiy as one moves from the low- to high-field regimes (-0.36 to -0.03 cm/kV, respectively) suggesting that the extrinsic response is much more susceptible to suppression with external fields. Additionally, the zero-field permittivity in the low- and high-field regimes is ~272 (close to that observed near zero-field, Figure 5.9) and ~126 (close to what is expected for monodomain $PbZr_{0.2}Ti_{0.8}O_3$).[301, 389] In other words, ~55% of the zero-field, room-temperature permittivity arises from extrinsic contributions (consistent with prior observations of such materials).[125]

In the 100 nm (20,80) compositionally-graded heterostructures, which possess a large built-in potential the nature of the response is fundamentally different, and thus its response cannot be fit in the same manner. To account for this difference, linear fits were conducted in each of three regions as previously described; however, the zero-field permittivity was calculated assuming the point of zero field to be the inflection point in the dielectric permittivity (at ~400 kV/cm) to account for the built-in potential. Starting our discussion with the response under negative bias (*i.e.* the up-poled and self-poling direction) we observe a single region of response with zero-field permittivity of ~79.1 and a tunabilitiy ~0.02 cm/kV. These values are similar to those reported in the intrinsic regime for the single-layer $PbZr_{0.2}Ti_{0.8}O_3$, implying that the response under negative bias in purely intrinsic in nature. Moving on to the response under positive bias, in the low-field region we observe a zero-field permittivity of ~90.8 and a tunabilitiy of ~0.05 cm/kV, both of which are significantly greater than observed under negative bias, but still much closer to the response observed in the high-field (intrinsic) regime in the single-layer $PbZr_{0.2}Ti_{0.8}O_3$ heterostructure. Finally,

fits to the high-field positive bias regime reveal a zero-field permittivity (~89.5) and tunabilitiy (~-0.04 cm/kV) nearly identical in magnitude to what is observed in the low-bias positive field regime.

Based on these results, we contest that when the applied field, polarization, and built-in potential direction all reinforce one another (as is the case under negative bias) the response is purely intrinsic in nature, showing a single regime of response with low permittivity and tunabilitiy. On the other hand, when the applied field opposes the polarization direction and built-in potential (as is the case under positive bias) the slight increase in zero-field permittivity and tunabilitiy (from the negative bias response) under small fields implies that extrinsic contributions to the permittivity are being activated by the positive bias. As the bias is increased, eventually the domain walls reach their terminal state under positive bias and any further increasing the bias serves only to suppress their contributions to the dielectric permittivity. Despite this slight activation of extrinsic domain wall contributions to the dielectric permittivity overall the dielectric permittivity in the 100 nm (20,80) heterostructures is always significantly lower than observed in the single-layer $PbZr_{0.2}Ti_{0.8}O_3$ with similar *c*/*a*/*c*/*a* domain structures. Once again, this suggests that the presence of the built-in potential can greatly diminish the extrinsic contributions to permittivity by stiffening the domain walls against motion under the application of small ac excitation fields.

All told, these studies reveal the through the use of compositional gradients that it is possible to dramatically alter the crystal and domain structure, creating combinations of ferroelectric and dielectric responses not possible in compositionally homogeneous ferroelectric heterostructures. Particularly interesting, the ability to generate large built-in potentials in strained compositionally-graded heterostructures is appealing for a wide variety of applications (e.g., piezoelectric vibrational energy scavenging) that require a constant and known polarization direction to enable repeatable and consistent device operation. In addition, to improve the performance of a material in piezoelectric vibrational (and pyroelectric) energy scavenging applications, one needs a material which simultaneously exhibits large piezoelectric (pyroelectric) response, low dielectric constant, and improved robustness to depolarization/aging. Traditionally this has been achieved in ferroelectrics by utilizing imprint or built-in electric fields that arise from the use of asymmetric electrodes. The use of compositionally-graded materials could provide a new pathway to improved performance in each of these areas. Due to the potential importance of heterostructures with large built-in potentials the remained of this chapter will focus on how the nature of the compositional

gradient can be used to control the built-in potential, ferroelectric, dielectric, and pyroelectric responses in these compositionally-graded heterostructures.

5.7 Effect of Heterostructure Design on the Dielectric and Ferroelectric response of Compositionally-Graded $PbZr_{1-x}Ti_xO_3$ Heterostructures

5.7.1 *Complex Evolution of Built-in Potential in Compositionally-Graded $PbZr_{1-x}Ti_xO_3$ Heterostructures*

To study the effect of heterostructure design on the built-in potential, ferroelectric, and dielectric response of compositionally-graded heterostructures we consider the six compositionally-graded heterostructures. For discussion we group these heterostructures into two categories. A set of four (20,80) compositionally-graded heterostructures of varying thickness (50, 75, 100 and 150 nm) and a set of three 100 nm thick compositionally-graded heterostructures with different gradient forms [*i.e.*, (20,45), (40,60), and (20,80)]. To quantify the built-in potential, ferroelectric hysteresis loops were measured for the various heterostructures at a range of frequencies (Figure 5.12a-b, for brevity, we show characteristic hysteresis loops measured at 1 kHz). Once again, similar to compositionally homogeneous ferroelectric thin films, all heterostructures studied show large saturation and remanent polarization. Similar to our previous studies, the built-in potential is quantified by the horizontal shift of the ferroelectric hysteresis loops along the voltage (or field) axis (*i.e.*, the difference between the coercive fields), and are plotted as a function of film thickness (Figure 5.12c). On the basis of common understanding of flexoelectric effects and built-in potentials,[164, 167, 170, 172, 390, 391] one would empirically expect that the magnitude of the built-in potential would be

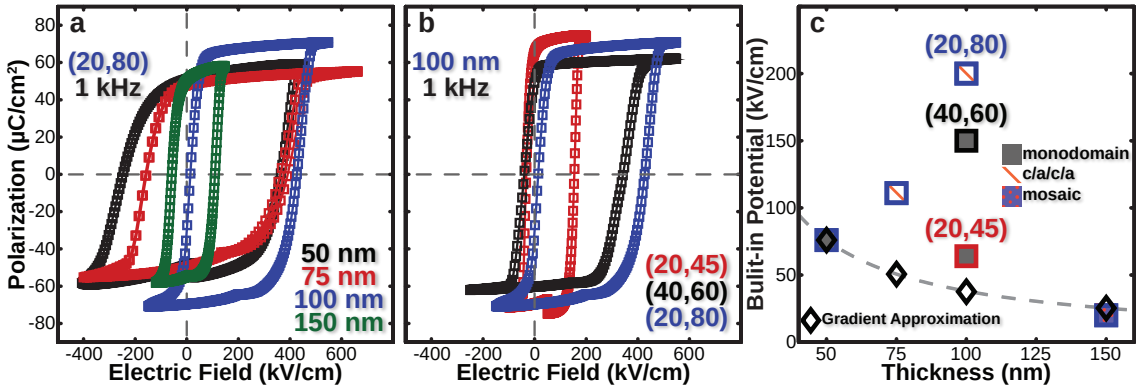

Figure 5.12. Room temperature polarization–electric field hysteresis loops of $PbZr_yTi_{1-y}O_3 \leftrightarrow PbZr_xTi_{1-x}O_3/SrRuO_3/GdScO_3$ heterostructures (sample name: (x,y)) measured at 1 kHz of various (a) (20,80) heterostructure thicknesses and (b) 100 nm thick compositional-gradient designs. (c) Plot of measured built-in potential as a function of film thickness for all compositionally-graded heterostructures studied. Dashed line and small diamond markers represents an estimation of the built-in potentials based on the flexo-chemo-electric coefficient of the 50 nm (20,80) heterostructures.

primarily governed by the magnitude of the strain gradient. Thus, for the thickness series of (20,80) heterostructures (Figure 5.12a), the magnitude of the built-in potential should be inversely proportional to the thickness. The actual results, however, do not follow this trend, and instead, the built-in potential is found to increase with film thickness until falling dramatically in the case of the 150 nm thick heterostructures. The measured built-in potential was found to be 0.380 ± 0.045 V (76 ± 9 kV/cm), 0.833 ± 0.038 V (111 ± 5 kV/cm), 2.00 ± 0.090 V (200 ± 9 kV/cm), and 0.4 ± 0.020 V (20 ± 1 kV/cm) for the 50, 75, 100, and 150 nm thick (20,80) heterostructures, respectively.

Only by returning to the differences in the crystal and domain structure can this trend be explained. Overall, as the thickness of the film increases the maximum average theoretical strain gradient and residual strain decreases, and therefore, (under the assumption that the built-in potential is primarily governed by the strain gradient) the built-in potential should monotonically decrease with thickness. In turn, this suggests that additional contributions to the built-in potential must be present. To shed more light on this concept, we can establish a frame of reference for the "intrinsic" strain- and composition-gradient contribution to the built-in potential by first considering the 50 nm thick (20,80) heterostructures. These heterostructures, which are coherently strained and monodomain therefore, possess a structure most closely matched with the "ideal" compositionally- and strain-graded heterostructure concept. Following the methods used in the community,[392] we can extract a coefficient of the same form and units as the flexoelectric coefficient, which we here call the *effective flexo-chemo-electric coefficient* (μ_{eff}), to acknowledge the inclusion of additional contributions, such as chemical-gradient effects, which are not traditionally considered in the flexoelectric coefficient. The effective flexo-chemo-electric coefficient is calculated by comparing the measured internal electric field (*i.e.* the built-in potential) to the maximum theoretical strain gradient as described in equation 5.7:

$$E_F = \frac{\mu_{eff}}{\varepsilon_0 \eta_{33}} \frac{\partial \varepsilon_{11}}{\partial x_3} \tag{5.7}$$

Where E_f is the built in electric field, ε_0 is the vacuum permittivity, η_{33} is the average intrinsic permittivity, and $\frac{\partial \varepsilon_{11}}{\partial x_3}$ is the in-plane strain gradient in the out-of-plane direction. Since, we have no way to measure the dielectric permittivity of the material in absence of the built-in potential we used a constant value for the entire compositionally-graded $PbZr_{1-x}Ti_xO_3$ of η_{33}=158 (which is based on the average high-field compositionally-dependent measurements of intrinsic permittivity in

$PbZr_{1-x}Ti_xO_3$).[128, 357, 392] Knowing that the strain gradient is 8.7×10^5 m^{-1} and that the built in potential is 0.38 V, we calculate the effective flexo-chemo-electric coefficient to be $|\mu_{eff}| = 12$ nC/m. This value lies directly in-between experimentally reported flexoelectric coefficients for the $PbZr_{1-x}Ti_xO_3$ system (500–2,000 nC/m, measured *via* bending of chemically homogeneous samples)[164, 392, 393] and first-principles calculations (which include only strain-gradient-based flexoelectric effects; for $PbTiO_3$ $\mu_{eff} = 0.165$ nC/m).[170, 215, 216] This comparison brings up a number of interesting points. First, as is typical, our experimental measures of these effects return values much larger than the first-principles predictions, suggesting that additional contributions to these effects could be present. Second, our experimental values are considerably smaller than most experimental values, which might suggest that the chemical-gradient effect could be of the opposite sign to that of the classic strain-gradient effects.

Using this effective flexo-chemo-electric coefficient, we can then make a simple prediction of how the built-in potential should scale with thickness (dashed line, Figure 5.12c). Since the maximum theoretical strain gradient is inversely proportional to the heterostructure thickness the built-in potential should fall off with increasing thickness. What is clear, however, is that the built-in potentials measured for the 75 and 100 nm thick (20,80) heterostructures variants are greatly enhanced compared to this expected trend. To explain this unexpected observation requires consideration of the strain state and domain structure of the heterostructures. Both the 75 and 100 nm thick (20,80) heterostructures exhibit a *c*/*a*/*c*/*a* domain structure where the size and density of the *a* domains increases with thickness, matching the observed trend in the built-in potential. This implies that the formation of ferroelastic domains could be responsible for the larger built-in potential. We hypothesize that the presence of ferroelastic *a* domains and the corresponding rotation of the polarization direction at such domain boundaries, gives rise to large, localized strain gradients[166, 394] and fields[394, 395] that contribute to the built-in potential. Since the largest built-in potential is observed in the 100 nm thick (20,80) heterostructures despite the significant reduction in strain gradient, this suggests that the *c*/*a*/*c*/*a* domain structures are key in defining the evolution of these effects. Finally, in the 150 nm thick heterostructures, which possess the most severe strain relaxation and domain structures indicative of complete or near-complete relaxation at the surface of the film, the relaxation must be severe enough that the strain gradient barely persists in the film, thereby dramatically reducing the overall built-in potential.

A similar analysis of the built-in potentials for the 100 nm thick (20,45), (40,60), and (20,80) heterostructures (Figure 5.12b), where the built-in potentials were measured to be 0.64 ± 0.03 V (64 ± 3 kV/cm), 1.5 ± 0.09 V (150 ± 9 kV/cm), and 2.0 ± 0.09 V (200 ± 9 kV/cm), respectively, can be completed. Recall that the theoretical strain gradients for the (20,45) and (40,60) heterostructures are approximately half of that of the (20,80) heterostructures and that both heterostructures exhibit a monodomain structure. Beginning with the (40,60) heterostructures, the lattice parameters defining the strain gradient increase rapidly, in a nonlinear fashion, upon transitioning through the MPB composition.[316] We hypothesize that the presence of locally enhanced strain gradients within the film associated with the MPB compositions could greatly increase the magnitude of the macroscopic built-in potential, even in the absence of domain structures. It should be noted, that heterostructures encompassing the MPB could also exhibit enhanced built-in potentials because of a local variation in the magnitude of the flexoelectric coefficient, which is typically larger near the MPB.[170, 396] Additionally, the fact that the built-in potential of the (40,60) heterostructures are larger than that of the 50 nm thick (20,80) heterostructures suggests that the chemical-potential-gradient effects are likely smaller (because of the reduced compositional range); yet, are still of the opposite sign of the strain-gradient effects. On the other hand, in the (20,45) heterostructures the reduced built-in potential is like the result of the fact that the composition range probed exists entirely on the tetragonal side of the $PbZr_{1-x}Ti_xO_3$ phase diagram, and that the lattice parameters increase smoothly with increasing Zr content, thereby excluding any locally enhanced strain gradients in the films. Additionally, the chemical-gradient effects in the (20,45) heterostructures should also be relatively small in magnitude (compared to the 50 nm thick (20,80) heterostructures), but again we cannot fully decouple these effects in a manner that allow us to quantify the magnitude of the chemical-gradient effect uniquely. All told, the ultimate manifestation of built-in potential in the compositionally-graded heterostructures varies in a rather complex and, at times, unintuitive manner as a function of film thickness, lattice parameter variation, domain formation, strain relaxation, compositional end members, and much more. Overall, the built-in potentials are larger when locally enhanced strain gradients exist such as those that occur upon transitioning through the MPB composition and at/near ferroelastic domain boundaries. These observations suggest that the macroscopic manifestation of built-in potential includes aspects of flexoelectric effects (*i.e.*, polarization–strain gradient coupling), chemical-gradient effects (*i.e.*, polarization–chemical potential

gradient coupling), and local inhomogeneities that enhance strain (and/or chemical) gradients, which occur preferentially in areas with rapid lattice parameter evolution like near the MPB composition or near ferroelastic domain boundaries.

5.7.2 Dielectric Response of Compositionally-Graded $PbZr_{1-x}Ti_xO_3$ Heterostructures

From a materials design perspective, however, we care about the nature of and how to control the built-in potential in these heterostructures because it can have profound effects on the material properties. Based on our prior studies of compositionally-graded $PbZr_{1-x}Ti_xO_3$ heterostructures which recognized that the presence of built-in potentials can reduce the dielectric permittivity, by acting to stiffen both intrinsic (*i.e.*, within the bulk of a domain) and extrinsic (*i.e.*, from motion of domain walls) domain wall motion under application of small ac fields, we set out to explore how the dielectric permittivity evolves in these various compositionally-graded heterostructures. To do this, the low-field dielectric permittivity was measured as a function of frequency for all heterostructures (we show characteristic permittivity measurements at an ac excitation of 8 mV from 1-100 kHz). Prior to measuring the frequency dependent dielectric response the small-signal field dependence of the permittivity was measured to ensure the measurement was conducted within the reversible Rayleigh regime. All heterostructures showed low losses (tan δ < 0.15) across all measurement frequencies. Again, we begin by exploring the thickness series of (20,80) heterostructures (Figure 5.13a-b) where the dielectric permittivity was found to be 71.8, 68.5, 86.2, and 158.2 (at 10 kHz) for 50, 75, 100, and 150 nm thick heterostructures, respectively. Beginning with the 50 nm thick heterostructures (which are monodomain, with a built-in potential of 76 ± 9 kV/cm) the permittivity is suppressed to a

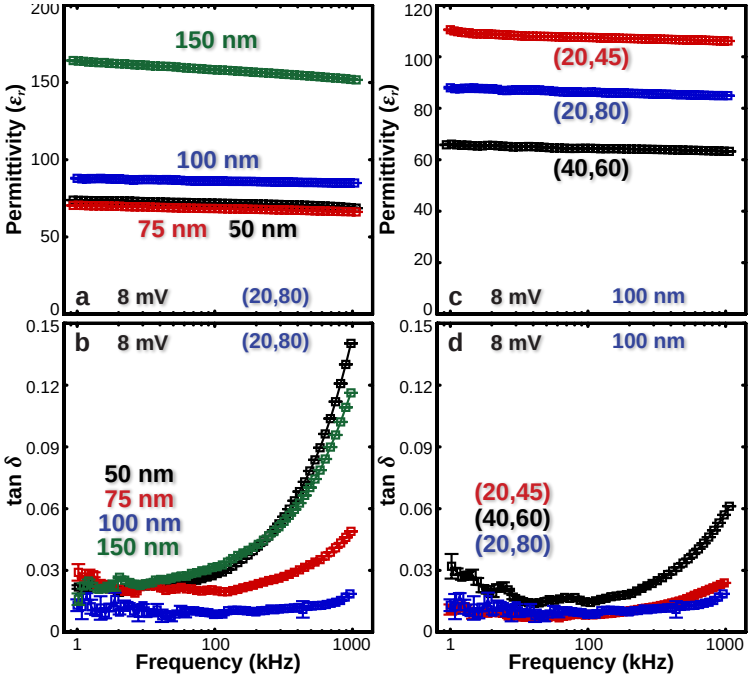

Figure 5.13. Room temperature dielectric response (measured at V_{ac} = 8 mV, error <7%) as a function of frequency for $PbZr_yTi_{1-y}O_3 \leftrightarrow PbZr_xTi_{1-x}O_3/SrRuO_3/GdScO_3$ (110) compositionally-graded heterostructures (sample name: (*x*,*y*)); for (20,80) heterostructure of various thickness (a) dielectric permittivity and (b) dielectric loss, and for 100 nm thick compositional-graded heterostructures of various heterostructure designs (c) dielectric permittivity and (d) dielectric loss.

value lower than that previously reported for intrinsic permittivity (~90) of monodomain, homogeneous $PbZr_{0.2}Ti_{0.8}O_3$ thin films.[301] This observation is readily understood since there are no extrinsic contributions (as there are no domain walls) combined with the sizable built-in potential, which serves to reduce the intrinsic susceptibility and thus the overall response. As the heterostructure thickness increases, domain structures emerge that influence the permittivity in competing ways. The presence of ferroelastic domains is known to give rise to extrinsic contributions to the dielectric permittivity, which typically enhances the dielectric permittivity,[125, 294, 296] and this work has shown that their formation also corresponds to an increases the magnitude of the built-in potential, which should work to suppress both the intrinsic and extrinsic contributions. Thus, in the 75 nm thick heterostructures where there is a small density of domains and a larger built-in field (111 ± 5 kV/cm), the combination manifests as a similar dielectric permittivity to the 50 nm thick heterostructures (within the error of measurement). By the time the thickness reaches 100 nm, however, the presence of a robust and denser domain structure and the associated extrinsic contributions to the dielectric permittivity overcomes the effects of the built-in field (200 ± 9 kV/cm), causing a slight increase in permittivity (although it is still smaller than that reported for monodomain, homogeneous $PbZr_{0.2}Ti_{0.8}O_3$ films). Finally, in the 150 nm thick heterostructures, which have complex, mosaic-like domain structures, with the smallest built-in potential of 20 ± 1 kV/cm, the largest permittivity is observed; a result of the minimally suppressed intrinsic and extrinsic contributions to permittivity.

Using a similar approach, we can also understand the evolution of the permittivity in the 100 nm thick (20,45), (40,60), and (20,80) heterostructures (Figure 5.13c-d). In this set of heterostructures, the (20,45) variants have the largest permittivity (~107.5 at 10 kHz) and the (40,60) heterostructures have the lowest permittivity (~64.4 at 10 kHz). Again, we can rationalize these trends through the evolution of the crystal and domain structure, and built-in potential. First, for the (20,45) heterostructures (with monodomain structure and a built-in potential of 64 ± 3 kV/cm), the measured permittivity is close to the expected permittivity for a monodomain, homogeneous $PbZr_{0.2}Ti_{0.8}O_3$ thin film,[301] indicating that the dielectric response is dominated by the intrinsic response of the monodomain structure, and that the small built-in potential does not significantly influence the dielectric response. For the (40,60) heterostructures (with monodomain structure and sizable built-in potential of 150 ± 9 kV/cm), the larger built-in potential greatly reduces the

intrinsic permittivity, and since there are no domain walls, there are no extrinsic contribution, resulting in the lowest observed dielectric response. We note that to the best of our knowledge that these are the lowest permittivity values reported for any $PbZr_{1-x}Ti_xO_3$ thin film to date. Progressing to the (20,80) heterostructures, *c*/*a*/*c*/*a* domain structures are formed generating an extrinsic response, which enhances the permittivity more than the increase in built-in potential can suppress it, causing a slight increase in permittivity compared to the 100 nm thick (40,60) heterostructures. Regardless, the observation of the lowest reported room temperature dielectric permittivity for the $PbZr_{1-x}Ti_xO_3$ system measured in the (40,60) heterostructures, which are compositionally close to the MPB (where a maximum in dielectric permittivity should be expected) demonstrates the efficacy of compositional-gradients in generating built-in potentials, which can provide routes to strongly decouple the ferroic and dielectric responses.

Altogether, through judicious exploration of a range of compositionally-graded heterostructures we have demonstrated that the ferroelectric and dielectric response is highly influenced by the crystal and domain structure, which can be manipulated by the gradient and heterostructure design. Specifically, we show that the magnitude of the built-in potential is only minimally influenced by the magnitude of the average strain gradient and instead is determined a combination of flexoelectric effects (*i.e.*, polarization–strain gradient coupling), chemical-gradient effects (*i.e.*, polarization–chemical potential gradient coupling), and local inhomogeneities that locally enhance strain (and/or chemical) gradients. These regions of enhanced strain gradients include areas with rapid lattice parameter evolution (like that near the MPB composition) or near ferroelastic domain boundaries. This work highlights the importance of local nanoscale strain gradients in generating large macroscopic built-in potentials, yielding new perspectives on how to design ferroelectric thin films to maximize built-in potentials while having minimal effect on the ferroic responses. In turn, these results provide a facile route to independently tune susceptibilities in ferroelectric thin films essential for optimizing materials figure of merit for a range of applications.

5.8 Pyroelectric Response of Compositionally-Graded $PbZr_{1-x}Ti_xO_3$ Heterostructures

The prior sections in this chapter have established the role of the built-in potential in dramatically suppressing the dielectric response while having minimal impact on the saturation and remanent polarization. Reducing the permittivity is key for optimizing materials for advanced na

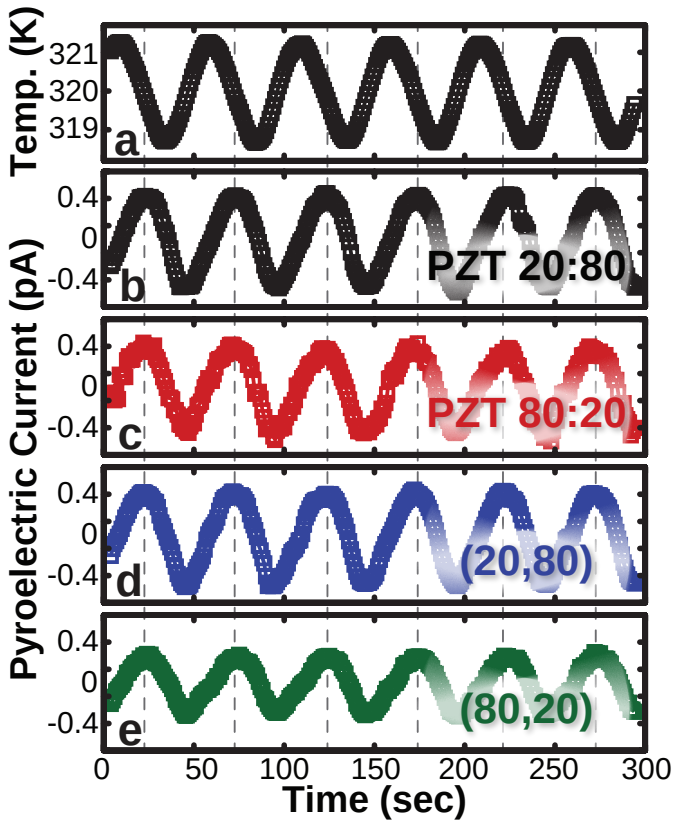

Figure 5.14. (a) Sinusoidal temperature variation applied to extract pyroelectric responses of 100 nm thick (b) single layer $PbZr_{0.2}Ti_{0.8}O_3$, (c) single-layer $PbZr_{0.8}Ti_{0.2}O_3$, and compositionally-graded (d) (20,80), and (e) (80,20) heterostructures.

noscale applications where the figures of merit for electromechanical[26, 397, 398] ($FoM_{EM}=d_{ijk}^2/c\varepsilon_{33}\varepsilon_0$, where d_{ijk} is the direct-effect piezoelectric coefficient and c is the material stiffness, ε_{33} is the dielectric permittivity, and ε_0 is the permittivity of free space), pyroelectric energy conversion ($FOM_{PEC}=\pi^2/\varepsilon_{33}\varepsilon_0$, where π is the pyroelectric coefficient),[24, 26, 27] and infrared sensing and electron emission[399, 400] ($FOM_{IR}=\pi^2/C_E\varepsilon_{33}\varepsilon_0$, where C_E is the heat capacity) are all inversely proportional to the dielectric permittivity. In general, routes to tune material stiffness, heat capacity, *etc.*, are limited and thus the ability to tune these figures of merit is confined to routes that decouple the piezoelectric or pyroelectric responses from the dielectric response. In turn, all that is required to achieve enhanced figures of merit in these compositionally-graded heterostructures is a large built-in potentials which suppress the dielectric permittivity and a large or comparable pyroelectric/piezoelectric response.

In the following section, we explore the pyroelectric responses and figures of merit of these compositionally-graded heterostructures. For this study, we limit our focus to four heterostructures: 100 nm thick, single-layer $PbZr_{0.2}Ti_{0.8}O_3$ and $PbZr_{0.8}Ti_{0.2}O_3$ heterostructures, and 100 nm thick, (20,80) and (80,20) compositionally-graded heterostructures, whose structure and electrical responses were discussed previously. The pyroelectric studies were completed using the phase sensitive measurement technique (as described, section 2.3.2) with a sinusoidally varying temperature excitation centered about a background temperature of 320 K, with a 1.25 K amplitude, at a frequency of 0.02 Hz (Figure 5.14a). The pyroelectric currents from the single-layer $PbZr_{0.2}Ti_{0.8}O_3$ and $PbZr_{0.8}Ti_{0.2}O_3$, and compositionally-graded heterostructures were measured and their response was fit to calculate the pyroelectric coefficient as previously described (Figure 5.14b-e).

The magnitude of the pyroelectric current and therefore the pyroelectric coefficient of the heterostructures can be grouped into two categories. The single-layer $PbZr_{0.2}Ti_{0.8}O_3$ and (20,80) compositionally-graded heterostructures have similar pyroelectric coefficients (−300 and −291 μC/m²K, respectively), ~30% greater than the single-layer $PbZr_{0.8}Ti_{0.2}O_3$ and (80,20) compositionally-graded heterostructures (−229 μC/m²K and −185 μC/m²K, respectively). Note that the $PbZr_{0.52}Ti_{0.48}O_3$ heterostructures (section 4.6.2) have a similar pyroelectric response to the $PbZr_{0.8}Ti_{0.2}O_3$ and (80,20) compositionally-graded heterostructures (~-200 μC/m²K). The observed differences are consistent with the ferroelectric domain structures observed in these heterostructures. The $PbZr_{0.2}Ti_{0.8}O_3$ and (20,80) compositionally-graded heterostructures exhibit *c*/*a*/*c*/*a* domain structures with a large volume fraction of *c* domains (which are out-of-plane polarization), contributing to a relatively large pyroelectric response. On other hand, the $PbZr_{0.8}Ti_{0.2}O_3$ heterostructures exhibit a mosaic (rhombohedral) domain structure, and the (80,20) compositionally-graded heterostructures have a high density of in-plane oriented tetragonal domains, both of which do not contribute to the pyroelectric current when measured along the [001] (*i.e.*, the out-of-plane direction), as measured herein, resulting in a lower pyroelectric response (compared to heterostructures which are primarily out-of-plane polarized). The most impactful observation from these studies is that the presence of a large built-in potential in the 100 nm (20,80) compositionally-graded heterostructures (~200 kV/cm) has almost no impact on the pyroelectric response compared to the other heterostructures studied, yet significantly reduces the dielectric permittivity.

The importance of the suppressed dielectric permittivity in systems with large pyroelectric responses (as is the case in the (20,80) compositionally-graded heterostructures) is highlighted by calculating the pyroelectric figures of merit, as previously described. Here we compare FoM_{IR} and FoM_{PEC} for the four heterostructure variants (Figure 5.15). The heat capacity for the single-layer and compositionally-graded $PbZr_{1-x}Ti_xO_3$ heterostructures is assumed to be ~3 J/cm³K, consistent with published reports,[28] and is assumed constant for all films. Typically $PbZr_{1-x}Ti_xO_3$ is not useful for pyroelectric applications as is illustrated by the single-layer $PbZr_{0.2}Ti_{0.8}O_3$ which despite possessing a large pyroelectric coefficient, the correspondingly large dielectric constant results in a rather pedestrian FoM. Among the four heterostructure variants, however, the 100 nm (20,80) compositionally-graded heterostructures, as expected, reveals the largest figures of merit (FoM_{IR} = 0.129 m²/C and FoM_{PEC} = 0.0113) due to the presence of a large pyroelectric coefficient and low

dielectric permittivity. For both the $PbZr_{0.8}Ti_{0.2}O_3$ and (80,20) compositionally-graded heterostructures, the large dielectric permittivity (resulting from a complex domain structure) paired with rather small pyroelectric coefficients (resulting from the presence of a large fraction of ferroelastic domains) gives rise to low figures of merit. The large figures of merit for the 100 nm (20,80) compositionally-graded heterostructures; however, are comparable or in some cases better than the traditionally utilized systems. For thermal imaging and pyroelectric energy conversion applications, 100 nm (20,80) compositionally-graded heterostructures are 1.1–1.2 times and 1.8–4.2 times larger than the figures of merit for ferroelectric single crystals of $LiNbO_3$ and $LiTaO_3$, respectively. These findings are important because this is the first time it has been demonstrated that large pyroelectric figures of merit, important for a range of technologically relevant devices can be achieved in high-quality thin films. It should also be noted that the $PbZr_{1-x}Ti_xO_3$ family of materials has experienced considerable attention as both ferroelectric memories and for actuator/sensor applications, and thus existing infrastructure and knowledge bases exist on how to create these materials *via* scalable methods. Furthermore, the approach (*i.e.*, the application of compositionally gradients) should be applicable to a wide range of materials and systems. Research on compositionally-graded ferroelectric thin films has not been widely developed, and additional systems—potentially including Pb-free alternatives—may be developed. Additionally, the findings may have impacts beyond thermal applications to both tunable dielectrics, piezoelectrics, piezoelectric energy harvesting, and more. Overall, the approach illustrated herein suggests that compositionally grading materials may give researchers the ability to deterministically tune and control dielectric, ferroelectric, and pyroelectric properties individually—thereby decoupling these effects and allowing for exacting design of high-performance materials.

	π ($\mu C/m^2K$)	ε_{33} (100 kHz)	C_E (J/cm^3K)	FOM_{IR} ($x10^{-2}, m^2/C$)	FOM_{PEC} ($x10^{-3}$,300K)
$PbZr_{0.2}Ti_{0.8}O_3$	-300 ± 7	235	~3	4.81	4.33
$PbZr_{0.8}Ti_{0.8}O_3$	-299 ± 11	453	~3	1.90	1.31
100 nm (20,80)	-291 ± 4	85	~3	12.9	11.3
100 nm (80,20)	-185 ± 13	409	~3	1.70	0.95
$LiNbO_3$	-83	31	2.8	10.8	2.69
$LiTaO_3$	-176	54	3.2	11.6	6.15

Figure 5.15. Pyroelectric coefficients (π), dielectric permittivity (ε_{33}), heat capacity (C_E), and the figures of merit for thermal imaging (FOM_{IR}) and pyroelectric energy conversion (FOM_{PEC}) for single-layer, compositionally-graded heterostructures, and common commercially used pyroelectric single crystals.

5.9 Conclusions

In this chapter, we have explored how deterministic control of compositionally-graded heterostructure form (in terms of the nature of the compositional gradient and heterostructure

thickness) can be used to tune the crystal and domain structure; and have evaluated its influence on the evolution of built-in potentials, ferroelectric, dielectric, and pyroelectric responses in compositionally-graded $PbZr_{1-x}Ti_xO_3$ thin films. We observe that the strain state and domain structure is highly dependent on the misfit strain at the substrate film interface where when closely lattice matched the strain stabilize the tetragonal crystal and domains structures, and enables large residual strains and strain gradients to persists. These large strain (and potentially chemical) gradient results in large built-in potentials and suppressed dielectric permittivity while having minimal influence on the magnitude of the polarization. On the other hand, when there is a large lattice mismatch at the substrate film interface the heterostructures relax, giving rise to a complex strain state and domains structure with large extrinsic contributions to the dielectric permittivity. We explore the evolution of the magnitude of the built-in potential in strained compositionally-graded heterostructures and find that the build-in potential does not scale directly with the magnitude of the strain gradient as would be expected. Instead, it is found that enhanced built-in potentials are observed in the compositionally-graded heterostructures which contain locally enhanced strain gradients occurring when traversing chemistries associated with structural phase boundaries (where there are abrupt changes in material lattice parameter) and at/near ferroelastic domain boundaries. These observations suggest that the built-in potential observed in these materials is likely a manifestation of a combination of flexoelectric effects (*i.e.*, polarization-strain gradient coupling), chemical-gradient effects (*i.e.*, polarization-chemical potential gradient coupling), and local inhomogeneities that enhance strain (and/or chemical) gradients. Regardless of origin, large built-in potentials act to suppress the dielectric permittivity, while having minimal impact on the magnitude of the polarization or pyroelectric responses which is proven to be an effective route to engineer materials with improved pyroelectric and potentially piezoelectric figures of merit.

Chapter 6

Labile Ferroelastic Domain walls in Compositionally-Graded $PbZr_{1-x}Ti_xO_3$

In the previous chapter, we explored how compositionally-graded heterostructures can be designed to retain large residual compressive strains and strain gradients, and evaluated the influence of this new modality of strain engineering on the crystal and domain structure, and built-in potential, as well as its ultimate influence on the ferroelectric, dielectric, and pyroelectric response. Specifically, it was observed that through the use of compositional and strain gradients that it is possible to stabilize tetragonal crystal and domain structures (*c*/*a*/*c*/*a*-like) in sections of films with chemistries which are rhombohedral in the bulk. Surprisingly, it was found that the presence of these domain structures significantly enhance the built-in potential beyond what is expected from the magnitude of the strain gradient alone. In this chapter, we use transmission electron microscopy-based nanobeam diffraction (NBED) and nanoscale band-excitation switching spectroscopy to explore the nanoscale structure and ferroelectric response of these ferroelastic domains. We show that strain gradients in compositionally-graded $PbZr_{1-x}Ti_xO_3$ heterostructures can stabilize needle-like ferroelastic domains which terminate inside the film. Local piezoelectric probes indicate that these needle-like domains are highly-labile in the out-of-plane direction under applied electric fields and produce locally enhanced piezoresponse. Based on these experiments we derive a switching mechanism in these compositionally-graded heterostructures with needle-like domains which explains their role in enhancing the macroscopic built-in potential. This work demonstrates the efficacy of composition and strain gradients in providing new modalities of domain engineering, enabling the design of novel domain structures, and the potential for domain wall-based devices and applications unachievable in homogeneous thin films.

6.1 Introduction

Domains and domain walls are known to dramatically impact the properties of ferroic materials. In ferroelectric thin films, domains tend to form highly-ordered ferroelastic domain structures that minimize the sum of elastic and electrostatic energies.[12, 401] In practice, a diverse range of ferroelastic domain structures and their associated domain walls can be produced, of which the most common are 90° (in tetragonal systems) [127, 194, 402] and 71° or 109° (in rhombohedral systems) domain walls.[172, 183] In the previous chapters, we have demonstrated the ability to controllably produce such domain structures in ferroelectric thin films and this ability can be eloquently exploited to understand contributions to- and to enhance the electrical (dielectric),[125] mechanical (piezoelectric),[192] and thermal (pyroelectric) [194, 374] response of materials. For simplicity, up until now, we have assumed that the strain which guides ferroelastic domain formation is homogeneous, however, it is likely that strain gradients can shape the fine features of the domain structures, with the potential to create new forms of ferroelastic domains with novel structures and modes of response responses. This potential new modality of domain structure engineering is particularly intriguing for designing high-density, nanoscale devices derived from the unique properties existing at these domain boundaries.[64, 158, 403-409] While there has been significant work on using magnetic domain walls for nanoscale devices (which are typically 10-100 nm in width),[410, 411] ferroelectric domain walls which can be considered analogous to magnetic domain walls are particularly intriguing because of their much smaller size (typically 1-10 nm in width) and additional modalities of response, making their consideration for use in this regard a natural one.

Utilizing these ferroelastic domain walls for nanoscale devices requires that they are easily indexable (*i.e.*, spatially localized) and can be manipulated (*i.e.*, writable/erasable, change shape or orientation, *etc.*) by application of an external stimuli (*i.e.*, mechanical or (preferably) electrical) in a controllable and repeatable manner. While it has been shown that ferroelectric, 180° domain walls can be created and moved long distances,[412] in general, ferroelastic domain walls are elastically pinned rendering them essentially immobile.[413-415] Recently, it has been shown that it is possible to create, annihilate, and/or manipulate ferroelastic domains by locally switching ferroelectric thin films; however, these approaches have limited specificity for how or where the domain walls move.[126, 127, 416]

To explore the influence of compositional and strain gradients on the domain structure and response, we focus on two heterostructure variants: 1) compositionally homogeneous, 100 nm thick $PbZr_{0.2}Ti_{0.8}O_3$ heterostructures (henceforth referred to as homogeneous heterostructures) and 2) linear compositionally-graded, 100 nm thick $PbZr_{0.8}Ti_{0.2}O_3$ (top of film) ⇔ $PbZr_{0.2}Ti_{0.8}O_3$ (bottom of film) heterostructures (henceforth referred to as (20,80) compositionally-graded heterostructures); whose crystal and domain structure, and macroscopic properties were explored in chapter 5. As a reminder, the compositional gradient used is nearly compositionally centered between the Ti-rich, tetragonal and the Zr-rich, rhombohedral phases exhibiting an increasing bulk in-plane lattice parameter as one transitions from the bottom to the top of the film. All heterostructures studied herein are grown on 30 nm $SrRuO_3/GdScO_3$ (110) substrates (with lattice parameters a = 5.45 Å, b = 5.75 Å, and c = 7.93 Å corresponding to a pseudocubic a_{pc} = 3.968 Å) producing an effective lattice mismatch which varies from 0.71% to -3.64% from the substrate to film surface in the compositionally-graded heterostructures (for additional description of these heterostructures see section 5.4). Asymmetric reciprocal space mapping (RSM) studies reveal that both the homogeneous (Figure 3.5a) and compositionally-graded heterostructures (Figure 5.3c) are nearly coherently strained to the substrate, and therefore the homogeneous heterostructures are homogeneously strained while the compositionally-graded heterostructures have a strain gradient approaching 4.35 x 10^5 m^{-1}.

6.2 Domain Structure Characterization

6.2.1 Band-Excitation Piezoresponse Force Microscopy Imaging

Conventional single-frequency (and dual frequency) PFM is highly effectual at imaging the general form of a domain structure, however, due to changes in tip contact resonance these techniques commonly result in stochastic false contrast which masks the fine details of the structure.[328] To overcome some of these limitations, the ferroelectric domain structure including both the vertical and lateral components of the homogeneous (Figure 6.1a-b) and compositionally-graded (Figure 6.1c-d) heterostructures were imaged using band-excitation piezoresponse force microscopy (BE-PFM). Unlike conventional PFM techniques, which measure the local piezoresponse with a scanning probe at a single- or dual-frequencies near the cantilever resonance, BE-PFM measures piezoresponse using a frequency band near the cantilever resonance, enabling direct measurement of the full cantilever resonance characteristics (as described in Section 2.4.1). The use of band

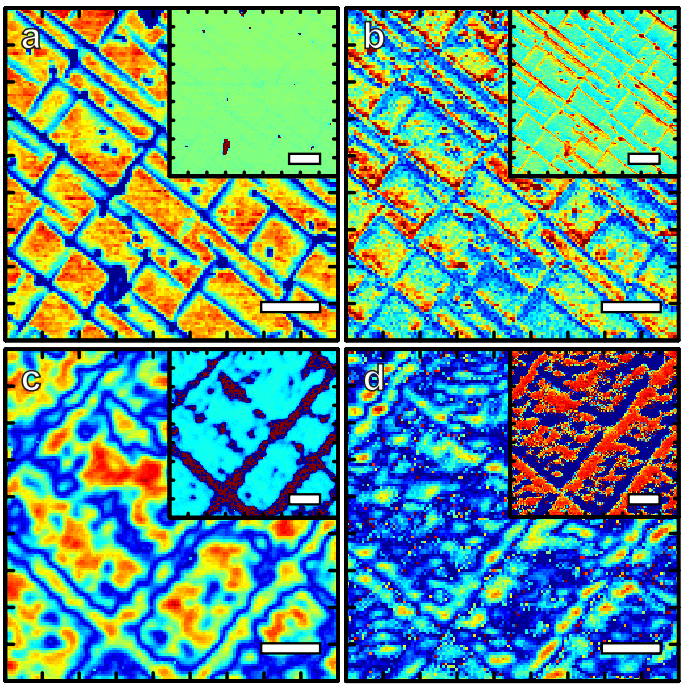

Figure 6.1. Band-excitation piezoresponse force microscopy (a) vertical amplitude (phase inset) and (b) lateral amplitude (phase inset) images of homogeneous $PbZr_{0.2}Ti_{0.8}O_3$ heterostructures. Band-excitation piezoresponse force microscopy (c) vertical amplitude (phase inset) and (d) lateral amplitude (phase inset) images of compositionally-graded $PbZr_{0.2}Ti_{0.8}O_3$←→$PbZr_{0.8}Ti_{0.2}O_3$ heterostructures. Scale bars in all images are 500 nm.

excitation for these measurements is crucial as it minimizes effects from changing tip-sample contact resonance that can alter the observed response, enabling the measurement of piezoresponse consistent throughout multiple dimensions (*i.e.*, frequency, spatial, voltage, time, *etc.*, See section 2.4.1).[328] Both the homogeneous and compositionally-graded heterostructures reveal features reminiscent of *c/a/c/a* domain structures which are made up of out-of-plane polarized *c* domains and in-plane polarized *a* domains separated by 90° domain walls (see section 3.3).[82] At first glance the similarity of these domain structures is surprising because at the free surface of the compositionally-graded heterostructures the film is compositionally rhombohedral and should exhibit a complex mosaic domain structure (See Figure 3.6g-i). As shown in chapter 5, it is likely that the presence of the compositional gradient and the associated strain gradient can stabilize the tetragonal phase and domain structure even in a film with more than 50% of the volume compositionally on the rhombohedral side of the phase diagram.[172, 173, 195] Closer inspection of the piezoresponse images, however, reveal some difference. Specifically, focusing on the amplitude response within the *a* domains, the homogeneous heterostructures exhibit highly-suppressed vertical piezoresponse (compared to the *c* domains), whereas the compositionally-graded heterostructures have similar (or slightly enhanced) piezoresponse within the *a* domains. This is suggestive that additional differences in these domain structures may be present.

6.2.2 *Transmission Electron Microscopy Studies of Compositionally-Graded $PbZr_{1-x}Ti_xO_3$ Heterostructures*

To gain more insight into the fine-structure of the ferroelastic domains we conducted detailed cross-sectional, high-angle annular dark field (HAADF)-STEM imaging and strain mapping studies. While it has been shown[417-419] that homogeneous heterostructures (particularly under tensile strain) primarily form parallelepiped-shaped ferroelastic domains with two (nearly) parallel 90° domains walls along the {101} (which transverses the thickness of the film), similar studies on compositionally-graded heterostructure have not been reported. Cross-sectional samples were prepared using the focused-ion beam machining lift out technique and subsequently attached to a Cu grid. Final polishing was done in a nanomill using a 500 eV argon beam. Representative HAADF- STEM images of the domain structure of the compositionally-graded heterostructure (Figure 6.2a) reveal a *c*/*a*/*c*/*a*-like domain structure; however, instead of continuing the entire way through the thickness of the film the *a* domains terminate within the thickness of the film, forming

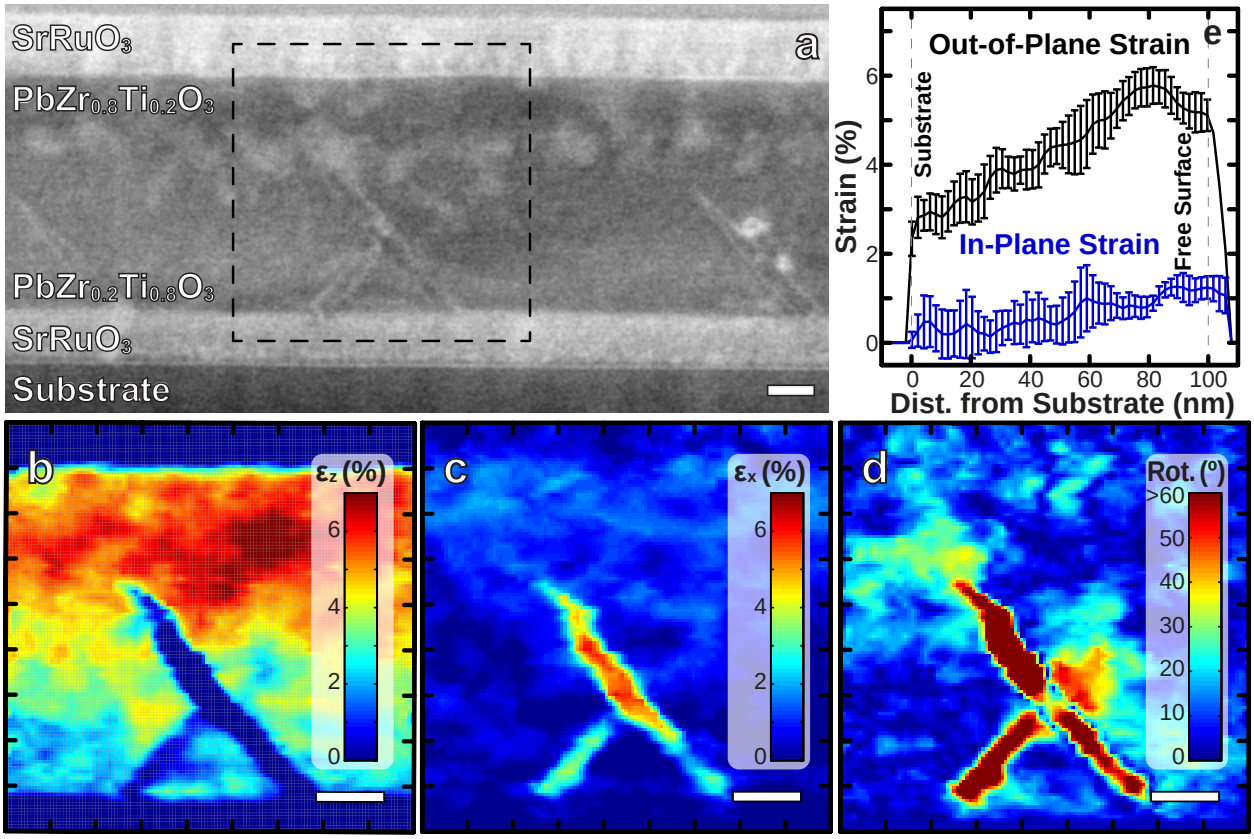

Figure 6.2. (a) High-angle angular dark field scanning transmission electron microscopy image of a compositionally-graded heterostructure revealing the presence of ferroelastic domain structures with needle-like shapes. Nanobeam diffraction-based strain mapping of compositionally-graded heterostructures reveals the (b) out-of-plane and (c) in-plane strain state of the film as well as the (d) local unit cell rotation. (e) Thickness-dependent average of in-plane and out-of-plane strain calculated from the nanobeam diffraction strain mapping. All strain is normalized to the substrate. All scale bars are 25 nm.

a tapered needle-like tip where the two 90° domain walls meet. Images taken at various locations throughout the heterostructure all consistently show the same tapered, needle-like domain structures.

Additional STEM-based nanobeam diffraction (NBED) studies were used to probe the local strain and strain gradients in the compositionally-graded heterostructures. In brief, elastic strain and local crystal rotation mapping about the domain structures was conducted using nanobeam diffraction in an FEI Titan, operated at 300 kV. Individual diffraction patterns were collected at 2.5 nm intervals over a 160 nm x 160 nm region. Diffraction peak locations were identified relative to a reference pattern using cross-correlation analysis, which was then used to calculate the local elastic strain and crystal rotation. Additional details of the elastic strain mapping approach can be found in (section 2.4.4 and Ref. 338). This analysis approach was chosen as it allows for the high resolution imaging of the two dimensional strain tensor over areas much larger that possible with other standard techniques such as geometric phase analysis.

Starting with the out-of-plane strain (Figure 6.2b), there is evidence of a strain gradient consistent with an increasing out-of-plane lattice parameter as one transitions from the substrate to the free surface. Similar analysis of the in-plane strain (Figure 6.2c) reveals nearly homogeneous in-plane strain punctuated by *a* domains which show large relativistic in-plane strains; however, overall the heterostructures are nearly coherently strained to the substrate in-the-plane. Finally, one can also map the unit cell rotation (Figure 6.2d) which shows that (as expected) the *a* domains are rotated ~90° with respect to the *c* domains (indicating that their polarization is in-plane oriented). Thickness-dependent averaging of the strain state measured relative to the substrate (Figure 6.2e, excluding the *a* domains) reveals an out-of-plane strain differential of ~3.8% and an in-plane strain differential of ~1.2% across the thickness of the film.

From these maps it is possible to calculate the thickness dependent epitaxial strain by averaging each line (perpendicular to the out-of-plane direction) excluding those values associated with the *a* domains (those with an in-plane oriented *c* axis). To isolate/partition the *c* domain regions from the *a* domains and substrate/bottom electrode, an arbitrary cutoff strain of -1.5% (in reference to the global mean strain) was used. The partitioned region (Figure 6.3) shows that this cutoff is effective to partition the *c* domains from the *a* domains and substrate/bottom electrode.

Using the calculated thickness-dependent average strain we are able to quantify the strain gradient in the material and compare this to the average theoretical maximum strain gradient of the heterostructures. The strain in the top- and bottom of the $PbZr_{1-x}Ti_xO_3$ layer can be calculated using $\varepsilon = \frac{a_f - a_b}{a_b}$, where ε is the local strain, a_f is the lattice parameter of the film, and a_b is the bulk lattice parameter. In the case of the maximum theoretical strain gradient, we are under the working assumption that the film is coherently strained to the substrate, and therefore, $a_f = a_s = 3.968$ Å, while a_b is 3.94 Å and 4.118 Å for $PbZr_{0.2}Ti_{0.8}O_3$ and $PbZr_{0.8}Ti_{0.2}O_3$, respectively. Using these values and assumptions, the misfit strain for the $PbZr_{0.2}Ti_{0.8}O_3$ and $PbZr_{0.8}Ti_{0.2}O_3$ layers are 0.0071 (tensile) and -0.0364 (compressive), respectively. Since this strain transitions over the film thickness (100 nm) the maximum theoretical strain gradient is ~4.35 x 10^5 m^{-1}. To quantify the actual strain gradient based on the NBED studies, we calculate the average measured lattice parameter of the $PbZr_{0.2}Ti_{0.8}O_3$ and $PbZr_{0.8}Ti_{0.2}O_3$ by multiplying the measured strain (in reference to the substrate lattice parameters) by the substrate pseudocubic lattice parameter. Using this approach, we find the lattice parameters to be 3.9704 Å and 4.0144 Å at the substrate-film interface ($PbZr_{0.2}Ti_{0.8}O_3$) and at the free surface ($PbZr_{0.8}Ti_{0.2}O_3$), respectively. By replacing a_f with these measured values, we calculate the local strain to be, 0.0077 (tensile) and -.0251 (compressive) for the $PbZr_{0.2}Ti_{0.8}O_3$ and $PbZr_{0.8}Ti_{0.2}O_3$, respectively; giving rise to an actual strain gradient of 3.28 x 10^5 m^{-1}. While this actual strain gradient is slightly less than the maximum theoretical strain gradient, it is still very large, demonstrating the efficacy of controlled compositional gradients in generating large strain gradients.

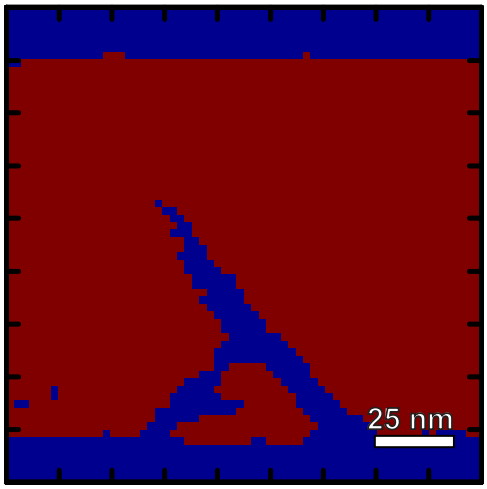

Figure 6.3. Calculated partition used to quantify the average strain gradient from NBED in compositionally-graded heterostructures. Red regions represent the pixels used for the averaging.

Closer inspection of the strain maps provides additional insights. For instance, focusing on the strain near the tip of the domain, there is evidence for increased and reduced strain along the top and bottom edges of the ferroelastic domain, respectively, an observation consistent with phase-field models of needle-like *a* domains.[395] Furthermore, focusing again on the tip of the needle-like domain, we observe unit cell rotation near the leading edge, an indication of a local structural instability associated with the highly-energetic domain wall. The observation of needle-like

domains which terminate within the thickness of the film can be understood considering the strain and strain gradients present in the compositionally-graded heterostructures. Data shows that as the unit cell tetragonality increases from the substrate to the free surface the volume fraction of *a* domains necessary to accommodate the strain state likewise reduces, causing the domain walls to taper to a point. This tapering wall is, however, geometrically required to deviate from the ideal electrical boundary along the {101} and, to minimize the energy of this high-energy boundary, localized polarization rotation occurs. Such high-energy structures are likely relatively unstable and should be highly responsive under electrical and mechanical stimuli.[166, 394] Collectively, these results demonstrate the potential for deterministic compositional and strain gradients to be used to modify the elastic conditions driving ferroelastic domain formations thereby enabling the stabilization of needle-like domains.

6.3 Probing Ferroelectricity on the Nanoscale in Single-Layer and Compositionally-Graded $PbZr_{1-x}Ti_xO_3$ Heterostructures

To explore how variation in ferroelastic domain shape and structure influences the domain wall response, we proceeded to conduct detailed BE-PFM switching spectroscopy (BE-SS) studies. This technique measures piezoresponse hysteresis loops analogous to macroscopic ferroelectric hysteresis loops with the primary exception that it is conducted with a nanoscale scanning probe which enables mapping of variations in response with nanoscale resolution. To complete these measurement a small-signal BE voltage waveform is used to measure the local piezoresponse at various voltage steps along a bipolar triangular switching waveform at remanence. The extracted local piezoresponse at each voltage step provides spatial maps that can be used to visualize and understand the switching process (see section 2.4.2 for more details).

6.3.1 Band-Excitation Switching Spectroscopy of Homogeneous $PbZr_{0.2}Ti_{0.8}O_3$ Heterostructures

To demonstrate the capabilities of this technique we first investigate the homogeneous heterostructures, whose switching process is better understood. For reference, we show a representative macroscopic hysteresis loop (measured at 10 kHz, Figure 6.4a). It is important to note that this hysteresis loop is symmetric (*i.e.*, possessing no voltage offset) implying that there is no macroscopic preference for the up- or down-poled state. A selection of amplitude (indicating the vertical piezoresponse at remanence) and phase (indicative of the out-of-plane polarization direction)

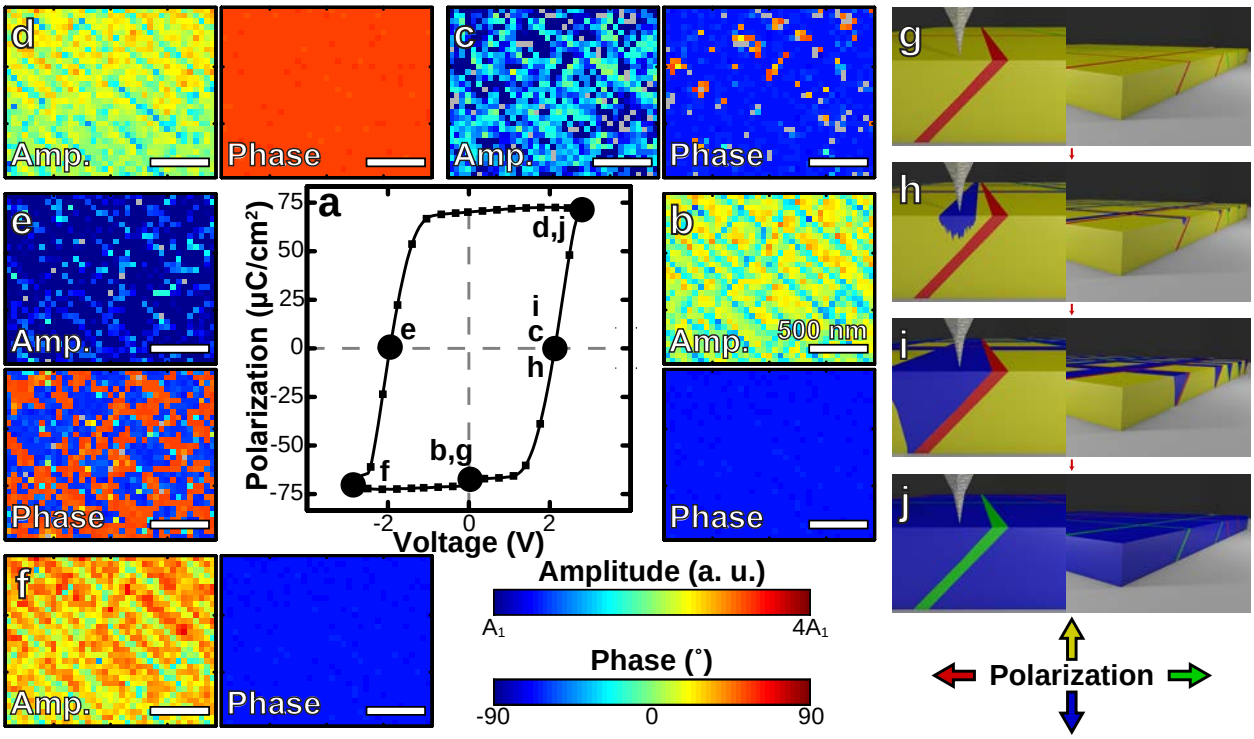

Figure 6.4. (a) Typical macroscopic ferroelectric hysteresis loop of a homogeneous $PbZr_{0.2}Ti_{0.8}O_3$ heterostructure measured at 10 kHz. (b-f) Corresponding band-excitation switching spectroscopy amplitude (left/top) and phase (right/bottom) images of the same homogeneous $PbZr_{0.2}Ti_{0.8}O_3$ heterostructure measured at various stages of ferroelectric switching (as labeled). All scale bars are 500 nm. (g-j) Schematic illustrations of the switching process in the homogeneous $PbZr_{0.2}Ti_{0.8}O_3$ heterostructures. Only the positive-bias half of the switching process is shown. Switching from the down-poled to the up-poled state happens in a similar manner, but with polarization of opposite sense. The color key on the bottom right labels the polarization directions in the illustrations.

maps of the local piezoresponse at various voltages throughout the switching cycle are provided (Figure 6.4b-f, additions images are provided in Appendix D, as a flip book starting from the last page of this thesis, and movies compiled from the complete set of measurements are available online). Starting with the entire region up-poled, as indicated by a uniform blue phase image (Figure 6.4b), the amplitude is, as expected, larger in the *c* domains (where the polarization and measurement direction are parallel) compared to the *a* domains (where the polarization and measurement direction are perpendicular). Application of positive bias results in rapid 180° switching to the down-poled state, as indicated by a change in phase from blue to red (Figure 6.4c). As the voltage increases, the region eventually reaches a final state with a similar amplitude response, but with phase of opposite sense as the original state (uniformly red, Figure 6.4d), indicating that ferroelectric switching to the down-poled state has occurred. Upon application of negative bias (Figure 6.4e-f), this process proceeds in reverse returning to its initial up-poled state. Throughout multiple switching cycles the *a* domains remain in the same location, an indication that they are effectively immobile. While there is some evidence of random domain structure reconfiguration following

the BE-SS measurements, consistent with recent reports, the vast majority of the domains remain fixed.[126, 127, 416]

These results are readily understood based on conventional theories and observations of ferroelectric switching in homogeneous heterostructures.[415, 419] Starting with the sample in the up-poled state (Figure 6.4g), the polarization of a particular *a* domain is fixed to avoid forming a charged domain wall. Ferroelectric switching occurs by nucleating a down-poled *c* domain which tends to nucleate near (or at) an *a* domain (Figure 6.4h). This down-poled domain then grows until being hindered by the presence of a 90° domain wall (which is now charged, Figure 6.4i). As the bias increases, this *a* domain can undergo 180° switching, eliminating the charged domain wall and allowing the film to switch to completion (Figure 6.4j). The final up- and down-poled states are energetically equivalent and therefore switching in reverse occurs in an identical manner. This switching process is hysteretic in nature and shows nearly identical response during repeated voltage cycling.

6.3.2 Band-Excitation Switching Spectroscopy of (20,80) Compositionally-Graded Heterostructures

In the compositionally-graded heterostructures, on the other hand, similar BE-SS studies reveal a vastly different response. Again, for reference, we show a representative macroscopic ferroelectric hysteresis loop (measured at 10 kHz, Figure 6.5a) which reveals a significant offset along the voltage axis (~200 kV/cm). As previously shown (see section 5.7.1), The observed voltage-offset of the hysteresis loops, or built-in potential, is not the result of imprint of asymmetric electrodes,[240] and instead, is caused by the presence of strain and/or chemical gradient as well as other intrinsic symmetry breaking (such as defects and domain structures).[164, 166, 167, 212, 223] The presence of this voltage offset implies that the film has a macroscopic preference to be self-poled in the up direction.

Local switching studies, again starting with the sample in the up-poled state (the self- poling direction, Figure 6.5b), reveal a large amplitude response within the up-poled *c* domains (as compared to the *a* domains) as observed in the homogeneous heterostructures. As positive bias is applied (starting the switch the film to the down-poled state, Figure 6.5c), there is evidence of a change in phase near the domain boundary (orange regions in phase images); along with suppressed piezoresponse in both the *c* and *a* domains, indicative of switching occurring at or near the domain boundaries. Increasing the positive bias further (Figure 6.5d) results in an increase

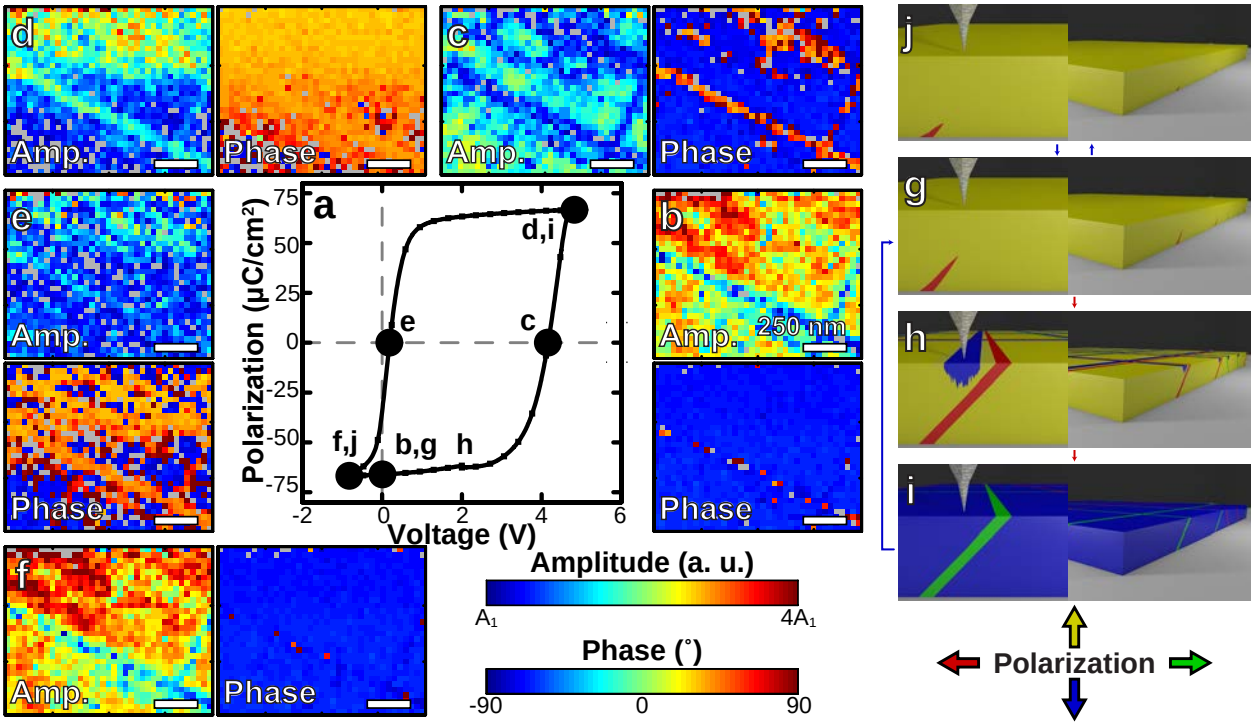

Figure 6.5. (a) Typical, macroscopic ferroelectric hysteresis loop of a 100 nm compositionally-graded (20,80) heterostructure measured at 10 kHz. (b-f) Corresponding band-excitation switching spectroscopy amplitude (left/top) and phase (right/bottom) images of the same compositionally-graded $PbZr_{1-x}Ti_xO_3$ heterostructure measured at various stages of ferroelectric switching (as labeled). All scale bars are 250 nm. (g-j) Schematic illustrations of the switching process in the compositionally-graded $PbZr_{1-x}Ti_xO_3$ heterostructures. The color key on the bottom right labels the polarization directions in the illustrations.

of the areal fraction of switched region (i.e., orange regions of the phase image). Additionally, we note that there is an enhancement in the local piezoresponse at the *a* domains as compared to the *c* domains. As the bias is reduced in magnitude (Figure 6.5e), the film begins to back switch (driven by the self-poling), the *a* domains reduce their presence, and the piezoresponse appears nearly uniform. Eventually, under large enough negative biases, evidence of the domains in the phase image nearly disappears (Figure 6.5f). This negative-bias state (Figure 6.5f) has an inversed relative local piezoelectric response from the high-field, positive-bias state (Figure 6.5d). This switching process observed here is highly asymmetric in nature with application of positive and negative fields producing vastly different responses both in the *c* and *a* domains (see additional images provided in appendix E, flip book starting on the last page of this thesis, and movies available online).

The switching process in compositionally-graded heterostructures with needle-like domains has not been explored to date. Using our understanding of the structure and the insight from the BE-SS it is possible to develop a model for the switching process. Starting with the film in the up-poled state (the self-poling direction, Figure 6.5g) application of positive bias drives the

polarization towards the down-poled state. In doing so, *via* the piezoelectric effect, there is a slight decrease in tetragonality (up until switching), which should drive an increase in the total volume fraction of *a* domains. While changes in the volume fraction of *a* domains are limited in homogeneous heterostructures with parallelepiped-like domains, in the case of compositionally-graded heterostructures, the high-energy tip of the needle-like domain can expand towards the free surface (Figure 6.5h). The ability to undergo such a *c* → *a* transitions is associated with a large change in the out-of-plane lattice parameter which translates to a large piezoelectric response at the *a* domains (under positive bias). As the needle-like domains grow, it is important to consider the changing elastic and electrical conditions. As the domains grow there is an increase in elastic energy, as the shape of the domain deviates from its as-grown state, as well as a reduction in electrical energy associated with converting the high-energy domain front (evidenced by the observed polarization rotation at the tip of the needle-like domain) to a nominally-uncharged, parallelepiped-like domain with coherent interfaces with the neighboring *c* domain along the {101}. Once the needle-like domain transverses the thickness of the film, it is possible to switch the film to the down-poled state (final state shown in Figure 6.5i, in a manner identical to the homogeneous heterostructure, Figure 6.4i-j). Note that nucleation of a down-poled domain prior to the *a* domain traversing the film is unlikely since the system would have to 1) overcome the preference for the up-poled state (defined by the self-poling direction), 2) form a charged domain wall, and 3) transition through a cubic-like state that drives expansion of the needle-like domains. Upon releasing the bias, a combination of the strong macroscopic self-poling and stored elastic energy drives the film and domain structure to switch back to its initial state (as indicated by the blue arrow, Figure 6.5i→g).

Conversely, from the as-grown state, upon application of negative bias (driving the heterostructure towards the self-poled direction), the tetragonality of the film increases *via* the piezoelectric effect, begetting a reduction in the volume fraction of *a* domains. This results in the contraction of the ferroelastic domains (Figure 6.5j). Complete removal of the *a* domain is unlikely because of the strain state of the film and substrate clamping. We note that in-situ electrical and structural characterization using TEM of needle-like domains have observed that these domains cannot be completely excluded even under fields approaching the breakdown voltage (~2000 kV/cm).[394] Additionally, because these ferroelastic domains are typically pinned at the substrate film interface, as the *a* domains shrink, due to geometric requirements, there is an increasing deviation

of the domain wall orientation from the nominally-uncharged {101}, which gives rise to an electrical energy cost which significantly suppresses further domain wall contraction under negative bias.[394] Therefore, given the large associated electrical energy to undergo an *a*→*c* transition at the ferroelastic domain, we would expect, as observed, suppressed piezoelectric response within the *a* domains (under negative bias). Upon releasing the electric field these domains once again release their stored electrical and elastic energy, returning to their as-grown state.

6.3.3 *Comparison of Nanoscale Switching in Homogeneous $PbZr_{0.2}Ti_{0.8}O_3$ and (20,80) Compositionally-Graded Heterostructures*

The main differences in the switching process can be highlighted by examining a voltage-lapse images of a small section centered around a ferroelastic domain in both the homogeneous (Figure 6.6a) and compositionally-graded (Figure 6.6b) heterostructures. In the homogeneous heterostructures, we see that switching (phase inversion) occurs abruptly and the amplitude in the *c* domain, although changing in magnitude, is universally larger than in the *a* domains. Conversely, in the compositionally-graded heterostructures, switching (phase inversion) happens more gradually and is localized near the domain boundary. Additionally, the compositionally-graded heterostructures show variations in the relative piezoresponse, having suppressed piezoresponse in the *a* domains (similar to the homogeneous heterostructures) in the as-grown state and under application of negative bias, but enhanced piezoresponse under large positive biases.

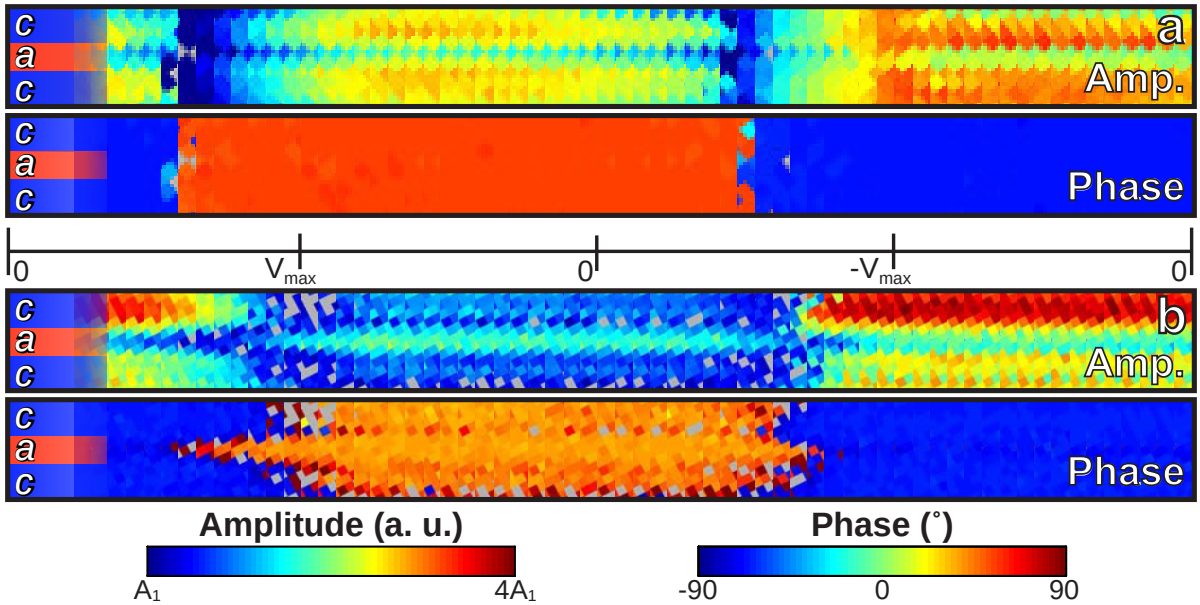

Figure 6.6. Voltage-lapse images near an *a* domain of (a) homogeneous $PbZr_{0.2}Ti_{0.8}O_3$ and (b) compositionally-graded $PbZr_{1-x}Ti_xO_3$ heterostructures imaged throughout an entire switching cycle.

6.3.4 *Comparison of Average Piezoresponse Loops in Homogeneous $PbZr_{0.2}Ti_{0.8}O_3$ and (20,80) Compositionally-Graded Heterostructures*

Since at each point in these measurements there is a corresponding piezoelectric hysteresis loop it is possible to cluster and calculate the spatially-averaged response of the loops based on the domain structure and response. To extract average hysteresis loops reflective of the response within the *a* and *c* domains the spatial maps of the response were partitioned. To do this an arbitrary cutoff considering the amplitude and offset was chosen to partition the regions of the homogeneous and compositionally-graded heterostructures to generate an image reflective of the domain structure (Figure 6.7a-b). From these figures it is clear that the partitioning method was effective at isolating the *c* and *a* domains. Once partitioned the mean piezoresponse along each voltage step can be calculated in both the *c* and *a* domain regions, forming an average piezoresponse loop (as shown for the homogeneous $PbZr_{0.2}Ti_{0.8}O_3$ and compositionally-graded heterostructures, Figure 6.7c-d, respectively).

Starting with the homogeneous $PbZr_{0.2}Ti_{0.8}O_3$ heterostructures we observe that the average hysteresis loop of the *c* domains has a significantly larger piezoresponse and slightly reduced coercivity, compared to the *a* domains. In addition, the centroid (*i.e.* the center of mass) of the hysteresis loop can be calculated (as shown by the hatched circles). The loop centroids for the homogeneous heterostructures show essentially no spatially-correlated shift along the voltage axis between the *a* and *c* domains. Moving on to the compositionally-graded heterostructures we notice that the *a* and *c* domains have nearly invariant piezoresponse at remanence. Changing our focus to the loop centroid we notice a significant shift (toward negative bias direction) at the *a* domains compared to

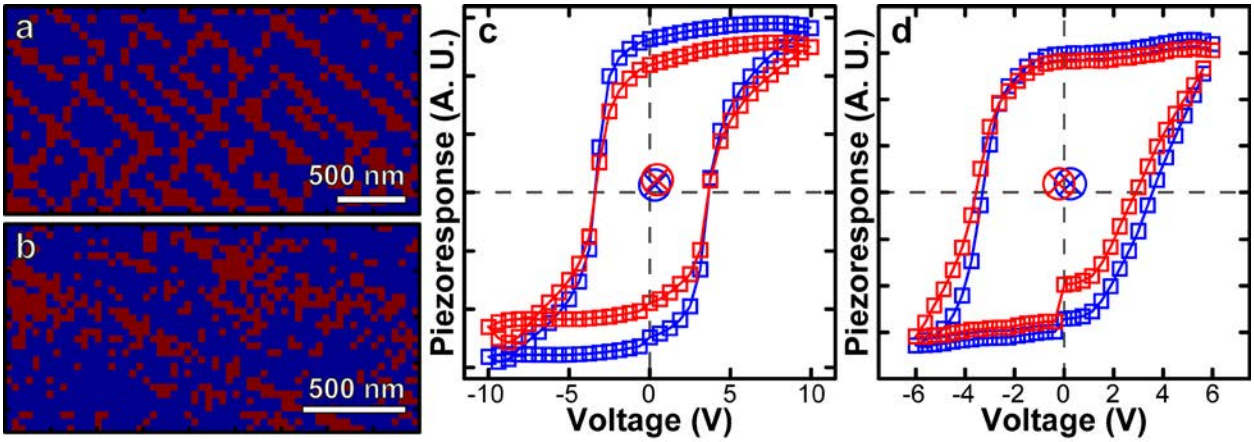

Figure 6.7. Maps of *a* and *c* domain partitions in (a) homogeneous $PbZr_{0.2}Ti_{0.8}O_3$ and (b) compositionally-graded $PbZr_{1-x}Ti_xO_3$ heterostructures. Average piezoelectric hysteresis loops of *a* domains (red) and *c* domains (blue) in (c) homogeneous $PbZr_{0.2}Ti_{0.8}O_3$ and (d) compositionally-graded $PbZr_{1-x}Ti_xO_3$ heterostructures. Loop centroids are marked with the cross hatched circle.

the *c* domains. While analyzing the data using this approach provides some insight, analyzing the data based on clustering and averaging the response has many flaws. First, because of the size of the datasets, outlier data points are difficult to exclude, yet can significantly impact the average loop shape. Secondly, clustering and averaging in this manner requires that the user define the bounds for clustering meaning only features which are already known to the user are revealed.

6.3.5 *Comparison of Loop Fitting Parameters in Homogeneous $PbZr_{0.2}Ti_{0.8}O_3$ and (20,80) Compositionally-Graded Heterostructures*

To visualize the data more analytically with less human imposed bias, we fit each of the piezoelectric loops to an empirical model where the fitting parameters represent tangible loop shape features (see section 2.4.3). Here, we show spatial maps of the magnitude (i.e., the absolute value) of the negative (E_c^-) and positive (E_c^+) coercive fields and offset (i.e., the midpoint between these values) for the homogeneous (Figure 6.8a-c, maps of other loop shape parameters are included in Appendix F) and compositionally-graded (Figure 6.8d-f, maps of other loop shape parameters are included in Appendix F) heterostructures. The homogeneous heterostructures shows an increase in the magnitude of the coercive field at the *a* domains; however, this increase in coercivity is symmetric, causing no variance in the offset. This result indicates that the heterostructure (both in the *c* and *a* domains) has a similar preference to be in the up- or down-poled state. While these results are consistent with the extracted average piezoelectric loops these features are much easier to visualize based on maps of the loop fitting parameters, demonstrating the utility of this analysis approach. Moving on to the compositionally-graded heterostructures, the E_c^- is found to be nearly invariant while there is a reduction in E_c^+ near the *a* domains. The combination of these two results gives rise to a spatially-correlated

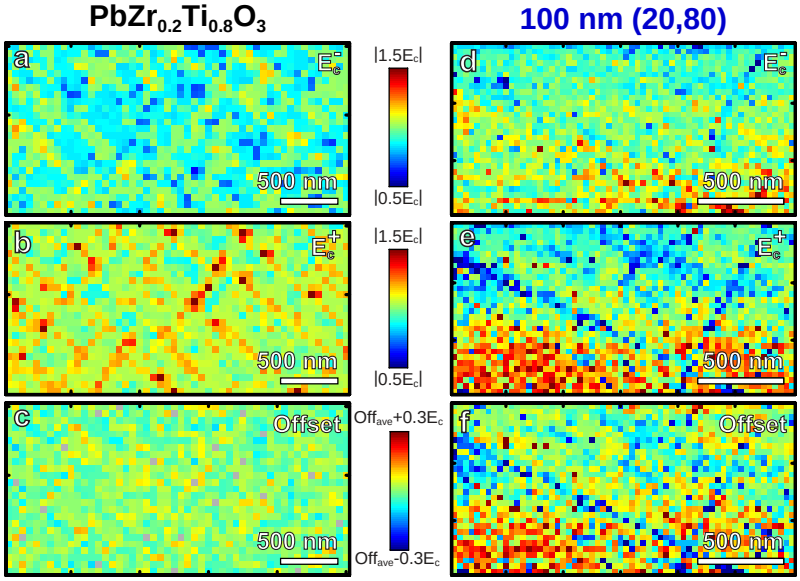

Figure 6.8. (a) Negative coercive field (E_c^-), (b) positive coercive field (E_c^+), and (c) voltage offset for homogeneous $PbZr_{0.2}Ti_{0.8}O_3$ heterostructures extracted from fits of the piezoelectric hysteresis loops. (d) Negative coercive field (E_c^-), (e) positive coercive field (E_c^+), and (f) voltage offset for 100 nm compositionally-graded (20,80) heterostructures extracted from fits of the piezoelectric hysteresis loops.

negative offset near the *a* domains; indicating that the *a* domains have a preference to be in their positive bias configuration (*i.e.*, the "down-poled state").

The negligible offset in the homogeneous heterostructures is the result of the fact that the structure is symmetric and the interaction between the *a* and *c* domains is independent of field direction. The response in the compositionally-graded heterostructures is more complex. The observed offset at/near the *a* domains is opposite that of the macroscopic hysteresis loops a measurement sensitive to the nature of the *c* domains, which occupy the vast majority of the heterostructure. In turn, this suggests that the different domains essentially transfer energy between one another under external bias, acting like a "spring" in that each drives a return of the other to the favorable as-grown state upon release of the applied bias. In other words, the associated change in the shape of the ferroelastic domains under bias will, in turn, generate a restoring force to its "equilibrium" as-grown state. We contest that the primary energy responsible for this asymmetry is the electrostatic energy. Although there is an elastic energy change under both positive and negative bias, this change is likely similar in magnitude and thus cannot be used to explain the offset. The electrostatic energy change, however, would be expected to be different, because of the change in the angle of inclination of the domain wall under negative and positive bias is not the same. Under negative bias, the *a* domains are driven to be nearly excluded from the film, causing the domain walls to deviate from the nominally-uncharged {101} (forming an energetic, charged domain wall) while under positive bias, the *a* domains are driven to be parallelepiped-like, which in the process converts a charged domain wall to a nominally-uncharged domain wall (reducing its energy). This elastic restoring force caused by the presence of ferroelastic domain walls provides a suitable mechanism to explain the anomalous enhancement in built-in potential observed in compositionally-graded heterostructure with ferroelastic domains.[173] Overall, the spring-like interaction of the *a* and *c* domains demonstrate the importance of the elastic boundary conditions in stabilizing these high energy and responsive domain structures.

6.3.6 High Field Local Piezoresponse of Homogeneous $PbZr_{0.2}Ti_{0.8}O_3$ and (20,80) Compositionally-Graded Heterostructures

To demonstrate the tangible implications of the observed differences in domain structure and switching mechanics we measured the local, high-field piezoresponse (at $V_{ac} \approx \frac{1}{2}E_c$) using BE-PFM for the homogeneous (Figure 6.9a) and compositionally-graded heterostructures (Figure

6.9b). In the homogeneous heterostructures we observe larger piezoresponse within the *c* domains and lower response within the *a* domains; which matches our intuition given that the polarization is parallel (perpendicular) to the measurement direction in the *c* (*a*) domains. The opposite response is observed in the compositionally-graded heterostructure where the piezoresponse is significantly larger within the *a* domains as compared to the *c* domains. This is a manifestation of the highly labile needle-like ferroelastic domains and the corresponding *c*→*a* and *a*→*c* transitions that take place under applied bias. These large structural transitions produce locally-enhanced piezoresponse demonstrating the efficacy of compositional and strain gradients in stabilizing highly susceptible, high energy domain structures with large localized piezoresponse.

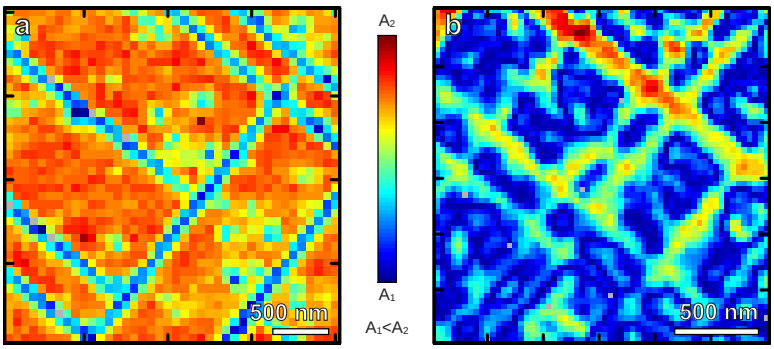

Figure 6.9. High-field (½E_c) piezoresponse force microscopy images of (a) homogeneous $PbZr_{0.2}Ti_{0.8}O_3$ heterostructures and (b) 100 nm (20,80) compositionally-graded heterostructures showing inverted responses.

6.4 Conclusions

In conclusions, we demonstrate how compositional and strain gradients can be used to modify ferroelastic domain structures facilitating the design of highly-labile and springy ferroelectric domains. Specifically, we observe that compositional and strain gradients can preferentially stabilize highly-energetic, needle-like domains, which under electrical excitation, are highly labile in the out-of-plane direction (while remain spatially fixed in the plane) throughout successive field cycling. These labile domain walls give rise to locally enhanced piezoresponse at the *a* domains as the result of a switching mechanism where the *a* domains expand towards the free surface or are nearly excluded from the film (depending on the direction of applied bias). This work presents new modalities of domain structure engineering through the use of controlled compositional and strain gradients with significant implications for designing novel forms of ferroelastic domains that are indexable, yet highly mobile, providing new routes to design novel domain wall functionalities inconceivable in homogeneous thin films. These new route to design domain wall structure and response using compositional and strain gradients has the potential to revolutionize the burgeoning field of nanoscale domain wall devices.

Chapter 7

Summary of Findings, Preliminary Work, and Suggestions for Future Work

7.1 Summary of Findings

In this thesis, we have explored new modalities of strain engineering through the use of chemical pressure, strain, and strain gradients to achieve novel modes of ferroelectric/ferroelastic response, and ultimately unique combinations of ferroelectric, dielectric, and pyroelectric susceptibilities impossible in more conventional systems. We began our discussion by conducting a systematic study of crystal and domain structures in epitaxial $PbZr_{1-x}Ti_xO_3$ thin films across the composition phase diagram. Using these model systems, we establish a framework to understand how chemical composition, and crystal and domain structure influences the ferroelectric, dielectric, and piezoelectric responses of these heterostructures.

We then took an in-depth look at how epitaxial strain, in the form of lattice mismatch, can impact the evolution of crystal and domain structure, and in the end the properties of $PbZr_{0.52}Ti_{0.48}O_3$ thin films, which are chemically close to the MPB. In general, we highlighted the complexity of strain evolution in highly-adaptable $PbZr_{0.52}Ti_{0.48}O_3$ thin films and revealed how the innate flat energy landscape and resulting phase competition can skirt classical assumptions of epitaxial strain. Ultimately, we showed that high-quality, single-phase films of $PbZr_{0.52}Ti_{0.48}O_3$ exhibit significantly different dielectric responses when grown on various substrates despite the appearance of a "relaxed" crystal structure. We used local probes of switching in these heterostructures to reveal distinct differences in the average switched area of the heterostructures, and correlate this difference to the lattice mismatch, and its role in modifying the elastic boundary conditions of the heterostructures. Subsequent dielectric and ferroelectric studies revealed transitions in ferroelectric switching at ultra-low frequencies and in the dielectric response at high dc fields, which suggests that reduced residual strain promotes full adaptability of the structure under applied fields and, as a result, enhanced electric-field susceptibility. Overall, we showed that $PbZr_{0.52}Ti_{0.48}O_3$ thin films – and other systems with phase competition – may not be beholden to the classic effects of epitaxial strain in

the same manner as more conventional materials.

Building off our knowledge of how chemistry, strain, strain relaxation, and crystal and domain structure can tune the susceptibilities of epitaxial $PbZr_{1-x}Ti_xO_3$ thin films, we explored how compositionally-gradient form (in terms of the nature of the compositional gradient and heterostructure thickness) can be used to tune the crystal and domain structure, and evaluated its influence on the evolution of the built-in potential, ferroelectric, dielectric and pyroelectric responses. We observed that the strain state and domain structure are highly dependent on the misfit strain at the substrate film interface, where when closely lattice matched the strain stabilizes a tetragonal crystal and domain structure, and enables large residual strains and strain gradients to persists. These large strain (and potentially chemical) gradients result in large built-in potentials and suppressed dielectric susceptibilities while having minimal influence on the magnitude of the polarization. On the other hand, when there is a large lattice mismatch at the substrate film interface the heterostructures relax, giving rise to a complex strain state and domains structure with large extrinsic contributions to the dielectric permittivity. In our exploration of these heterostructures we found that the built-in potential in strained, compositionally-graded heterostructures does not scale directly with the magnitude of the strain gradient as would be expected. Instead, it was found that the built-in potential is enhanced in compositionally-graded heterostructures which contain locally enhanced strain gradients, which occur when traversing chemistries associated with structural phase boundaries (where there are abrupt changes in the lattice parameter) and at/near ferroelastic domain boundaries. Therefore, we posit that the built-in potential observed in these materials is likely a manifestation of a combination of flexoelectric effects (*i.e.*, polarization-strain gradient coupling), chemical-gradient effects (*i.e.*, polarization-chemical potential gradient coupling), and local inhomogeneities that enhance strain (and/or chemical) gradients. Regardless of origin, large built-in potentials act to suppress the dielectric permittivity, while having minimal impact on the magnitude of the polarization or pyroelectric responses; which we prove to be an effective route to engineer materials with improved pyroelectric and potentially piezoelectric figures of merit.

To explain the anomalous enhancement in built-in potential observed in compositionally-graded heterostructure with ferroelastic domains we employed detailed transmission electron microscopy-based nanobeam diffraction and nanoscale band-excitation switching spectroscopy to explore the nanoscale structure and response of these ferroelastic domains. We demonstrated how

compositional and strain gradients can be used to modify ferroelastic domain structures facilitating the design of highly-labile and "springy" ferroelectric domains. Specifically, we observed that compositional and strain gradients can preferentially stabilize highly-energetic, needle-like domains which under electrical excitation are highly labile in the out-of-plane direction (while remaining spatially fixed in the plane) throughout successive field cycling. These labile domain walls give rise to locally enhanced piezoresponse at the *a* domains as the result of a switching mechanism where the *a* domains expand towards the free surface or are nearly excluded from the film (depending on the direction of applied bias). This work presented new modalities of domain structure engineering through the use of controlled compositional and strain gradients with significant implications for designing novel forms of ferroelastic domains that are indexable, yet highly mobile, and providing new routes to design novel domain wall functionalities inconceivable in homogeneous thin films.

All told, this work develops new routes of strain-based crystal and domain structure engineering using chemical composition, epitaxial strain, and chemical and strain gradients to stabilize new phases and domain structures, and to promote phase competition. Furthermore, this work demonstrates some of the practical implications of these novel strain-engineered structures in terms of their ability to control dielectric, ferroelectric, piezoelectric, and pyroelectric responses, and hints at other potential nanoscale impacts of these engineered materials and structures. Throughout this work, due to the complexity of the materials and types of responses in the materials we were presented with a number of major experimental hurdles that necessitated the development of new approaches or techniques. Some of the major technical contributions include:

- Development of a low-cost, high-bias field method to extract extrinsic and intrinsic dielectric permittivity and tunabilitiy.
- The development of an approach and methodology to quantify strain relaxation in compositionally-graded heterostructures.
- Expansion of the approach and methodologies used to extract physically significant insight from band-excitation switching spectroscopy.
- Demonstration of the first direct measurement of strain gradients in compositionally-graded heterostructures using nanobeam electron diffraction.

While significant progress in developing new materials, characterization tools, and physical

understanding of phenomena has been made in this work, we have not reached our limitations. Instead, we have just laid the groundwork necessary to intelligently design and understand new, more complex, material systems, with a slightly expanded toolbox of techniques capable of peering into their structures and modes of response at new depths. The following sections will highlight some of the areas most primed for exploration and discovery.

7.2 Preliminary Work

7.2.1 Introduction to Mixed-Phase Structures

Throughout this thesis we focused on new strain-based routes to engineer materials using thin-film epitaxy. One of the primary limitations in our ability to impose epitaxial strain has been the availability of substrate and electrode materials with suitable lattice parameters. Particularly, up until very recently, there was dearth of available substrates and electrode materials with lattice parameters approaching 4.0 Å, capable of imposing large tensile strains on $PbZr_{1-x}Ti_xO_3$. Within the last few years, the slight increase in availability of rare earth scandate substrates [*i.e.* $SmScO_3$ (110, a_{pc}=3.985 Å), $NdScO_3$ (110, a_{pc}=4.01 Å) and $PyScO_3$ (110, a_{pc}=4.02 Å)] as well as familiarity growing $Ba_{0.5}Sr_{0.5}RuO_3$ (a_{pc}=3.967 Å) a conductive perovskite oxide has expanded the range of tensile strains which can be imposed. The ability to grow heterostructures on substrates with large tensile strains is particularly interesting as the lattice parameters of these substrates falls between the in-plane lattice parameters of the phases and domain variants which can exist. In turn, applying strain of this form has the possibility of driving phase competition to accommodate the strain state.

Such strain-engineered phase competition is not a new concept and has been employed in highly compressively strained $BiFeO_3$ (~4.5% compressive, traditionally a rhombohedral distorted perovskite phase), to stabilizes, in some areas, a tetragonally distorted perovskite phase, creating mixed-phase structures.[64] These mixed-phase structures possess stripe-like features of a tetragonal-like phase (which is actually a monoclinically-distorted version of a super-tetragonal structure) and a small fraction of rhombohedral-like phase (which is also actually monoclinic, but a derivative of the parent rhombohedral phase).[118, 187, 420-423] These structures are particularly interesting as they have been shown to exhibit enhanced electromechanical responses, the ability to locally write and alter the domain structures, and allow for stimuli-induced (*i.e.* electrical, thermal, mechanical) structural phase transformations which tend to produce large susceptibilities (*i.e.* dielectric,

pyroelectric, piezoelectric, *etc.*).[187, 374, 424-426] While these mixed-phase structures in $BiFeO_3$ are interesting from a scientific standpoint their practical implications are limited by the relatively high conductivity of $BiFeO_3$ thin films.[427-429] This ability to use strain to generate and control phase competition in other systems (with acceptable leakage characteristics) would provide new routes to enhance dielectric, piezoelectric, pyroelectric, and potentially electrocaloric responses in materials that could be easily integrated into functional devices.

7.2.2 Design of Mixed-Phase $PbTiO_3$ Heterostructures

Now considering the $PbZr_{1-x}Ti_xO_3$ system specifically, when applying moderate tensile strains tetragonal $PbZr_{1-x}Ti_xO_3$ accommodates the strain by forming increasing fractions of in-plane oriented *a* domains. At some point, however, the tensile strain will become so large that in order to minimize the total energy the strain is accommodated by forming a hierarchical mixed-phase structure, with some fraction of *c*/*a*/*c*/*a* and $a_1/a_2/a_1/a_2$ super-domains.[430] For our initial investigation of highly-tensile strained $PbZr_{1-x}Ti_xO_3$ we choose to grow 100 nm thick films of $PbTiO_3$ (a = 3.9045 Å, c = 4.1524 Å) /15 nm $Ba_{0.5}Sr_{0.5}RuO_3$ on substrates with various misfit strains [ranging from 2.1% (4.0%) to 2.9% (3.1%) tensile (compressive) for the *c* and *a* axis, respectively). $PbTiO_3$ was chosen for our initial studies as it has the smallest in plane lattice parameter within the $PbZr_{1-x}Ti_xO_3$ system.

7.2.3 Domain Structure of Mixed-Phase $PbTiO_3$ Heterostructures

All heterostructures, showed mixed-phase regions consisting of regions of *c*/*a*/*c*/*a*-like stripes surrounded by $a_1/a_2/a_1/a_2$-like super-domain regions, where the relative areal fraction of the $a_1/a_2/a_1/a_2$ super-domains increases with increasing tensile misfit strain. It is worth mentioning that during the time of this work, a single publication showing similar mixed-phase structures in $PbZr_{0.1}Ti_{0.9}O_3$ thin films grown on $SmScO_3$ (110) was reported.[119] For brevity in this discussion, we focus our attention solely on the heterostructure grown on $SmScO_3$ (110), as the other heterostructures showed similar features. Starting by looking at the topographic features of these heterostructures (Figure 7.1a) we observe a hierarchical structure of *c*/*a*/*c*/*a* and $a_1/a_2/a_1/a_2$ super-domain regions oriented as if they were a conventional *c*/*a*/*c*/*a* domain structure, within which there is a finer scale domain structure. Looking at the topography in these super-domain regions a sawtooth-like topography is observed in the *c*/*a*/*c*/*a* super-domain regions while the $a_1/a_2/a_1/a_2$ regions appear essentially flat. A line trace taken across the top surface of a *c*/*a*/*c*/*a* region (Figure 7.1b) reveals that

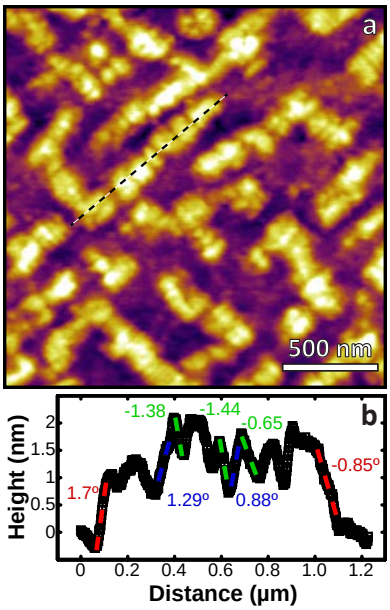

Figure 7.1. (a) Topography image of mixed phase $PbTiO_3$ heterostructures on $SmScO_3$ (110) showing regions of *c*/*a*/*c*/*a*-like and $a_1/a_2/a_1/a_2$-like domain structures. (b) line trace across a *c*/*a*/*c*/*a*-like regions indicating the tilt angles of the domains

the *c*/*a*/*c*/*a* regions are elevated ~1.5 nm above the $a_1/a_2/a_1/a_2$ and are tilted ~0.85-1.7° in reference to the substrate normal.

To observe the domain structure in more detail we conducted detailed piezoresponse force microscopy in both the vertical and lateral directions (Figure 7.2a-b). These studies confirm our initial hypothesis regarding the structure which consists of bands of *c*/*a*/*c*/*a*-like super-domain regions [which appear bright (dark) in the vertical (lateral) amplitude images] and $a_1/a_2/a_1/a_2$-like super-domain regions [which appear dark (bright) in the vertical (lateral) amplitude images]. Now looking at the phase images, and starting with the vertical response, we observe that the heterostructures are primarily poled in a single direction, with just a few antipolar (or 180°) domains. Moving on to the lateral phase images we observe fine bands within the in-plane polarized region which appear nearly vertical in the image (*i.e.*, along the $<110>_{pc}$) indicative of a fine $a_1/a_2/a_1/a_2$ domain structure of

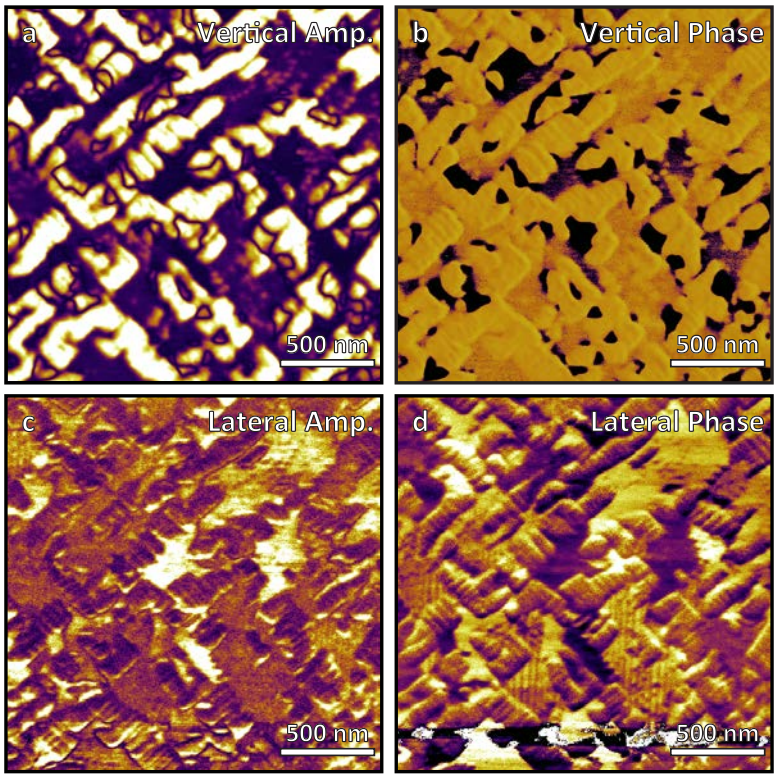

Figure 7.2. Vertical piezoresponse (a) amplitude and (b) phase. Lateral piezoresponse (c) amplitude and (d) phase of mixed phase $PbTiO_3$ heterostructures grown on $SmScO_3$ (110).

in-plane oriented 90° domain walls. Upon finer inspection, it is apparent that the *c*/*a*/*c*/*a* regions intersect the $a_1/a_2/a_1/a_2$ at an angle of ~135° with what appears to be the same periodicity, an indication that these domains must form in order to minimize the electrostatic and elastic energy of these domain walls.

7.2.4 Band-Excitation Switching Spectroscopy of Mixed-Phase $PbTiO_3$ Heterostructures

To explore the nanoscale susceptibility of this domain structure we have conducted detailed band-excitation piezoresponse force microscopy switching spectroscopy (as described in section 2.4.2, piezoresponse switching images included in appendix G and movies are available onine). During these measurements, we notice that it was common to observe piezoelectric hysteresis loops with multiple steps in the switching process (as shown in Figure 7.3a). Such transitions are likely related to collective switching of small domain regions, at some critical bias, akin to Barkhausen pulses observed when switching magnetic domains.[431, 432]

Since piezoelectric hysteresis loops of this form have multiple switching events these loops cannot be fit to the conventional model. To fit these hysteresis loops, SHO fits of the cantilever resonance and extraction of piezoelectric hysteresis loops (based on phase optimization) were completed as previously described (see section 2.4.3). To fit loops with multiple steps we derived a new set of model equations (7.1-7.8) capable of fitting piezoelectric loops with up to three transitions.

$$\Gamma_1 = a_1 + (a_2 - a_1)\frac{erf\left(\frac{V_{bot} + A_{l1}}{\sigma_1}\right)+1}{2} + (a_3 - a_2)\frac{erf\left(\frac{V_{bot} + A_{l2}}{\sigma_2}\right)+1}{2} + (a_4 - a_3)\frac{erf\left(\frac{V_{bot} + A_{l3}}{\sigma_2}\right)+1}{2} + a_7 V_{bot} \tag{7.1}$$

$$\Gamma_2 = a_1 + (a_5 - a_1)\frac{erf\left(\frac{V_{top} + A_{U1}}{\sigma_4}\right)+1}{2} + (a_6 - a_5)\frac{erf\left(\frac{V_{top} + A_{U2}}{\sigma_5}\right)+1}{2} + (a_4 - a_6)\frac{erf\left(\frac{V_{top} + A_{U3}}{\sigma_6}\right)+1}{2} + a_7 V_{top} \tag{7.2}$$

$$\sigma_1 = \left(\frac{b_1 + b_2}{2}\right) + \left(\frac{b_2 - b_1}{2}\right) erf\left(\frac{V_{bot} - C_1}{D_1}\right) \tag{7.3}$$

$$\sigma_2 = \left(\frac{b_3 + b_4}{2}\right) + \left(\frac{b_4 - b_3}{2}\right) erf\left(\frac{V_{bot} - C_2}{D_2}\right) \tag{7.4}$$

$$\sigma_3 = \left(\frac{b_5 + b_6}{2}\right) + \left(\frac{b_6 + b_5}{2}\right) erf\left(\frac{V_{bot} - C_3}{D_3}\right) \tag{7.5}$$

$$\sigma_4 = \left(\frac{b_7 + b_8}{2}\right) + \left(\frac{b_8 - b_7}{2}\right) erf\left(\frac{V_{top} - C_4}{D_4}\right) \tag{7.6}$$

$$\sigma_5 = \left(\frac{b_9 + b_{10}}{2}\right) + \left(\frac{b_{10} - b_9}{2}\right) erf\left(\frac{V_{top} - C_5}{D_5}\right) \tag{7.7}$$

$$\sigma_6 = \left(\frac{b_{11} + b_{12}}{2}\right) + \left(\frac{b_{12} - b_{11}}{2}\right) erf\left(\frac{V_{top} - C_6}{D_6}\right) \tag{7.8}$$

where $a_{1\text{-}6}$ represents the various plateaus in amplitude, a_7 is the linear tilt, $A_{l1\text{-}3}$ and $A_{U1\text{-}3}$ represent the coercive fields, $b_{1\text{-}12}$ determine the rate of transition, $C_{1\text{-}6}$ define the bias of inflection between b parameters, $D_{1\text{-}6}$ determines the rate of transition between b parameters, and V_{bot}/V_{top} is the voltage of the top and bottom branches (Figure 7.3b). Fitting of the hysteresis loops to these equations was accomplished using a custom script written in Matlab™. To begin, derivatives of the piezoresponse voltage curves (of the top and bottom branches) were calculated from local linear fits of 3-7 data points with a sliding voltage window. The switching regions (*i.e.*, those with large slopes) were found using a peak finding algorithm *findpeaks* in the Matlab™ base package. The three most prominent peaks were found and sorted in order of occurrence.

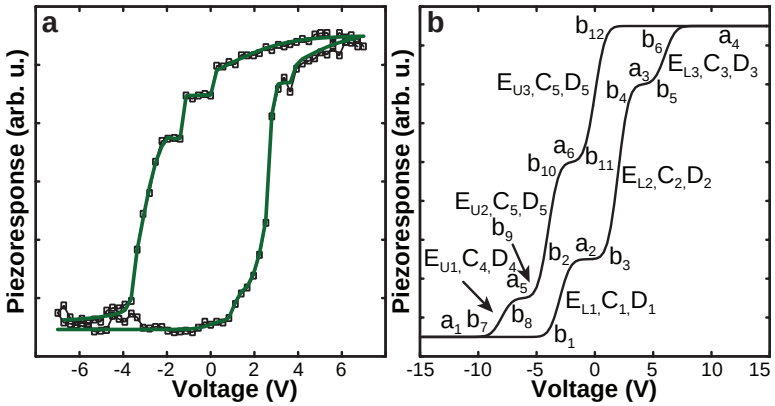

Figure 7.3. (a) Example local piezoelectric hysteresis loop measured in mixed-phase $PbTiO_3$ with multiple steps demonstrating the quality of the loop fit (green line). (b) Example hysteresis loop demonstrating how the variables in the objective function correlate to the loop shape in piezoelectric hysteresis loop with multiple switching events.

The characteristics of the peaks and shape of the hysteresis loop were then used to establish the start points and upper and lower bounds of each of the fitting parameters. The equations were then fit to the data using a non-linear least squares fitting algorithm *lsqcurvefit*[433-435] set to search for global minimum using the *multistart* method available in the Matlab™ Optimization Toolbox.[436, 437] In short, this technique generates a series of guesses near the start point, between the defined bounds, and compares the error of each of the guesses by minimizing the sum of the squares, optimizing the guesses until finding a local minimum. *Multistart* complements *lsqcurvefit* by generating a random set of initial guesses which allows for the global minimum to be found. Since the quality of the fit in each of the sections is scaled by the number of points this fitting approach is exceedingly poor at fitting sharp features (as there is a lower data density); and therefore, to get the curves to fit well the fits were weighted by the normalized derivatives and optimized using an optimization algorithm

included in Matlab Optimization Toolbox™ enabling high quality fits to be obtained (Figure 7.3a, green curve).

Unfortunately, due to the extremely fine domain size, finite tip radius, instrumental drift and length of the switching studies (~6-8 hours per scan), we do not have the resolution necessary to observe the spatial variances in the switching mechanisms related to the fine features of the domain structure (see a small subset of the spatial maps included in Appendix H).

7.2.5 Domain Structure of Mixed-Phase $PbZr_{0.2}Ti_{0.8}O_3$ Heterostructures

To observe the fine features of the domain structure using BE-SS heterostructures with similar domain structures, yet larger scale is needed. As a rule of thumb, the domain size tends to increase with the thickness in accordance with Kittel's law,[438] and therefore, we chose to grow 400 nm thick $PbZr_{0.2}Ti_{0.8}O_3/Ba_{0.5}Sr_{0.5}RuO_3$ (20 nm)/$NdScO_3$ (110) heterostructures using PLD. Looking at the domain structure (topography Figure 7.4a, piezoresponse vertical amplitude and phase Figure 7.4b-c, and lateral amplitude and phase Figure 7.4d-e), we observe the same general domain features (as observed in the thinner $PbTiO_3$ heterostructures) on a much large scale. These images once again, reveal a hierarchical super-domain structure of *c*/*a*/*c*/*a*-like domains [which appears

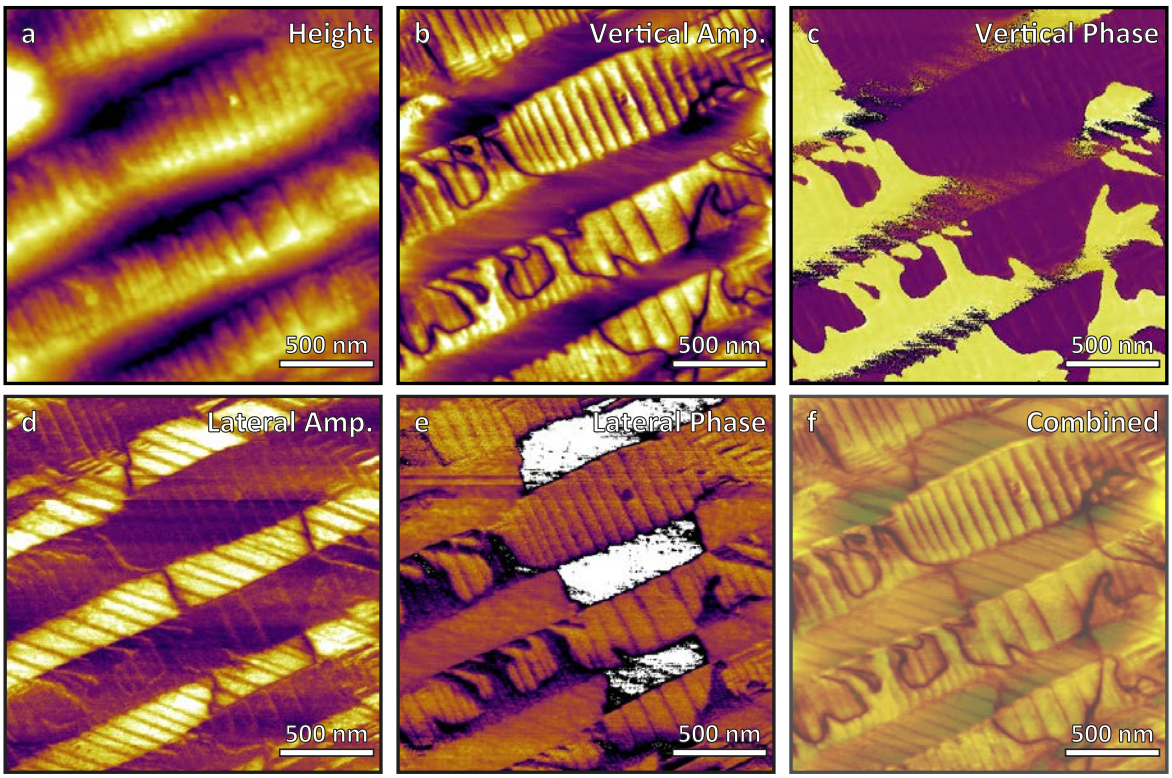

Figure 7.4. (a) Topography, and Piezoresponse force microscopy vertical (b) amplitude and (c) phase, lateral (d) amplitude and (c) phase, and combined amplitude images of 400 nm thick mixed-phase $PbZr_{0.2}Ti_{0.8}O_3$ heterostructures on $NdScO_3$ (110) showing a super-domain structure of *c*/*a*/*c*/*a*-like and $a_1/a_2/a_1/a_2$-like super-domain regions.

bright (dark) in the vertical (lateral) amplitude images] and $a_1/a_2/a_1/a_2$-like domains [which appear dark (bright) in the vertical (lateral) amplitude images]. These thicker heterostructures however, have super-domains of width >500 nm and length on the order of microns, which contain a fine structure of nanodomains with domain width of ~10-20 nm. This is much larger than observed in the thinner heterostructures which have a super-domain width of <50 nm, length <500 nm, and nanodomain width of <5 nm. To visualize the intersection between the domain wall of the *c*/*a*/*c*/*a*-like and $a_1/a_2/a_1/a_2$-like super-domains we combined the vertical and lateral amplitude images by subtracting the regions of low response (*i.e.*, the purple regions) from both images and superimposing them on one another (Figure 7.4f). Using this approach, we see, once again, the domain walls from the *c*/*a*/*c*/*a* and $a_1/a_2/a_1/a_2$ super-domain regions have a high degree of coherency. Upon closer inspection, it is noticeable the nearly every boundary from the $a_1/a_2/a_1/a_2$ super-domain regions intersects the neighboring *c*/*a*/*c*/*a* super-domain at a *c*/*a* domain wall, while there are some additional *c*/*a* domain walls which do not have a corresponding a_1/a_2 domain wall. Finally, in a select few regions, such as in the top right hand corner there is some evidence regions with a dense herringbone-like *c*/*a*/*c*/*a* domain structure. Poling studies of these heterostructures (not included in this discussion) have found that after sequential poling the structure stabilizes into a herringbone structure very much similar to what is observed in this region; indicating that the mixed-phase super-domain structure might be a metastable structure. All told, these heterostructures appear identical in form to the thinner $PbTiO_3$ heterostructures with the exception of scale. While this should have significant implication for the macroscopic responses and properties, when studying the nanoscale switching mechanism the larger scale of the domain structure is necessary to observe the details of the switching process.

7.2.6 Crystal Structure of Mixed-Phase $PbZr_{0.2}Ti_{0.8}O_3$ Heterostructures

Before studying the nanoscale switching of these heterostructures detailed symmetric reciprocal space maps were conducted about the 220- and 002-diffraction conditions of the substrate and film, respectively (Figure 7.5). From these studies we observe two sets of peaks. The first set of three peaks has out-of-plane lattice parameters nearly identical to what is expected for bulk $PbZr_{0.2}Ti_{0.8}O_3$. Of these three peaks, the central peak is nearly aligned with the out-of-plane axis of the substrate (PZT_c 002) while the other two reflections ($PZT_{c\text{-}tilt}$ 002) are indicative of a tetragonal phase which is monoclinically distorted by ~0.6° along the <100> relative to the [001] substrate

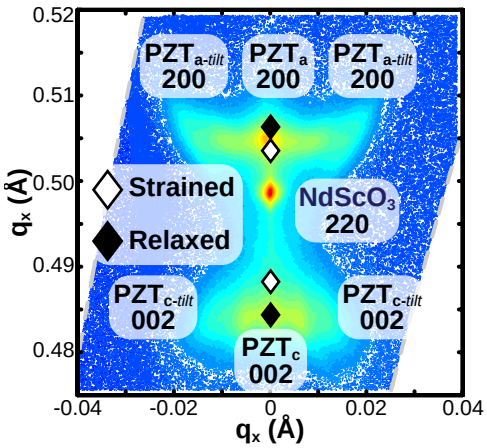

Figure 7.5. Symmetric reciprocal space map of 400 nm thick mixed-phase $PbZr_{0.2}Ti_{0.8}O_3$ heterostructures on $NdScO_3$ (110) obtained about the 220 diffraction condition of the substrate. Strain and relaxed peak positions of the film are indicated.

normal. The second set of 3 peaks, is observed with out-of-plane lattice parameters of ~3.96 Å, nearly halfway in-between the expected lattice parameter for the strained and relaxed *a* domain peak position. Once again, of these three peaks, there is a central peak which is nearly aligned with the substrate normal (PZT_a 200), surrounded by two additional peaks ($PZT_{a\text{-}tilt}$ 200) representing *a* domains which are tilted by ~1° along the <100> relative to the [001] substrate normal. Comparing these results to the topographic images, it is likely that these tilted *a* domains are from within the *c*/*a*/*c*/*a* super-domains as they have a saw-tooth-like topography with clear crystallographic tilts. Whereas, the untilted *a* domains are likely located within the $a_1/a_2/a_1/a_2$ super-domains where crystallographic tilts are not geometrically required, as seen by the relatively flat topography within these regions.

7.2.7 Band-Excitation Switching Spectroscopy of Mixed-Phase $PbZr_{0.2}Ti_{0.8}O_3$ Heterostructures

Using this understanding of the crystal and domain structure we set out to study the nanoscale switching mechanisms using BE-SS as previously described (see section 2.4.2). Prior to switching the heterostructures topographic and vertical piezoresponse images and were obtained (Figure 7.6a-c). To aid in the explanation of the switching spectroscopy we provide an example ferroelectric hysteresis loop to highlight the various points in the switching process being imaged (Figure 7.6d). A selection of amplitude (indicating the vertical piezoresponse at remanence) and phase (generally indicative of the out-of-plane polarization direction) maps of the local piezoresponse at various voltages throughout the switching cycle are provided (Figure 7.6e-i, additional images are provided in appendix I, in a flip book starting from appendix A, and movies compiled from the complete set of measurements are available online). Starting with the entire region uppoled, as indicated by a uniform red phase image (Figure 7.6e), the amplitude is, as expected, larger in the *c*/*a*/*c*/*a*-like super-domain regions (where a large proportion of the polarization direction is parallel to the measurement direction) compared to the $a_1/a_2/a_1/a_2$-like super-domains (where the polarization and measurement direction are perpendicular). Application of positive bias results in switching (Figure 7.6f phase/amplitude) which appears to initiate (at least from the phase image)

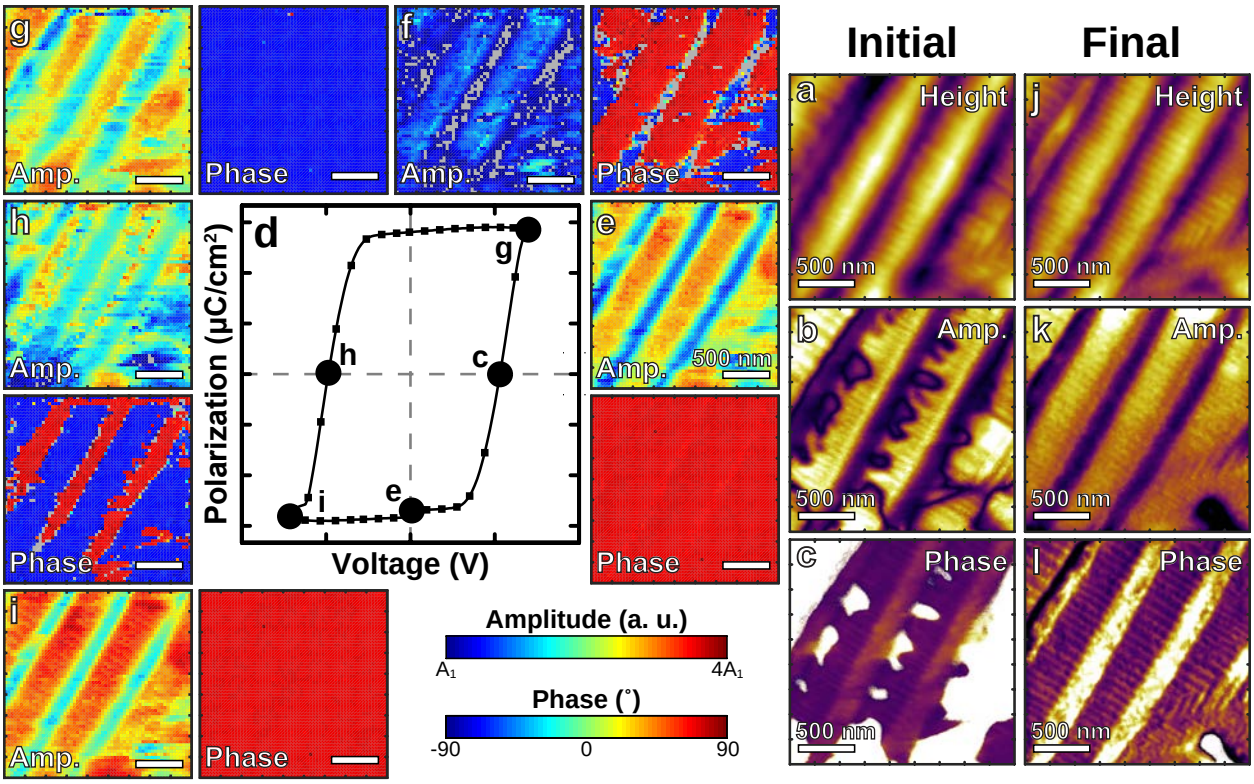

Figure 7.6. (a) Topography, and vertical piezoresponse force microscopy (a) amplitude and (b) phase images of 400 nm thick mixed-phase $PbZr_{0.2}Ti_{0.8}O_3/Ba_{0.5}Sr_{0.5}RuO_3$ (15 nm)/$NdScO_3$ (110) heterostructures prior to BE-SS measurements. (d) Typical macroscopic ferroelectric hysteresis loop used for reference only. (e-i) Corresponding band-excitation switching spectroscopy amplitude (left/top) and phase (right/bottom) images of the same 400 nm thick mixed-phase $PbZr_{0.2}Ti_{0.8}O_3/Ba_{0.5}Sr_{0.5}RuO_3$ (15 nm)/$NdScO_3$ (110) heterostructures measured at various stages of ferroelectric switching (as labeled). (j) Topography, and vertical piezoresponse force microscopy (k) amplitude and (l) phase images of 400 nm thick mixed-phase $PbZr_{0.2}Ti_{0.8}O_3/Ba_{0.5}Sr_{0.5}RuO_3$ (15 nm)/$NdScO_3$ (110) heterostructures following BE-SS measurements. All scale bars are 500 nm.

from within the $a_1/a_2/a_1/a_2$-like super-domains; however, one must be careful when trying to interpret phase images during switching. The phase response which is actually being imaged is a convolution of a number effects including: piezoresponse, electrostatic forces, lateral cross-talk into the vertical response, *etc.*, and, in turn, phase contrast can sometimes be misleading. If we focus instead on the amplitude images, we see that the piezoresponse is locally enhanced at the super-domain boundaries, indicating, instead, that nucleation of downward poled domains likely occurs at these super-domain boundaries. As the positive bias increases, the film switches to saturation, poling the heterostructure down, as indicated by the uniformly blue phase image (Figure 7.6g). In this down-poled state the amplitude response looks nearly identical to the initial, up-poled state. As the applied bias switches from positive to negative we notice that switching once again appears to start within the $a_1/a_2/a_1/a_2$ super-domains (as indicated by the red regions in the phase image). Unlike under positive bias however, the vertical amplitude starts to increase first within the $a_1/a_2/a_1/a_2$

super-domains (as shown in appendix I, filp book starting in appendix A and movie available online), before finally giving way to switching which nucleates at the super-domain boundaries. As the applied bias is increased further (in the negative direction) the heterostructure switches to saturation (poling the heterostructure up), back to the initial state (as indicated by the uniformly red phase image). In this negative-bias state the heterostructure has nearly identical response as observed in the positive-bias state. Response and switching of the same general form is observed through multiple switching cycles. Following switching topographic and piezoresponse force microscopy images reveal significant changes in the domain structure. First, in the top left-hand corner of the image there is the emergence of a *c*/*a*/*c*/*a*-like region within what used to be a purely a_1/a_2/a_1/a_2 super-domain region. This observation indicates that the application of an applied electric field, can at times, result in conversion of an a_1/a_2/a_1/a_2 super-domain to a *c*/*a*/*c*/*a*-like super-domain. Additionally, in the bottom right hand corner of the region we observe the re-orientation and expansion of what used to be a *c*/*a*/*c*/*a* region with a single primary orientation to a herringbone-like *c*/*a*/*c*/*a* domain region.

While we are still working on developing a comprehensive picture of the switching mechanisms in these heterostructures there are many useful conclusions which can be made. First, we clearly show that the switching nucleates at the super-domain boundaries. While it is well established that nucleation tends to preferentially occur near ferroelastic domain boundaries, the observation that nucleation occurs preferentially at the super-domain boundaries compared to at the nanodomain (within the super-domains) implies that these super-domain boundaries are more effective in acting as nucleation centers than traditional ferroelastic domains. In turn, designing heterostructures with super-domain structures could provide a route to significantly reduce coercivity. Additionally, the asymmetry in the switching observed in the a_1/a_2/a_1/a_2 super-domains (as indicated by the increased amplitude within this region when switching to the up-poled state compared to the down-poled state) might be an indication of possible strain gradients which may arise as a result of the dense ferroelastic domain structure. Finally, the observation of the emergence of a *c*-like domain within an a_1/a_2/a_1/a_2 super-domain and expansion of the herringbone-like region demonstrates the possibility of long range collective reorientation of the ferroelastic domain structure by the application of externally applied electric fields.

Once again, because at each pixel in the switching spectroscopy image there exists a full

piezoelectric hysteresis loop, it is possible to visualize the loops from within each of these super-do main regions. We show representative piezoelectric hysteresis loops from within a *c*/*a*/*c*/*a* and $a_1/a_2/a_1/a_2$ super-domain regions (Figure 7.7). Starting with the piezoelectric hysteresis loop from within the *c*/*a*/*c*/*a* super-domain region, we observe nearly square loops that saturate well. Moving on to the loops from within the $a_1/a_2/a_1/a_2$ super-domain regions, we observe highly-tilted piezoelectric hysteresis loop with significantly reduced piezoresponse. By calculating the loop centroid (cross hatched circle) it is found that the loops in this region are positively shifted along the voltage axis. Finally, looking at the fine structure of these piezoelectric hysteresis there are noticeable jumps in the piezoelectric response, which appear to be of the general form as those observed in the thinner $PbTiO_3$ heterostructures with the exception that these features are more gradual and less frequent.

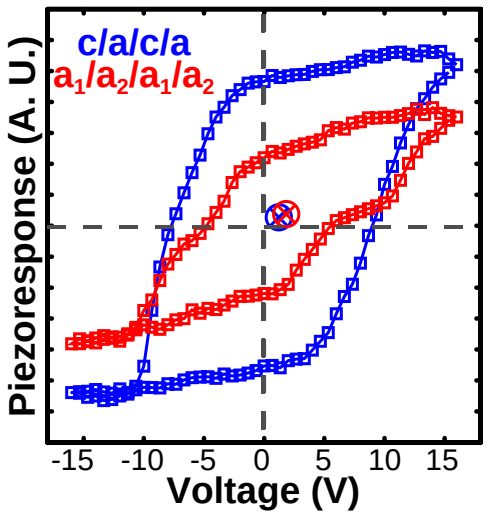

Figure 7.7. Representative piezoelectric hysteresis loops taken from within the *c*/*a*/*c*/*a* (blue curve) and $a_1/a_2/a_1/a_2$ (red curve) super-domain regions of a 400 nm thick mixed-phase $PbZr_{0.2}Ti_{0.8}O_3/Ba_{0.5}Sr_{0.5}RuO_3$ (15 nm)/ $NdScO_3$ (110) heterostructure.

The observed variance in the loop shape within these regions can be explained as follows. Starting with the loops in the *c*/*a*/*c*/*a* super-domain regions, we observe that the loops switch in a single step, nearly identical to what is observed in *c* domains of conventional heterostructures with *c*/*a*/*c*/*a* domain structures. This indicates that the response in these regions is dominated by the response of the *c* domains. The piezoresponse loops within the $a_1/a_2/a_1/a_2$ region, on the other hand, has a more complex response. Starting with the general loop shape features, it is observed, that there is a slightly reduced out-of-plane piezoresponse within the $a_1/a_2/a_1/a_2$ super-domains, an expected result considering that the polarization is oriented primarily perpendicular to the measurement direction (in comparison to the *c*/*a*/*c*/*a* super-domain regions where the polarization and measurement direction are nearly parallel to one another). Now looking at the slant of the loop, it is found that the $a_1/a_2/a_1/a_2$ super-domains have a much large loop slant (than the *c*/*a*/*c*/*a* super-domain regions). To explain this observation one must first consider origins of the slanted piezoelectric hysteresis loops. Conventionally, ferroelectric switching is a nucleation limited process, where once a domain is nucleated switching happens rapidly to completion, resulting in square piezoelectric loops. If, for instance, the growth of ferroelectric domains during switching is

impeded, one would expect that the loops would appear more slanted. Considering the very high density of in-plane oriented ferroelastic $a_1/a_2/a_1/a_2$ domains within the $a_1/a_2/a_1/a_2$ super-domain regions it is likely that switching and growth of a domain (in the out-of-plane direction) requires a collective reordering of the ferroelastic domain structure, in order to reduce to the electrical and elastic strain energy. Therefore, the collective nature of the switching process would likely impede the growth of a ferroelectric domain during switching. This hypothesis is corroborated by the observation of positive shifted piezoelectric hysteresis loops which could be related to elastic restoring forces that arise during switching away from the as grown or current equilibrium domain structure (similar to what is observed in the compositionally-graded heterostructures). Finally, throughout the switching process there are many jumps in the piezoelectric loop. These jumps are likely the manifestation of these large scale collective ferroelastic switching events which results in the reorientation of the ferroelastic domain structure (*i.e.* the nucleation of a new *c*/*a*/*c*/*a* or expansion of the herringbone-like *c*/*a*/*c*/*a* domain structure).

To explore the variance in loop shape features on a more statistically relevant scale the ferroelectric hysteresis loops were fit with using the standard loop fitting model (see section 2.4.3 for details). While this model does not take into account the multiple transition observed in the $a_1/a_2/a_1/a_2$ super-domains it is effective at modeling the general loop shape features (we are currently in the process of optimizing the fitting software and analysis methodology to account for these piezoelectric hysteresis loops with multiple transitions). Here, we show a small subset of the loop shape parameters obtain from fitting the piezoelectric hysteresis loops (Figure 7.8a-d, additional loop shape parameters are included in the appendix J). Starting with the voltage centroid of the fitted loop (Figure 7.8a), as observed from the single loop data there is a clear shift of the loop (in the positive bias direction) within the $a_1/a_2/a_1/a_2$ super-domain regions (compared to the *c*/*a*/*c*/*a* super-domain regions). As previously stated, this might be an indication of the presence of electric or elastic restoring forces that result during ferroelectric switching from the as grown (or poled) structure/state. Now, focusing on the work of switching (or loop area, Figure 7.8b), we observe an increase in the work of switching (loop area) in the primarily out-of-plane polarized *c*/*a*/*c*/*a* super-domains (compared to the $a_1/a_2/a_1/a_2$ super-domains), an expected result considering the orientation of the polarization and measurement direction. In addition, using the fitted loops and comparing it to the raw piezoresponse loop it is possible to create spatial maps of the difference in

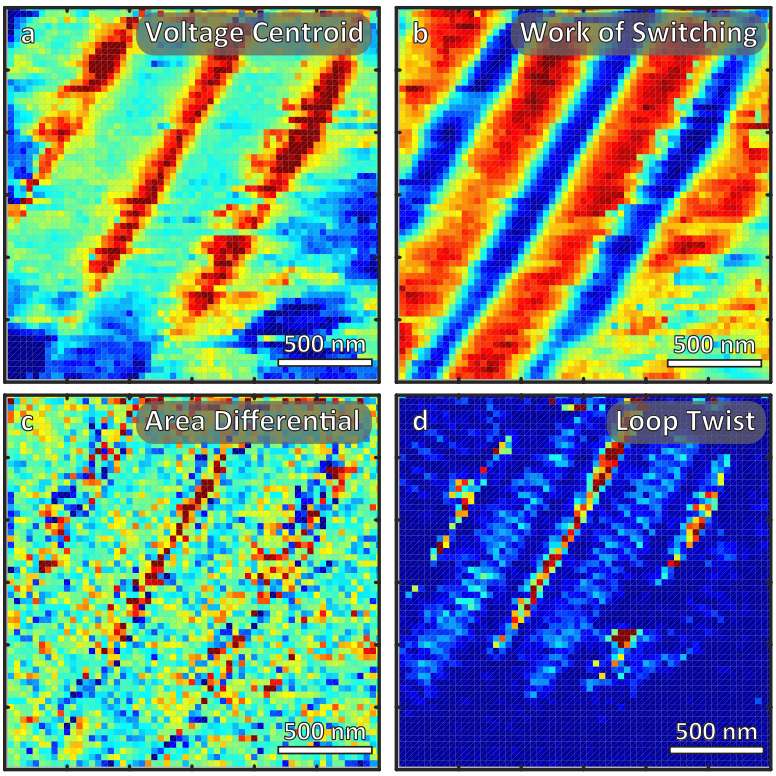

Figure 7.8. Maps of (a) voltage centroid, (b) work of switching, (c) area differential, and (d) loop twist extracted from loop fitting of piezoresponse loops obtained from band-excitation switching spectroscopy measurements on 400 nm thick mixed-phase $PbZr_{0.2}Ti_{0.8}O_3/Ba_{0.5}Sr_{0.5}RuO_3$ (15 nm)/$NdScO_3$ (110) heterostructures.

area (or fit error). The results of this calculation provide insight into how well the model represents the raw data. Looking at this image (Figure 7.8c) the fits are found to be particular poor (red in color) within the $a_1/a_2/a_1/a_2$ regions. This observation makes sense considering that the loops within these regions show multiple transitions which are not accounted for in the fitting model. Finally, we show maps of the degree of twist in the piezoelectric hysteresis loop (Figure 7.8d). While the concept of what is actually being represented in this parameter is a little bit obtuse; in general, larger loop twists are observed when there is a change in the electrical-mechanical coupling of the total mechanical system (composed of the cantilever and ferroelectric) during the switching (such as would be the case when switching a near a ferroelastic domain wall, see loop twist parameter of conventional $PbZr_{0.2}Ti_{0.8}O_3$ heterostructures on $GdScO_3$ for comparison appendix F). Under these assumptions we observed, as expected, enhanced loop twist within the $a_1/a_2/a_1/a_2$ super-domains and near the c/a boundaries in the $c/a/c/a$ super-domains indicating that switching in these regions has more ferroelastic character.

While these results reveal many interesting preliminary findings it also exposes the shortcomings of the current techniques and methodologies used to visualize and interpret multi-dimensional piezoresponse force microscopy data. It is fairly easy to visualize the data on 2-dimensions (*i.e.* piezoresponse-voltage, *etc.*), or even 3-dimensions (*i.e.* piezoresponse-spatial (x,y), *etc.*); however, it is exceedingly difficult to visualize the data in a higher dimensional space. These higher dimensional spaces however, might hold the clues needs to describe and understand the underlying mechanisms of response and physics of the system. At times, even visualizing 3-dimensional data

can be challenging as finding the appropriate scales to make the response modes of interest (which might be unknown) visible to the naked eye is not known *a priori*. To try and reduce the dimensionality of the data it is possible to fit the data to a model and extract parameters which represent the data features; however, this approach is only as good as the fitting model. In turn, utilizing this method of dimensionally reduction requires that the all features of significance are known *a priori* and can be incorporated into the fitting model, limiting its suitability in observing new nanoscale phenomena which might be buried deep within in these "big data" sets. Given the ever growing size and dimensionality of these datasets it is important that we devise new autonomous approaches to analyze and visualize the materials responses collected from these sorts of multidimensional measurements.

7.3 Suggestions for Future Work

7.3.1 Advances in "Big Data" Analytics to Uncover New Physics Across Multiple Dimensions

Traditionally, when collecting experimental data, experimental computational limitations set a manageable threshold on the acquired data size (typically on the order of thousand to millions data points). In turn, these data sets are relatively easily screened and visualized using brute force graphing and analysis techniques. More recently, the increased accessibility of high bandwidth electronics, increased computing power, and desire to understand coupled and correlated materials responses has caused the common measurement to balloon in size. For instance, band-excitation piezoresponse switching spectroscopy measurements (as conducted in this work) can easily contain an excess of 1 billion data points over an 8-diminsional data space (frequency, amplitude, loss, phase, x, y, voltage, time, *etc*.), and the size and dimensionality of these data sets is growing at an ever expanding rate. Trying to analyze such a large data set manually presents an insurmountable and unrealistic challenge and therefore, to handle this data some sort of dimensionality reduction is necessary. Using a basic knowledge of the systems, human guided approaches based on confining the data space or fitting, make it possible to skim the surface of these "big data" sets; however, such an approach requires that you know *a priori* the data dimension which the features of interest lies. Even if human driven dimensionality reduction can produce useful insight it is still only analyzing the data at the most cursory level.

To surmount this computational barrier approaches of "big data analytics"[439, 440] such as

unsupervised learning, dimensionality reduction, and clustering, widely used in everyday life, need to be adapted and adopted by the scientific research community.[441] To make strides towards this goal there are many challenges which need to be overcome. Both the experimental scientist and data analytics communities have reached a high degree of sophistication, to the point where the overlap, and even the language and terminology shared between these communities is small. To bridge this gap an increased dialog and cross-disciplinary approach is needed. Recently, the importance of this cross-disciplinary approach has been realized, and publications have started to trickle in.[442-448] These "big data" analytic tools are on the brink of revolutionizing how we analyze data, what is needed is time, familiarity and acceptance amongst the broader scientific community to understand the importance of these tools to turn the "big data" collected, into "deep data" which can synergistically combine physical knowledge of the system with data analytics to uncover new physics.

7.3.2 Control of Ferroelectric Domain Structure and Response Using Compositionally-Graded Heterostructures

Much of the work in this thesis has focused on the effect of compositional and strain gradients in controlling the crystal and domain structure, and ultimately the responses (electrical, ferroelectric, dielectric, *etc*.) of compositionally-graded heterostructures.[172, 173, 195, 449] This work however, has just scratched the surface of what is possible. Throughout this work we have limited our scope to some of the simplest heterostructure designs possible in order to simplify the analysis and interpretation of what is an inherently complex system. While many significant discoveries and insights were made, there is much more that can be done. The concept of compositionally-grading heterostructures can be expanded to other ferroelectric systems or even trinary compositional gradients where the magnitude of the maximum strain and strain gradients can be increased. Additional, more complex compositional gradient forms can be designed such that the strain and chemical gradients are not continuous in magnitude or direction, enabling the design of novel combinations of electrical, ferroelectric, mechanical and potentially thermal responses. At the nanoscale level, in this work we have shown that the presence of compositional and strain gradients can direct the shape the structure and response of ferroelastic domains.[449] This is particularly interesting as it provides new routes to finely control the shape of ferroelastic domains through control of the form and magnitude of the compositional and strain gradients. This unique capability is in need of

exploration; but, holds the potential to enable an unprecedented level of control in designing new modalities of electromechanical responses at ferroelastic domain walls important for the burgeoning field of domain wall nanoelectronics.

7.3.3 Design and Fabrication of Free-Standing Epitaxial Heterostructures

Conventionally, when one thinks of a ferroelectric thin film one automatically assumes that the substrates is semi-infinite and perfectly rigid; however, if one were able to fabricate heterostructures where the substrate and film were of comparable thickness the properties of the heterostructure would depend on the elastic properties of both layers in a more nuanced way.[450, 451] This method to control of the mechanical boundary conditions of heterostructures would enable the precise control of the strain state, crystal and domain structure, and ultimately the properties of the active layer in ways not currently possible. To date however, there are many practical challenges that need to be addressed before such structures can be fabricated. The main challenge is finding the correct sacrificial layer, and/or etching protocol necessary to fabricate these epitaxially-strained free standing heterostructures. Once these practical challenges are solved these free standing heterostructures will not only enable new modalities of strain engineering but also will facilitate the exploration of new physics. For instance, if free standing cantilever structures can be fabricated, controlled bending experiments can be designed to explore flexoelectric effects and extract flexoelectric coefficients with unprecedented accuracy. From a device perspective the ability to fabricate free standing heterostructures will enable the use of epitaxial strain to optimize materials to increase performance and sensitivity for potential applications in vibrational and thermal energy harvesting, and thermal/mechanical sensing.

7.3.4 Epitaxial Strain Engineering of Ferroelectrics on Virtual Substrates

Throughout this work, one of the primary limitations in our ability to strain materials using thin-film epitaxy has been availability of substrates with suitable lattice parameters capable of imposing the desired degree of strain. Even if a substrate with the desired lattice parameter is sold commercially, there are typically only a few good suppliers with very limited supplies. To make matters worse some of the perovskite materials with larger lattice parameters [*i.e.* $PrScO_3$ (110, a_{pc}=4.0138), $CeScO_3$ (110, a_{pc}=4.0235), $LaScO_3$ (110, a_{pc}=4.0473)], which are particularly interesting due to their small lattice mismatch with the Zr-rich compositions of $PbZr_{1-x}Ti_xO_3$, are either available in extremely limited supply, or cannot be grown using the Czochralski growth method

(or other common single-crystal growth methods) due to their high melting temperatures.[452] Despite the limited availability of single crystals of these materials pressed ceramic targets of these materials are readily available. To circumvent these limitations it is possible to use pulsed-laser deposition (or other thin-film epitaxy techniques) to grow thick epitaxial layers of these materials (on more commonly available perovskite substrates), such that they act as virtual substrates which can impose strain on subsequent layers of much lower thickness. The concept of growing a material as a virtual substrate is not a new concept and has been widely adopted in the semiconductor industry;[453-456] yet, has barely been explored in perovskite thin films. The use of virtual substrates also creates new possibilities as it would be possible to create solid solutions of similar perovskites materials enabling the continuous tuning of substrate lattice parameter. Ultimately, the development and implementation of virtual substrates in epitaxial strain engineering provides the potential to dramatically expand the accessibility and possibilities of epitaxial strain engineering important for the study of wide variety of materials systems.

7.3.5 Effects of Growth Kinetics and Chemistry on the Structure and Properties of $PbZr_{1-x}Ti_xO_3$ Thin Films

Traditionally, when growing materials using pulsed laser deposition stoichiometric transfer from the target to the substrate is assumed *a piori*.[78, 457] Recently, this classical assumption has received significant scrutiny as it has been found that both the angle between the target normal and the substrate,[458, 459] and the laser fluence[460-462] can have a significant influence on the stoichiometry, structure,[150, 463] dielectric response[458, 464-466] and thermal condutivity[458, 467] in a variety of material systems; however, to data no such systematic study in the $PbZr_{1-x}Ti_xO_3$ system has been undertaken. Moreover, it has very recently been shown that the amalgamation of strain and defect chemical defects can give rise to defect dipole alignment changing the nature of how strain in accommodated in thin films.[150] Throughout our study of the $PbZr_{1-x}Ti_xO_3$ we have noticed that through control of laser fluence, growth rate, and temperature the crystal and domain structures between heterostructure can vary wildly, despite them being considered identical based on the conventional nomenclature of the community. Furthermore, preliminary studies have revealed that by altering the growth conditions it is possible to generate chemical gradient in Pb and B-site astoichiometry. The ability to control defects during growth is particularly interesting as it provides new routes to controllably generate strain gradients. Additionally, these preliminary studies (within our

group) have uncovered that the electrical properties of these heterostructure vary in a non-intuitive fashion where the crystallographic quality of the heterostructure and films resistivity are inversely correlated. Figuring out the ultimate dependence of growth conditions, defect chemistry, structure, and electrical conductivity in this class of materials is of paramount importance to paint a more accurate picture of the response and physics of these complex material systems. This new knowledge will facilitate the design of heterostructures with improved electrical responses capable of being integrated into- and improving performance of- functional devices.

7.3.6 Exploration of Pyroelectric and Electrocaloric Responses of Ferroelectric Heterostructures

Measurement of pyroelectric and electrocaloric effects are relatively straightforward in bulk samples; however, are significantly more challenging in thin films as a result of the reduced sample dimensions, sample resistance, and magnitude of response. Traditionally pyroelectric response in ferroelectric thin films has been determined by measuring the change in remnant polarization as a function of temperature[59, 311, 322, 323] or using the so-called Byer-Roundy method which measures pyroelectric response during a series of linear temperature cycles;[314] however, neither of these methods are accurate when applied to ferroelectric thin films.[327] Recently, a more accurate phase-sensitive approach to pyroelectric measurements – which can separate the pyroelectric and thermally stimulated current, developed by Garn and Sharp,[319, 320] has been implemented in ferroelectric thin films,[326, 327, 374] as well as in this work. This technique, however, is far from perfect, suffering from exceedingly small pyroelectric currents (on the order of pico- to nano- amps) which typically fall below the noise floor when trying to measure at elevated temperatures.

Standard practices for measuring electrocaloric effects in literature are even less developed. Primarily electrocaloric has been determined using an indirect method relying on the assumption that the π has been accurately measured and that the Maxwell relation $\left(\partial P/\partial T\right)_E = \left(\partial S/\partial E\right)_T$ holds true, both of which are of suspect.[57, 59, 311, 322] This assumption is particularly problematic in thin films where elastocaloric effects can be large.[324] There have been some attempts in literature to directly measure electrocaloric effects in ferroelectric thin films, but these techniques have been primitive, consisting mainly of attaching a thermometer to the surface of a film.[58, 323] An alternative approach, using differential scanning calorimeters has been employed to directly measure electrocaloric response but has been limited to systems with large thermal mass (thick films or multilayer stacks), precluding the study of strained epitaxial thin films.[60, 468]

Throughout the time of this work, new approaches to measure pyroelectric and electrocaloric temperature changes over a wide range of frequencies and temperatures have been developed, including techniques based on 2ω method (pyroelectric) and laser intensity modulated methods (pyroelectric and electrocaloric).[324, 326, 327] While these methods have been demonstrated, only a very select few prototypical ferroelectric thin films have been studied using these approaches. In turn, a world of new materials systems and physics is awaiting exploration with these techniques.

Undoubtedly, as with all other ferroelectric susceptibilities the nanoscale nature of the pyroelectric and electrocaloric response will be of significant interest and importance. Utilizing some of the developments in new modes of scanning probe microscopy, particularly those which focus on rapidly measuring the fully cantilever dynamics,[448] it is important to start considering how it might be possible to adapt these techniques to locally measure electrocaloric or pyroelectric response. For instance, by measuring calibrating the thermal response of the cantilever, and with the capability of measuring the full cantilever dynamics (using a combination of laser interferometry and scanning laser spot position) it might be possible to observe local electrocaloric responses as an electric field is applied to a sample using a conductive tip. While development of this technique requires significant technological developments its future importance merits some consideration.

Appendix A

History, Mechanisms, and Growth Modes of Pulsed-Laser Deposition

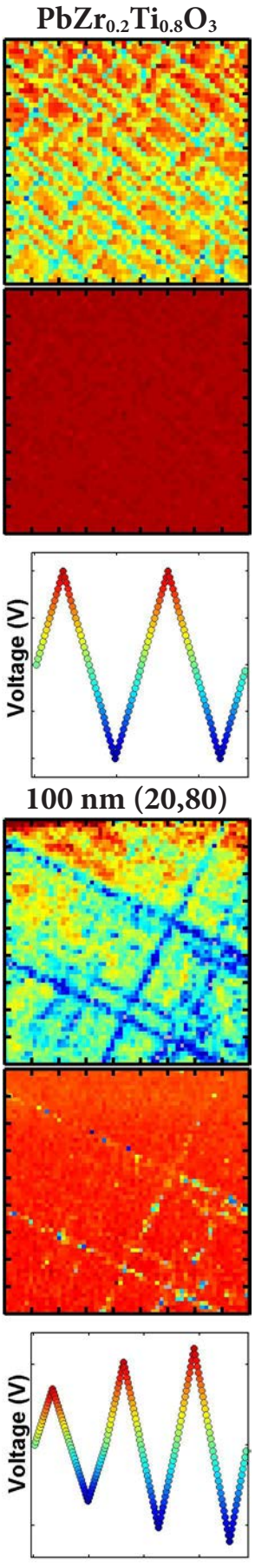

Historically, the concept of PLD began in the mid-1960's with the development of high powered lasers.[469] Soon after it was observed that these high powered lasers can ablate materials, and this was rapidly recognized as a promising route to grow thin films.[470] Since this discover there have been many developments in the laser technology including shorter pulse durations, lower wavelengths, and higher power[471, 472] which have enabled thin films to be grown with quality close to films grown by MBE.[473, 474] Within the past two decades the confluence of these early developments and experiences growing a wide variety of materials systems with PLD have led to it becoming a work-horse in thin-film epitaxy community. This widespread utilization of PLD is owed primarily to the relative simplicity of the techniques and ability to take a material system from conception to synthesis rapidly with minimal capital investment. This ability to somewhat haphazardly grow new materials is primarily the result of the preconceived notion that PLD results in near stoichiometric transfer from target-to-film. This concept arises primarily because PLD is a highly non-equilibrium growth process where only the interaction of the laser with the target materials is assumed to matter.

In actuality, there are many interactions beyond the laser target interaction which are important, including interactions between: the laser and plasma plume, ions within the plasma, and the plasma plume with the ambient scattering gas. In general, as the laser pulse reaches the target surface there are three types of absorption processes which can occur. 1) lattice absorption in the material volume, 2) free carrier absorption at the material surface, and 3) plume absorption.[475] The relative importance of each of these interactions depends on the materials properties of the ablated material. For instance, metallic materials primarily undergo free carrier absorption whereas, at the other extreme, dielectric materials are dominated by lattice

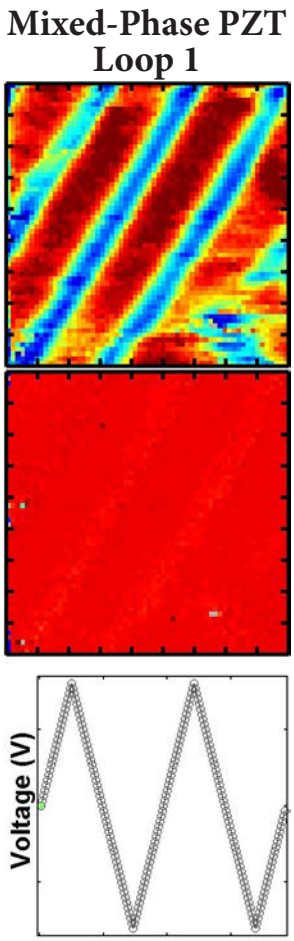

absorption. Once absorption has occurred a molten layer, the so-called Knudsen layer forms.[475] This melted region or front begins to propagate through the target as the material starts to vaporize from the melt. As more energy from the pulse is absorbed a plasma is formed, creating a plume which expands rapidly away from the target.

Once the plume is created, material transfer happens *via* a number of different methods including thermal, electronic, and macroscopic sputtering, of which the relative importance of each is growth condition and material dependent. Starting with the thermal sputtering process, which is likely the most intuitive to understand, the laser interaction with the target heats the target well above its boiling point resulting in the transfer of gaseous species. These thermal transfer processes are particularly prominent in materials with low boiling points, low thermal conductivity, low laser reflectivity, and high laser absorption. Electronic sputtering processes occur when the interaction of the target and laser pulse result in the electronic excitation and/or ionization of atoms. This process gives rise to a highly energetic repulsive plasma that rapidly expands away from the target. Electronic sputtering results in extremely high adatom velocities and temperatures (as high as 40,000 K, based on $\kappa_b T$).[476] Finally, it is possible to have macroscopic particulate ejection from the surface as a result of thermal shock waves which break the surface tension of the Knudsen layer. This process results in the expulsion of liquid droplets and other large volumes of material from the target. Typically, it is advisable to avoid this growth mechanism when trying to obtain films with good topography and crystal quality.

As the plume expands from the target it interacts with the ambient gas, scattering the adatom species.[477] The background pressure plays a significant role in defining the shape and dispersion of the plume. Generally, increased background pressures results in the focusing of the plume shape, a reduction in the front velocity, and can dramatically alter the growth rate. In addition, it is common, specifically in the oxide community to grow films in a reactive environment, such as O_2, S_2, *etc.*, resulting in the formation of molecules within the plasma which can alter the plume

dynamics. While observing the fine-details of the plume dynamics, and using it as feedback to optimize growth is not realistic, an understand of the mechanisms involved in the deposition process is useful. When optimizing growth of a material there are many knobs to turn (temperature, fluence, laser spot size, pressure, *etc.*) and even small changes to any of these parameters can result in significant and visible changes to the plume shape, and ultimately the film structure. The understanding of the plume dynamics provides insights into which knobs to turn and in what direction. In the end, using standard deposition conditions it is possible to deposit adatom with energies ranging from 1-100 eV with widely variable deposition rates.

Once these ablated adatoms adsorb onto the surface they diffuse around on the surface until nucleating a new cluster, joining a pre-existing nuclei, or desorbing from the surface. Growth of thin films tends to occur *via* three major growth modes: 1) Volmer-Weber or island growth,[478] 2) Frank-Van der Merwe or layer-by-layer growth,[479] and 3) Stranski-Krastanov growth.[480] Volmer-Weber island growth occurs when many stable clusters nucleate on the surface of the film and the subsequently deposited material has a strong preference to bond to the preexisting nuclei compared to the substrate surface, making well defined islands. This is most common when depositing dissimilar materials or onto a substrate with a high surface energy. Frank-Van der Merwe layer-by-layer growth has the opposite premise. In layer-by-layer growth the deposited material prefers to bond to the substrate and/or a preexisting step edge than to bond on top of a previously formed layer, tending to form 2d planar layers. The final growth mechanism Stranski-Krastanov growth represents a combination of these two mechanism where initially the adsorbed adatoms prefer to grow layer-by-layer. After a few layers however, the preference for layered growth no longer exist, giving way to three dimensional island growth.

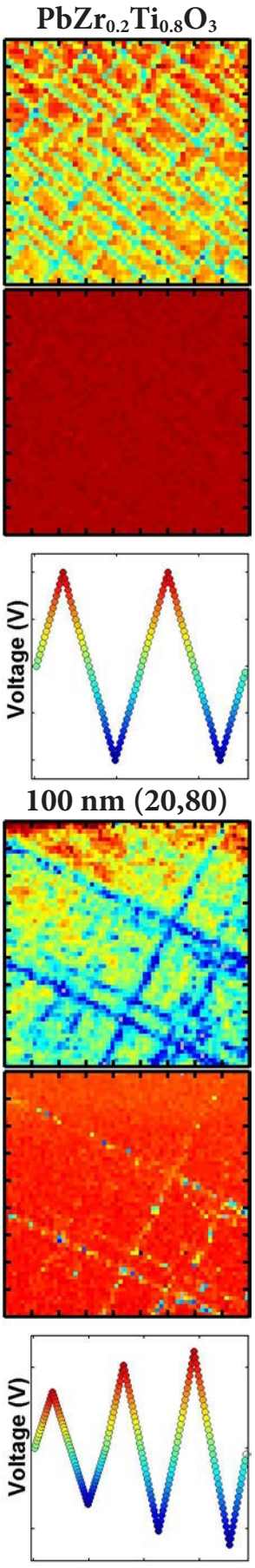

Mixed-Phase PZT

Loop 1

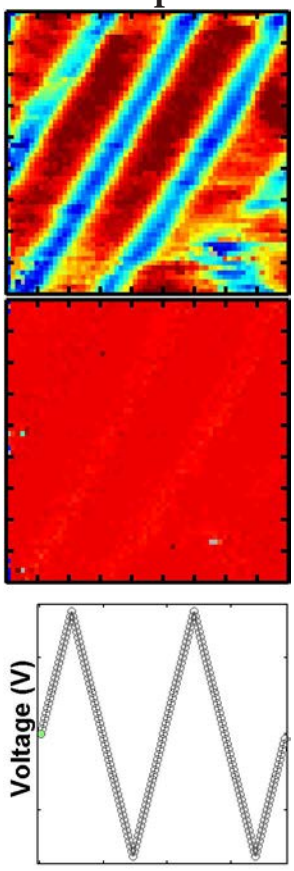

Loop 2

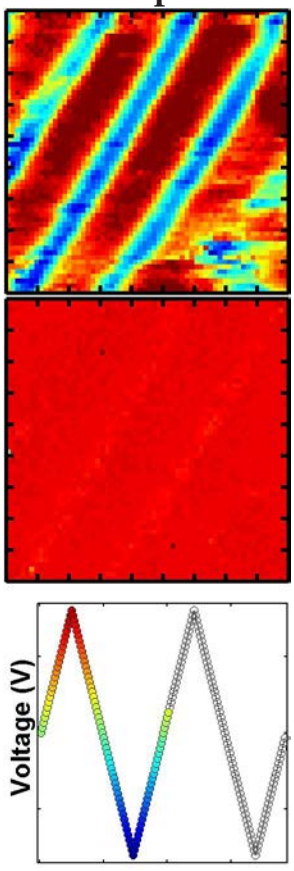

Appendix B

Measurement and Quantification of Laser Fluence

To calculate the laser fluence requires that both the laser spot size and laser energy are known. To measure this, the laser energy and optics were set to the typical growth conditions and the laser energy was measured from within the chamber. To measure the laser spot area, a single shot of the laser was fired onto a TiO_2 target, leaving a mark on the target. An image of the laser spot was then acquired by taking a high resolution scan of the target (dpi>600). From these ablation spots it is evident that the laser spot is non-uniform in nature. Since the exact spatial dependence of

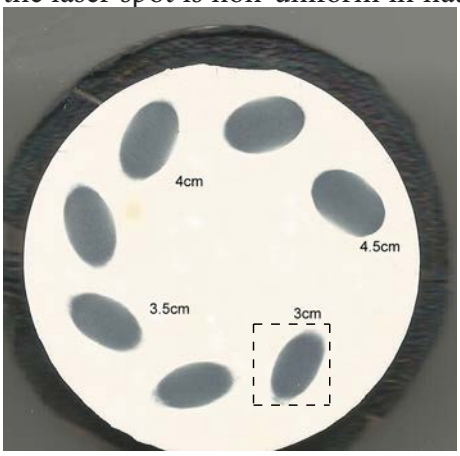

	Pixel Cutoff	Area (cm^2)	Fluence
Original Image	--	96.6135	1.0351
95%	252	96.5948	1.0353
90%	248	96.4641	1.0367
80%	239	95.5432	1.0466
70%	231	93.7971	1.0661
60%	222	91.5719	1.0920
50%	213	89.6205	1.1158
40%	205	88.0026	1.1363
30%	196	86.2068	1.1600
20%	187	84.5155	1.1832
10%	179	82.7258	1.2088
7.5%	176	82.0613	1.2186
5%	174	81.6954	1.2241
2.5%	172	81.2772	1.2304
20 pix	110	39.6231	2.5238

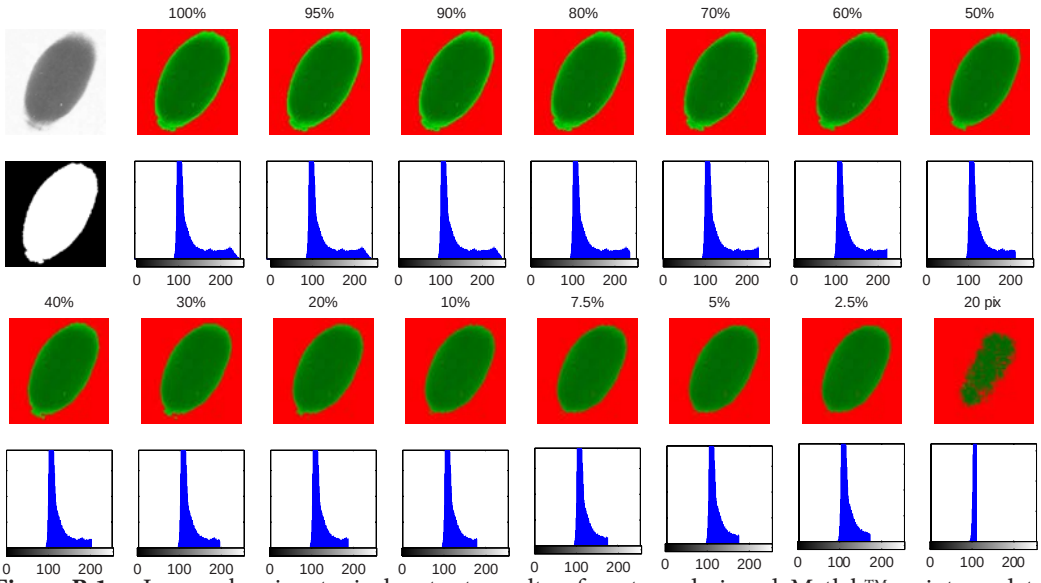

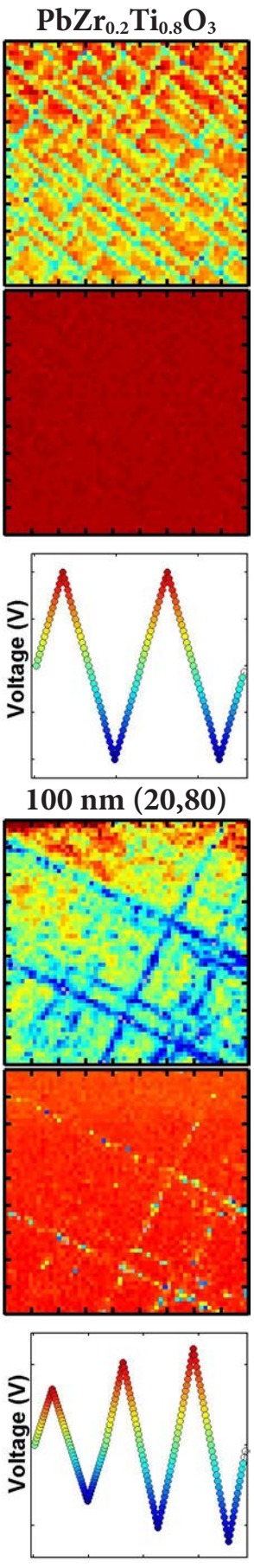

Figure B.1. Image showing typical output results of custom designed Matlab™ script used to quantify the laser spot area and fluence.

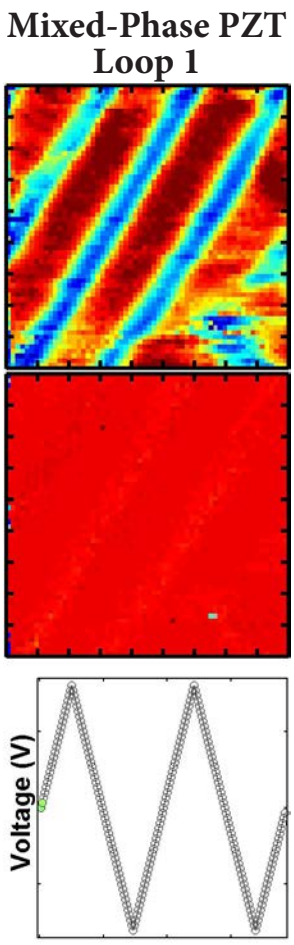

the laser spot energy is unknown averaging methodologies must be used to approximate the laser fluence. To do this, a custom Matlab™ script was written. This script imports a scanned image of the TiO_2 target, and requests that the user provide the image dpi and laser energy. After a region of interest is selected the script converts the image into a gray-scale image and displays images of the laser spot (in a green-red color scale) excluding those points below a threshold gray value. The number of pixels above the gray threshold are counted, converted to their real-space dimensions, and used as the area to calculate the laser fluence. A representative example of the results from this script is provided (Figure B.1). For all fluence calculations in this thesis a cutoff threshold of the darkest 10% of the pixels (in the image) was used to approximate the ablated area. Matlab™ scripts used to complete this calculation are provided online.

Appendix C

Additional Studies of $PbZr_{0.2}Ti_{0.8}O_3$ Heterostructures

C.1 Additional X-ray Diffraction Studies

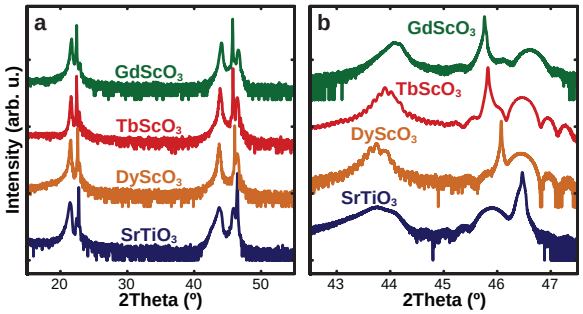

Figure C.1. (a) Full range and (b) high resolution x-ray diffraction 2θ-ω scans about the (00l)-diffraction conditions of $PbZr_{0.2}Ti_{0.8}O_3$.

Detailed XRD 2θ-ω scans of the $PbZr_{0.2}Ti_{0.8}O_3$ heterostructures on various substrates reveal that all heterostructures are single phase (00l)-oriented (Figure C.1a). High-resolution scans about the 002-diffraction condition reveal that the out-of-plane lattice parameter of the film increases with increasing compressive strain, and decreases with increasing tensile strain (Figure C.1b). To observe if any in-plane oriented *a* domains were present, we conducted XRD RSM which measures a series of 2θ-ω scans, at various ω values, about the 002-diffraction condition of $PbZr_{1-x}Ti_xO_3$ (Figure C.2a-d). These reciprocal space maps show no evidence of *a* domains in the compressively strained heterostructure on $SrTiO_3$ (Figure C.2a) or in the nearly lattice matched heterostructures on $DyScO_3$ (Figure C.2b). On the substrates with increasing tensile strain, $TbScO_3$ (Figure C.2c) and $GdScO_3$ (Figure C.2d) however, an increasing fraction of *a* domains is observed.

To further characterize the strain state detailed asymmetric RSM about the 103-diffraction condition for the $PbZr_{0.2}Ti_{0.8}O_3$ were measured (Figure C.3a-d).

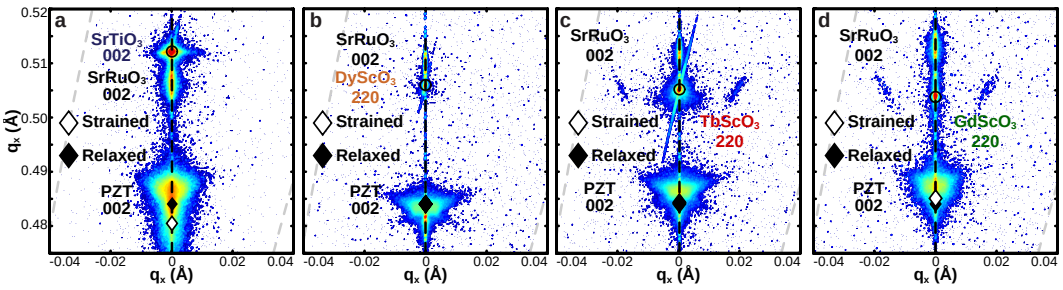

Figure C.2. Symmetric reciprocal space maps about the 002-diffraction condition for $PbZr_{0.2}Ti_{0.8}O_3$ for films grown on substrates with increasing tensile strain (a) $SrTiO_3$ (001) (b) $DyScO_3$ (110), (c) $TbScO_3$ (110) and (d) $GdScO_3$ (110).

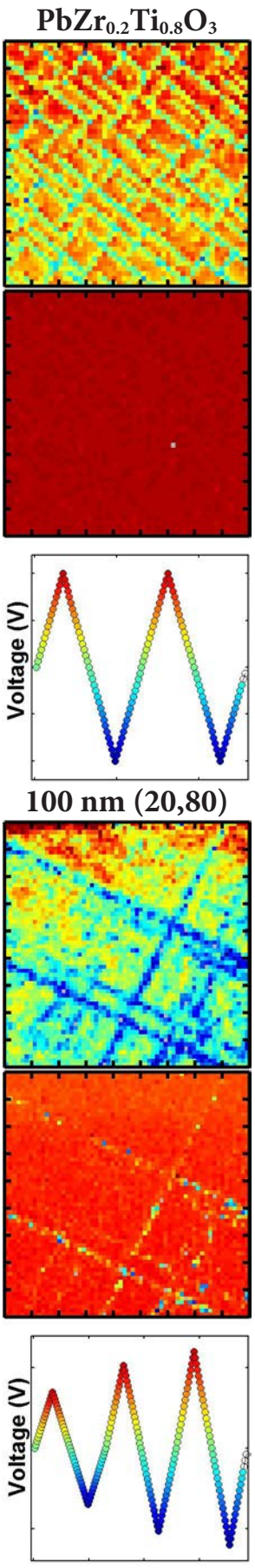

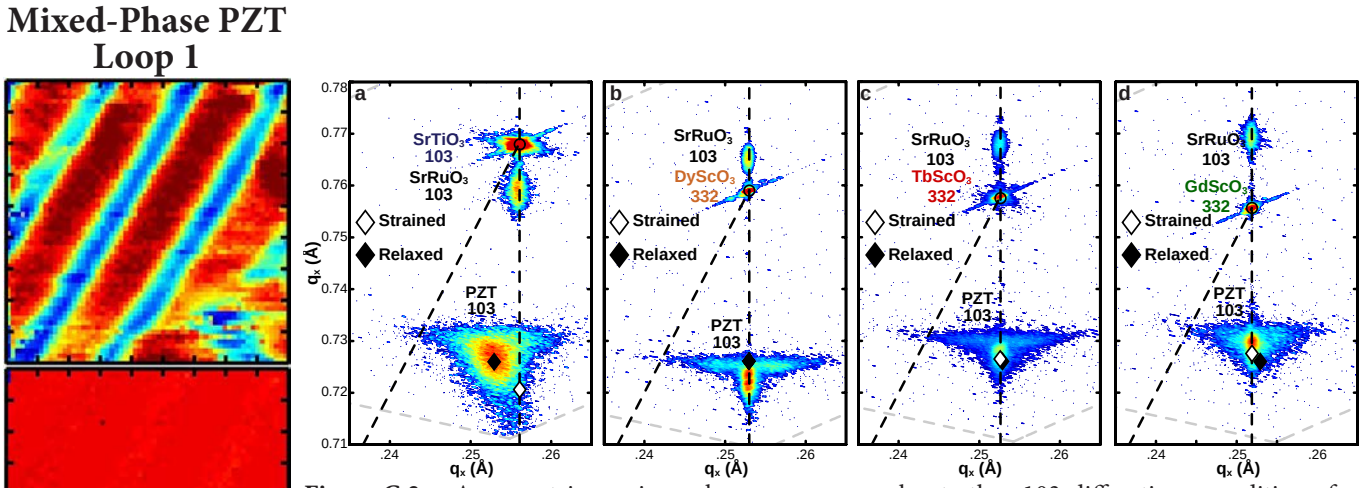

Figure C.3. Asymmetric reciprocal space maps about the 103-diffraction condition for $PbZr_{0.2}Ti_{0.8}O_3$ for films grown on substrates with increasing tensile strain (a) $SrTiO_3$ (001) (b) $DyScO_3$ (110), (c) $TbScO_3$ (110) and (d) $GdScO_3$ (110).

Initially, we notice that regardless of substrate all $SrRuO_3$ bottom electrodes have the same in-plane lattice parameter as the substrate meaning they are coherently strained to the substrate. Now focusing on the $PbZr_{0.2}Ti_{0.8}O_3$ layer, and starting with the film grown on $SrTiO_3$ (Figure C.3a), which imposes a compressive misfit strain of -0.8%, we notice that the $PbZr_{0.2}Ti_{0.8}O_3$ film is nearly fully relaxed, deviating significantly from the q_x value of the substrate; and aligning almost perfectly with the bulk lattice parameter. Moving on to the films on the scandate substrates (Figure C.3b-d) which imposes a tensile misfit strains ranging from 0.3-0.9% we observe that all heterostructures are coherently strained (having in-plane lattice parameters identical to the substrate which they are grown on). This tensile strain causes a reduction in the out-of-plane lattice parameter which matches well with the calculated out-of-plane strained lattice parameter (as indicated by the white-filled diamond). This difference in the ability to maintain strain under tensile verses compressive strains is likely caused by the ability to form ferroelastic domain under tensile strain which can accommodate strain without relaxing the film.

C.2 Leakage Measurements of $PbZr_{0.2}Ti_{0.8}O_3$ thin films.

The electrical properties of $PbZr_{0.2}Ti_{0.8}O_3$ heterostructures on various substrates were measured by fabricating parallel plate capacitors using the MgO hard mask process (as described in section 2.2.1). Initial leakage characterization of the capacitor structures for all heterostructures studied was completed by applying bias to the top circular electrode and measuring the leakage current through the

grounded bottom electrode (Figure C.4). For all measurements a dwell time between each voltage step (of 100 ms) was included to exclude switching currents. The $SrRuO_3/PbZr_{1-x}Ti_xO_3/SrRuO_3$ heterostructure can be understood by considering it to be a structure of back-to-back Schottky diodes. In this configuration the electrode under reverse bias will dominate the leakage characteristics. In turn, in this electrode configuration, the negative (positive) bias direction represents the leakage characteristic through the top (bottom) electrode. From these measurements we observe that the heterostructures are highly insulating, an indication of the quality of the epitaxial heterostructure. Comparing the characteristics of the top- and bottom- electrodes, there is slightly more leakage when the leakage characteristics are dominated by the top electrode (than the bottom electrode). This is likely due to the decreased quality of the top electrode as a result of the lower growth temperature. Overall the leakage current is nearly symmetric compared to electrodes fabricated using elemental metal electrodes.[240]

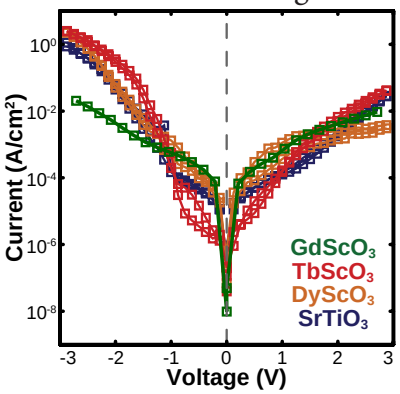

Figure C.4. Room temperature current-voltage response of $PbZr_{0.2}Ti_{0.8}O_3$ heterostructures grown on various substrates.

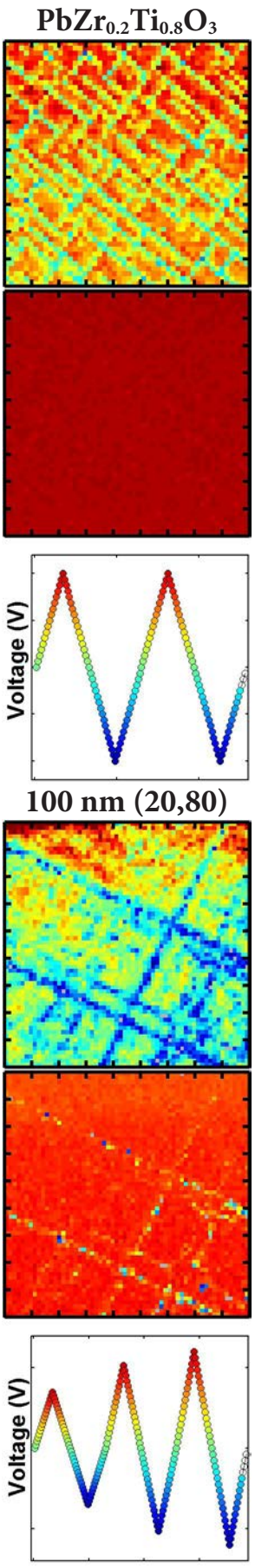

Mixed-Phase PZT
Loop 1

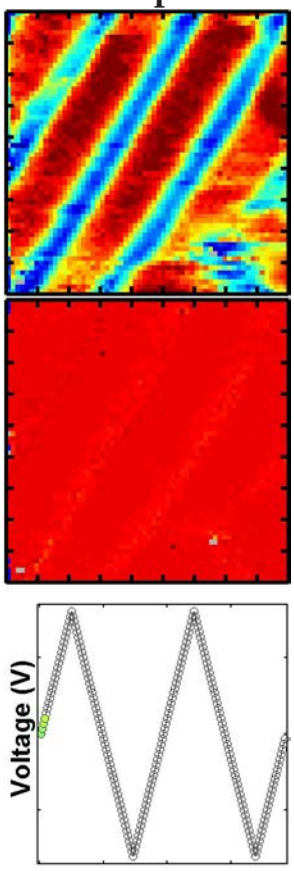

Loop 2

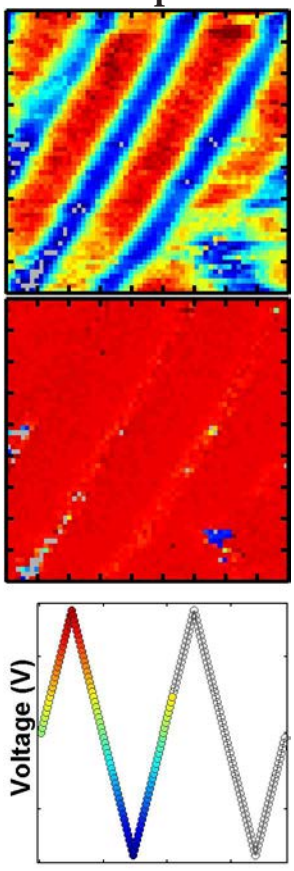

Appendix D

Additional Images of Band-Excitation Switching Spectroscopy of $PbZr_{0.2}Ti_{0.8}O_3$ Heterostructures

Included in this section is a subset of the BE-SS (amplitude, phase, loss, and resonance frequency) images of homogeneous $PbZr_{0.2}Ti_{0.8}O_3$ Heterostructures. Note that the scan size in all images is 2 μm.

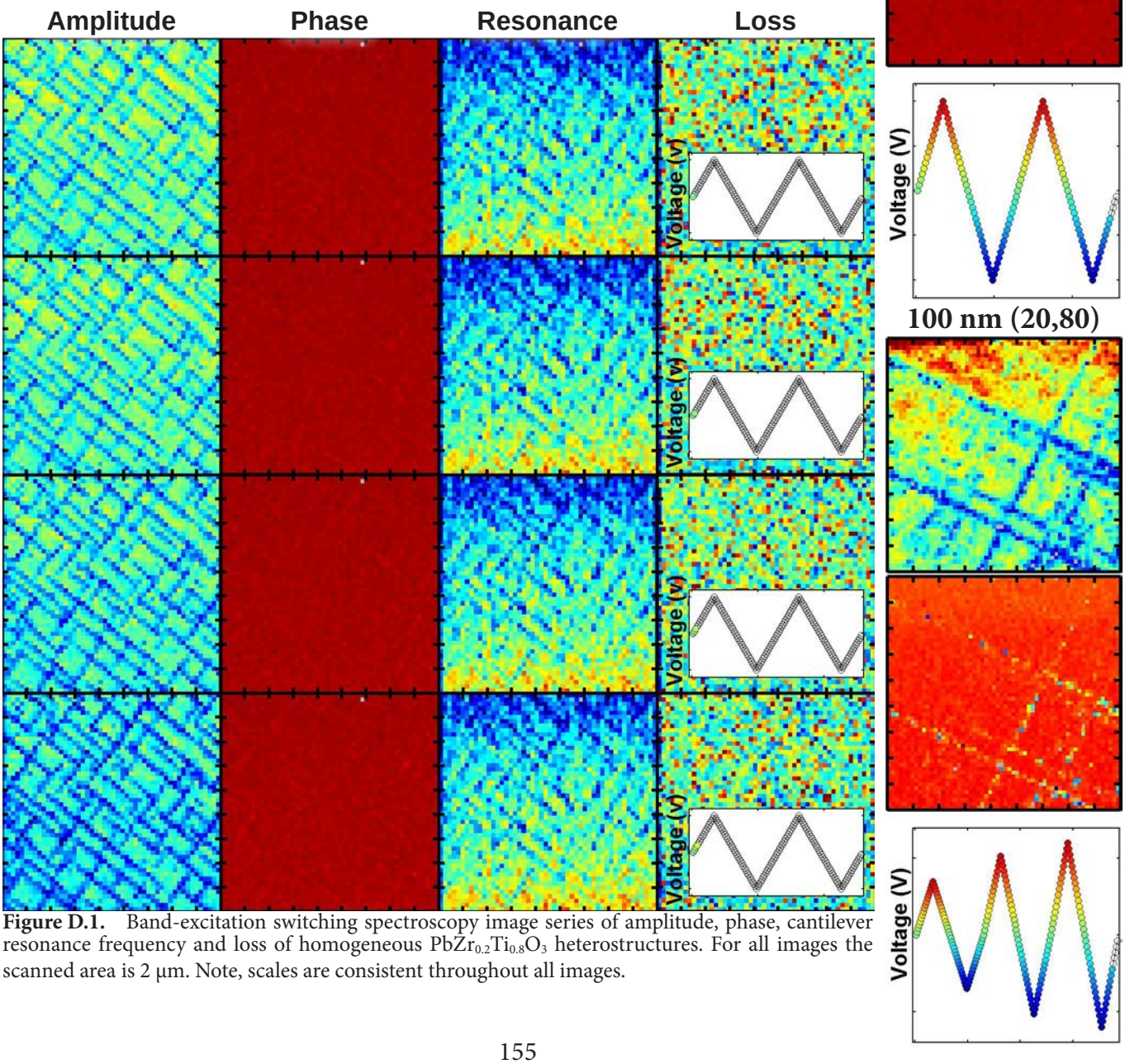

Figure D.1. Band-excitation switching spectroscopy image series of amplitude, phase, cantilever resonance frequency and loss of homogeneous $PbZr_{0.2}Ti_{0.8}O_3$ heterostructures. For all images the scanned area is 2 μm. Note, scales are consistent throughout all images.

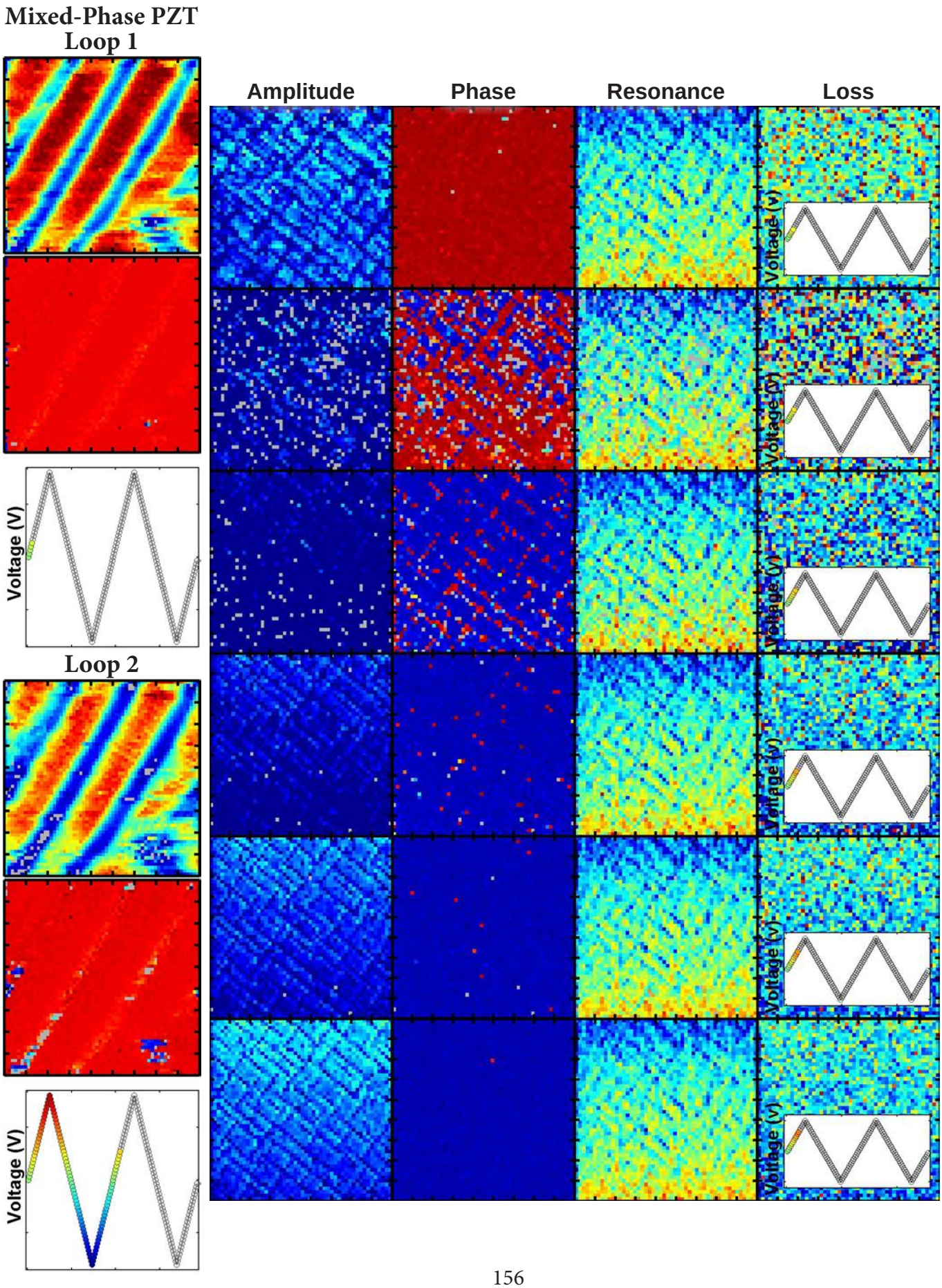
Mixed-Phase PZT
Loop 1
Amplitude
Phase
Resonance
Loss
Voltage (V)
Loop 2
Voltage (V)
Voltage (v)

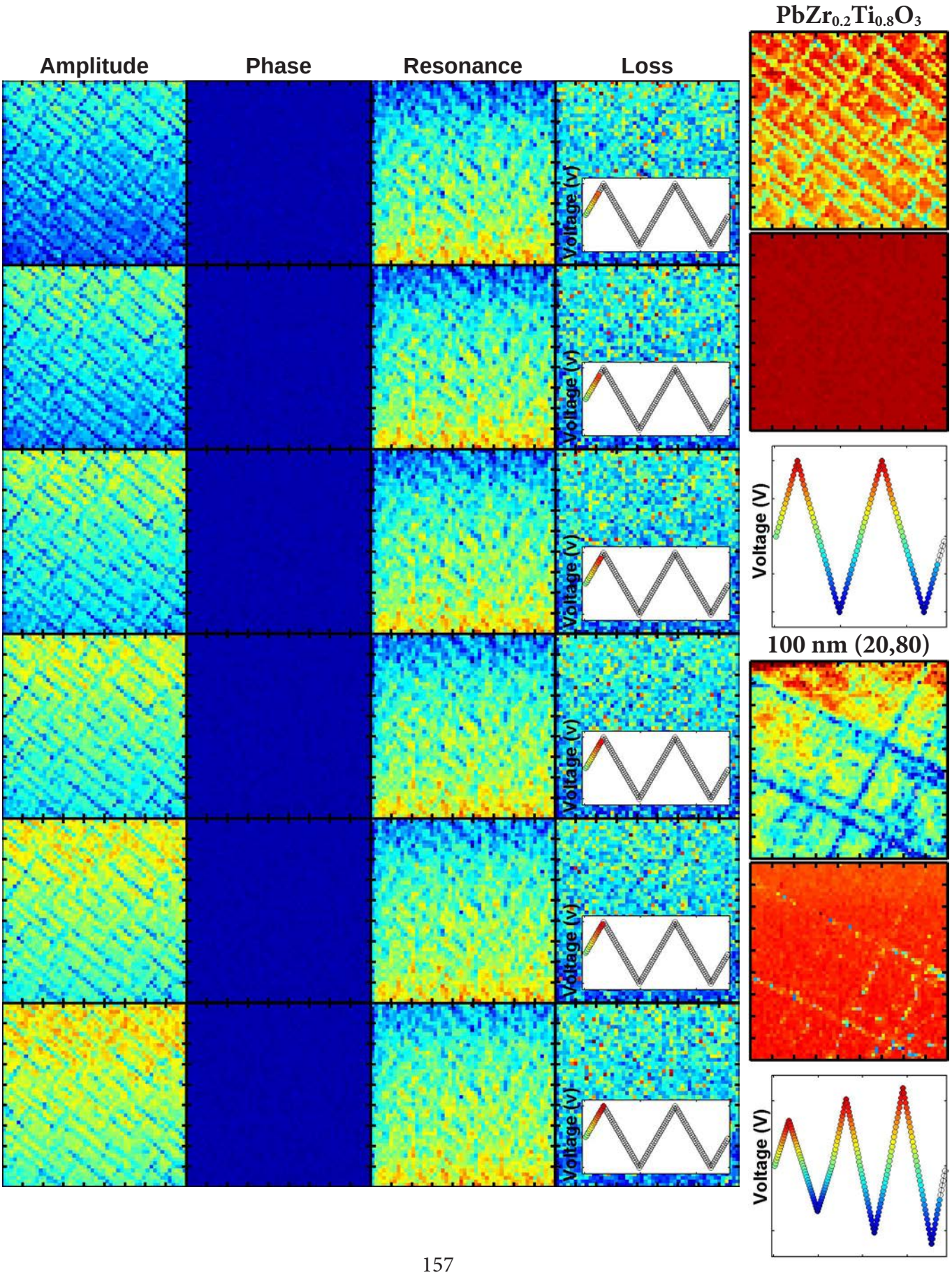
Amplitude
Phase
Resonance
Loss
Voltage (v)
PbZr0.2Ti0.8O3
Voltage (V)
100 nm (20,80)

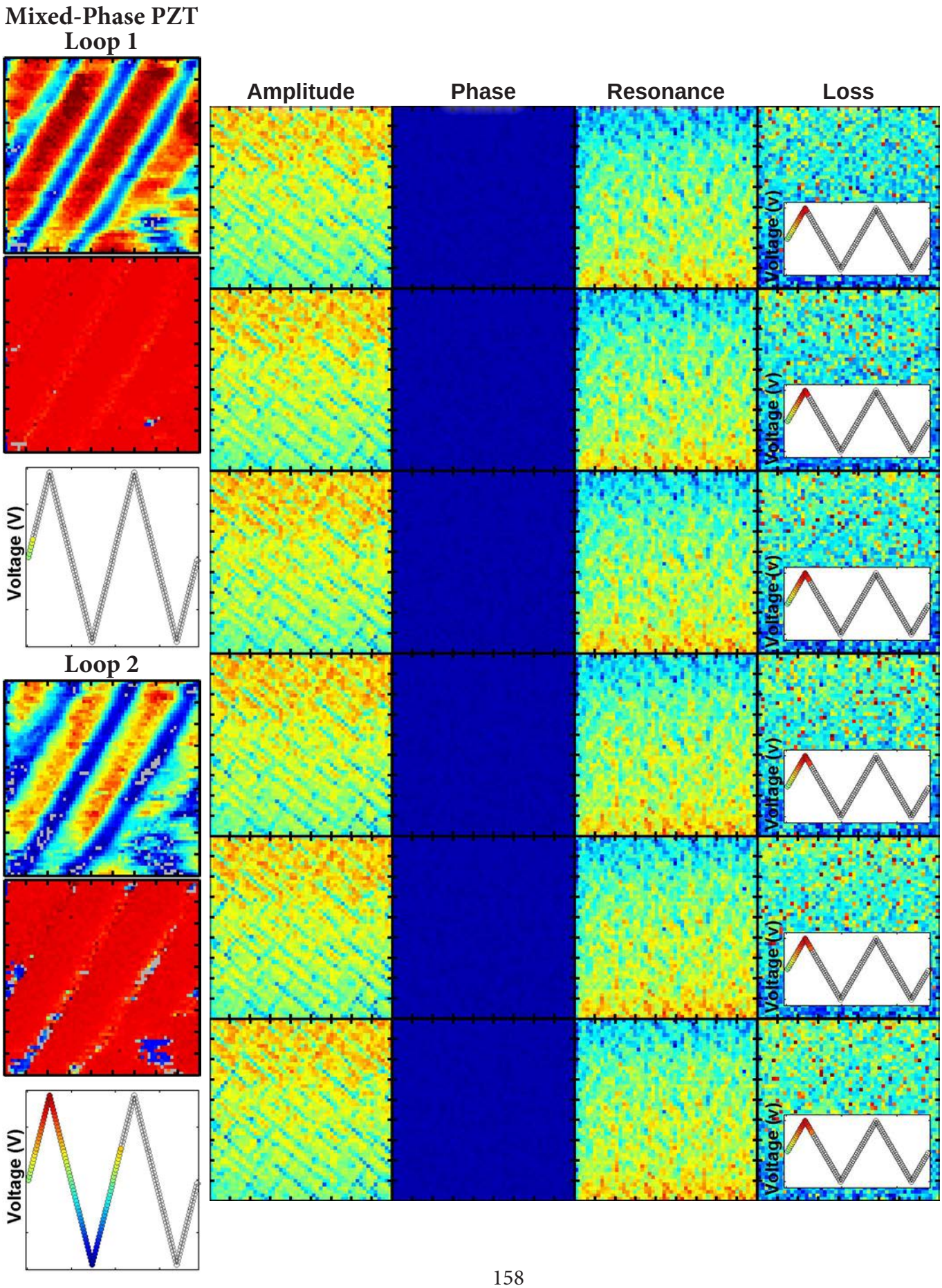
Mixed-Phase PZT
Loop 1
Amplitude
Phase
Resonance
Loss
Voltage (V)
Loop 2
Voltage (V)
Voltage (v)

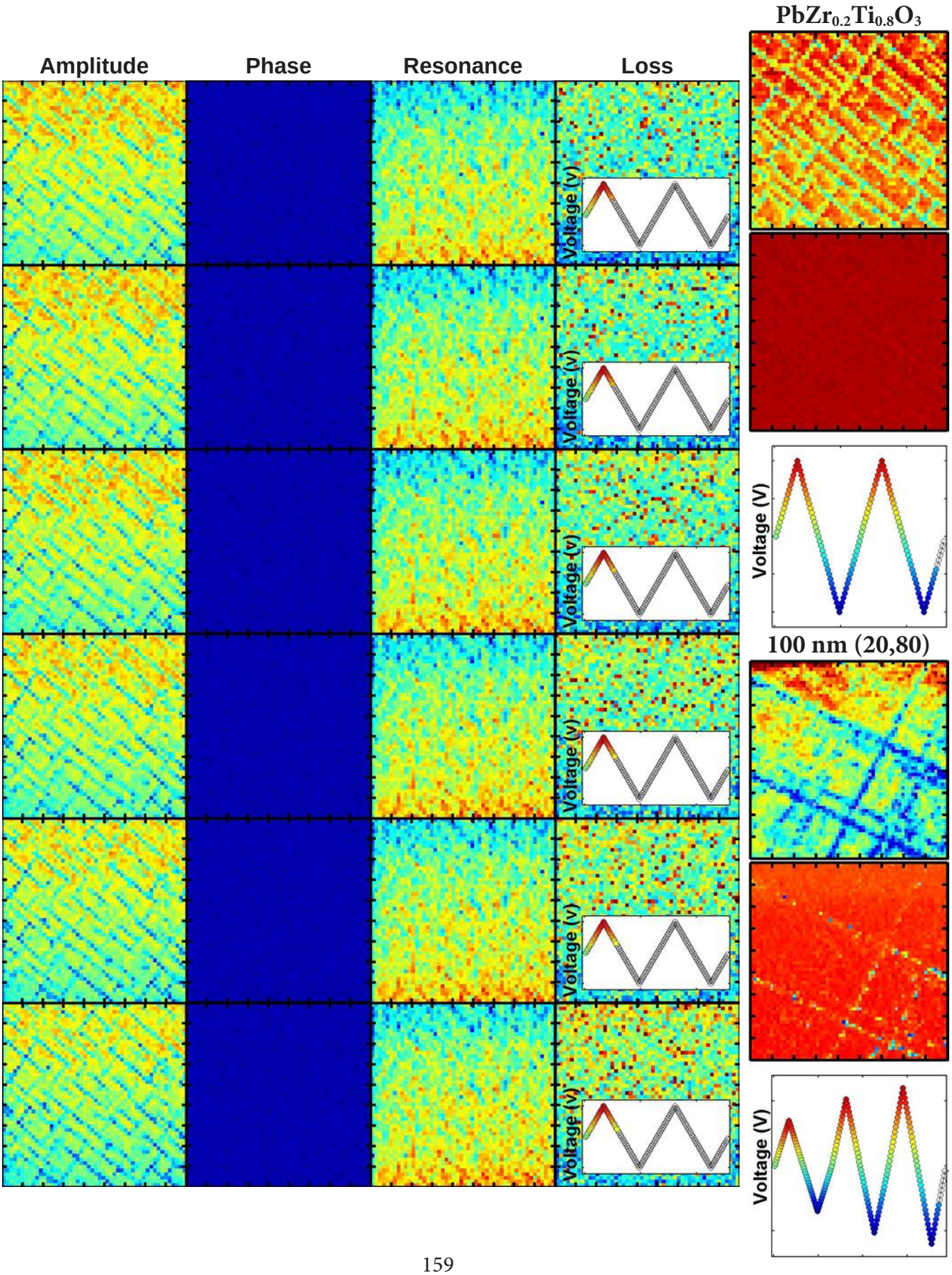
Amplitude
Phase
Resonance
Loss
Voltage (v)
PbZr0.2Ti0.8O3
Voltage (V)
100 nm (20,80)

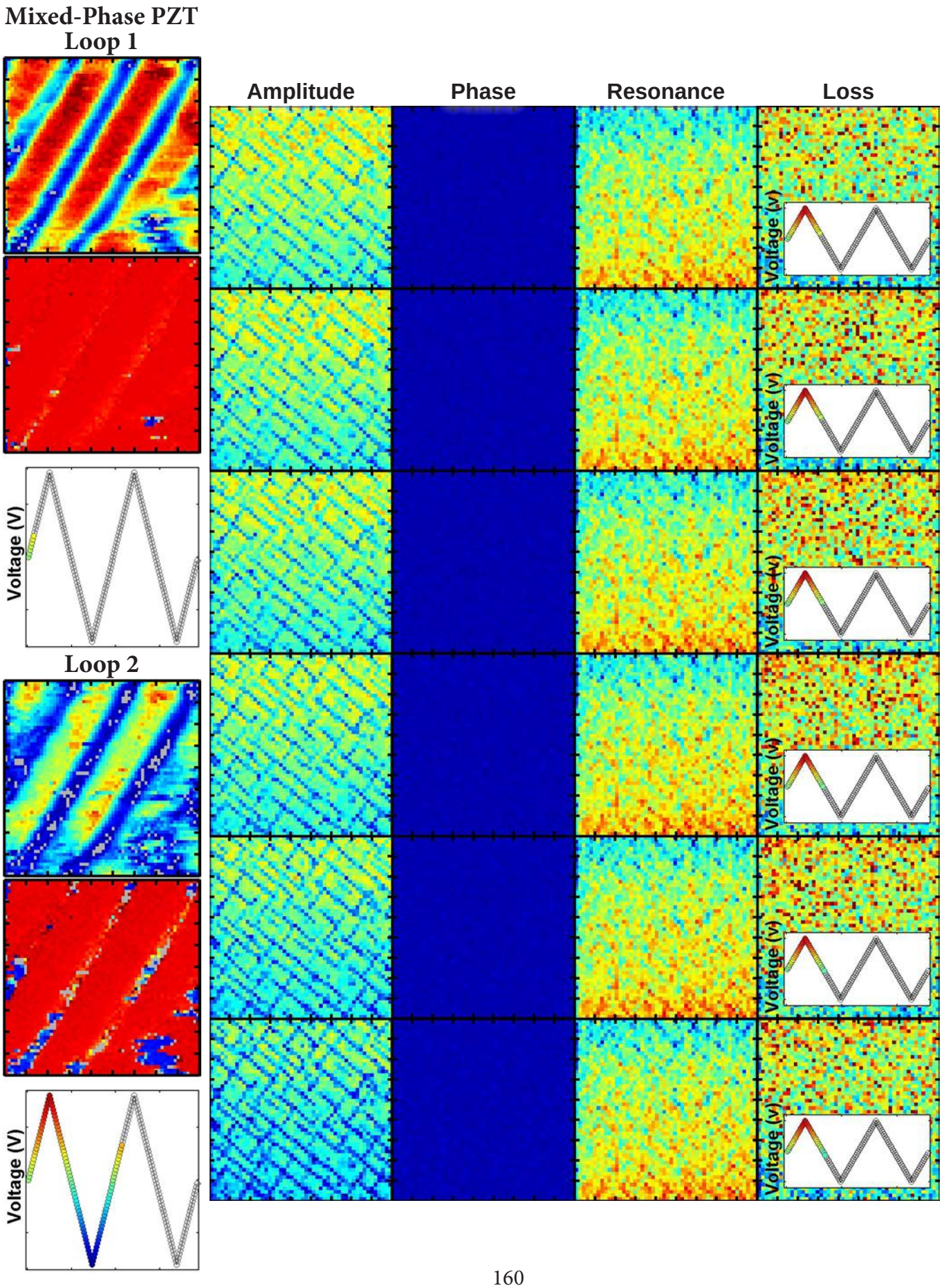
Mixed-Phase PZT
Loop 1
Amplitude
Phase
Resonance
Loss
Voltage (V)
Loop 2
Voltage (V)
Voltage (v)

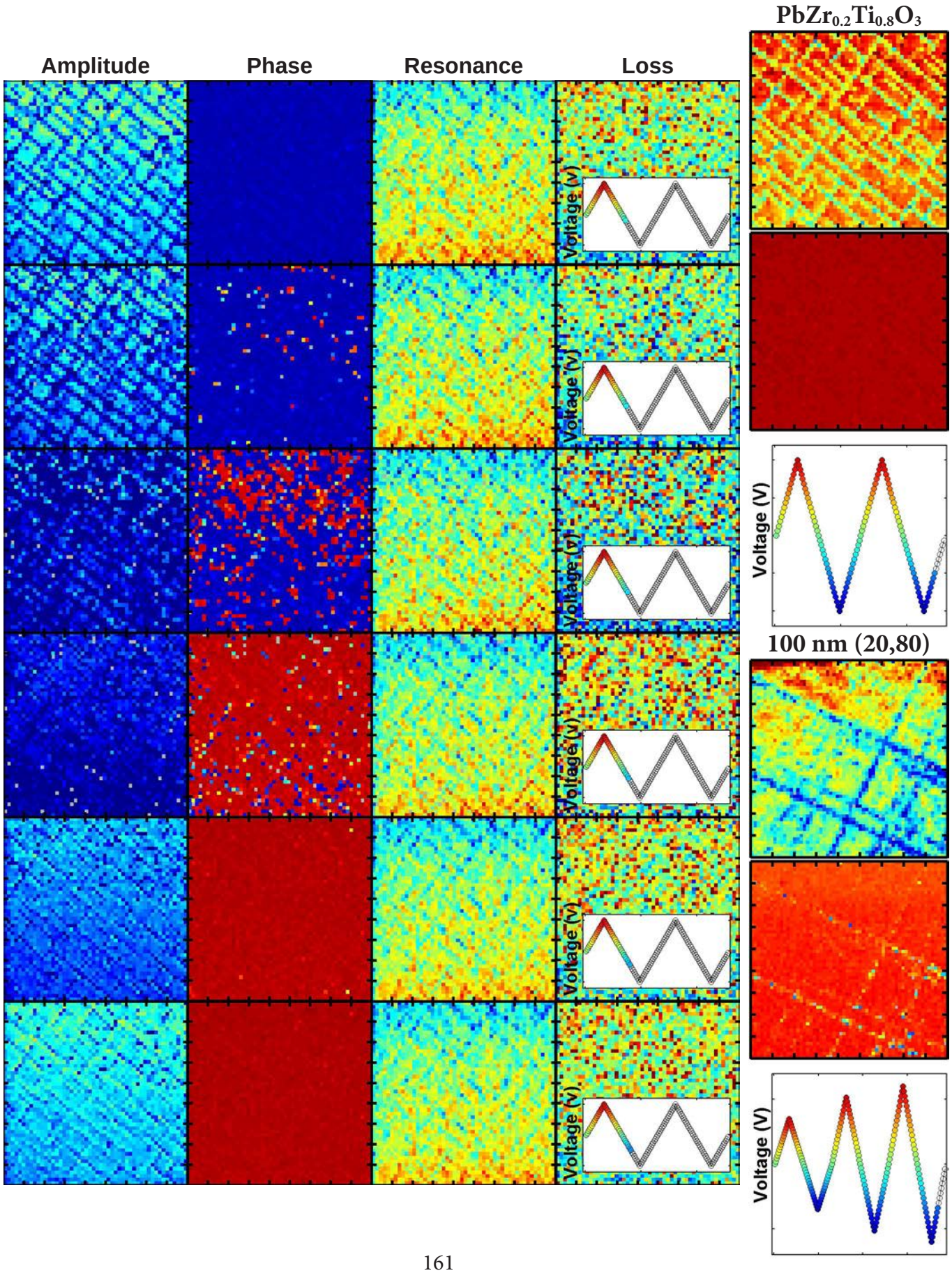
Amplitude
Phase
Resonance
Loss
Voltage (v)
PbZr0.2Ti0.8O3
Voltage (V)
100 nm (20,80)

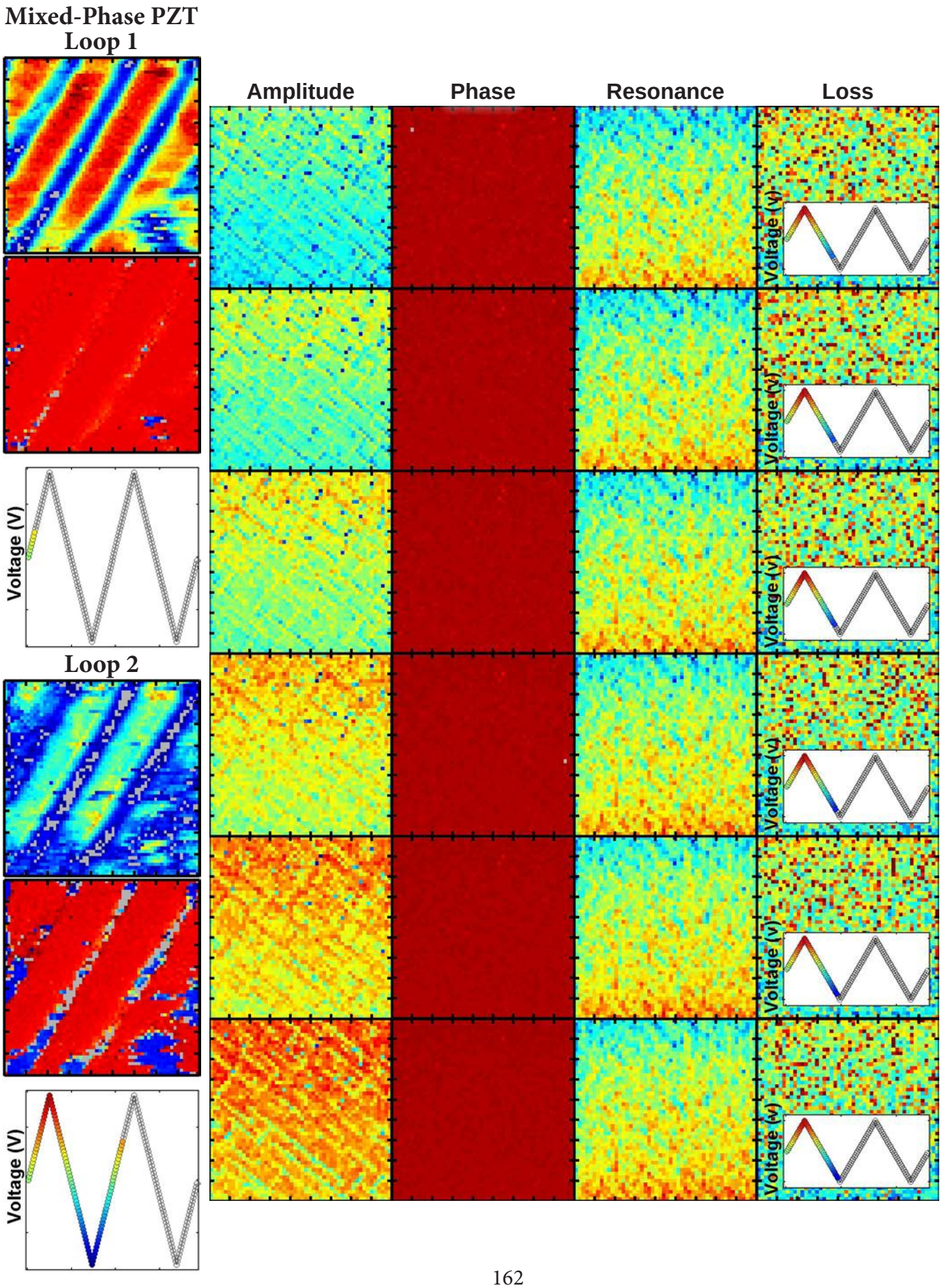
Mixed-Phase PZT
Loop 1
Amplitude
Phase
Resonance
Loss
Voltage (V)
Loop 2
Voltage (V)
Voltage (v)

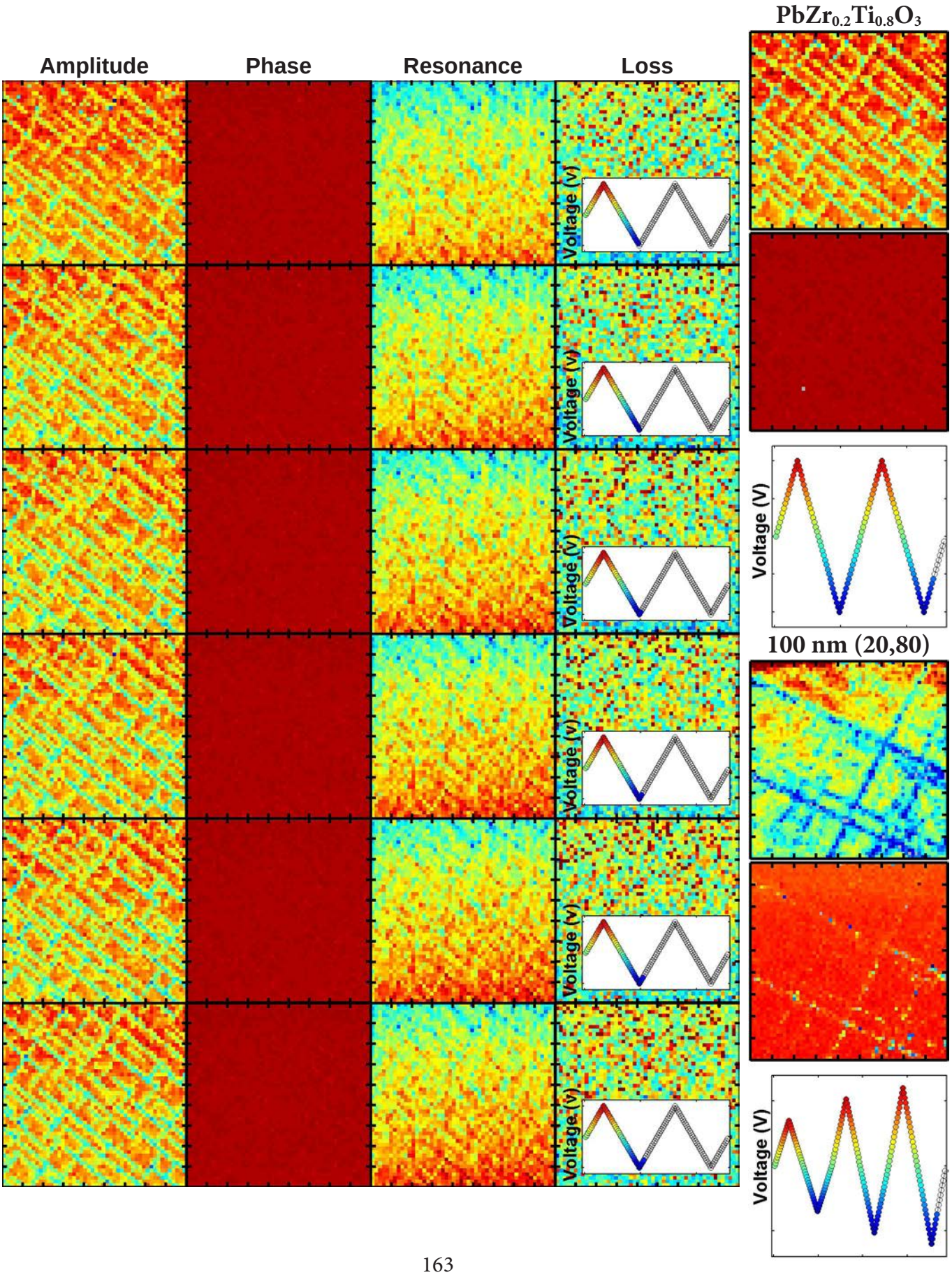
Amplitude
Phase
Resonance
Loss
Voltage (V)
PbZr0.2Ti0.8O3
Voltage (V)
100 nm (20,80)
Voltage (V)

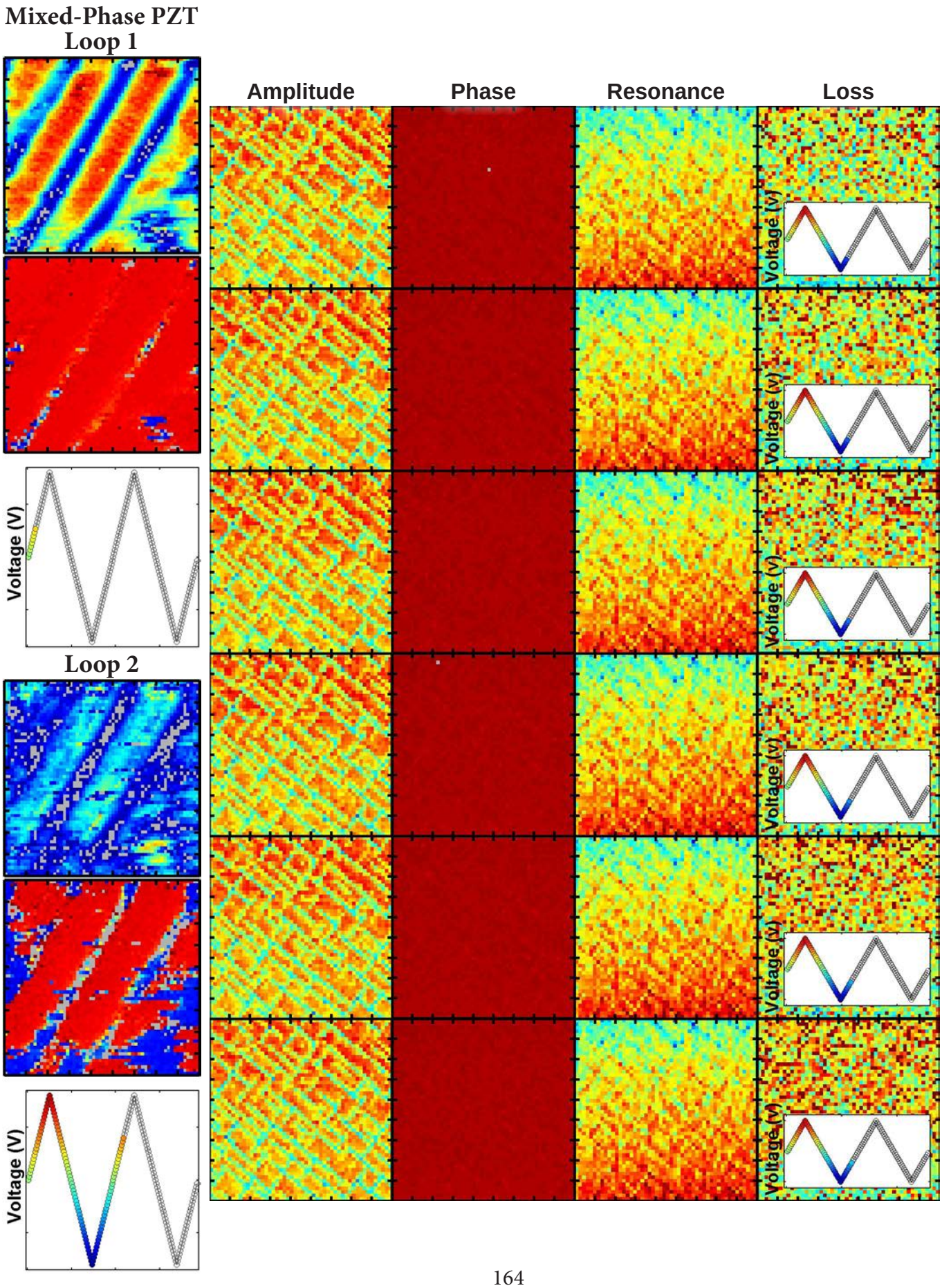
Mixed-Phase PZT
Loop 1
Amplitude
Phase
Resonance
Loss
Voltage (V)
Voltage (v)
Loop 2
Voltage (V)
Voltage (v)

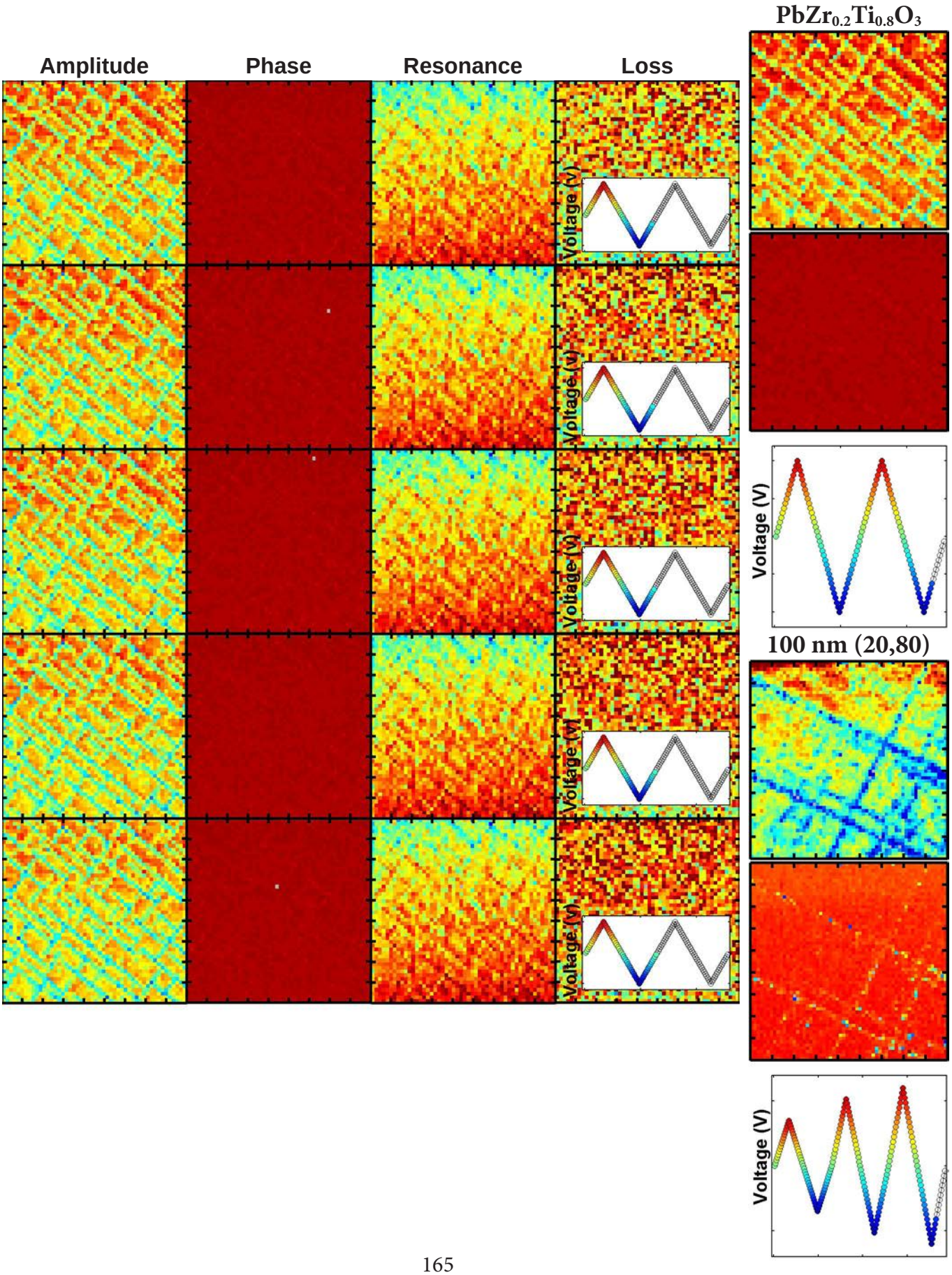
PbZr0.2Ti0.8O3
Amplitude
Phase
Resonance
Loss
Voltage (V)
Voltage (V)
Voltage (V)
Voltage (V)
Voltage (V)
Voltage (V)
100 nm (20,80)
Voltage (V)

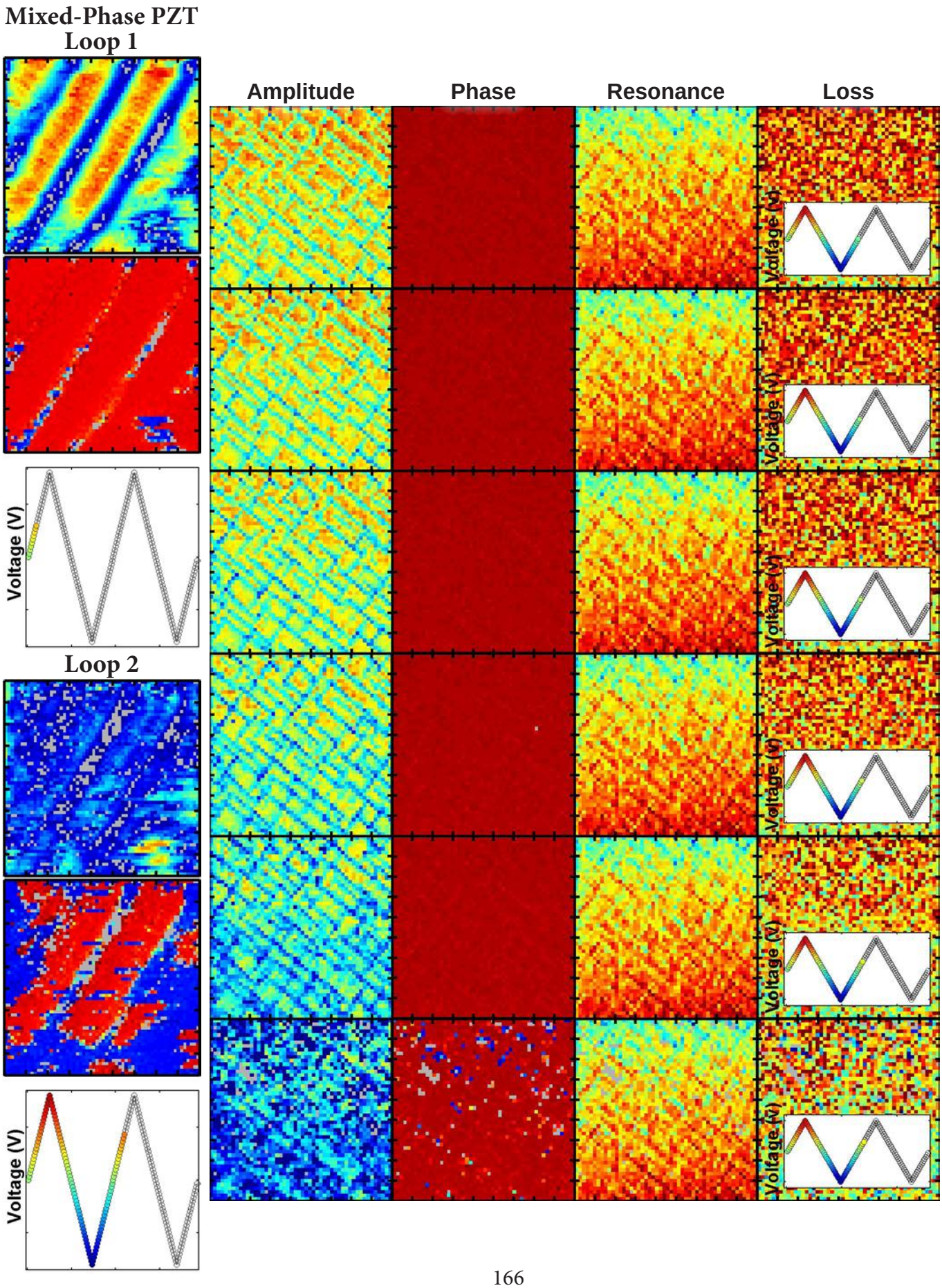
Mixed-Phase PZT
Loop 1
Amplitude
Phase
Resonance
Loss
Voltage (V)
Loop 2
Voltage (V)

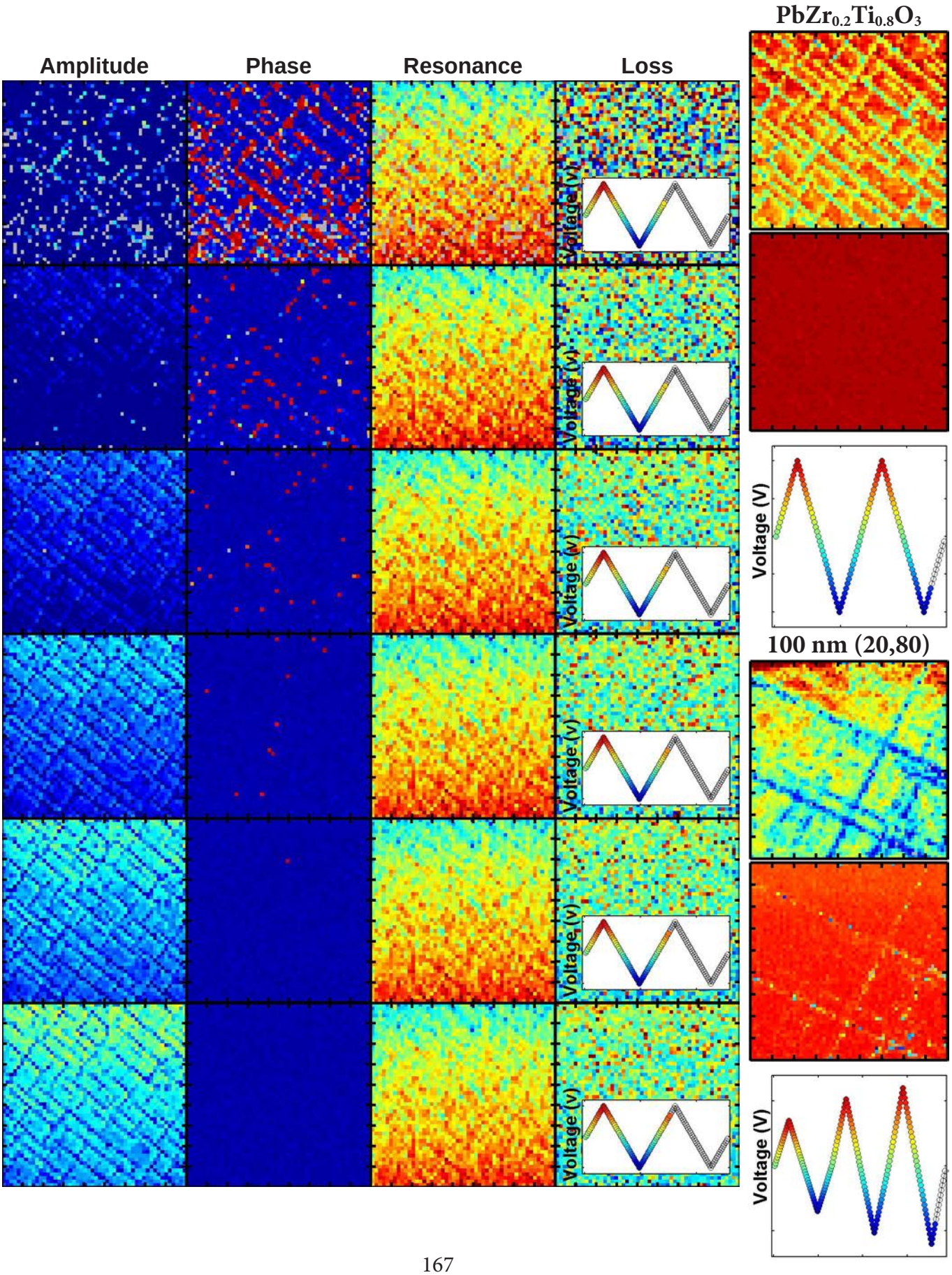
Amplitude
Phase
Resonance
Loss
Voltage (V)
PbZr0.2Ti0.8O3
Voltage (V)
100 nm (20,80)
Voltage (V)

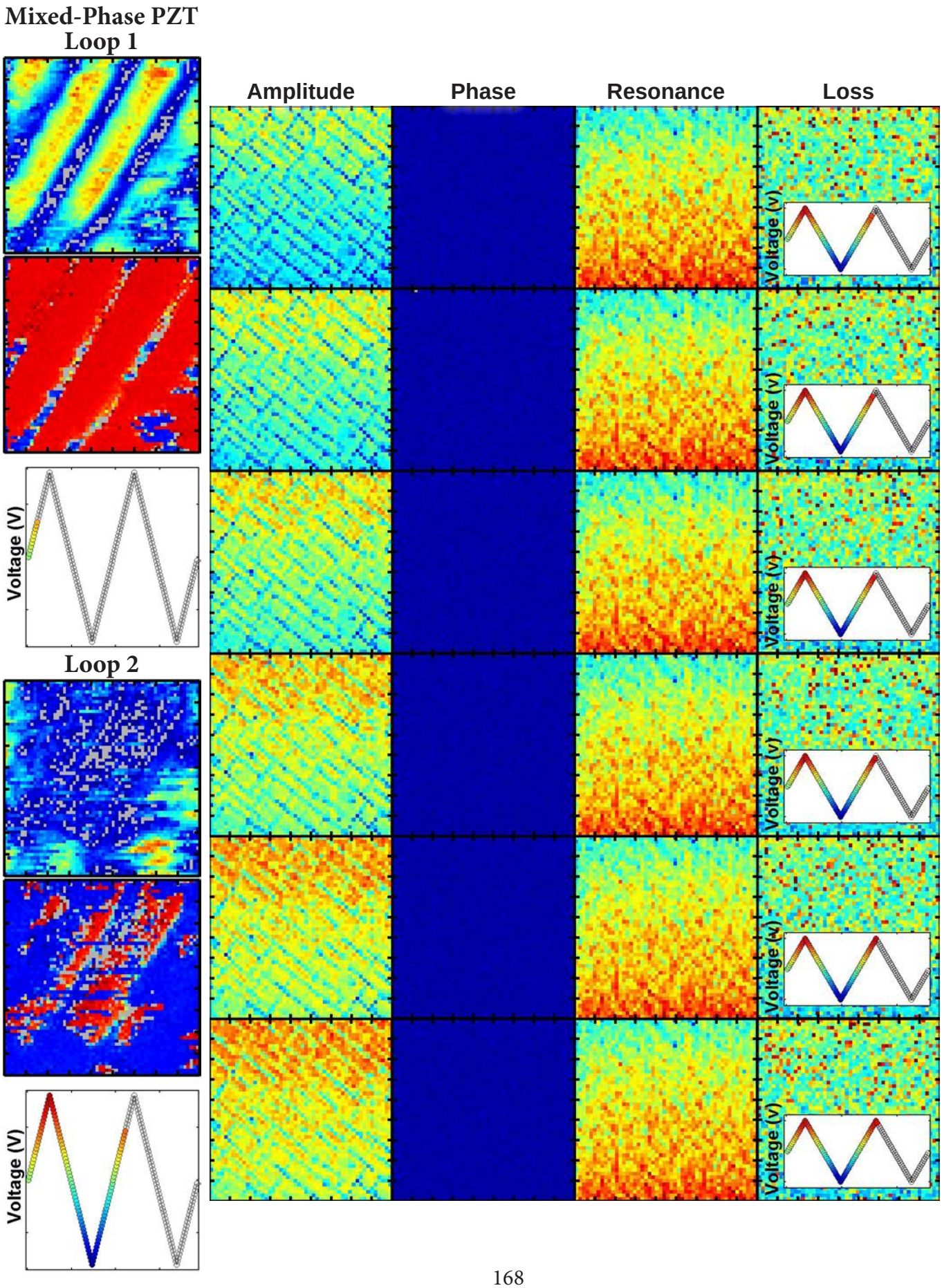
Mixed-Phase PZT
Loop 1
Amplitude
Phase
Resonance
Loss
Voltage (V)
Voltage (v)
Loop 2
Voltage (V)
Voltage (v)

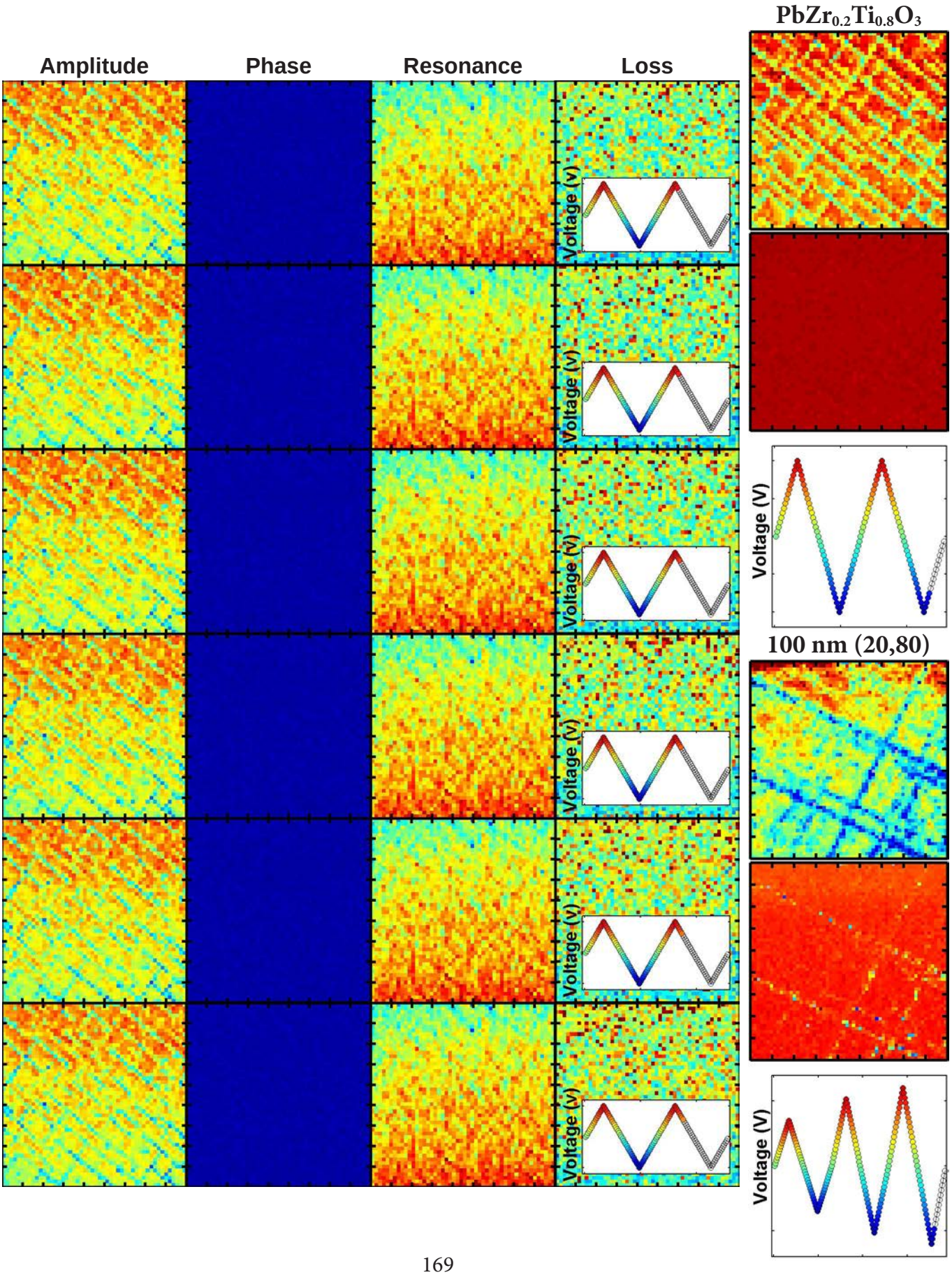
Amplitude
Phase
Resonance
Loss
Voltage (v)
PbZr0.2Ti0.8O3
Voltage (V)
100 nm (20,80)

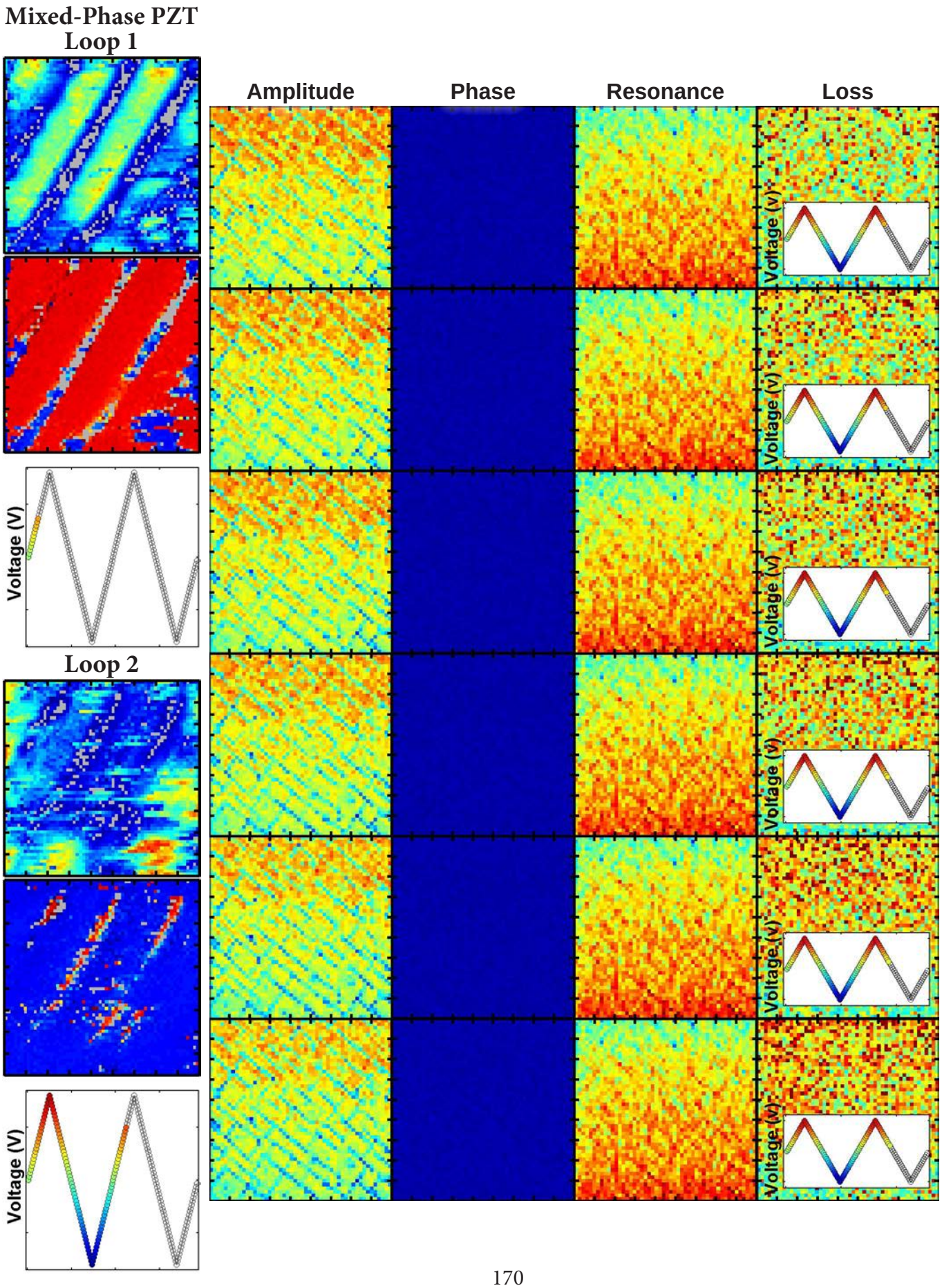
Mixed-Phase PZT
Loop 1
Amplitude
Phase
Resonance
Loss
Voltage (V)
Voltage (v)
Loop 2
Voltage (V)
Voltage (v)

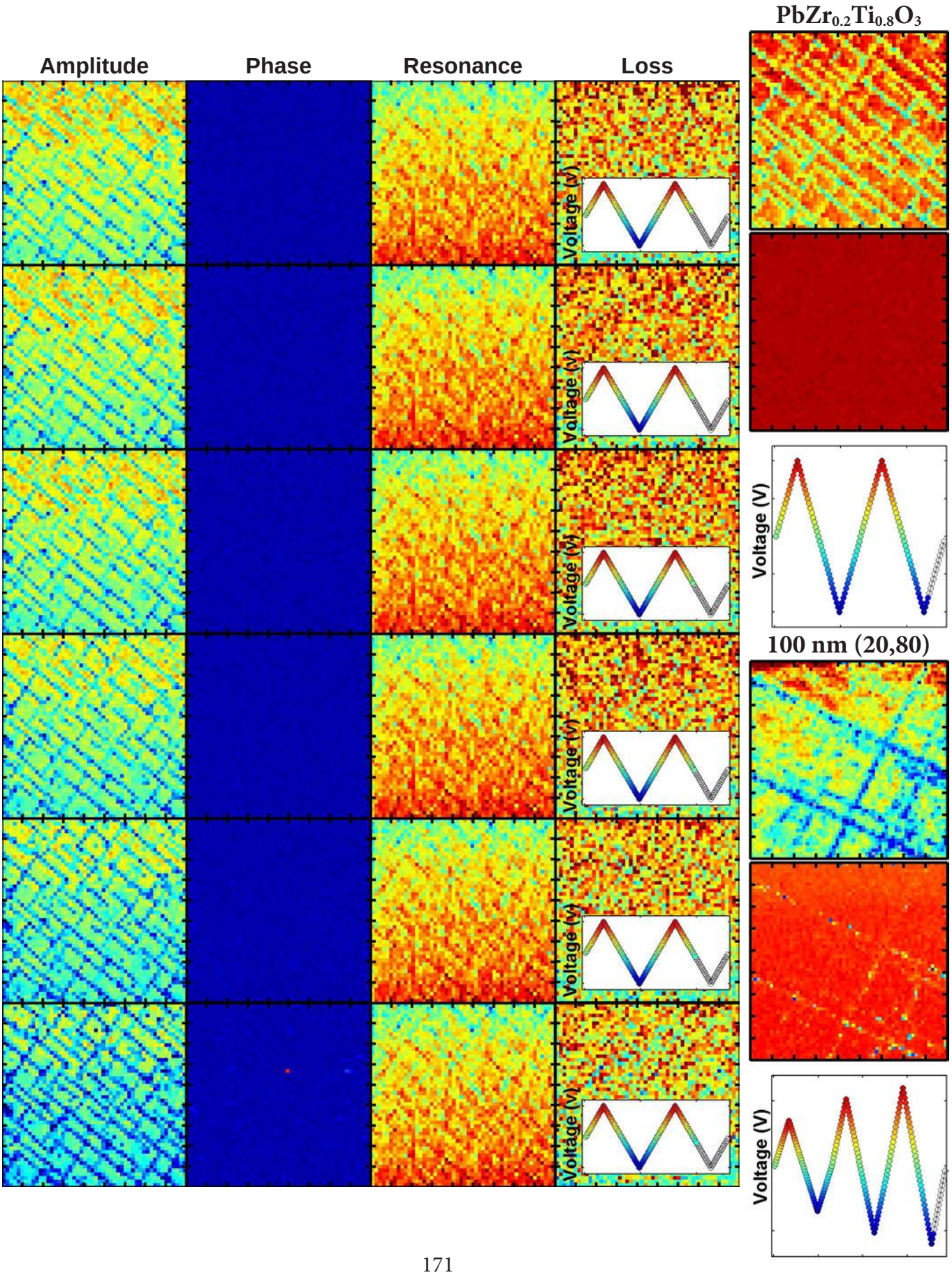
Amplitude
Phase
Resonance
Loss
Voltage (V)
PbZr0.2Ti0.8O3
100 nm (20,80)

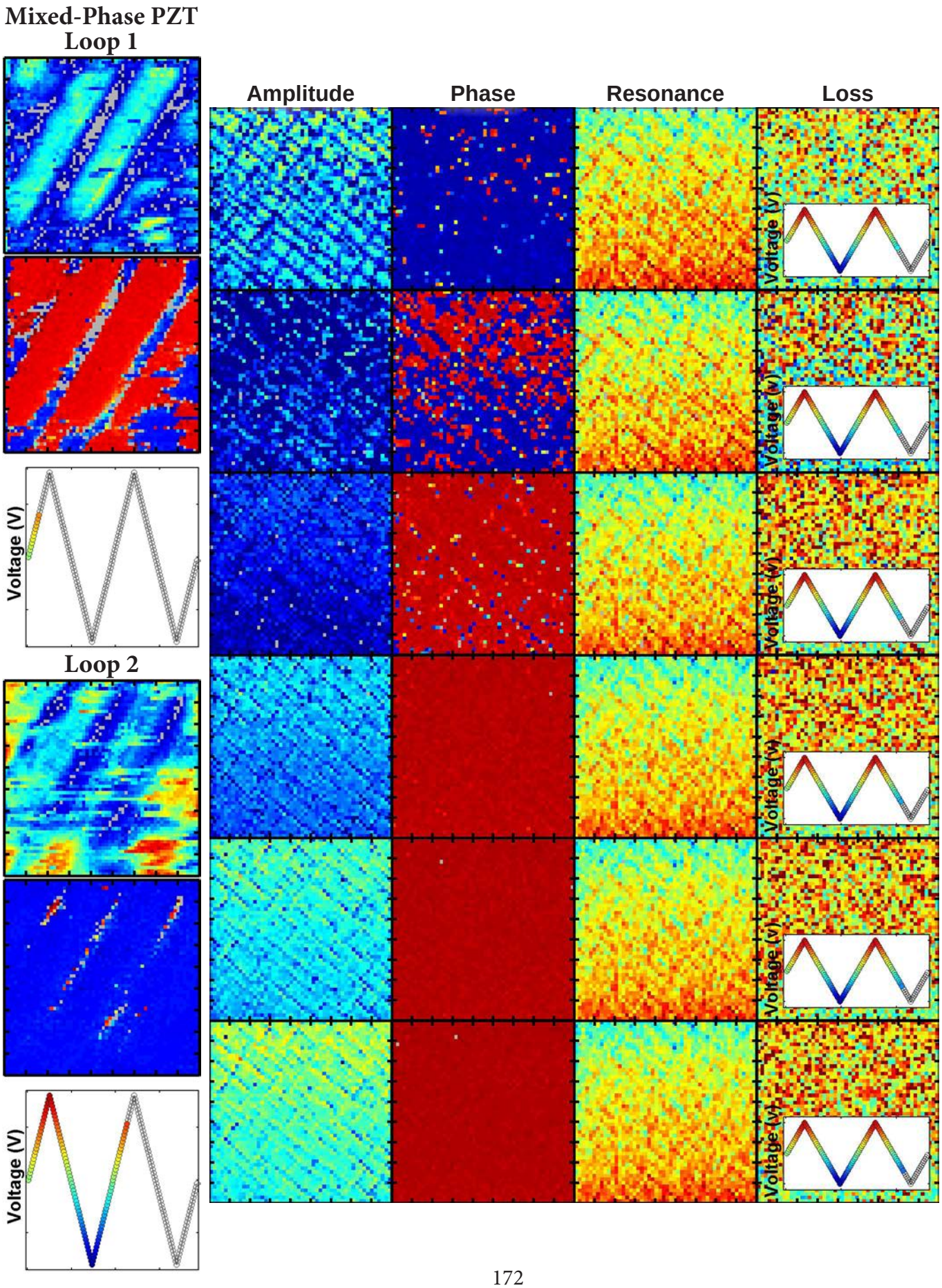
Mixed-Phase PZT
Loop 1
Amplitude
Phase
Resonance
Loss
Voltage (V)
Loop 2
Voltage (V)

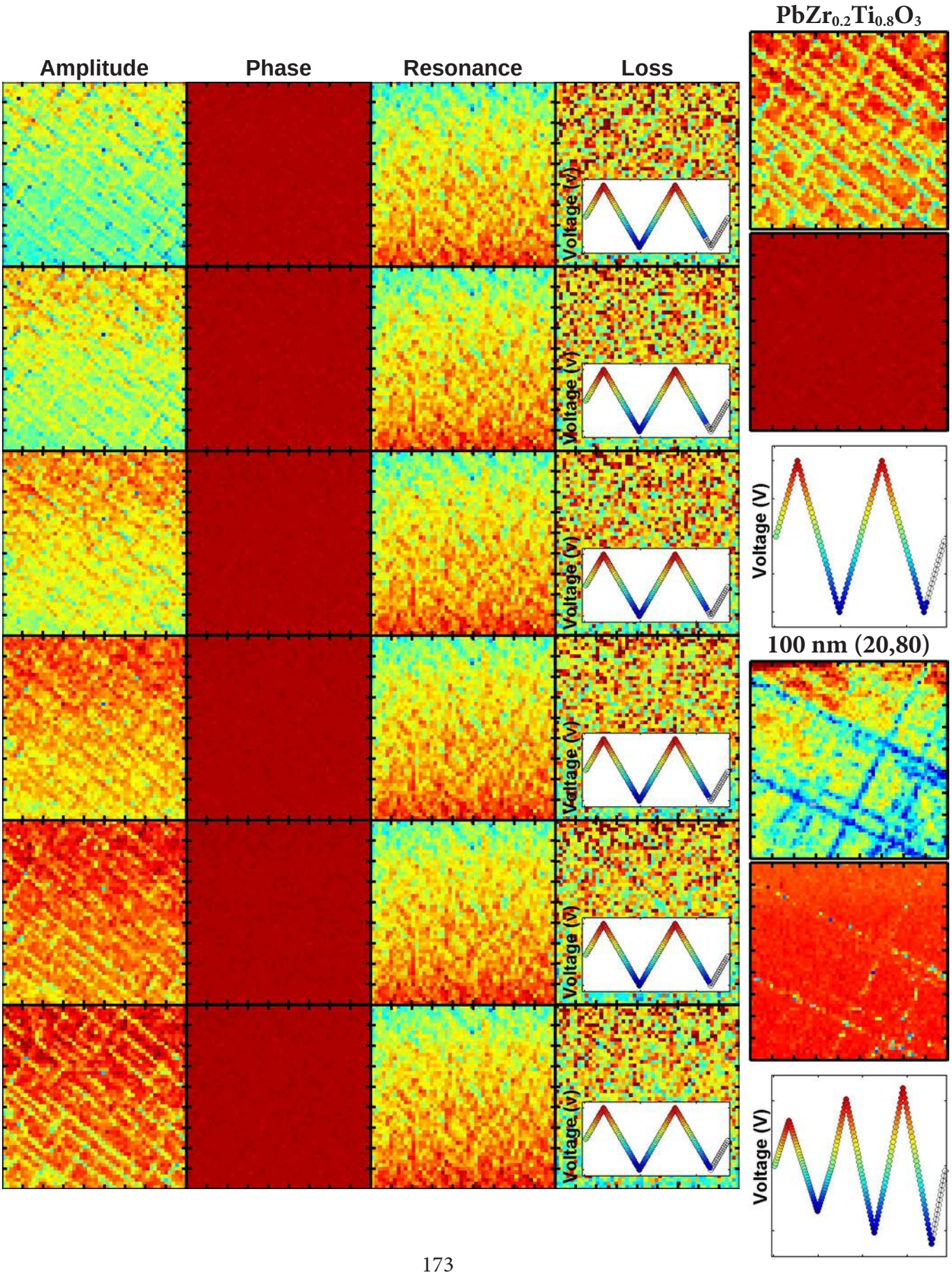
Amplitude
Phase
Resonance
Loss
Voltage (V)
PbZr0.2Ti0.8O3
100 nm (20,80)

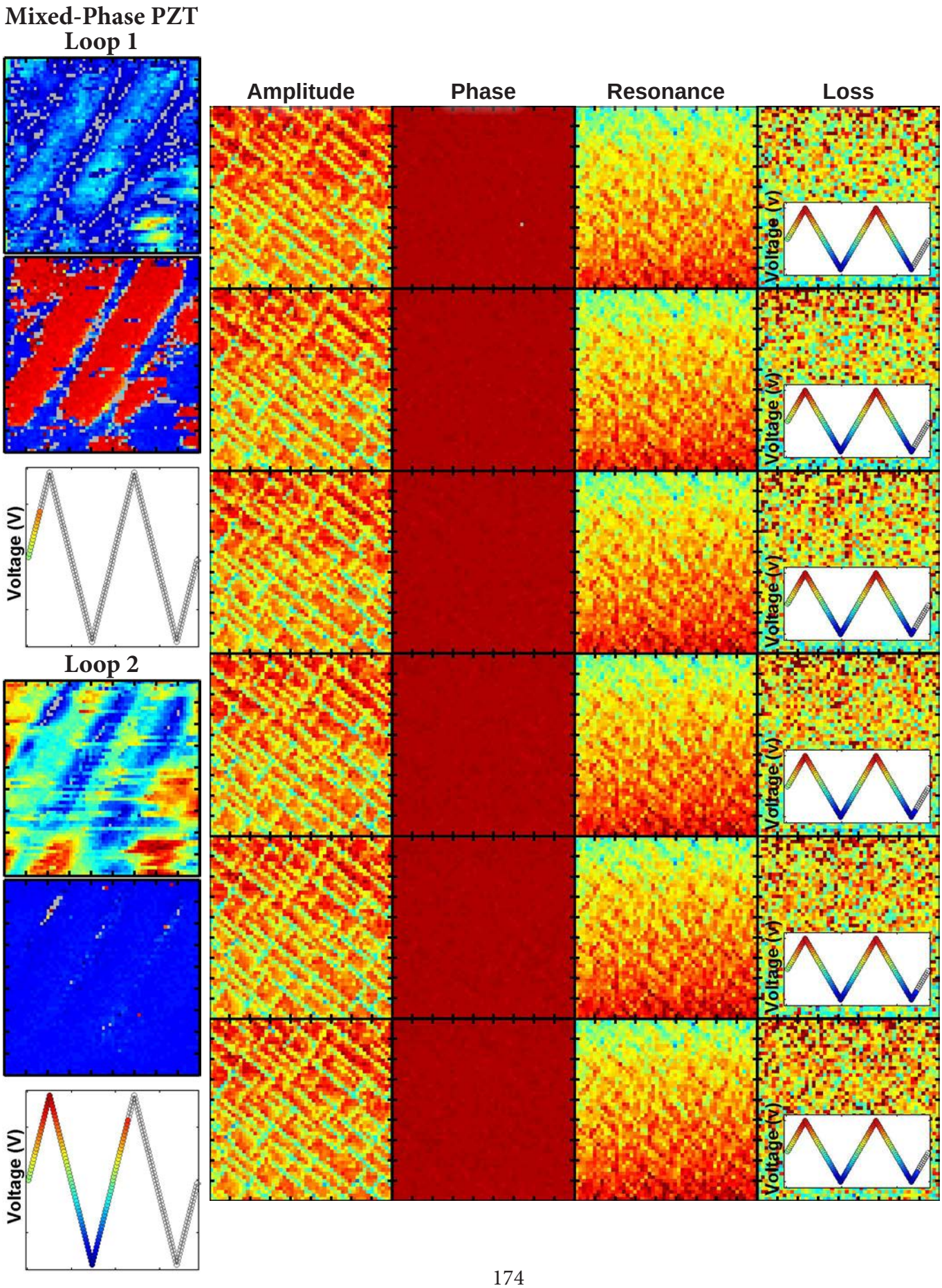
Mixed-Phase PZT
Loop 1
Amplitude
Phase
Resonance
Loss
Voltage (V)
Loop 2
Voltage (V)
Voltage (v)

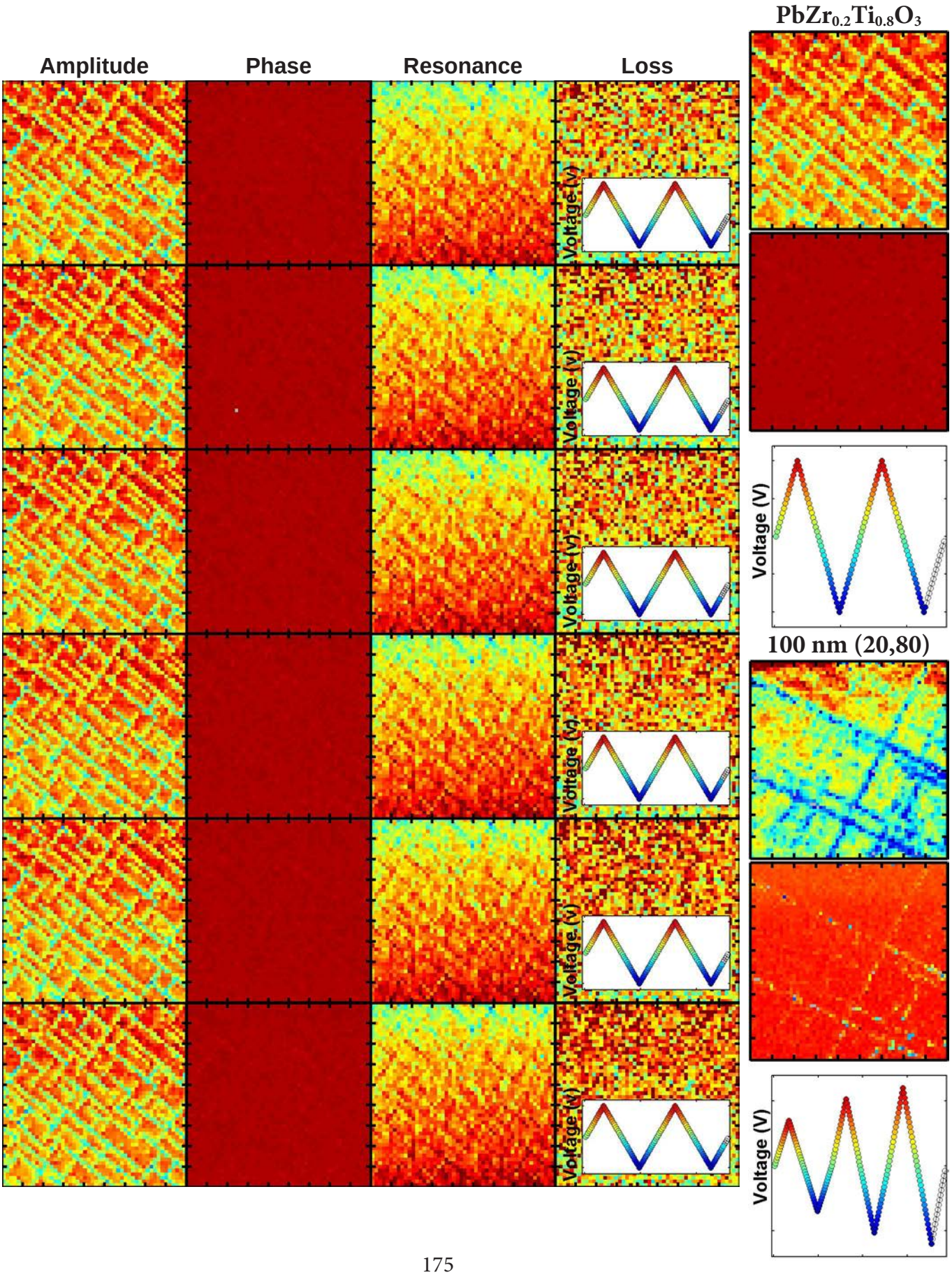
PbZr0.2Ti0.8O3
Amplitude
Phase
Resonance
Loss
Voltage (V)
Voltage (V)
Voltage (V)
Voltage (V)
Voltage (V)
Voltage (V)
Voltage (V)
100 nm (20,80)
Voltage (V)

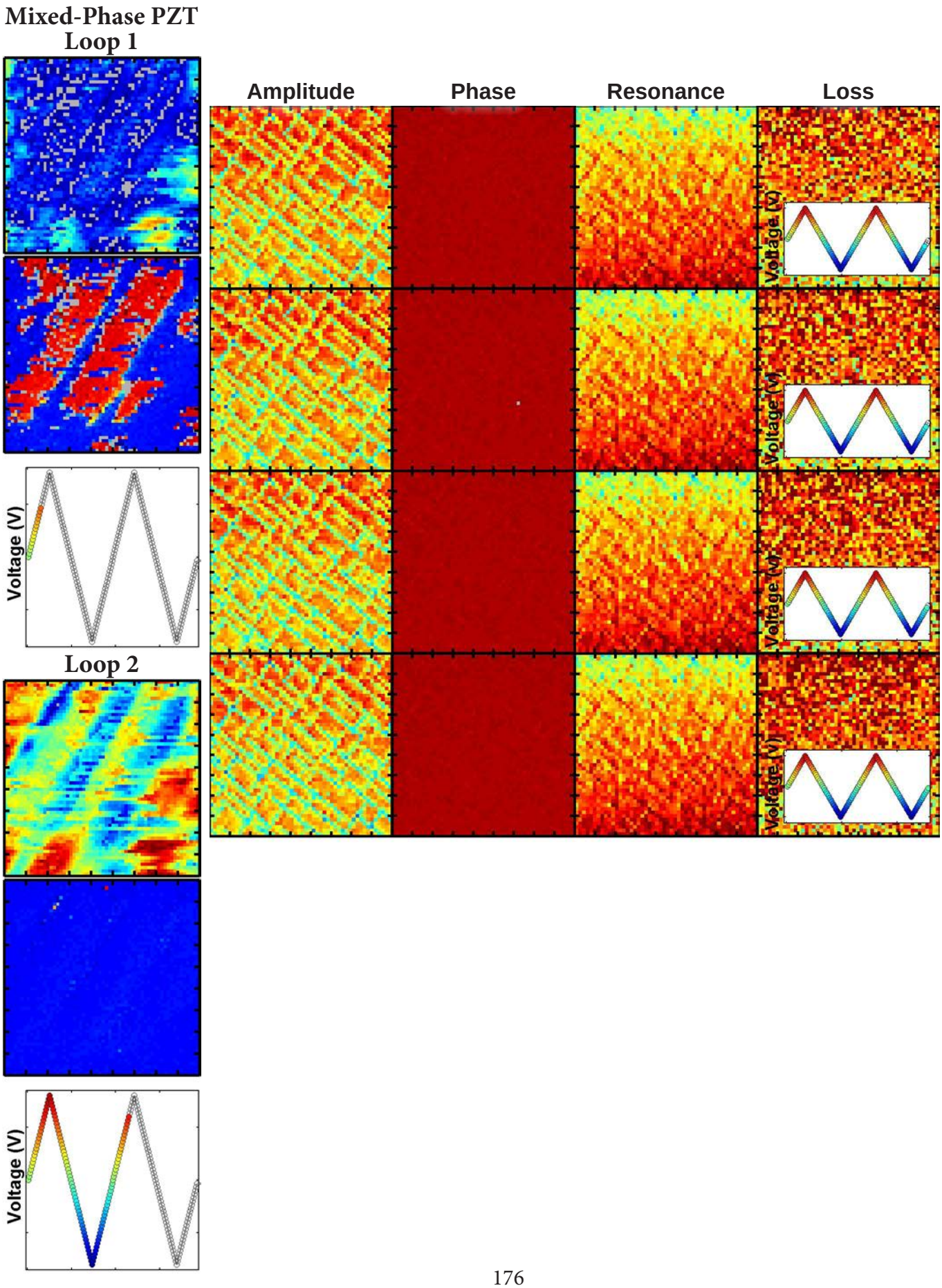
Mixed-Phase PZT
Loop 1
Amplitude
Phase
Resonance
Loss
Voltage (V)
Loop 2
Voltage (V)

Appendix E

Additional Images of Band-Excitation Switching Spectroscopy of Compositionally-Graded (20,80) Heterostructures

Included in this section is a subset of the BE-SS (amplitude, phase, loss, and resonance frequency) images of compositionally-graded (20,80) heterostructures. Note that the scan size in all images is 1.75 μm.

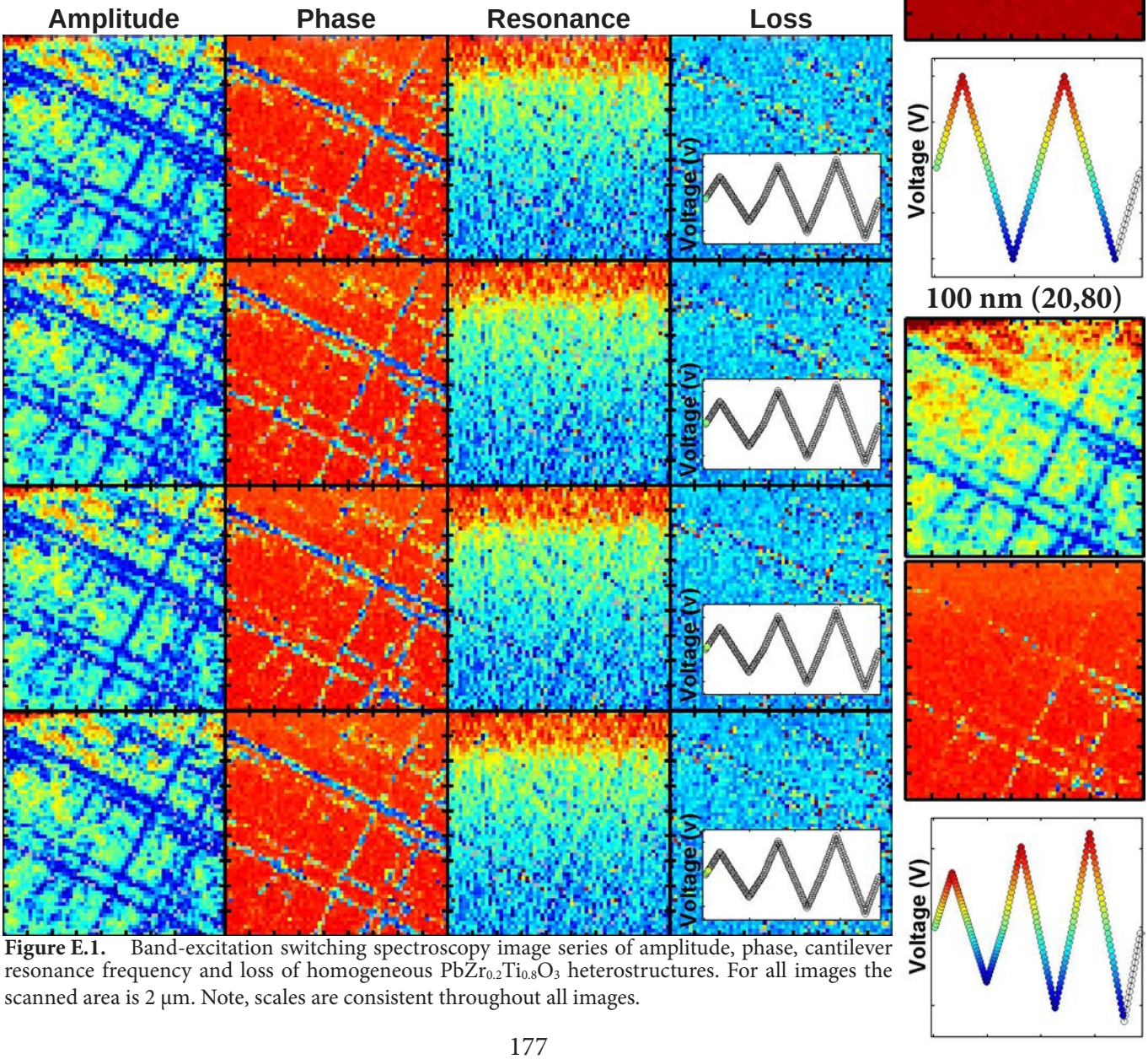

Figure E.1. Band-excitation switching spectroscopy image series of amplitude, phase, cantilever resonance frequency and loss of homogeneous $PbZr_{0.2}Ti_{0.8}O_3$ heterostructures. For all images the scanned area is 2 μm. Note, scales are consistent throughout all images.

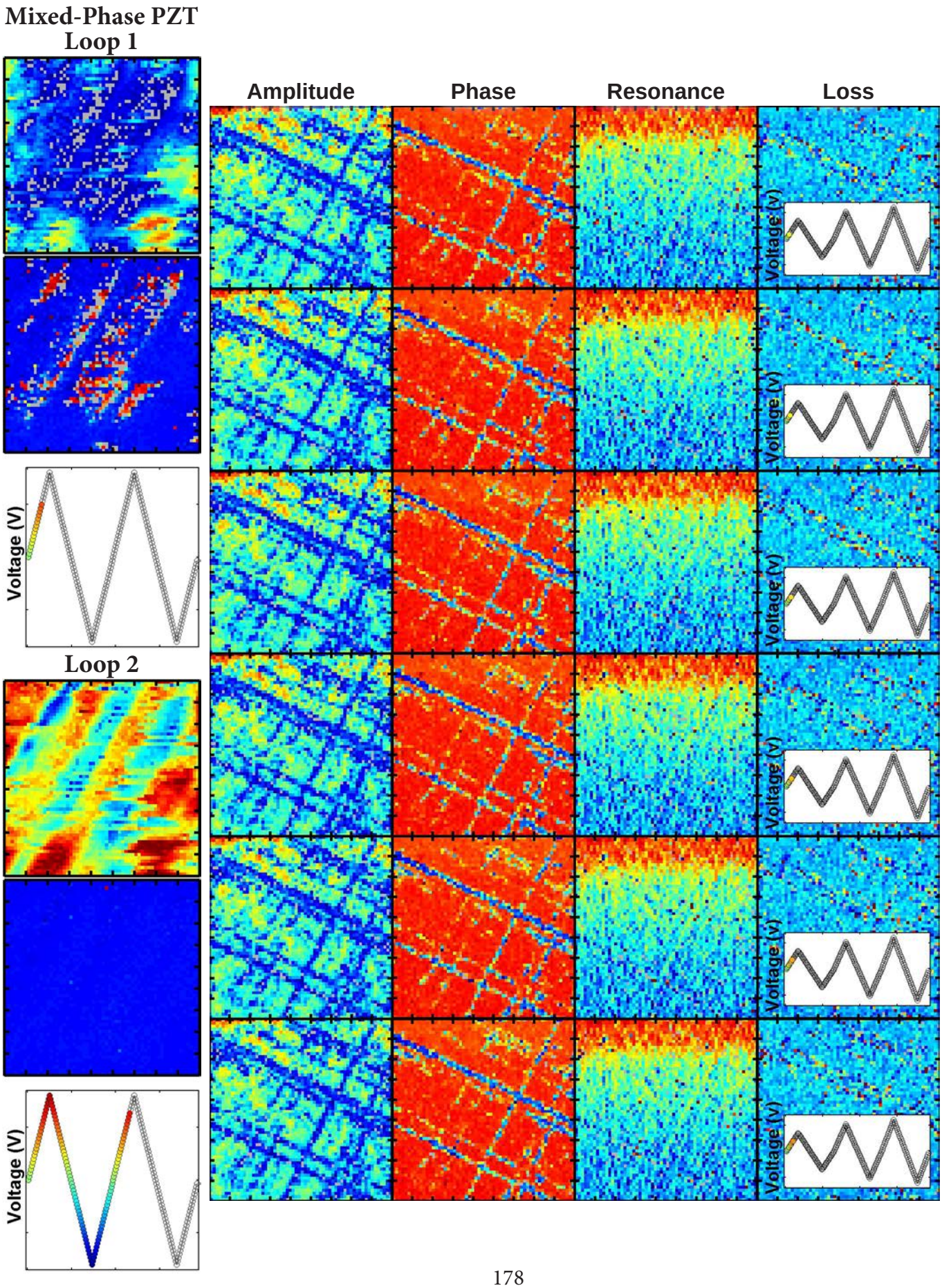
Mixed-Phase PZT
Loop 1
Amplitude
Phase
Resonance
Loss
Voltage (V)
Loop 2
Voltage (V)
Voltage (v)

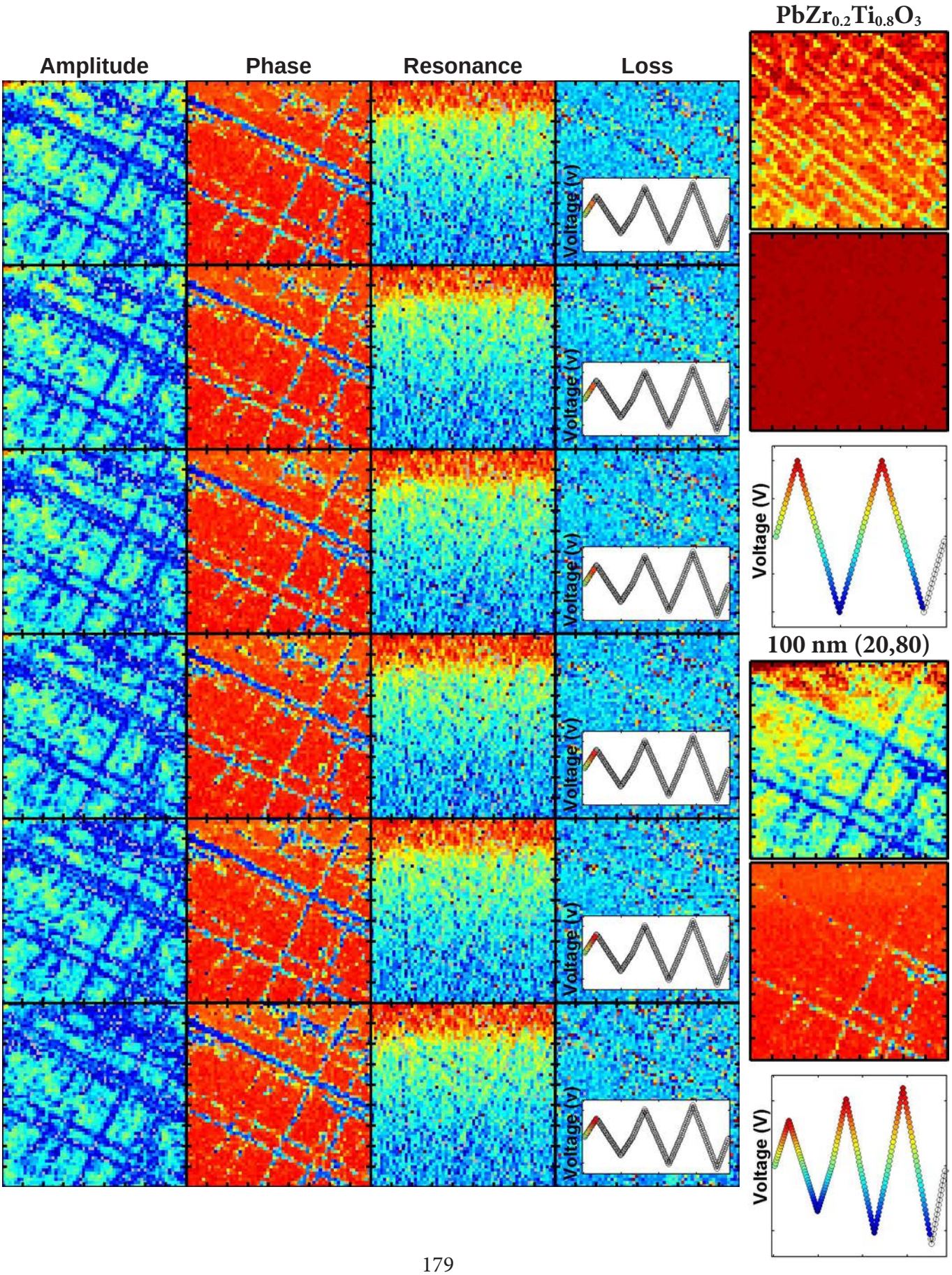
Amplitude
Phase
Resonance
Loss
Voltage (v)
PbZr0.2Ti0.8O3
Voltage (V)
100 nm (20,80)

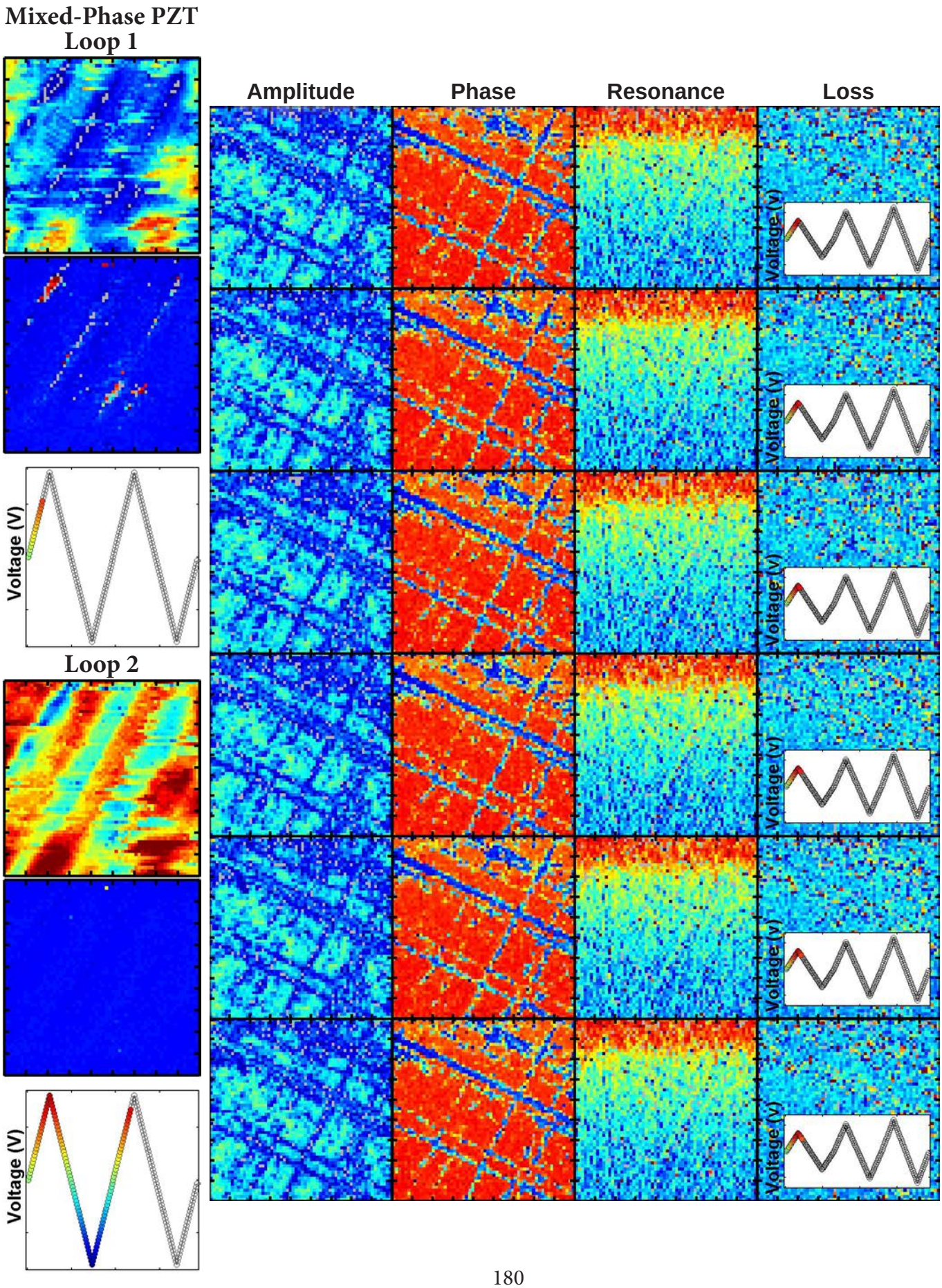
Mixed-Phase PZT
Loop 1
Amplitude
Phase
Resonance
Loss
Voltage (V)
Loop 2
Voltage (V)
Voltage (v)

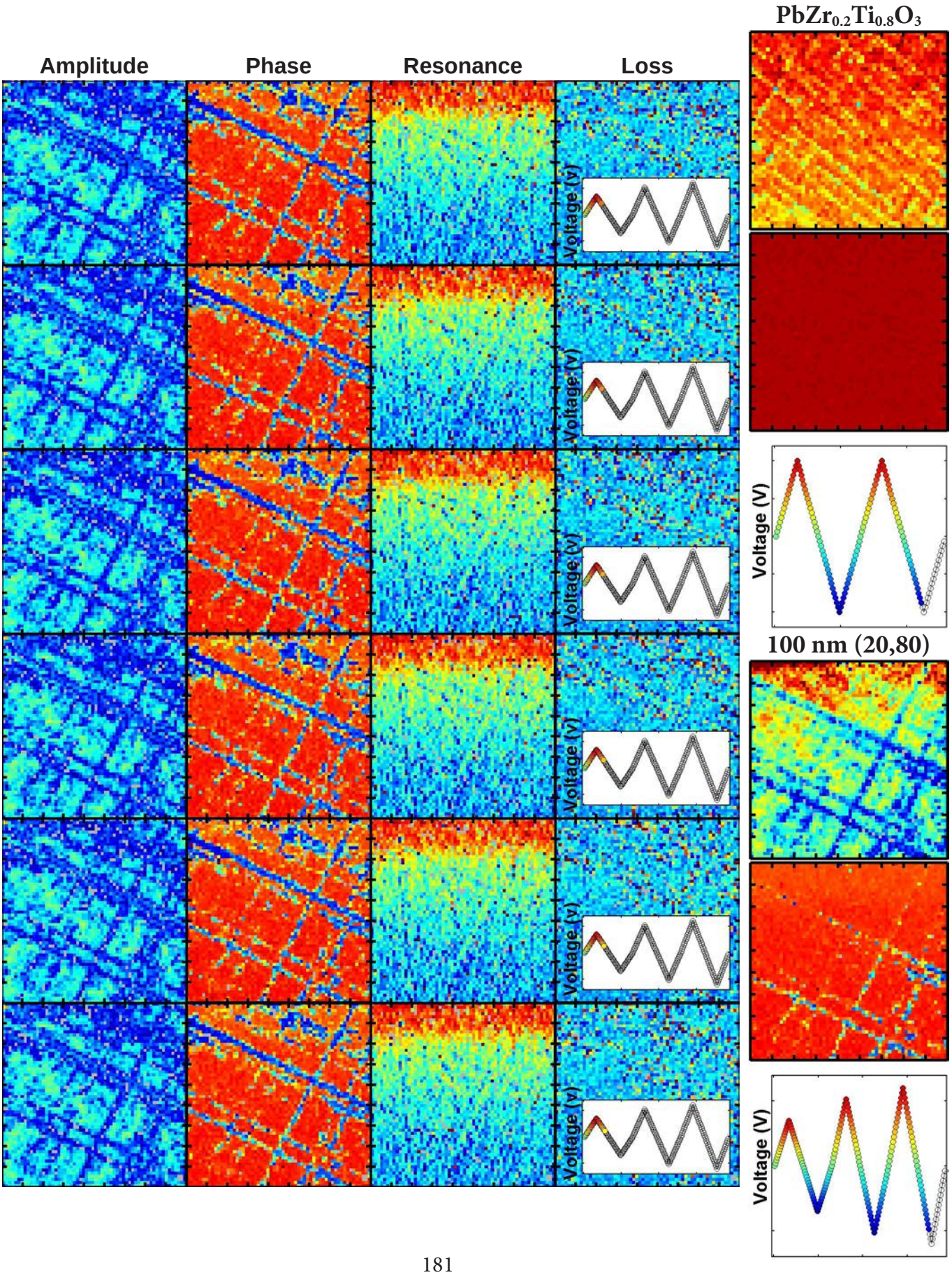
PbZr0.2Ti0.8O3
Amplitude
Phase
Resonance
Loss
Voltage (V)
Voltage (V)
Voltage (V)
Voltage (V)
Voltage (V)
Voltage (V)
Voltage (V)
100 nm (20,80)

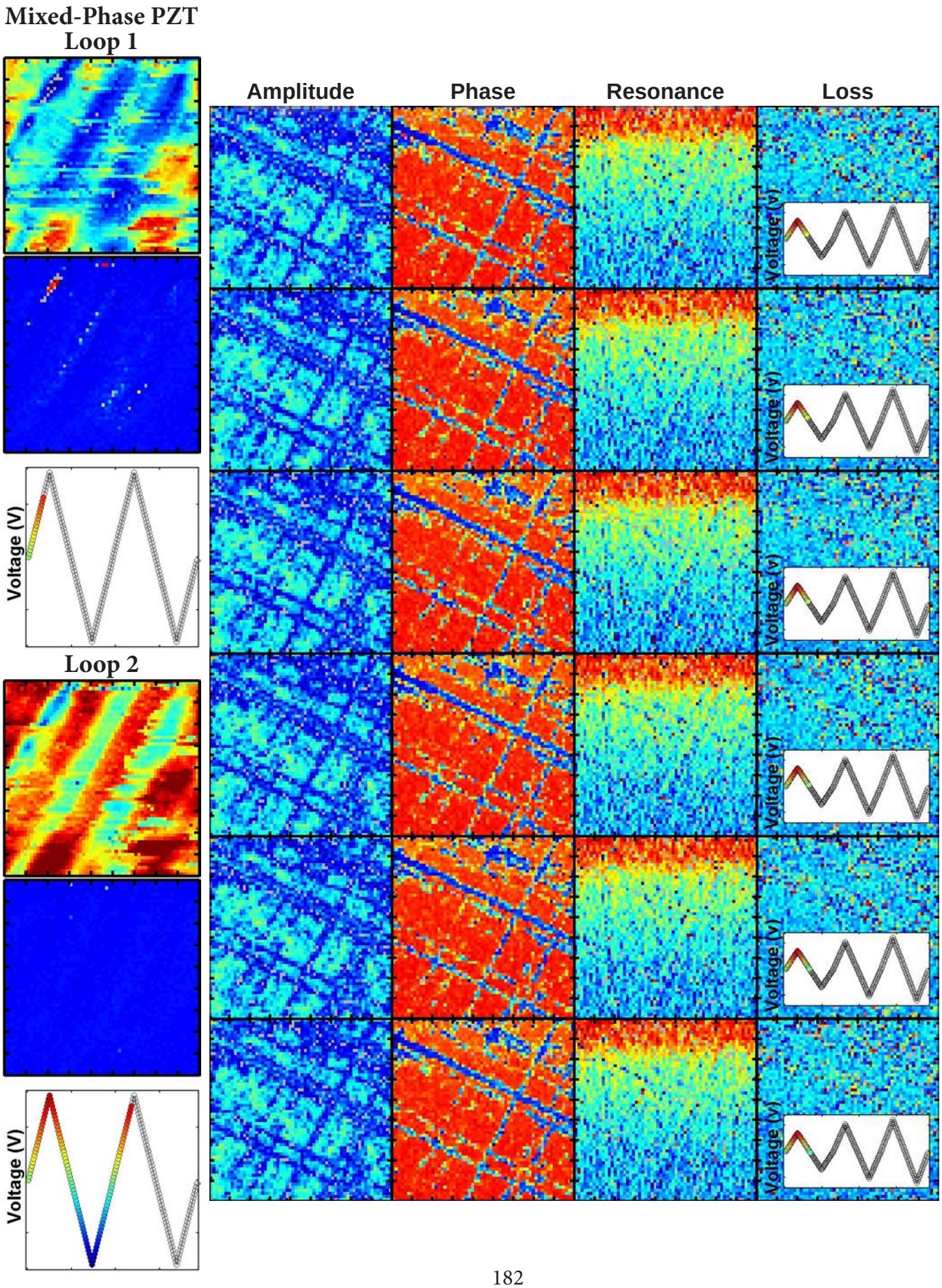
Mixed-Phase PZT
Loop 1
Amplitude
Phase
Resonance
Loss
Voltage (V)
Loop 2
Voltage (V)
Voltage (v)

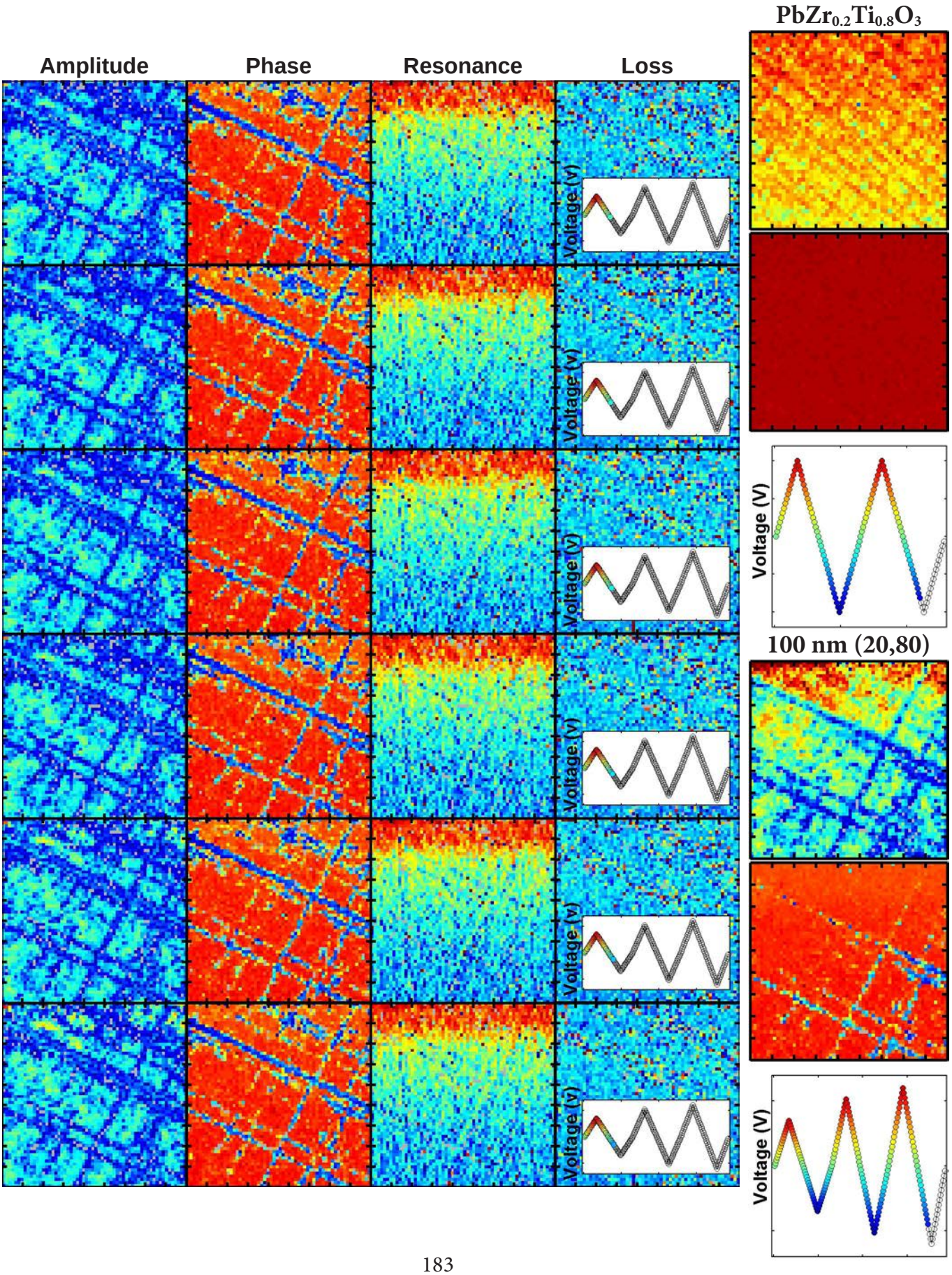
Amplitude
Phase
Resonance
Loss
Voltage (V)
PbZr0.2Ti0.8O3
Voltage (V)
100 nm (20,80)
Voltage (V)

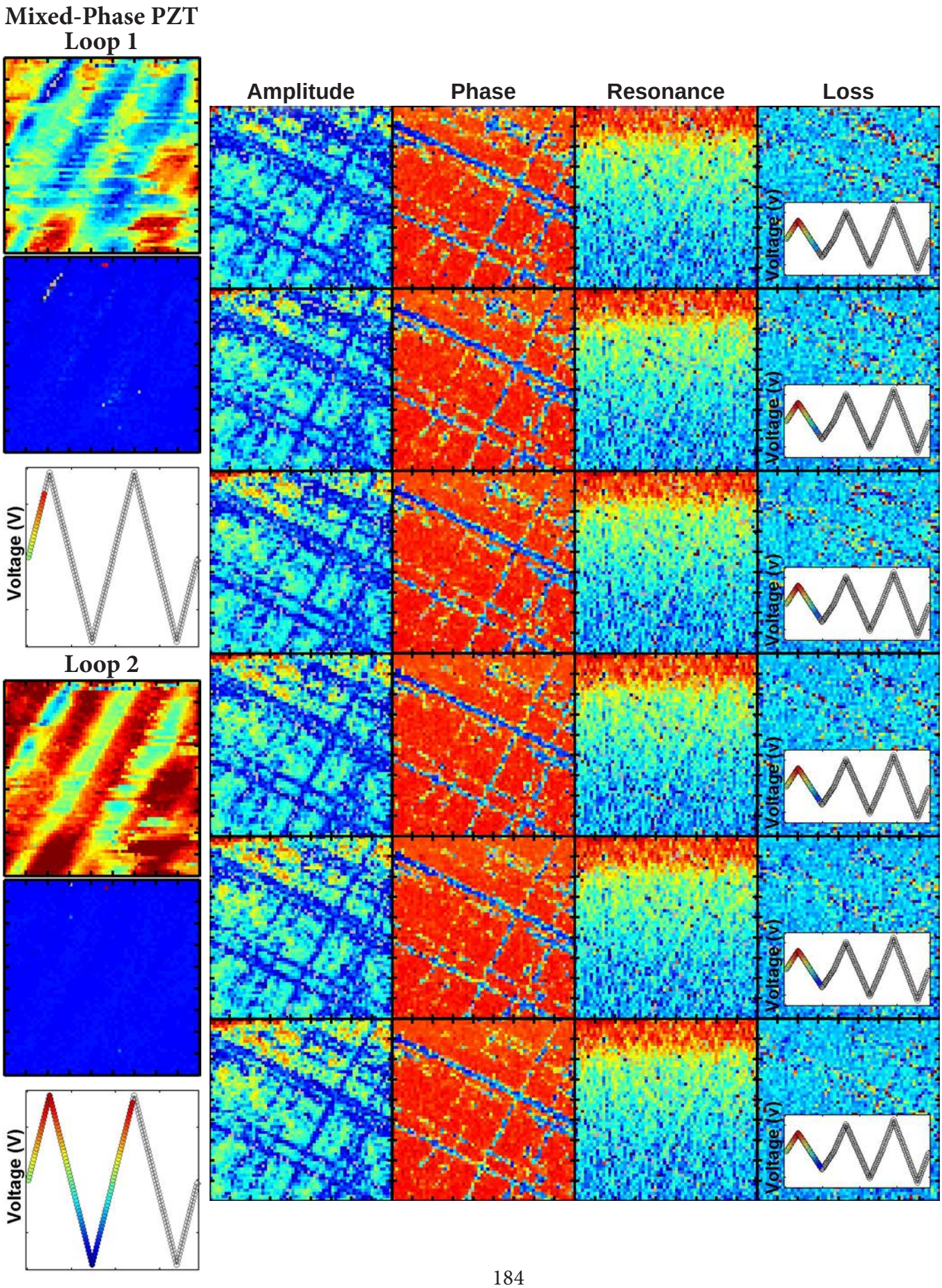
Mixed-Phase PZT
Loop 1
Amplitude
Phase
Resonance
Loss
Voltage (V)
Loop 2
Voltage (V)
Voltage (v)

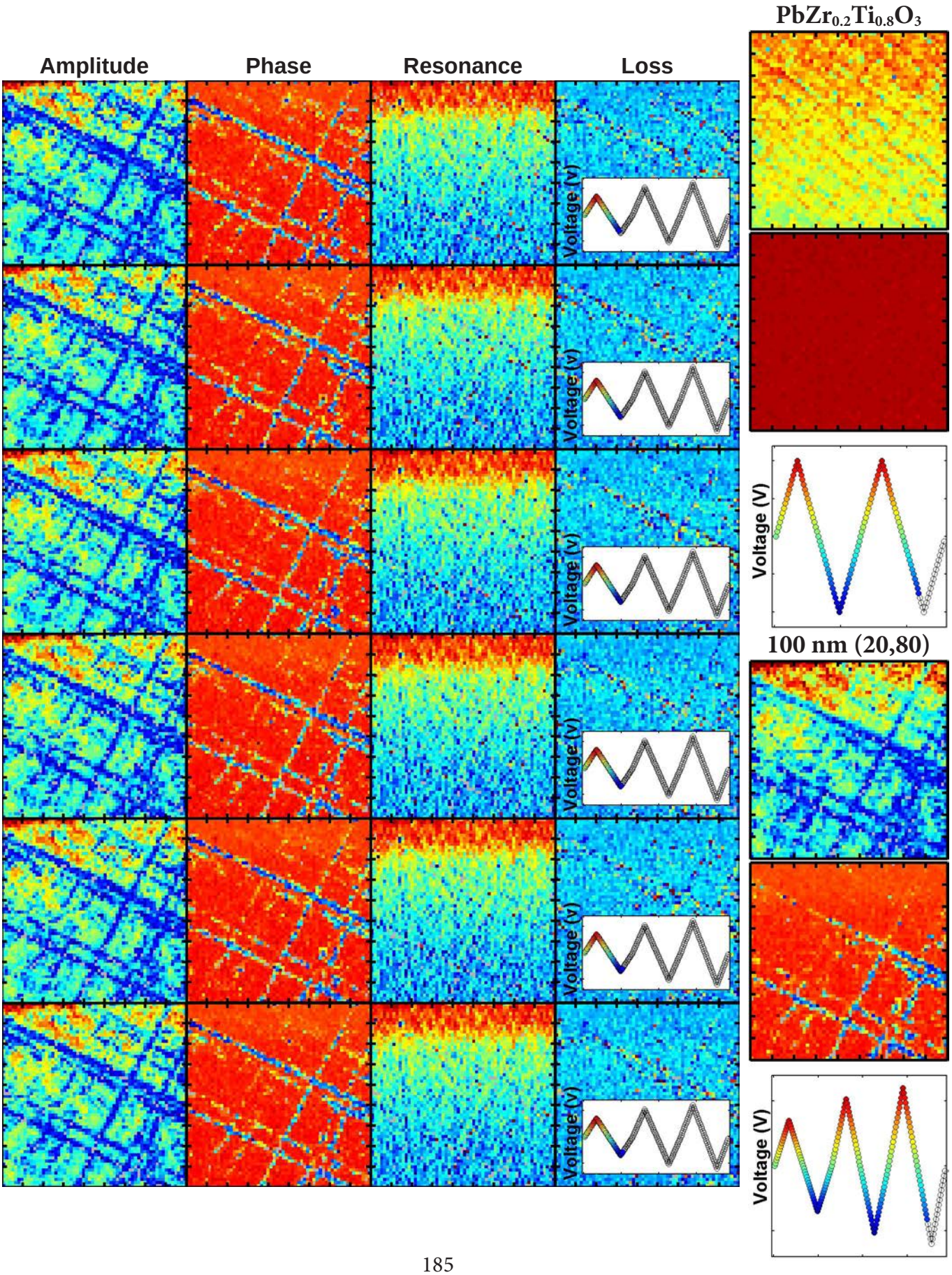
Amplitude
Phase
Resonance
Loss
Voltage (V)
PbZr0.2Ti0.8O3
Voltage (V)
100 nm (20,80)
Voltage (V)

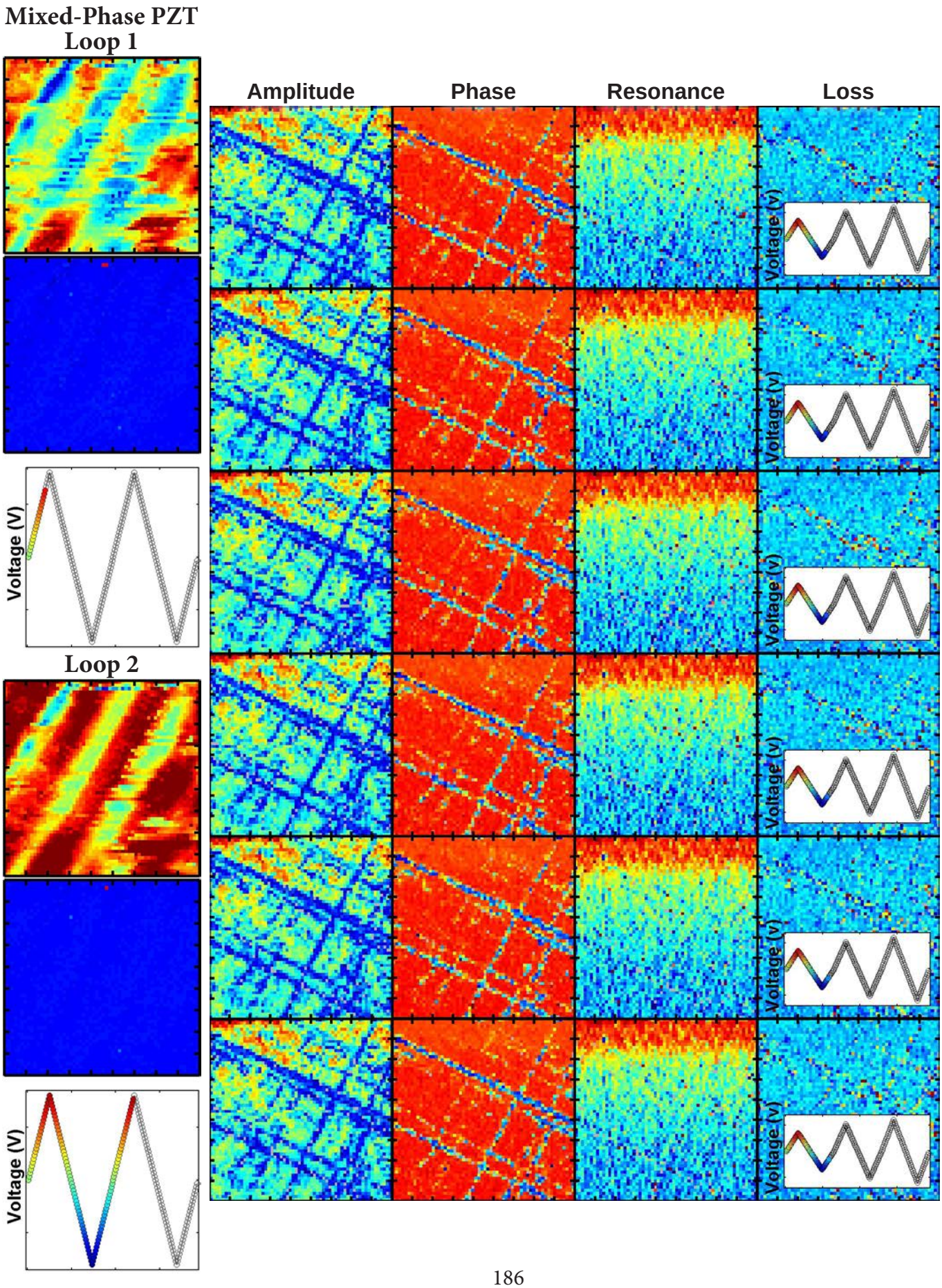
Mixed-Phase PZT
Loop 1
Amplitude
Phase
Resonance
Loss
Voltage (V)
Voltage (v)
Loop 2
Voltage (V)
Voltage (v)

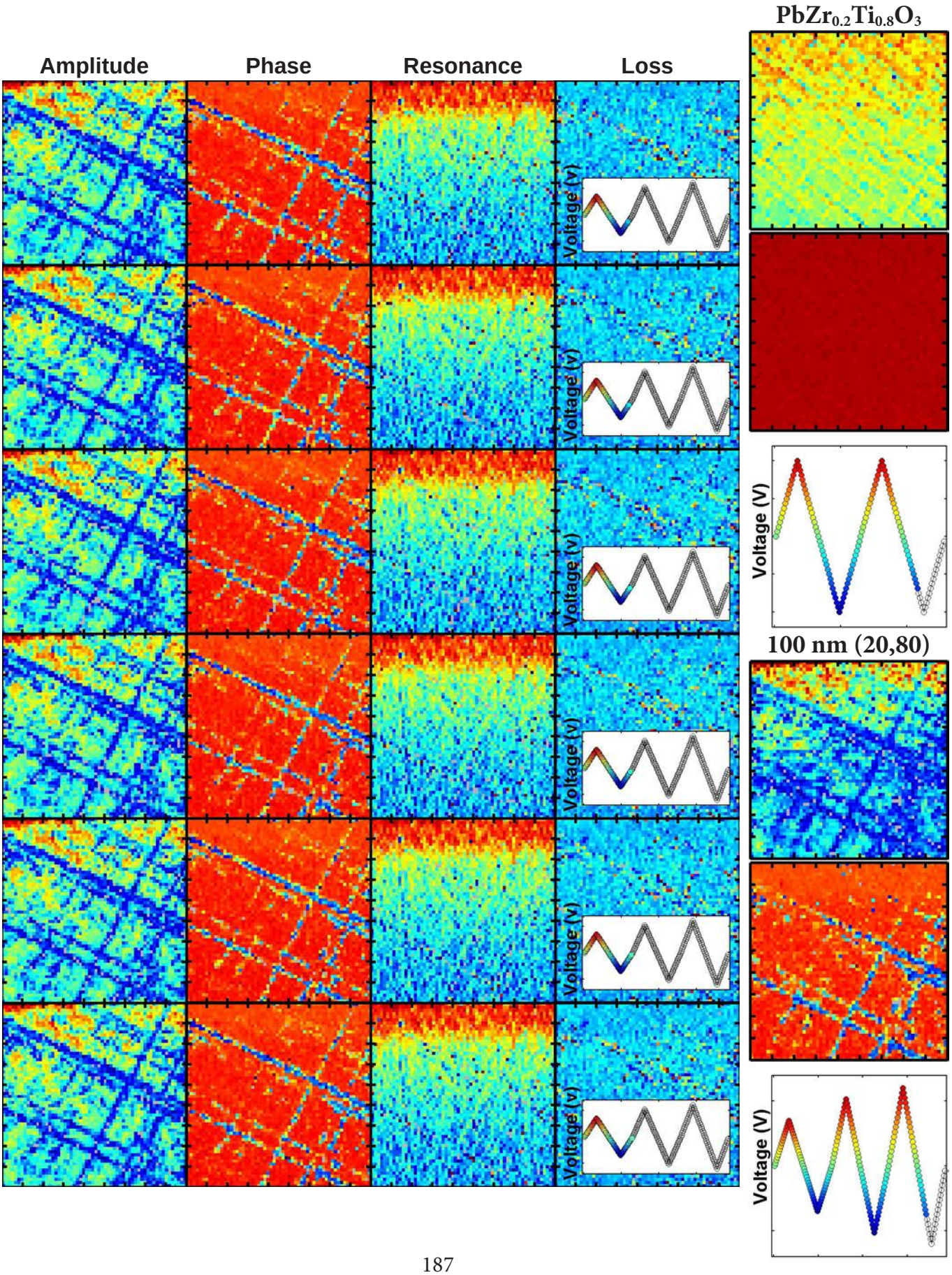
Amplitude
Phase
Resonance
Loss
Voltage (v)
PbZr0.2Ti0.8O3
Voltage (V)
100 nm (20,80)

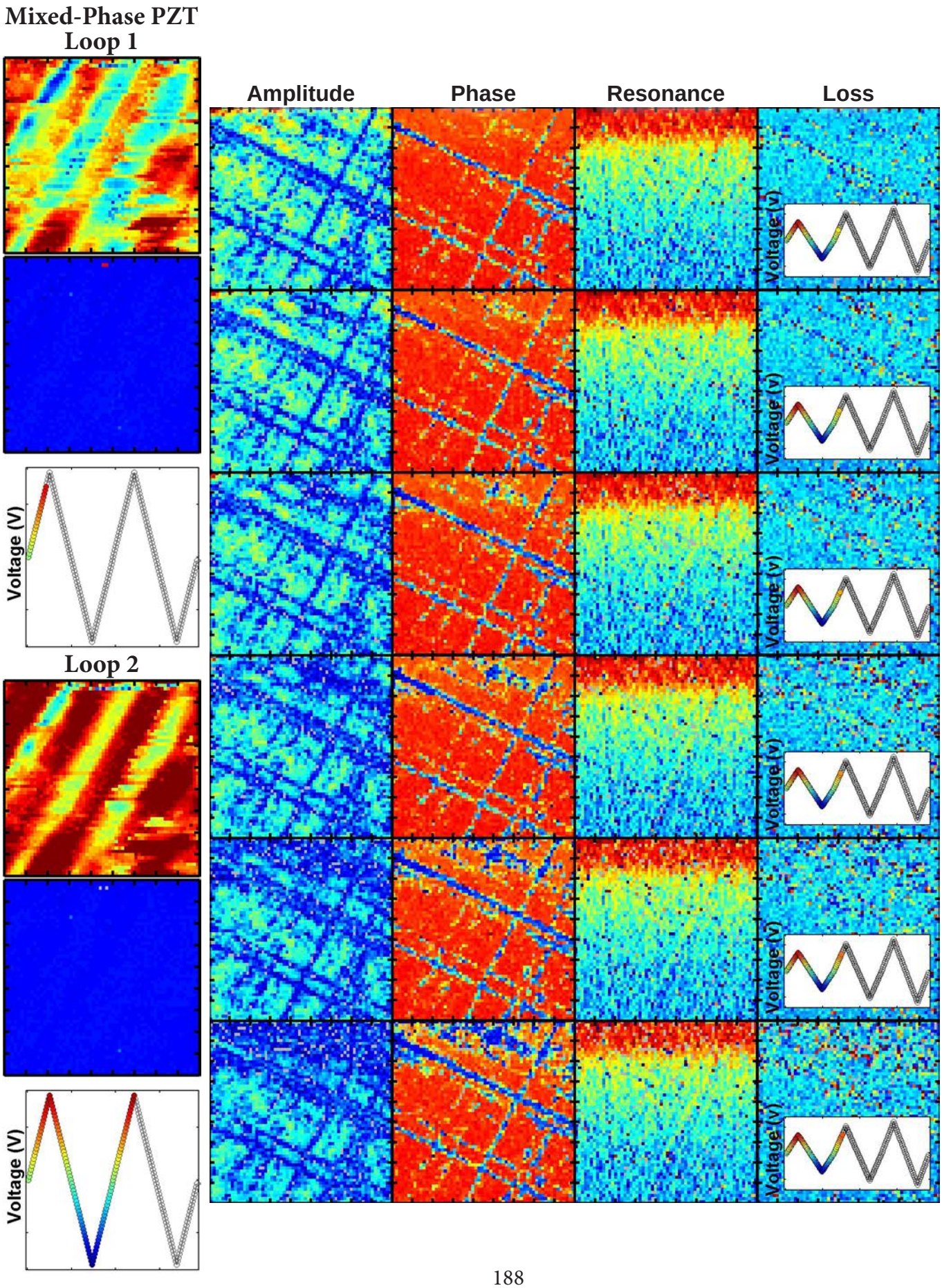
Mixed-Phase PZT
Loop 1
Amplitude
Phase
Resonance
Loss
Voltage (V)
Voltage (v)
Loop 2

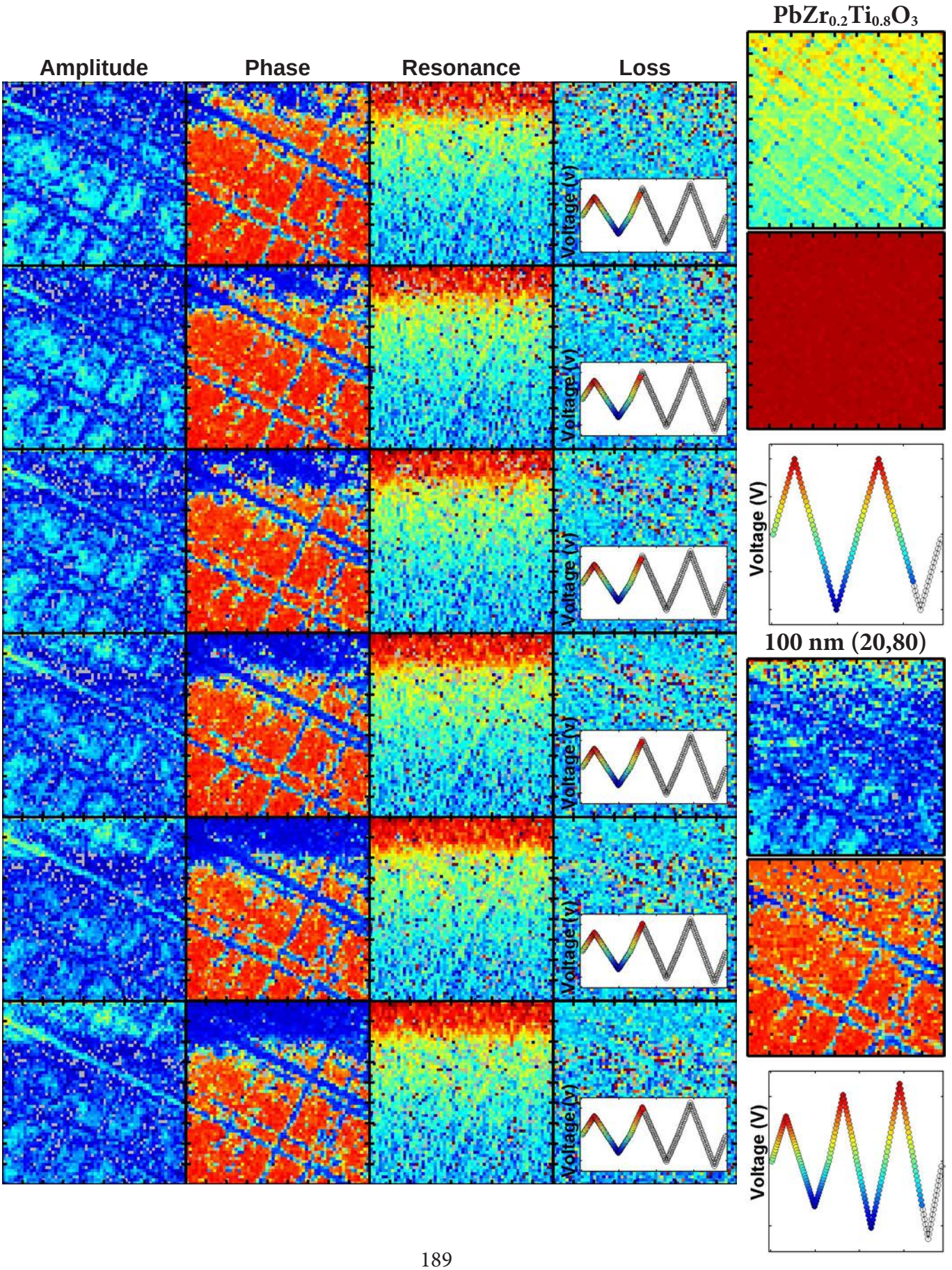
Amplitude
Phase
Resonance
Loss
Voltage (v)
PbZr0.2Ti0.8O3
Voltage (V)
100 nm (20,80)

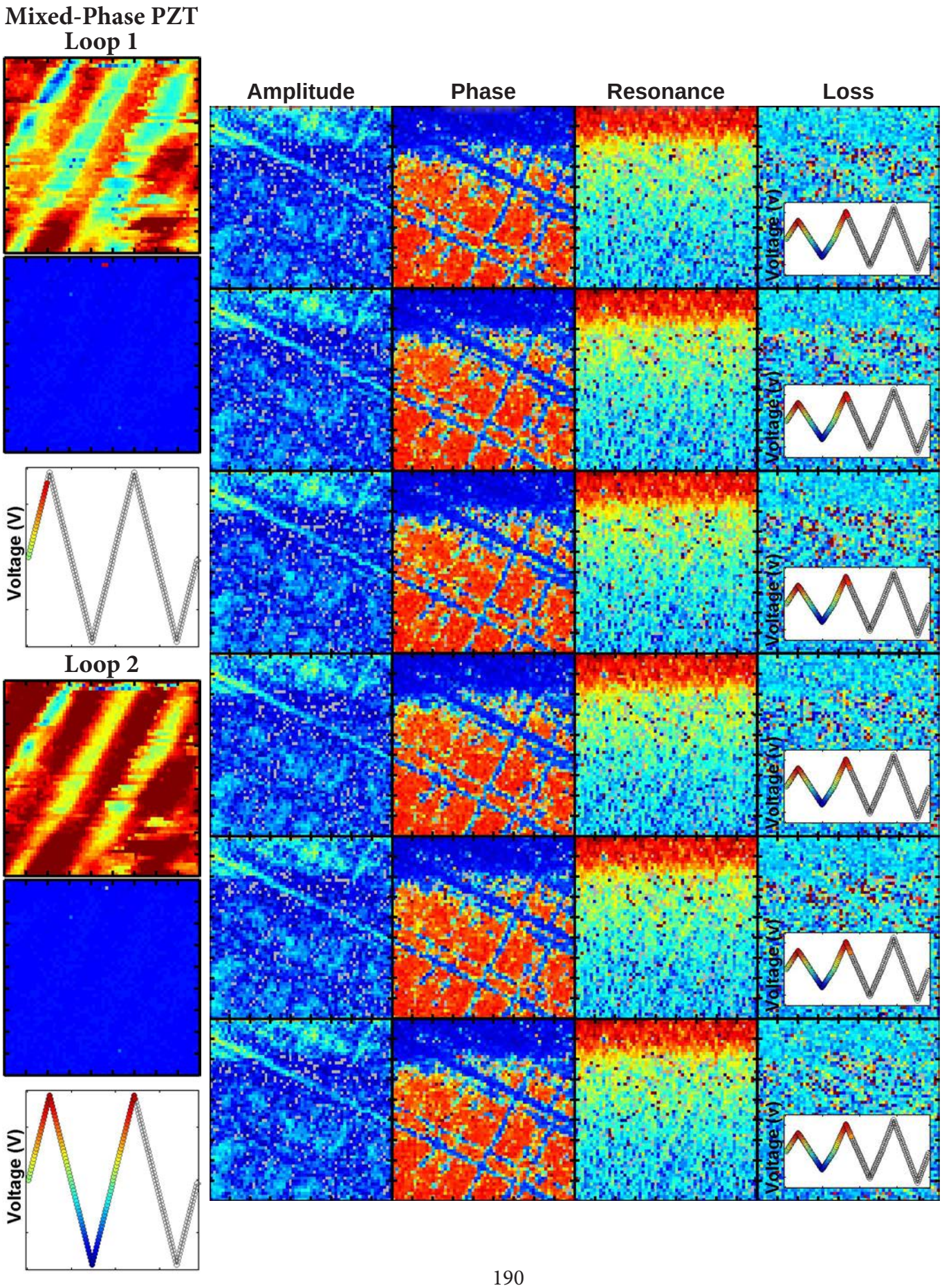
Mixed-Phase PZT
Loop 1
Amplitude
Phase
Resonance
Loss
Voltage (V)
Voltage (v)
Loop 2
Voltage (V)
Voltage (v)

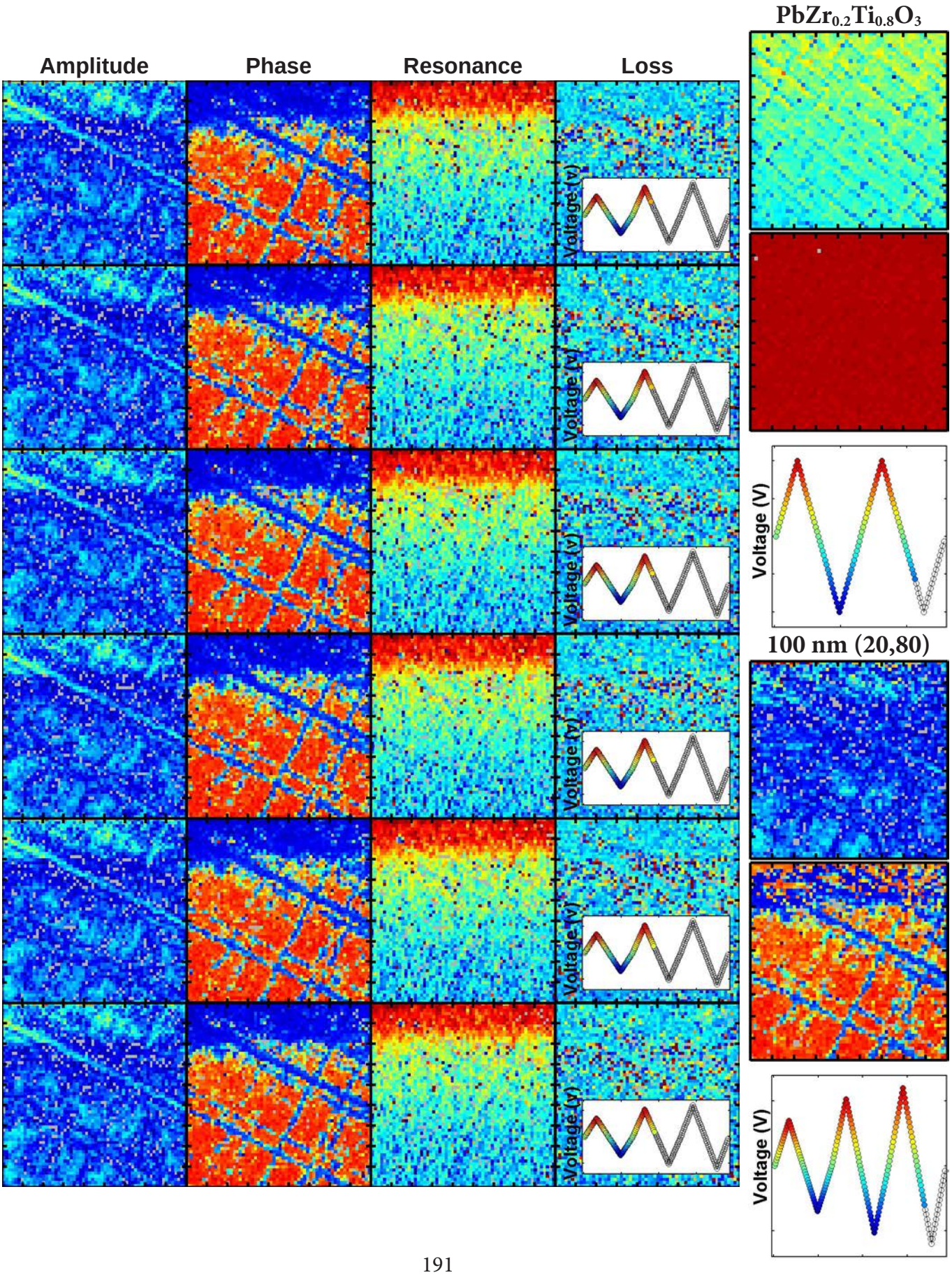
Amplitude
Phase
Resonance
Loss
Voltage (v)
PbZr0.2Ti0.8O3
Voltage (V)
100 nm (20,80)

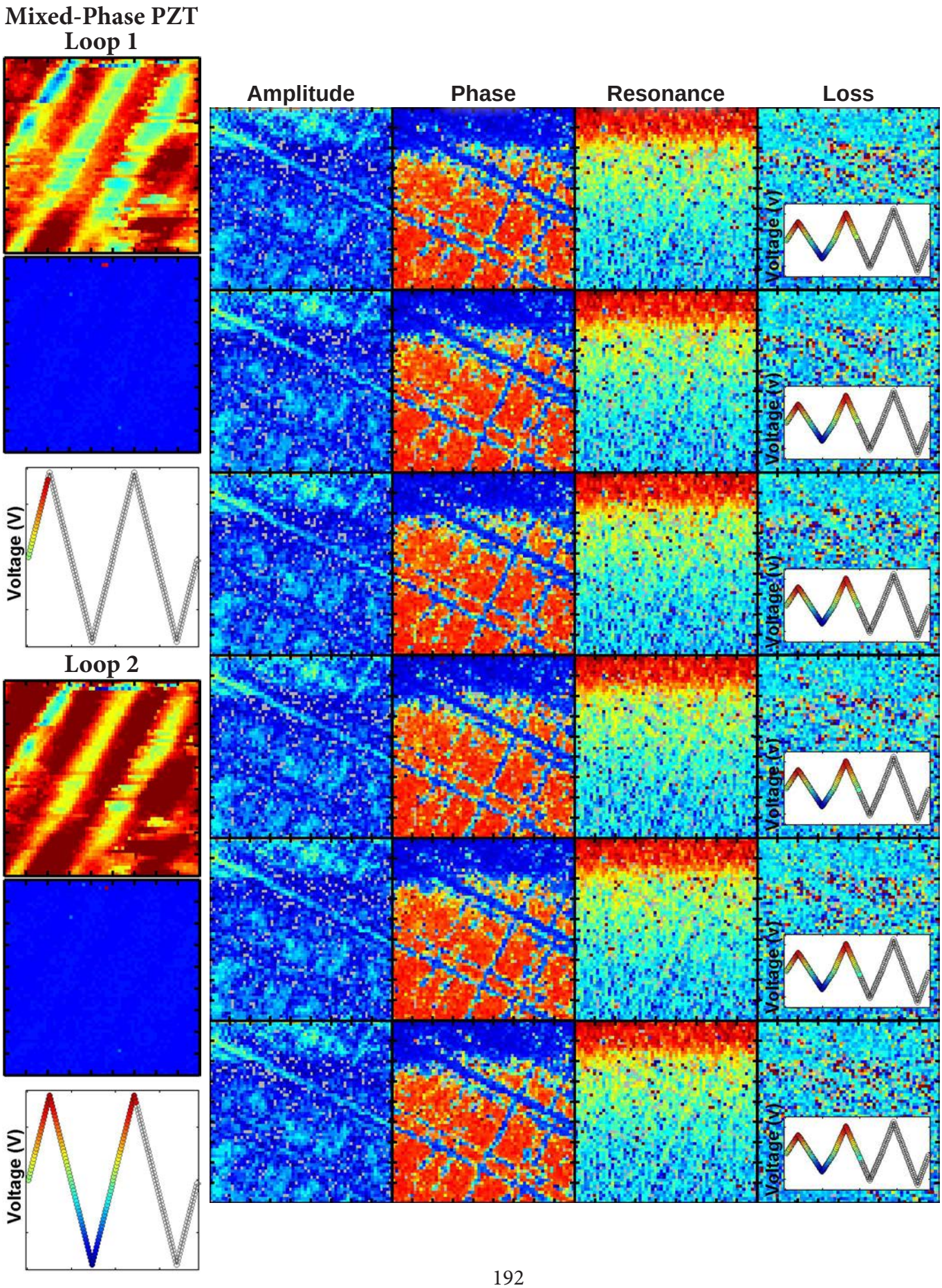
Mixed-Phase PZT
Loop 1
Amplitude
Phase
Resonance
Loss
Voltage (V)
Loop 2
Voltage (V)

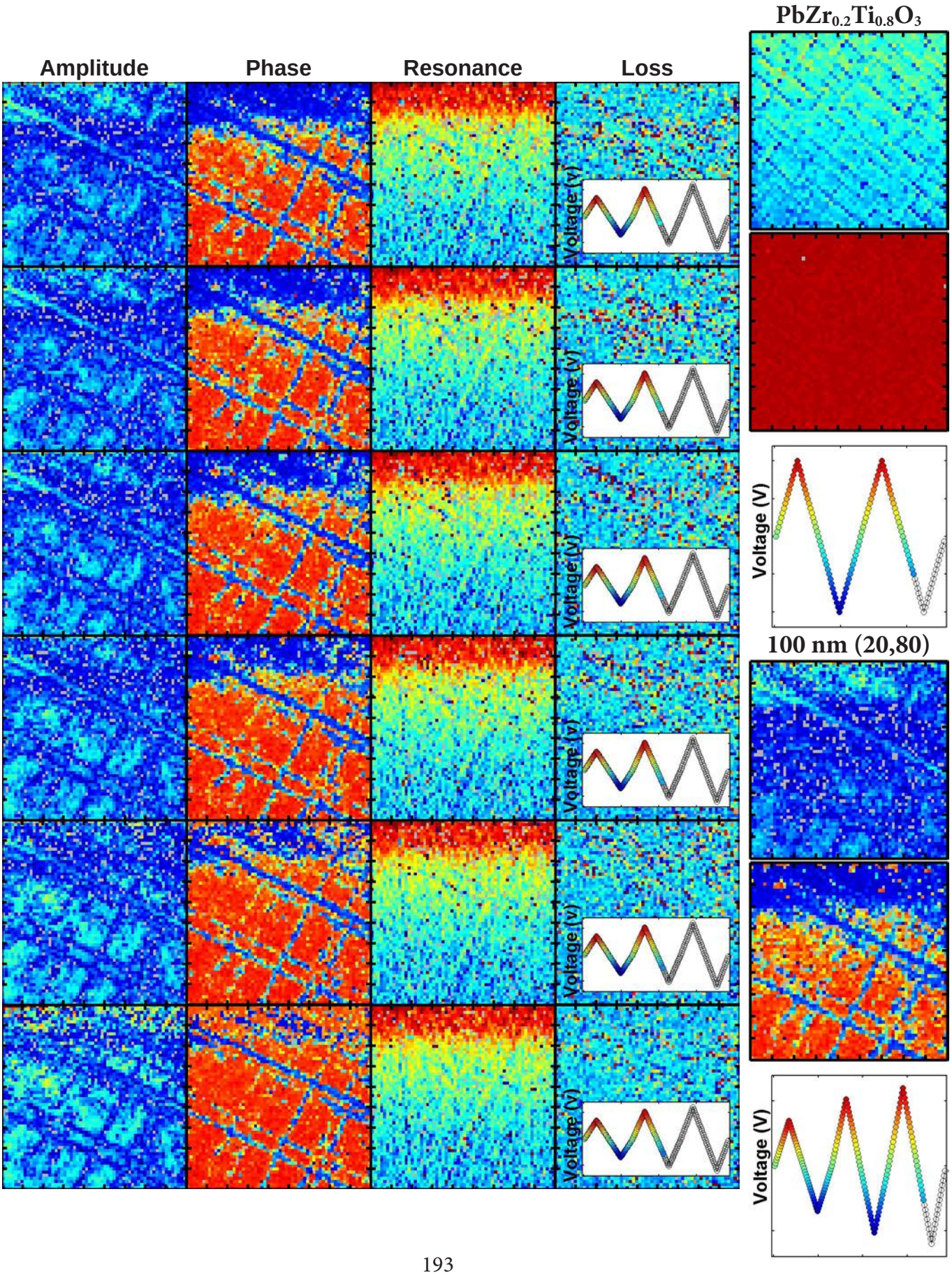
Amplitude
Phase
Resonance
Loss
Voltage (V)
PbZr0.2Ti0.8O3
Voltage (V)
100 nm (20,80)
Voltage (V)

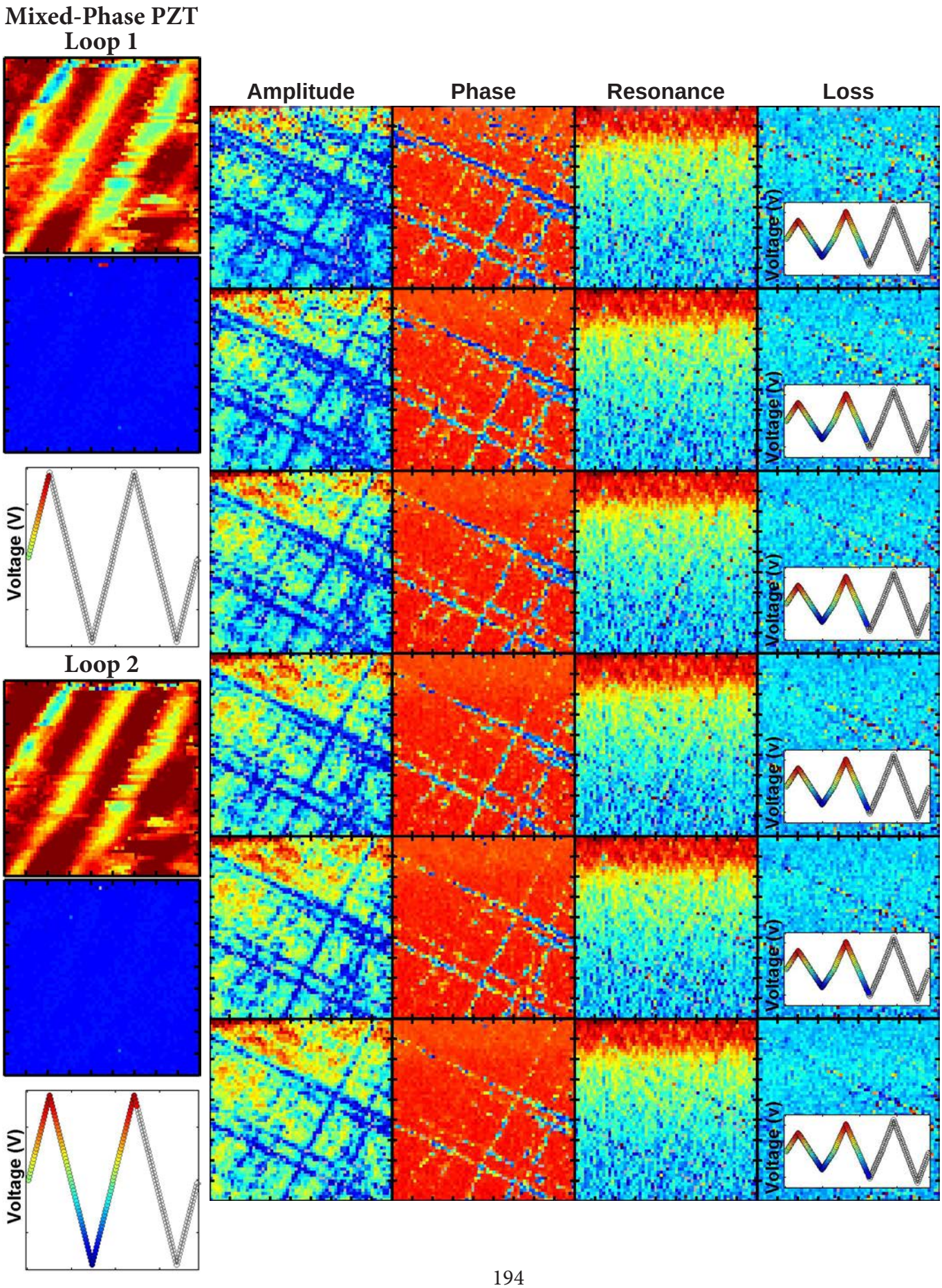
Mixed-Phase PZT
Loop 1
Amplitude
Phase
Resonance
Loss
Voltage (V)
Voltage (v)
Loop 2
Voltage (V)
Voltage (v)

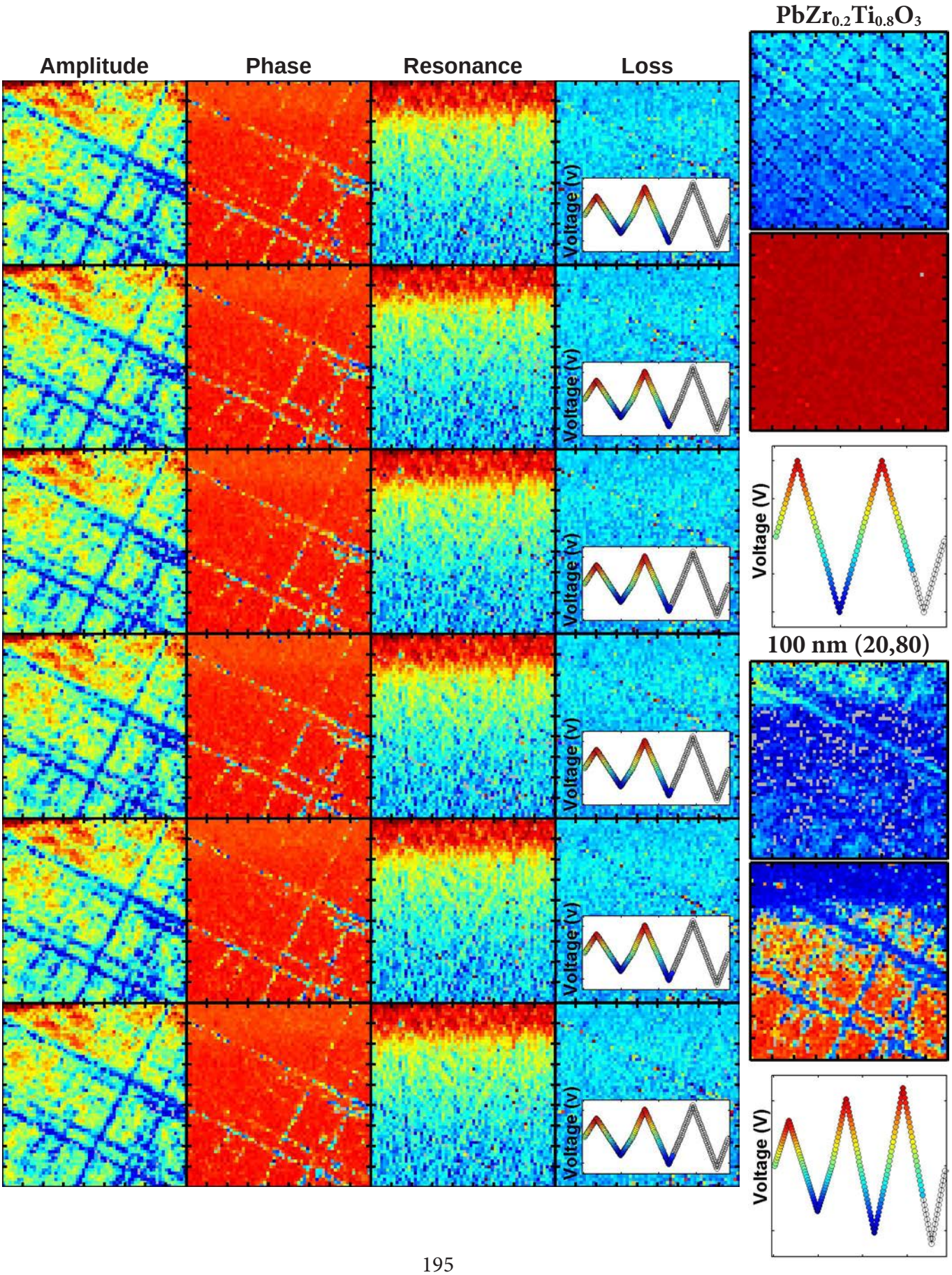
PbZr0.2Ti0.8O3
Amplitude
Phase
Resonance
Loss
Voltage (V)
Voltage (V)
Voltage (V)
Voltage (V)
Voltage (V)
Voltage (V)
Voltage (V)
100 nm (20,80)
Voltage (V)

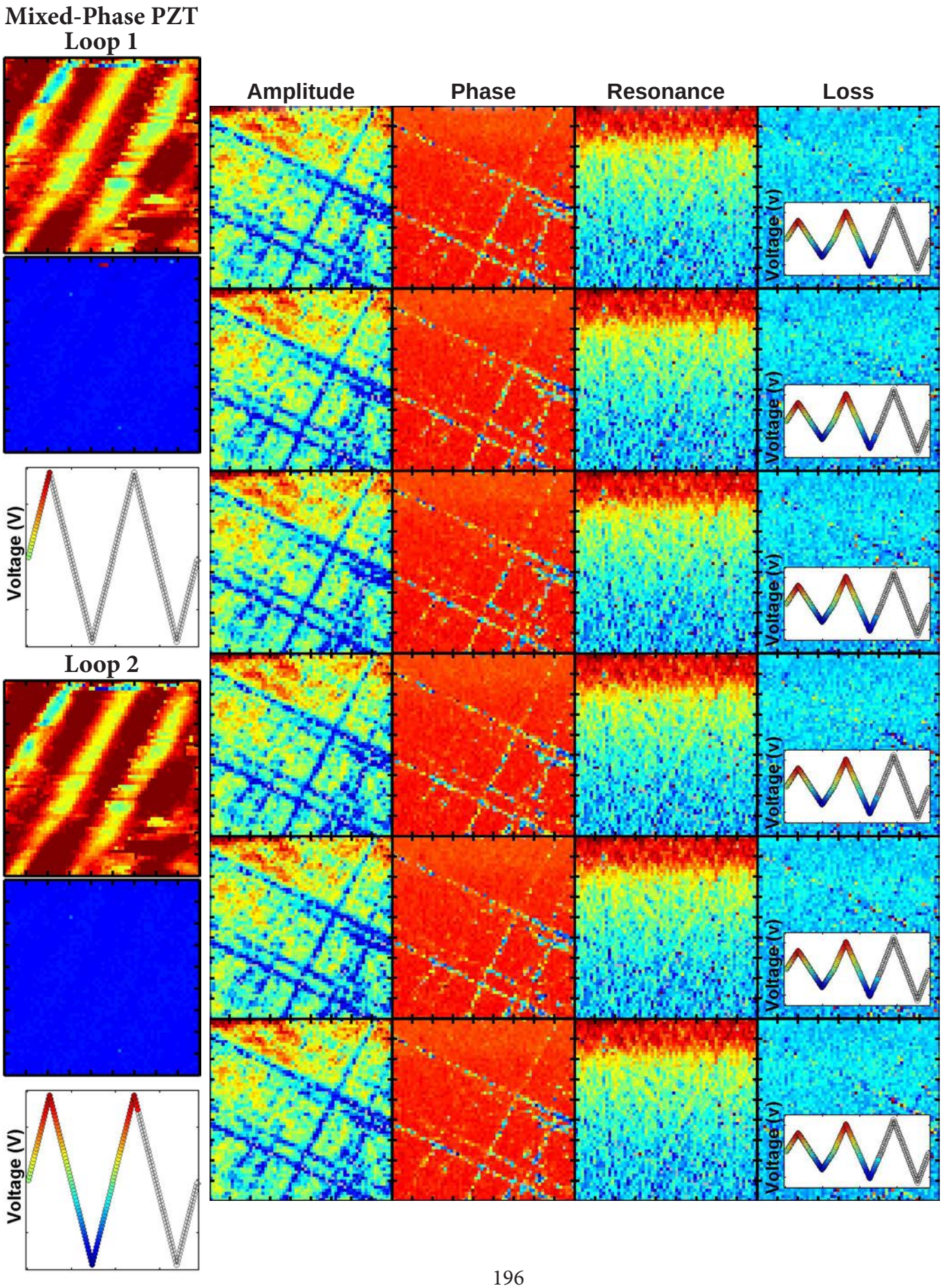
Mixed-Phase PZT
Loop 1
Amplitude
Phase
Resonance
Loss
Voltage (V)
Voltage (v)
Loop 2
Voltage (V)
Voltage (v)

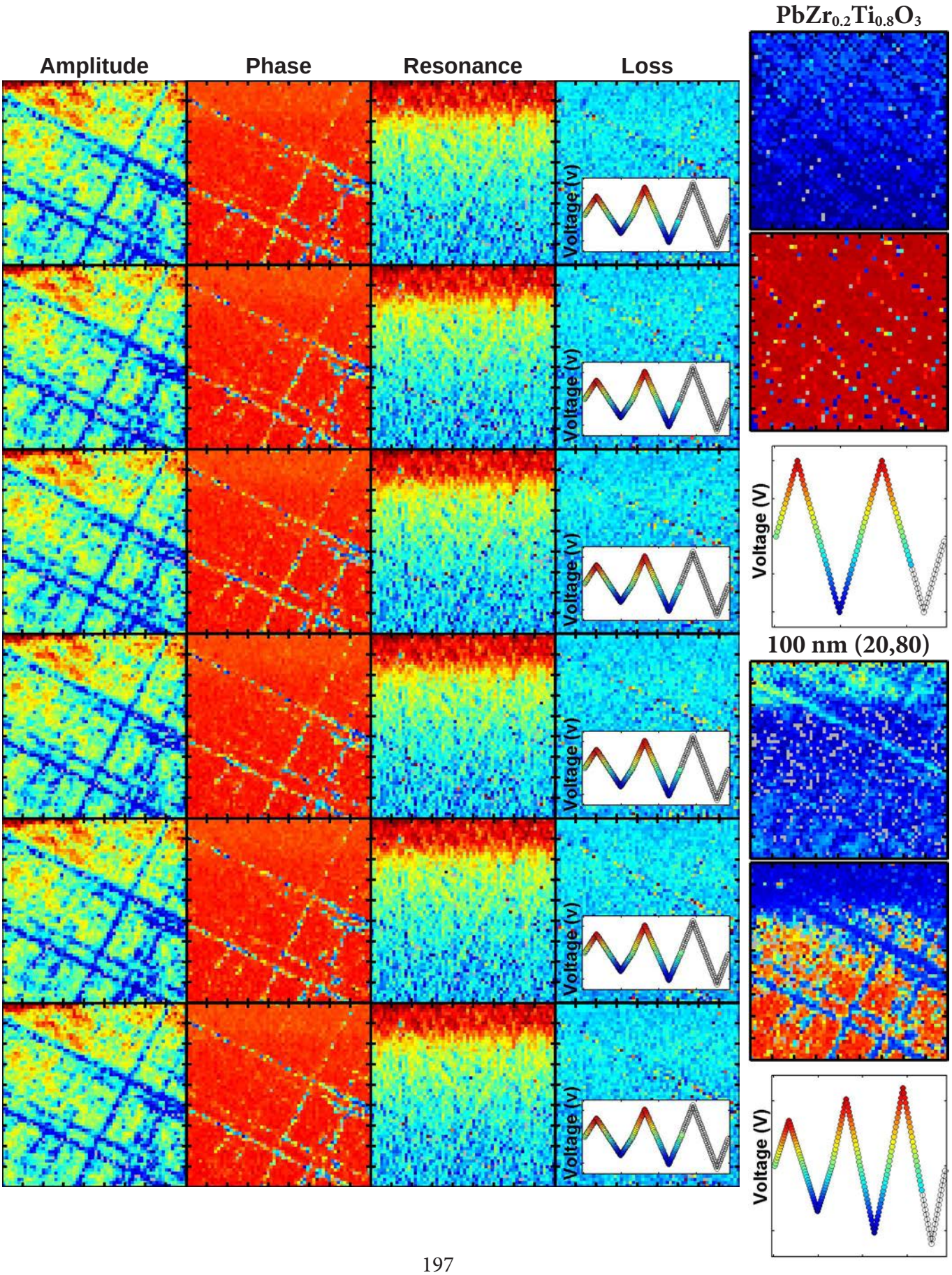
Amplitude
Phase
Resonance
Loss
Voltage (v)
PbZr0.2Ti0.8O3
Voltage (V)
100 nm (20,80)

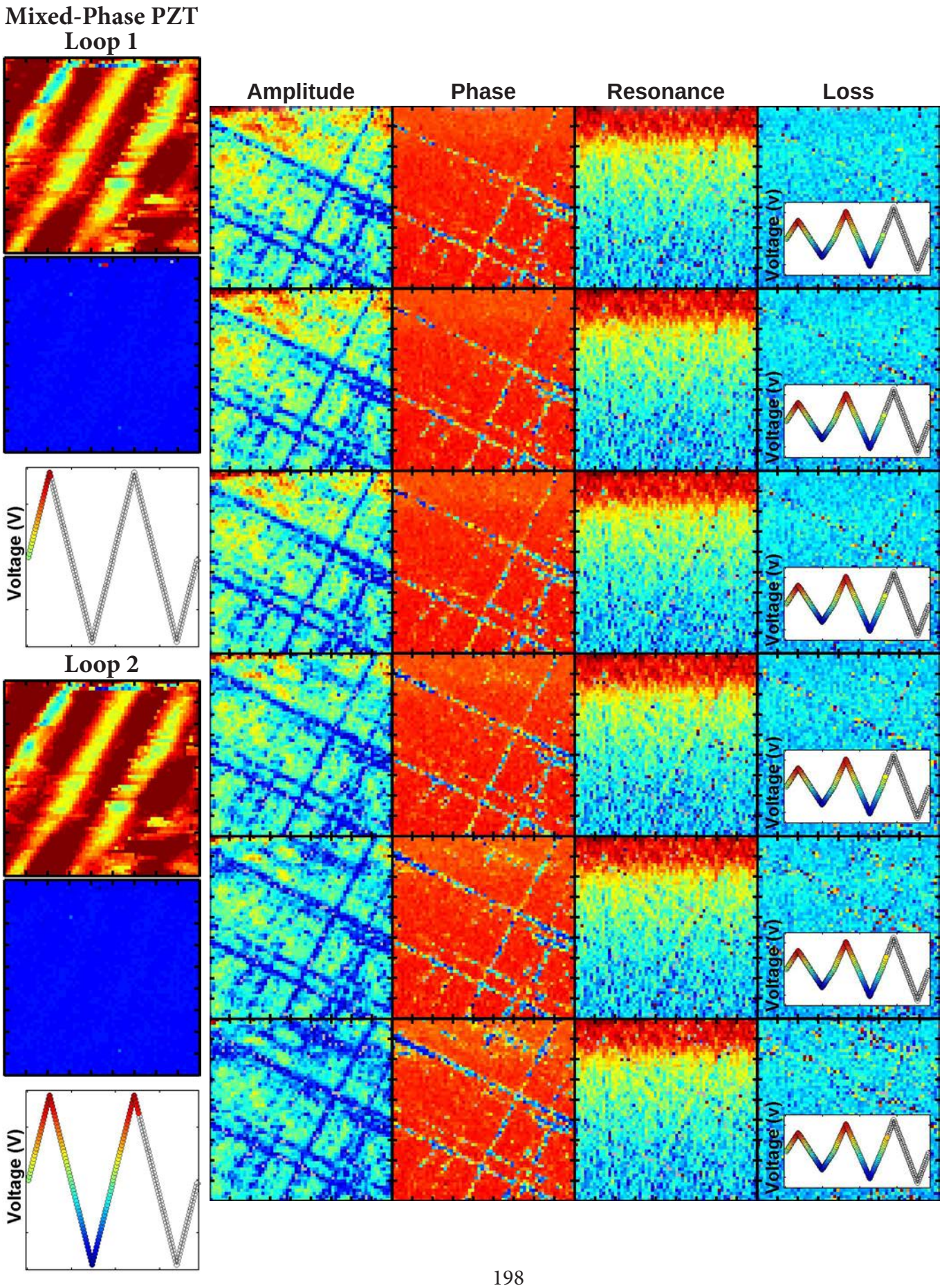
Mixed-Phase PZT
Loop 1
Amplitude
Phase
Resonance
Loss
Voltage (V)
Voltage (v)
Loop 2
Voltage (V)
Voltage (v)

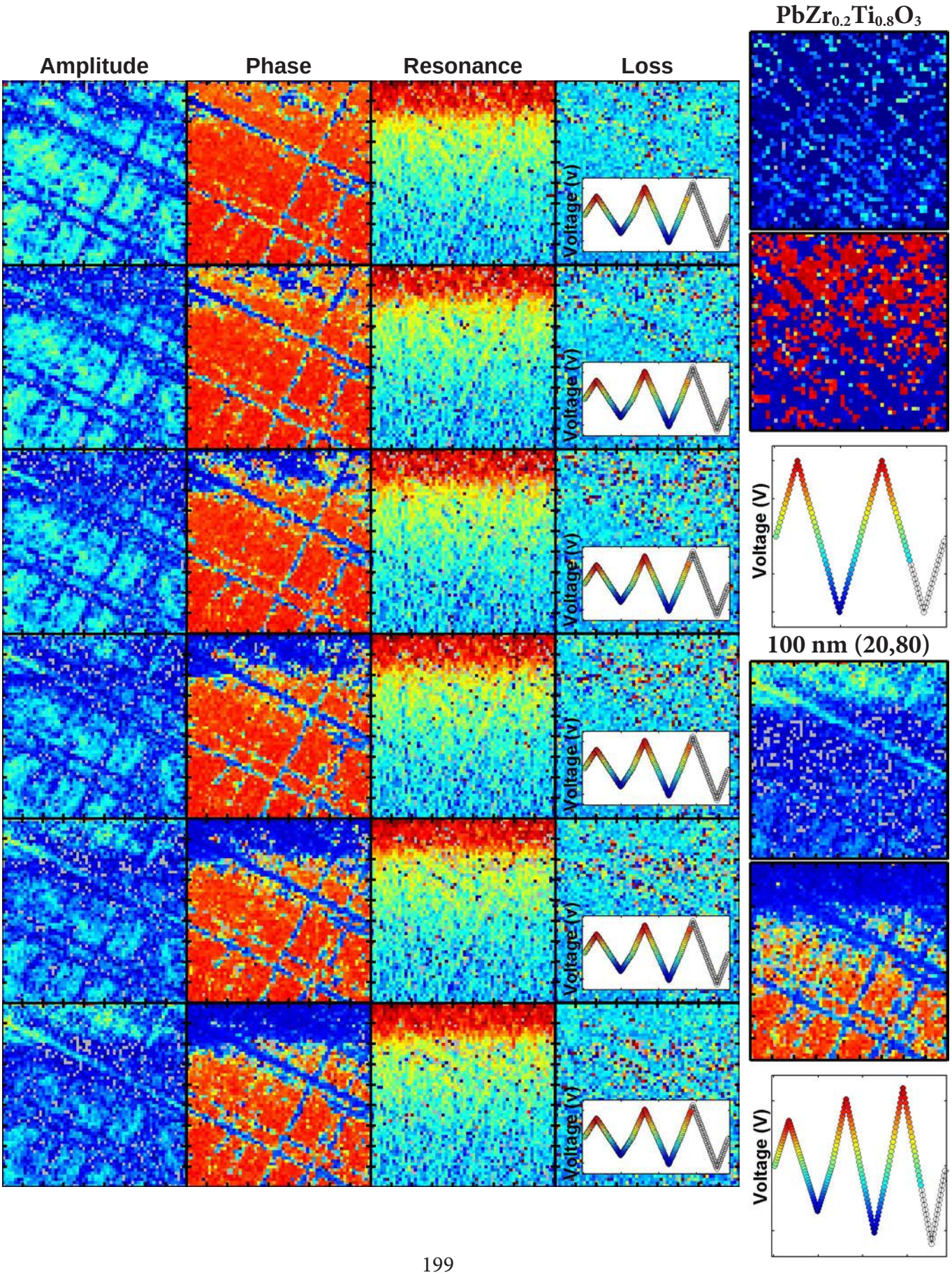
PbZr0.2Ti0.8O3
Amplitude
Phase
Resonance
Loss
Voltage (v)
Voltage (V)
100 nm (20,80)

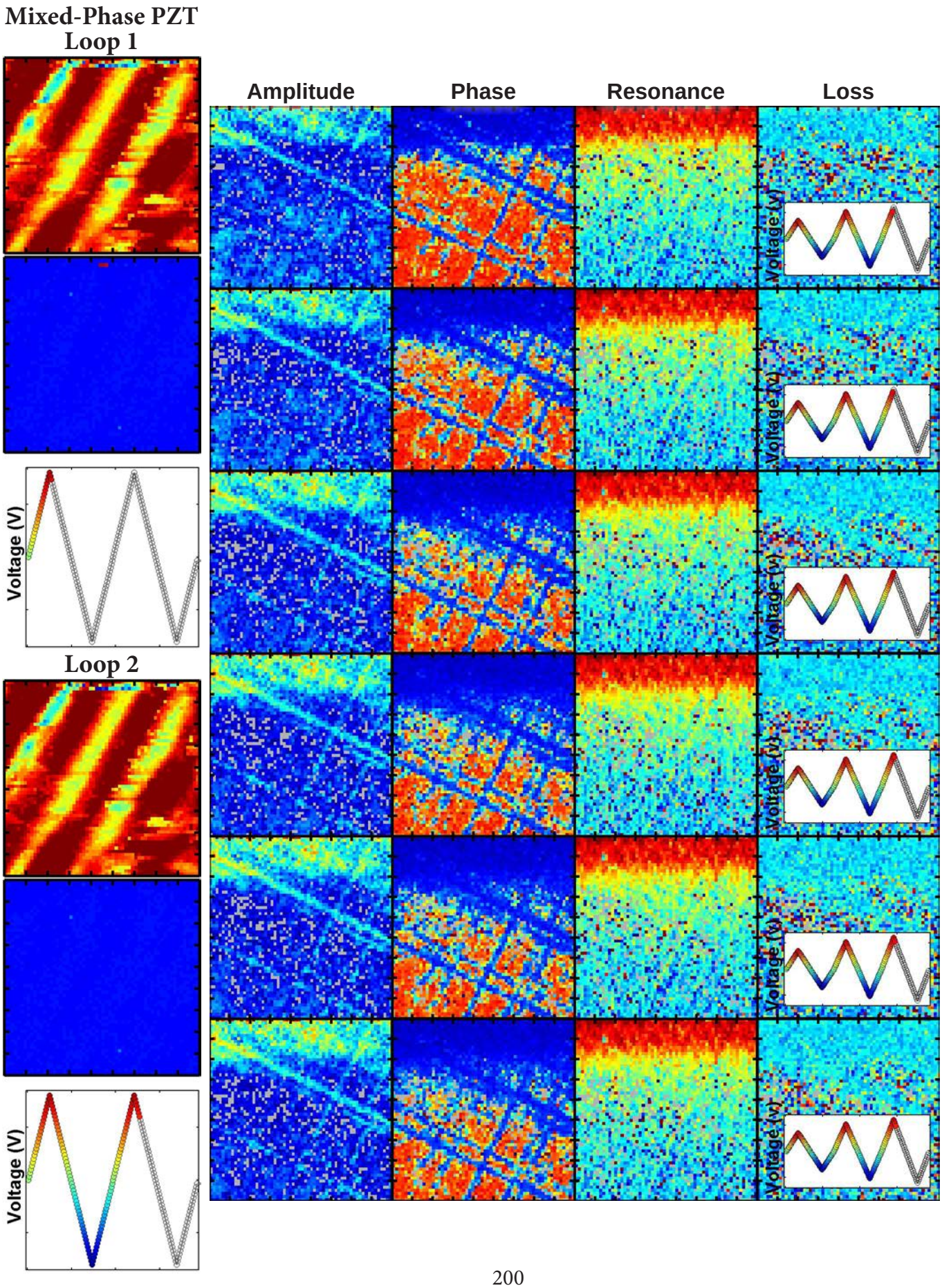
Mixed-Phase PZT
Loop 1
Amplitude
Phase
Resonance
Loss
Voltage (V)
Loop 2
Voltage (V)

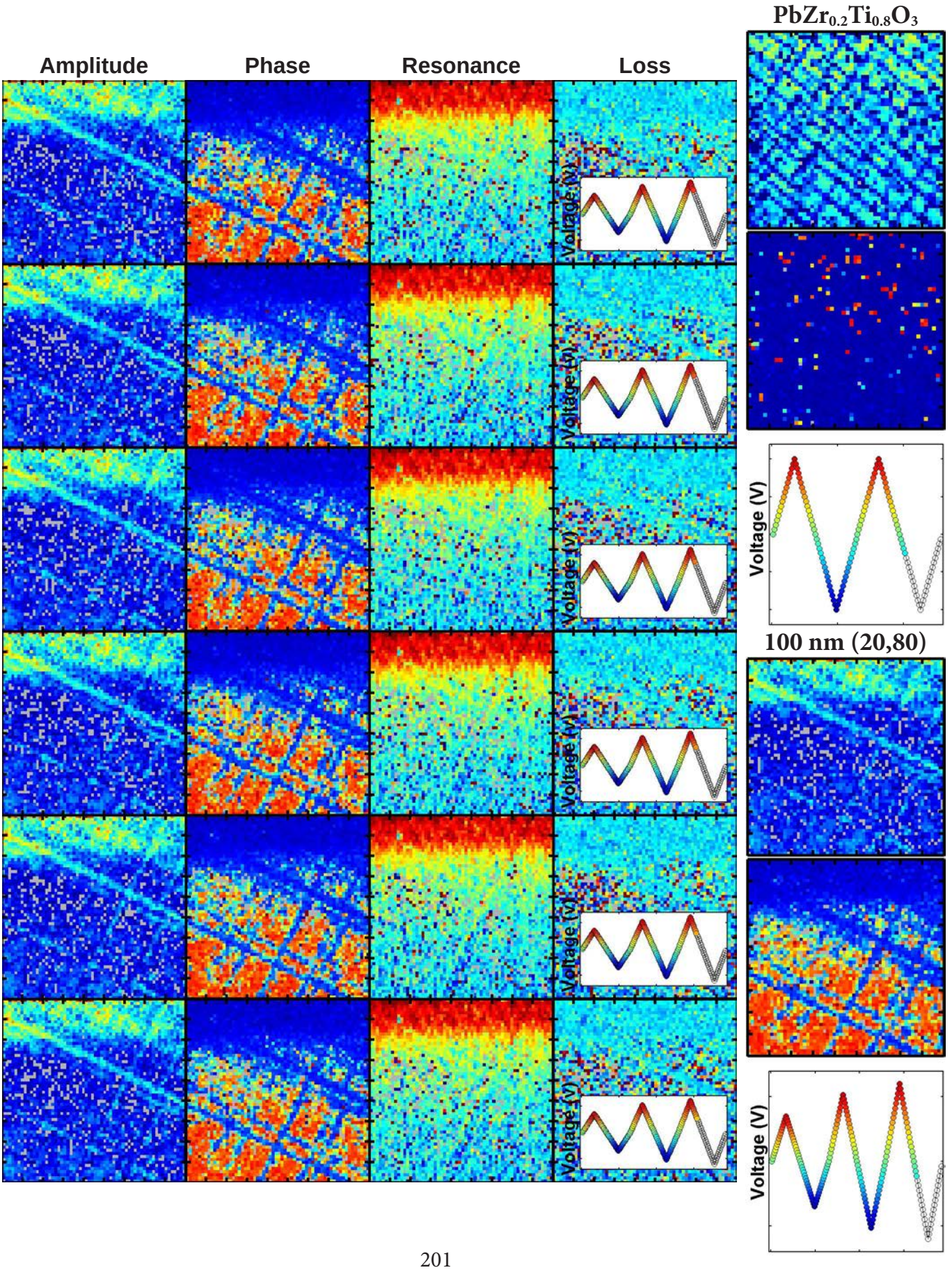
PbZr0.2Ti0.8O3
Amplitude
Phase
Resonance
Loss
Voltage (V)
100 nm (20,80)

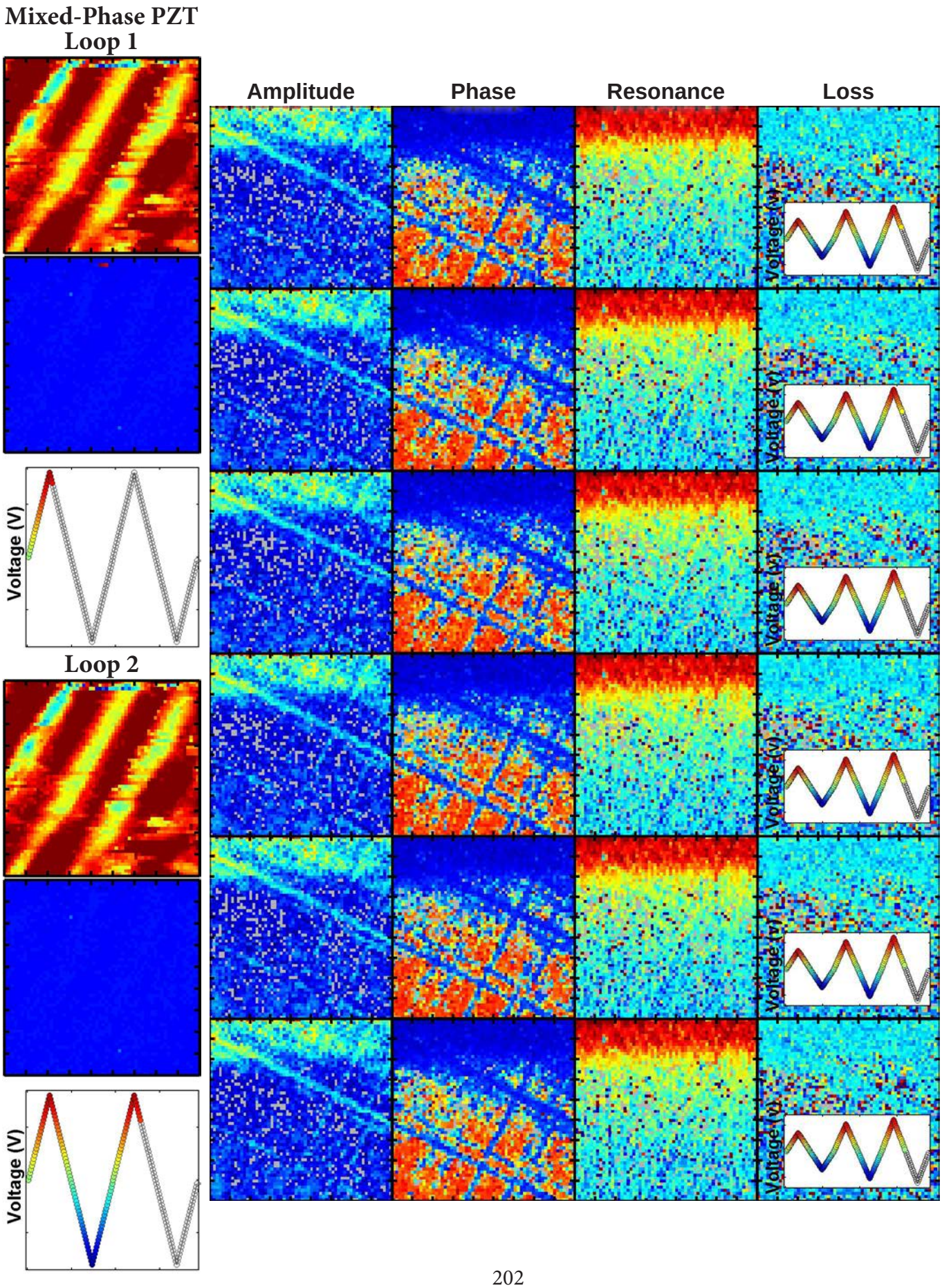
Mixed-Phase PZT
Loop 1
Amplitude
Phase
Resonance
Loss
Voltage (V)
Loop 2
Voltage (V)

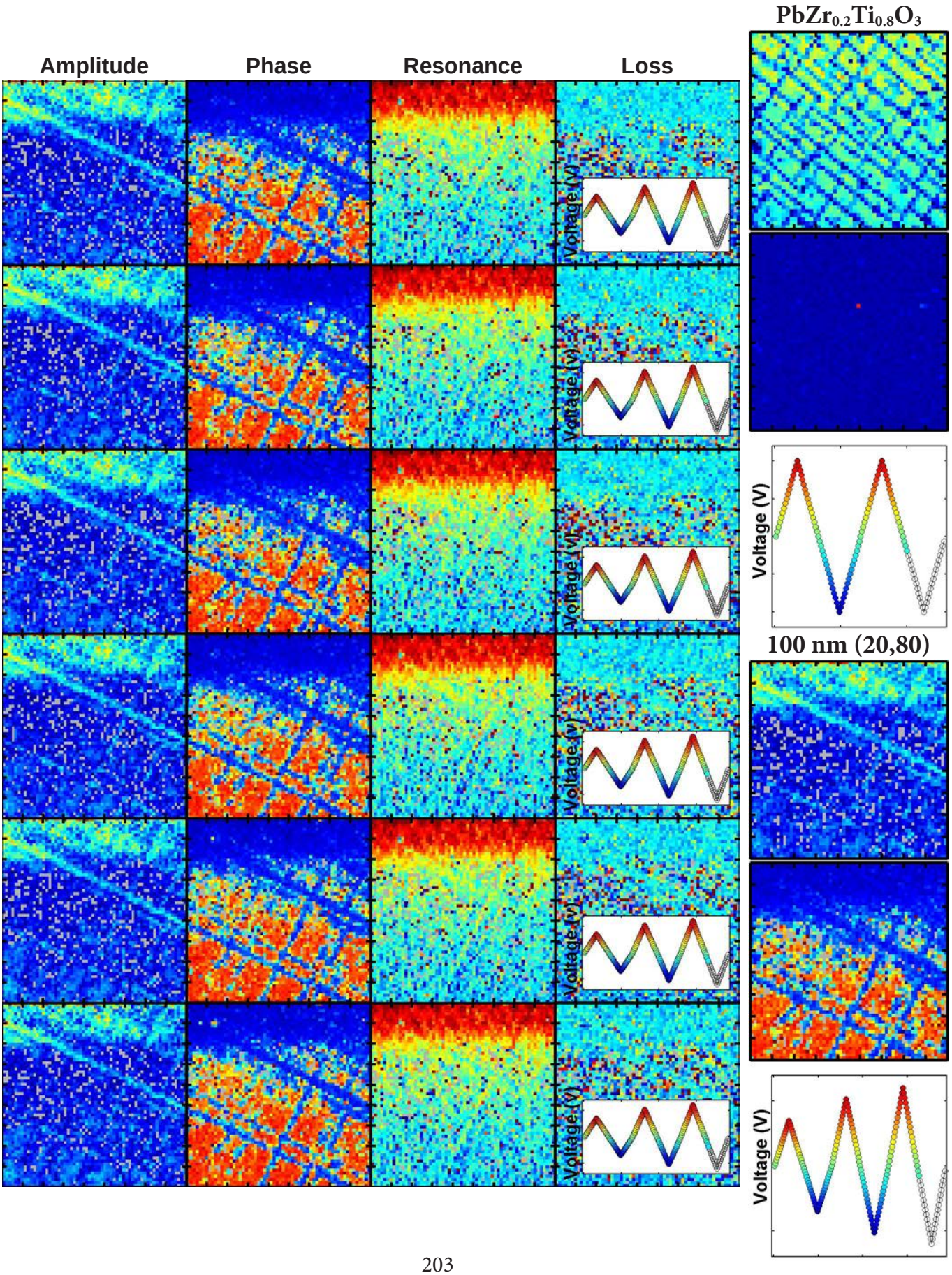
PbZr0.2Ti0.8O3
Amplitude
Phase
Resonance
Loss
Voltage (V)
Voltage (V)
Voltage (V)
Voltage (V)
Voltage (V)
Voltage (V)
Voltage (V)
100 nm (20,80)

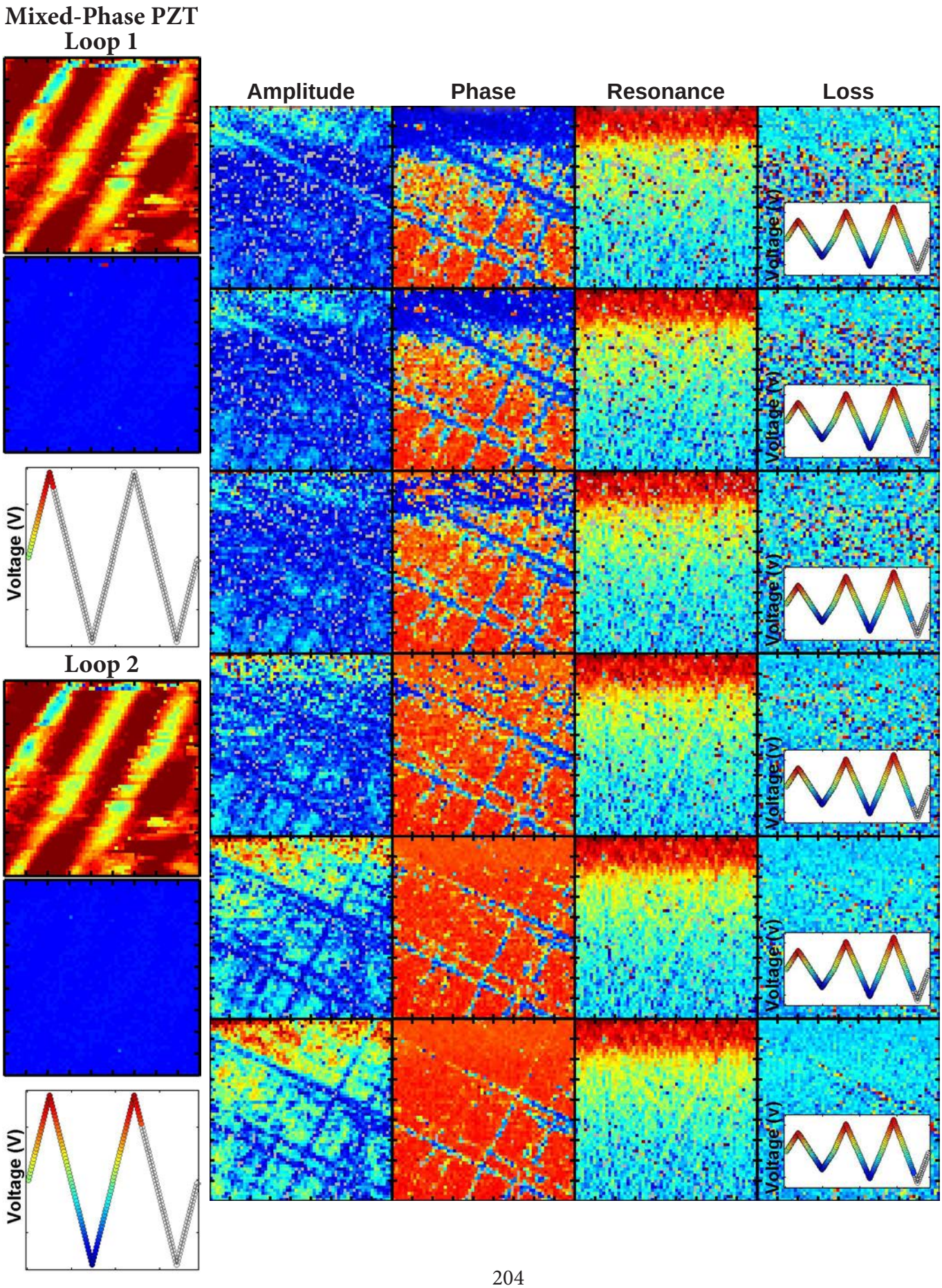
Mixed-Phase PZT
Loop 1
Amplitude
Phase
Resonance
Loss
Voltage (V)
Loop 2
Voltage (V)
Voltage (v)

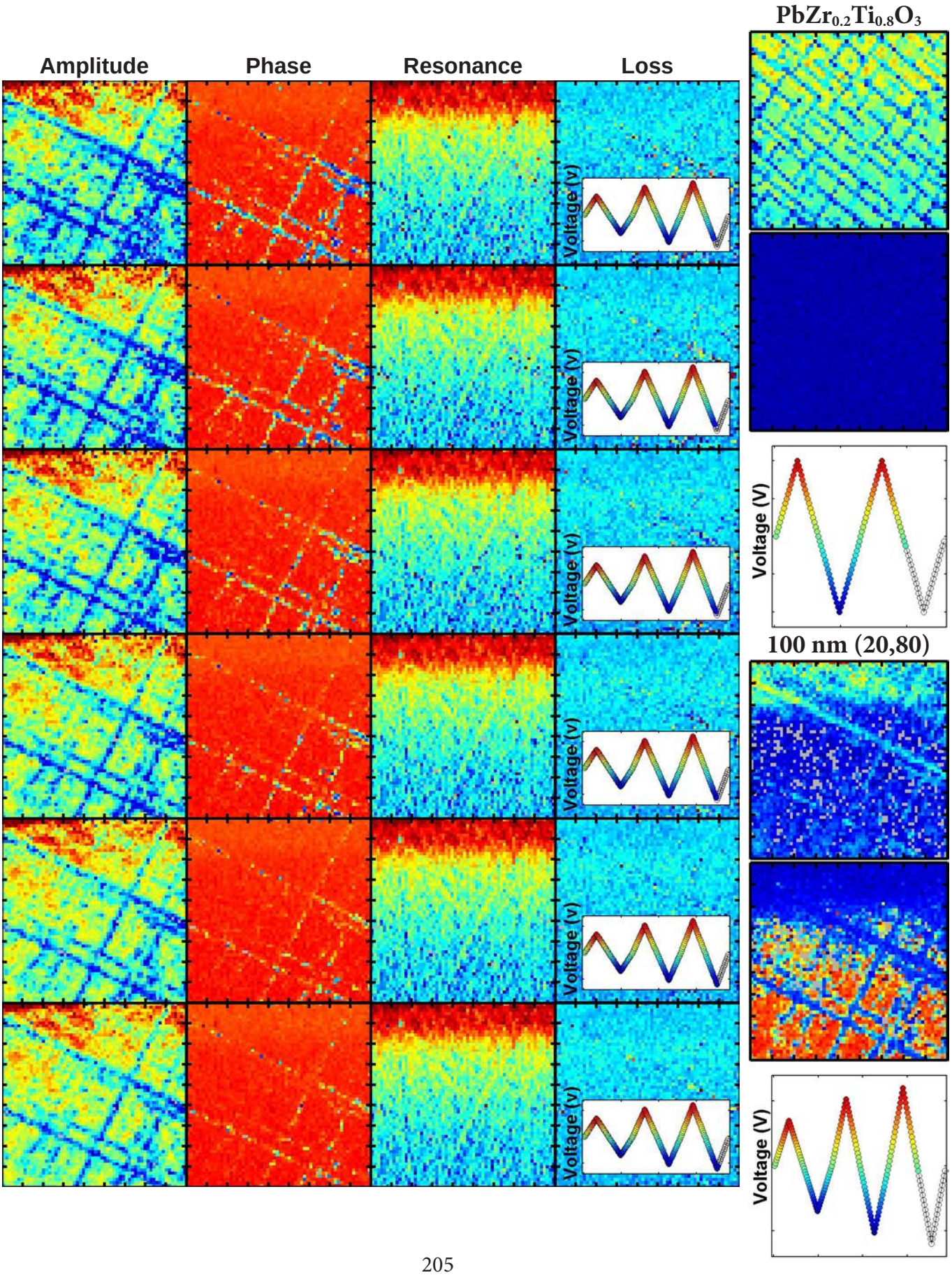
PbZr0.2Ti0.8O3
Amplitude
Phase
Resonance
Loss
Voltage (v)
Voltage (V)
100 nm (20,80)

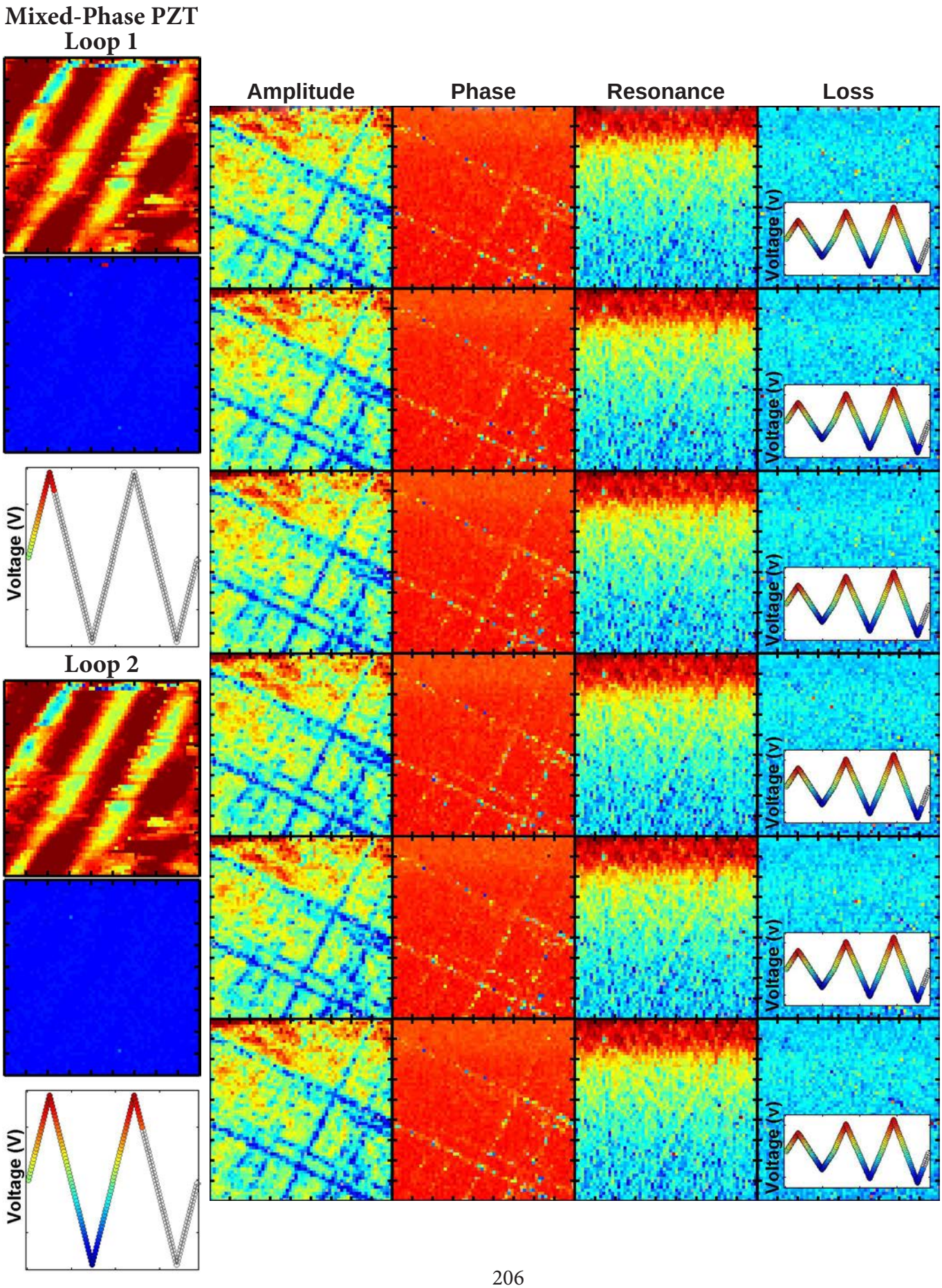
Mixed-Phase PZT
Loop 1
Amplitude
Phase
Resonance
Loss
Voltage (V)
Voltage (v)
Loop 2
Voltage (V)
Voltage (v)

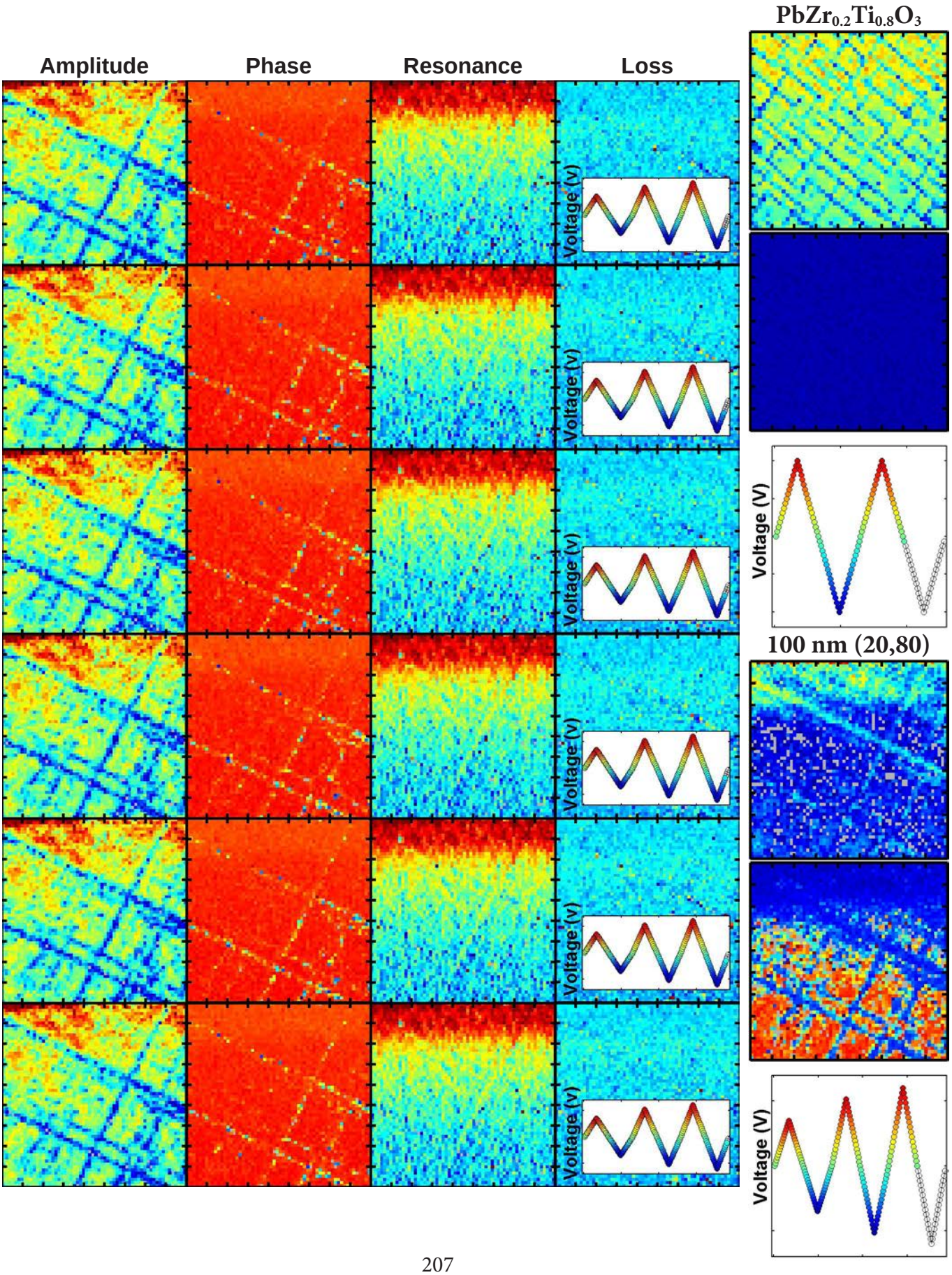
Amplitude
Phase
Resonance
Loss
Voltage (v)
Voltage (v)
Voltage (v)
Voltage (v)
Voltage (v)
Voltage (v)
PbZr0.2Ti0.8O3
Voltage (V)
100 nm (20,80)
Voltage (V)

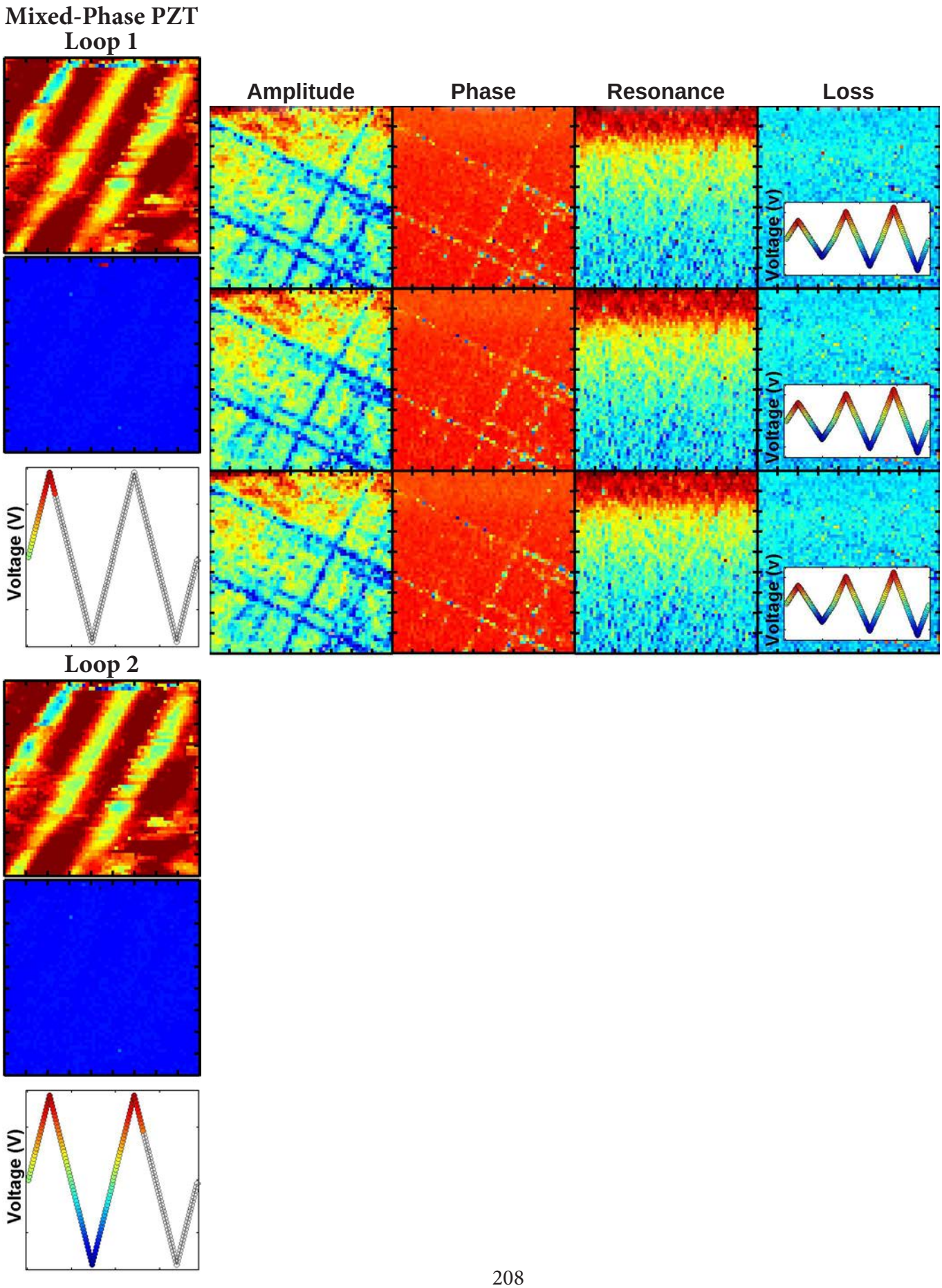
Mixed-Phase PZT
Loop 1
Amplitude
Phase
Resonance
Loss
Voltage (V)
Voltage (v)
Voltage (v)
Voltage (v)
Loop 2
Voltage (V)

Appendix F

Additional Loop Shape Parameters for Homogeneous $PbZr_{0.2}Ti_{0.8}O_3$ and Compositionally-Graded (20,80) Heterostructures

In conducting BE-SS measurements, obtaining useful and insightful data requires the consideration of many factors including: scan size, sample size, applied voltage, number of hysteresis loops, tip wear, *etc.*, and in turn, certain measurement parameters have better sensitivity to observe certain features of the response. While all measurements show the same fundamental modes of response and trends, we conducted multiple measurements of all heterostructures studied with slightly different measurement parameters which focused on highlighting certain pertinent features. In this appendix, we show the data with the set of scan parameters which makes the trends in response most pronounce.

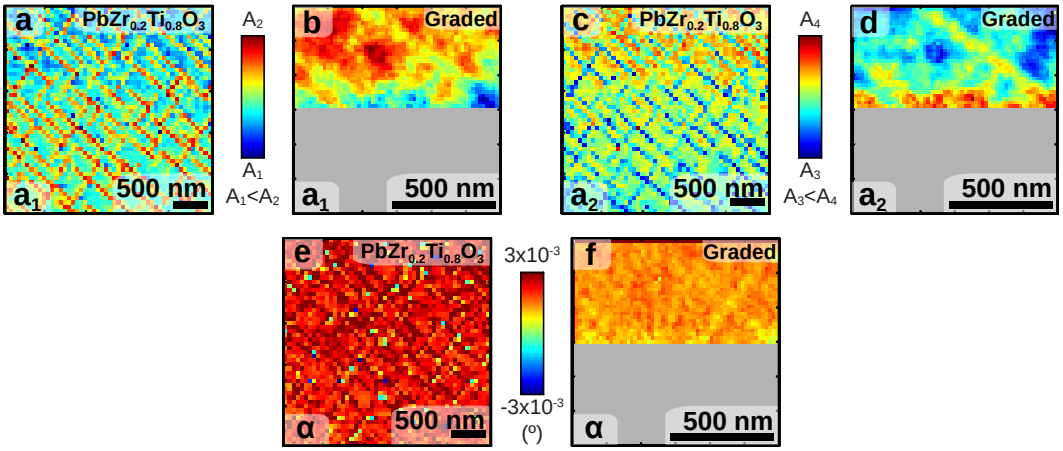

Figure F.1. Primary loop shape parameter obtained from loop fitting of a_1 the minimum saturation piezoresponse of (a) homogeneous $PbZr_{0.2}Ti_{0.8}O_3$ and (b) compositionally-graded heterostructures. a_2 the maximum saturation piezoresponse of (c) homogeneous $PbZr_{0.2}Ti_{0.8}O_3$ and (d) compositionally-graded heterostructures. Rotation angle α used to define a_3 of (e) homogeneous $PbZr_{0.2}Ti_{0.8}O_3$ and (f) compositionally-graded heterostructures.

We start our discussion with spatial maps of the minimum saturation piezoresponse amplitude (a_1, Figure F.1a-b), maximum saturation piezoresponse (a_2, Figure F.1c-d), and rotation angle (α, Figure F.1e-f) used to define (a_3) for the homogeneous $PbZr_{0.2}Ti_{0.8}O_3$ and compositionally-graded heterostructures. In the homogeneous heterostructures there is evidence of a slight increase in a_1 (Figure

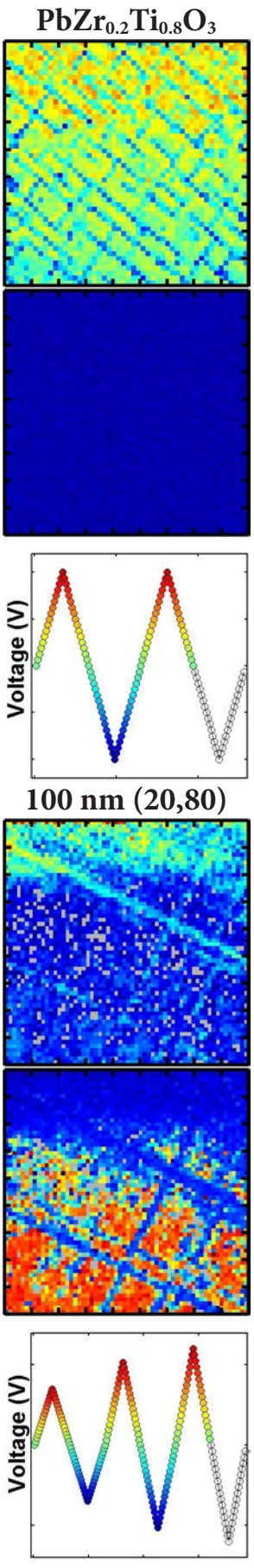

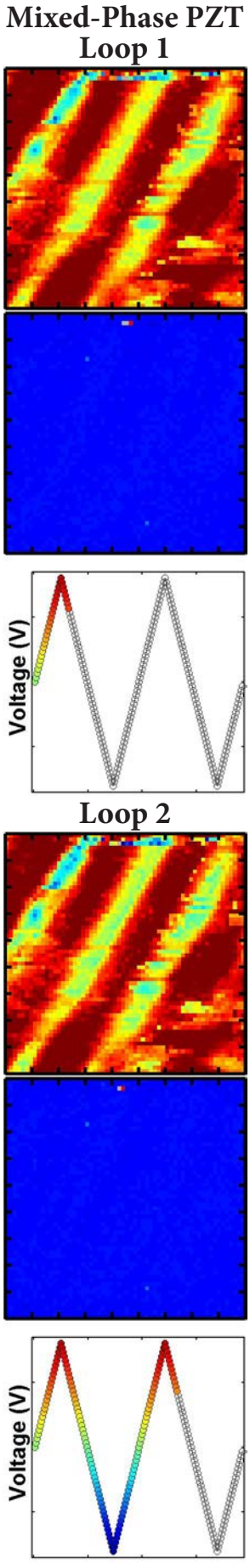

F.1a) and a slight decrease in a_2 (Figure F.1c) at or near the *a* domains compared to the *c* domains. Comparatively the compositionally-graded heterostructures show slightly suppressed minimum saturation piezoresponse (a_1, Figure F.1b) at or near the *a* domains; but, shows significant enhancement in a_2 (Figure F.1d) at the *a* domains compared to the *c* domains. This is likely related to the proposed mechanism of response at these *a* domains, where there is a difference in piezoresponse depending on the direction of the applied bias. Now, looking at α (Figure F.1e-f), we see an enhancement in the rotation angle at or near the *a* domains (compared to the *c* domains) in the homogeneous heterostructures; while the compositionally-graded heterostructures show an opposite response (slightly suppressed α at or near the *a* domains).

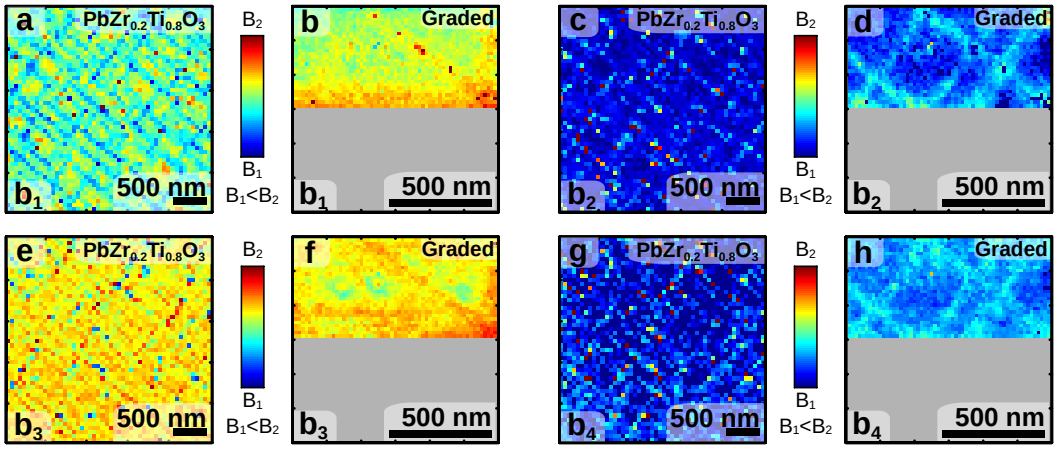

Figure F.2. Secondary loop shape parameter obtained from loop fitting of b_1 bottom left corner sharpness of (a) homogeneous $PbZr_{0.2}Ti_{0.8}O_3$ and (b) compositionally-graded heterostructures. b_2 top left corner sharpness of (c) homogeneous $PbZr_{0.2}Ti_{0.8}O_3$ and (d) compositionally-graded heterostructures. b_3 top right corner sharpness of (e) homogeneous $PbZr_{0.2}Ti_{0.8}O_3$ and (f) compositionally-graded heterostructures. b_4 bottom right corner sharpness of (g) homogeneous $PbZr_{0.2}Ti_{0.8}O_3$ and (h) compositionally-graded heterostructures.

Now, looking at the $b_{1\text{-}4}$ parameters (Figure F.2a-h) which represent the sharpness of the loop corner, starting our discussion with the homogeneous $PbZr_{0.2}Ti_{0.8}O_3$ heterostructures we see a slight suppression in b_1 at or near the *a* domains (sharper corners), while slight having a slightly enhanced $b_{2\text{-}4}$ values (rounder corners) at or near the *a* domains compared to the *c* domains. Overall, $b_{1,3}$ are significantly greater than $b_{2,4}$, indicating that saturation occurs more gradually than nucleation. In the case of the compositionally-graded heterostructure we observe slight enhancement in the $b_{1,3}$ values at or near the *a* domains, indicating saturation

occurs slightly more gradually at the *a* domains compared to the *c* domains. A more significant relative enhancement in $b_{2,4}$ is observed at the *a* domains compared to the *c* domains. This observation, implies that nucleation occurs more gradually at the *a* domains compared to the *c* domains and is consistent with our proposed switching/response mechanism which does not require nucleation and growth (commonly associated with sharp transitions). Overall, again, as observed in the homogeneous $PbZr_{0.2}Ti_{0.8}O_3$ heterostructures, $b_{1,3}$ are significantly greater than $b_{2,4}$, indicating that initial switching occurs more rapidly than saturation.

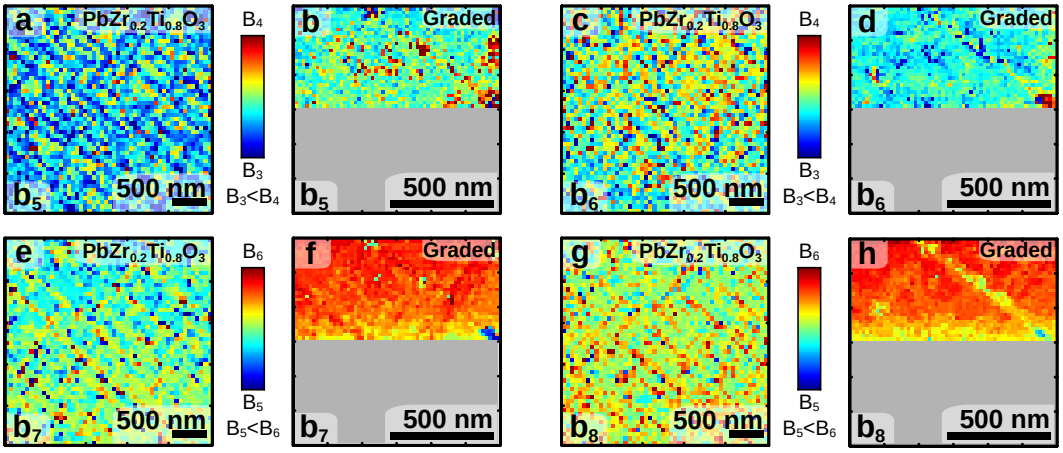

Figure F.3. Tertiary loop shape parameter obtained from loop fitting. b_5 relating to the transition between b_1 to b_2 of (a) homogeneous $PbZr_{0.2}Ti_{0.8}O_3$ and (b) compositionally-graded heterostructures. b_6 relating to the transition between b_3 to b_4 of (c) homogeneous $PbZr_{0.2}Ti_{0.8}O_3$ and (d) compositionally-graded heterostructures. b_7 locates the halfway point between the transition from b_1 to b_2 (e) homogeneous $PbZr_{0.2}Ti_{0.8}O_3$ and of (f) compositionally-graded heterostructures. b_8 locates the halfway point between the transition from b_3 to b_4 of (g) homogeneous $PbZr_{0.2}Ti_{0.8}O_3$ and (h) compositionally-graded heterostructures.

Moreover, it is possible to plot the ternary loop shape parameters (Figure F.3a-h) describing the rate of transitions between the loop shape curvatures and the curvature midpoints. While these parameters are necessary to obtain good fits of the piezoelectric loops their physical significance is a little bit obtuse. We are currently working on understanding the significance of these parameters.

In addition to the basic loop shape fitting parameters it is also possible to extract values related to the loop shape characteristics. Starting with the optimum rotation angle (Figure F.4a-b), which represents the phase shift necessary to maximize the real component and minimize the imaginary component of the piezoelectric hysteresis loop, we observe a slight increase in the optimum rotation angle at the

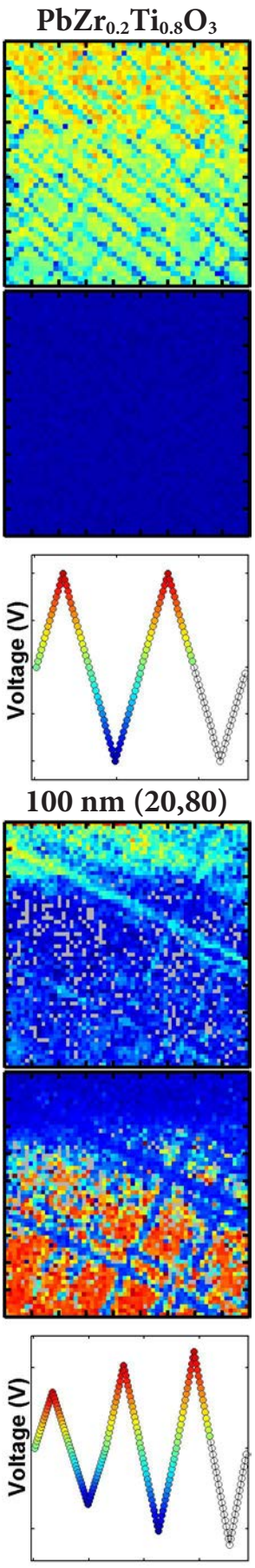

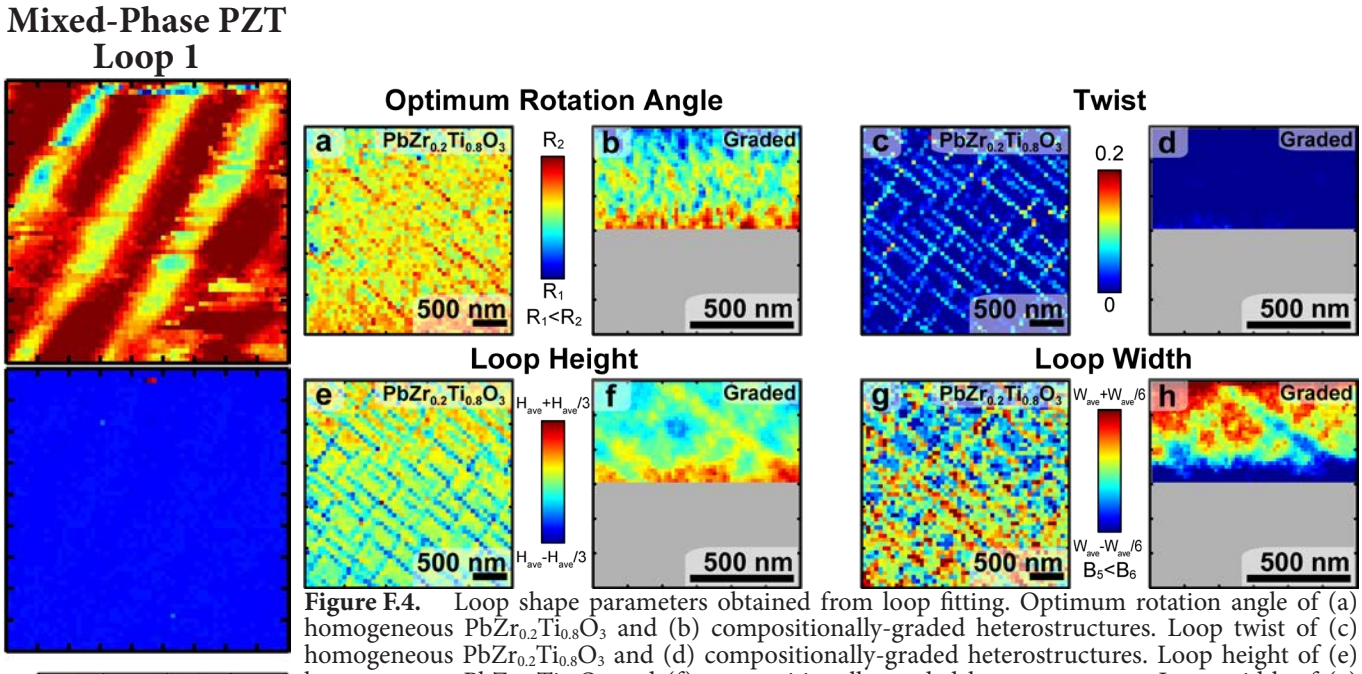

Figure F.4. Loop shape parameters obtained from loop fitting. Optimum rotation angle of (a) homogeneous $PbZr_{0.2}Ti_{0.8}O_3$ and (b) compositionally-graded heterostructures. Loop twist of (c) homogeneous $PbZr_{0.2}Ti_{0.8}O_3$ and (d) compositionally-graded heterostructures. Loop height of (e) homogeneous $PbZr_{0.2}Ti_{0.8}O_3$ and (f) compositionally-graded heterostructures. Loop width of (g) homogeneous $PbZr_{0.2}Ti_{0.8}O_3$ and (h) compositionally-graded heterostructures.

a domains (compared to the *c* domains) in the homogeneous $PbZr_{0.2}Ti_{0.8}O_3$ heterostructures, while there is no spatially correlated variance in the compositionally-graded heterostructures. Furthermore, we can calculate the loop twist which is thought to be reflective of the change in electromechanical coupling of the mechanical system composed of the film and the cantilever. For the case of the homogeneous $PbZr_{0.2}Ti_{0.8}O_3$ heterostructures (Figure F.4c) we see strongly enhanced loop twists at, or near, the *a* domains (compared to the c domains), whereas in the compositionally-graded heterostructures (Figure F.4d) we observe no spatially correlated contrast. Now focusing on the loop height, of the homogeneous $PbZr_{0.2}Ti_{0.8}O_3$ heterostructures (Figure F.4e), we observe suppressed piezoresponse at or near the in-plane oriented *a* domains (compared to the *c* domains), an expected result considering the uniformly enhanced piezoresponse observed in the *c* domains throughout the entire switching process. Once again, similar to the observations in the main text, we observe the opposite trend in the compositionally-graded heterostructure (Figure F.4f), which shows an enhancement in the measured loop height at, or near, the *a* domains (compared to the *c* domains). Changing our attention to the loop width, we observe an increased loop width in the homogeneous $PbZr_{0.2}Ti_{0.8}O_3$ heterostructures at, or near, the *a* domains (compared to the *c* domains), an indication that a larger voltage is needed to generate an out-of-plane response at, or near, the

in-plane oriented *a* domains. Once again, we observe the opposite trend in the compositionally-graded heterostructures, which reveals a local reduction in the loop width at, or near, the *a* domains. This reduction in the loop width at the *a* domains makes sense as the *a* domains are in an energetic quandary and can be easily excited by external bias. Additionally, based on our switching mechanism to switch the *c* domains in the out-of-plane direction requires that the *a* domains respond by changing shape first. Only once the *a* domains reach their terminal, high-bias state can the *c* domains switch, necessitating a local reduction in loop width at or near the *a* domains.

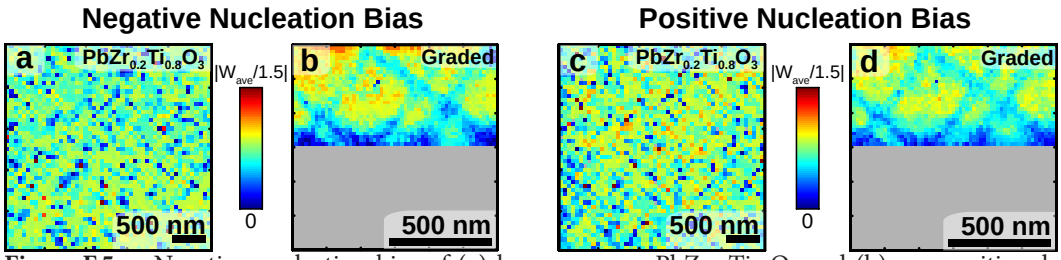

Figure F.5. Negative nucleation bias of (a) homogeneous $PbZr_{0.2}Ti_{0.8}O_3$ and (b) compositionally-graded heterostructures. Positive nucleation bias of (c) homogeneous $PbZr_{0.2}Ti_{0.8}O_3$ and (d) compositionally-graded heterostructures.

In addition, these fitted loops can be used to understand the nucleation process in these heterostructures. To do this, we can quantify (at each point in the spatial map) the nucleation bias, which we define as the voltage where the piezoresponse deviates 3% (of the loop height/piezoresponse) from the saturation piezoresponse values (Figure F.5a-d). Looking at these spatial maps, we observe that in the homogeneous heterostructures that both the positive (Figure F.5a) and negative (Figure F.5c) nucleation bias is slightly suppressed at, or near, the *a* domain. This observation is consistent with theories of ferroelectric switching in homogeneous $PbZr_{0.2}Ti_{0.8}O_3$ heterostructures, which has demonstrated that 180° switching preferentially nucleates at, or near, ferroelastic domain walls.[9] Similarly, in the compositionally-graded heterostructure we also see a significant reduction in both the negative (Figure F.5b) and positive (Figure F.5d) nucleation bias at, or near, the *a* domains (compared to the *c* domains). The reasons for this reduction in nucleation bias however, is not caused by preferential nucleation, but instead, is the result of having *a* domain in an energetic quandary which can be easily excited to respond

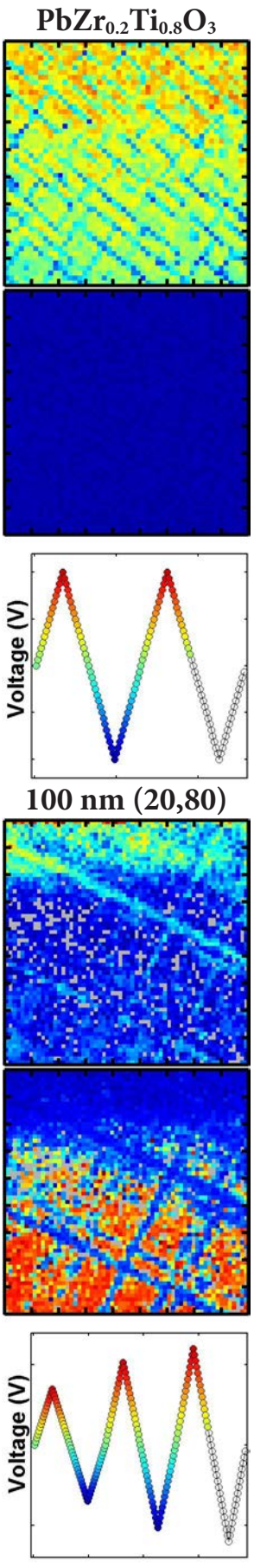

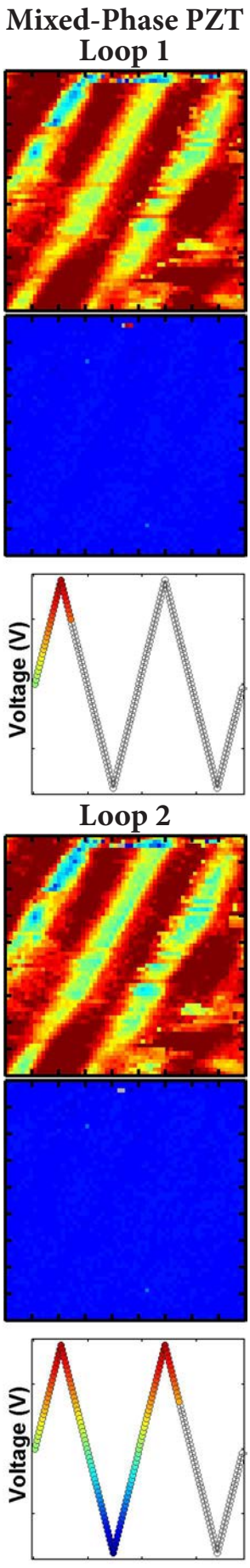

(by growing towards the free surface or by trying to be excluded from the film entirely) by the external bias applied to the tip.

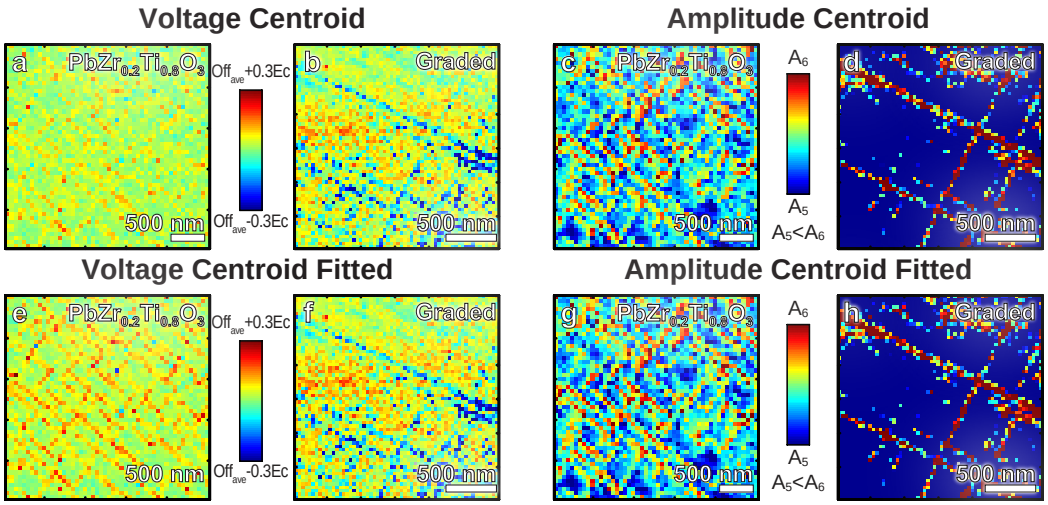

Figure F.6. Spatial maps of the voltage centroid, calculated from the raw piezoelectric hysteresis loop of (a) homogeneous $PbZr_{0.2}Ti_{0.8}O_3$ and (b) compositionally-graded heterostructures; calculated from fitted loop of (c) homogeneous $PbZr_{0.2}Ti_{0.8}O_3$ and (d) compositionally-graded heterostructures; amplitude centroid, the raw piezoelectric hysteresis loop of (e) homogeneous $PbZr_{0.2}Ti_{0.8}O_3$ and (f) compositionally-graded heterostructures; calculated from fitted loop of (g) homogeneous $PbZr_{0.2}Ti_{0.8}O_3$ and (h) compositionally-graded heterostructures.

Moving on, we can use the center of mass of the loops to calculate values for the voltage (Figure F.6a-d) and amplitude loop centroid (Figure F.6e-h) based on both the raw and fitted piezoelectric loop. In all cases the measured centroid based on triangulation and numerical integration are nearly indistinguishable, once again confirming the quality of the loop fits. Starting with the voltage centroids of the homogeneous $PbZr_{1-x}Ti_xO_3$ heterostructures (Figure F.6a,c) we observe no contrast in the image. This result is consistent with the measured voltage offset (included in the main text), a somewhat related loop shape parameter. In the case of the compositionally-graded heterostructures we observe a significant negative shift at or near the *a* domains (Figure F.6b,d), again consistent with the offset calculated in the main text. Now looking at the amplitude centroid for the homogeneous $PbZr_{0.2}Ti_{0.8}O_3$ (Figure F.6e,f) and compositionally-graded heterostructures (Figure F.6g,h) show local enhancement at or near the *a* domains.

Finally, we can calculate the work of switching (or loop area), using a method based on either triangulation of the raw piezoelectric loop or integration of the fitted loop (Figure F.7a-d). Once again, the spatial maps based on triangulation and

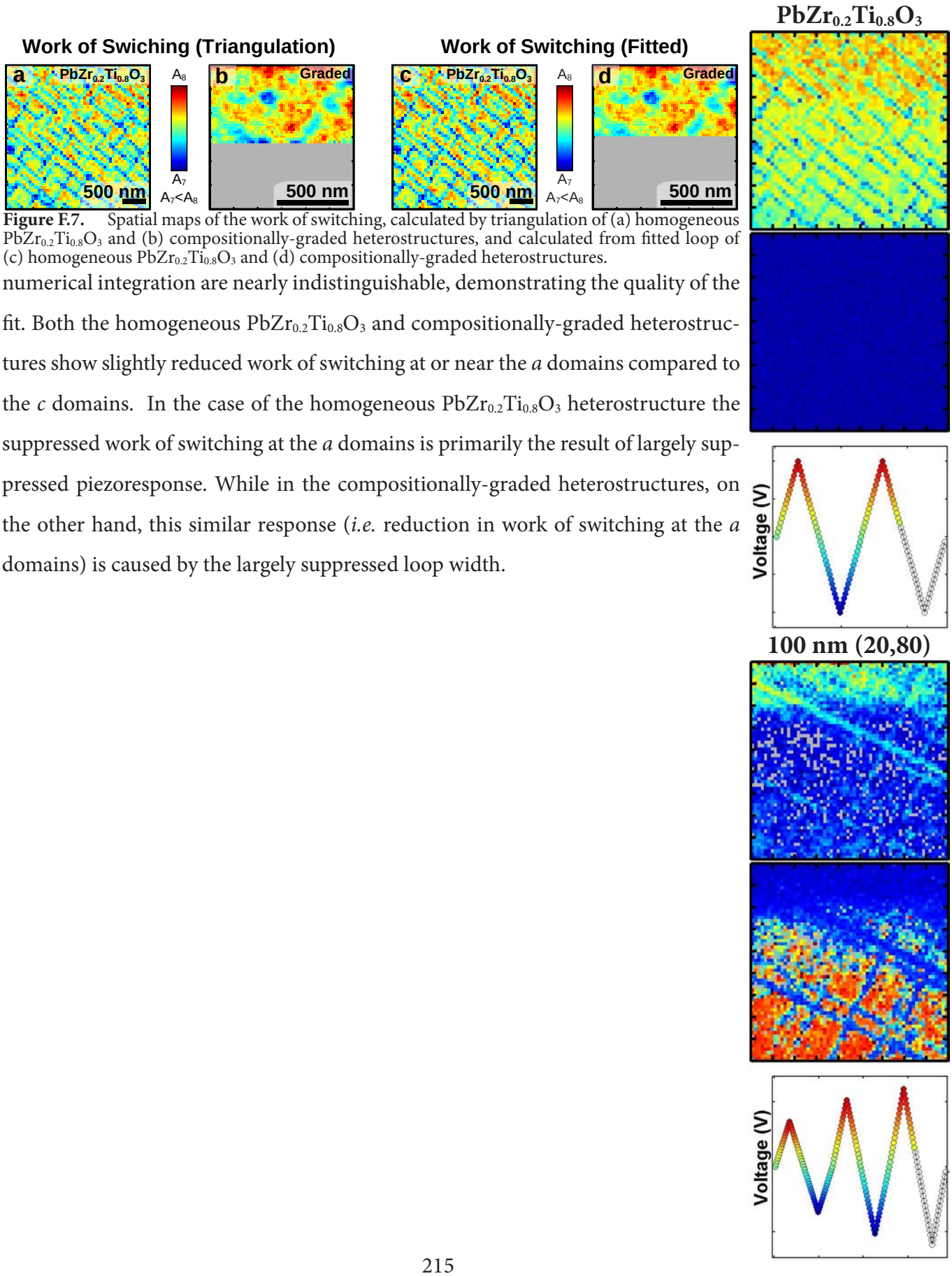

Figure F.7. Spatial maps of the work of switching, calculated by triangulation of (a) homogeneous $PbZr_{0.2}Ti_{0.8}O_3$ and (b) compositionally-graded heterostructures, and calculated from fitted loop of (c) homogeneous $PbZr_{0.2}Ti_{0.8}O_3$ and (d) compositionally-graded heterostructures.

numerical integration are nearly indistinguishable, demonstrating the quality of the fit. Both the homogeneous $PbZr_{0.2}Ti_{0.8}O_3$ and compositionally-graded heterostructures show slightly reduced work of switching at or near the *a* domains compared to the *c* domains. In the case of the homogeneous $PbZr_{0.2}Ti_{0.8}O_3$ heterostructure the suppressed work of switching at the *a* domains is primarily the result of largely suppressed piezoresponse. While in the compositionally-graded heterostructures, on the other hand, this similar response (*i.e.* reduction in work of switching at the *a* domains) is caused by the largely suppressed loop width.

Mixed-Phase PZT
Loop 1

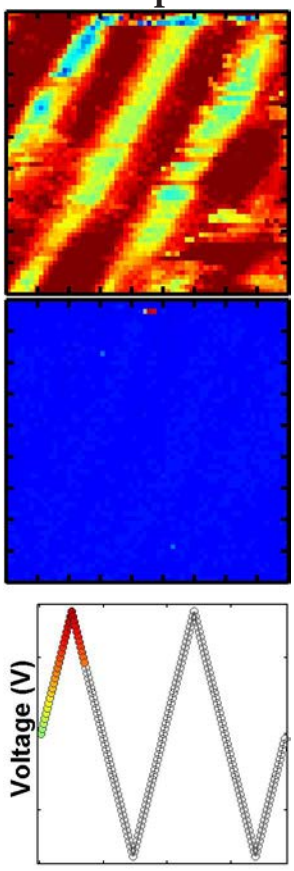

Loop 2

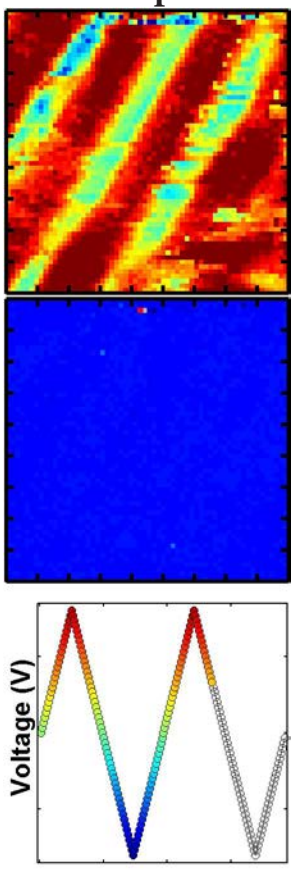

Appendix G

Mixed Phase $PbTiO_3$ Switching Spectroscopy

Included in this section is a subset of the BE-SS (amplitude, phase, loss, and resonance frequency) images of 100 nm thick mixed-phase $PbTiO_3$ heterostructures grown on $SmScO_3$ (110). Note that the scan size of all images is 400 nm.

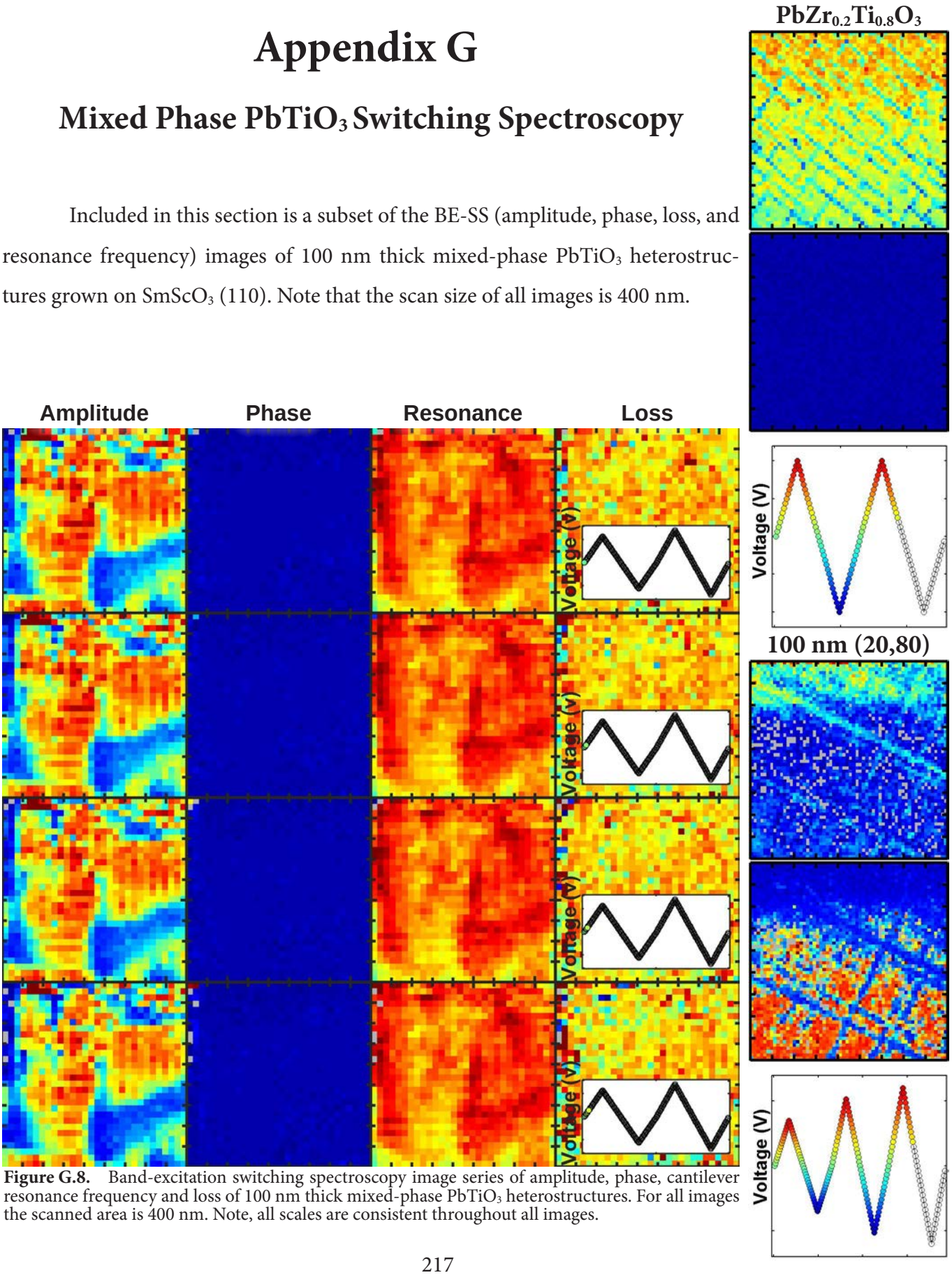

Figure G.8. Band-excitation switching spectroscopy image series of amplitude, phase, cantilever resonance frequency and loss of 100 nm thick mixed-phase $PbTiO_3$ heterostructures. For all images the scanned area is 400 nm. Note, all scales are consistent throughout all images.

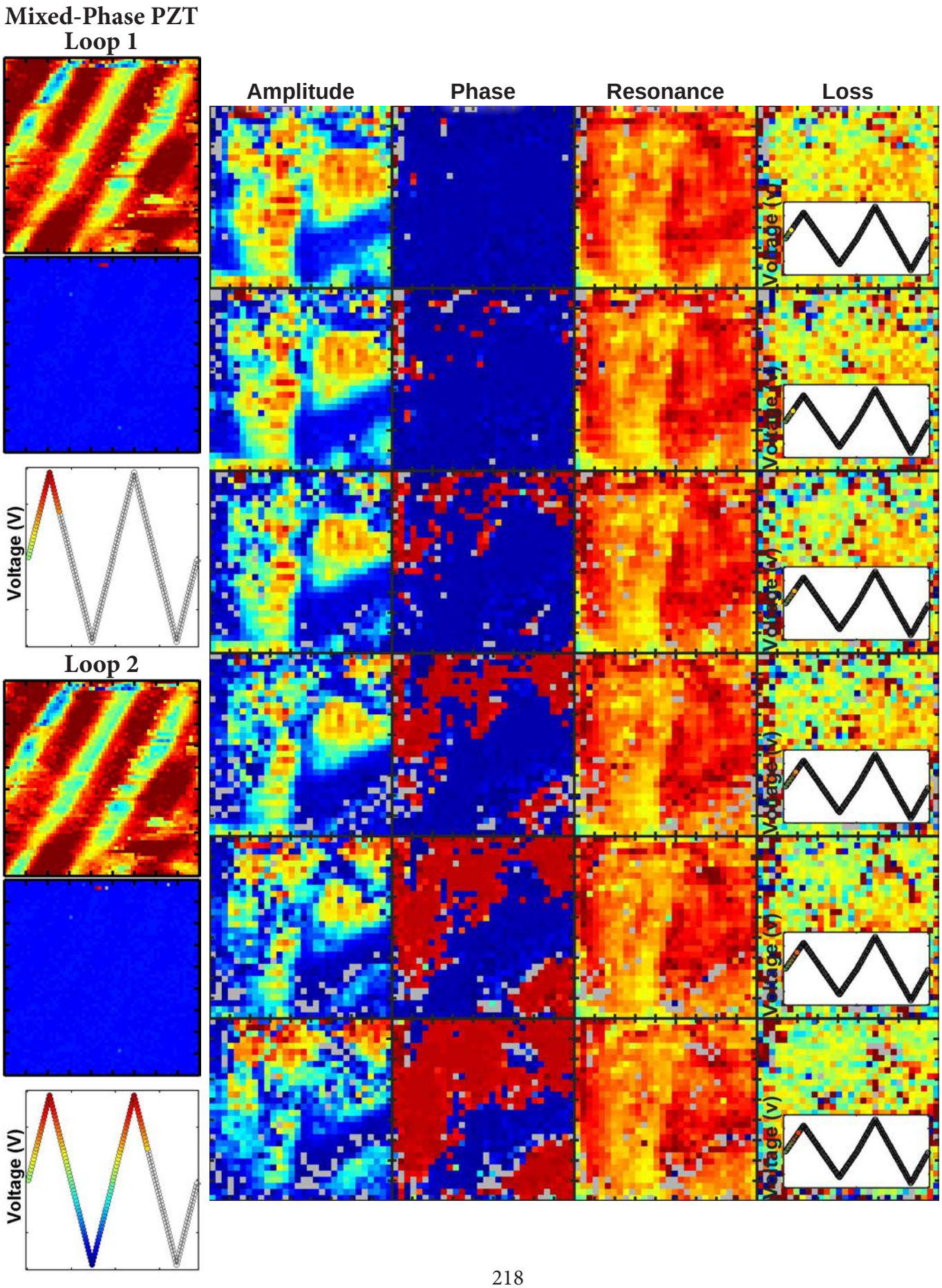
Mixed-Phase PZT
Loop 1
Amplitude
Phase
Resonance
Loss
Voltage (V)
Loop 2
Voltage (V)

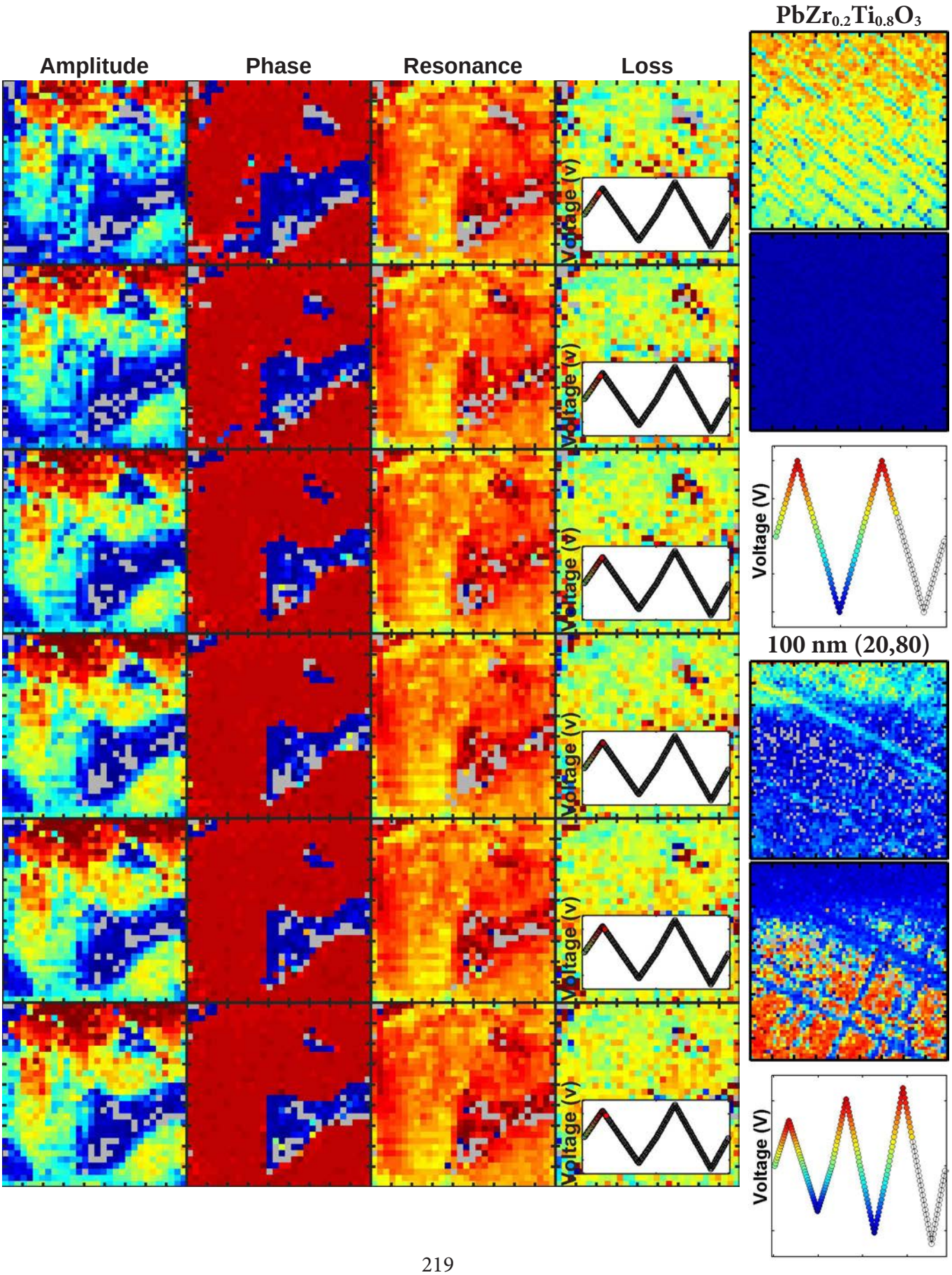
Amplitude
Phase
Resonance
Loss
Voltage (v)
PbZr0.2Ti0.8O3
Voltage (V)
100 nm (20,80)
Voltage (V)

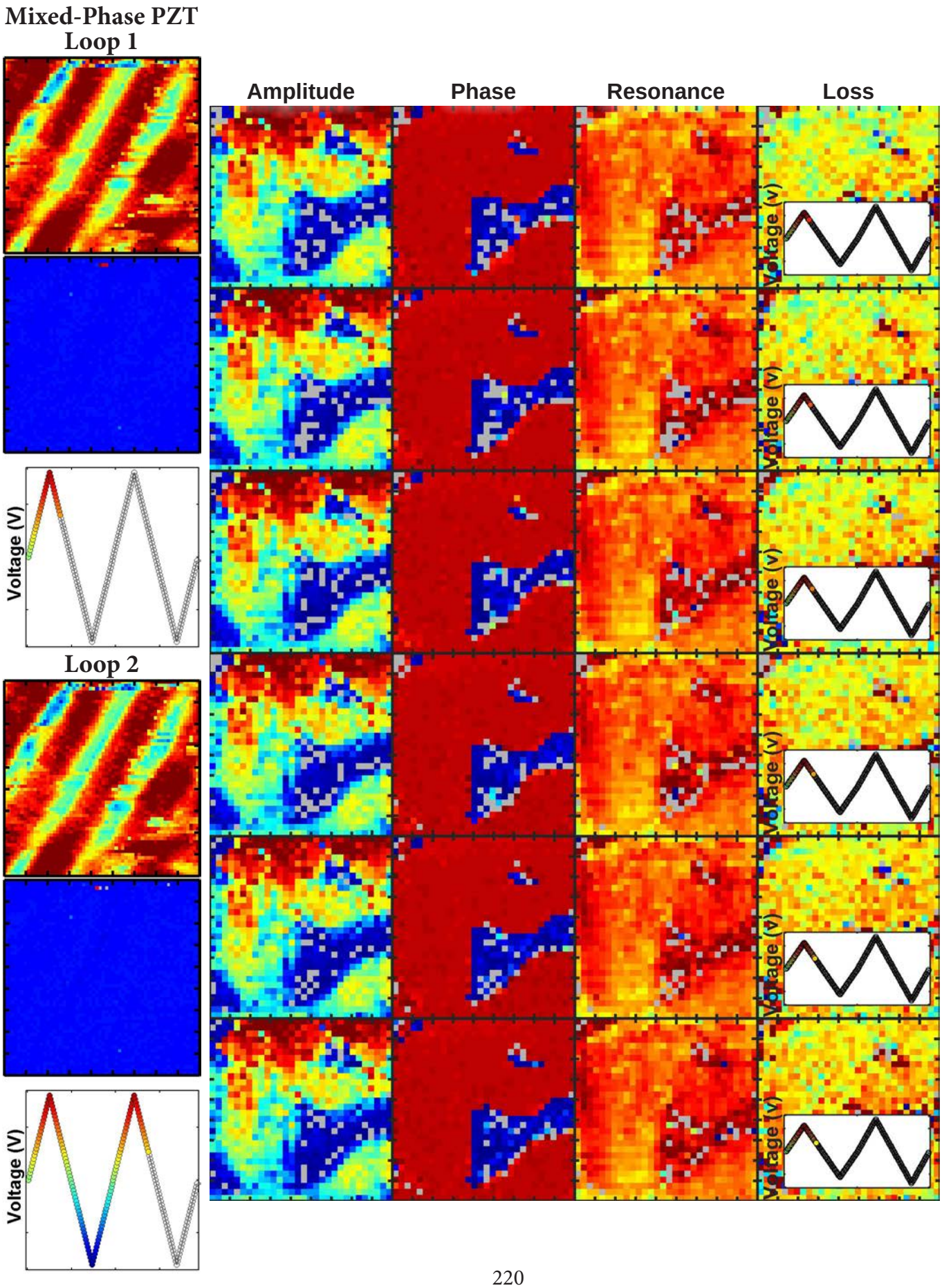
Mixed-Phase PZT
Loop 1
Amplitude
Phase
Resonance
Loss
Voltage (V)
Loop 2
Voltage (V)
Voltage (v)

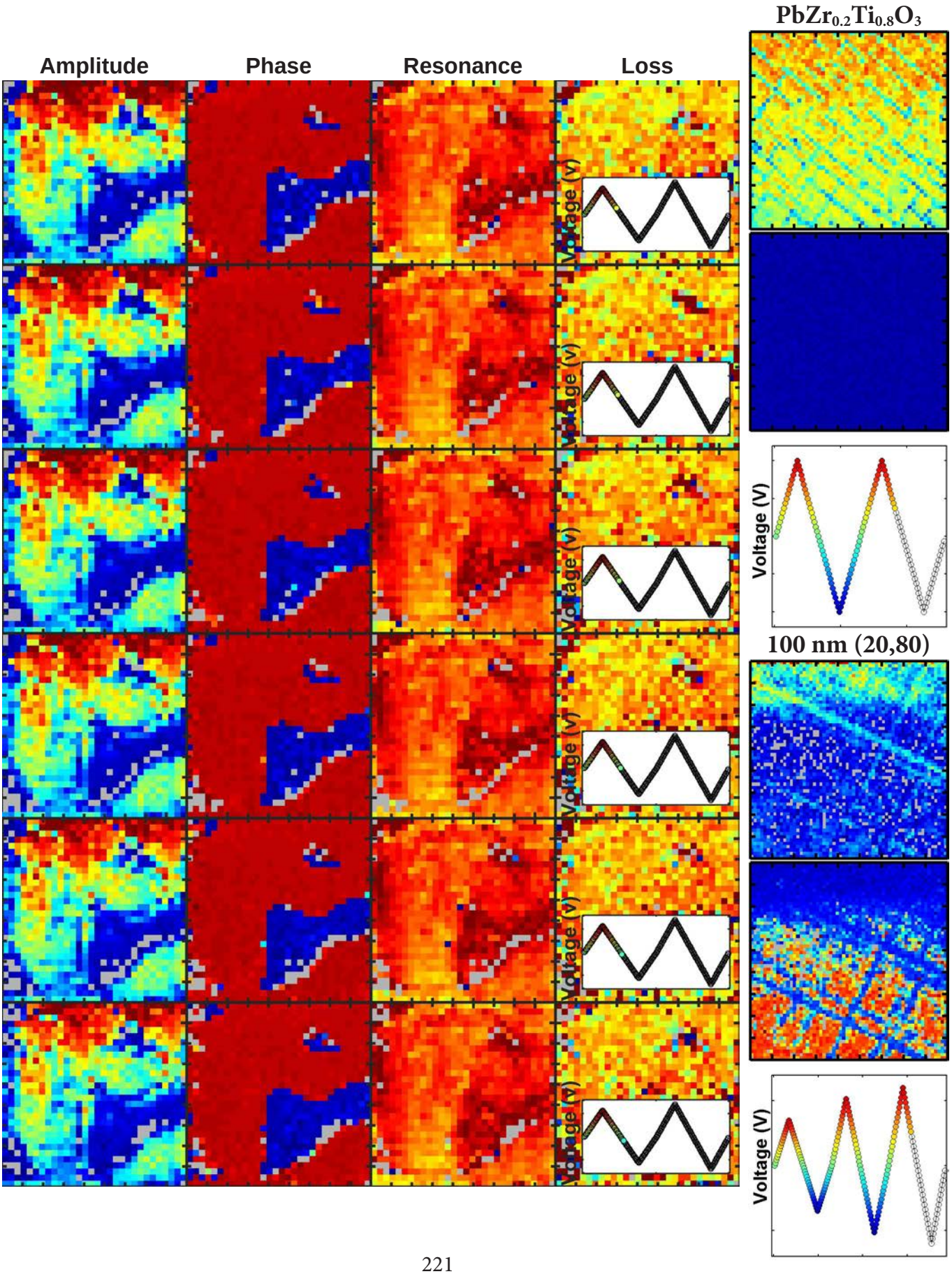
Amplitude
Phase
Resonance
Loss
Voltage (V)
PbZr0.2Ti0.8O3
Voltage (V)
100 nm (20,80)
Voltage (V)

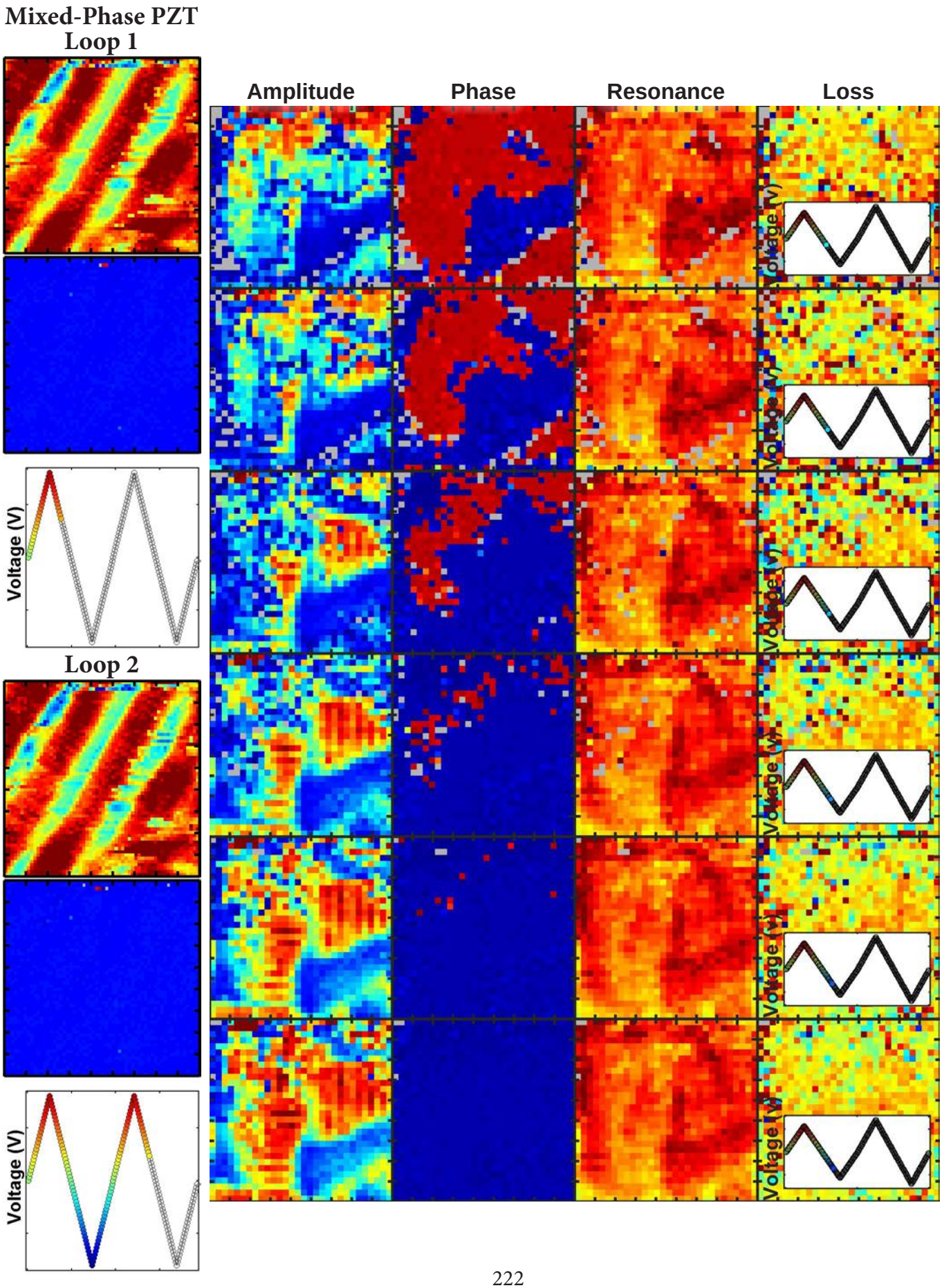
Mixed-Phase PZT
Loop 1
Amplitude
Phase
Resonance
Loss
Voltage (V)
Loop 2
Voltage (V)

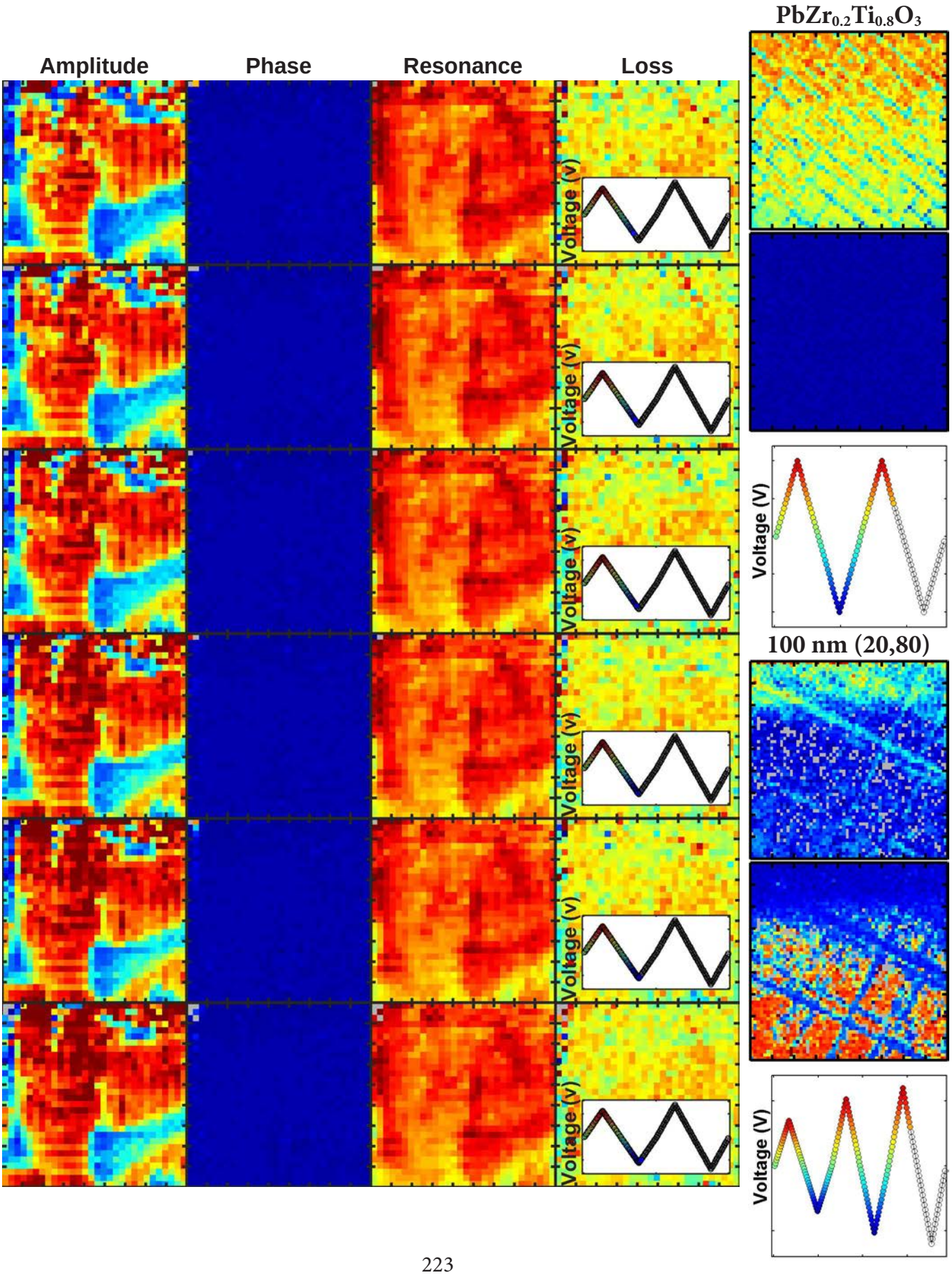
PbZr0.2Ti0.8O3
Amplitude
Phase
Resonance
Loss
Voltage (v)
Voltage (V)
100 nm (20,80)

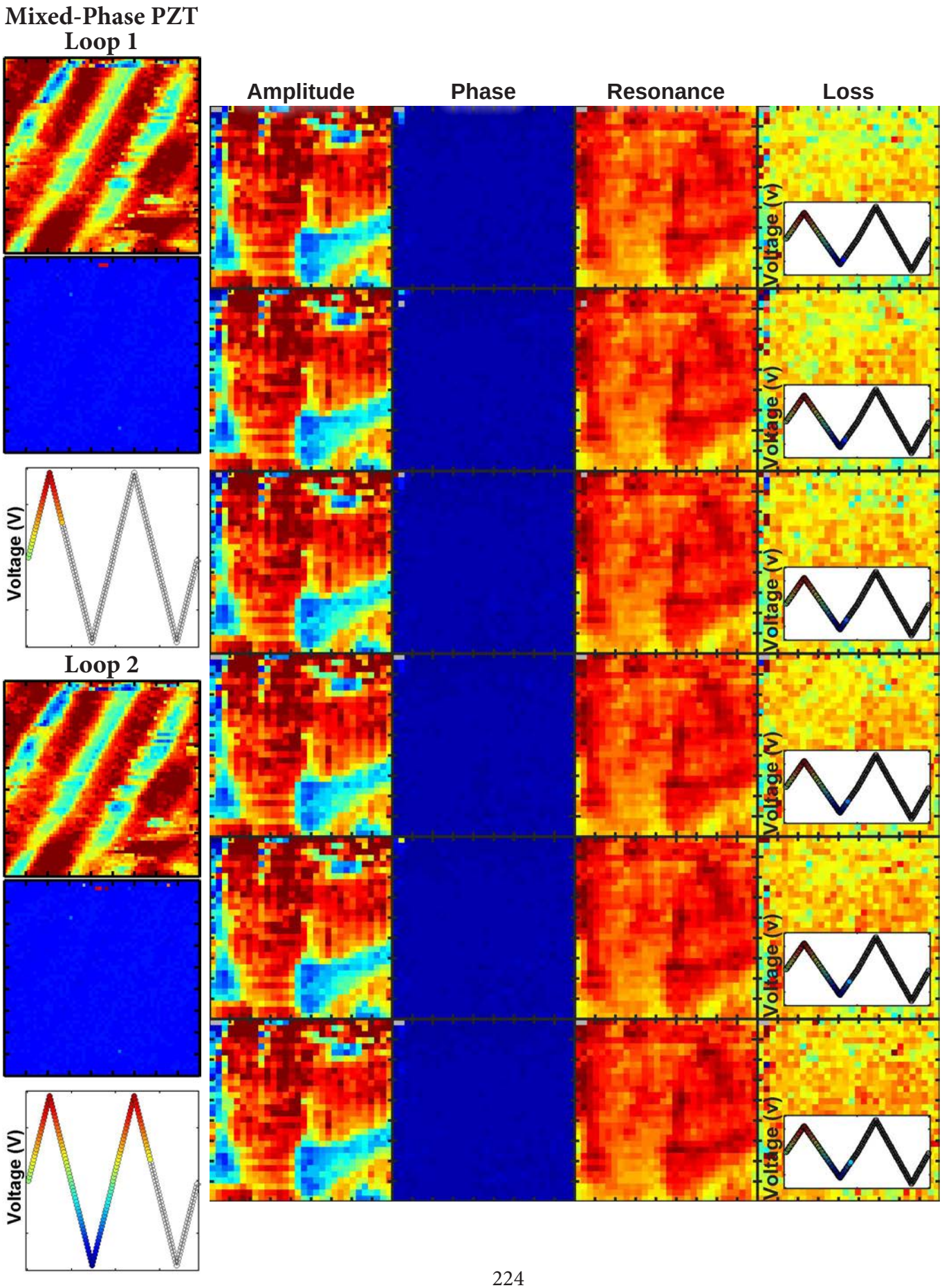
Mixed-Phase PZT
Loop 1
Amplitude
Phase
Resonance
Loss
Voltage (V)
Voltage (v)
Loop 2
Voltage (V)
Voltage (v)

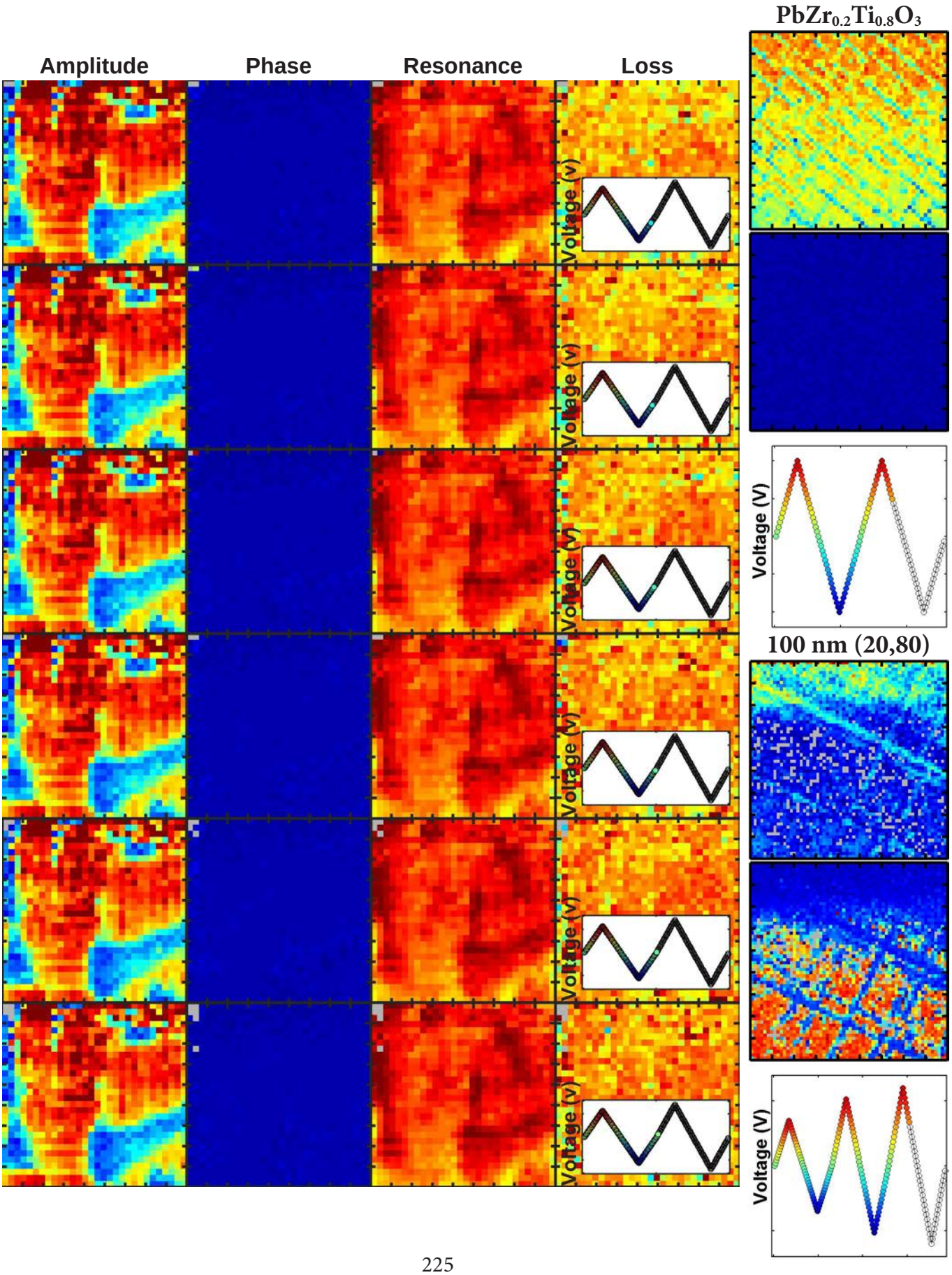
Amplitude
Phase
Resonance
Loss
Voltage (v)
PbZr0.2Ti0.8O3
Voltage (V)
100 nm (20,80)

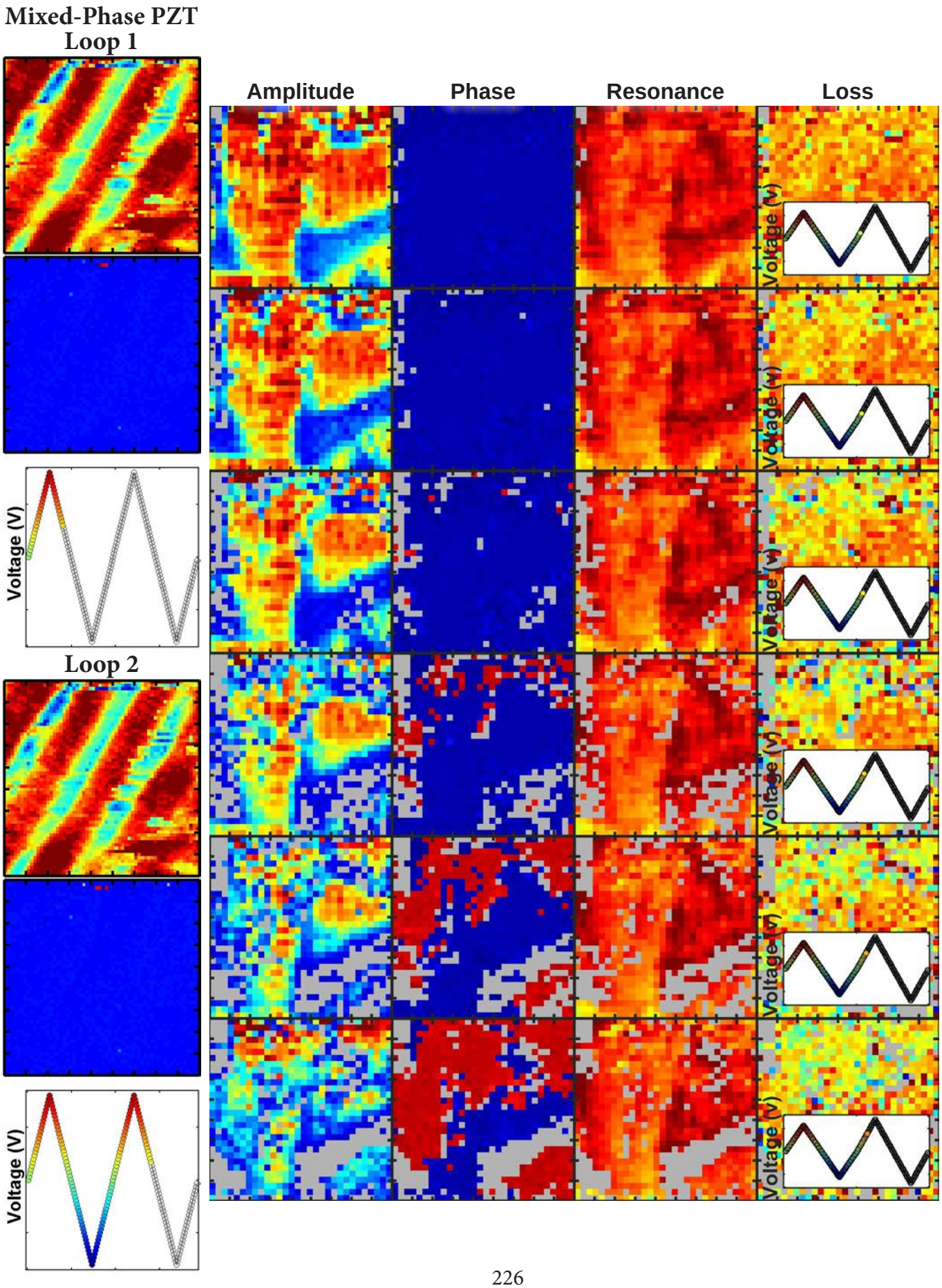
Mixed-Phase PZT
Loop 1
Amplitude
Phase
Resonance
Loss
Voltage (V)
Loop 2
Voltage (V)

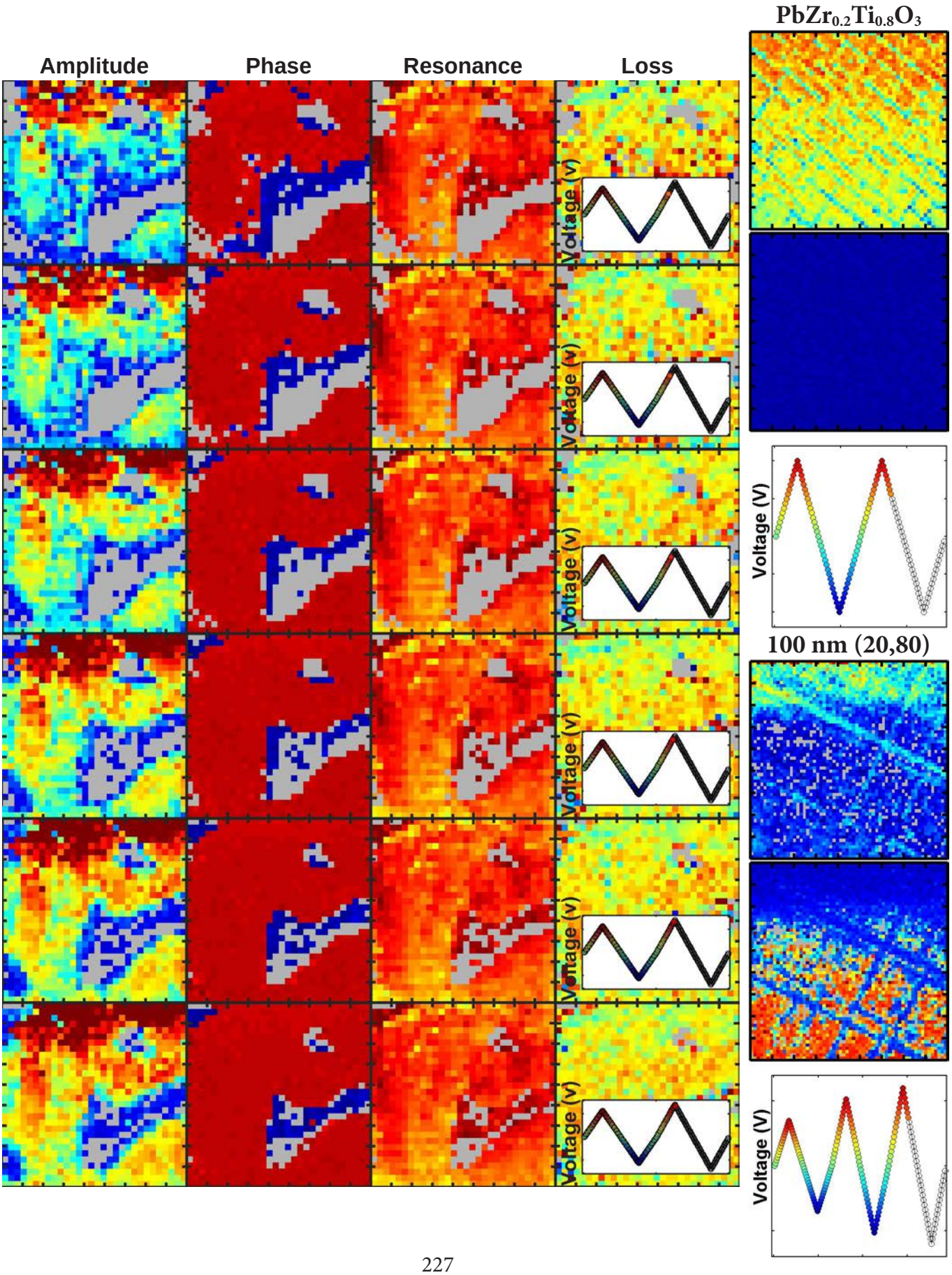
PbZr0.2Ti0.8O3
Amplitude
Phase
Resonance
Loss
Voltage (v)
Voltage (V)
100 nm (20,80)

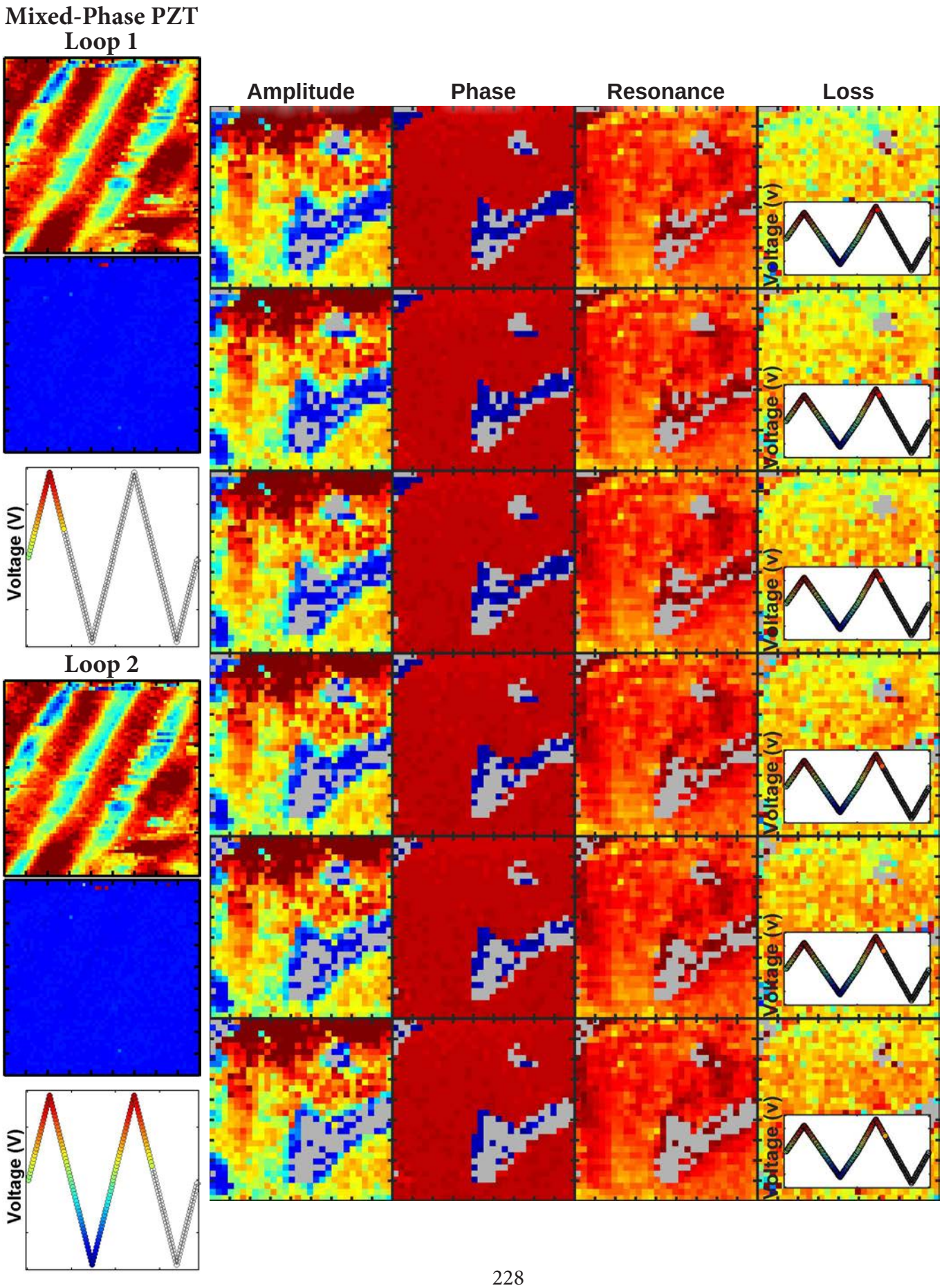
Mixed-Phase PZT
Loop 1
Amplitude
Phase
Resonance
Loss
Voltage (V)
Voltage (v)
Loop 2
Voltage (V)
Voltage (v)

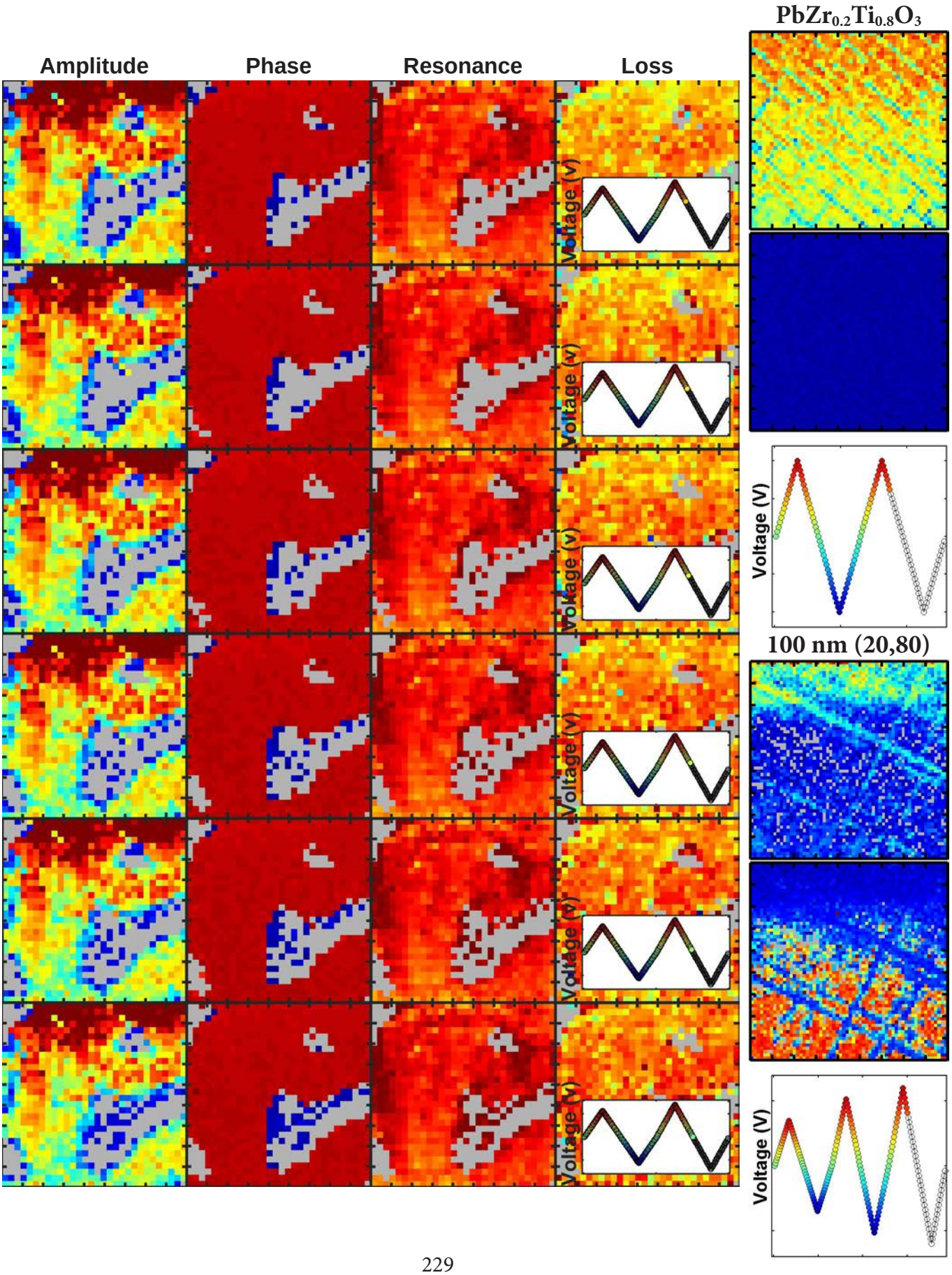
Amplitude
Phase
Resonance
Loss
Voltage (V)
PbZr0.2Ti0.8O3
100 nm (20,80)

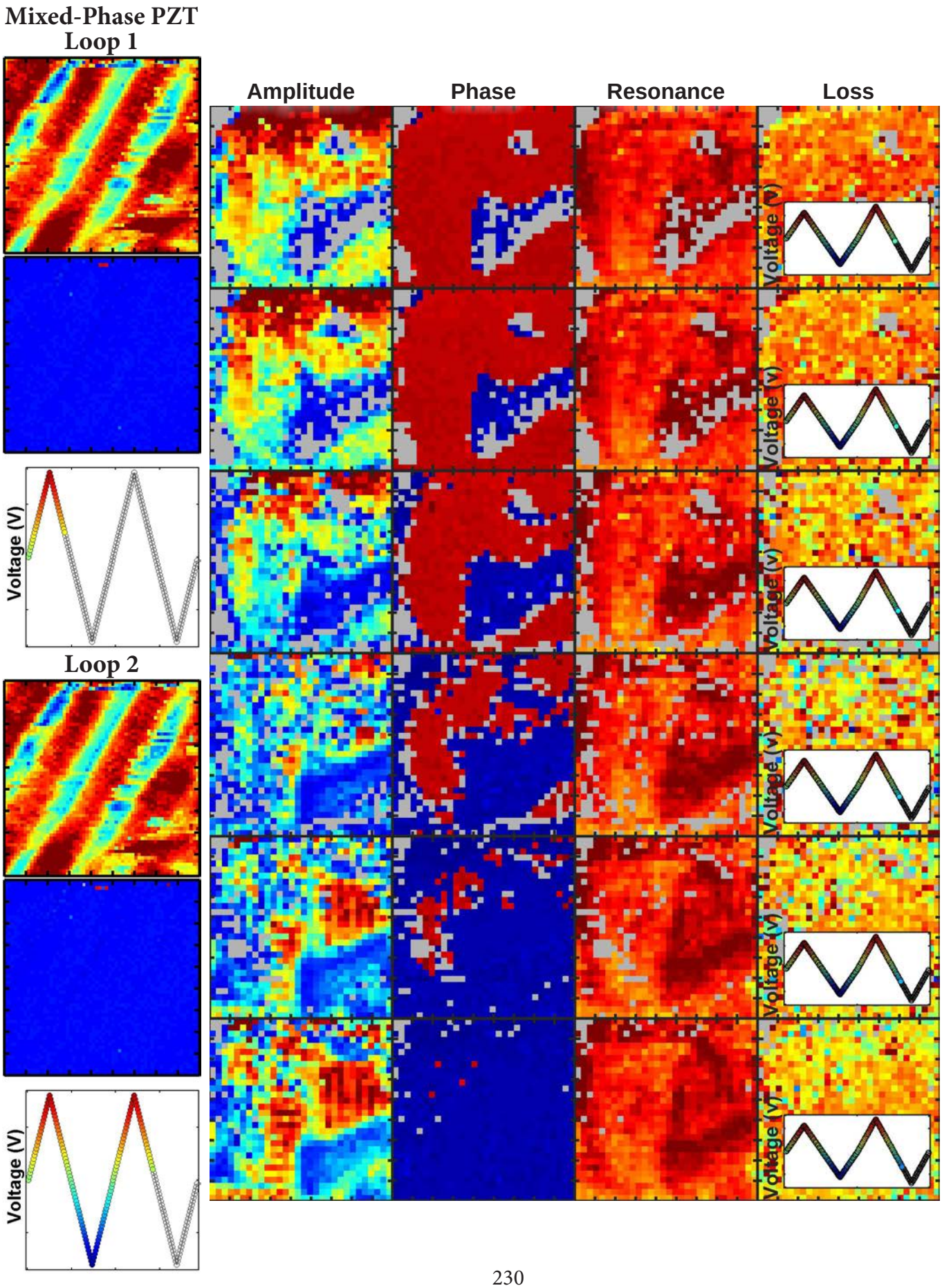
Mixed-Phase PZT
Loop 1
Amplitude
Phase
Resonance
Loss
Voltage (V)
Loop 2
Voltage (V)

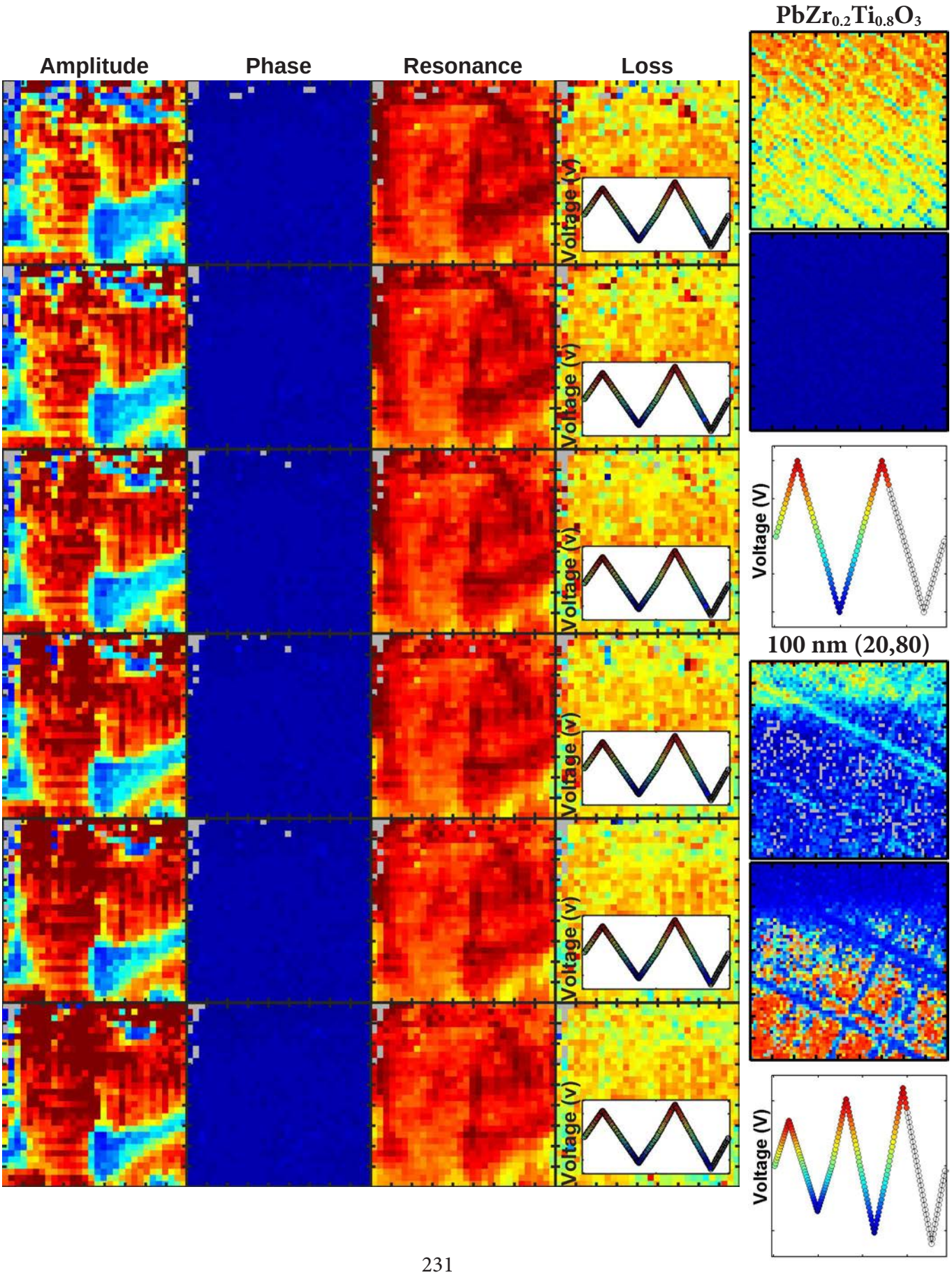
Amplitude
Phase
Resonance
Loss
Voltage (V)
PbZr0.2Ti0.8O3
100 nm (20,80)

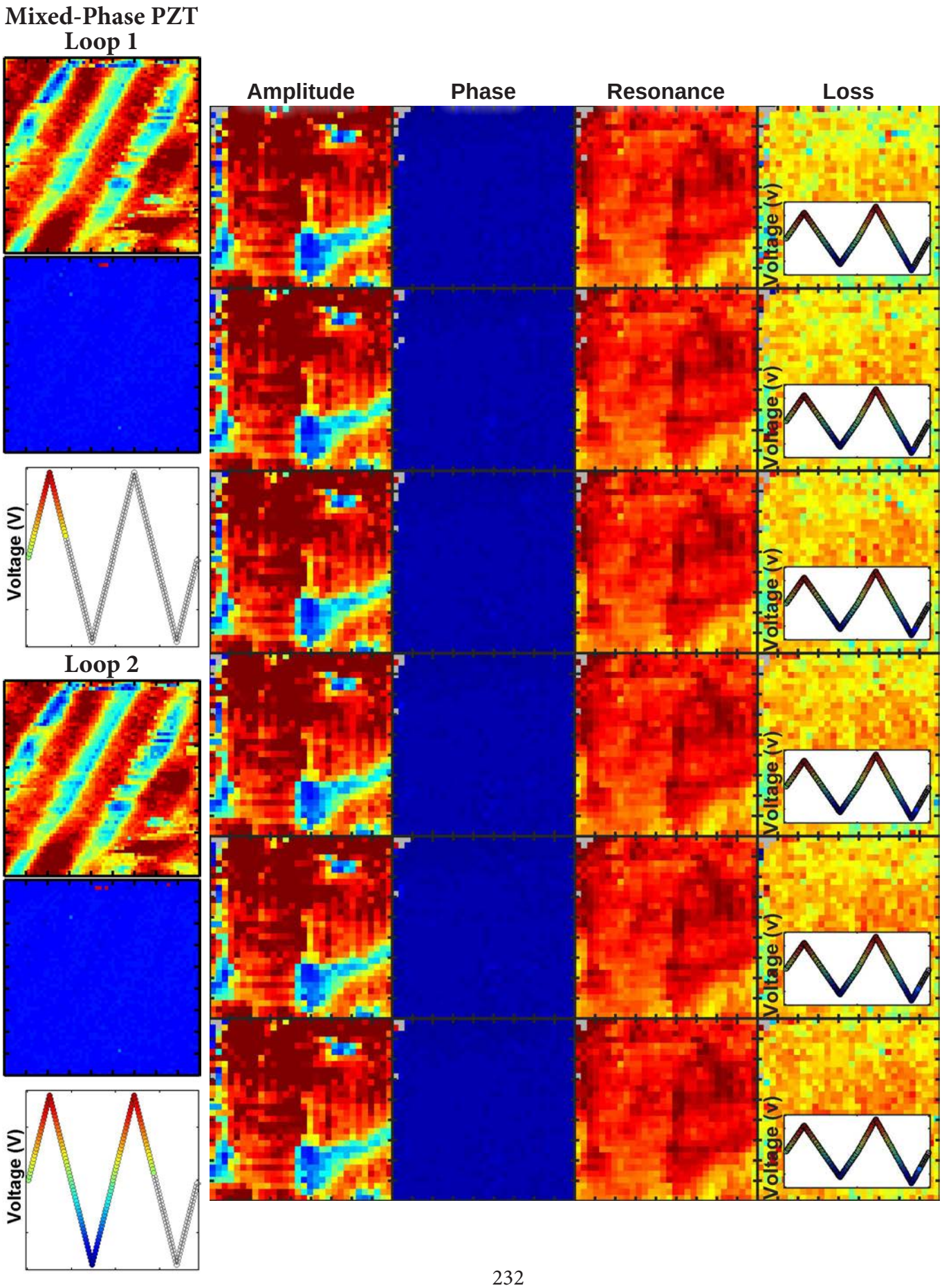
Mixed-Phase PZT
Loop 1
Amplitude
Phase
Resonance
Loss
Voltage (V)
Loop 2
Voltage (V)
Voltage (v)

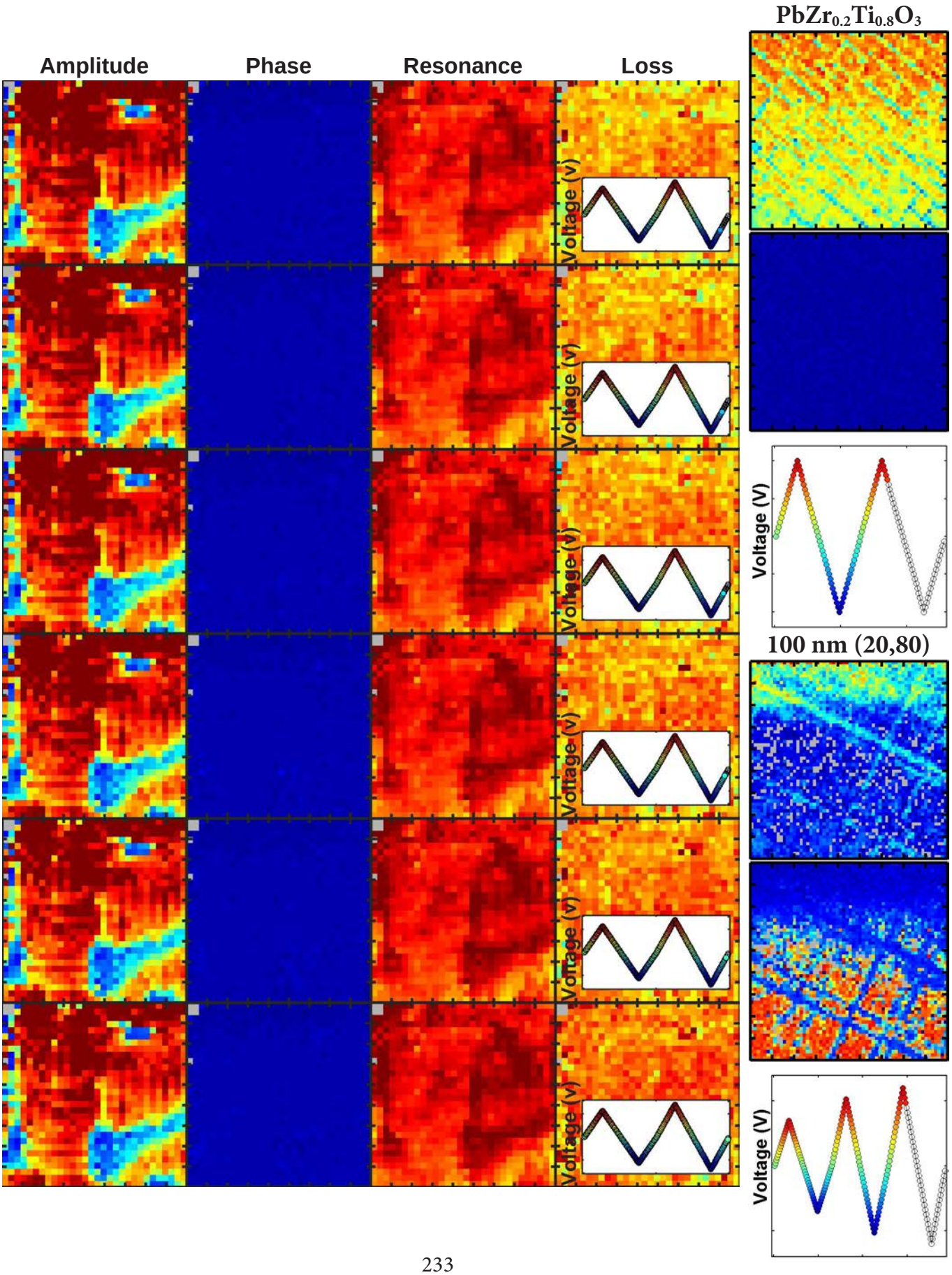
Amplitude
Phase
Resonance
Loss
Voltage (v)
PbZr0.2Ti0.8O3
Voltage (V)
100 nm (20,80)

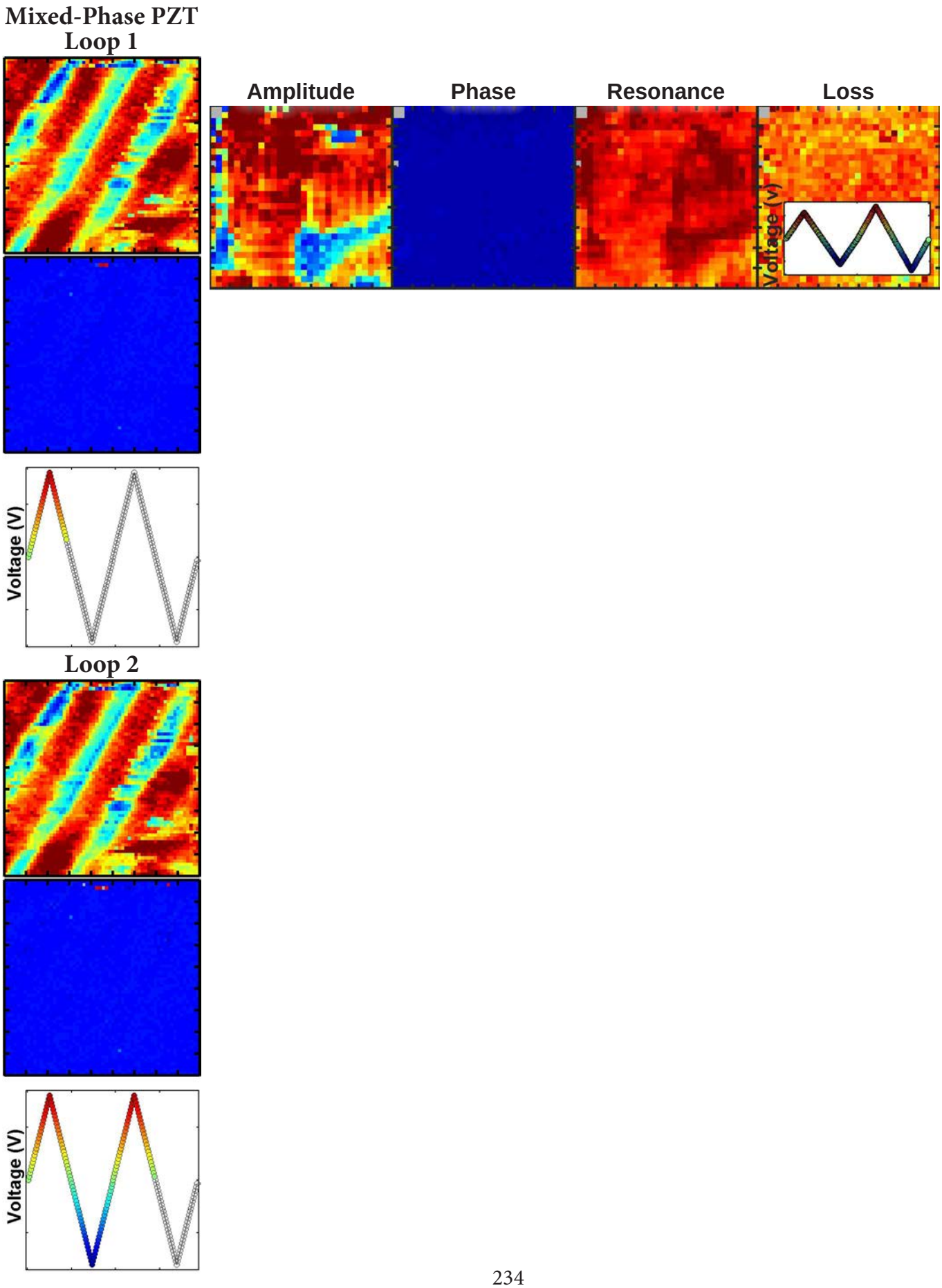
Mixed-Phase PZT
Loop 1
Amplitude
Phase
Resonance
Loss
Voltage (v)
Voltage (V)
Loop 2
Voltage (V)

Appendix H

Mixed-Phase $PbTiO_3$ Loop Shape Parameters

In this section we have included preliminary loop fitting results (from the switching spectroscopy measurement shown in Appendix G) on 100 nm thick mixed-phase $PbTiO_3/Ba_{0.5}Sr_{0.5}RuO_3$ (15 nm)/$SmScO_3$ (110). All loop fitting results are based on the custom multi-step loop fitting algorithm. The results presented in this section are preliminary and included in this thesis to demonstrate the methods, methodologies, and typical results. We are currently in the process of optimizing the experimental dataset, loop fitting algorithm, and analysis techniques to aid in deriving physical insight from these experiments. Note, all scanned regions are 400 nm x 400 nm.

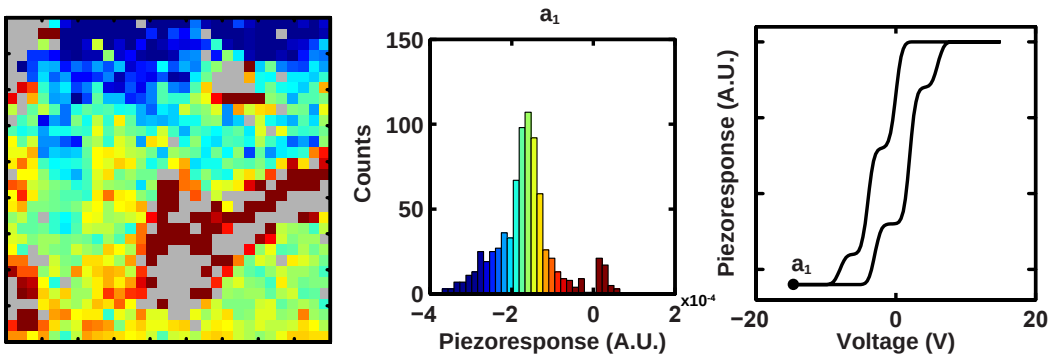

Figure H.1. Multi-step loop fitting result (a_1) of 100 nm thick mixed-phase $PbTiO_3$ on $SmScO_3$ (110).

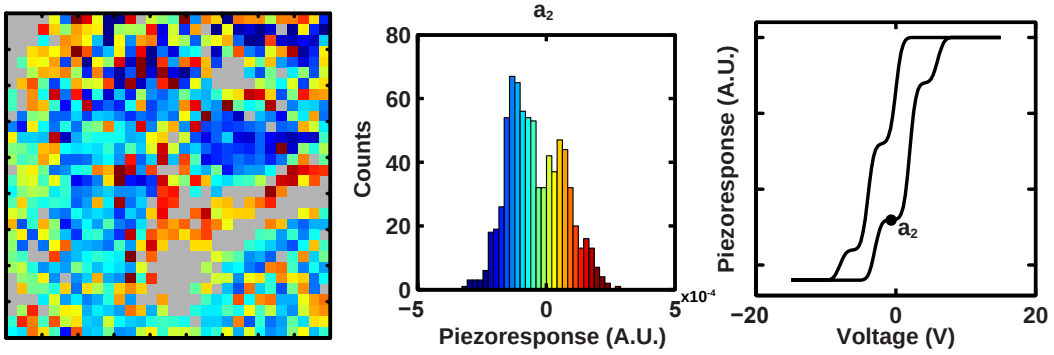

Figure H.2. Multi-step loop fitting result (a_2) of 100 nm thick mixed-phase $PbTiO_3$ on $SmScO_3$ (110).

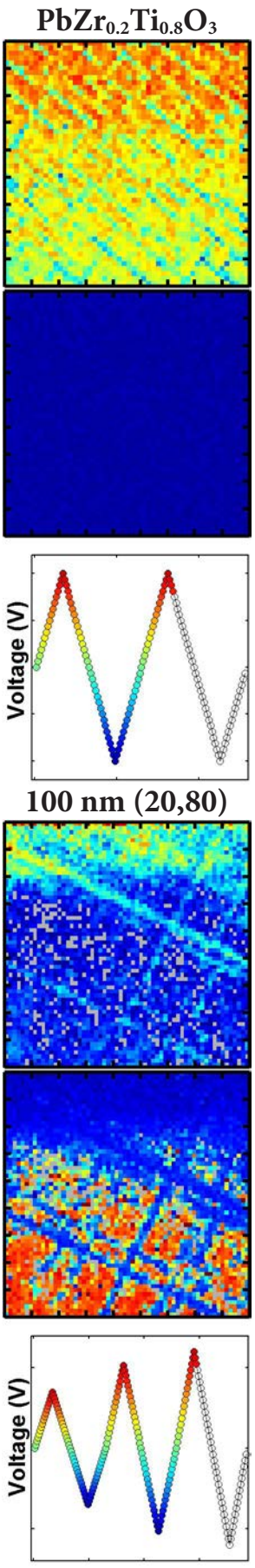

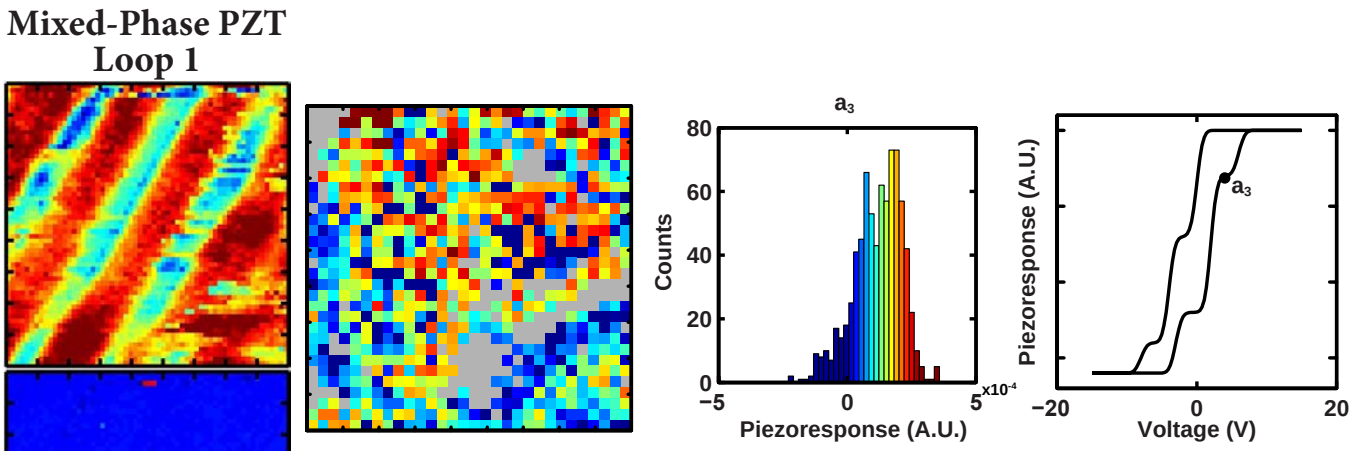

Figure H.3. Multi-step loop fitting result (a_3) of 100 nm thick mixed-phase $PbTiO_3$ on $SmScO_3$ (110).

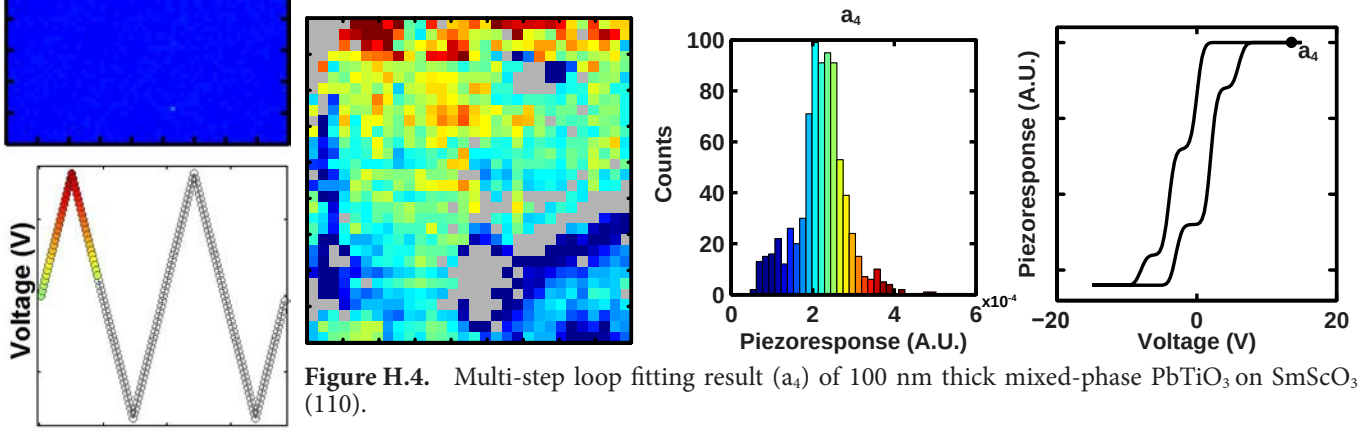

Figure H.4. Multi-step loop fitting result (a_4) of 100 nm thick mixed-phase $PbTiO_3$ on $SmScO_3$ (110).

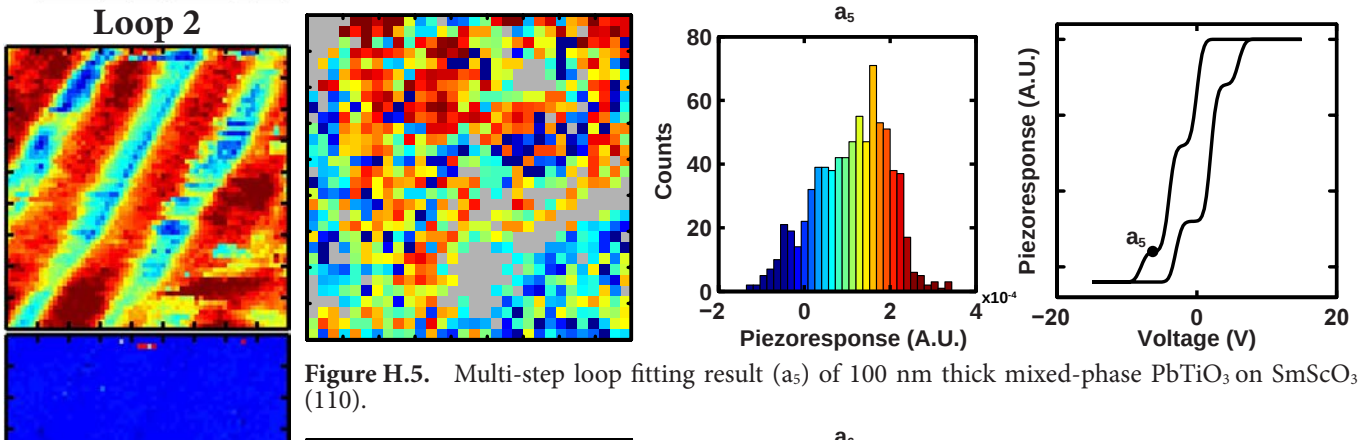

Figure H.5. Multi-step loop fitting result (a_5) of 100 nm thick mixed-phase $PbTiO_3$ on $SmScO_3$ (110).

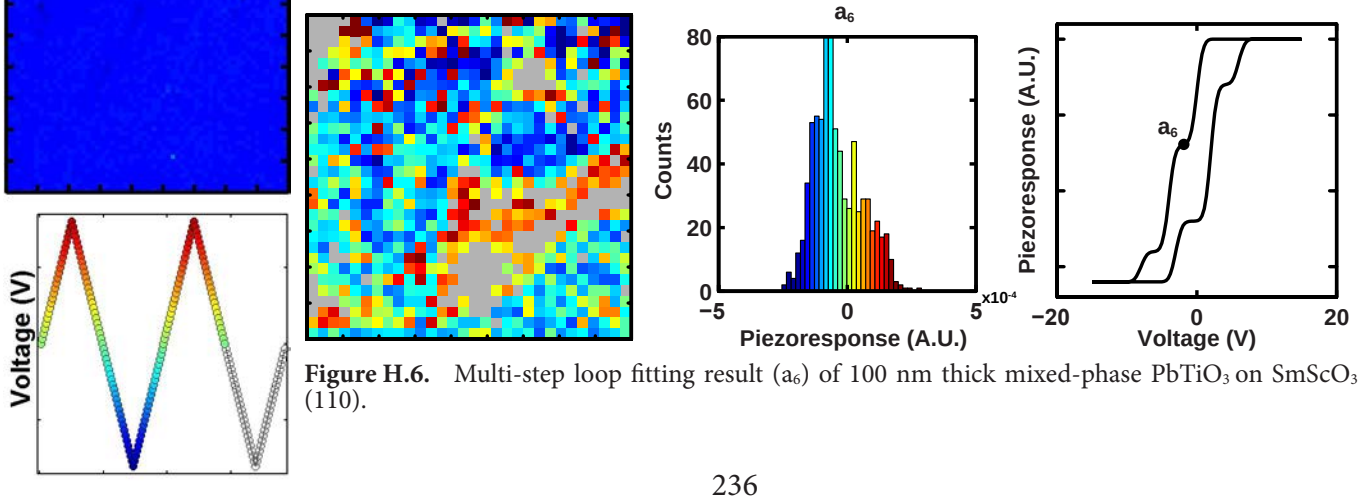

Figure H.6. Multi-step loop fitting result (a_6) of 100 nm thick mixed-phase $PbTiO_3$ on $SmScO_3$ (110).

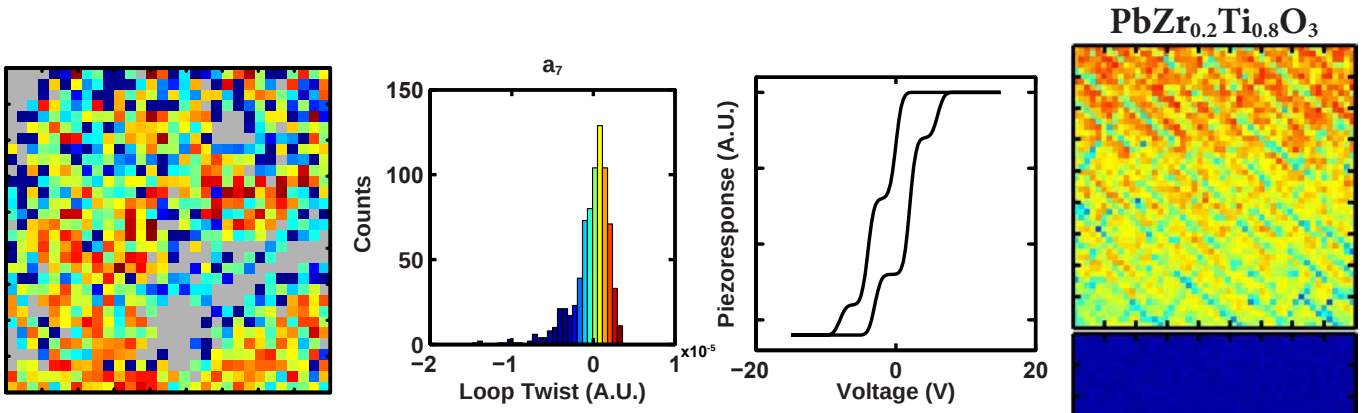

Figure H.7. Multi-step loop fitting result (a_7) of 100 nm thick mixed-phase $PbTiO_3$ on $SmScO_3$ (110).

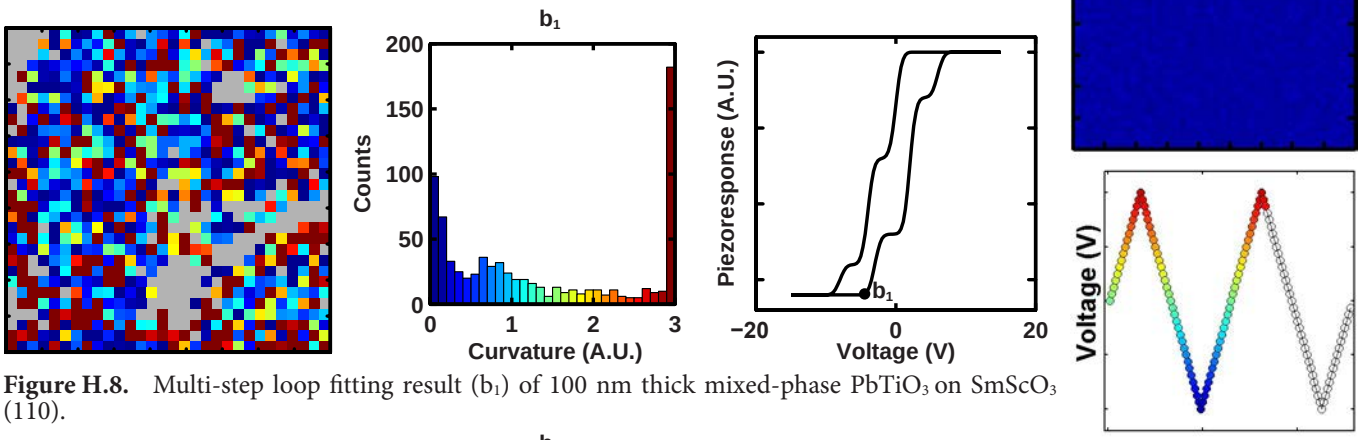

Figure H.8. Multi-step loop fitting result (b_1) of 100 nm thick mixed-phase $PbTiO_3$ on $SmScO_3$ (110).

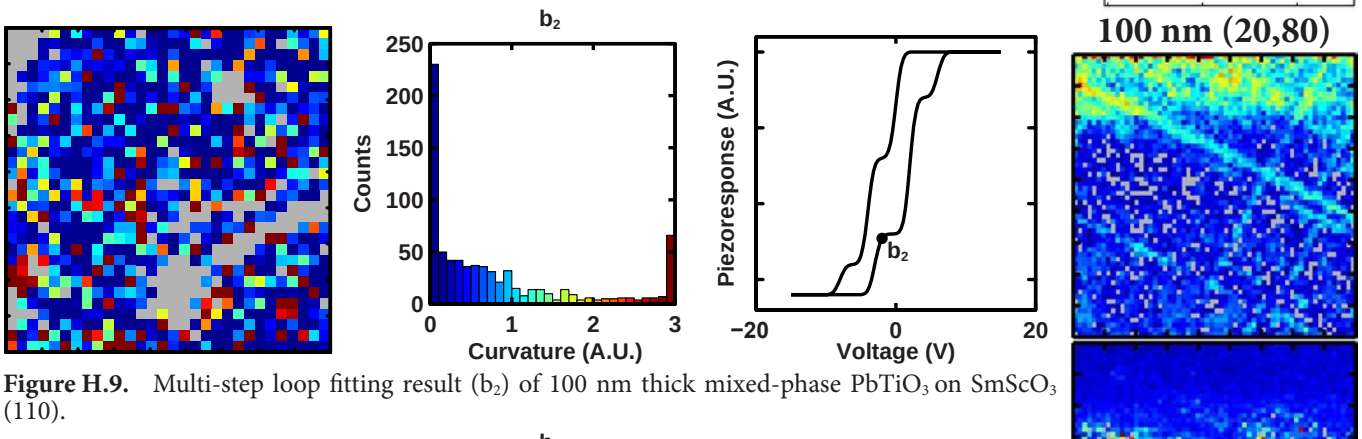

Figure H.9. Multi-step loop fitting result (b_2) of 100 nm thick mixed-phase $PbTiO_3$ on $SmScO_3$ (110).

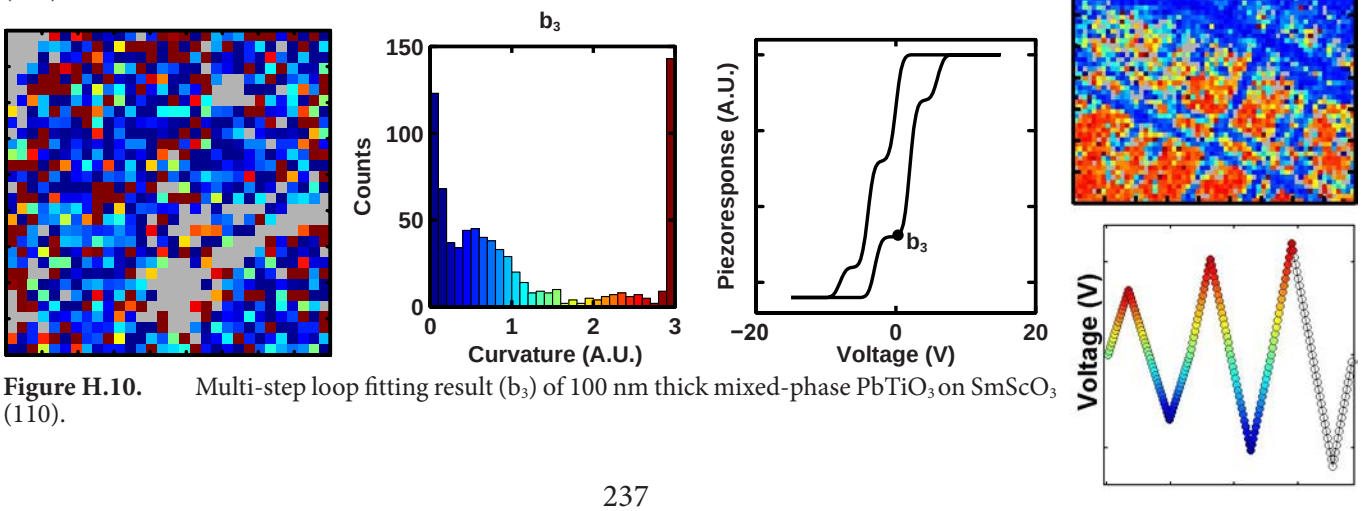

Figure H.10. Multi-step loop fitting result (b_3) of 100 nm thick mixed-phase $PbTiO_3$ on $SmScO_3$ (110).

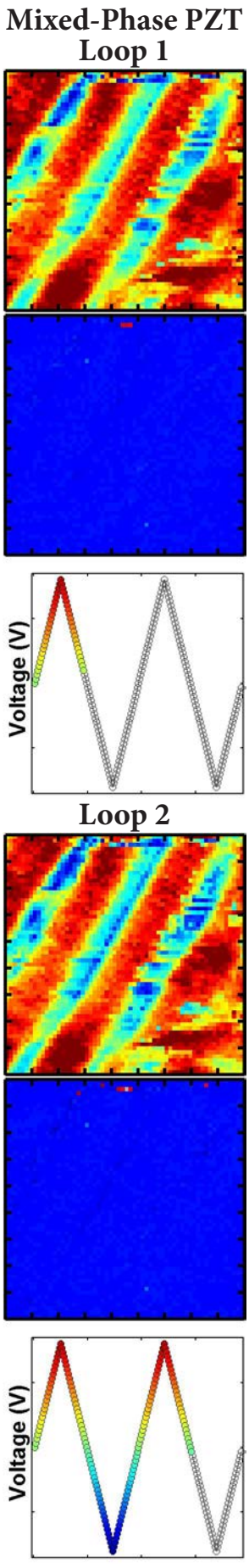

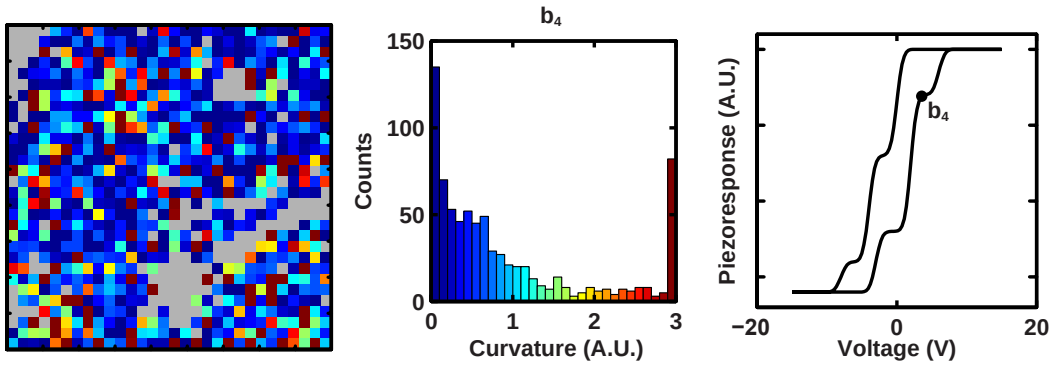

Figure H.11. Multi-step loop fitting result (b_4) of 100 nm thick mixed-phase $PbTiO_3$ on $SmScO_3$ (110).

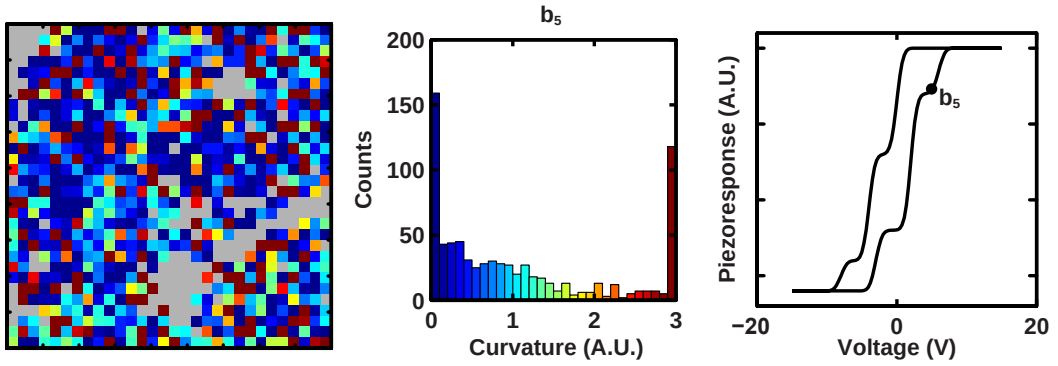

Figure H.12. Multi-step loop fitting result (b_5) of 100 nm thick mixed-phase $PbTiO_3$ on $SmScO_3$ (110).

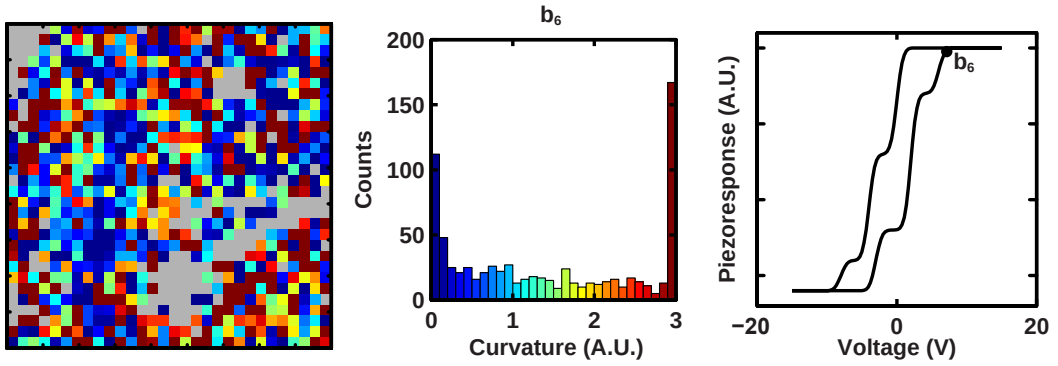

Figure H.13. Multi-step loop fitting result (b_6) of 100 nm thick mixed-phase $PbTiO_3$ on $SmScO_3$ (110).

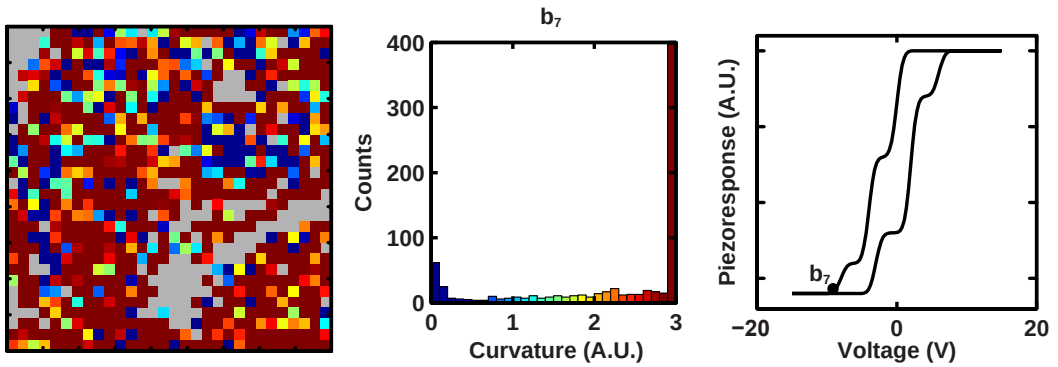

Figure H.14. Multi-step loop fitting result (b_7) of 100 nm thick mixed-phase $PbTiO_3$ on $SmScO_3$ (110).

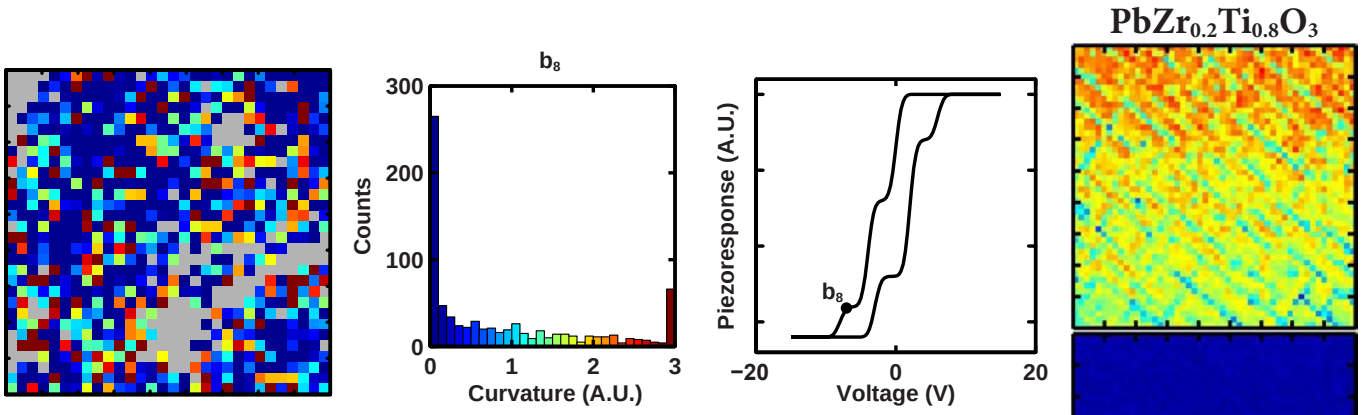

Figure H.15. Multi-step loop fitting result (b_8) of 100 nm thick mixed-phase $PbTiO_3$ on $SmScO_3$ (110).

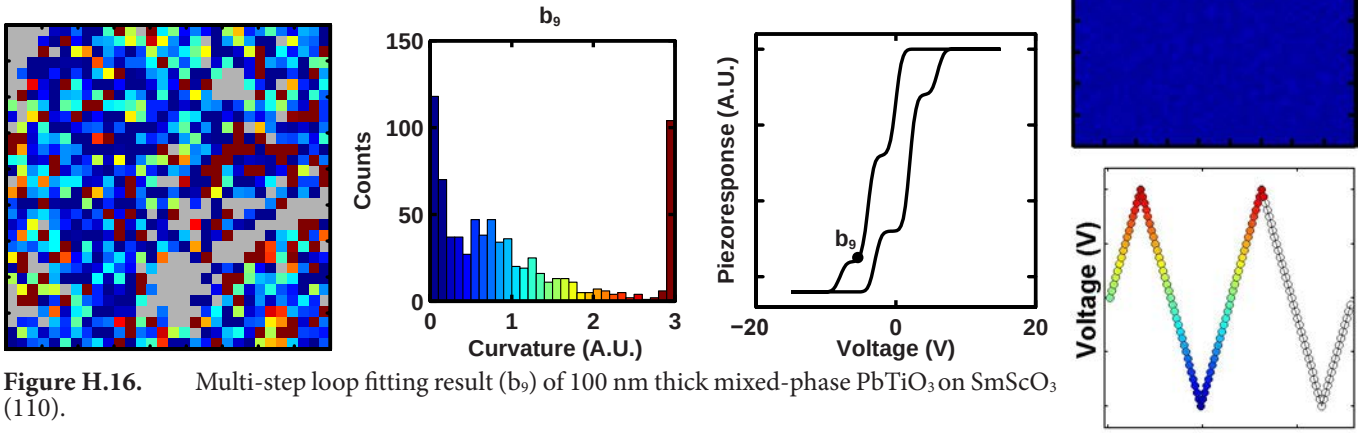

Figure H.16. Multi-step loop fitting result (b_9) of 100 nm thick mixed-phase $PbTiO_3$ on $SmScO_3$ (110).

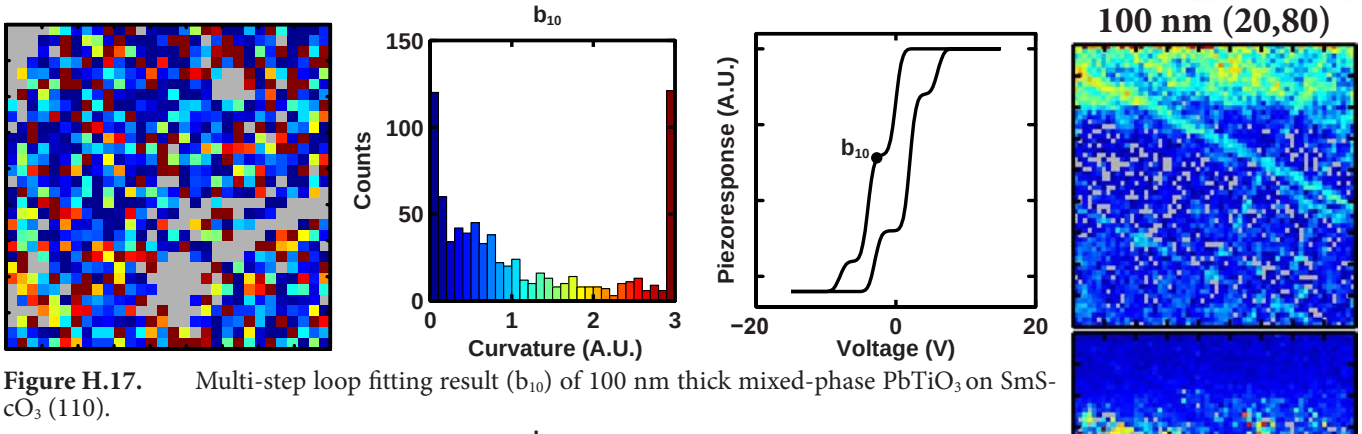

Figure H.17. Multi-step loop fitting result (b_{10}) of 100 nm thick mixed-phase $PbTiO_3$ on $SmScO_3$ (110).

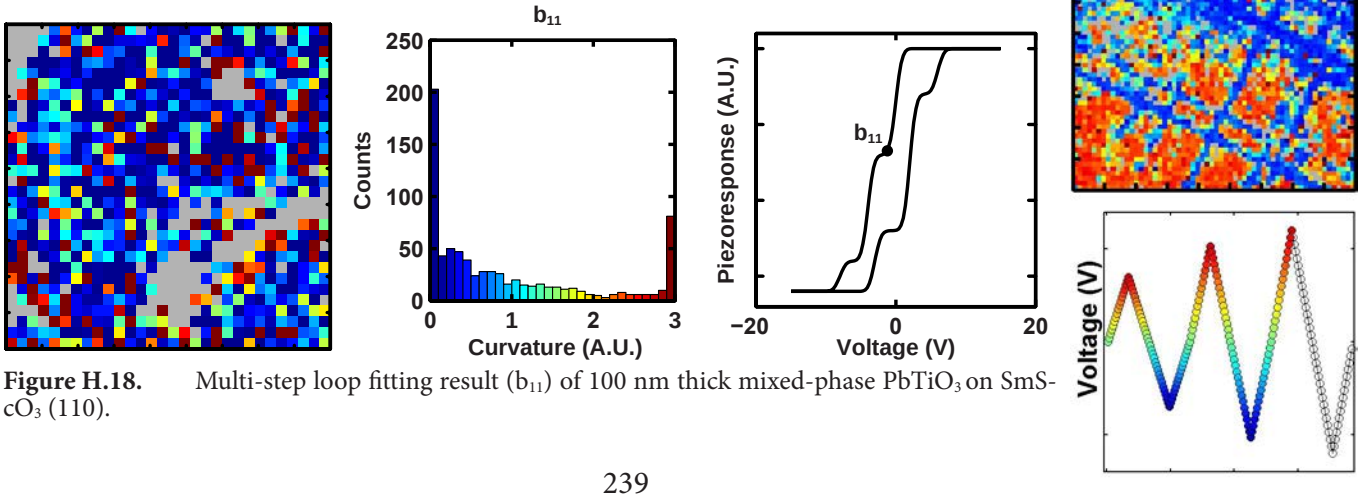

Figure H.18. Multi-step loop fitting result (b_{11}) of 100 nm thick mixed-phase $PbTiO_3$ on $SmScO_3$ (110).

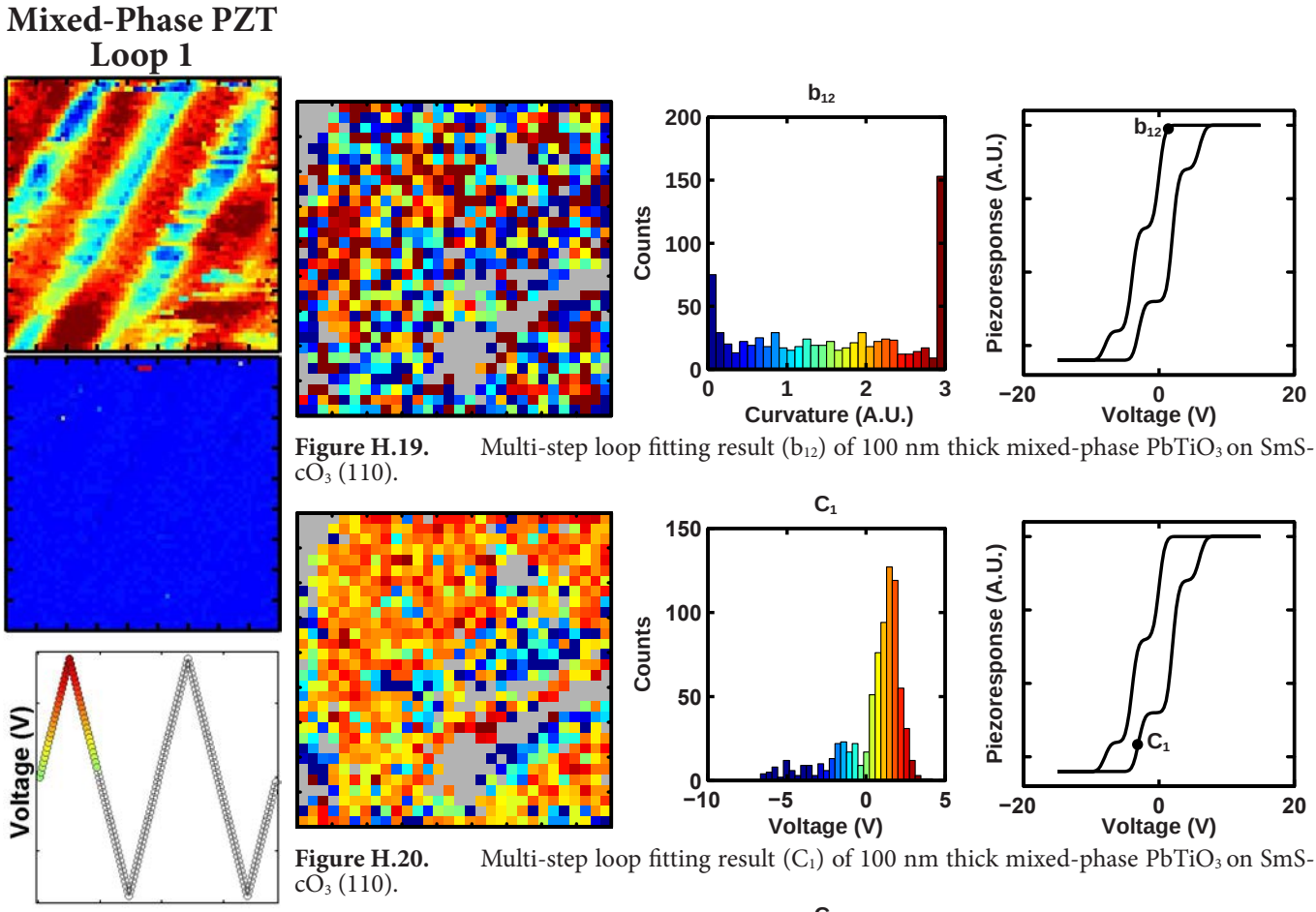

Figure H.19. Multi-step loop fitting result (b_{12}) of 100 nm thick mixed-phase $PbTiO_3$ on $SmScO_3$ (110).

Figure H.20. Multi-step loop fitting result (C_1) of 100 nm thick mixed-phase $PbTiO_3$ on $SmScO_3$ (110).

Figure H.21. Multi-step loop fitting result (C_2) of 100 nm thick mixed-phase $PbTiO_3$ on $SmScO_3$ (110).

Figure H.22. Multi-step loop fitting result (C_3) of 100 nm thick mixed-phase $PbTiO_3$ on $SmScO_3$ (110).

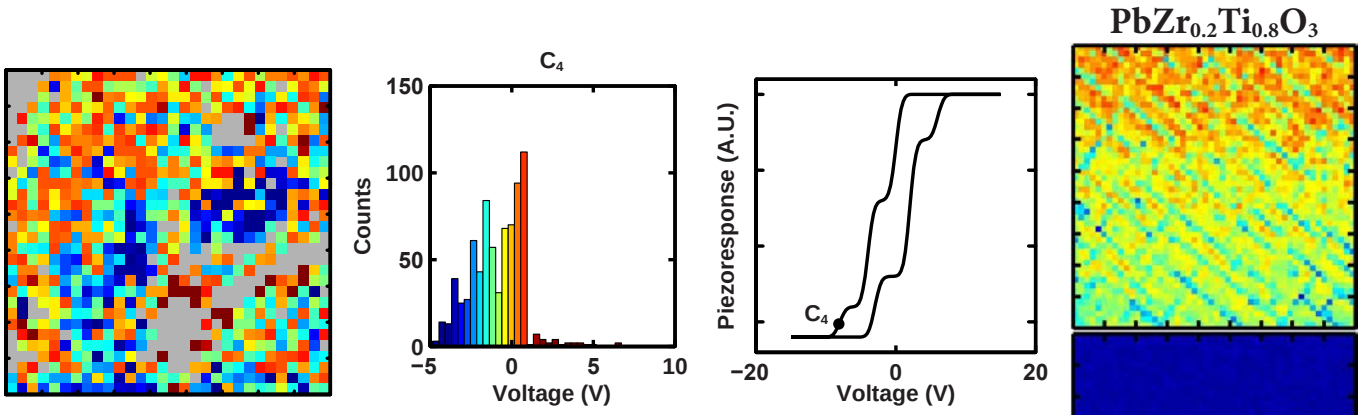

Figure H.23. Multi-step loop fitting result (C_4) of 100 nm thick mixed-phase $PbTiO_3$ on $SmScO_3$ (110).

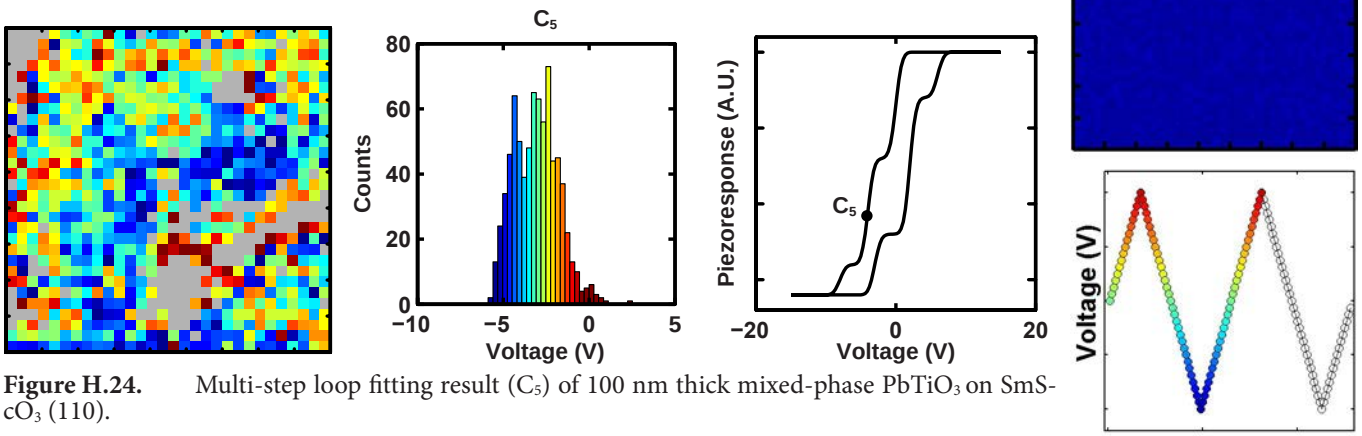

Figure H.24. Multi-step loop fitting result (C_5) of 100 nm thick mixed-phase $PbTiO_3$ on $SmScO_3$ (110).

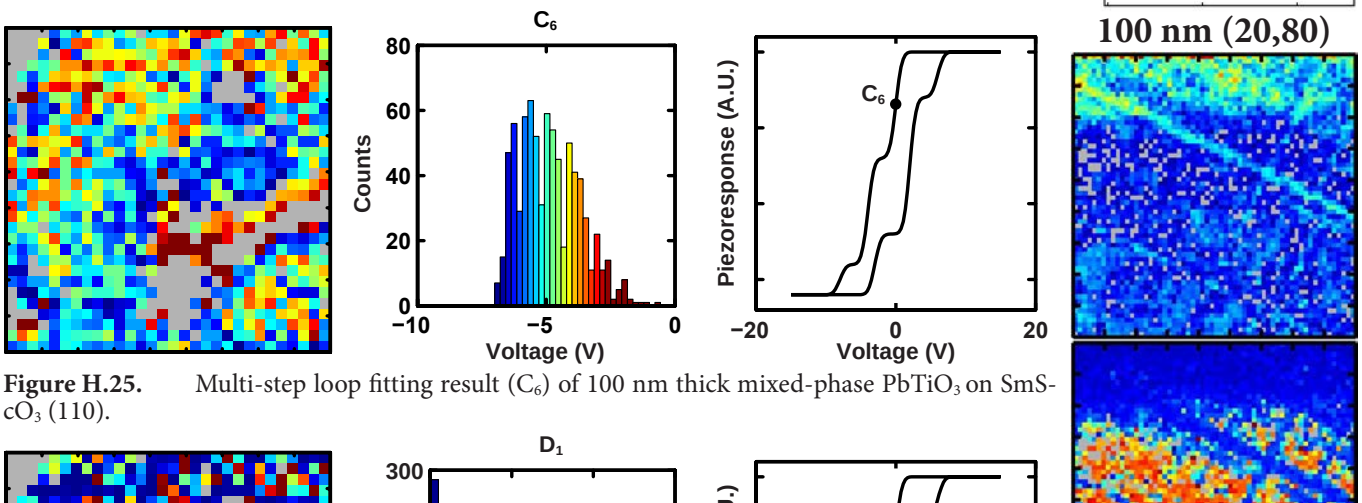

Figure H.25. Multi-step loop fitting result (C_6) of 100 nm thick mixed-phase $PbTiO_3$ on $SmScO_3$ (110).

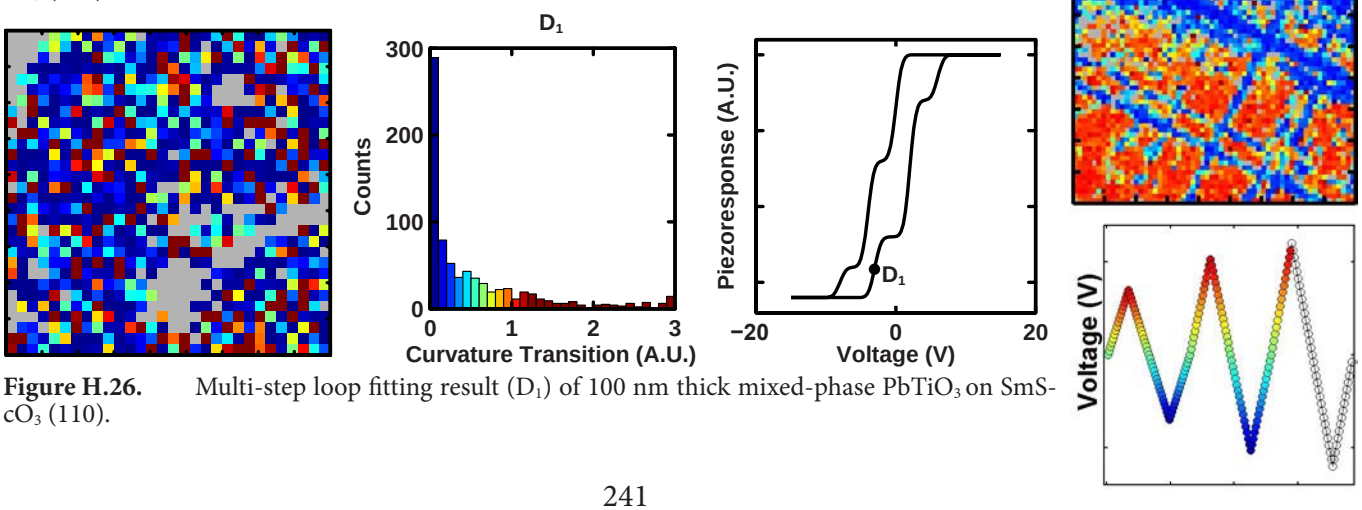

Figure H.26. Multi-step loop fitting result (D_1) of 100 nm thick mixed-phase $PbTiO_3$ on $SmScO_3$ (110).

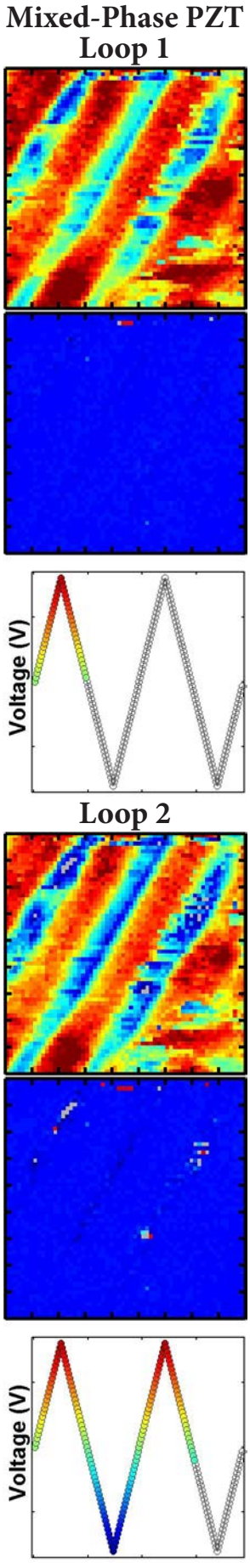

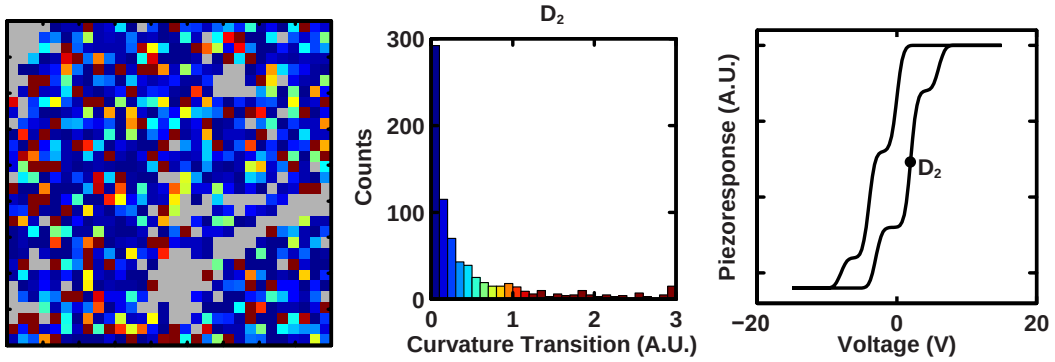

Figure H.27. Multi-step loop fitting result (D_2) of 100 nm thick mixed-phase $PbTiO_3$ on $SmScO_3$ (110).

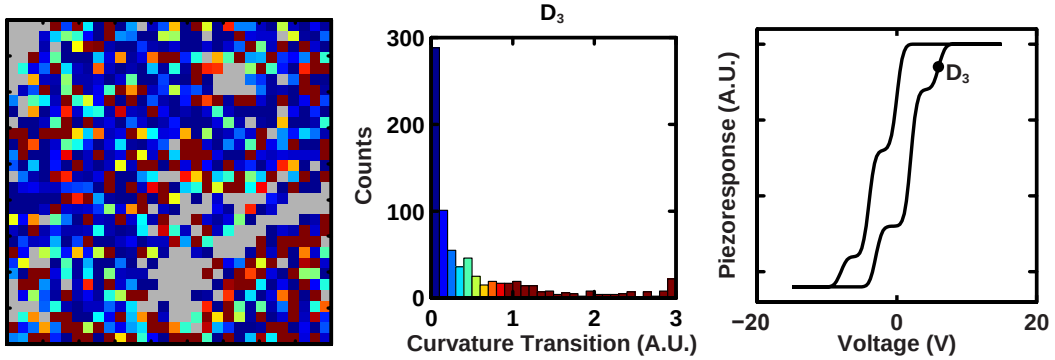

Figure H.28. Multi-step loop fitting result (D_3) of 100 nm thick mixed-phase $PbTiO_3$ on $SmScO_3$ (110).

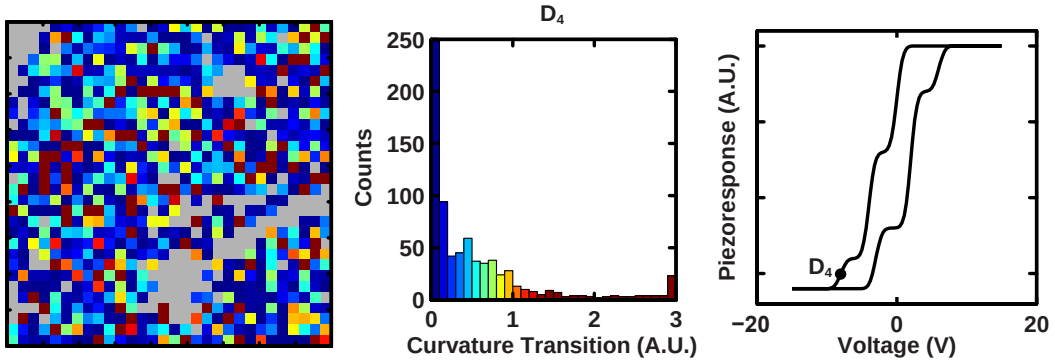

Figure H.29. Multi-step loop fitting result (D_4) of 100 nm thick mixed-phase $PbTiO_3$ on $SmScO_3$ (110).

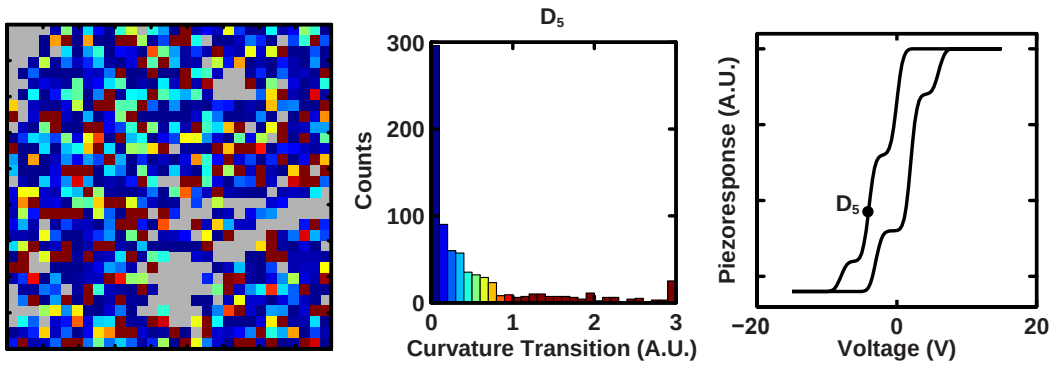

Figure H.30. Multi-step loop fitting result (D_5) of 100 nm thick mixed-phase $PbTiO_3$ on $SmScO_3$ (110).

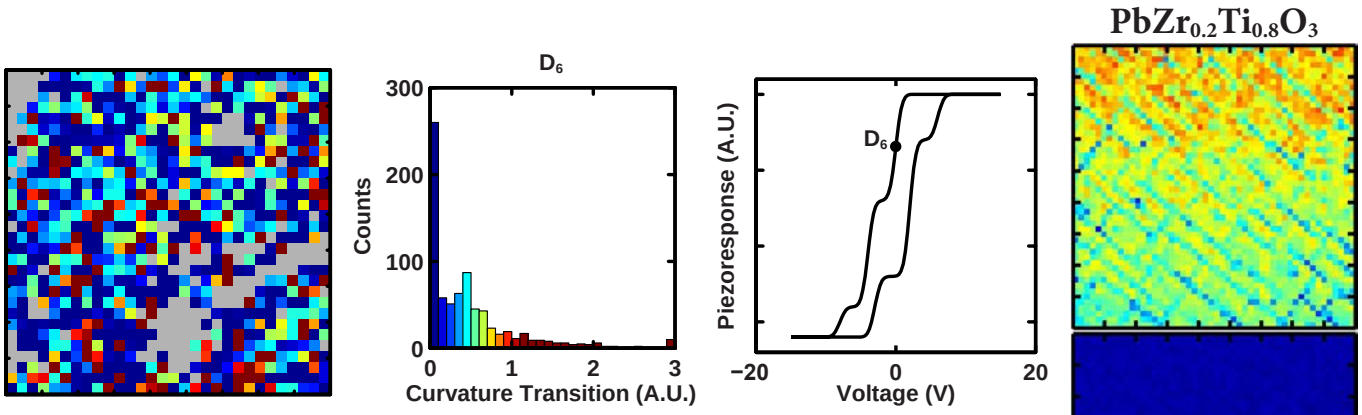

Figure H.31. Multi-step loop fitting result (D_6) of 100 nm thick mixed-phase $PbTiO_3$ on $SmScO_3$ (110).

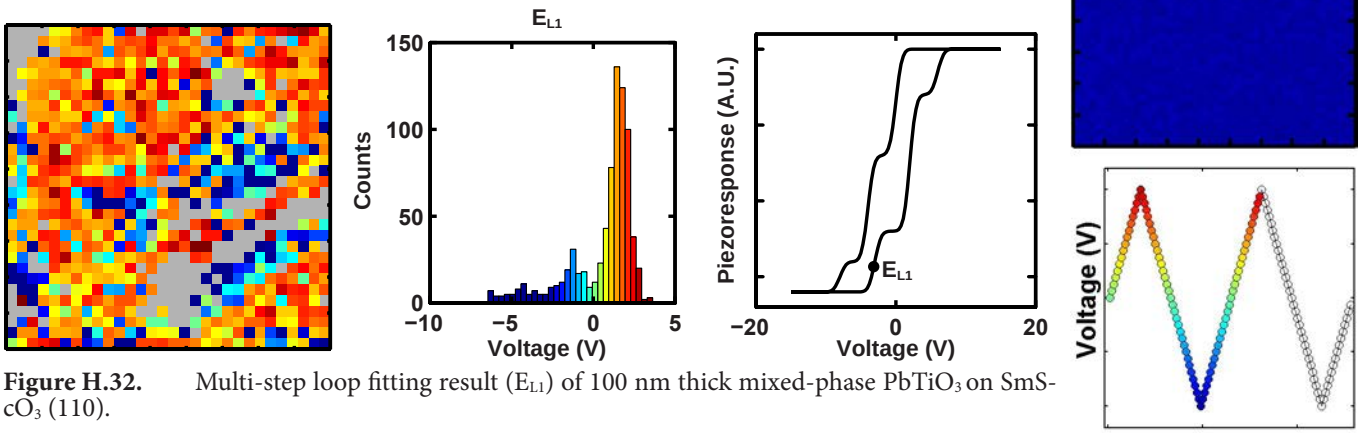

Figure H.32. Multi-step loop fitting result (E_{L1}) of 100 nm thick mixed-phase $PbTiO_3$ on $SmScO_3$ (110).

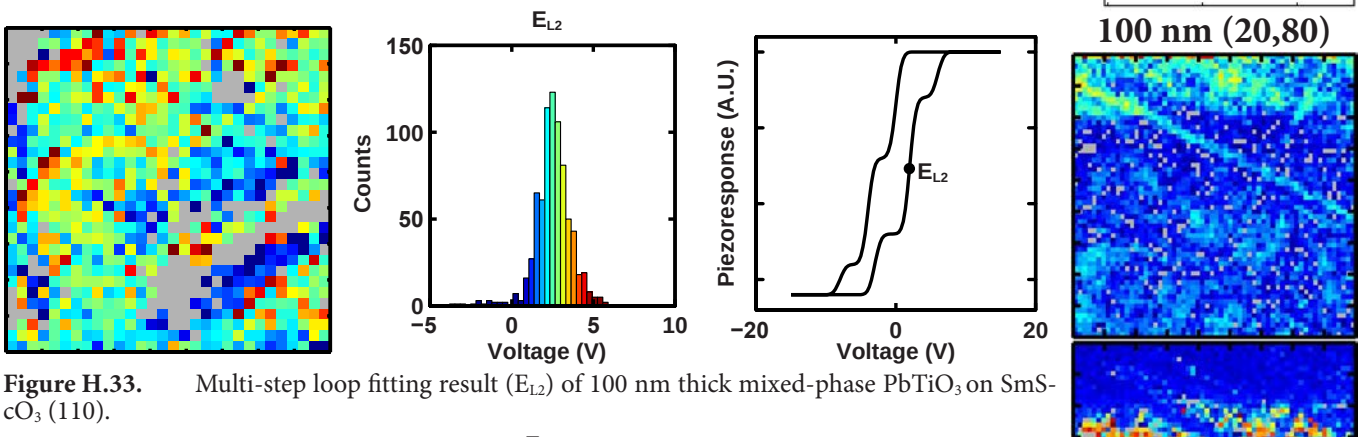

Figure H.33. Multi-step loop fitting result (E_{L2}) of 100 nm thick mixed-phase $PbTiO_3$ on $SmScO_3$ (110).

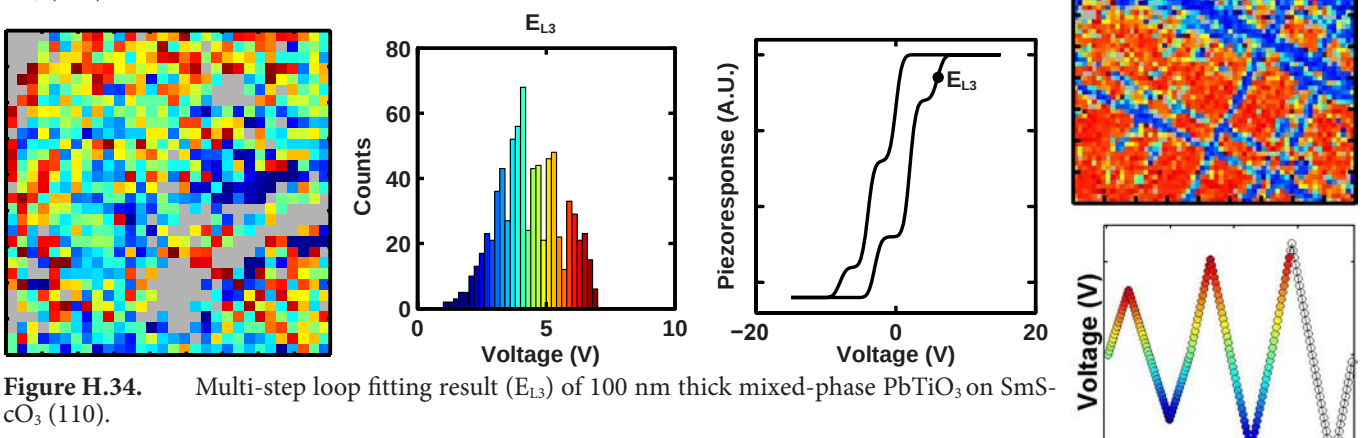

Figure H.34. Multi-step loop fitting result (E_{L3}) of 100 nm thick mixed-phase $PbTiO_3$ on $SmScO_3$ (110).

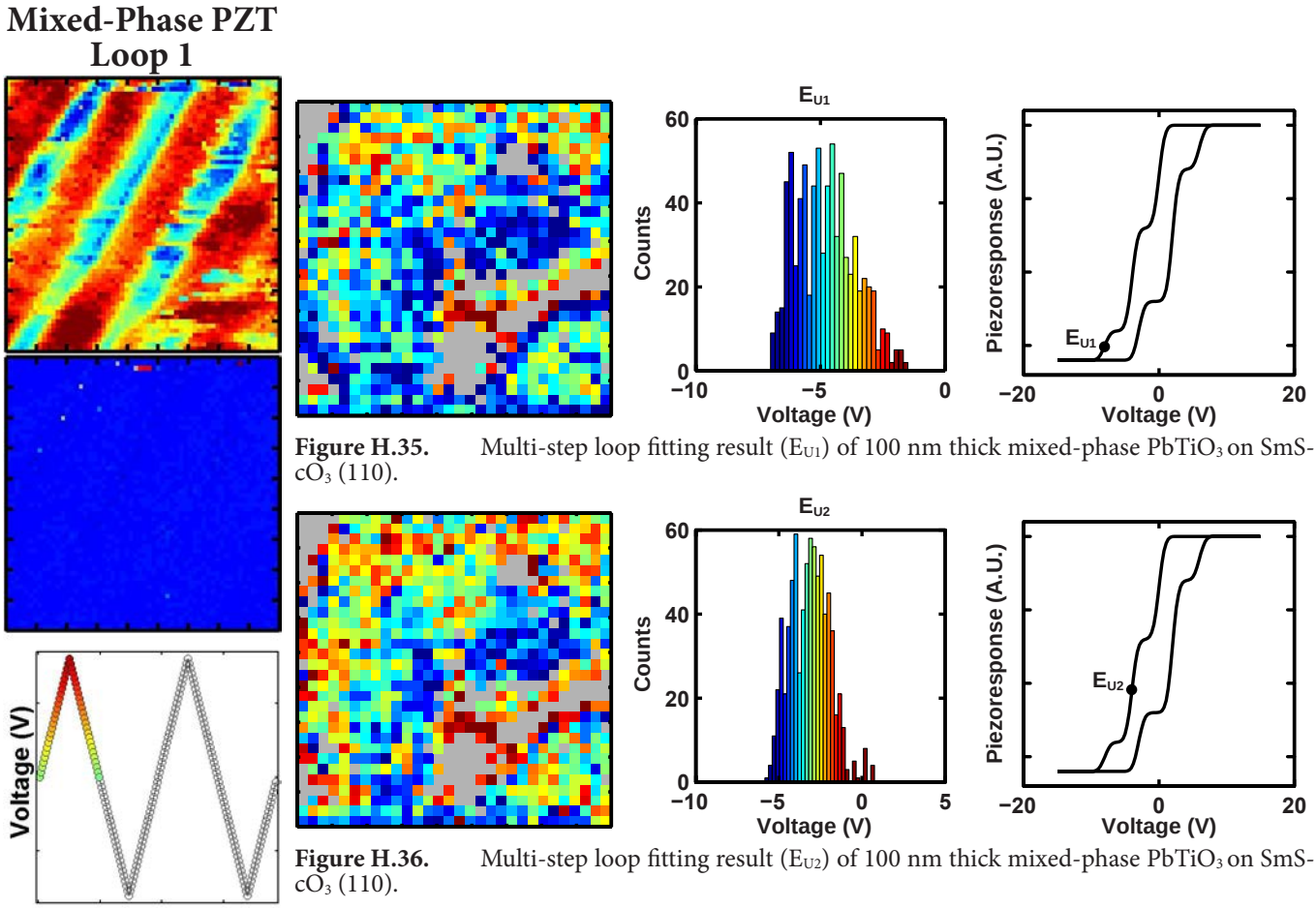

Figure H.35. Multi-step loop fitting result (E_{U1}) of 100 nm thick mixed-phase $PbTiO_3$ on $SmScO_3$ (110).

Figure H.36. Multi-step loop fitting result (E_{U2}) of 100 nm thick mixed-phase $PbTiO_3$ on $SmScO_3$ (110).

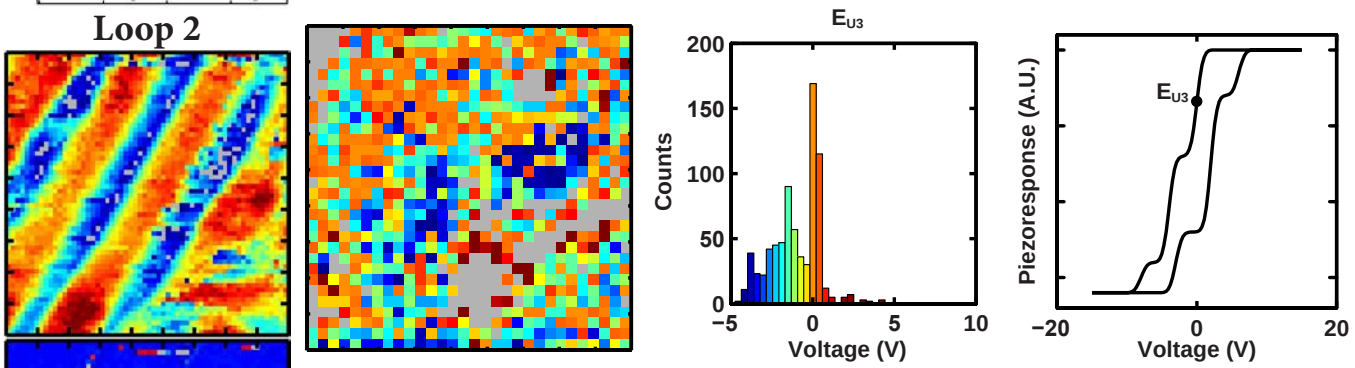

Figure H.37. Multi-step loop fitting result (E_{U3}) of 100 nm thick mixed-phase $PbTiO_3$ on $SmScO_3$ (110).

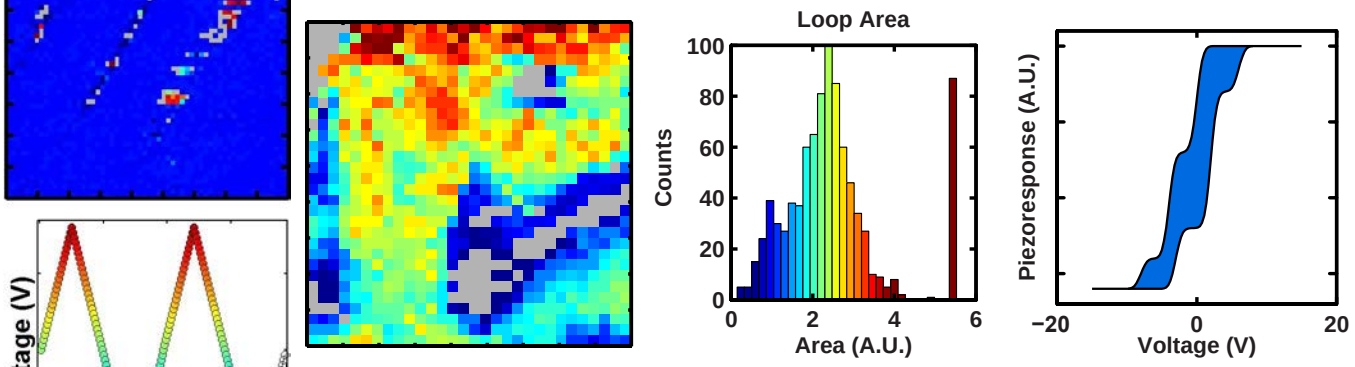

Figure H.38. Multi-step loop fitting result loop area of 100 nm thick mixed-phase $PbTiO_3$ on $SmScO_3$ (110).

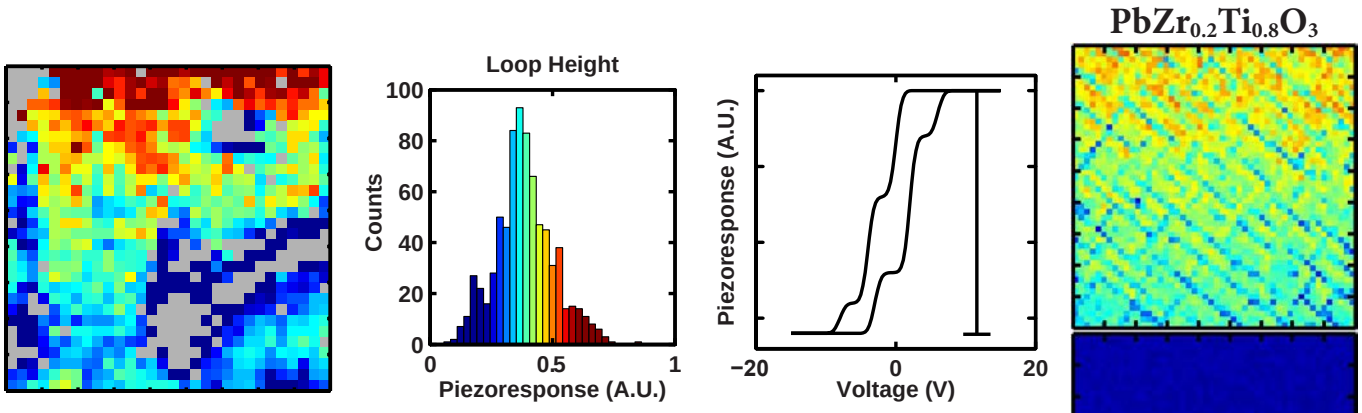

Figure H.39. Multi-step loop fitting result loop height of 100 nm thick mixed-phase $PbTiO_3$ on $SmScO_3$ (110).

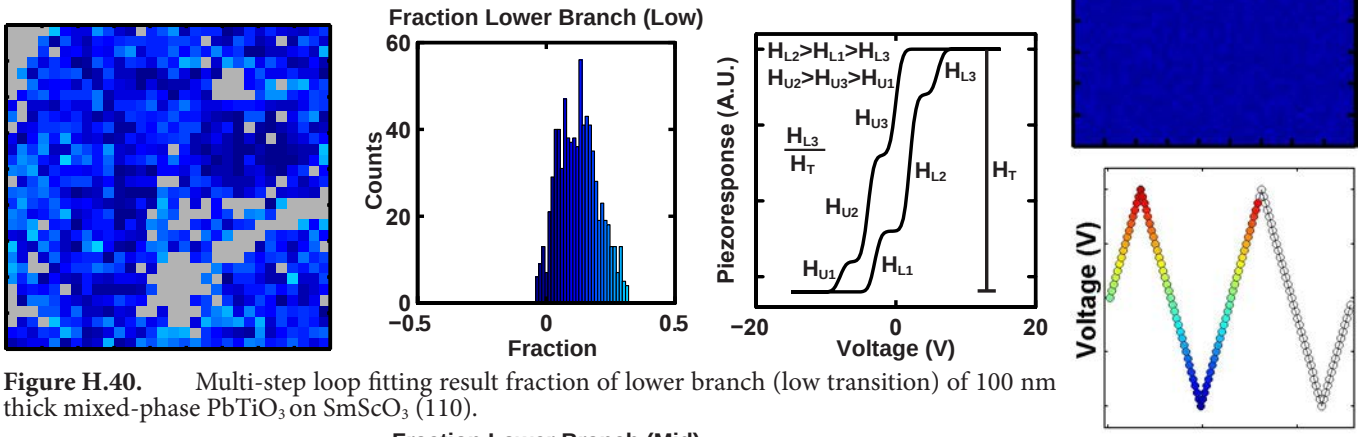

Figure H.40. Multi-step loop fitting result fraction of lower branch (low transition) of 100 nm thick mixed-phase $PbTiO_3$ on $SmScO_3$ (110).

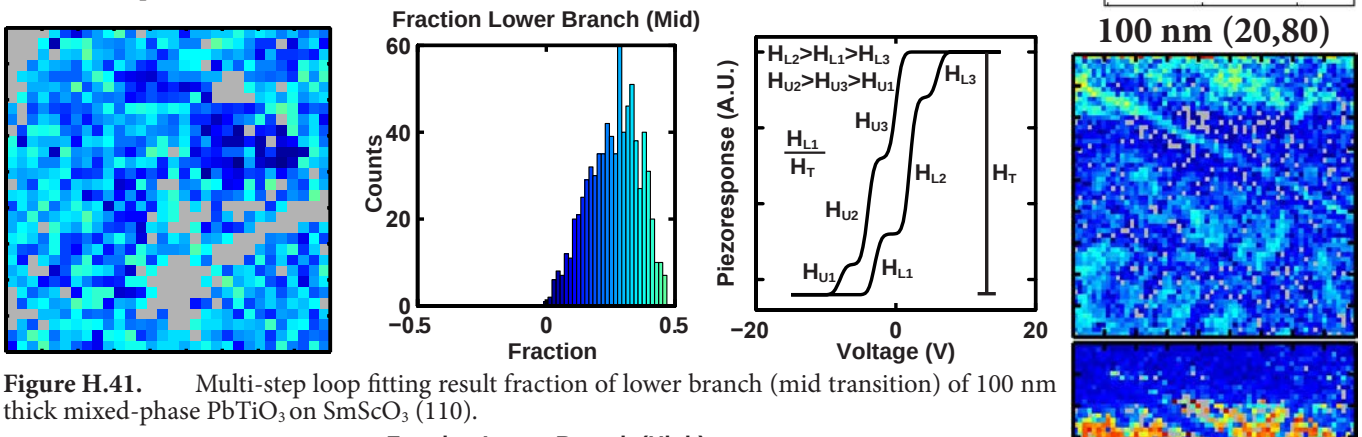

Figure H.41. Multi-step loop fitting result fraction of lower branch (mid transition) of 100 nm thick mixed-phase $PbTiO_3$ on $SmScO_3$ (110).

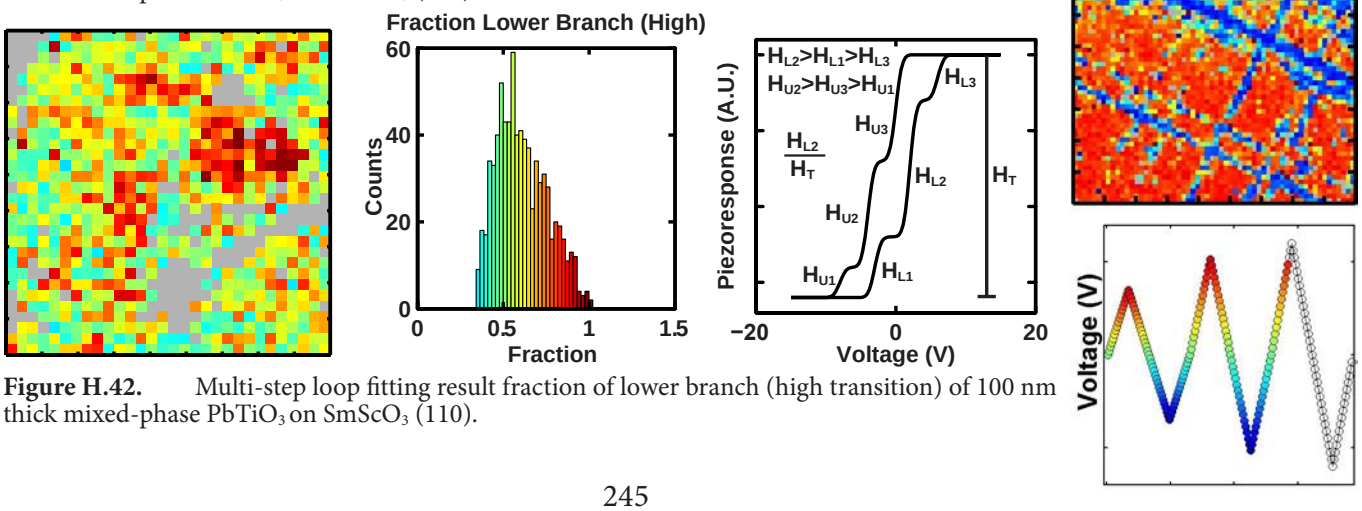

Figure H.42. Multi-step loop fitting result fraction of lower branch (high transition) of 100 nm thick mixed-phase $PbTiO_3$ on $SmScO_3$ (110).

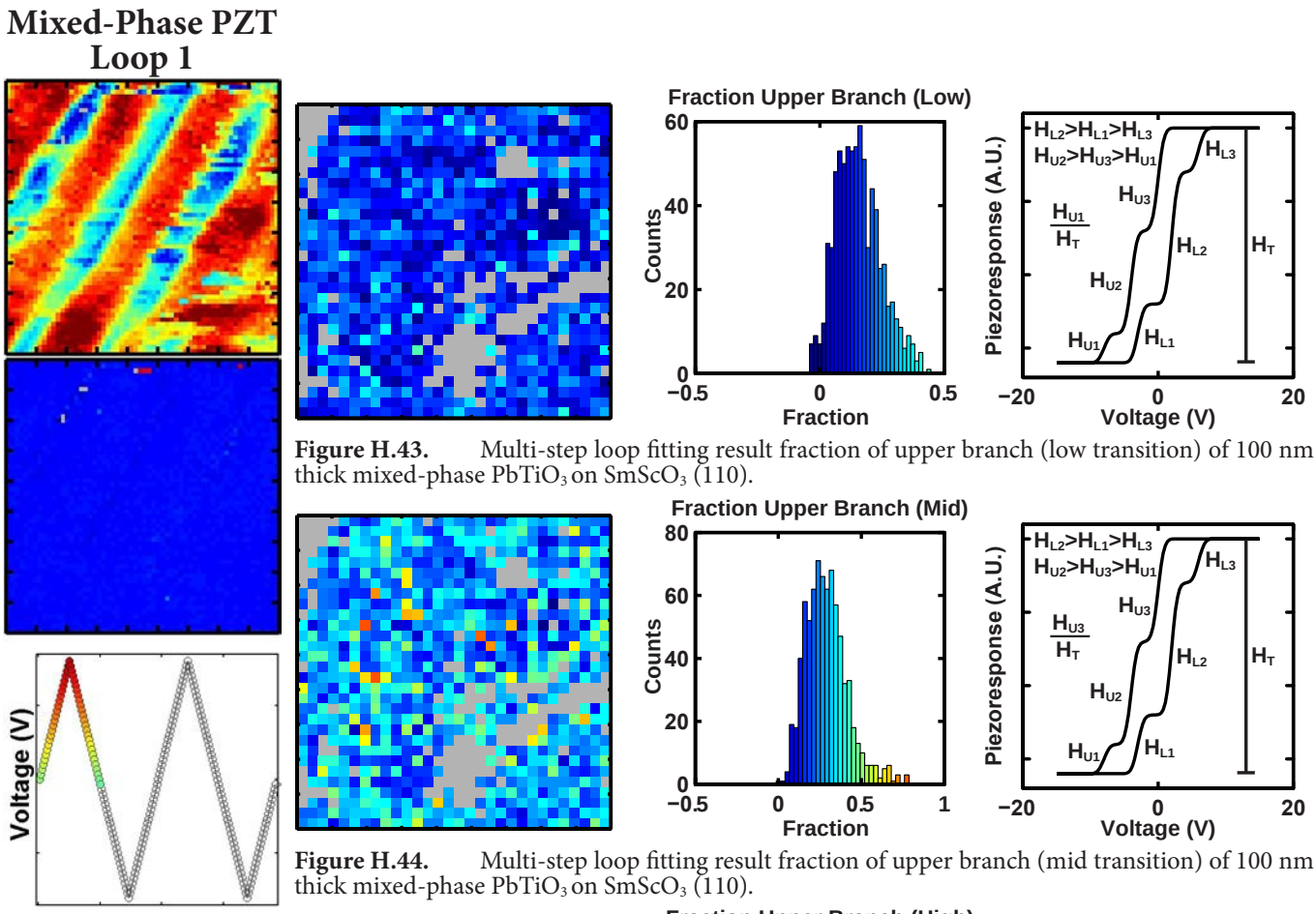

Figure H.43. Multi-step loop fitting result fraction of upper branch (low transition) of 100 nm thick mixed-phase $PbTiO_3$ on $SmScO_3$ (110).

Figure H.44. Multi-step loop fitting result fraction of upper branch (mid transition) of 100 nm thick mixed-phase $PbTiO_3$ on $SmScO_3$ (110).

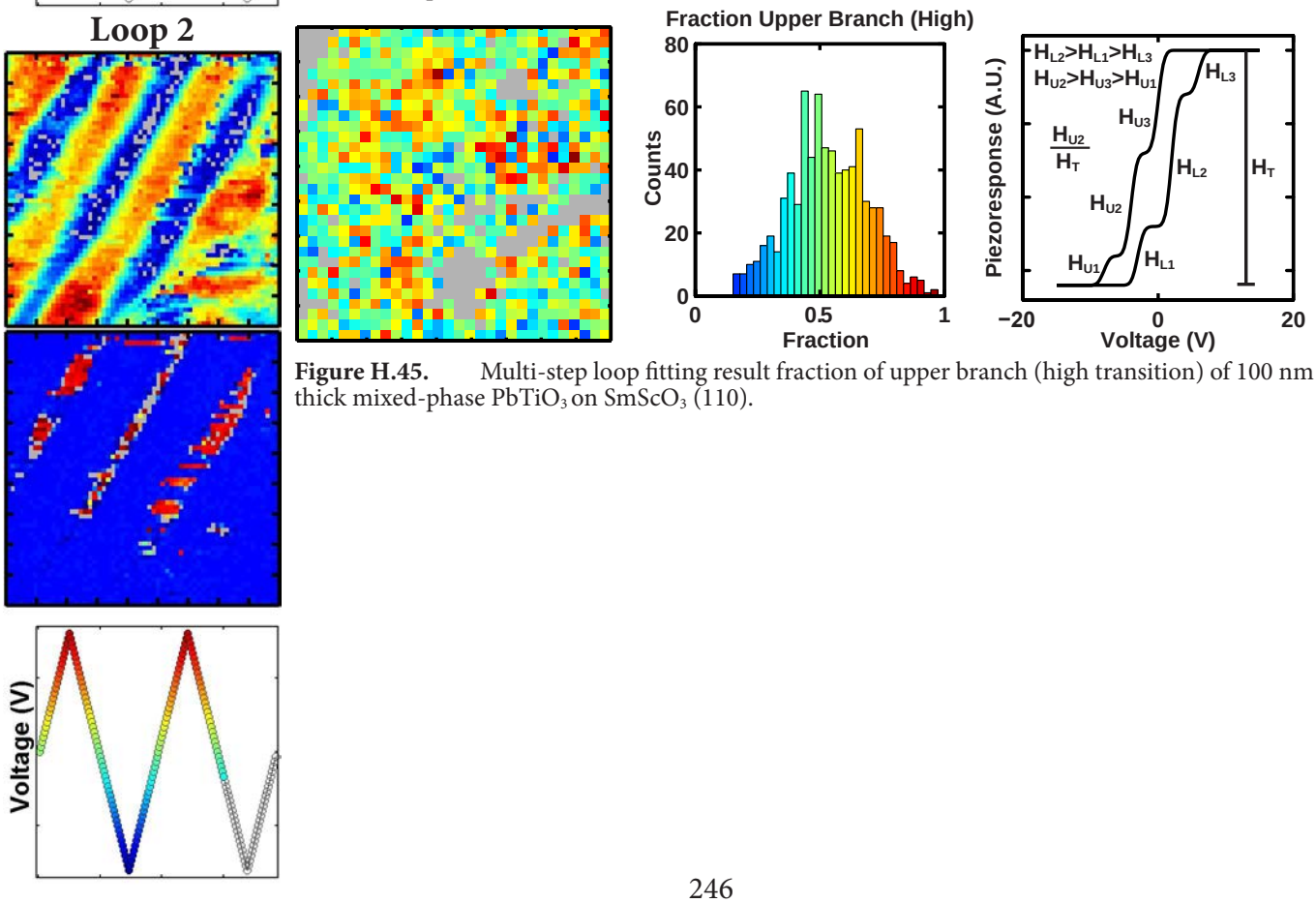

Figure H.45. Multi-step loop fitting result fraction of upper branch (high transition) of 100 nm thick mixed-phase $PbTiO_3$ on $SmScO_3$ (110).

Appendix I

Mixed-Phase $PbZr_{0.2}Ti_{0.8}O_3$ Switching Spectroscopy

Included in this section is a subset of the BE-SS (amplitude, phase, loss, and resonance frequency) images of 400 nm thick mixed-phase $PbZr_{0.2}Ti_{0.8}O_3$ heterostructures grown on $NdScO_3$ (110). Note that the scan size in all images is 2 μm.

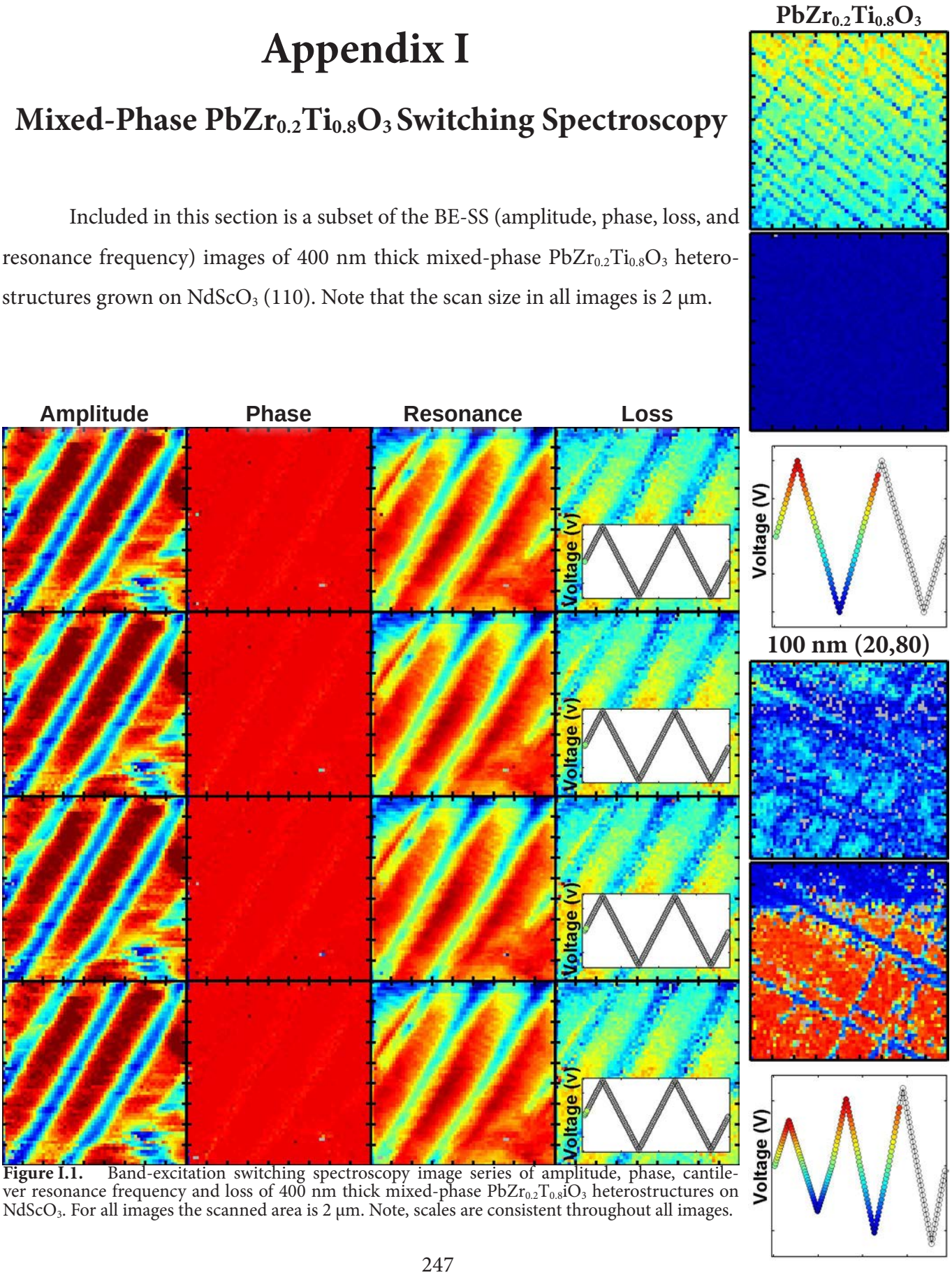

Figure I.1. Band-excitation switching spectroscopy image series of amplitude, phase, cantilever resonance frequency and loss of 400 nm thick mixed-phase $PbZr_{0.2}T_{0.8}iO_3$ heterostructures on $NdScO_3$. For all images the scanned area is 2 μm. Note, scales are consistent throughout all images.

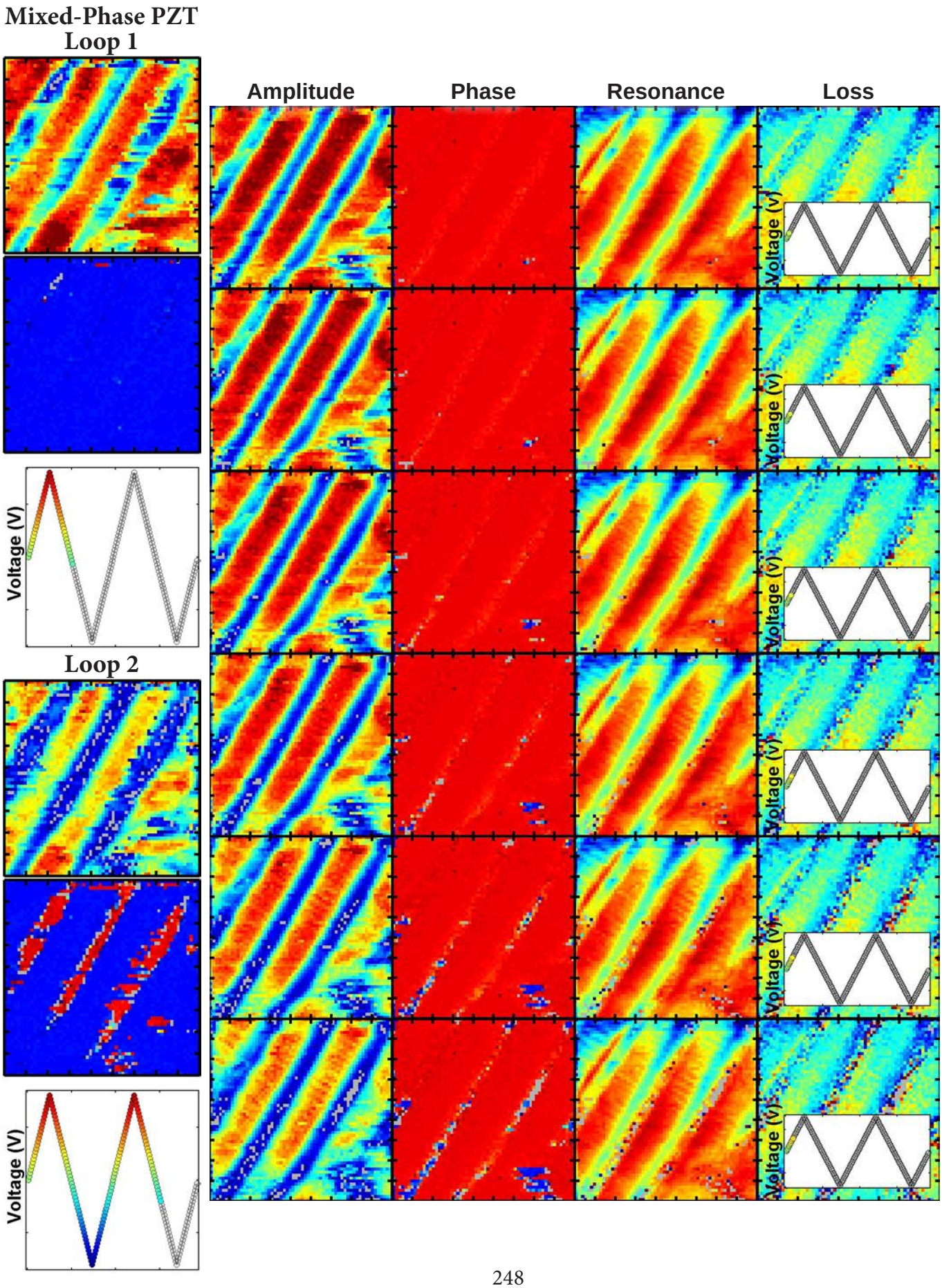
Mixed-Phase PZT
Loop 1
Amplitude
Phase
Resonance
Loss
Voltage (V)
Loop 2
Voltage (V)
Voltage (V)

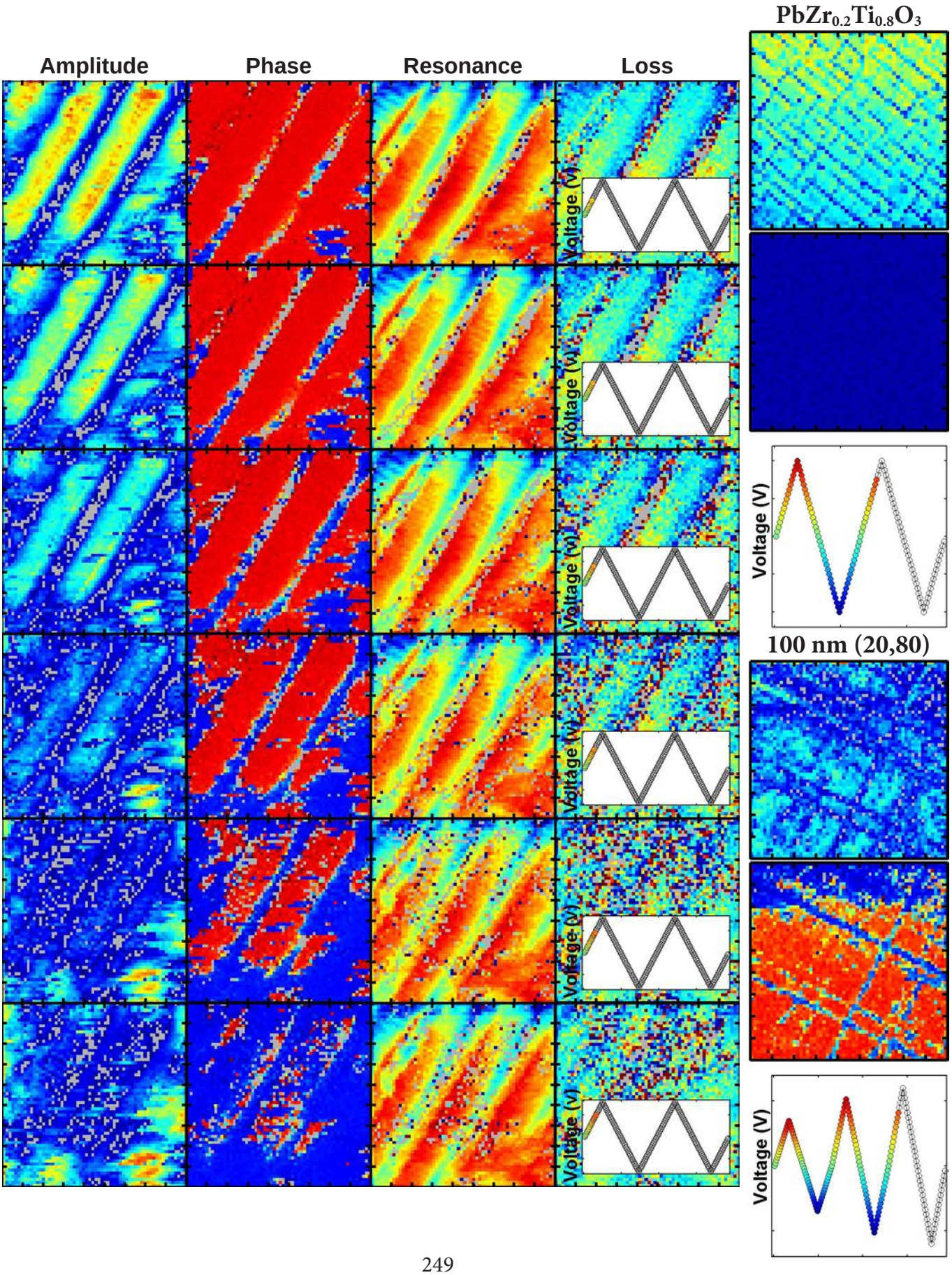
PbZr0.2Ti0.8O3
Amplitude
Phase
Resonance
Loss
Voltage (V)
Voltage (V)
Voltage (V)
Voltage (V)
Voltage (V)
Voltage (V)
100 nm (20,80)

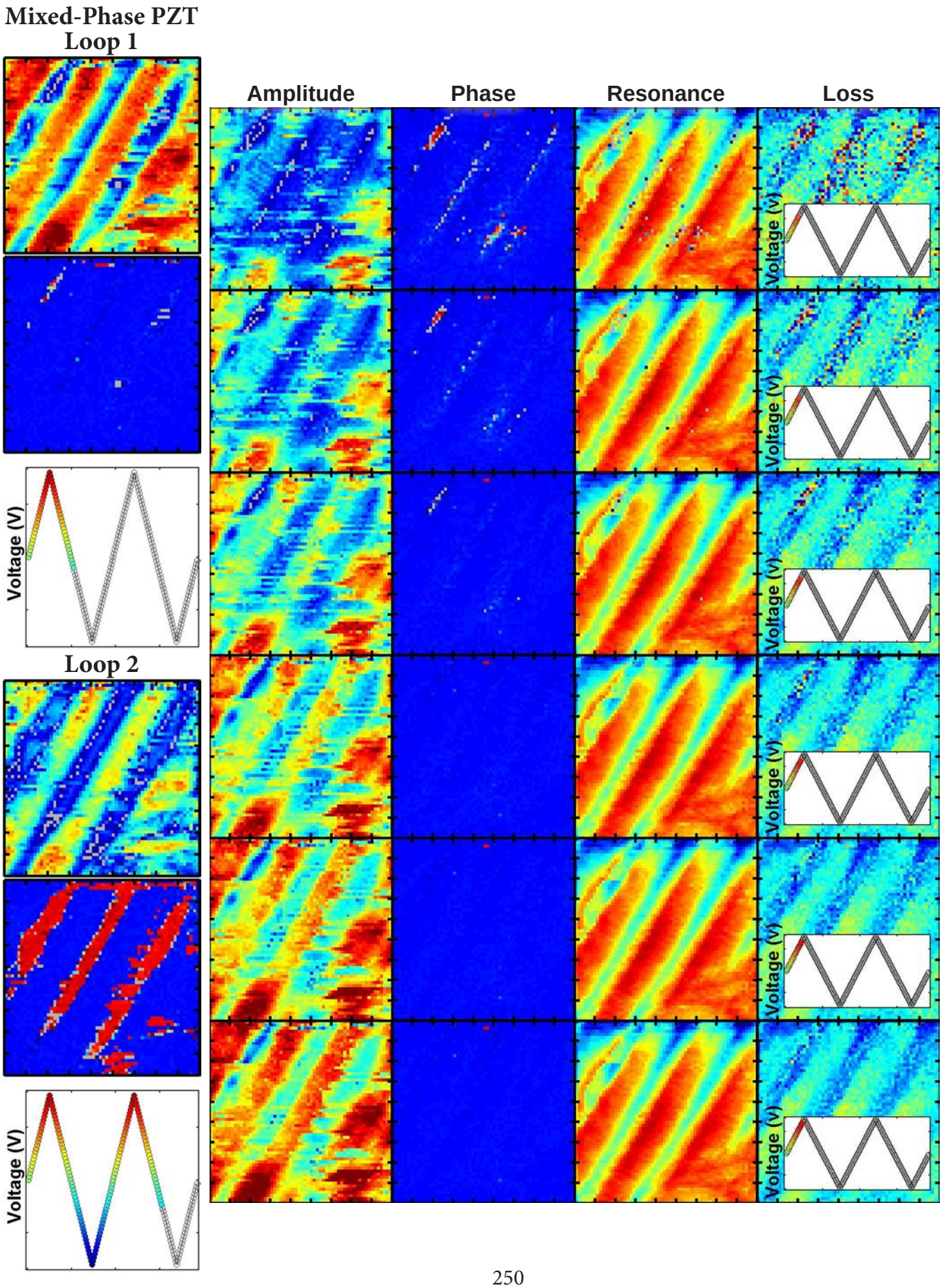
Mixed-Phase PZT
Loop 1
Amplitude
Phase
Resonance
Loss
Voltage (V)
Loop 2
Voltage (V)
Voltage (v)

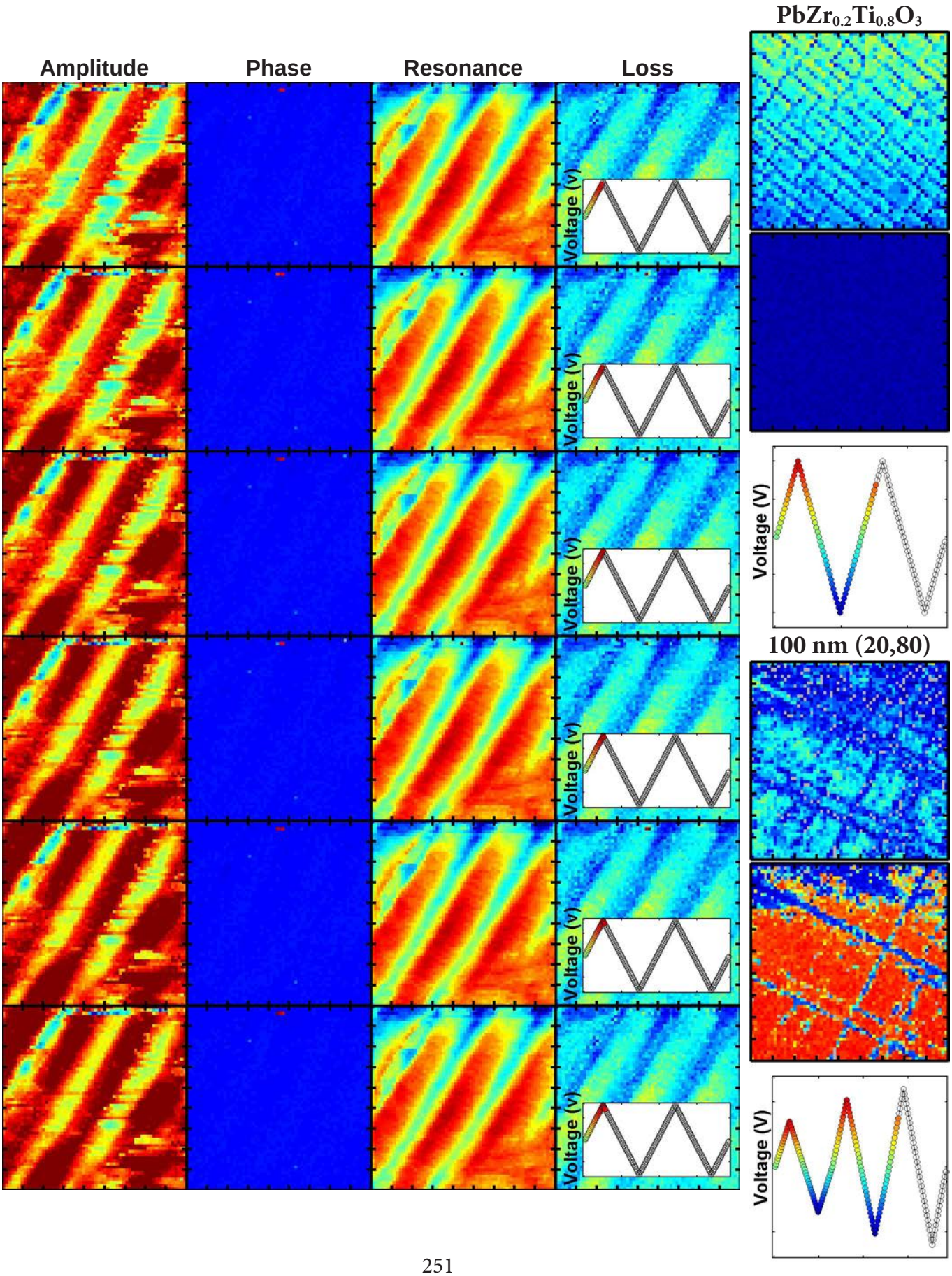
Amplitude
Phase
Resonance
Loss
Voltage (V)
PbZr0.2Ti0.8O3
100 nm (20,80)

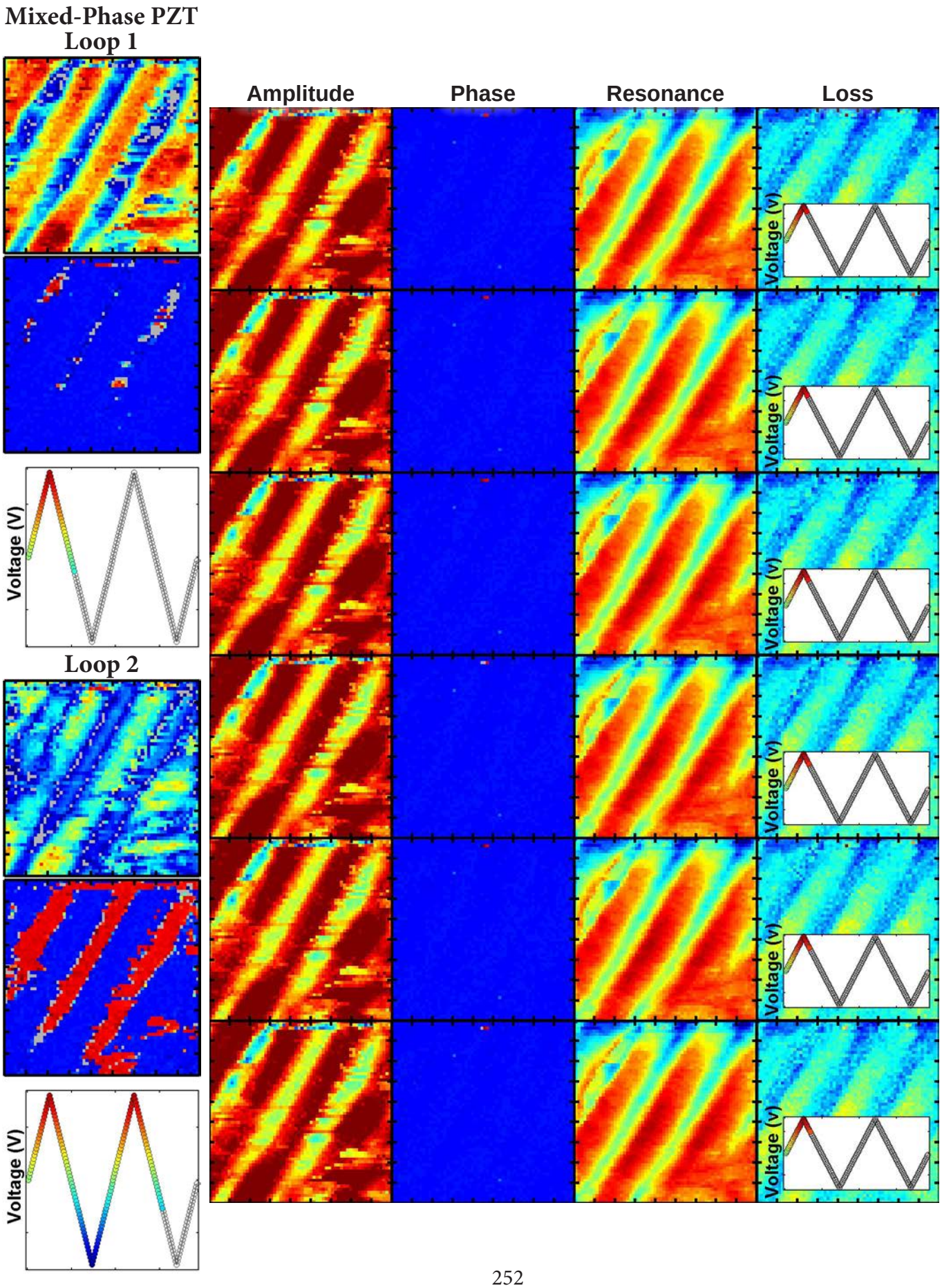
Mixed-Phase PZT
Loop 1
Amplitude
Phase
Resonance
Loss
Voltage (V)
Loop 2
Voltage (V)
Voltage (v)

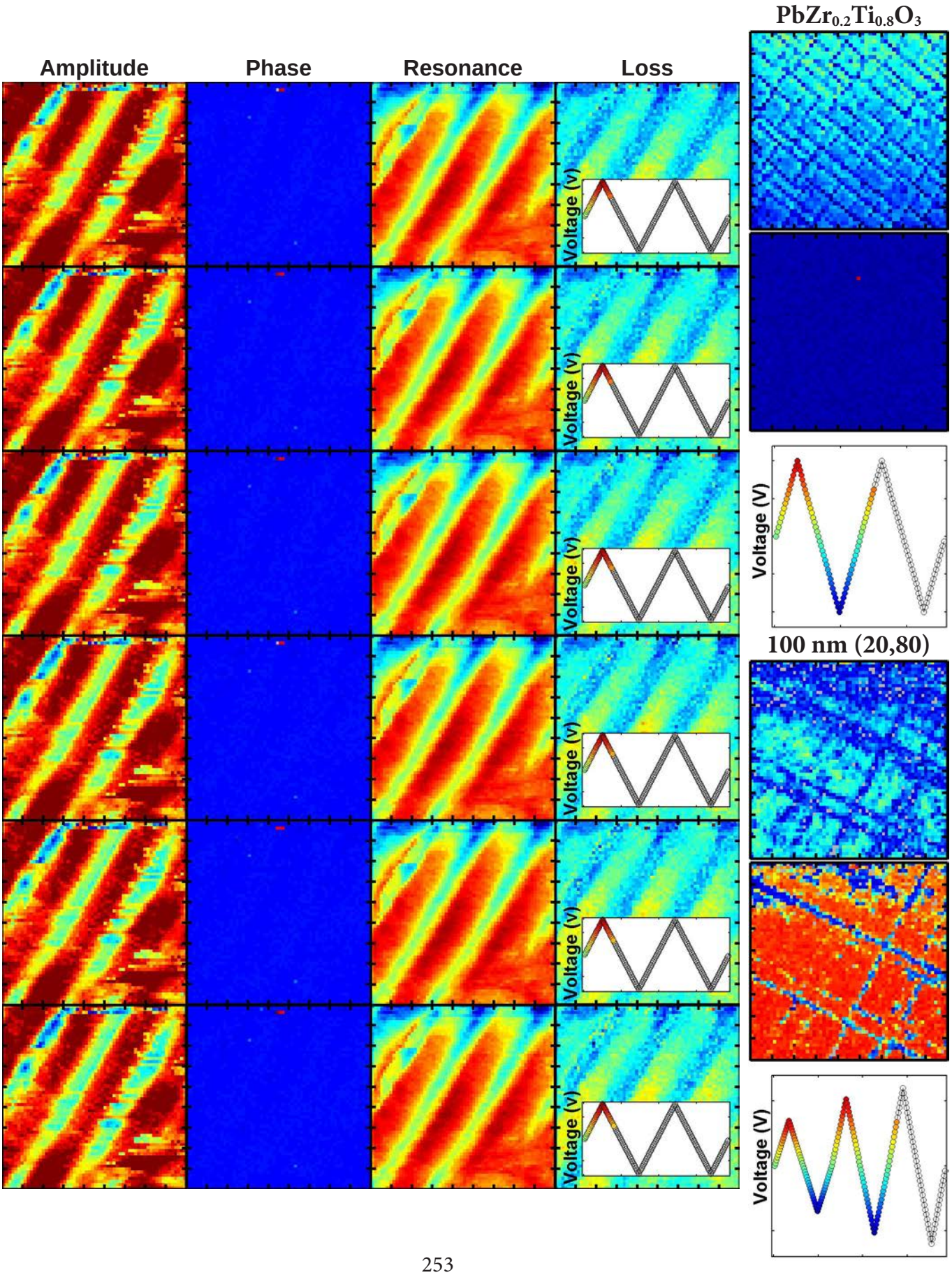
PbZr0.2Ti0.8O3
Amplitude
Phase
Resonance
Loss
Voltage (V)
100 nm (20,80)

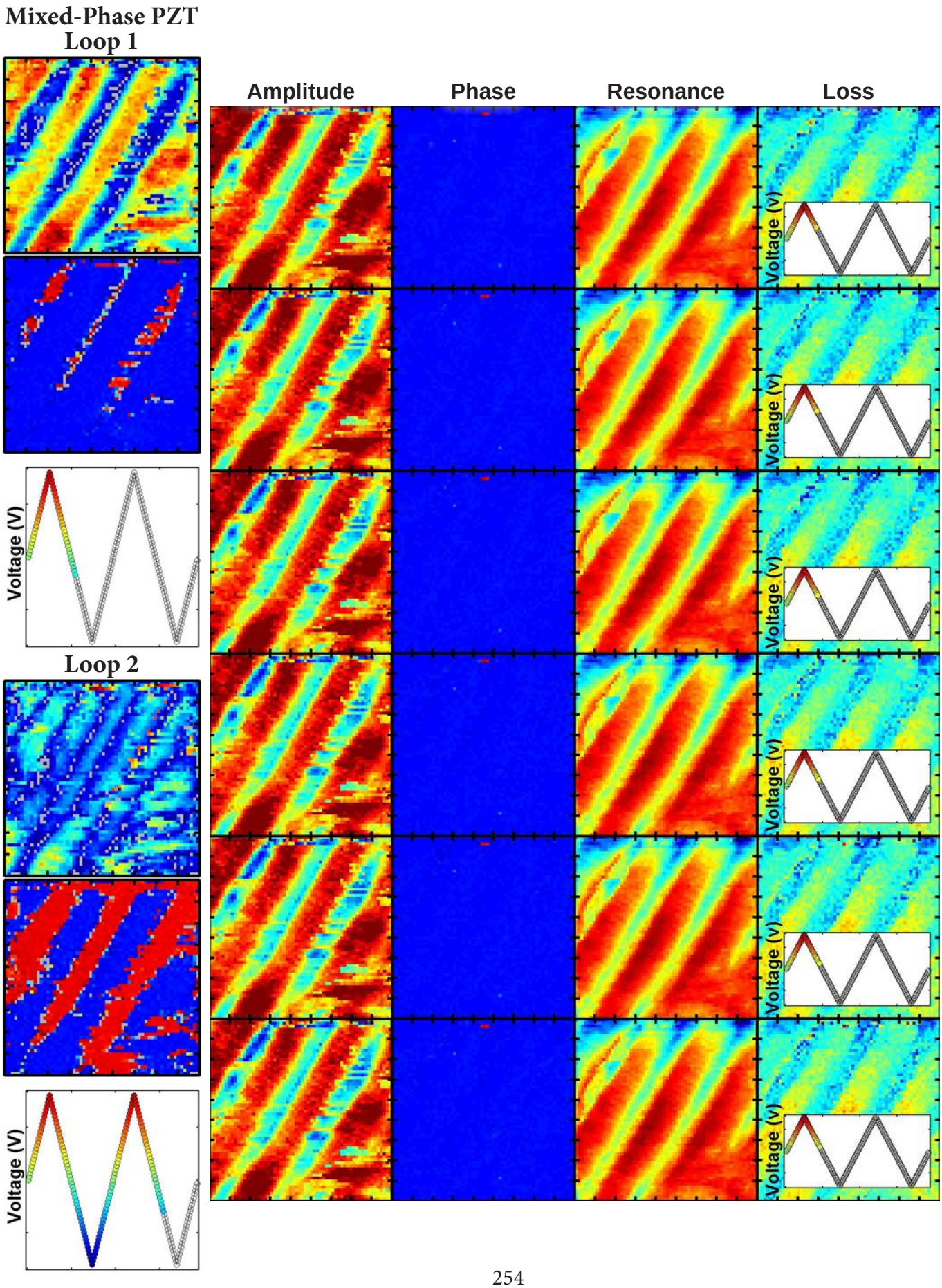
Mixed-Phase PZT
Loop 1
Amplitude
Phase
Resonance
Loss
Voltage (V)
Loop 2
Voltage (V)
Voltage (v)

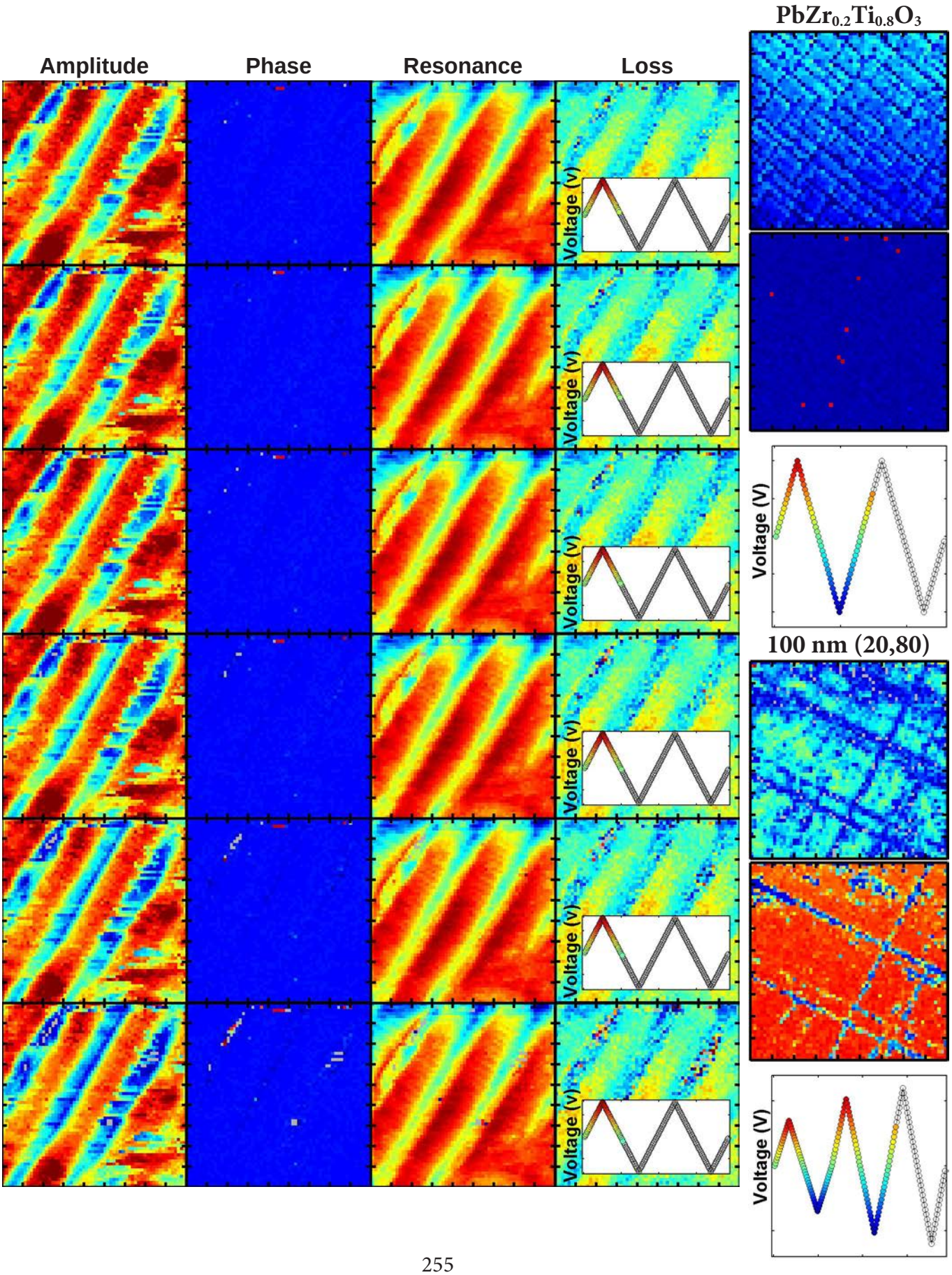
PbZr0.2Ti0.8O3
Amplitude
Phase
Resonance
Loss
Voltage (v)
Voltage (V)
100 nm (20,80)

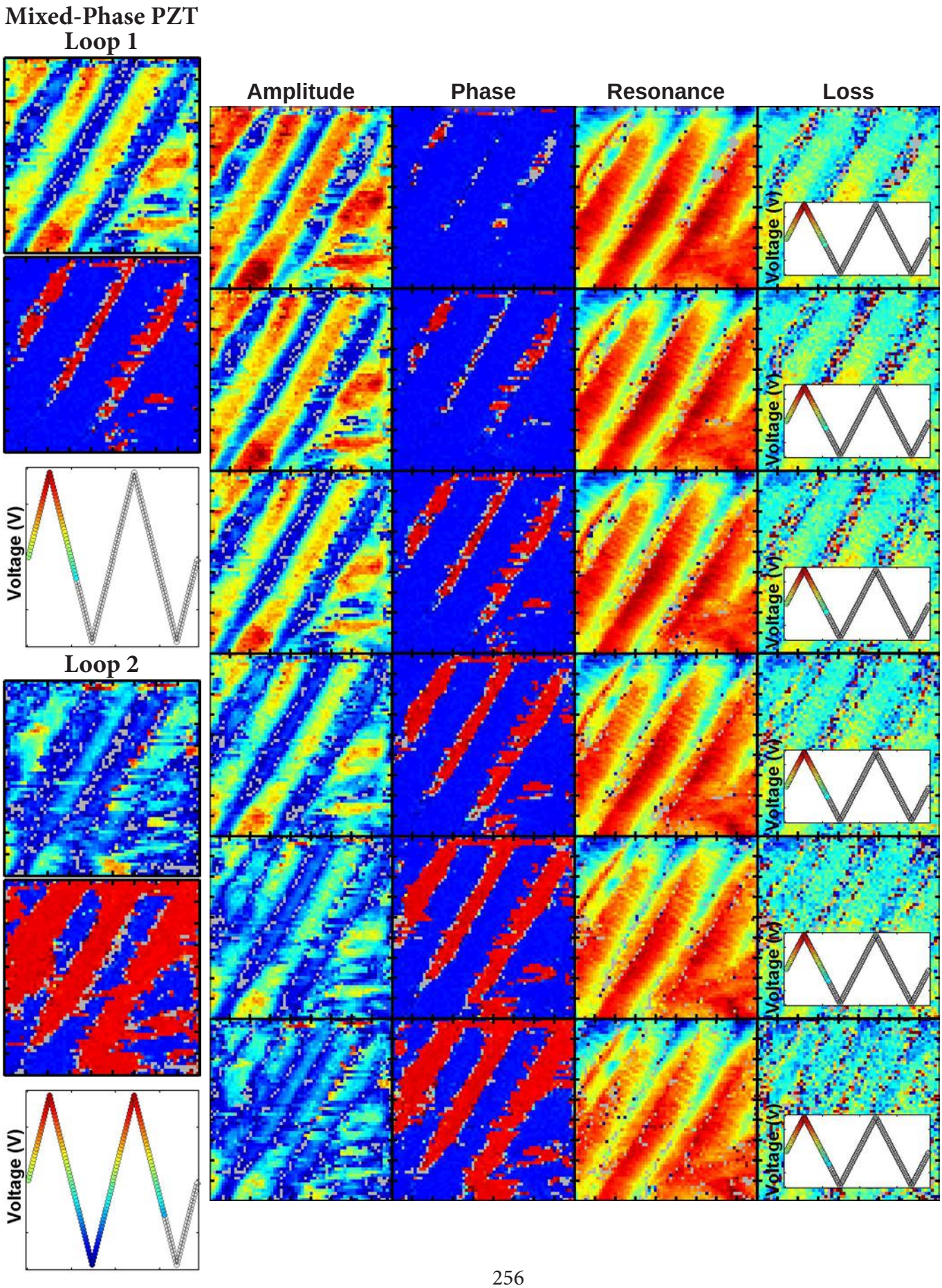
Mixed-Phase PZT
Loop 1
Amplitude
Phase
Resonance
Loss
Voltage (V)
Loop 2
Voltage (V)

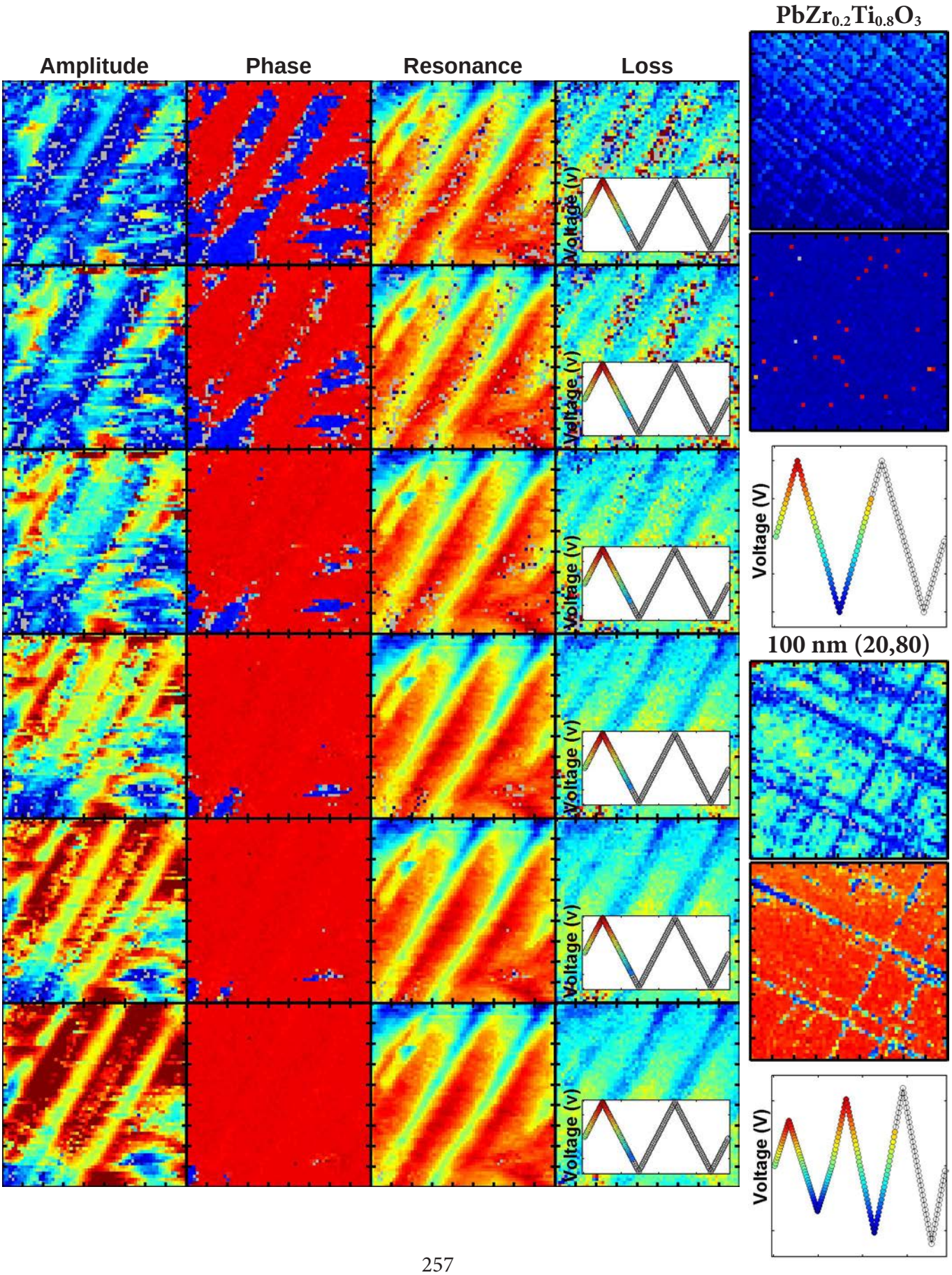
Amplitude
Phase
Resonance
Loss
Voltage (V)
PbZr0.2Ti0.8O3
100 nm (20,80)

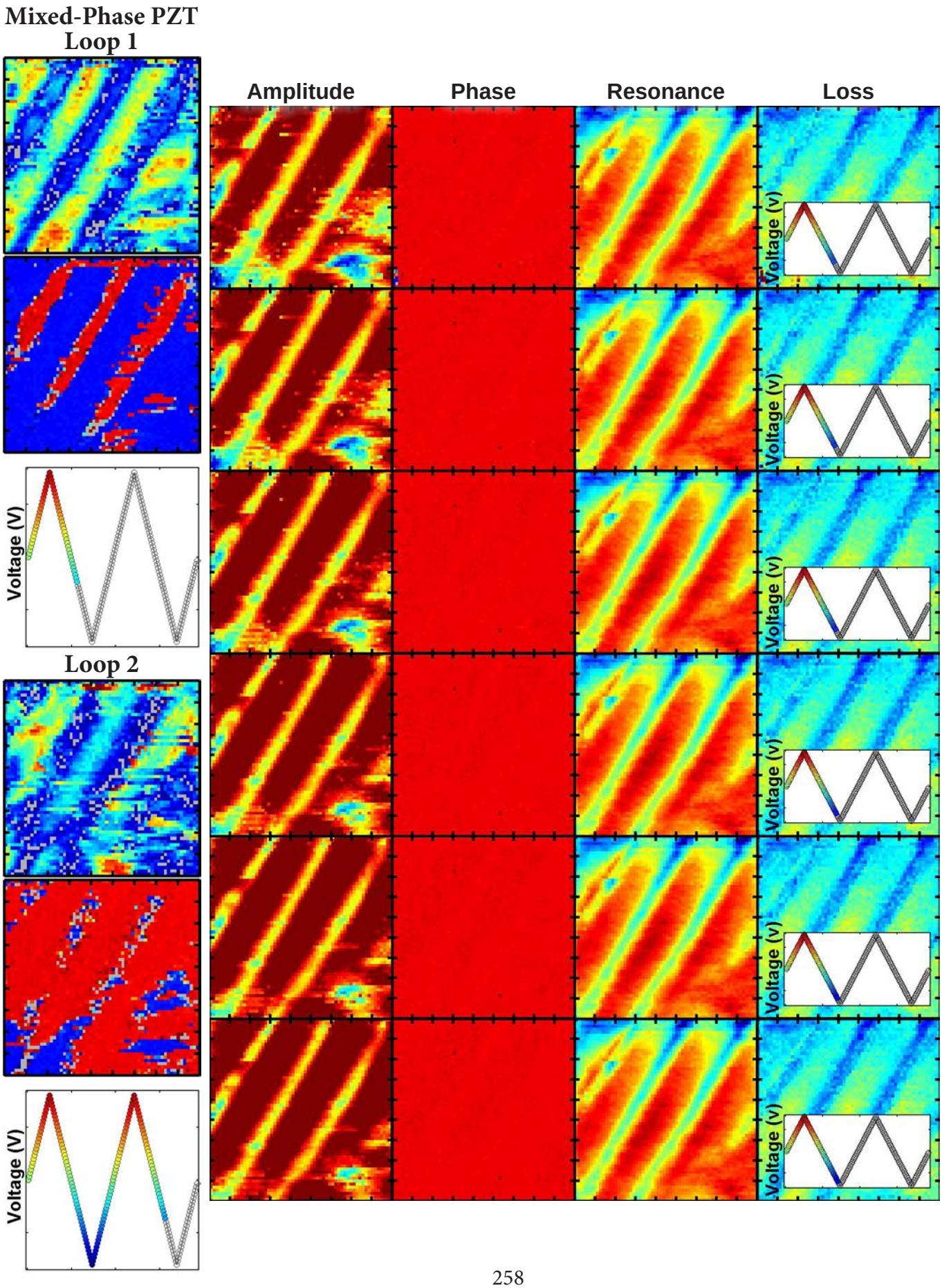
Mixed-Phase PZT
Loop 1
Amplitude
Phase
Resonance
Loss
Voltage (V)
Loop 2
Voltage (V)
Voltage (v)

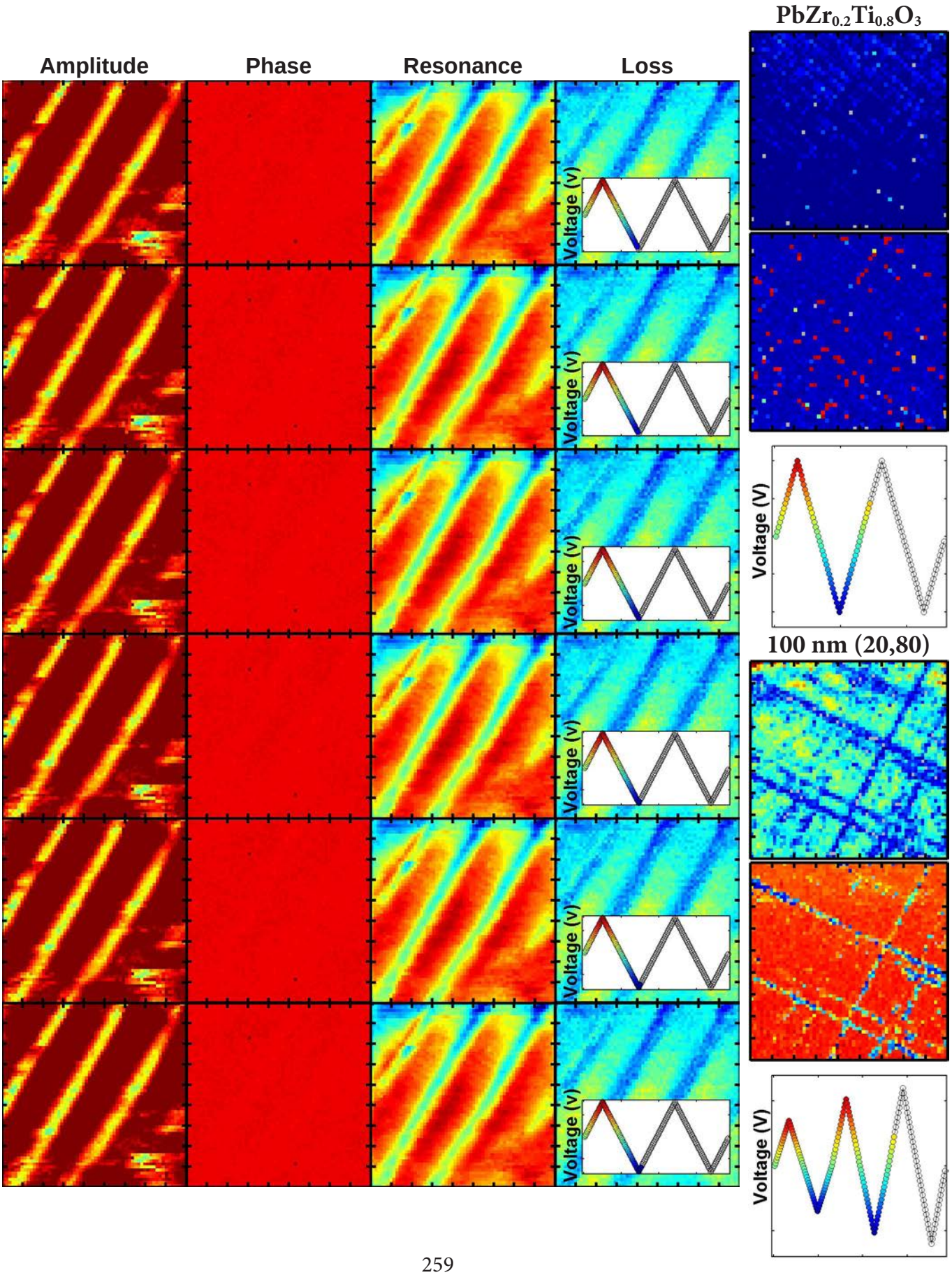
Amplitude
Phase
Resonance
Loss
Voltage (v)
PbZr0.2Ti0.8O3
Voltage (V)
100 nm (20,80)

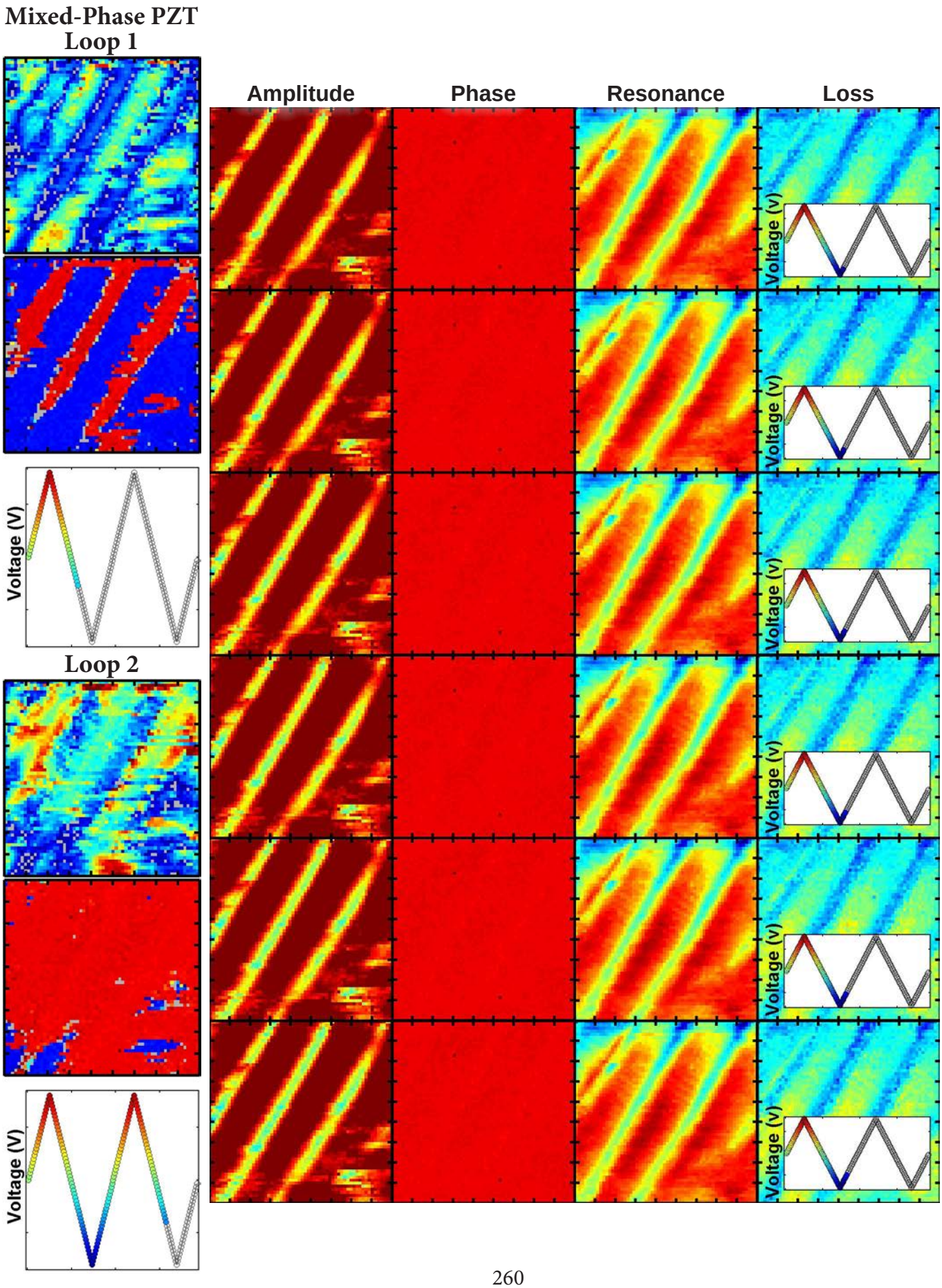
Mixed-Phase PZT
Loop 1
Amplitude
Phase
Resonance
Loss
Voltage (V)
Loop 2
Voltage (V)
Voltage (v)

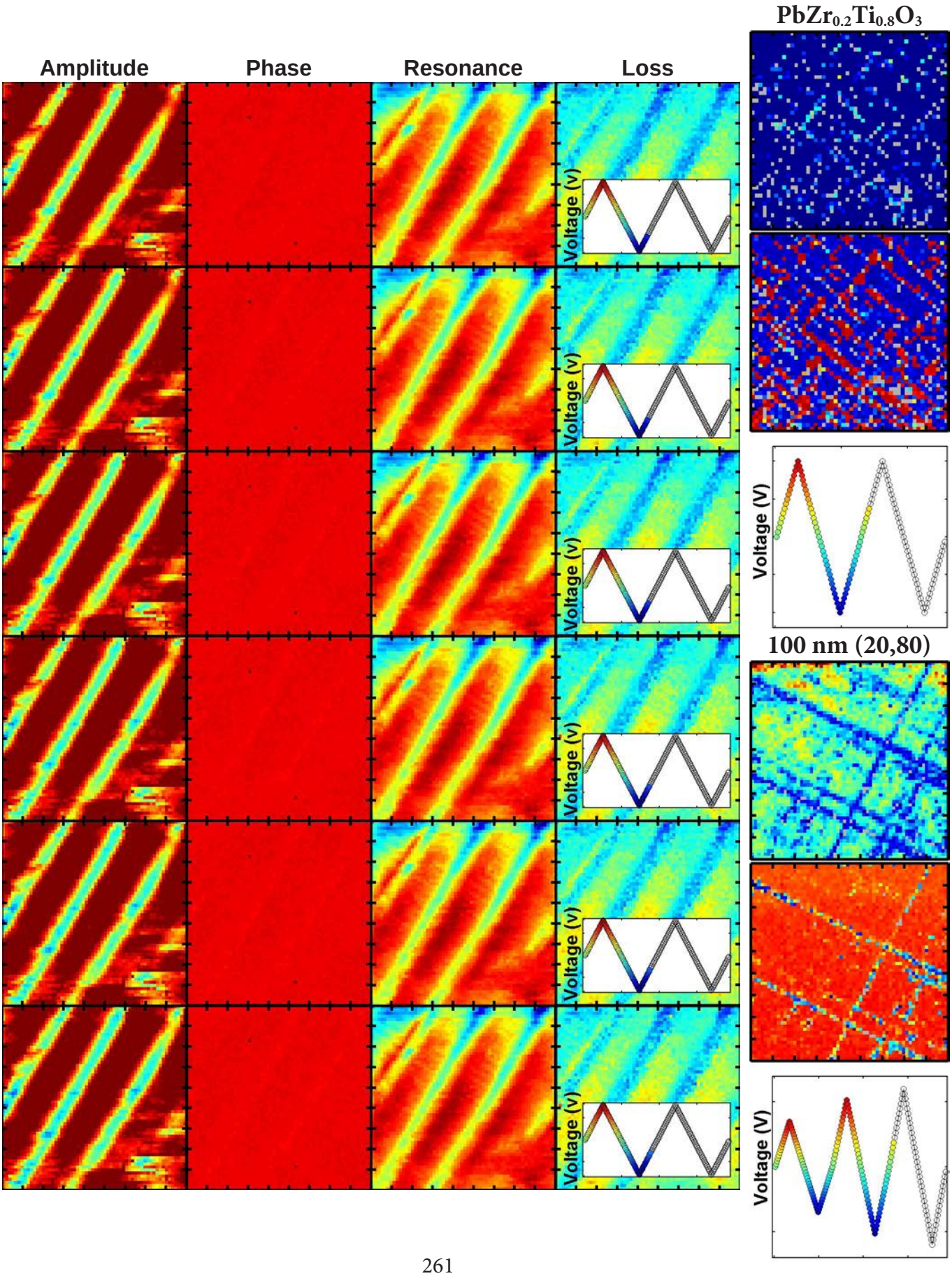
Amplitude
Phase
Resonance
Loss
Voltage (v)
PbZr0.2Ti0.8O3
Voltage (V)
100 nm (20,80)

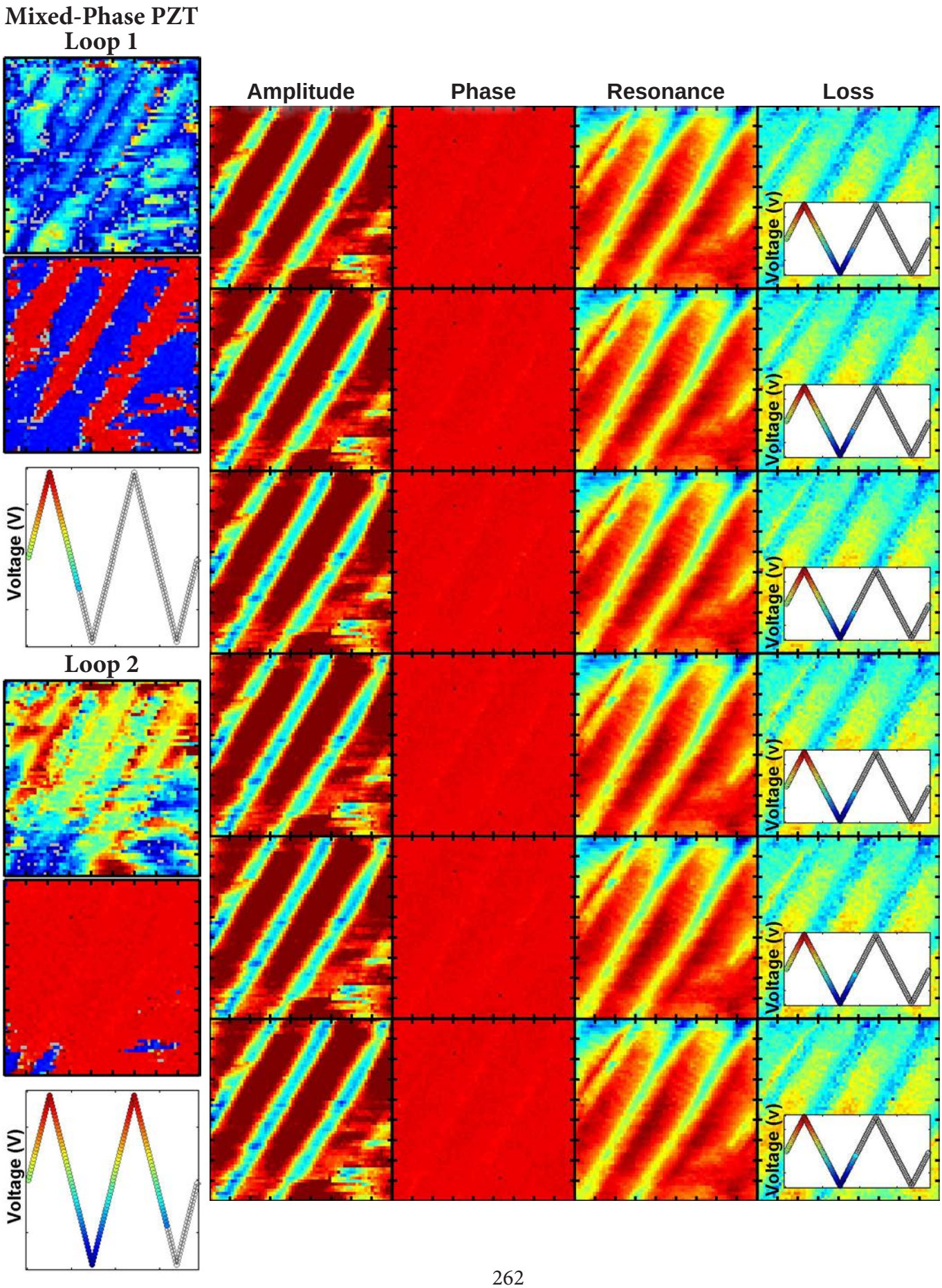
Mixed-Phase PZT
Loop 1
Amplitude
Phase
Resonance
Loss
Voltage (V)
Loop 2
Voltage (V)
Voltage (v)

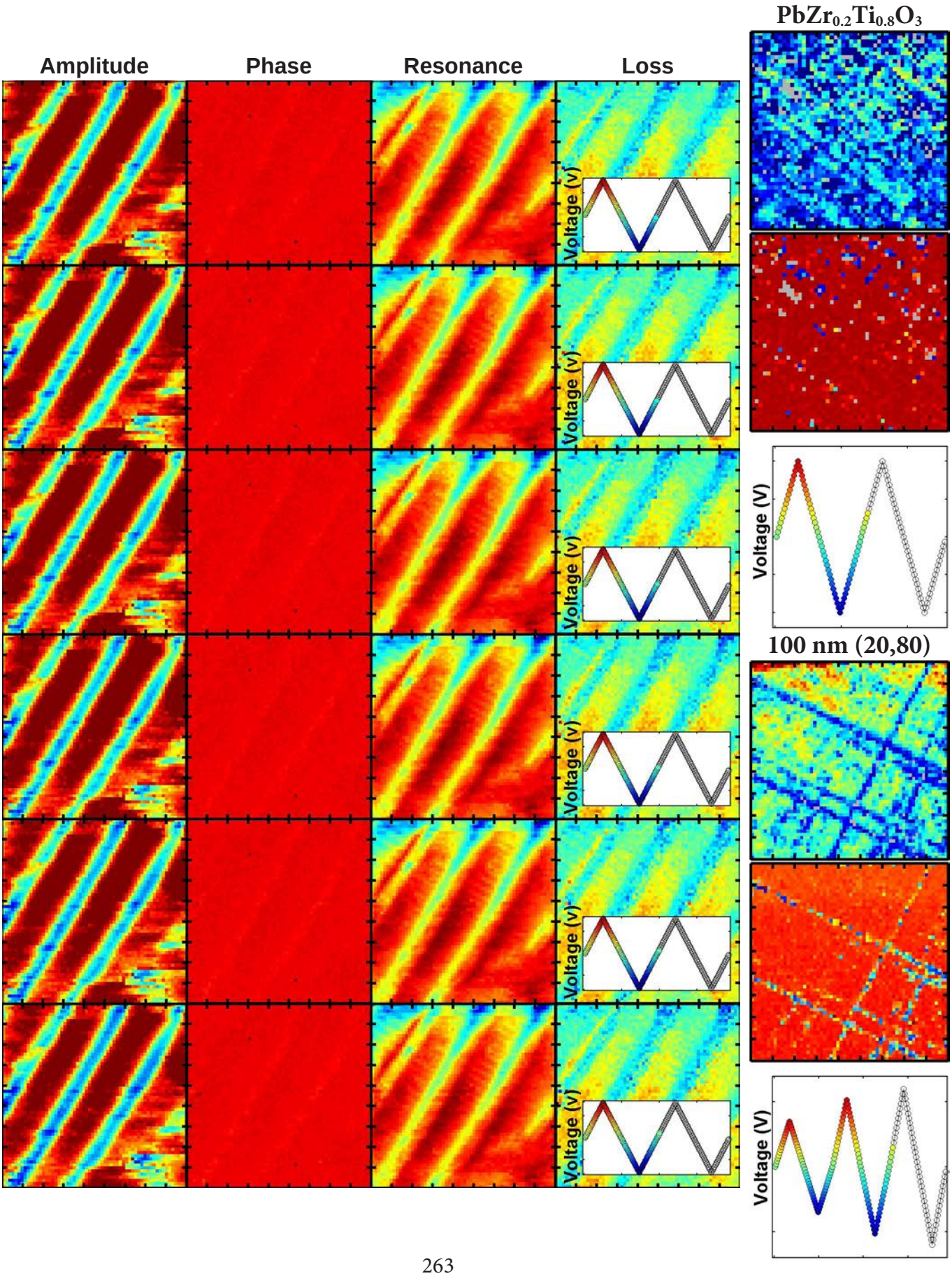
PbZr0.2Ti0.8O3
Amplitude
Phase
Resonance
Loss
Voltage (v)
Voltage (V)
100 nm (20,80)

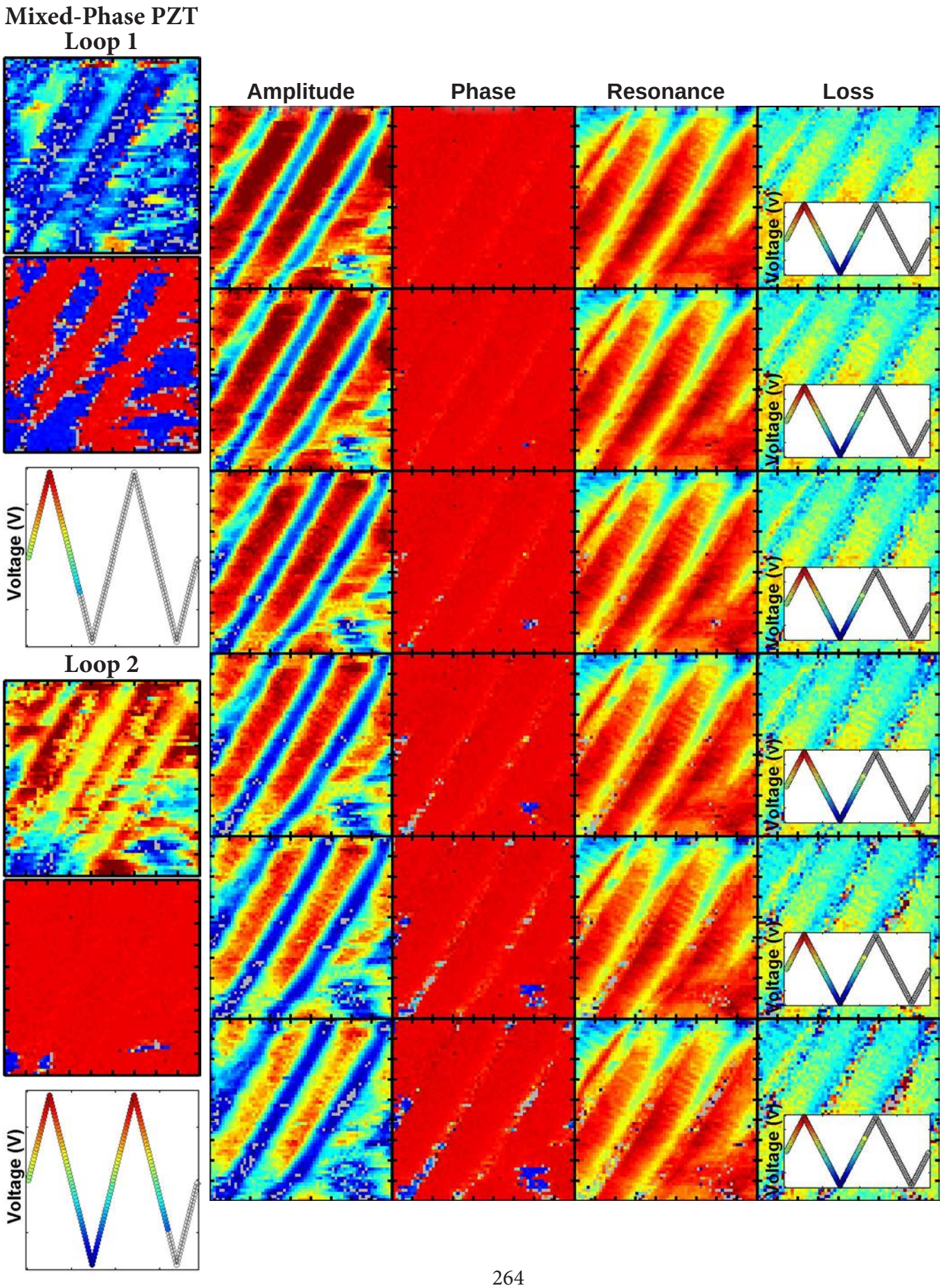
Mixed-Phase PZT
Loop 1
Amplitude
Phase
Resonance
Loss
Voltage (V)
Loop 2
Voltage (V)
Voltage (v)

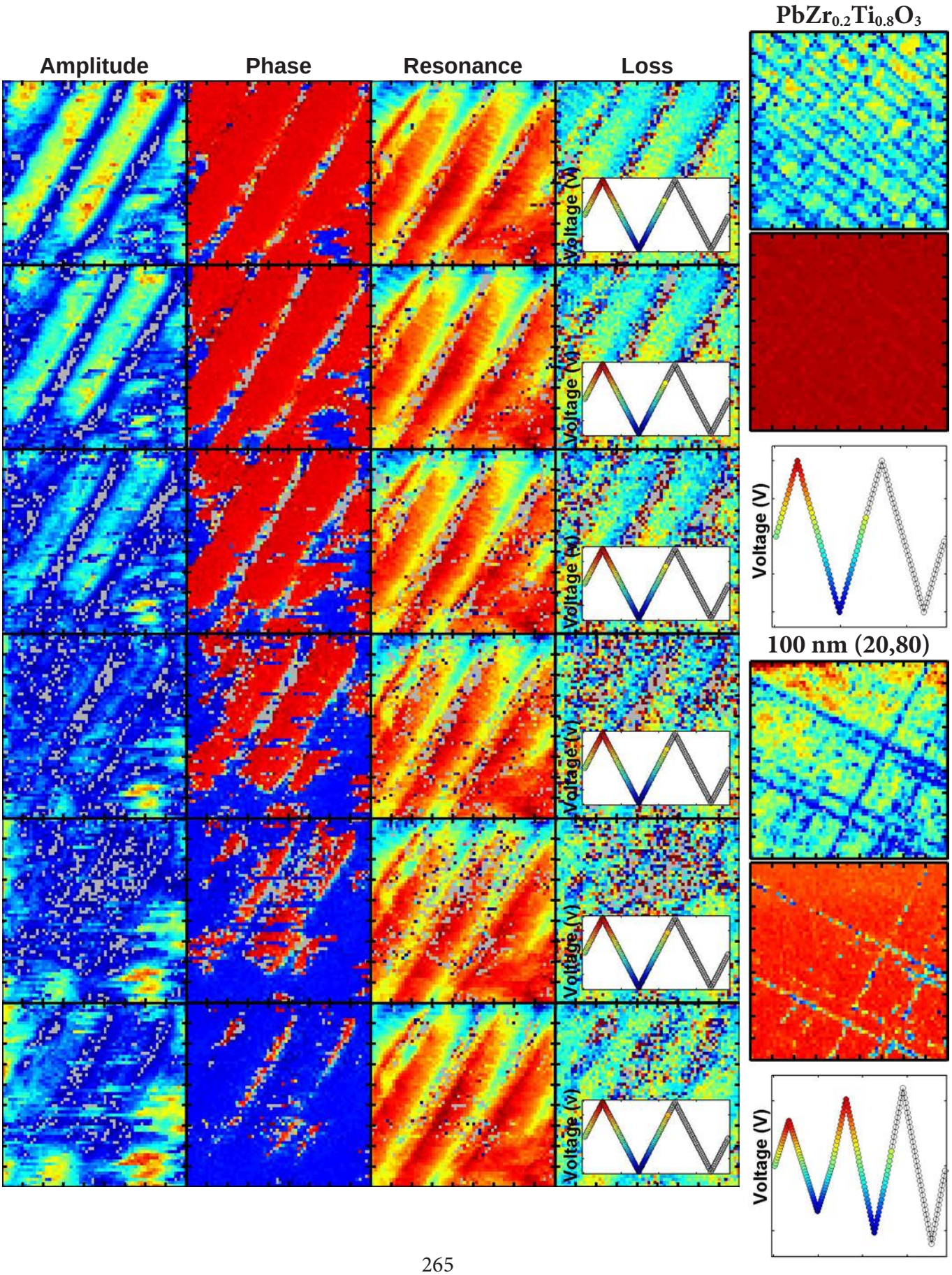
Amplitude
Phase
Resonance
Loss
Voltage (V)
PbZr0.2Ti0.8O3
100 nm (20,80)

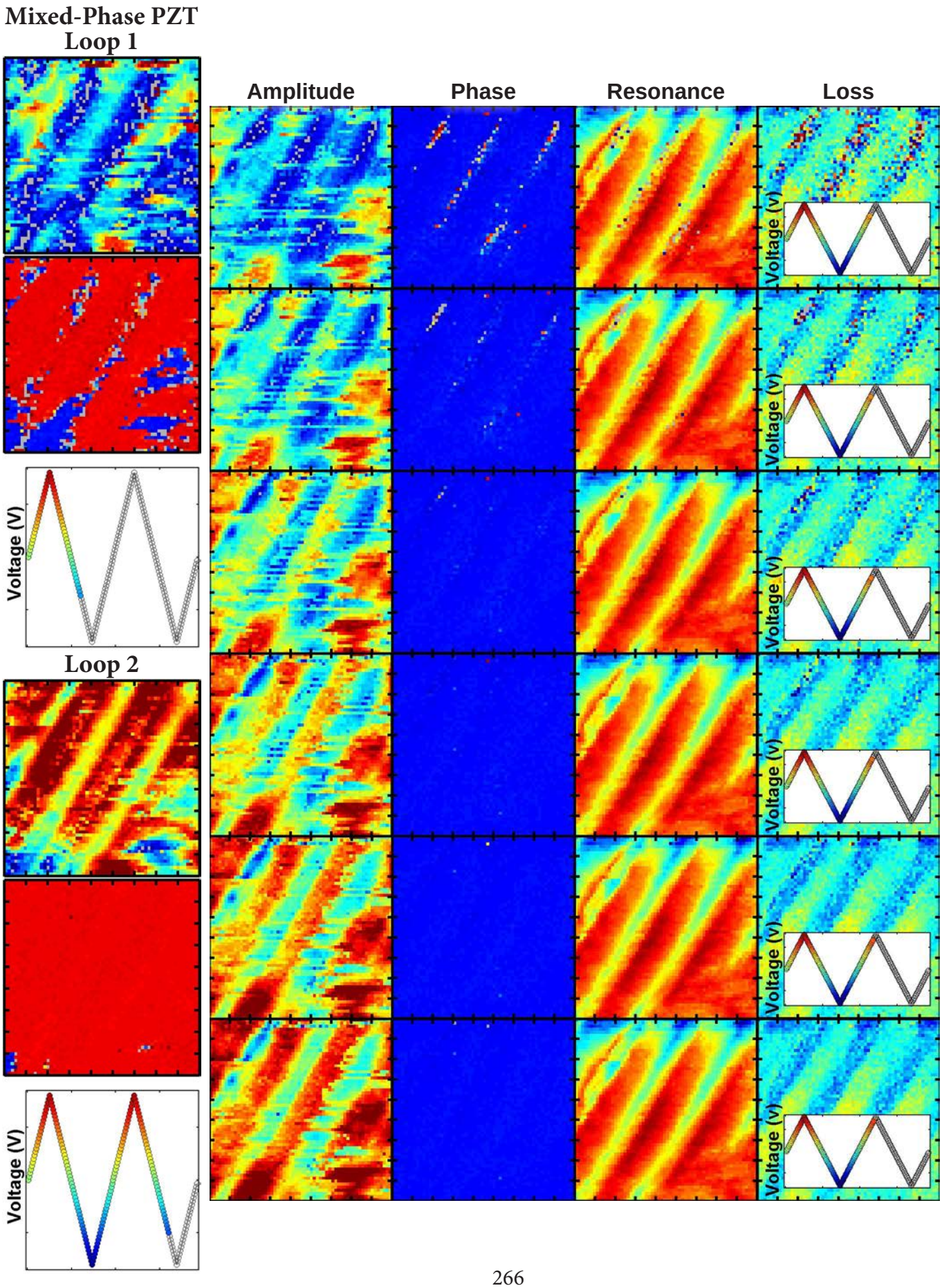
Mixed-Phase PZT
Loop 1
Amplitude
Phase
Resonance
Loss
Voltage (V)
Loop 2
Voltage (V)
Voltage (v)

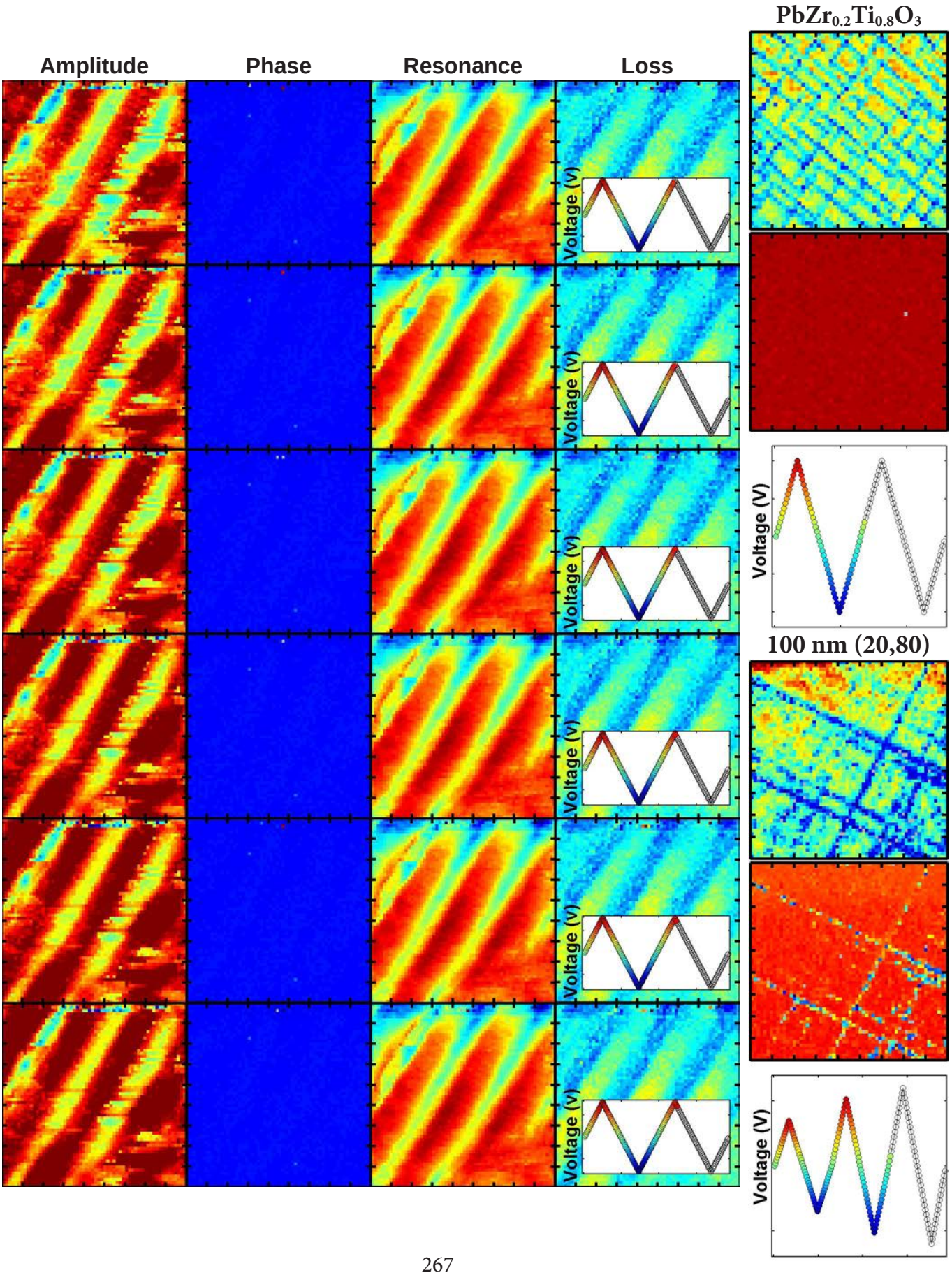
Amplitude
Phase
Resonance
Loss
Voltage (V)
PbZr0.2Ti0.8O3
100 nm (20,80)

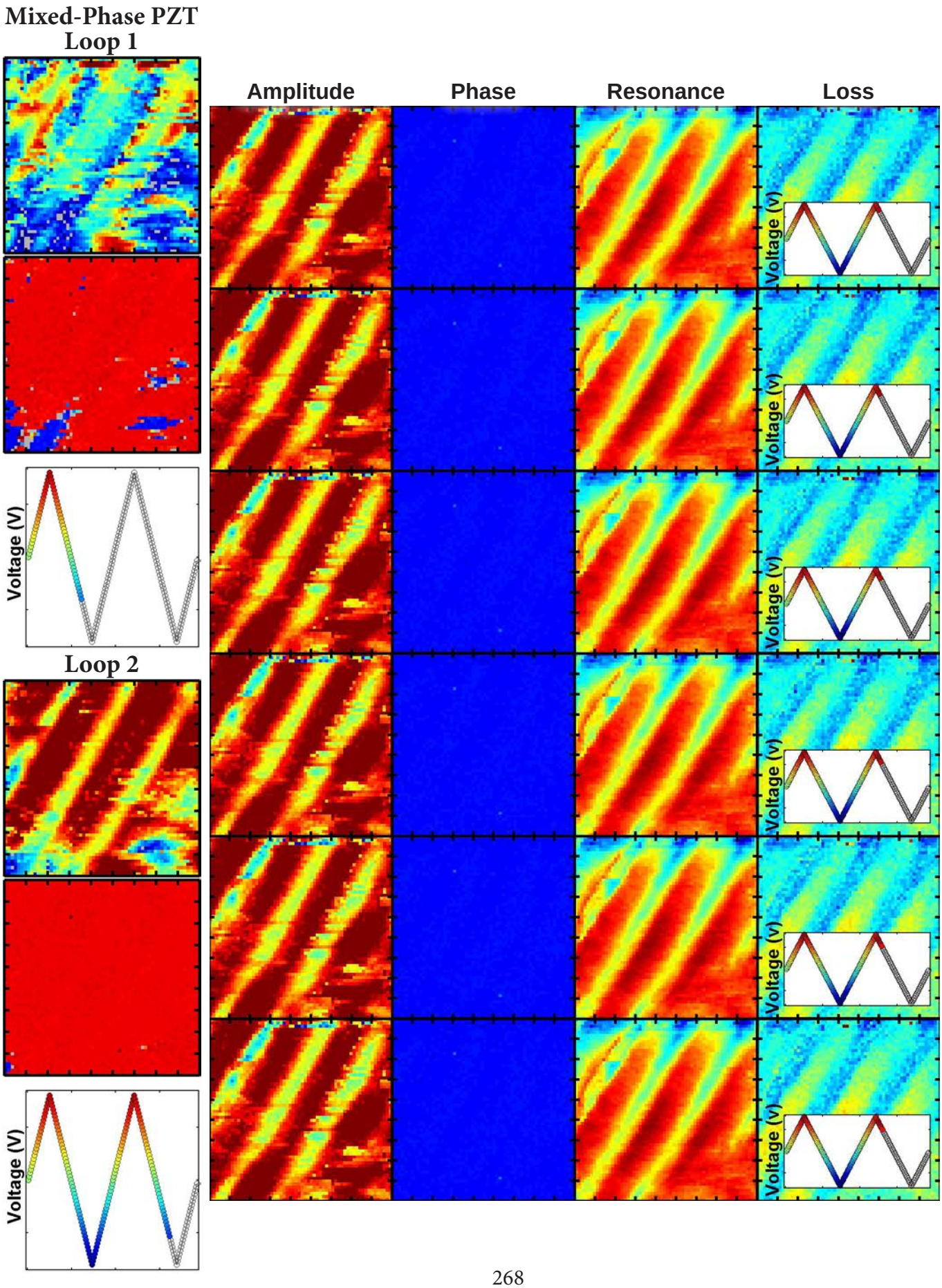
Mixed-Phase PZT
Loop 1
Amplitude
Phase
Resonance
Loss
Voltage (V)
Loop 2
Voltage (V)
Voltage (v)

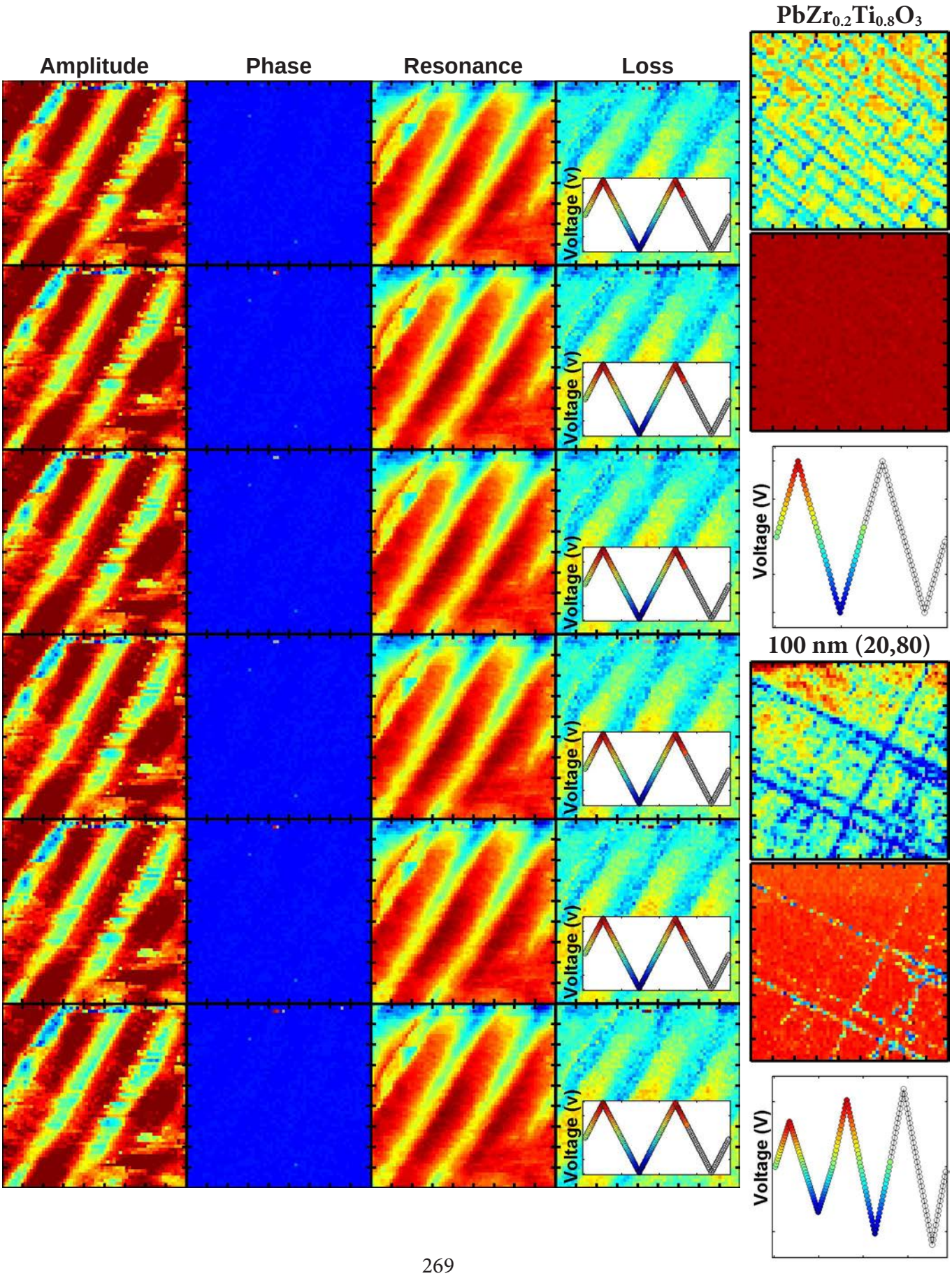
Amplitude
Phase
Resonance
Loss
Voltage (V)
PbZr0.2Ti0.8O3
100 nm (20,80)

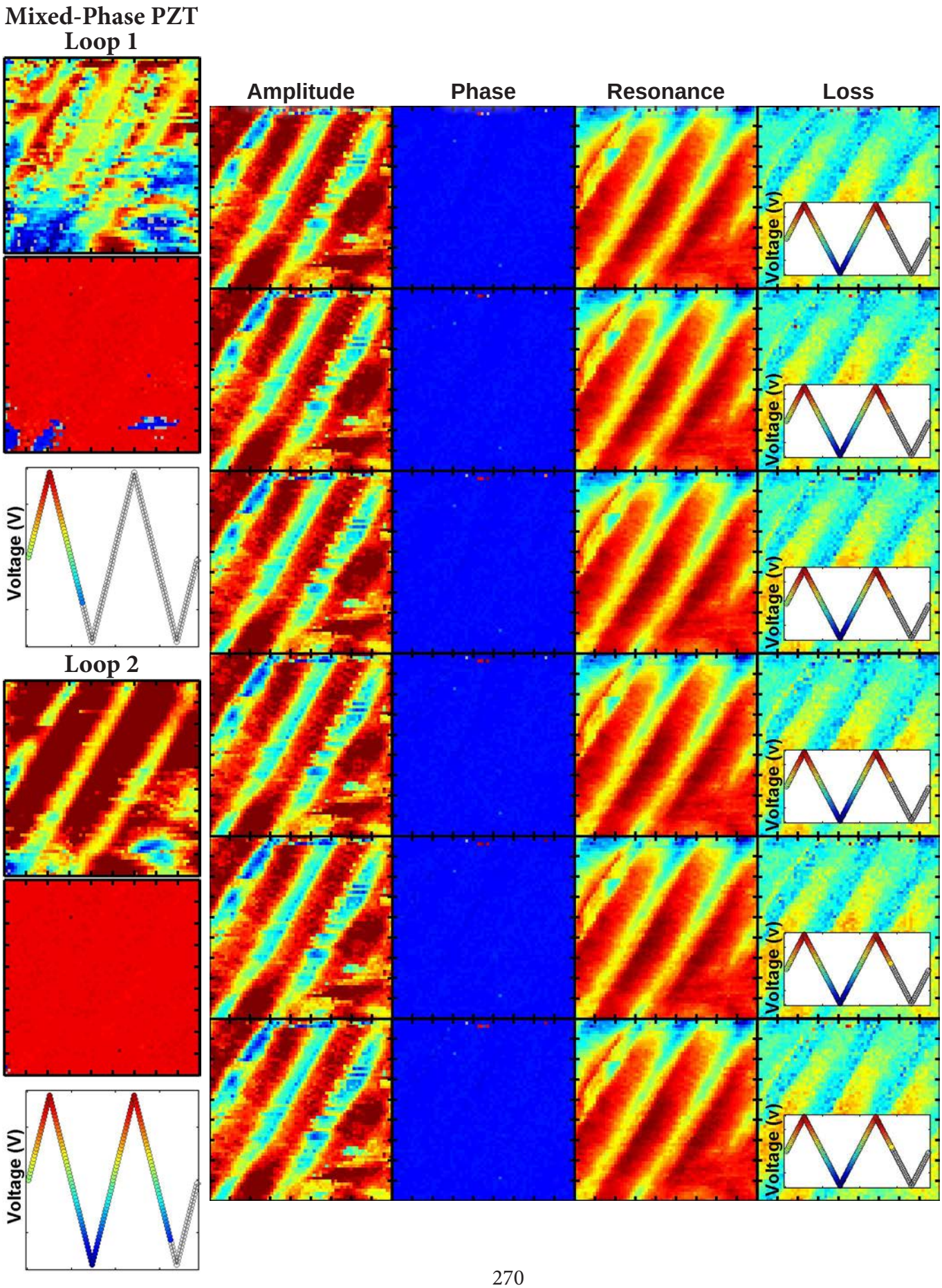
Mixed-Phase PZT
Loop 1
Amplitude
Phase
Resonance
Loss
Voltage (V)
Loop 2
Voltage (V)
Voltage (v)

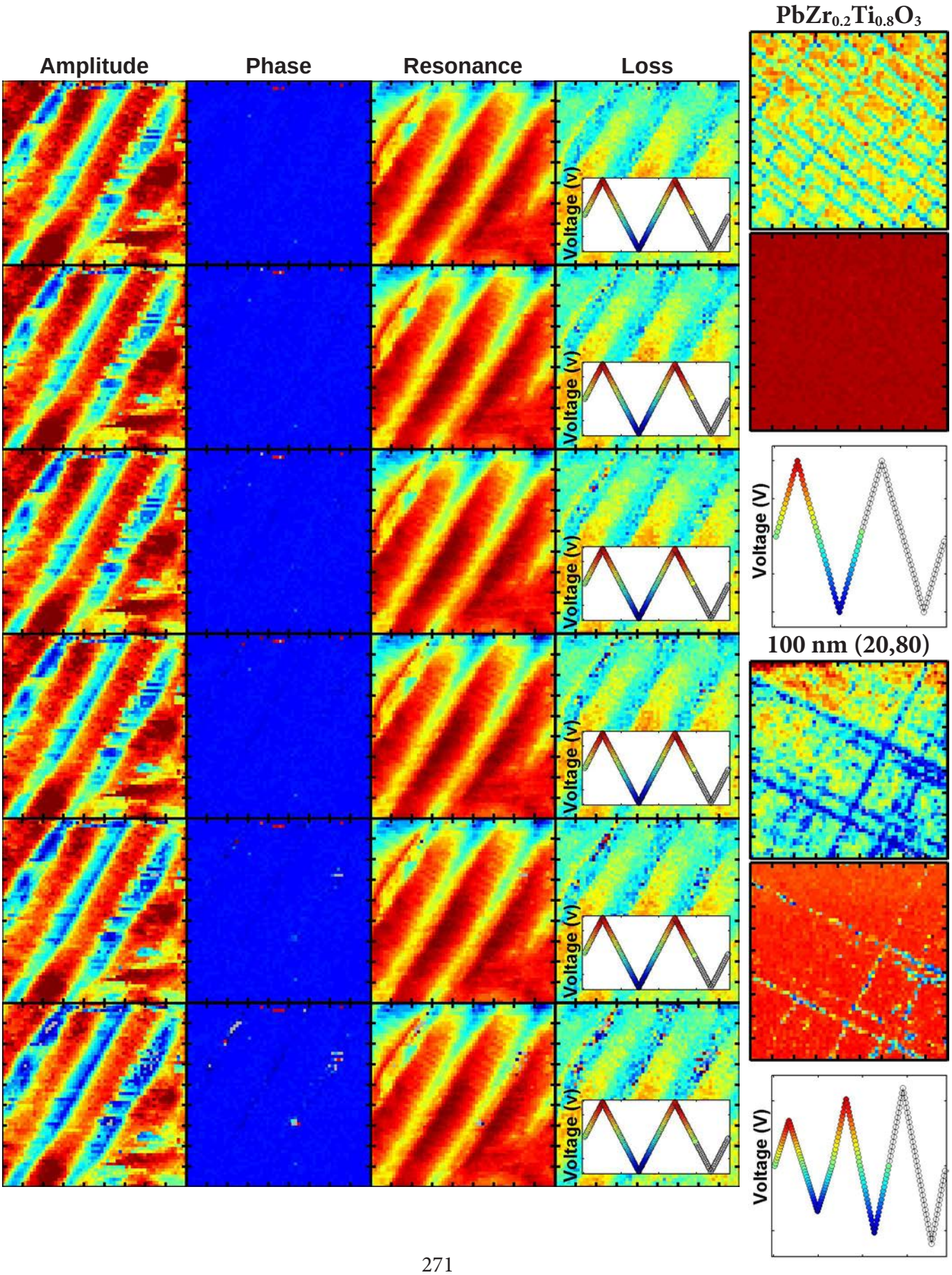
Amplitude
Phase
Resonance
Loss
Voltage (v)
PbZr0.2Ti0.8O3
Voltage (V)
100 nm (20,80)

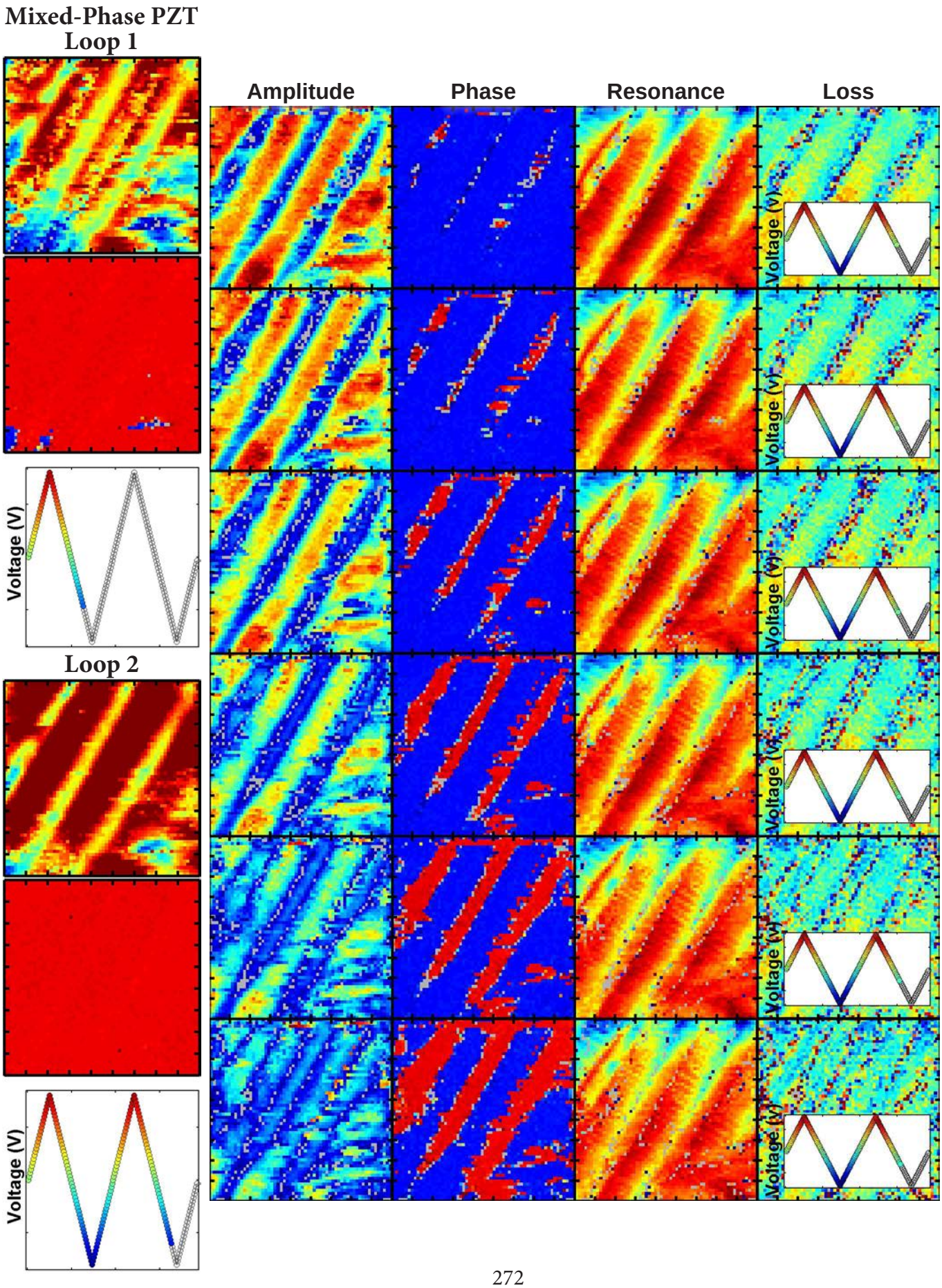
Mixed-Phase PZT
Loop 1
Amplitude
Phase
Resonance
Loss
Voltage (V)
Loop 2
Voltage (V)
Voltage (v)
Voltage (v)
Voltage (v)
Voltage (v)
Voltage (v)

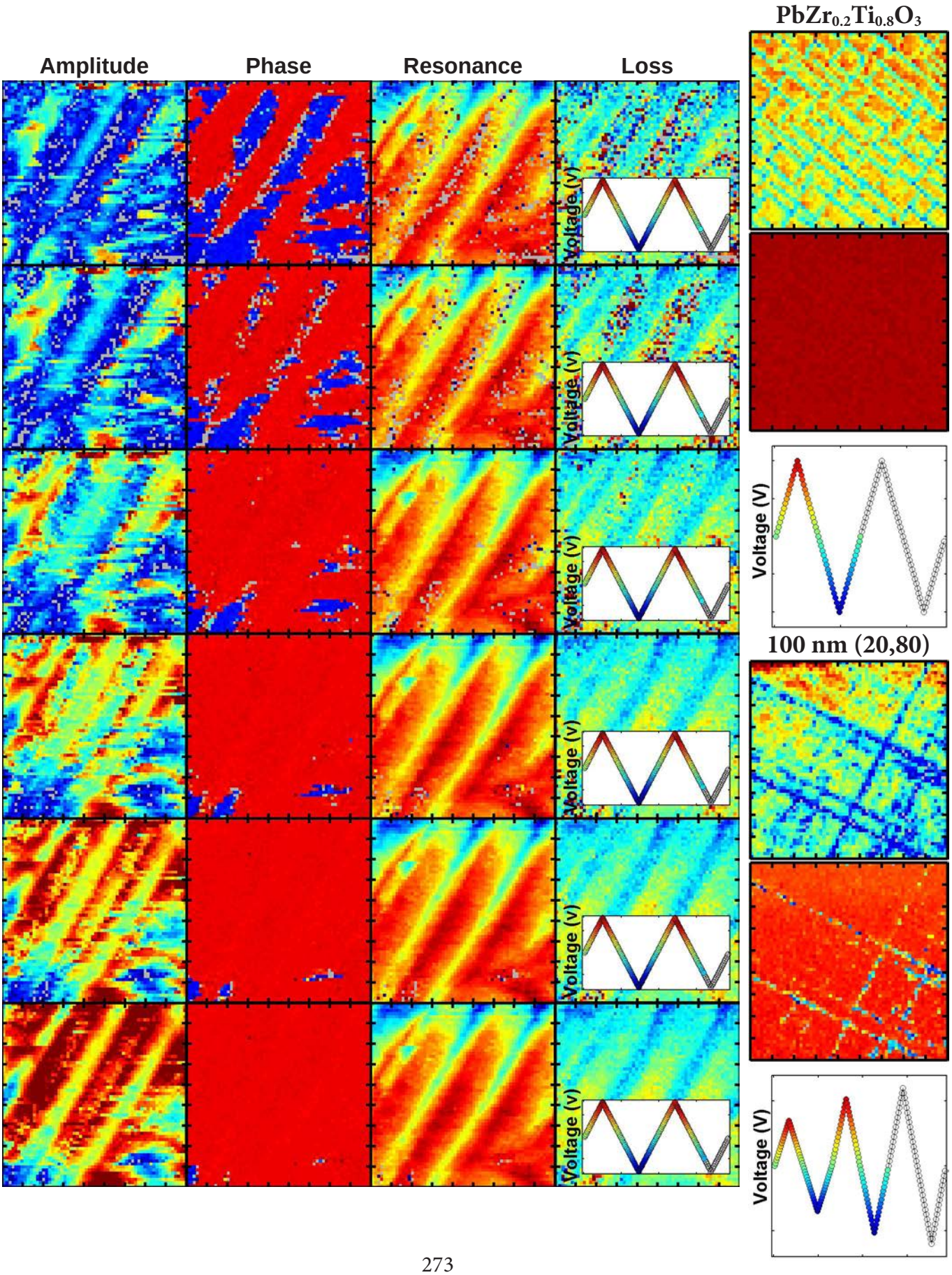
Amplitude
Phase
Resonance
Loss
Voltage (V)
PbZr0.2Ti0.8O3
100 nm (20,80)

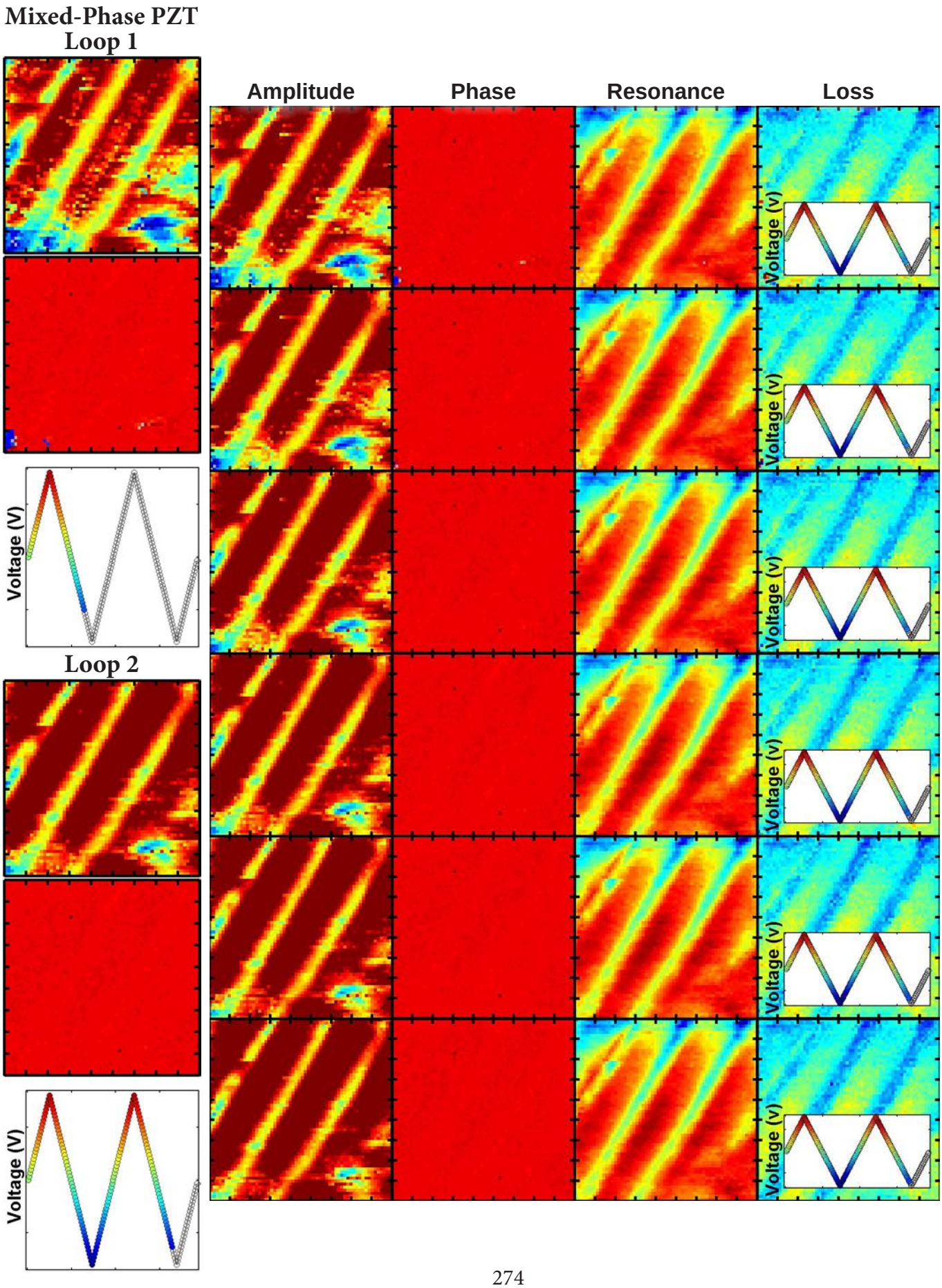
Mixed-Phase PZT
Loop 1
Amplitude
Phase
Resonance
Loss
Voltage (V)
Loop 2
Voltage (V)
Voltage (v)

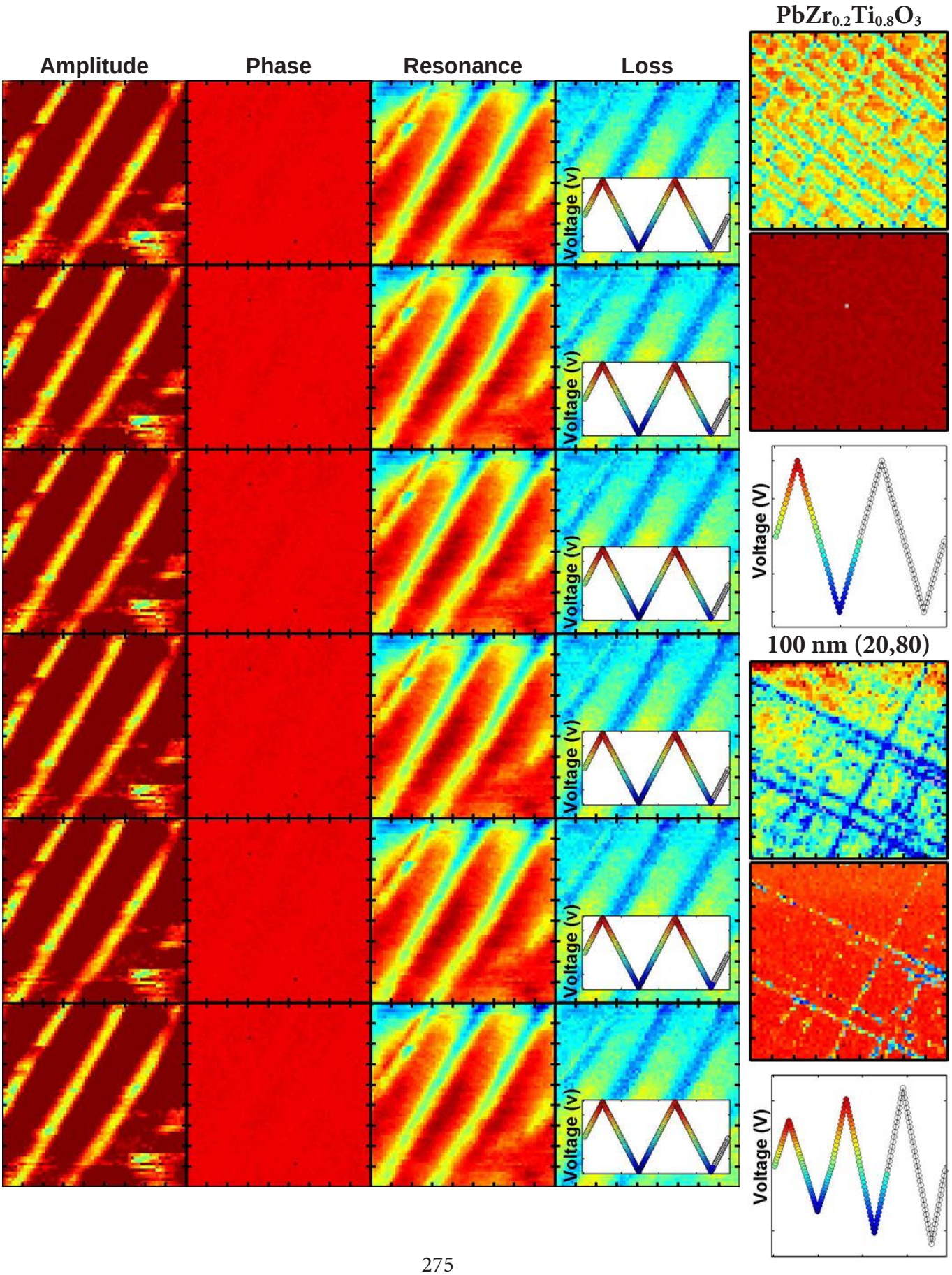
Amplitude
Phase
Resonance
Loss
Voltage (v)
PbZr0.2Ti0.8O3
Voltage (V)
100 nm (20,80)

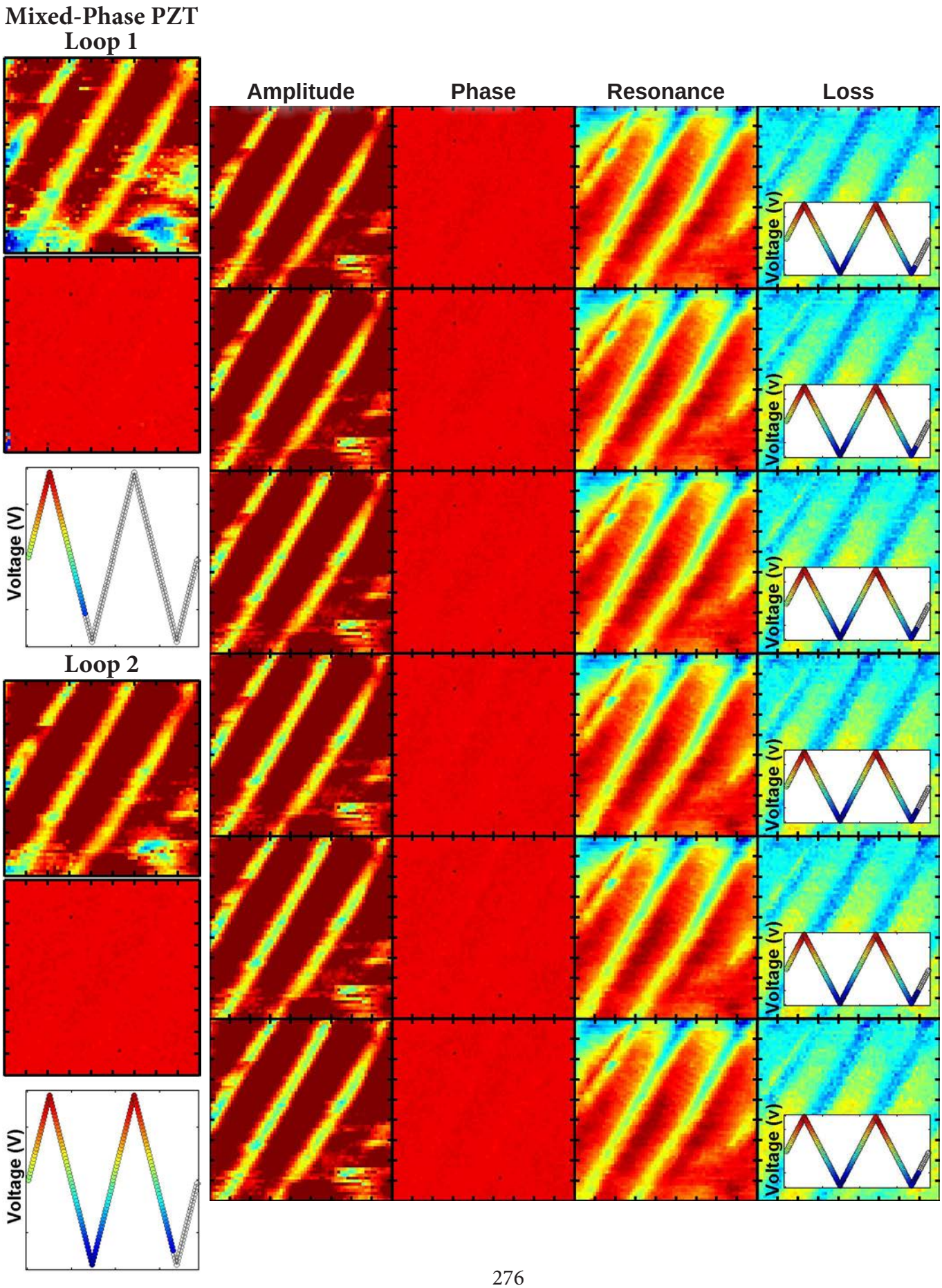
Mixed-Phase PZT
Loop 1
Amplitude
Phase
Resonance
Loss
Voltage (V)
Loop 2
Voltage (V)
Voltage (v)

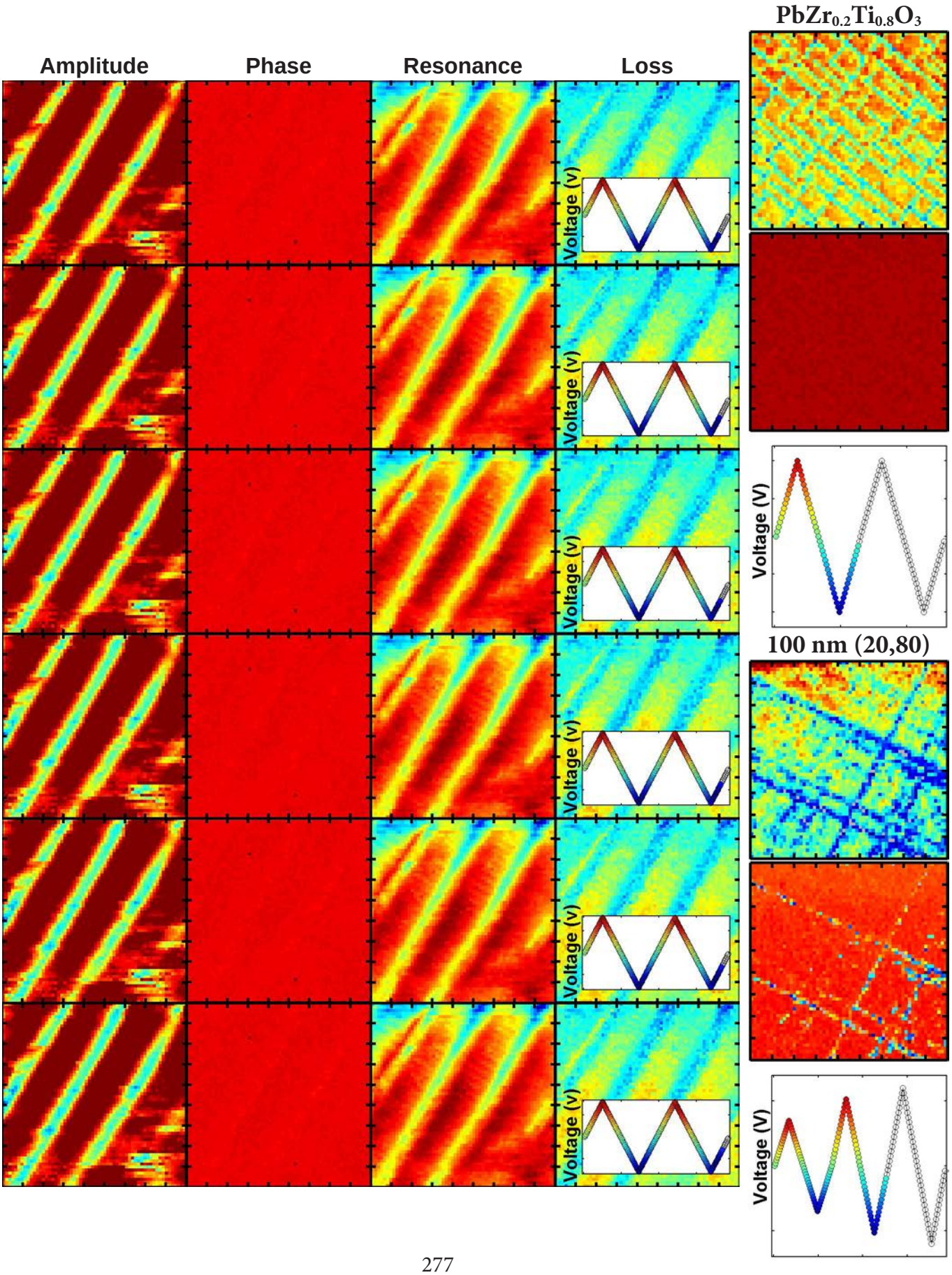
Amplitude
Phase
Resonance
Loss
Voltage (v)
PbZr0.2Ti0.8O3
Voltage (V)
100 nm (20,80)

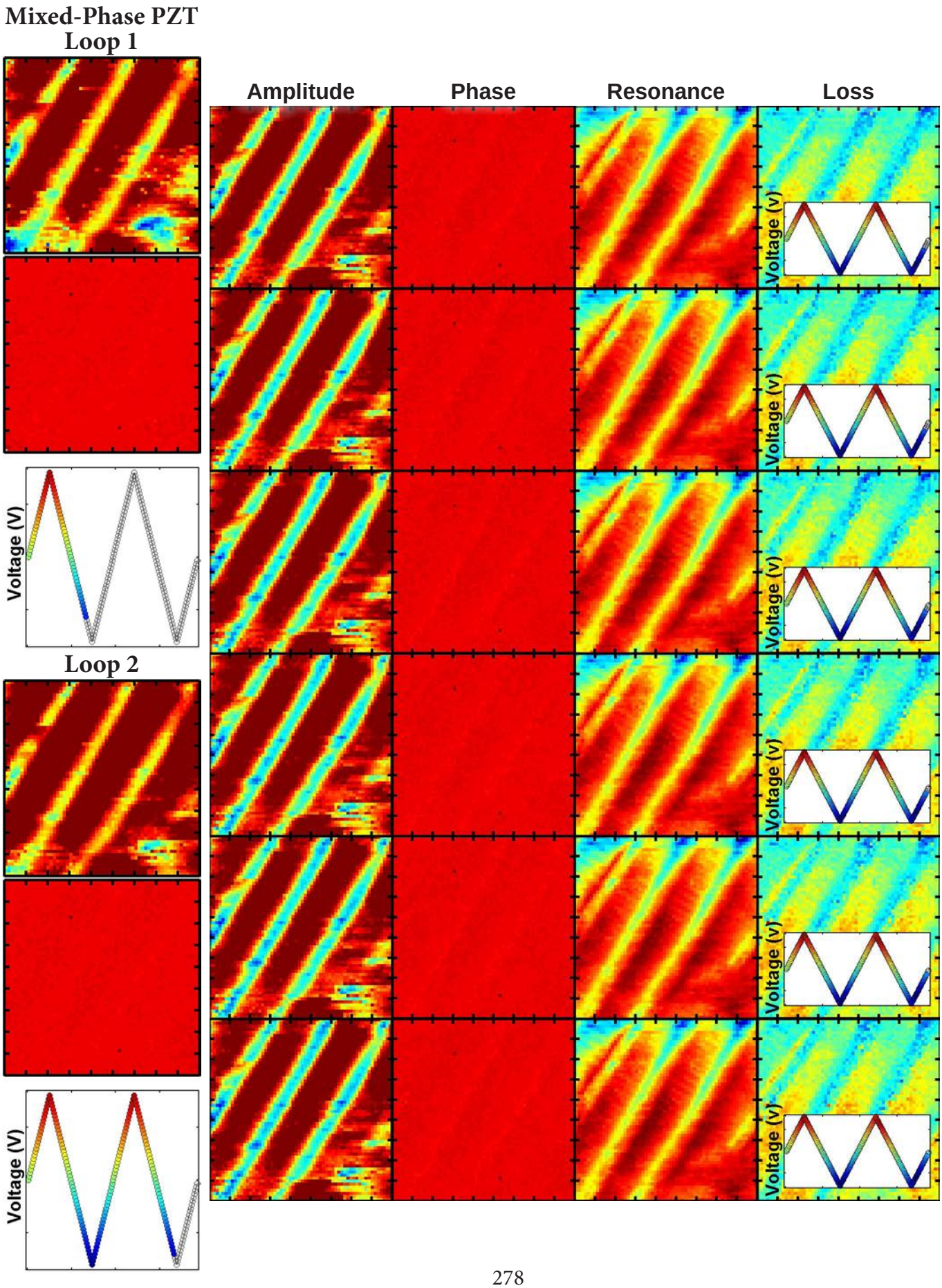
Mixed-Phase PZT
Loop 1
Amplitude
Phase
Resonance
Loss
Voltage (V)
Loop 2
Voltage (V)
Voltage (v)

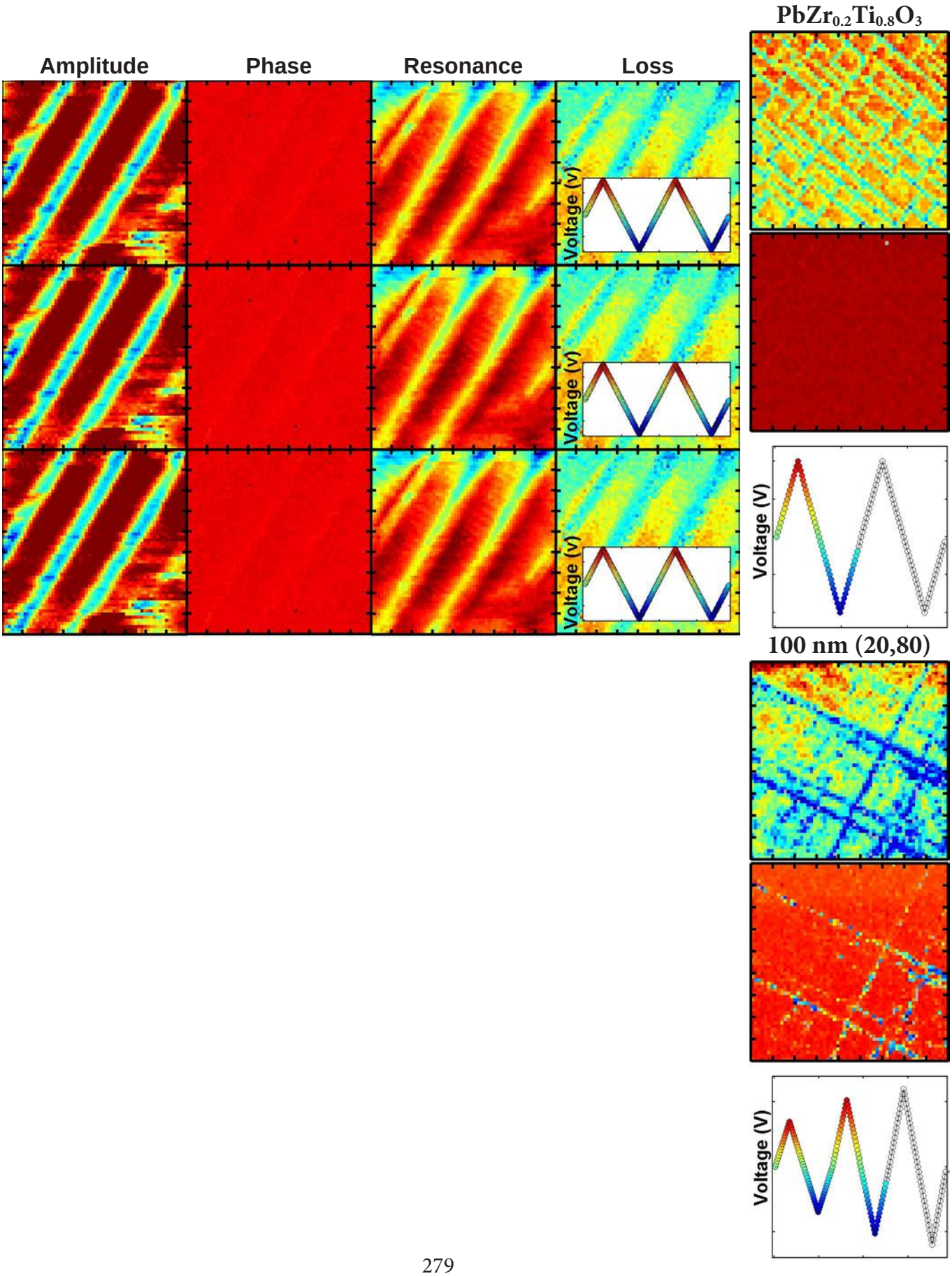
Amplitude
Phase
Resonance
Loss
Voltage (V)
Voltage (V)
Voltage (V)
PbZr0.2Ti0.8O3
Voltage (V)
100 nm (20,80)
Voltage (V)

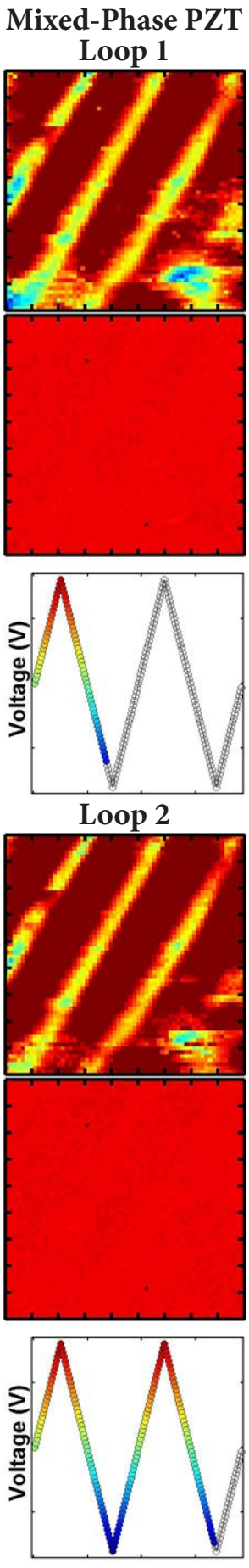
Mixed-Phase PZT
Loop 1
Voltage (V)
Loop 2
Voltage (V)

Appendix J

Mixed-Phase $PbZr_{0.2}Ti_{0.8}O_3$ Loop Shape Parameters

In this section we have included preliminary loop fitting results (from the switching spectroscopy measurement shown in Appendix I) on 400 nm thick mixed-phase $PbZr_{0.2}Ti_{0.8}O_3/Ba_{0.5}Sr_{0.5}RuO_3$ (15 nm)/$NdScO_3$ (110). All loop fitting results are based on the single-transition loop fitting algorithm. The results presented in this section are preliminary and included in this thesis to demonstrate the methods, methodologies, and typical results. We are currently in the process of optimizing the experimental dataset, loop fitting algorithm and analysis techniques to aid in deriving physical insight from these experiments. All scans sizes are 2 μm.

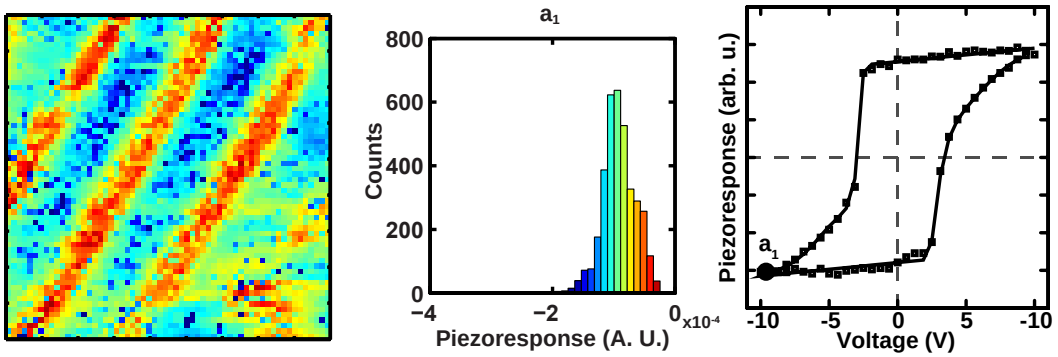

Figure J.1. Loop fitting result (a_1) of 400 nm thick mixed-phase $PbZr_{0.2}Ti_{0.8}O_3$ heterostructures on $NdScO_3$ (110).

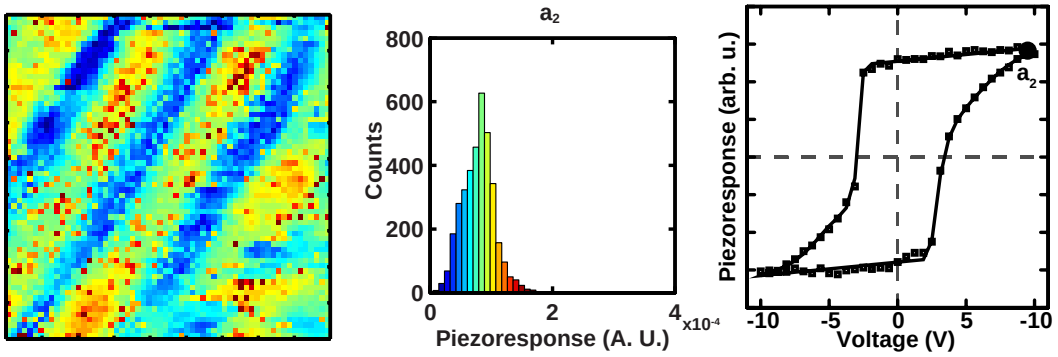

Figure J.2. Loop fitting result (a_2) of 400 nm thick mixed-phase $PbZr_{0.2}Ti_{0.8}O_3$ heterostructures on $NdScO_3$ (110).

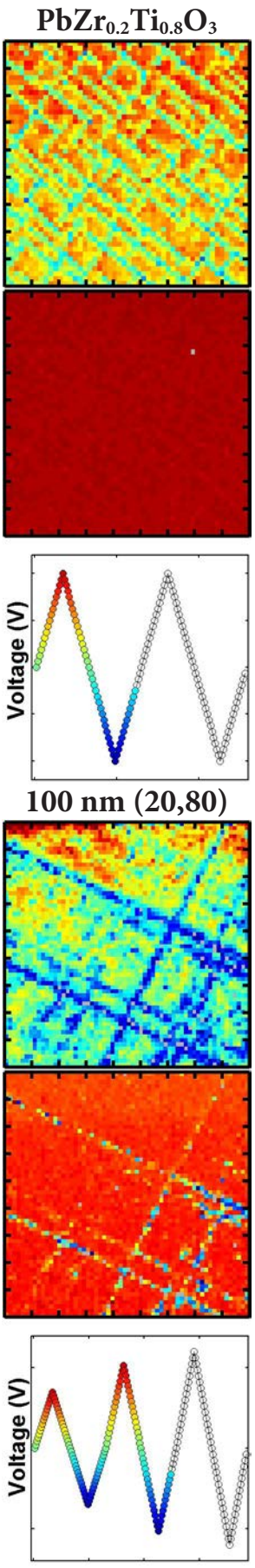

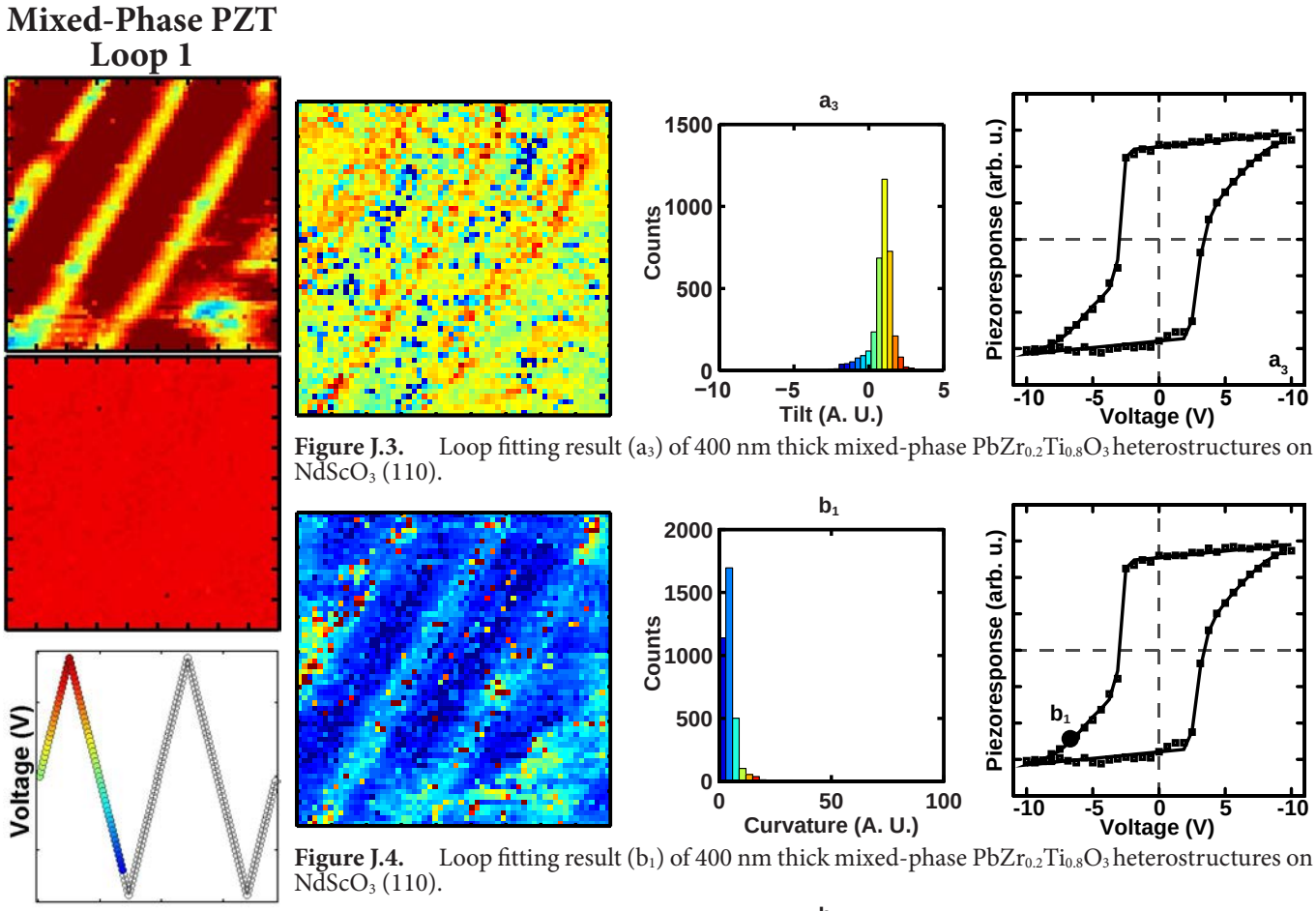

Figure J.3. Loop fitting result (a_3) of 400 nm thick mixed-phase $PbZr_{0.2}Ti_{0.8}O_3$ heterostructures on $NdScO_3$ (110).

Figure J.4. Loop fitting result (b_1) of 400 nm thick mixed-phase $PbZr_{0.2}Ti_{0.8}O_3$ heterostructures on $NdScO_3$ (110).

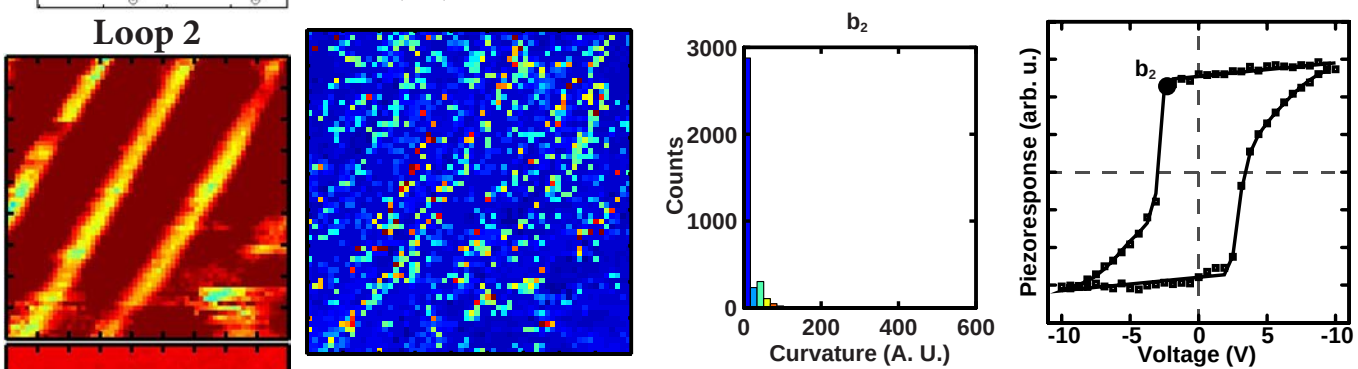

Figure J.5. Loop fitting result (b_2) of 400 nm thick mixed-phase $PbZr_{0.2}Ti_{0.8}O_3$ heterostructures on $NdScO_3$ (110).

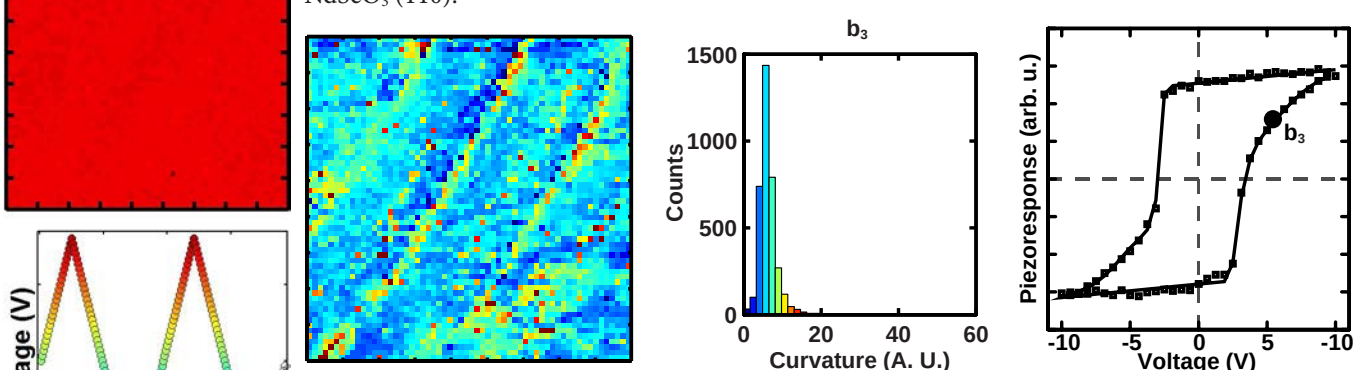

Figure J.6. Loop fitting result (b_3) of 400 nm thick mixed-phase $PbZr_{0.2}Ti_{0.8}O_3$ heterostructures on $NdScO_3$ (110).

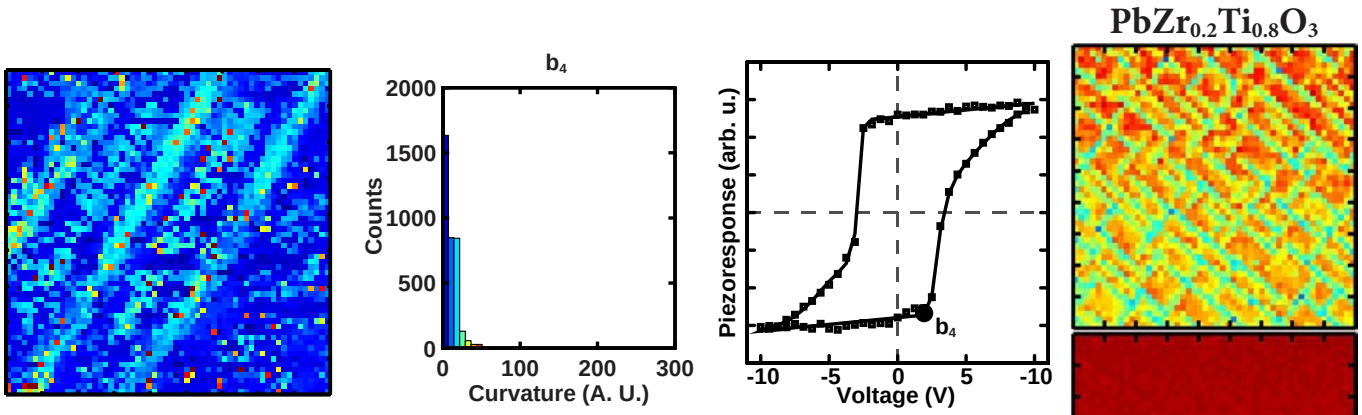

Figure J.7. Loop fitting result (b_4) of 400 nm thick mixed-phase $PbZr_{0.2}Ti_{0.8}O_3$ heterostructures on $NdScO_3$ (110).

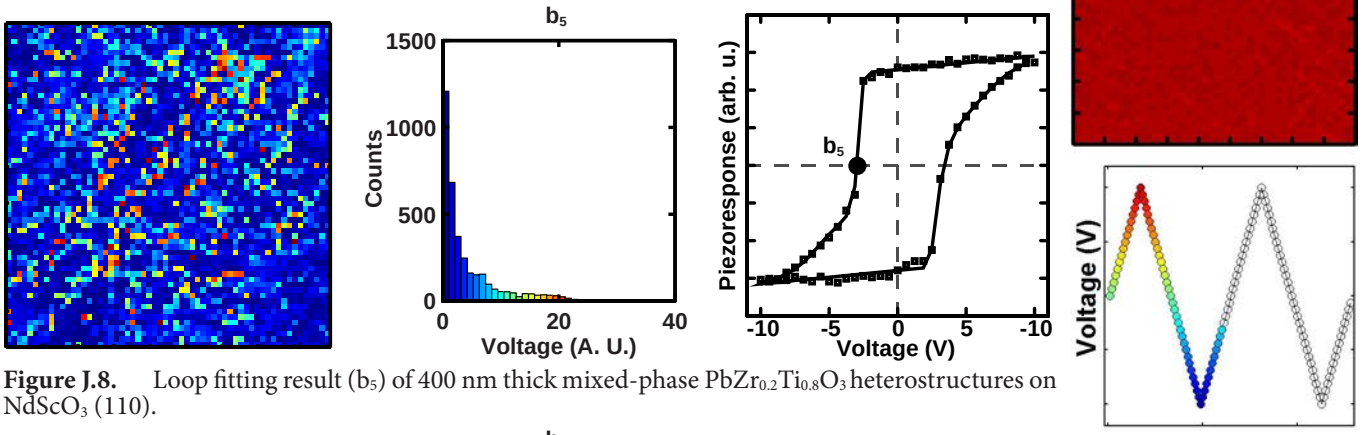

Figure J.8. Loop fitting result (b_5) of 400 nm thick mixed-phase $PbZr_{0.2}Ti_{0.8}O_3$ heterostructures on $NdScO_3$ (110).

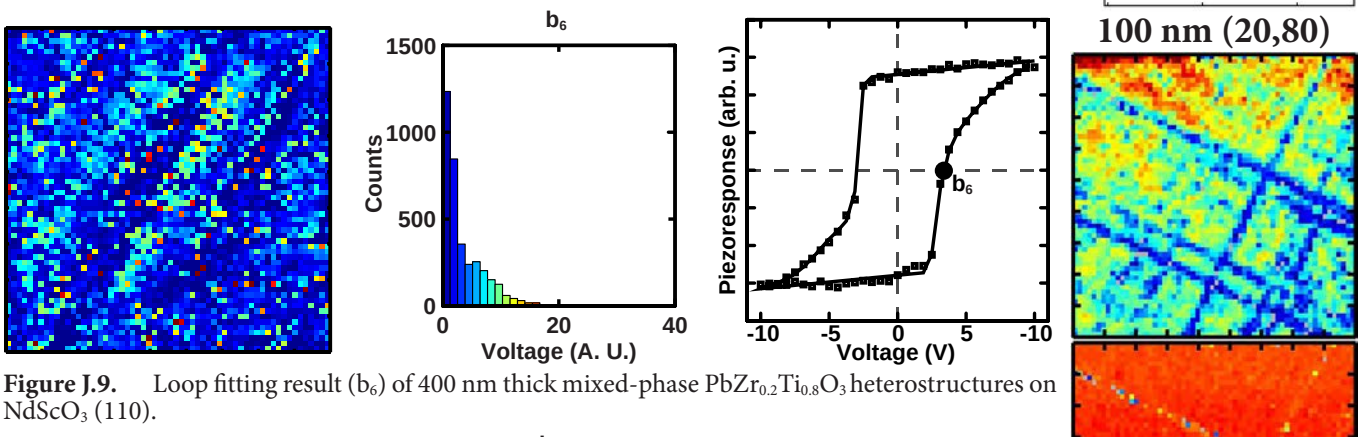

Figure J.9. Loop fitting result (b_6) of 400 nm thick mixed-phase $PbZr_{0.2}Ti_{0.8}O_3$ heterostructures on $NdScO_3$ (110).

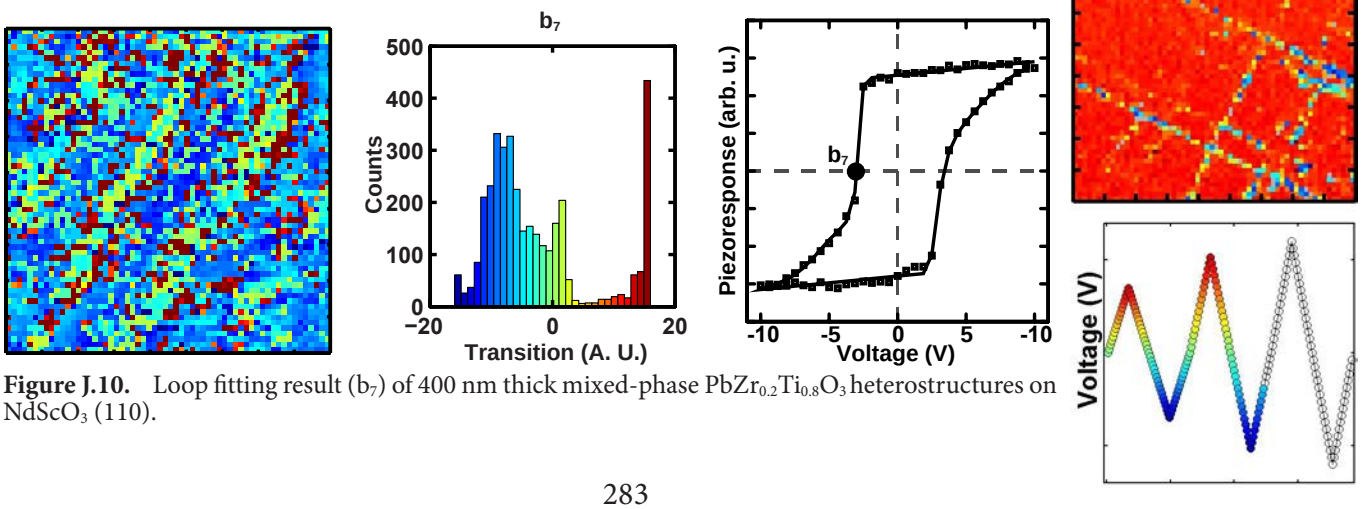

Figure J.10. Loop fitting result (b_7) of 400 nm thick mixed-phase $PbZr_{0.2}Ti_{0.8}O_3$ heterostructures on $NdScO_3$ (110).

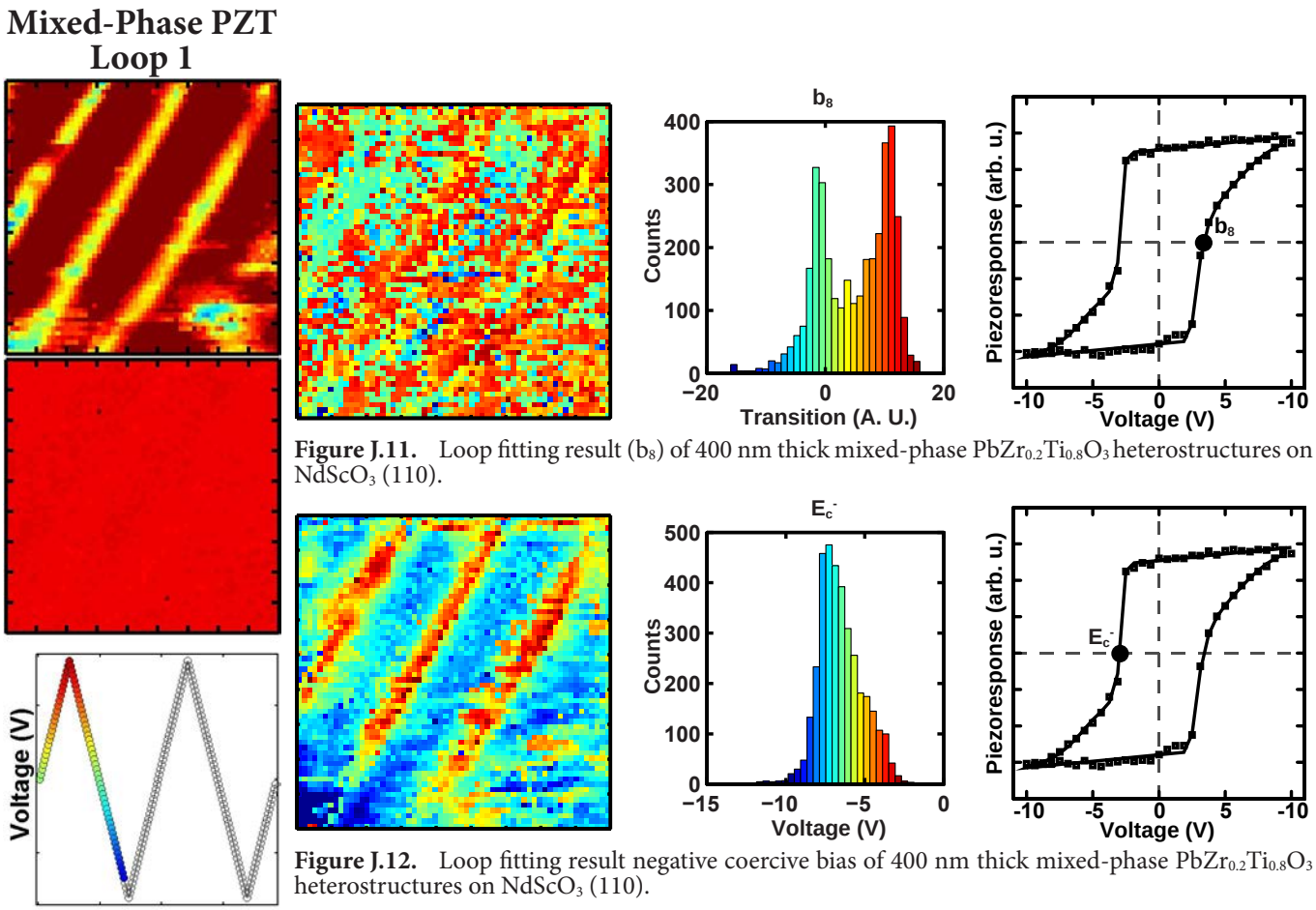

Figure J.11. Loop fitting result (b_8) of 400 nm thick mixed-phase $PbZr_{0.2}Ti_{0.8}O_3$ heterostructures on $NdScO_3$ (110).

Figure J.12. Loop fitting result negative coercive bias of 400 nm thick mixed-phase $PbZr_{0.2}Ti_{0.8}O_3$ heterostructures on $NdScO_3$ (110).

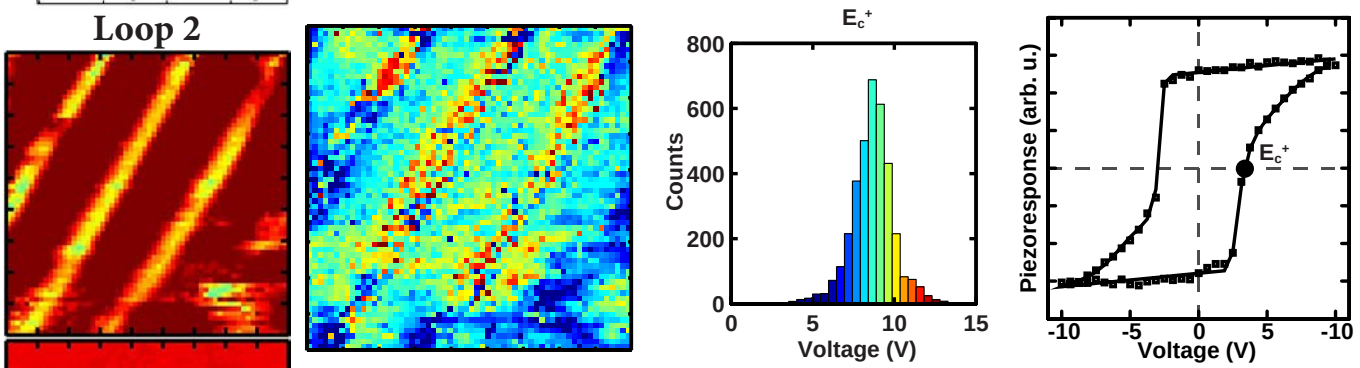

Figure J.13. Loop fitting result positive coercive bias of 400 nm thick mixed-phase $PbZr_{0.2}Ti_{0.8}O_3$ heterostructures on $NdScO_3$ (110).

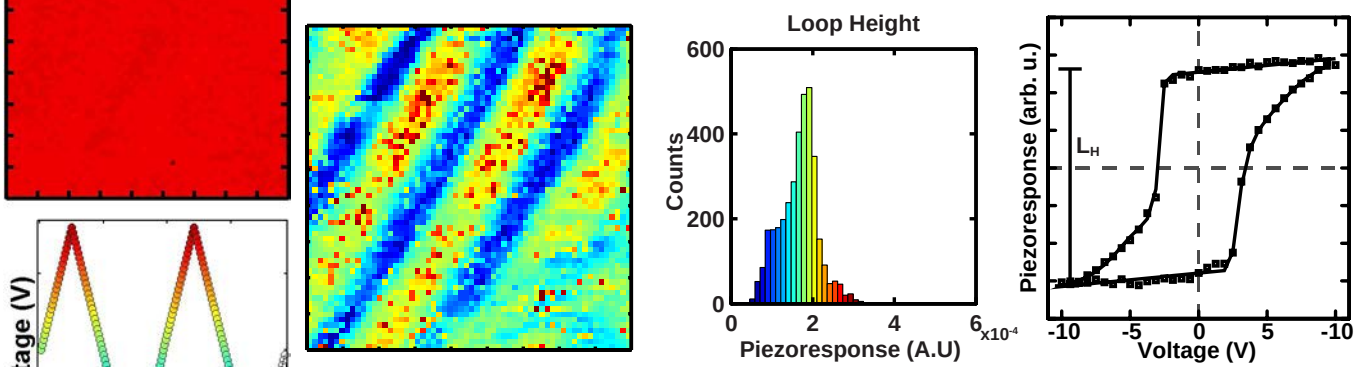

Figure J.14. Loop fitting result loop height of 400 nm thick mixed-phase $PbZr_{0.2}Ti_{0.8}O_3$ heterostructures on $NdScO_3$ (110).

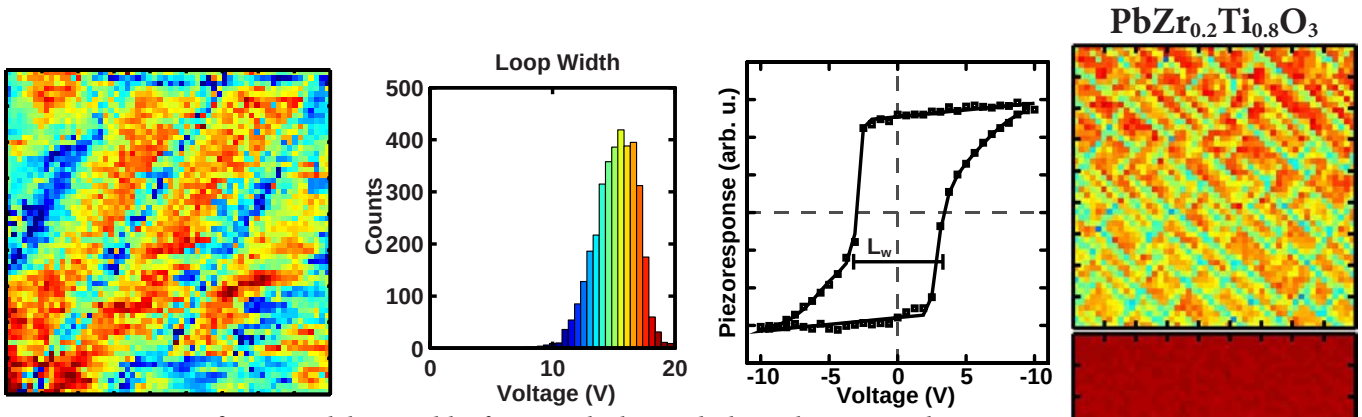

Figure J.15. Loop fitting result loop width of 400 nm thick mixed-phase $PbZr_{0.2}Ti_{0.8}O_3$ heterostructures on $NdScO_3$ (110).

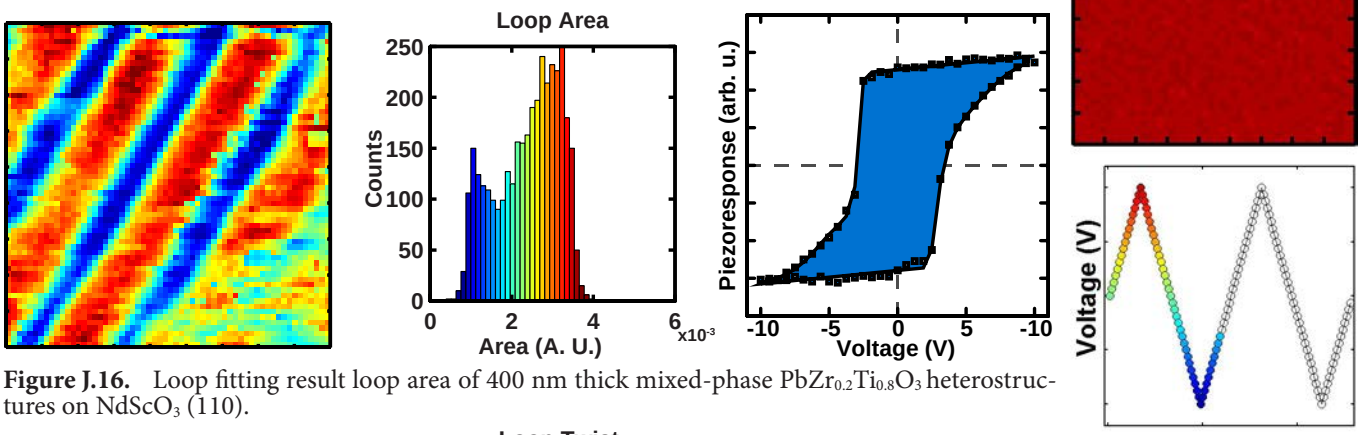

Figure J.16. Loop fitting result loop area of 400 nm thick mixed-phase $PbZr_{0.2}Ti_{0.8}O_3$ heterostructures on $NdScO_3$ (110).

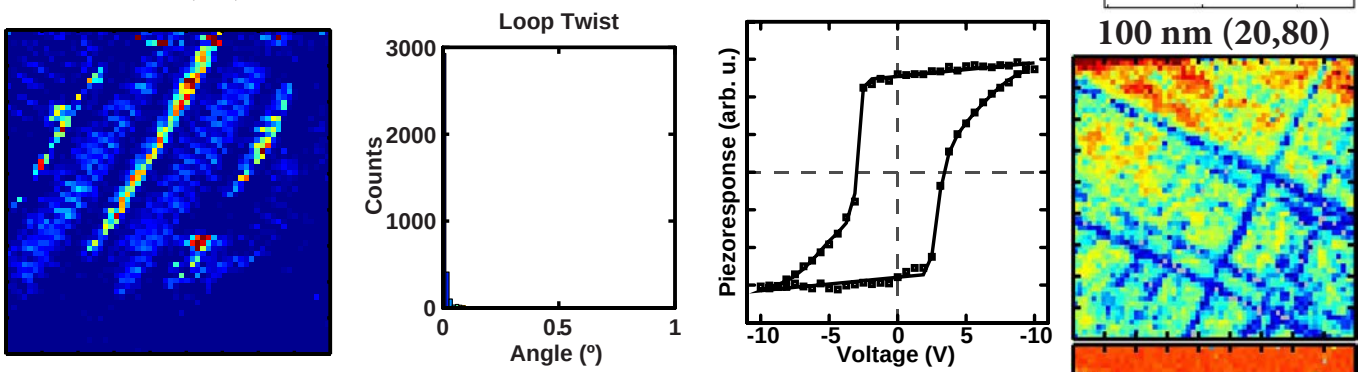

Figure J.17. Loop fitting result loop twist of 400 nm thick mixed-phase $PbZr_{0.2}Ti_{0.8}O_3$ heterostructures on $NdScO_3$ (110).

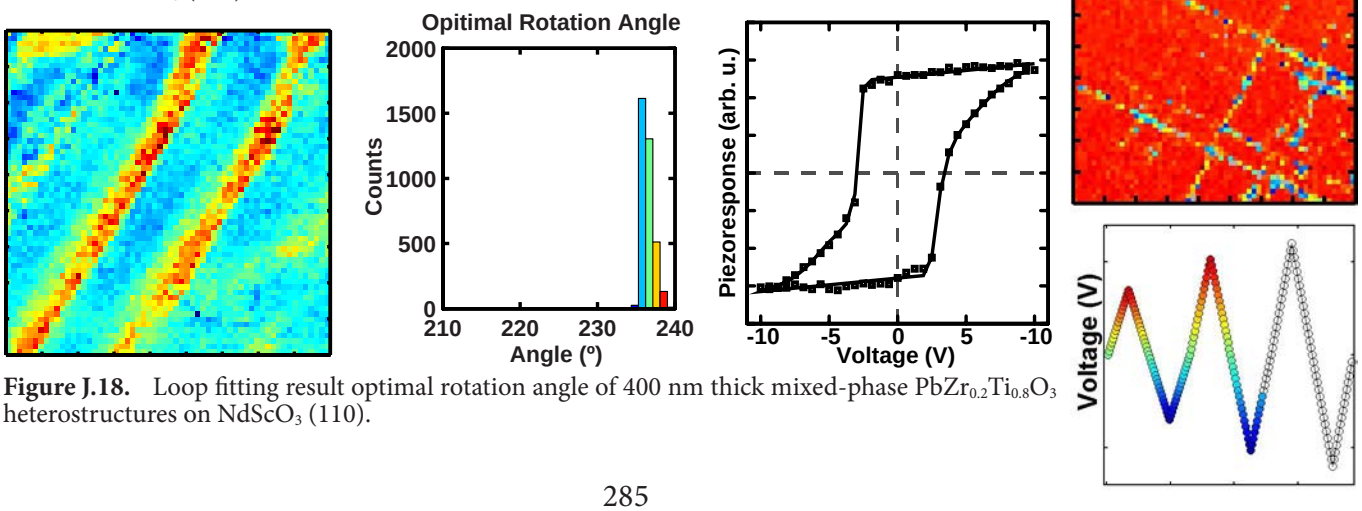

Figure J.18. Loop fitting result optimal rotation angle of 400 nm thick mixed-phase $PbZr_{0.2}Ti_{0.8}O_3$ heterostructures on $NdScO_3$ (110).

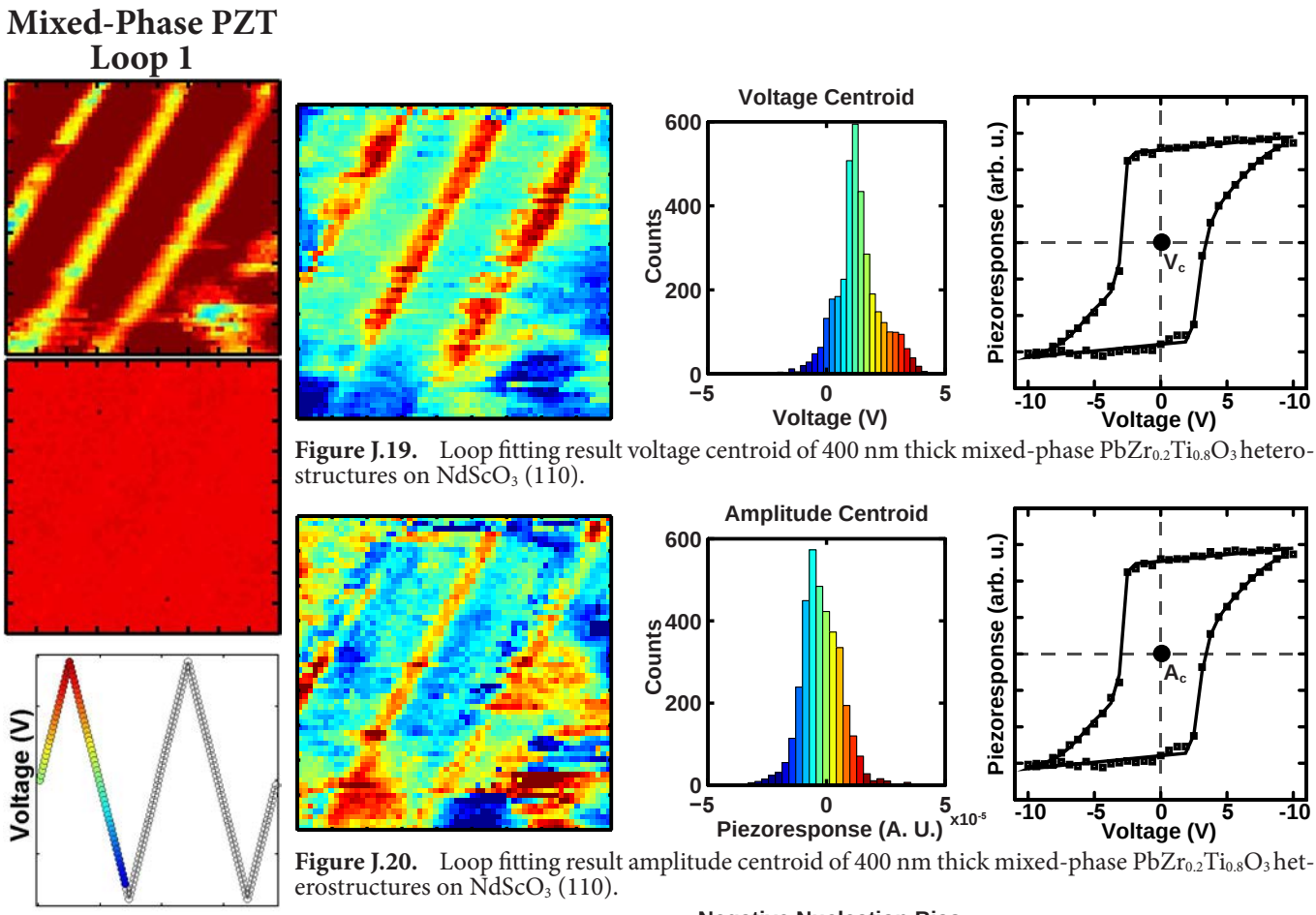

Figure J.19. Loop fitting result voltage centroid of 400 nm thick mixed-phase $PbZr_{0.2}Ti_{0.8}O_3$ heterostructures on $NdScO_3$ (110).

Figure J.20. Loop fitting result amplitude centroid of 400 nm thick mixed-phase $PbZr_{0.2}Ti_{0.8}O_3$ heterostructures on $NdScO_3$ (110).

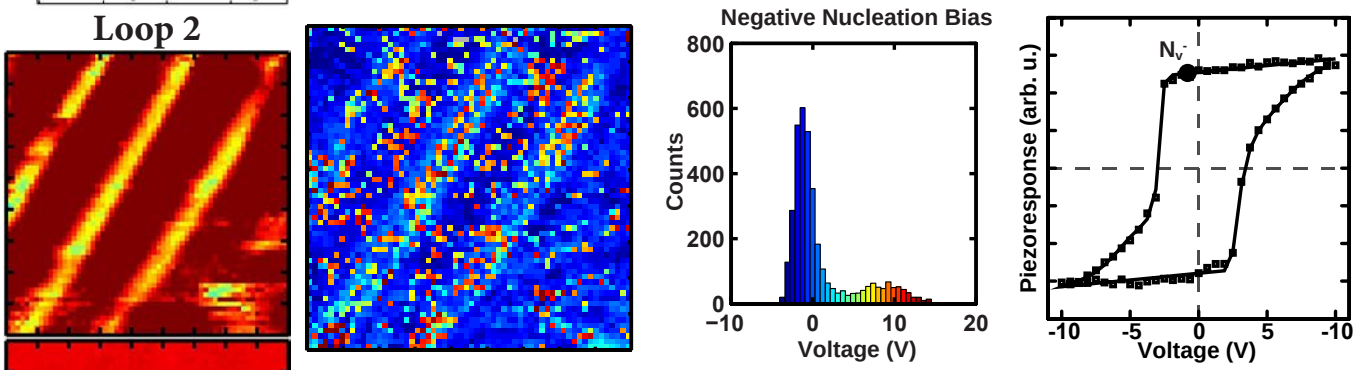

Figure J.21. Loop fitting result negative nucleation bias of 400 nm thick mixed-phase $PbZr_{0.2}Ti_{0.8}O_3$ heterostructures on $NdScO_3$ (110).

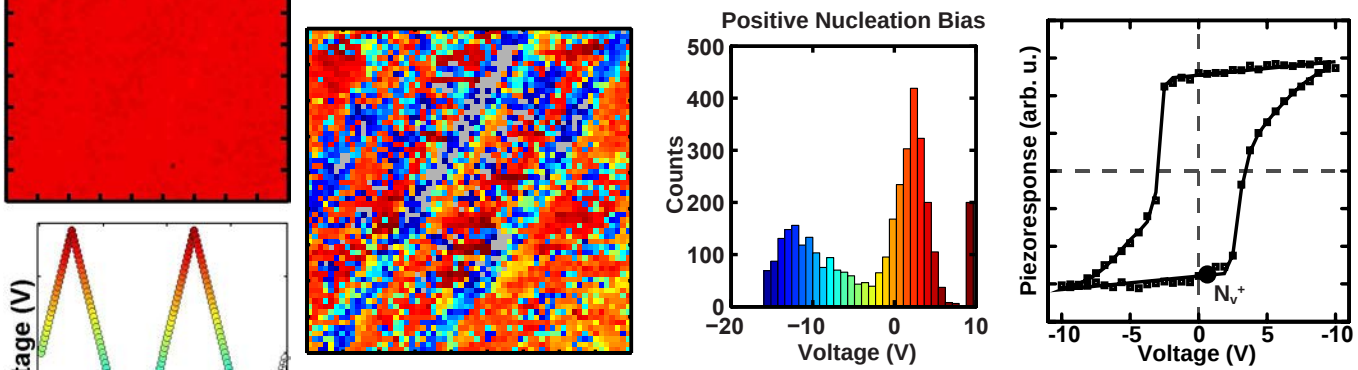

Figure J.22. Loop fitting result positive nucleation bias of 400 nm thick mixed-phase $PbZr_{0.2}Ti_{0.8}O_3$ heterostructures on $NdScO_3$ (110).

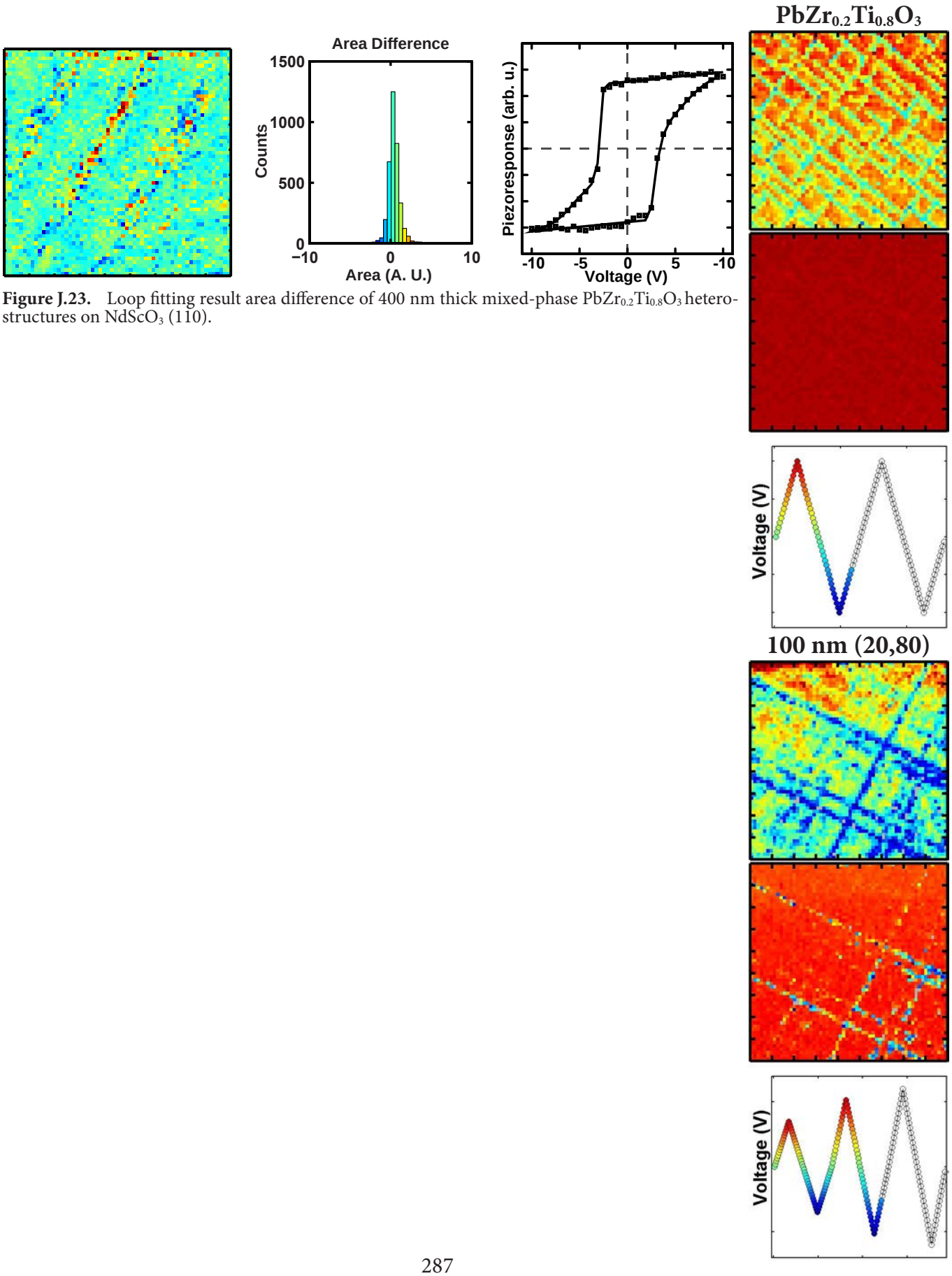

Figure J.23. Loop fitting result area difference of 400 nm thick mixed-phase $PbZr_{0.2}Ti_{0.8}O_3$ heterostructures on $NdScO_3$ (110).

Mixed-Phase PZT
Loop 1

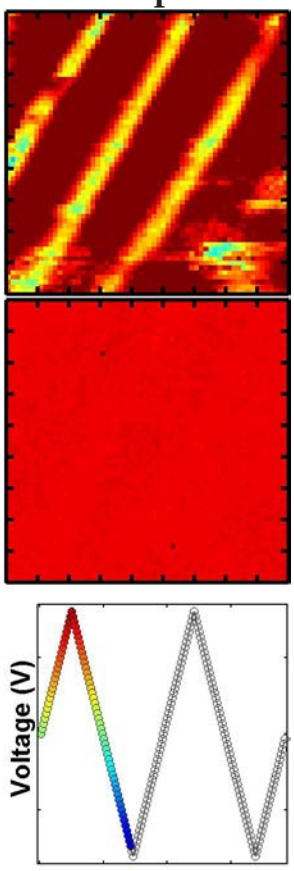

Loop 2

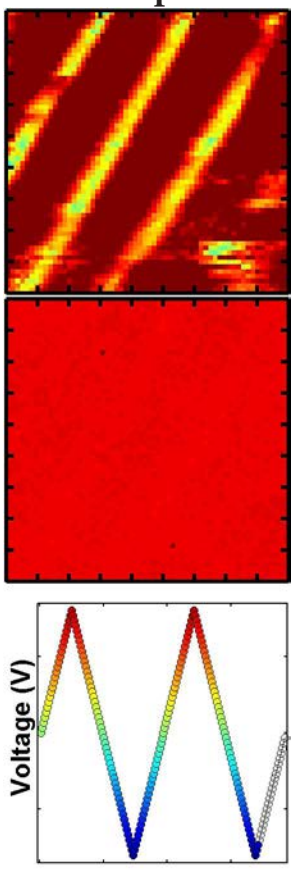

References

1. Curie, P. & Curie, P. Development by pressure of polar electricity in hemihedral crystals with inclined faces. *Bull. soc. min. de France* **3**, 90-294 (1880).

2. Lindsay, R. B. in *Acoustics: Historical and Philosophical Development* (Dowden, Hutchinson \& Ross, 1976).

3. Pockels, F. On the effect of an electrostatic field on the optical behaviour of piezo-electric crystals. *Abh. Gott.* **39**, 1-7 (1894).

4. Debye, P. Einige resultate einer kinetischen theorie der isolatoren. *Phisik. Zeits.* **13**, 97-100 (1912).

5. Hoffmann, D. in *Erwin Schrödinger* (Springer-Verlag, 2013).

6. Valasek, J. Piezo-electric activity of Rochelle salt under various conditions. *Phys. Rev.* **19**, 478-491 (1922).

7. Valasek, J. Dielectric anomalies in Rochelle salt crystals. *Phys. Rev.* **24**, 560-568 (1924).

8. Valasek, J. Piezo-electric and allied phenomena in Rochelle salt. *Phys. Rev.* **17**, 475-481 (1921).

9. Busch, G. & Scherrer, P. Eine neue seignette-elektrische Substanz. *Naturwissen-schaften* **23**, 737-737 (1935).

10. Busch, G. & Scherrer, P. A new seignette-electric substance. *Ferroelectrics* **71**, 15-16 (1987).

11. Wul, B. & Goldman, I. Dielectric constants of titanates of metals of the second group. *Compt. Rend. Acad. Sci. URSS* **46**, 139-142 (1945).

12. Setter, N. *et al*. Ferroelectric thin films: review of materials, properties, and applications. *J. Appl. Phys.* **100**, 051606-1-46 (2006).

13. Schlom, D. G. *et al*. Strain Tuning of Ferroelectric Thin Films. *Annu. Rev. Mater. Res.* **37**, 589-626 (2007).

14. Martin, L. W. & Schlom, D. G. Advanced synthesis techniques and routes to new single-phase multiferroics. *Curr. Opin. Solid State Mater. Sci.* **16**, 199-215 (2012).

15. Martin, L. W., Chu, Y. H. & Ramesh, R. Advances in the growth and characterization of magnetic, ferroelectric, and multiferroic oxide thin films. *Mater. Sci. Eng. R-Rep.* **68**, 89-133 (2010).

16. Li, H., Deng, Z. D. & Carlson, T. J. Piezoelectric materials used in underwater acoustic transducers. *Sens. Lett.* **10**, 679-697 (2012).

17. Dimos, D. & Mueller, C. H. Perovskite thin films for high-frequency capacitor applications. *Annu. Rev. Mater. Sci.* **28**, 397-419 (1998).

18. Kong, L. B. *et al*. Electrically tunable dielectric materials and strategies to improve their performances. *Prog. Mater. Sci.* **55**, 840-893 (2010).

19. Muralt, P. PZT thin films for microsensors and actuators: Where do we stand?

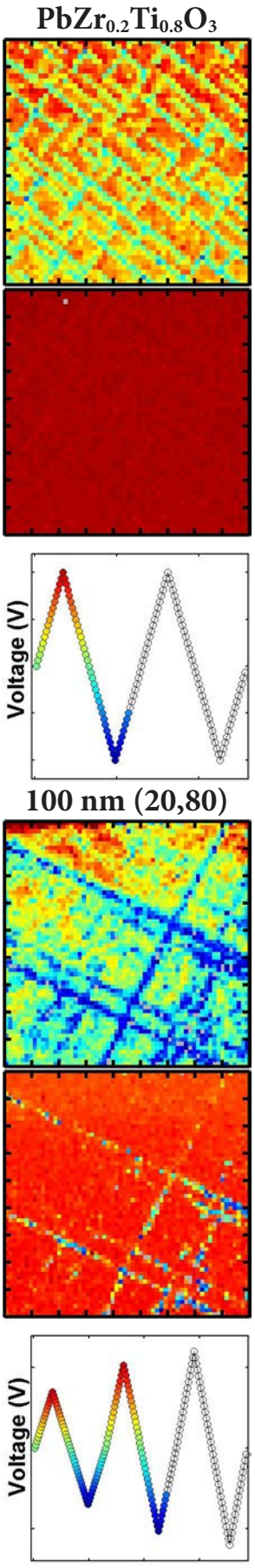

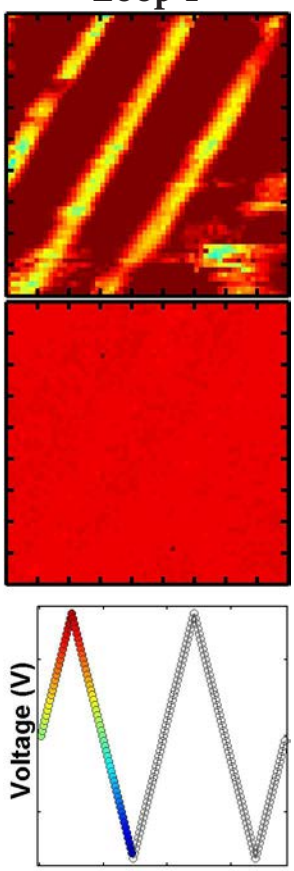

IEEE Trans. Ultrason. Ferroelect. Freq. Control **47**, 903-915 (2000).

20. Polla, D. L. & Francis, L. F. Processing and characterization of piezoelectric materials and integration into microelectromechanical systems. *Annu. Rev. Mater. Sci.* **28**, 563-597 (1998).

21. Roedel, J. *et al*. Perspective on the development of lead-free piezoceramics. *J. Am. Ceram. Soc.* **92**, 1153-1177 (2009).

22. Sinclair, D. C. & West, A. R. Impedance and modulus spectroscopy of semiconducting $BaTiO_3$ showing positive temperature coefficient of resistance. *J. Appl. Phys.* **66**, 3850-3856 (1989).

23. Okano, M., Watanabe, Y. & Cheong, S. W. Nonlinear positive temperature coefficient of resistance of $BaTiO_3$ film. *Appl. Phys. Lett.* **82**, 1923-1925 (2003).

24. Sebald, G. *et al*. Electrocaloric and pyroelectric properties of $0.75Pb(Mg_{1/3}Nb_{2/3})O_3$–$0.25PbTiO_3$ single crystals. *J. Appl. Phys.* **100**, 124112-1-6 (2006).

25. Yang, Y. *et al*. Pyroelectric nanogenerators for harvesting thermoelectric energy. *Nano Lett.* **12**, 2833-2838 (2012).

26. Sebald, G., Lefeuvre, E. & Guyomar, D. Pyroelectric energy conversion: optimization principles. *IEEE Trans. Ultrason. Ferroelect. Freq. Control* **55**, 538-551 (2008).

27. Navid, A. & Pilon, L. Pyroelectric energy harvesting using Olsen cycles in purified and porous poly(vinylidene fluoride-trifluoroethylene) [P(VDF-TrFE)] thin films. *Smart Mater. Struct.* **20**, 025012-1-9 (2011).

28. Muralt, P. Ferroelectric thin films for micro-sensors and actuators: a review. *J Micromech. Microeng.* **10**, 136-146 (2000).

29. Wang, Z. L. & Song, J. Piezoelectric nanogenerators based on zinc oxide nanowire arrays. *Science* **312**, 242-246 (2006).

30. Wang, Z. L. Zinc oxide nanostructures: growth, properties and applications. *J. Phys. Condens. Matter.* **16**, R829-R858 (2004).

31. Trolier-McKinstry, S. *et al*. Designing Piezoelectric Films for Micro Electromechanical Systems. *IEEE Trans. Ultrason. Ferroelect. Freq. Control* **58**, 1782-1792 (2011).

32. Anton, S. R. & Sodano, H. A. A review of power harvesting using piezoelectric materials (2003–2006). *Smart Mater. Struct.* **16**, R1-R21 (2007).

33. Kumar, A. K. S. *et al*. High-frequency surface acoustic wave device based on thin-film piezoelectric interdigital transducers. *Appl. Phys. Lett.* **85**, 1757-1759 (2004).

34. Inoue, Y., Matsukawa, M. & Sato, K. Effect of Surface Acoustic-Wave Generated on Ferroelectric Support upon Catalysis. *J. Am. Chem. Soc.* **111**, 8965-8966 (1989).

35. Chang, R., Chu, S., Lin, Y., Hong, C. & Wong, Y. An investigation of $(Na_{0.5}K_{0.5})NbO_3$-$CaTiO_3$ based lead-free ceramics and surface acoustic wave devices. *J. Eur. Ceram. Soc.* **27**, 4453-4460 (2007).

36. Laser, D. J. & Santiago, J. G. A review of micropumps. *J. Micromech. Microeng.* **14**, R35-R64 (2004).

37. Crawley, E. F. & Deluis, J. Use of piezoelectric actuators as elements of intelligent structures. *AIAA J.* **25**, 1373-1385 (1987).

38. Baeumer, C., Rogers, S. P., Xu, R., Martin, L. W. & Shim, M. Tunable carrier type and density in graphene/$PbZr_{0.2}Ti_{0.8}O_3$ hybrid structures through ferroelectric switching. *Nano Lett.* **13**, 1693-1698 (2013).

39. Naber, R. C. G. *et al*. High-performance solution-processed polymer ferroelectric field-effect transistors. *Nat. Mater.* **4**, 243-248 (2005).

40. Mathews, S., Ramesh, R., Venkatesan, T. & Benedetto, J. Ferroelectric field effect transistor based on epitaxial perovskite heterostructures. *Science* **276**, 238-240 (1997).

41. Miller, S. L. & Mcwhorter, P. J. Physics of the Ferroelectric Nonvolatile Memory Field-Effect Transistor. *J. Appl. Phys.* **72**, 5999-6010 (1992).

42. Scott, J. F. & Paz de Araujo, C. A. Ferroelectric memories. *Science* **246**, 1400-1405 (1989).

43. Lu, H. *et al*. Mechanical Writing of Ferroelectric Polarization. *Science* **336**, 59-61 (2012).

44. Salje, E. K. H. Multiferroic Domain Boundaries as Active Memory Devices: Trajectories Towards Domain Boundary Engineering. *ChemPhysChem* **11**, 940-950 (2010).

45. Kholkin, A. L., Pertsev, N. A. & Goltsev, A. V. in 17-38 (Springer US, 2008).

46. Goldschmidt, V. The laws of crystal chemistry. *Naturwissenschaften* **14**, 477-485 (1926).

47. Benedek, N. A. & Fennie, C. J. Why are there so few perovskite ferroelectrics? *J. Phys. Chem. C* **117**, 13339-13349 (2013).

48. Jahn, H. A. &Teller, E. *Stability of polyatomic molecules in degenerate electronic states. I. Orbital degeneracy* (Proceedings of the Royal Society of London A: Mathematical, Physical and Engineering Sciences Ser. 161, The Royal Society, 1937).

49. Jahn, H. *Stability of polyatomic molecules in degenerate electronic states. II. Spin degeneracy* (Proc. Roy. Soc.(London) A Ser. 164, 1938).

50. Opik, U. &Pryce, M. *Studies of the Jahn-Teller effect. I. A survey of the static problem* (Proceedings of the Royal Society of London A: Mathematical, Physical and Engineering Sciences Ser. 238, The Royal Society, 1957).

51. Cohen, R. E. Origin of ferroelectricity in perovskite oxides. *Nature* **358**, 136-138 (1992).

52. Harwood, M., Popper, P. & Rushman, D. Curie point of barium titanate. *Nature* **160**, 58-59 (1947).

53. Jaffe, B., Cook, W. R. & Jaffe, H. L. in *Piezoelectric ceramics* (Academic Press, 1971).

54. Seshadri, R. & Hill, N. A. Visualizing the role of Bi 6s "lone pairs" in the off-center distortion in ferromagnetic $BiMnO_3$. *Chem. Mater.* **13**, 2892-2899 (2001).

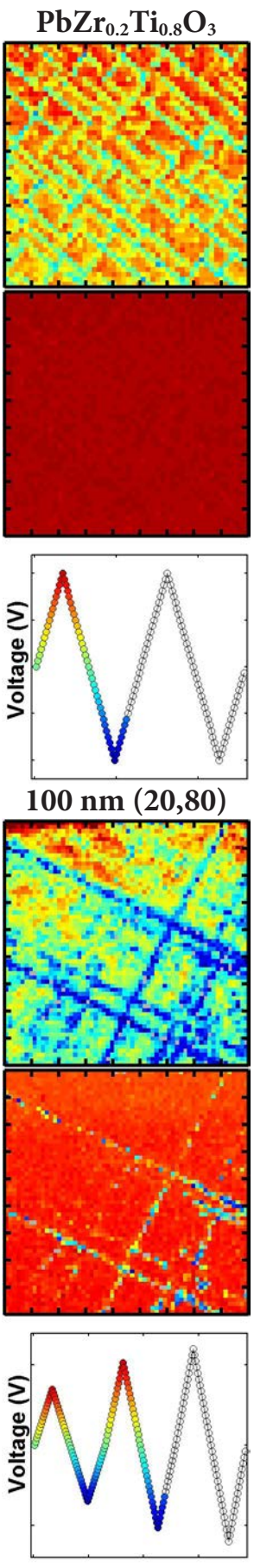

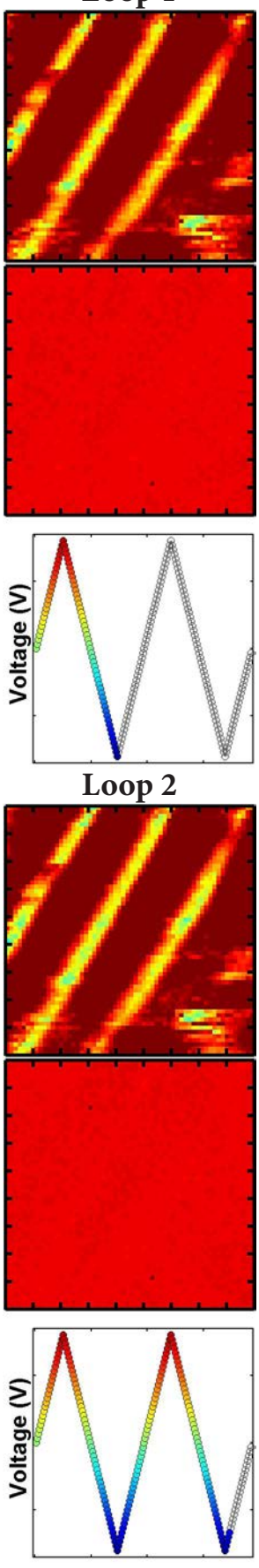

55. Scott, J. F. in *Ferroelectric memories* (Springer Science & Business Media, 2000).

56. Nye, J. F. in *Physical properties of crystals: their representation by tensors and matrices* (Oxford university press, 1985).

57. Lu, S. G. *et al.* Comparison of directly and indirectly measured electrocaloric effect in relaxor ferroelectric polymers. *Appl. Phys. Lett.* **97**, 2029012-1-3 (2010).

58. Jia, Y. & Sungtaek Ju, Y. Direct characterization of the electrocaloric effects in thin films supported on substrates. *Appl. Phys. Lett.* **103**, 042903-1-4 (2013).

59. Mischenko, A. S., Zhang, Q., Scott, J. F., Whatmore, R. W. & Mathur, N. D. Giant Electrocaloric Effect in Thin-Film $PbZr_{0.95}Ti_{0.05}O_3$. *Science* **311**, 1270-1271 (2006).

60. Li, X. *et al.* Tunable temperature dependence of electrocaloric effect in ferroelectric relaxor poly(vinylidene fluoride-trifluoroethylene-chlorofluoroethylene terpolymer. *Appl. Phys. Lett.* **99**, 052907-1-3 (2011).

61. Izyumskaya, N. *et al.* Processing, Structure, Properties, and Applications of PZT Thin Films. *Crit. Rev. Solid State Mater. Sci.* **32**, 111-202 (2007).

62. Luo, J. & Zhang, S. Advances in the Growth and Characterization of Relaxor-PT-Based Ferroelectric Single Crystals. *Crystals* **4**, 306-330 (2014).

63. Gumbsch, P., Taeri-Baghbadrani, S., Brunner, D., Sigle, W. & Rühle, M. Plasticity and an inverse brittle-to-ductile transition in strontium titanate. *Phys. Rev. Lett.* **87**, 085505-1-4 (2001).

64. Zeches, R. J. *et al.* A strain-driven morphotropic phase boundary in $BiFeO_3$. *Science* **326**, 977-980 (2009).

65. Christen, H. M., Nam, J. H., Kim, H. S., Hatt, A. J. & Spaldin, N. A. Stress-induced R–M_A–M_C–T symmetry changes in $BiFeO_3$ films. *Physical Review B* **83**, 144107-1-7 (2011).

66. Chen, P. *et al.* Optical properties of quasi-tetragonal $BiFeO_3$ thin films. *Appl. Phys. Lett.* **96**, 131907-1-3 (2010).

67. Schwartz, R. W. *et al.* Sol-Gel Processing of PZT Thin-Films - a Review of the State-Of-The-Art and Process Optimization Strategies. *Integr. Ferroelectr.* **7**, 259-277 (1995).

68. Schwartz, R. W., Schneller, T. & Waser, R. Chemical solution deposition of electronic oxide films. *C. R. Chim.* **7**, 433-461 (2004).

69. Yamakawa, K., Trolier-McKinstry, S., Dougherty, J. & Krupanidhi, S. Reactive magnetron co-sputtered antiferroelectric lead zirconate thin films. *Appl. Phys. Lett.* **67**, 2014-2016 (1995).

70. Nam, S. & Tsurumi, T. In situ epitaxial growth of lead zirconate titanate films by bias sputtering at high RF power. *Jpn. J. Appl. Phys.* **43**, 2672-2676 (2004).

71. Auciello, O., Foster, C. M. & Ramesh, R. Processing technologies for ferroelectric thin films and heterostructures. *Annu. Rev. Mater. Sci.* **28**, 501-531 (1998).

72. Jones, A. C. Molecular design of improved precursors for the MOCVD of electroceramic oxides. *J. Mater. Chem.* **12**, 2576-2590 (2002).

73. Wessels, B. W. Metal-Organic Chemical-Vapor-Deposition of Ferroelectric Oxide Thin-Films for Electronic and Optical Application. *Annu. Rev. Mater. Sci.* **25**, 525-546 (1995).

74. Theis, C. D., Yeh, J., Schlom, D. G., Hawley, M. E. & Brown, G. W. Adsorption-controlled growth of PbTiO3 by reactive molecular beam epitaxy. *Thin Solid Films* **325**, 107-114 (1998).

75. Theis, C. D. & Schlom, D. G. Epitaxial lead titanate grown by MBE. *J. Cryst. Growth* **174**, 473-479 (1997).

76. Mckee, R. A., Walker, F. J., Conner, J. R., Specht, E. D. & Zelmon, D. E. Molecular-Beam Epitaxy Growth of Epitaxial Barium Silicide, Barium Oxide, and Barium-Titanate on Silicon. *Appl. Phys. Lett.* **59**, 782-784 (1991).

77. Chrisey, D. B. & Hubler, G. K. in *Pulsed laser deposition of thin films* (Wiley New York, 1994).

78. Eason, R. in *Pulsed laser deposition of thin films: applications-led growth of functional materials* (John Wiley & Sons, 2007).

79. Willmott, P. & Huber, J. Pulsed laser vaporization and deposition. *Rev. Mod. Phys.* **72**, 315-328 (2000).

80. Kimmel, A. V., Weaver, P. M., Cain, M. G. & Sushko, P. V. Defect-Mediated Lattice Relaxation and Domain Stability in Ferroelectric Oxides. *Phys. Rev. Lett.* **109**, 117601-1-5 (2012).

81. Speck, J. S. & Pompe, W. Domain Configurations due to Multiple Misfit Relaxation Mechanisms in Epitaxial Ferroelectric Thin Films. I. Theory. *J. Appl. Phys.* **76**, 466-476 (1994).

82. Speck, J. S., Seifert, A., Pompe, W. & Ramesh, R. Domain configurations due to multiple misfit relaxation mechanisms in epitaxial ferroelectric thin films. II. experimental verification and implications. *J. Appl. Phys.* **76**, 477-483 (1994).

83. Speck, J. S., Daykin, A. C., Seifert, A., Romanov, A. E. & Pompe, W. Domain Configurations due to Multiple Misfit Relaxation Mechanisms in Epitaxial Ferroelectric Thin Films. III. Interfacial Defects and Domain Misorientations. *J. Appl. Phys.* **78**, 1696-1706 (1995).

84. Kwak, B. S. *et al.* Strain relaxation by domain formation in epitaxial ferroelectric thin films. *Phys. Rev. Lett.* **68**, 3733-3736 (1992).

85. Johnston, K. E., Mitchell, M. R., Blanc, F., Lightfoot, P. & Ashbrook, S. E. Structural Study of $La_{1-x}Y_xScO_3$, Combining Neutron Diffraction, Solid-State NMR, and First-Principles DFT Calculations. *J. Phys. Chem. C* **117**, 2252-2265 (2013).

86. Liferovich, R. P. & Mitchell, R. H. A structural study of ternary lanthanide orthoscandate perovskites. *J. Solid State Chem.* **177**, 2188-2197 (2004).

87. Faucher, M. & Caro, P. Aff inement de structure et transitions electroniques de $EuScO_3$. *Mater. Res. Bull.* **10**, 1-7 (1975).

88. Slater, P., Irvine, J., Ishihara, T. & Takita, Y. The structure of the oxide ion

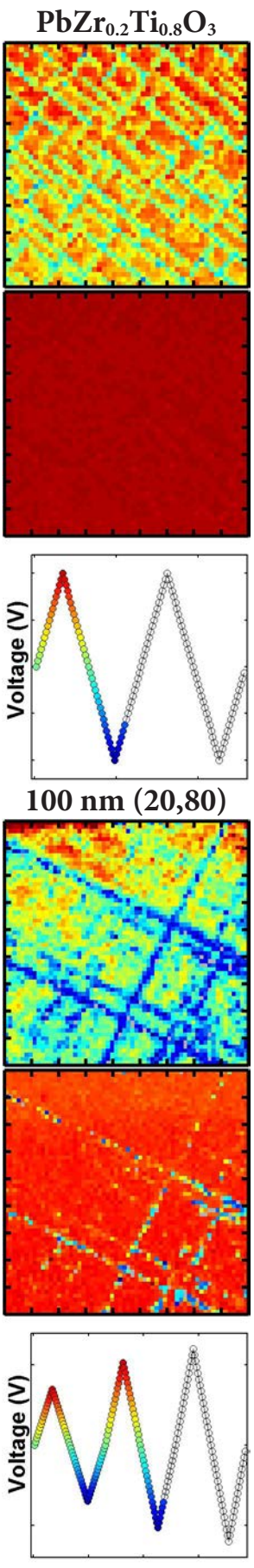

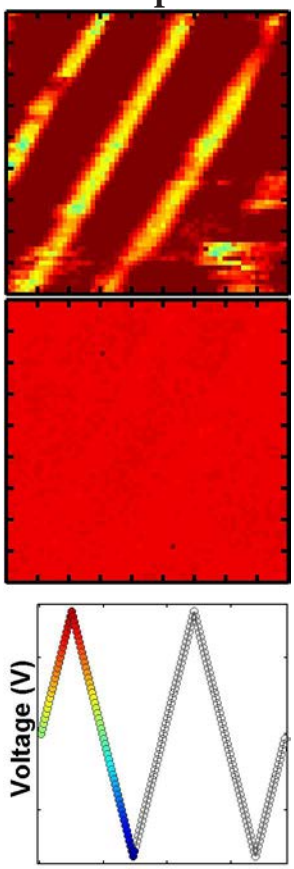

conductor $La_{0.9}Sr_{0.1}Ga_{0.8}Mg_{0.2}O_{2.85}$ by powder neutron diffraction. *Solid State Ionics* **107**, 319-323 (1998).

89. Marti, W., Fischer, P., Altorfer, F., Scheel, H. & Tadin, M. Crystal structures and phase transitions of orthorhombic and rhombohedral $RGaO_3$ (R= La, Pr, Nd) investigated by neutron powder diffraction. *J. Phys. Condens. Matter* **6**, 127-135 (1994).

90. Angel, R. *et al*. High-pressure structural evolution of a perovskite solid solution $(La_{1-x}Nd_x)GaO_3$. *J. Solid State Chem.* **180**, 3408-3424 (2007).

91. Pawlak, D. A. *et al*. Structure and spectroscopic properties of $(AA')(BB')O_3$ mixed-perovskite crystals. *J. Mater. Res.* **20**, 3329-3337 (2005).

92. Britten, J. F. *et al*. Czochralski-Grown $SrLaGaO_4$. *Acta Crystallogr. Sect. C: Cryst. Struct. Commun.* **51**, 1975-1977 (1995).

93. Zhao, J., Ross, N. & Angel, R. Polyhedral control of the rhombohedral to cubic phase transition in $LaAlO_3$ perovskite. *J. Phys. Condens. Matter* **16**, 8763-8773 (2004).

94. Vasylehko, L., Trots, D., Senyshyn, A. & Lukasiewicz, T. Low-temperature structural properties of $LuAlO_3$ and $TbAlO_3$. *2006 HASYLAB Annual Report* **1**, 605-606 (2006).

95. Park, S., Chung, S., Kim, I. & Hong, K. S. Nonstoichiometry and the Long-Range Cation Ordering in Crystals of $(Na_{1/2}Bi_{1/2})TiO_3$. *J. Am. Ceram. Soc.* **77**, 2641-2647 (1994).

96. Yasukawa, M., Ioroi, A., Ikeuchi, K. & Kono, T. Thermoelectric properties of La-doped $SrPbO_3$ ceramics prepared by coprecipitation method. *Mater. Lett.* **58**, 3536-3539 (2004).

97. Hegde, M., Satyalakshmi, K., Manoharan, S. S. & Kumar, D. Superconducting and non-superconducting oxide multilayers. *Mater. Sci. Eng. , B* **32**, 239-245 (1995).

98. Jona, F., Shirane, G., Mazzi, F. & Pepinsky, R. X-Ray and Neutron Diffraction Study of Antiferroelectric Lead Zirconate, $PbZrO_3$. *Phys. Rev.* **105**, 849-856 (1957).

99. Joseph, J., Vimala, T., Sivasubramanian, V. & Murthy, V. Structural investigations on Pb $(Zr_xT_{1-x})O_3$ solid solutions using the X-ray Rietveld method. *J. Mater. Sci.* **35**, 1571-1575 (2000).

100. Prodjosantoso, A. K., Zhou, Q. & Kennedy, B. J. Synchrotron X-ray diffraction study of the $Ba_{1-x}SrSnO_3$ solid solution. *J. Solid State Chem.* **200**, 241-245 (2013).

101. Slodczyk, A., Kania, A., Daniel, P. & Ratuszna, A. Structural, vibrational and dielectric studies of 0.91 PMN–0.09 PT single crystals. *J. Phys. D* **38**, 2910-2918 (2005).

102. Baettig, P., Seshadri, R. & Spaldin, N. A. Anti-polarity in ideal $BiMnO_3$. *J. Am. Chem. Soc.* **129**, 9854-9855 (2007).

103. Rae, A. D., Thompson, J. & Withers, R. L. Structure refinement of commensurately modulated bismuth strontium tantalate, $Bi_2SrTa_2O_9$. *Acta Crystallogr. Sect. B: Struct. Sci* **48**, 418-428 (1992).

104. Köhler, J., Dinnebier, R. & Bussmann-Holder, A. Structural instability of Eu-TiO_3 from X-ray powder diffraction. *Phase Transit.* **85**, 949-955 (2012).

105. Belik, A. A. *et al.* Neutron powder diffraction study on the crystal and magnetic structures of $BiCrO_3$. *Chem. Mater.* **20**, 3765-3769 (2008).

106. Beno, M. *et al.* Structure of the single-phase high-temperature superconductor $YBa_2Cu_3O_{7-\delta}$. *Appl. Phys. Lett.* **51**, 57-59 (1987).

107. Dorrian, J., Newnham, R., Smith, D. & Kay, M. Crystal structure of $Bi_4Ti_3O_{12}$. *Ferroelectrics* **3**, 17-27 (1972).

108. Torardi, C. *et al.* Structures of the superconducting oxides $Tl_2Ba_2CuO_6$ and $Bi_2Sr_2CuO_6$. *Phys. Rev. B* **38**, 225-231 (1988).

109. Logvenov, G., Sveklo, I. & Bozovic, I. Combinatorial molecular beam epitaxy of $La_{2-x}Sr_xCuO_{4+\delta}$. *Phys. C* **460**, 416-419 (2007).

110. Xu, Y. in *Ferroelectric materials and their applications* (Elsevier, 2013).

111. Choi, K. J. *et al.* Enhancement of Ferroelectricity in Strained $BaTiO_3$ Thin Films. *Science* **306**, 1005-1009 (2004).

112. Gariglio, S., Stucki, N., Triscone, J. M. & Triscone, G. Strain relaxation and critical temperature in epitaxial ferroelectric $Pb(Zr_{0.20}Ti_{0.80})O_3$ thin films. *Appl. Phys. Lett.* **90**, 202905-1-3 (2007).

113. Specht, E. D., Christen, H. M., Norton, D. P. & Boatner, L. A. X-ray diffraction measurement of the effect of layer thickness on the ferroelectric transition in epitaxial $KTaO_3/KNbO_3$ multilayers. *Phys. Rev. Lett.* **80**, 4317-4320 (1998).

114. Abe, K. *et al.* Modification of ferroelectricity in heteroepitaxial $(Ba,Sr)TiO_3$ films for non-volatile memory applications. *Integrated Ferroelectr.* **21**, 197-206 (1998).

115. Infante, I. C. *et al.* Bridging Multiferroic Phase Transitions by Epitaxial Strain in $BiFeO_3$. *Phys. Rev. Lett.* **105**, 079901-1-4 (2010).

116. Haeni, J. H. *et al.* Room-temperature ferroelectricity in strained $SrTiO_3$. *Nature* **430**, 758-761 (2004).

117. Bea, H. *et al.* Evidence for Room-Temperature Multiferroicity in a Compound with a Giant Axial Ratio. *Phys. Rev. Lett.* **102**, 217603-1-5 (2009).

118. Chen, Z. *et al.* Low symmetry monoclinic M-C phase in epitaxial $BiFeO_3$ thin films on $LaSrAlO_4$ substrates. *Appl. Phys. Lett.* **97**, 242903-1-3 (2010).

119. Feigl, L., McGilly, L. J. & Setter, N. Superdomain Structure in Epitaxial Tetragonal PZT Thin Films Under Tensile Strain. *Ferroelectrics* **465**, 36-43 (2014).

120. Chen, Z. *et al.* Coexistence of ferroelectric triclinic phases in highly strained $BiFeO_3$ films. *Physical Review B* **84**, 094116-1-6 (2011).

121. Chu, Y. *et al.* Domain control in mulfiferroic $BiFeO_3$ through substrate vicinality. *Adv. Mater.* **19**, 2662-2666 (2007).

122. Chu, Y. *et al.* Nanoscale domain control in multiferroic $BiFeO_3$ thin films. *Adv.*

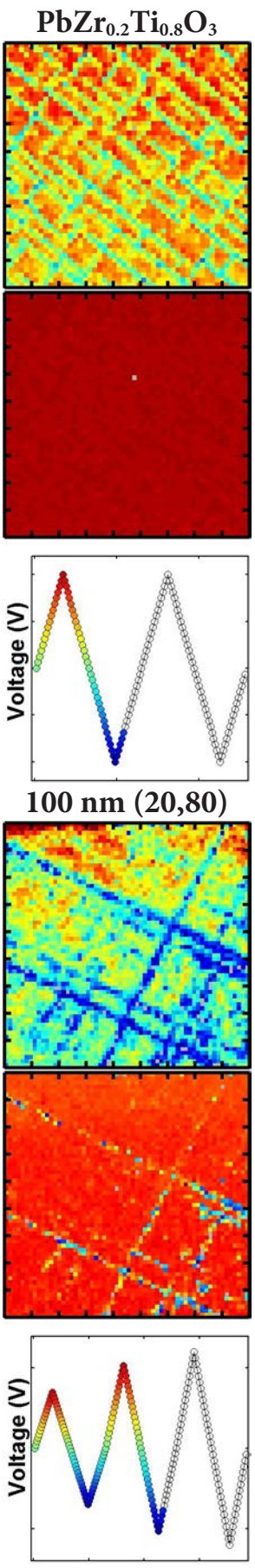

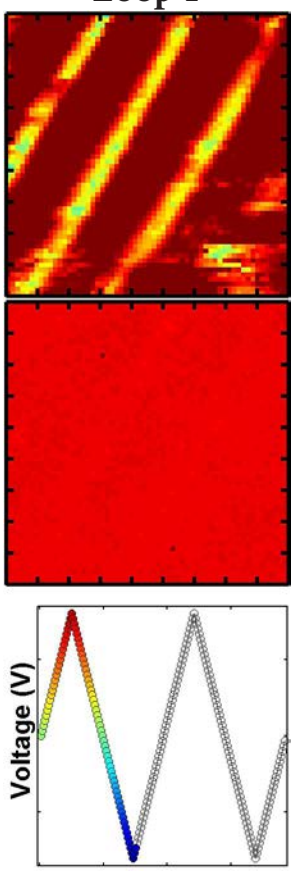

Mater. **18**, 2307-2311 (2006).

123. Lee, K. & Baik, S. Ferroelastic domain structure and switching in epitaxial ferroelectric thin films. *Annu. Rev. Mater. Res.* **36**, 81-116 (2006).

124. Vlooswijk, A. H. G. *et al*. Smallest 90° domains in epitaxial ferroelectric films. *Appl. Phys. Lett.* **91**, 112901-1-3 (2007).

125. Karthik, J., Damodaran, A. R. & Martin, L. W. Effect of 90° domain walls on the low-field permittivity of $PbZr_{0.2}Ti_{0.8}O_3$ thin films. *Phys. Rev. Lett.* **108**, 167601-1-5 (2012).

126. Feigl, L., McGilly, L., Sandu, C. & Setter, N. Compliant ferroelastic domains in epitaxial $Pb(Zr,Ti)O_3$ thin films. *Appl. Phys. Lett.* **104**, 172904-1-4 (2014).

127. Feigl, L. *et al*. Controlled stripes of ultrafine ferroelectric domains. *Nat. Commun.* **5**, 4677-1-9 (2014).

128. Agar, J. C. *et al*. Tuning Susceptibility via Misfit Strain in Relaxed Morphotropic Phase Boundary $PbZr_{1-x}Ti_xO_3$ Epitaxial Thin Films. *Adv. Mater. Interfaces* **1**, 1400098-1-8 (2014).

129. Takahashi, R., Dahl, O., Eberg, E., Grepstad, J. K. & Tybell, T. Ferroelectric stripe domains in $PbTiO_3$ thin films: Depolarization field and domain randomness. *J. Appl. Phys.* **104**, 064109-1-8 (2008).

130. Streiffer, S. K. *et al*. Observation of nanoscale 180 degrees stripe domains in ferroelectric $PbTiO_3$ thin films. *Phys. Rev. Lett.* **89**, 067601-1-4 (2002).

131. Warusawithana, M. P., Colla, E. V., Eckstein, J. N. & Weissman, M. B. Artificial Dielectric Superlattices with Broken Inversion Symmetry. *Phys. Rev. Lett.* **90**, 036802-1-4 (2003).

132. Bastani, Y. & Bassiri-Gharb, N. Enhanced dielectric and piezoelectric response in PZT superlattice-like films by leveraging spontaneous Zr/Ti gradient formation. *Acta Mater.* **60**, 1346-1352 (2012).

133. Callori, S. J. *et al*. Ferroelectric $PbTiO_3/SrRuO_3$ Superlattices with Broken Inversion Symmetry. *Phys. Rev. Lett.* **109**, 067601-1-5 (2012).

134. Nakhmanson, S. M., Rabe, K. M. & Vanderbilt, D. Polarization enhancement in two- and three-component ferroelectric superlattices. *Appl. Phys. Lett.* **87**, 102906-1-3 (2005).

135. Dawber, M. *et al*. Tailoring the Properties of Artificially Layered Ferroelectric Superlattices. *Adv. Mater.* **19**, 4153-4159 (2007).

136. Dawber, M. *et al*. Unusual Behavior of the Ferroelectric Polarization in $PbTiO_3$/$SrTiO_3$ Superlattices. *Phys. Rev. Lett.* **95**, 177601-1-5 (2005).

137. Lee, H. N., Christen, H. M., Chisholm, M. F., Rouleau, C. M. & Lowndes, D. H. Strong polarization enhancement in asymmetric three-component ferroelectric superlattices. *Nature* **433**, 395-399 (2005).

138. Ahn, C. H., Rabe, K. M. & Triscone, J. M. Ferroelectricity at the nanoscale: local polarization in oxide thin films and heterostructures. *Science* **303**, 488-491 (2004).

139. Tang, Y. *et al*. Observation of a periodic array of flux-closure quadrants in strained ferroelectric $PbTiO_3$ films. *Science*, 1259869-1259878 (2015).

140. Jia, C. L., Urban, K. W., Alexe, M., Hesse, D. & Vrejoiu, I. Direct observation of continuous electric dipole rotation in flux-closure domains in ferroelectric Pb(Zr,-Ti)O_3. *Science* **331**, 1420-1423 (2011).

141. Sinsheimer, J. *et al*. Engineering Polarization Rotation in a Ferroelectric Superlattice. *Phys. Rev. Lett.* **109**, 167601-1-5 (2012).

142. Rogdakis, K. *et al*. Tunable ferroelectricity in artificial tri-layer superlattices comprised of non-ferroic components. *Nat. Commun.* **3**, 1064-1-6 (2012).

143. Peng, L. S., Xi, X., Moeckly, B. H. & Alpay, S. Strain relaxation during in situ growth of $SrTiO_3$ thin films. *Appl. Phys. Lett.* **83**, 4592-4594 (2003).

144. Akcay, G., Alpay, S., Rossetti Jr, G. & Scott, J. Influence of mechanical boundary conditions on the electrocaloric properties of ferroelectric thin films. *J. Appl. Phys.* **103**, 024104-1-7 (2008).

145. Zhang, J., Cole, M. & Alpay, S. Pyroelectric properties of barium strontium titanate films: Effect of thermal stresses. *J. Appl. Phys.* **108**, 054103-1-7 (2010).

146. Okatan, M., Cole, M. & Alpay, S. Dielectric tunability of graded barium strontium titanate multilayers: Effect of thermal strains. *J. Appl. Phys.* **104**, 104107-1-7 (2008).

147. Cai, B. *et al*. Anisotropic ferroelectric properties of anisotropically strained epitaxial $NaNbO_3$ films. *J. Appl. Phys.* **115**, 224103-1-7 (2014).

148. Wördenweber, R. *et al*. Impact of compressive in-plane strain on the ferroelectric properties of epitaxial $NaNbO_3$ films on (110) $NdGaO_3$. *Appl. Phys. Lett.* **103**, 132908-1-4 (2013).

149. Schwarzkopf, J., Braun, D., Schmidbauer, M., Duk, A. & Wördenweber, R. Ferroelectric domain structure of anisotropically strained $NaNbO_3$ epitaxial thin films. *J. Appl. Phys.* **115**, 204105-1-10 (2014).

150. Damodaran, A. R., Breckenfeld, E., Chen, Z., Lee, S. & Martin, L. W. Enhancement of ferroelectric curie temperature in $BaTiO_3$ films via strain-induced defect dipole alignment. *Adv. Mater.* **26**, 6341-6347 (2014).

151. Lee, D., Yang, S. M., Yoon, J. & Noh, T. W. Flexoelectric rectification of charge transport in strain-graded dielectrics. *Nano. Lett.* **12**, 6436-6440 (2012).

152. Lee, D. *et al*. Giant Flexoelectric Effect in Ferroelectric Epitaxial Thin Films. *Phys. Rev. Lett.* **107**, 057602-1-4 (2011).

153. Lee, D. *et al*. Active Control of Ferroelectric Switching Using Defect-Dipole Engineering. *Adv. Mater.* **24**, 6490-6495 (2012).

154. Ren, X. B. Large electric-field-induced strain in ferroelectric crystals by point-defect-mediated reversible domain switching. *Nat. Mater.* **3**, 91-94 (2004).

155. Hu, W. *et al*. Electron-pinned defect-dipoles for high-performance colossal permittivity materials. *Nat. Mater.* **12**, 821-826 (2013).

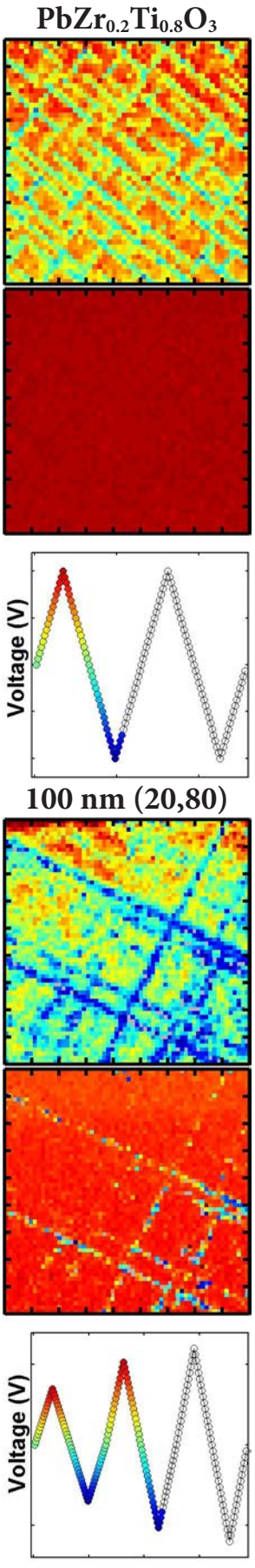

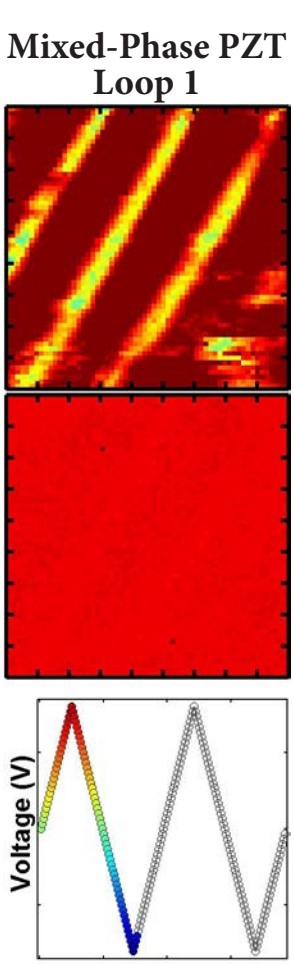

156. Lee, S., Randall, C. A. & Liu, Z. Comprehensive Linkage of Defect and Phase Equilibria through Ferroelectric Transition Behavior in BaTiO3-Based Dielectrics: Part 1. Defect Energies Under Ambient Air Conditions. *J. Am. Ceram. Soc.* **91**, 1748-1752 (2008).

157. Lee, S., Randall, C. A. & Liu, Z. Comprehensive Linkage of Defect and Phase Equilibria Through Ferroelectric Transition Behavior in BaTiO3-Based Dielectrics: Part 2. Defect Modeling Under Low Oxygen Partial Pressure Conditions. *J. Am. Ceram. Soc.* **91**, 1753-1761 (2008).

158. Xu, R., Karthik, J., Damodaran, A. R. & Martin, L. W. Stationary domain wall contribution to enhanced ferroelectric susceptibility. *Nat. Commun.* **5**, 3120-1-7 (2014).

159. Xu, R. *et al.* Ferroelectric polarization reversal via successive ferroelastic transitions. *Nat. Mater.* **14**, 79-86 (2014).

160. Ramesh, R. & Schlom, D. Orienting ferroelectric films. *Science* **296**, 1975-1976 (2002).

161. Dutta, S., Jeyaseelan, A. A. & Sruthi, S. Ferroelectric and Piezoelectric properties of (111) oriented lanthanum modified lead zirconate titanate film. *Thin Solid Films* **562**, 190-194 (2014).

162. Xu, R., Zhang, J., Chen, Z. & Martin, L. W. Orientation-dependent structural phase diagrams and dielectric properties of $PbZr_{1-x}Ti_xO_3$ polydomain thin films. *Physical Review B* **91**, 144106-1-11 (2015).

163. Wang, Y. U. Diffraction theory of nanotwin superlattices with low symmetry phase. *Phys. Rev. B* **74**, 104109-1-4 (2006).

164. Zubko, P., Catalan, G. & Tagantsev, A. K. Flexoelectric effect in solids. *Annu. Rev. Mater. Res.* **43**, 387-421 (2013).

165. Lee, D. *et al.* Flexoelectric control of defect formation in ferroelectric epitaxial thin films. *Adv. Mater.* **26**, 5005-5011 (2014).

166. Catalan, G. *et al.* Flexoelectric rotation of polarization in ferroelectric thin films. *Nat. Mater.* **10**, 963-967 (2011).

167. Yudin, P. & Tagantsev, A. Fundamentals of flexoelectricity in solids. *Nanotechnology* **24**, 432001-1-36 (2013).

168. Karthik, J., Mangalam, R. V. K., Agar, J. C. & Martin, L. W. Large built-in electric fields due to flexoelectricity in compositionally graded ferroelectric thin films. *Phys. Rev. B* **87**, 024111-1-6 (2013).

169. Narvaez, J. & Catalan, G. Origin of the enhanced flexoelectricity of relaxor ferroelectrics. *Appl. Phys. Lett.* **104**, 162903-1-4 (2014).

170. Tagantsev, A. K. Piezoelectricity and flexoelectricity in crystalline dielectrics. *Phys. Rev. B* **34**, 5883-5889 (1986).

171. Zhang, J., Xu, R., Damodaran, A. R., Chen, Z. H. & Martin, L. W. Understanding order in compositionally graded ferroelectrics: Flexoelectricity, gradient, and

depolarization field effects. *Phys. Rev. B* **89**, 224101-1-11 (2014).

172. Mangalam, R. V. K., Karthik, J., Damodaran, A. R., Agar, J. C. & Martin, L. W. Unexpected crystal and domain structures and properties in compositionally graded $PbZr_{1-x}Ti_xO_3$ thin films. *Adv. Mater.* **25**, 1761-1767 (2013).

173. Agar, J. C. *et al.* Complex Evolution of Built-in Potential in Compositionally-Graded $PbZr_{1-x}Ti_xO_3$ Thin Films. *ACS Nano* **9**, 7332-7342 (2015).

174. Meyer, B. & Vanderbilt, D. Ab initio study of ferroelectric domain walls in $PbTiO_3$. *Phys. Rev. B* **65**, 104111-1-12 (2002).

175. Kvasov, A. & Tagantsev, A. K. Role of high-order electromechanical coupling terms in thermodynamics of ferroelectric thin films. *Phys. Rev. B* **87**, 184101-1-10 (2013).

176. Qiu, Q., Nagarajan, V. & Alpay, S. Film thickness versus misfit strain phase diagrams for epitaxial $PbTiO_3$ ultrathin ferroelectric films. *Phys. Rev. B* **78**, 064117-1-13 (2008).

177. Kukhar, V., Pertsev, N., Kohlstedt, H. & Waser, R. Polarization states of polydomain epitaxial Pb $(Zr_{1-x}Ti_x)O_3$ thin films and their dielectric properties. *Phys. Rev. B* **73**, 214103-1-9 (2006).

178. Li, Y., Hu, S. & Chen, L. Ferroelectric domain morphologies of (001) $PbZr_{1-x}Ti_xO_3$ epitaxial thin films. *J. Appl. Phys.* **97**, 034112-1-7 (2005).

179. Pertsev, N., Kukhar, V., Kohlstedt, H. & Waser, R. Phase diagrams and physical properties of single-domain epitaxial $Pb(Zr_{1-x}Ti_x)O_3$ thin films. *Phys. Rev. B* **67**, 054107-1-10 (2003).

180. Koukhar, V., Pertsev, N. & Waser, R. Thermodynamic theory of epitaxial ferroelectric thin films with dense domain structures. *Phys. Rev. B* **64**, 214103-1-15 (2001).

181. Pertsev, N. A. & Zembilgotov, A. G. Domain populations in epitaxial ferroelectric thin films: Theoretical calculations and comparison with experiment. *J. Appl. Phys.* **80**, 6401-6406 (1996).

182. Nagarajan, V. *et al.* Thickness dependence of structural and electrical properties in epitaxial lead zirconate titanate films. *Journal of Applied Physics* **86**, 595-602 (1999).

183. Seidel, J. *et al.* Conduction at domain walls in oxide multiferroics. *Nat. Mater.* **8**, 229-234 (2009).

184. Streiffer, S. *et al.* Domain patterns in epitaxial rhombohedral ferroelectric films. I. Geometry and experiments. *J. Appl. Phys.* **83**, 2742-2753 (1998).

185. Schmitt, L. A. *et al.* Composition dependence of the domain configuration and size in $Pb(Zr_{1-x}Ti_x)O_3$ ceramics. *J. Appl. Phys.* **101**, 074107-1-7 (2007).

186. Xu, F. *et al.* Domain wall motion and its contribution to the dielectric and piezoelectric properties of lead zirconate titanate films. *J. Appl. Phys.* **89**, 1336-1348 (2001).

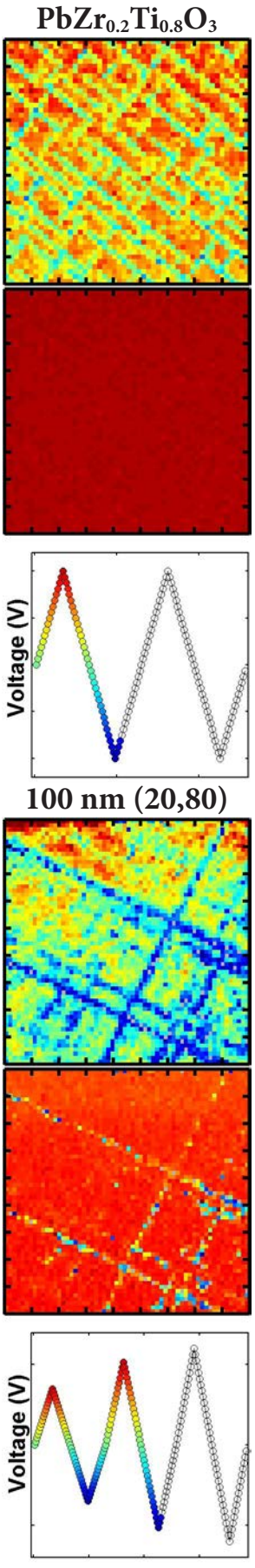

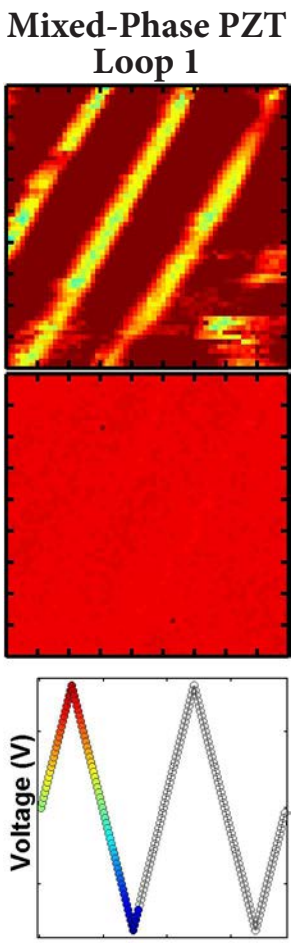

187. Damodaran, A. R. *et al.* Nanoscale structure and mechanism for enhanced electromechanical response of highly strained $BiFeO_3$ thin films. *Adv. Mater.* **23**, 3170-3175 (2011).

188. Fujino, S. *et al.* Combinatorial discovery of a lead-free morphotropic phase boundary in a thin-film piezoelectric perovskite. *Appl. Phys. Lett.* **92**, 202904-1-3 (2008).

189. Lewis, B. Energy loss processes in ferroelectric ceramics. *Proc. Phys. Soc.* **73**, 17-24 (1959).

190. Plessner, K. Ageing of the dielectric properties of barium titanate ceramics. *Proc. Phys. Soc. B.* **69**, 1261-1268 (1956).

191. Kittel, C. Domain boundary motion in ferroelectric crystals and the dielectric constant at high frequency. *Phys. Rev.* **83**, 458 (1951).

192. Zednik, R. J., Varatharajan, A., Oliver, M., Valanoor, N. & McIntyre, P. C. Mobile ferroelastic domain walls in nanocrystalline PZT films: the direct piezoelectric effect. *Adv. Funct. Mater.* **21**, 3104-3110 (2011).

193. Pramanick, A., Damjanovic, D., Daniels, J. E., Nino, J. C. & Jones, J. L. Origins of electro-mechanical coupling in polycrystalline ferroelectrics during subcoercive electrical loading. *J. Am. Chem. Soc.* **94**, 293-309 (2011).

194. Karthik, J., Agar, J. C., Damodaran, A. R. & Martin, L. W. Effect of 90° domain walls and thermal expansion mismatch on the pyroelectric properties of epitaxial $PbZr_{0.2}Ti_{0.8}O_3$ thin films. *Phys. Rev. Lett.* **109**, 257602-1-5 (2012).

195. Mangalam, R. V. K., Agar, J. C., Damodaran, A. R., Karthik, J. & Martin, L. W. Improved pyroelectric figures of merit in compositionally graded $PbZr_{1-x}Ti_xO_3$ thin films. *ACS Appl. Mater. Interfaces* **5**, 13235-13241 (2013).

196. Catalan, G., Sinnamon, L. J. & Gregg, J. M. The effect of flexoelectricity on the dielectric properties of inhomogeneously strained ferroelectric thin films. *J. Phys. Condens. Matter* **16**, 2253-2264 (2004).

197. Catalan, G., Noheda, B., McAneney, J., Sinnamon, L. J. & Gregg, J. M. Strain gradients in epitaxial ferroelectrics. *Phys. Rev. B* **72**, 020102-1-4 (2005).

198. Indenbom, V., Loginov, E. & Osipov, M. Flexoelectric effect and crystal-structure. *Kristallografiya* **26**, 1157-1162 (1981).

199. Wen, Z. *et al.* Mechanical switching of ferroelectric polarization in ultrathin $BaTiO_3$ films: The effects of epitaxial strain. *Appl. Phys. Lett.* **104**, 042907-1-5 (2014).

200. Gruverman, A. *et al.* Mechanical stress effect on imprint behavior of integrated ferroelectric capacitors. *Appl. Phys. Lett.* **83**, 728-730 (2003).

201. Mantese, J. V., Schubring, N. W., Micheli, A. L. & Catalan, A. B. Ferroelectric thin films with polarization gradients normal to the growth surface. *Appl. Phys. Lett.* **67**, 721-723 (1995).

202. Mantese, J. V. *et al.* Slater model applied to polarization graded ferroelectrics. *Appl. Phys. Lett.* **71**, 2047-2049 (1997).

203. Ma, W. & Cross, L. E. Flexoelectricity of barium titanate. *Appl. Phys. Lett.* **88**, 2902-1-3 (2006).

204. Fu, J. Y., Zhu, W., Li, N., Smith, N. B. & Cross, L. E. Gradient scaling phenomenon in microsize flexoelectric piezoelectric composites. *Appl. Phys. Lett.* **91**, 182910-1-3 (2007).

205. Fu, J. Y., Zhu, W., Li, N. & Cross, L. E. Experimental studies of the converse flexoelectric effect induced by inhomogeneous electric field in a barium strontium titanate composition. *J. Appl. Phys.* **100**, 024112-1-6 (2006).

206. Baskaran, S., He, X., Chen, Q. & Fu, J. Y. Experimental studies on the direct flexoelectric effect in alpha-phase polyvinylidene fluoride films. *Appl. Phys. Lett.* **98**, 2901-1-3 (2011).

207. Ma, W. & Cross, L. E. Flexoelectric polarization of barium strontium titanate in the paraelectric state. *Appl. Phys. Lett.* **81**, 3440-3442 (2002).

208. Ma, W. & Cross, L. E. Large flexoelectric polarization in ceramic lead magnesium niobate. *Appl. Phys. Lett.* **79**, 4420-4422 (2001).

209. Ma, W. & Cross, L. E. Observation of the flexoelectric effect in relaxor $Pb(Mg_{1/3}Nb_{2/3})O_3$ ceramics. *Appl. Phys. Lett.* **78**, 2920-2921 (2001).

210. Hana, P. *et al.* Study of the inverse flexoelectric phenomena in ceramic lead magnesium niobate-lead titanate. *Ferroelectrics* **336**, 137-144 (2006).

211. Hana, P. Study of flexoelectric phenomenon from direct and from inverse flexoelectric behavior of PMNT ceramic. *Ferroelectrics* **351**, 196-203 (2007).

212. Cross, L. E. Flexoelectric effects: charge separation in insulating solids subjected to elastic strain gradients. *J. Mater. Sci.* **41**, 53-63 (2006).

213. Ma, W. & Cross, L. E. Flexoelectric effect in ceramic lead zirconate titanate. *Appl. Phys. Lett.* **86**, 072905-1-3 (2005).

214. Chu, B., Zhu, W., Li, N. & Eric Cross, L. Flexure mode flexoelectric piezoelectric composites. *J. Appl. Phys.* **106**, 104109-1-3 (2009).

215. Ponomareva, I., Tagantsev, A. & Bellaiche, L. Finite-temperature flexoelectricity in ferroelectric thin films from first principles. *Phys. Rev. B* **85**, 104101-1-5 (2012).

216. Hong, J. & Vanderbilt, D. First-principles theory and calculation of flexoelectricity. *Phys. Rev. B* **88**, 174107-1-24 (2013).

217. Frenkel, A. I. *et al.* Origin of polarity in amorphous $SrTiO_3$. *Phys. Rev. Lett.* **99**, 215502-1-4 (2007).

218. Kleemann, W., Schäfer, F. & Fontana, M. Crystal optical studies of spontaneous and precursor polarization in $KNbO_3$. *Phys. Rev. B* **30**, 1148-1154 (1984).

219. Aktas, O., Carpenter, M. A. & Salje, E. K. Polar precursor ordering in $BaTiO_3$ detected by resonant piezoelectric spectroscopy. *Appl. Phys. Lett.* **103**, 142902-1-4 (2013).

220. Burns, G. & Dacol, F. Crystalline ferroelectrics with glassy polarization behavior. *Phys. Rev. B* **28**, 2527-2530 (1983).

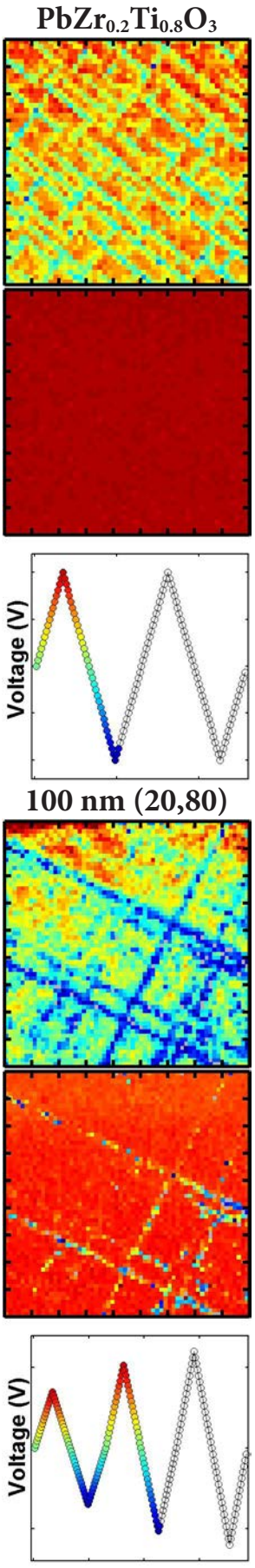

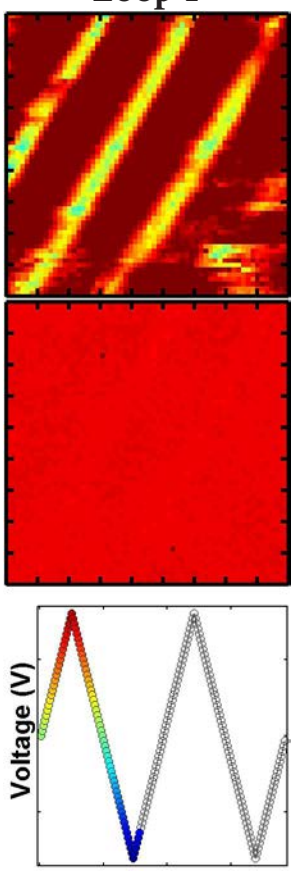

221. Liu, W. & Randall, C. A. Thermally Stimulated Relaxation in Fe-Doped $SrTiO_3$ Systems: II. Degradation of $SrTiO_3$ Dielectrics. *J. Am. Ceram. Soc.* **91**, 3251-3257 (2008).

222. Aschauer, U., Pfenninger, R., Selbach, S. M., Grande, T. & Spaldin, N. A. Strain-controlled oxygen vacancy formation and ordering in $CaMnO_3$. *Phys. Rev. B* **88**, 054111-1-7 (2013).

223. Tagantsev, A. K. & Yurkov, A. S. Flexoelectric effect in finite samples. *J. Appl. Phys.* **112**, 044103-1-7 (2012).

224. Stengel, M. Microscopic response to inhomogeneous deformations in curvilinear coordinates. *Nat. Commun.* **4**, 2693-1-8 (2013).

225. Axe, J., Harada, J. & Shirane, G. Anomalous acoustic dispersion in centrosymmetric crystals with soft optic phonons. *Phys. Rev. B* **1**, 1227-1234 (1970).

226. Farhi, E. *et al.* Low energy phonon spectrum and its parameterization in pure $KTaO_3$ below 80 K. *EPJ B* **15**, 615-623 (2000).

227. Hehlen, B. *et al.* Brillouin-scattering observation of the TA-TO coupling in $SrTiO_3$. *Phys. Rev. B* **57**, R13989-R13992 (1998).

228. Mirzade, F. K. Influence of flexoelectricity on the propagation of nonlinear strain waves in solids. *Phys. Status Solidi B* **244**, 529-544 (2007).

229. Biancoli, A., Fancher, C. M., Jones, J. L. & Damjanovic, D. Breaking of macroscopic centric symmetry in paraelectric phases of ferroelectric materials and implications for flexoelectricity. *Nat. Mater.* **14**, 224-229 (2015).

230. Yudin, P., Ahluwalia, R. & Tagantsev, A. Upper bounds for flexoelectric coefficients in ferroelectrics. *Appl. Phys. Lett.* **104**, 082913-1-3 (2014).

231. Jeon, B. C. *et al.* Flexoelectric effect in the reversal of self-polarization and associated changes in the electronic functional properties of $BiFeO_3$ thin films. *Adv. Mater.* **25**, 5643-5649 (2013).

232. Williamson, G. K. & Hall, W. H. X-ray line broadening from filed aluminium and wolfram. *Acta. Metall. Mater.* **1**, 22-31 (1953).

233. Hÿtch, M., Snoeck, E. & Kilaas, R. Quantitative measurement of displacement and strain fields from HREM micrographs. *Ultramicroscopy* **74**, 131-146 (1998).

234. Brazier, M., McElfresh, M. & Mansour, S. Unconventional hysteresis behavior in compositionally graded $Pb(Zr,Ti)O_3$ thin films. *Appl. Phys. Lett.* **72**, 1121-1123 (1998).

235. Zhong, S., Alpay, S. P., Ban, Z. G. & Mantese, J. V. Effective pyroelectric response of compositionally graded ferroelectric materials. *Appl. Phys. Lett.* **86**, 092903-1-3 (2005).

236. Akcay, G., Zhong, S., Allimi, B., Alpay, S. & Mantese, J. Strain induced internal potentials of compositionally graded epitaxial ferroelectric thin films. *Appl. Phys. Lett.* **91**, 012904-1-3 (2007).

237. Brazier, M., McElfresh, M. & Mansour, S. Origin of anomalous polarization

offsets in compositionally graded Pb(Zr,Ti)O_3 thin films. *Appl. Phys. Lett.* **74**, 299-301 (1999).

238. Lee, K., Kim, Y. & Lee, W. Physical modeling of the effect of the asymmetric electrode configuration on the hysteresis curves of ferroelectric film capacitors. *Ferroelectrics* **271**, 179-185 (2002).

239. Park, B., Noh, T., Lee, J., Kim, C. & Jo, W. Effects of interface charges on imprint of epitaxial $Bi_4Ti_3O_{12}$ thin films. *Appl. Phys. Lett.* **70**, 1101-1103 (1997).

240. Karthik, J., Damodaran, A. R. & Martin, L. W. Epitaxial ferroelectric heterostructures fabricated by selective area epitaxy of $SrRuO_3$ using an MgO mask. *Adv. Mater.* **24**, 1610-1615 (2012).

241. Narayanan, M., Tong, S., Liu, S., Ma, B. & Balachandran, U. Estimation of intrinsic contribution to dielectric response of $Pb_{0.92}La_{0.08}Zr_{0.52}Ti_{0.48}O_3$ thin films at low frequencies using high bias fields. *Appl. Phys. Lett.* **102**, 062906-1-4 (2013).

242. Lee, D. *et al*. Polarity control of carrier injection at ferroelectric/metal interfaces for electrically switchable diode and photovoltaic effects. *Phys. Rev. B* **84**, 125305-1-9 (2011).

243. Bragg, W. & Bragg, W. The reflection of X-rays by crystals. *Proceedings of the Royal Society of London.Series A, Containing Papers of a Mathematical and Physical Character*, 428-438 (1913).

244. Hirano, K. *et al*. Formation of interference fringes in the Bragg-(Bragg)(m)-Laue mode. *Acta Crystallogr. Sect. A* **65**, 253-258 (2009).

245. Ern, C., Donner, W., Dosch, H., Adams, B. & Nowikow, D. Temperature-Dependent Interfacial Stiffness of the Disorder Layer in a Thin Cu 3 Au Alloy Film. *Phys. Rev. Lett.* **85**, 1926-1929 (2000).

246. Pietsch, U., Holy, V. & Baumbach, T. in *High-resolution X-ray scattering: from thin films to lateral nanostructures* (Springer Science & Business Media, 2013).

247. Zhong, Q., Inniss, D., Kjoller, K. & Elings, V. Fractured polymer/silica fiber surface studied by tapping mode atomic force microscopy. *Surf. Sci. Lett.* **290**, L688-L692 (1993).

248. Garcıa, R. & Perez, R. Dynamic atomic force microscopy methods. *Surf. Sci. Rep.* **47**, 197-301 (2002).

249. Giessibl, F. J. Advances in atomic force microscopy. *Rev. Mod. Phys.* **75**, 949-963 (2003).

250. Neuman, K. C. & Nagy, A. Single-molecule force spectroscopy: optical tweezers, magnetic tweezers and atomic force microscopy. *Nat. Mater.* **5**, 491-505 (2008).

251. Rief, M., Oesterhelt, F., Heymann, B. & Gaub, H. E. Single Molecule Force Spectroscopy on Polysaccharides by Atomic Force Microscopy. *Science* **275**, 1295-1297 (1997).

252. Bhushan, B., Israelachvili, J. N. & Landman, U. Nanotribology: friction, wear and lubrication at the atomic scale. *Nature* **374**, 607-616 (1995).

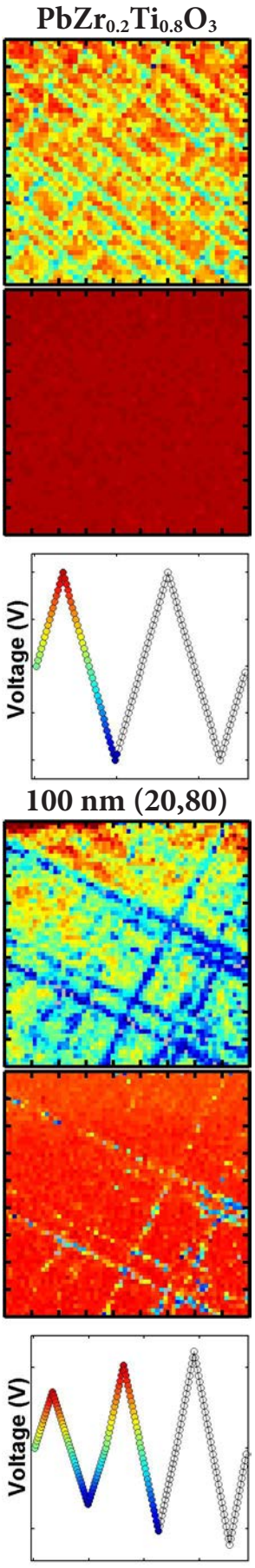

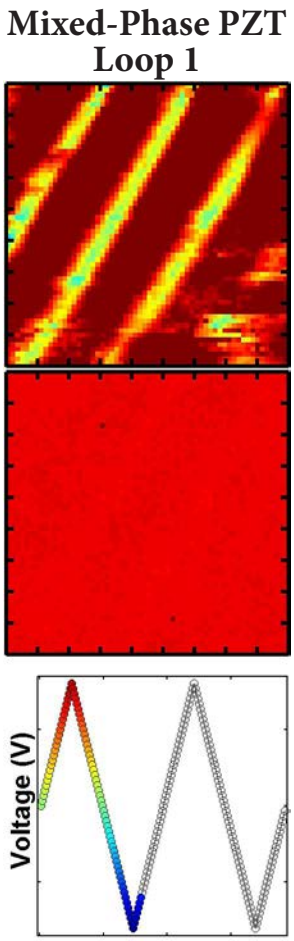

253. Landman, U., Luedtke, W. D., Burnham, N. A. & Colton, R. J. Atomistic mechanisms and dynamics of adhesion, nanoindentation, and fracture. *Science* **248**, 454-461 (1990).

254. Girard, P. Electrostatic force microscopy: principles and some applications to semiconductors. *Nanotechnology* **12**, 485-490 (2001).

255. Weaver, J. & Abraham, D. W. High resolution atomic force microscopy potentiometry. *J. Vac. Sci. Technol.* **9**, 1559-1561 (1991).

256. Puntes, V. F., Gorostiza, P., Aruguete, D. M., Bastus, N. G. & Alivisatos, A. P. Collective behaviour in two-dimensional cobalt nanoparticle assemblies observed by magnetic force microscopy. *Nat. Mater.* **3**, 263-268 (2004).

257. Hartmann, U. Magnetic force microscopy. *Annu. Rev. Mater. Sci.* **29**, 53-87 (1999).

258. Martin, Y. & Wickramasinghe, H. K. Magnetic imaging by "force microscopy"with 1000 Å resolution. *Appl. Phys. Lett.* **50**, 1455-1457 (1987).

259. Garcia, R., Knoll, A. W. & Riedo, E. Advanced scanning probe lithography. *Nat. Nanotechnol.* **9**, 577-587 (2014).

260. Liu, G., Xu, S. & Qian, Y. Nanofabrication of self-assembled monolayers using scanning probe lithography. *Acc. Chem. Res.* **33**, 457-466 (2000).

261. Friedman, S., Amster, O. & Yang, Y. *Recent advances in scanning Microwave Impedance Microscopy (sMIM) for nano-scale measurements and industrial applications* (SPIE NanoScience Engineering, International Society for Optics and Photonics, 2014).

262. Gramse, G. *et al.* Quantitative sub-surface and non-contact imaging using scanning microwave microscopy. *Nanotechnology* **26**, 135701-1-9 (2015).

263. Anderson, M. S. Locally enhanced Raman spectroscopy with an atomic force microscope. *Appl. Phys. Lett.* **76**, 3130-3132 (2000).

264. Sonntag, M. D., Pozzi, E. A., Jiang, N., Hersam, M. C. & Van Duyne, R. P. Recent advances in tip-enhanced Raman spectroscopy. *J. Phys. Chem. Lett* **5**, 3125-3130 (2014).

265. Cain, M. G. in *Characterisation of Ferroelectric Bulk Materials and Thin Films* (Springer Netherlands, 2014).

266. Rodriguez, B. J., Callahan, C., Kalinin, S. V. & Proksch, R. Dual-frequency resonance-tracking atomic force microscopy. *Nanotechnology* **18**, 475504-1-6 (2007).

267. Jesse, S., Kalinin, S. V., Proksch, R., Baddorf, A. P. & Rodriguez, B. J. The band-excitation method in scanning probe microscopy for rapid mapping of energy dissipation on the nanoscale. *Nanotechnology* **18**, 435503-1-8 (2007).

268. Nagarajan, V. *et al.* Size effects in ultrathin epitaxial ferroelectric heterostructures. *Appl. Phys. Lett.* **84**, 5225-5227 (2004).

269. Gerra, G., Tagantsev, A., Setter, N. & Parlinski, K. Ionic polarizability of conductive metal oxides and critical thickness for ferroelectricity in $BaTiO_3$. *Phys. Rev.*

Lett. **96**, 107603-1-4 (2006).

270. Kim, Y. *et al.* Ferroelectric properties of $SrRuO_3$/$BaTiO_3$/$SrRuO_3$ ultrathin film capacitors free from passive layers. *Appl. Phys. Lett.* **88**, 072909-1-3 (2006).

271. Stengel, M., Vanderbilt, D. & Spaldin, N. A. Enhancement of ferroelectricity at metal–oxide interfaces. *Nat. Mater.* **8**, 392-397 (2009).

272. Tagantsev, A., Landivar, M., Colla, E. & Setter, N. Identification of passive layer in ferroelectric thin films from their switching parameters. *J. Appl. Phys.* **78**, 2623-2630 (1995).

273. Pertsev, N. *et al.* Coercive field of ultrathin $Pb(Zr_{0.52}Ti_{0.48})O_3$ epitaxial films. *Appl. Phys. Lett.* **83**, 3356-3358 (2003).

274. Tagantsev, A., Stolichnov, I., Colla, E. & Setter, N. Polarization fatigue in ferroelectric films: Basic experimental findings, phenomenological scenarios, and microscopic features. *J. Appl. Phys.* **90**, 1387-1402 (2001).

275. Dawber, M. & Scott, J. A model for fatigue in ferroelectric perovskite thin films. *Appl. Phys. Lett.* **76**, 1060-1062 (2000).

276. Morimoto, T. *et al.* Ferroelectric properties of $Pb(Zi,Ti)O_3$ capacitor with thin $SrRuO_3$ films within both electrodes. *Jpn. J. Appl. Phys.* **39**, 2110-2113 (2000).

277. Nagaraj, B., Aggarwal, S. & Ramesh, R. Influence of contact electrodes on leakage characteristics in ferroelectric thin films. *J. Appl. Phys.* **90**, 375-382 (2001).

278. Eom, C. *et al.* Fabrication and properties of epitaxial ferroelectric heterostructures with ($SrRuO_3$) isotropic metallic oxide electrodes. *Appl. Phys. Lett.* **63**, 2570-2572 (1993).

279. Pintilie, L., Vrejoiu, I., Hesse, D., LeRhun, G. & Alexe, M. Ferroelectric polarization-leakage current relation in high quality epitaxial $Pb(Zr,Ti)O_3$ films. *Physical Review B* **75**, 104103-1-14 (2007).

280. Robertson, J. High dielectric constant gate oxides for metal oxide Si transistors. *Rep. Prog. Phys.* **69**, 327-396 (2006).

281. Von Hippel, A., Breckenridge, R. G., Chesley, F. & Tisza, L. High dielectric constant ceramics. *Ind. Eng. Chem. Res.* **38**, 1097-1109 (1946).

282. Ribes, G. *et al.* Review on high-k dielectrics reliability issues. *IEEE Trans. Device Mater. Rel.* **5**, 5-19 (2005).

283. Volksen, W., Miller, R. D. & Dubois, G. Low Dielectric Constant Materials. *Chem. Rev.* **110**, 56-110 (2010).

284. Maex, K. *et al.* Low dielectric constant materials for microelectronics. *J. Appl. Phys.* **93**, 8793-8841 (2003).

285. Tagantsev, A. K., Sherman, V. O., Astafiev, K. F., Venkatesh, J. & Setter, N. Ferroelectric materials for microwave tunable applications. *J. Electroceram.* **11**, 5-66 (2003).

286. Damjanovic, D. & Taylor, D. V. Contributions to the nonlinear dielectric and piezoelectric response of ferroelectric thin films and ceramics. *Ferroelectrics* **221**,

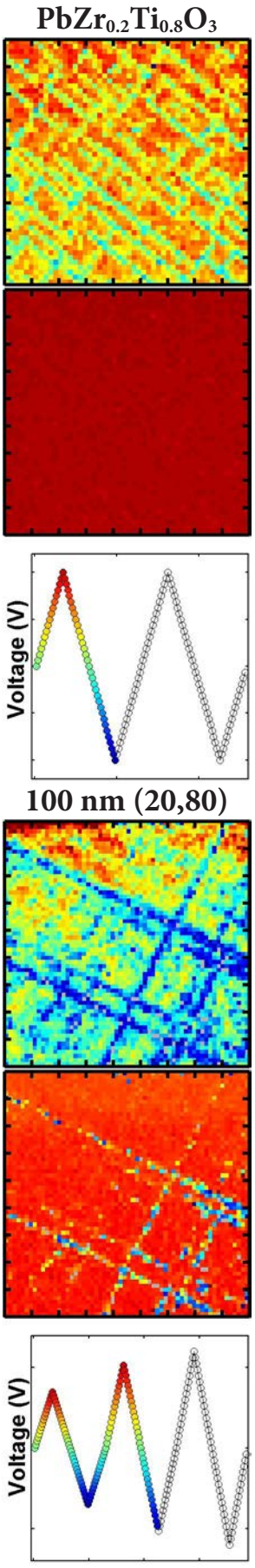

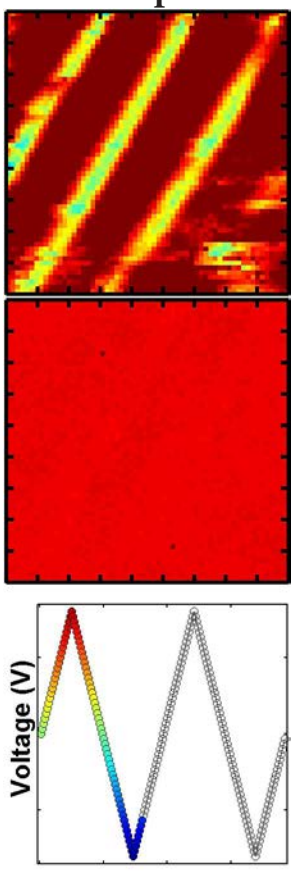

137-146 (1999).

287. Damjanovic, D. Ferroelectric, dielectric and piezoelectric properties of ferroelectric thin films and ceramics. *Rep. Prog. Phys.* **61**, 1267-1324 (1998).

288. Lee, C. *et al*. Exploiting dimensionality and defect mitigation to create tunable microwave dielectrics. *Nature* **502**, 532-536 (2013).

289. Hall, D. A. Review nonlinearity in piezoelectric ceramics. *J. Mater. Sci.* **36**, 4575-4601 (2001).

290. Bassiri-Gharb, N. *et al*. Domain wall contributions to the properties of piezoelectric thin films. *J. Electroceram.* **19**, 49-67 (2007).

291. Rayleigh, L. XXV. Notes on electricity and magnetism.—III. On the behaviour of iron and steel under the operation of feeble magnetic forces. *The London, Edinburgh, and Dublin Phil. Mag. and J. of Sci.* **23**, 225-245 (1887).

292. Néel, L. Théorie du traînage magnétique des substances massives dans le domaine de Rayleigh. *J. Phys. Radium* **11**, 49-61 (1950).

293. Néel, L. Theorie des Lois D'aimantation de Lord Rayleigh. *J. Phys. Radium* **12**, 1-16 (1942).

294. Damjanovic, D. & Demartin, M. Contribution of the irreversible displacement of domain walls to the piezoelectric effect in barium titanate and lead zirconate titanate ceramics. *J. Phys. Condens. Matter* **9**, 4943-2953 (1997).

295. Hagemann, H. Loss mechanisms and domain stabilisation in doped $BaTiO_3$. *J. Phys. Chem. C* **11**, 3333-3344 (1978).

296. Hall, D. A. Rayleigh behaviour and the threshold field in ferroelectric ceramics. *Ferroelectrics* **223**, 319-328 (1999).

297. Taylor, D. V. & Damjanovic, D. Evidence of domain wall contribution to the dielectric permittivity in PZT thin films at sub-switching fields. *J. Appl. Phys.* **82**, 1973-1975 (1997).

298. Taylor, D. & Damjanovic, D. Domain wall pinning contribution to the nonlinear dielectric permittivity in $Pb(Zr,Ti)O_3$ thin films. *Appl. Phys. Lett.* **73**, 2045-2047 (1998).

299. Sawyer, C. B. & Tower, C. Rochelle salt as a dielectric. *Phys. Rev.* **35**, 269 (1930).

300. Scott, J. Ferroelectrics go bananas. *J. Phys. Condens. Matter* **20**, 021001-1-2 (2008).

301. Vrejoiu, I. *et al*. Intrinsic Ferroelectric Properties of Strained Tetragonal $PbZr_{0.2}Ti_{0.8}O_3$ Obtained on Layer-by-Layer Grown, Defect-Free Single-Crystalline Films. *Adv. Mater.* **18**, 1657-1661 (2006).

302. Jin, L., Porokhonskyy, V. & Damjanovic, D. Domain wall contributions in $Pb(Zr,Ti)O_3$ ceramics at morphotropic phase boundary: A study of dielectric dispersion. *Appl. Phys. Lett.* **96**, 242902-1-3 (2010).

303. Kersten, O. & Schmidt, G. Dielectric dispersion in PZT ceramics. *Ferroelectrics* **67**, 191-197 (1986).

304. Arlt, G., Böttger, U. & Witte, S. Dielectric dispersion of ferroelectric ceramics and single crystals at microwave frequencies. *Ann. Phys.* **506**, 578-588 (1994).

305. Böttger, U. & Arlt, G. Dielectric microwave dispersion in PZT ceramics. *Ferroelectrics* **127**, 95-100 (1992).

306. Zhuang, Z., Haun, M. J., Jang, S. & Cross, L. E. Composition and temperature dependence of the dielectric, piezoelectric and elastic properties of pure PZT ceramics. *IEEE Trans. Ultrason. Ferroelect. Freq. Control* **36**, 413-416 (1989).

307. Zhang, X., Chen, Z., Cross, L. E. & Schulze, W. Dielectric and piezoelectric properties of modified lead titanate zirconate ceramics from 4.2 to 300 K. *J. Mater. Sci.* **18**, 968-972 (1983).

308. Ang, C. & Yu, Z. Dielectric behavior of $PbZr_{0.52}Ti_{0.48}O_3$ thin films: Intrinsic and extrinsic dielectric responses. *Appl. Phys. Lett.* **85**, 3821-3823 (2004).

309. Herbert, J. M. in *Ferroelectric Transducers and Sensors* (Gordon and Breach Science Publishers, 1982).

310. Lang, S. B. Pyroelectricity: from ancient curiosity to modern imaging tool. *Phys Today* **58**, 31-36 (2005).

311. Mischenko, A. S., Zhang, Q., Whatmore, R. W., Scott, J. F. & Mathur, N. D. Giant electrocaloric effect in the thin film relaxor ferroelectric $0.9PbMg_{1/3}Nb_{2/3}O_3$–$0.1PbTiO_3$ near room temperature. *Appl. Phys. Lett.* **89**, 242912-1-3 (2006).

312. Zhang, Q. & Whatmore, R. Improved ferroelectric and pyroelectric properties in Mn-doped lead zirconate titanate thin films. *J. Appl. Phys.* **94**, 5228-5233 (2003).

313. Chynoweth, A. Dynamic method for measuring the pyroelectric effect with special reference to barium titanate. *J. Appl. Phys.* **27**, 78-84 (1956).

314. Byer, R. L. & Roundy, C. B. Pyroelectric coefficient direct measurement technique and application to a nsec response time detector. *Ferroelectrics* **3**, 333-338 (1972).

315. Zhao, S. *et al.* Time dependent dc resistance degradation in lead-based perovskites: $0.7PbMgNb_{2/3}O_3$–$0.3PbTiO_3$. *J. Appl. Phys.* **105**, 053705-1-7 (2009).

316. Takayama, R. & Tomita, Y. Preparation of epitaxial $Pb(Zr_xTi_{1-x})O_3$ thin films and their crystallographic, pyroelectric, and ferroelectric properties. *J. Appl. Phys.* **65**, 1666-1670 (1989).

317. Liu, W., Ko, J. S. & Zhu, W. Preparation and properties of multilayer Pb(Zr,Ti)O_3/$PbTiO_3$ thin films for pyroelectric application. *Thin Solid Films* **371**, 254-258 (2000).

318. Zhang, Q. & Whatmore, R. Sol-gel PZT and Mn-doped PZT thin films for pyroelectric applications. *J. Phys. D* **34**, 2296-2310 (2001).

319. Garn, L. E. & Sharp, E. J. Use of low-frequency sinusoidal temperature waves to separate pyroelectric currents from nonpyroelectric currents. Part I. Theory. *J. Appl. Phys.* **53**, 8974-8979 (1982).

320. Sharp, E. J. & Garn, L. E. Use of low-frequency sinusoidal temperature waves to

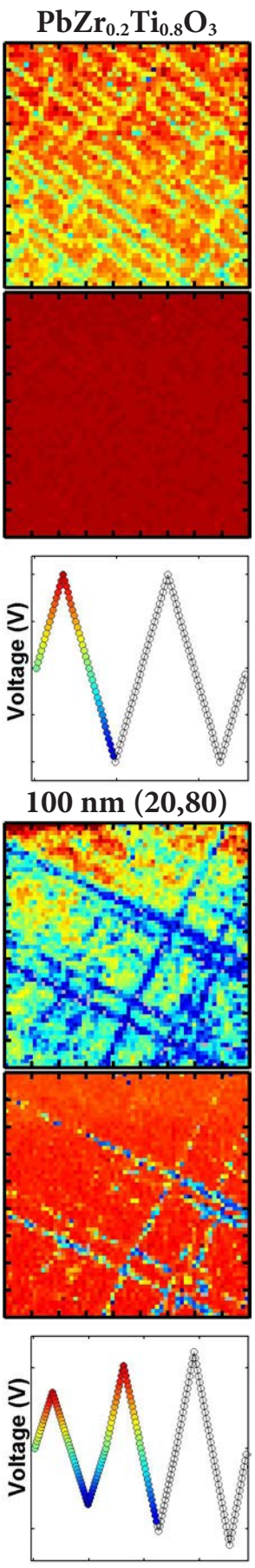

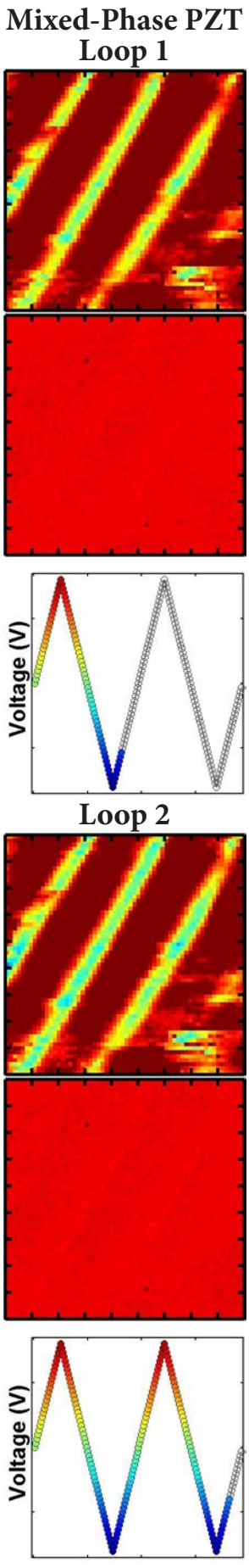

separate pyroelectric currents from nonpyroelectric currents. Part II. Experiment. *J. Appl. Phys.* **53**, 8980-8987 (1982).

321. Peng, B., Fan, H. & Zhang, Q. A Giant Electrocaloric Effect in Nanoscale Antiferroelectric and Ferroelectric Phases Coexisting in a Relaxor $Pb_{0.8}Ba_{0.2}ZrO_3$ Thin Film at Room Temperature. *Advanced Functional Materials* **23**, 2987-2992 (2013).

322. Chen, H., Ren, T., Wu, X., Yang, Y. & Liu, L. Giant electrocaloric effect in lead-free thin film of strontium bismuth tantalite. *Appl. Phys. Lett.* **94**, 182902-1-3 (2009).

323. Lu, S. G. *et al.* Organic and inorganic relaxor ferroelectrics with giant electrocaloric effect. *Appl. Phys. Lett.* **97**, 162904-1-3 (2010).

324. Tong, T., Karthik, J., Mangalam, R., Martin, L. W. & Cahill, D. G. Reduction of the electrocaloric entropy change of ferroelectric $PbZr_{1-x}Ti_xO_3$ epitaxial layers due to an elastocaloric effect. *Phys. Rev. B* **90**, 094116-1-8 (2014).

325. Tong, T., Karthik, J., Martin, L. W. & Cahill, D. G. Secondary effects in wide frequency range measurements of the pyroelectric coefficient of $Ba_{0.6}Sr_{0.4}TiO_3$ and $PbZr_{0.2}Ti_{0.8}O_3$ epitaxial layers. *Physical Review B* **90**, 155423-1-7 (2014).

326. Bhatia, B., Damodaran, A. R., Cho, H., Martin, L. W. & King, W. P. High-frequency thermal-electrical cycles for pyroelectric energy conversion. *J. Appl. Phys.* **116**, 194509-1-8 (2014).

327. Bhatia, B. *et al.* Pyroelectric current measurements on $PbZr_{0.2}Ti_{0.8}O_3$ epitaxial layers. *J. Appl. Phys.* **112**, 104106-1-6 (2012).

328. Jesse, S. & Kalinin, S. V. Band-excitation in scanning probe microscopy: sines of change. *J. Phys. D* **44**, 464006-1-16 (2011).

329. Jesse, S., Maksymovych, P. & Kalinin, S. V. Rapid multidimensional data acquisition in scanning probe microscopy applied to local polarization dynamics and voltage dependent contact mechanics. *Appl. Phys. Lett.* **93**, 112903-1-3 (2008).

330. Vasudevan, R. K. *et al.* Ferroelectric and electrical characterization of multiferroic $BiFeO_3$ at the single nanoparticle level. *Appl. Phys. Lett.* **99**, 252905-1-4 (2011).

331. Anbusathaiah, V. *et al.* Ferroelastic domain wall dynamics in ferroelectric bilayers. *Acta Mater.* **58**, 5316-5325 (2010).

332. Jesse, S. & Kalinin, S. V. Principal component and spatial correlation analysis of spectroscopic-imaging data in scanning probe microscopy. *Nanotechnology* **20**, 085714-1-10 (2009).

333. Guo, S. *et al.* Spatially resolved probing of Preisach density in polycrystalline ferroelectric thin films. *J. Appl. Phys.* **108**, 084103-1-10 (2010).

334. Strelcov, E. *et al.* Deep data analysis of conductive phenomena on complex oxide interfaces: physics from data mining. *ACS nano* **8**, 6449-6457 (2014).

335. Chu, M. *et al.* Impact of misfit dislocations on the polarization instability of epitaxial nanostructured ferroelectric perovskites. *Nat. Mater.* **3**, 87-90 (2004).

336. Dubourdieu, C. *et al.* Switching of ferroelectric polarization in epitaxial $BaTiO_3$ films on silicon without a conducting bottom electrode. *Nat. Nanotechnol.* **8**,

748-754 (2013).

337. Oni, A. *et al.* Large area strain analysis using scanning transmission electron microscopy across multiple images. *Appl. Phys. Lett.* **106**, 011601-1-4 (2015).

338. Ozdol, V. B. *et al.* Strain mapping at nanometer resolution using advanced nano-beam electron diffraction. *Appl. Phys. Lett.* **106**, 253107-1-5 (2015).

339. Gerber, P., Bottger, U. & Waser, R. Composition influences on the electrical and electromechanical properties of lead zirconate titanate thin films. *J. Appl. Phys.* **100**, 124105-1-8 (2006).

340. Jaffe, B., Roth, R. & Marzullo, S. Piezoelectric Properties of Lead Zirconate-Lead Titanate Solid-Solution Ceramics. *J. Appl. Phys.* **25**, 809-810 (1954).

341. Jaffe, B., Roth, R. S. & Marzullo, S. Properties of Piezoelectric Ceramics in the Solid-Solution Series Lead Titanate-Lead Zirconate-Lead Oxide - Tin Oxide and Lead Titanate-Lead Hafnate. *J. Res. Nat. Bur. Stand.* **55**, 239-254 (1955).

342. Foster, C. M., Pompe, W., Daykin, A. C. & Speck, J. S. Relative coherency strain and phase transformation history in epitaxial ferroelectric thin films. *J. Appl. Phys.* **79**, 1405-1415 (1996).

343. Shirane, G., Suzuki, K. & Takeda, A. Phase transitions in solid solutions of $PbZrO_3$ and $PbTiO_3$ (II) X-ray study. *J. Phys. Soc. Jpn.* **7**, 12-18 (1952).

344. Pandya, S. *et al.* Strain-induced growth instability and nanoscale surface patterning in perovskite thin films. *Nano Lett.*, Under Review (2015).

345. Damjanovic, D. A morphotropic phase boundary system based on polarization rotation and polarization extension. *Appl. Phys. Lett.* **97**, 062906-1-3 (2010).

346. Ouyang, J., Zhang, W., Alpay, S. P. & Roytburd, A. Effect of elastic domains on electromechanical response of epitaxial ferroelectric films with a three-domain architecture. *J. Adv. Ceram.* **2**, 1-10 (2013).

347. Liu, W. & Ren, X. Large Piezoelectric Effect in Pb-Free Ceramics. *Phys. Rev. Lett.* **103**, 257602-1-4 (2009).

348. Theissmann, R. *et al.* Nanodomains in morphotropic lead zirconate titanate ceramics: On the origin of the strong piezoelectric effect. *J. Appl. Phys.* **102**, 024111-1-6 (2007).

349. Oikawa, T., Aratani, M., Funakubo, H., Saito, K. & Mizuhira, M. Composition and orientation dependence of electrical properties of epitaxial $Pb(Zr_xTi_{1-x})O_3$ thin films grown using metalorganic chemical vapor deposition. *J. Appl. Phys.* **95**, 3111-3115 (2004).

350. Yokoyama, S. *et al.* Composition Dependency of Epitaxial $Pb(Zr,Ti)O_3$ Films with Different Film Thickness. *Ferroelectrics* **389**, 10-17 (2009).

351. Fu, H. & Cohen, R. E. Polarization rotation mechanism for ultrahigh electromechanical response in single-crystal piezoelectrics. *Nature* **403**, 281-283 (2000).

352. Bellaiche, L., García, A. & Vanderbilt, D. Electric-field induced polarization paths in $PbZr_{1-x}Ti_xO_3$ alloys. *Phys. Rev. B* **64**, 060103-1-4 (2001).

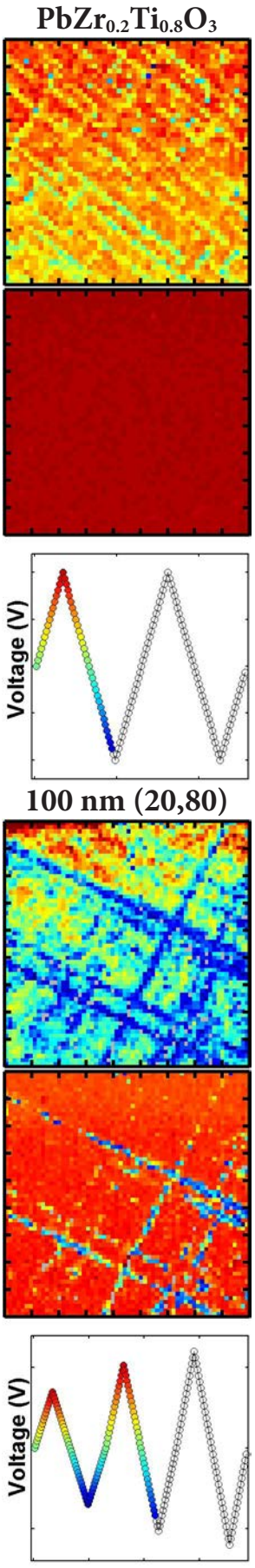

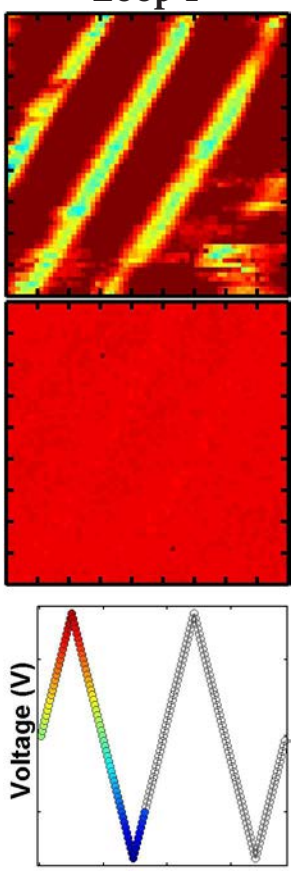

353. Noheda, B. *et al.* Electric-field-induced phase transitions in rhombohedral $Pb(Zn_{1/3}Nb_{2/3})_{1-x}Ti_xO_3$. *Phys. Rev. B* **65**, 224101-1-7 (2002).

354. Noheda, B. *et al.* Polarization Rotation via a Monoclinic Phase in the Piezoelectric $92\%PbZn_{1/3}Nb_{2/3}O_3$-$8\%PbTiO_3$. *Phys. Rev. Lett.* **86**, 3891-3894 (2001).

355. Noheda, B. *et al.* Stability of the monoclinic phase in the ferroelectric perovskite $PbZr_{1-x}Ti_xO_3$. *Phys. Rev. B* **63**, 014103-1-9 (2000).

356. Noheda, B. *et al.* Tetragonal-to-monoclinic phase transition in a ferroelectric perovskite: The structure of $PbZr_{0.52}Ti_{0.48}O_3$. *Phys. Rev. B* **61**, 8687-8695 (2000).

357. Kim, D., Maria, J., Kingon, A. I. & Streiffer, S. K. Evaluation of intrinsic and extrinsic contributions to the piezoelectric properties of $Pb(Zr_{1-x}Ti_x)O_3$ thin films as a function of composition. *J. Appl. Phys.* **93**, 5568-5575 (2003).

358. Damjanovic, D. Logarithmic frequency dependence of the piezoelectric effect due to pinning of ferroelectric-ferroelastic domain walls. *Phys. Rev. B* **55**, R649-R652 (1997).

359. Damjanovic, D. Stress and frequency dependence of the direct piezoelectric effect in ferroelectric ceramics. *J. Appl. Phys.* **82**, 1788-1797 (1997).

360. Bintachitt, P. *et al.* Collective dynamics underpins Rayleigh behavior in disordered polycrystalline ferroelectrics. *Proc. Natl. Acad. Sci. U. S. A.* **107**, 7219-7224 (2010).

361. Yokoyama, S. *et al.* Crystal structure and microstructure of epitaxial Pb(Zr,Ti)O_3 films consisting of mixed phases with tetragonal and rhombohedral symmetries grown on (100) $SrRuO_3$//(100)$SrTiO_3$ substrate by metalorganic chemical vapor deposition. *J. Mater. Res.* **22**, 1551-1557 (2007).

362. Schönau, K. A. *et al.* Nanodomain structure of Pb $[Zr_{1-x}Ti_x]O_3$ at its morphotropic phase boundary: Investigations from local to average structure. *Phys. Rev. B* **75**, 184117-1-10 (2007).

363. Wróbel, Z. Effect of proportional compositions of $Pb(Zr_xTi_{1-x})O_3$ solid solutions on their electric properties with particular regard to the morphotropic phase boundary. *Phys. Status Solidi A* **45**, K67-K69 (1978).

364. Berlincourt, D. A., Cmolik, C. & Jaffe, H. Piezoelectric Properties of Polycrystalline Lead Titanate Zirconate Compositions. *Proceedings of the IRE* **48**, 220-229 (1960).

365. Zhou, C. & Newns, D. M. Intrinsic dead layer effect and the performance of ferroelectric thin film capacitors. *J. Appl. Phys.* **82**, 3081-3088 (1997).

366. Drougard, M. E. & Landauer, R. On the Dependence of the Switching Time of Barium Titanate Crystals on Their Thickness. *J. Appl. Phys.* **30**, 1663-1668 (1959).

367. Gentner, J. O., Gerthsen, P., Schmidt, N. A. & Send, R. E. Dielectric losses in ferroelectric ceramics produced by domain-wall motion. *J. Appl. Phys.* **49**, 4485-4489 (1978).

368. Robels, U. & Arlt, G. Domain wall clamping in ferroelectrics by orientation of

defects. *J. Appl. Phys.* **73**, 3454-3460 (1993).

369. Eitel, R. E., Shrout, T. R. & Randall, C. A. Nonlinear contributions to the dielectric permittivity and converse piezoelectric coefficient in piezoelectric ceramics. *J. Appl. Phys.* **99**, 124110-1-7 (2006).

370. Griggio, F. *et al*. Composition dependence of local piezoelectric nonlinearity in (0.3)Pb($Ni_{0.33}Nb_{0.67}$)O_3-(0.7)Pb(Zr_xTi_{1-x})O_3 films. *J. Appl. Phys.* **110**, 044109-1-11 (2011).

371. Lang, S., Zhu, W. & Ye, Z. Specific heat of ferroelectric Pb($Zr_{1-x}Ti_x$)O_3 ceramics across the morphotropic phase boundary. *J. Appl. Phys.* **111**, 094102-1-5 (2012).

372. Kuwata, J., Uchino, K. & Nomura, S. Phase transitions in the Pb($Zn_{1/3}Nb_{2/3}$)O_3-$PbTiO_3$ system. *Ferroelectrics* **37**, 579-582 (1981).

373. Park, S. & Shrout, T. R. Characteristics of relaxor-based piezoelectric single crystals for ultrasonic transducers. *Ultrasonics, Ferroelectrics and Frequency Control, IEEE Transactions on* **44**, 1140-1147 (1997).

374. Karthik, J. & Martin, L. W. Pyroelectric properties of polydomain epitaxial Pb(Zr_{1-x},tTi_x)O_3 thin films. *Phys. Rev. B* **84**, 024102-1-9 (2011).

375. Anbusathaiah, V. *et al*. Labile Ferroelastic Nanodomains in Bilayered Ferroelectric Thin Films. *Adv Mater* **21**, 3497-3502 (2009).

376. Zhong, S., Alpay, S. P. & Mantese, J. V. Compositional symmetry breaking in ferroelectric bilayers. *Appl. Phys. Lett.* **87**, 102902 (2005).

377. Zheng, H. *et al*. Multiferroic $BaTiO_3$-$CoFe_2O_4$ Nanostructures. *Science* **303**, 661-663 (2004).

378. Bousquet, E. *et al*. Improper ferroelectricity in perovskite oxide artificial superlattices. *Nature* **452**, 732-736 (2008).

379. Vrejoiu, I., Alexe, M., Hesse, D. & Gösele, U. Functional perovskites—from epitaxial films to nanostructured arrays. *Adv. Funct. Mater* **18**, 3892-3906 (2008).

380. Tersoff, J. Dislocations and strain relief in compositionally graded layers. *Appl. Phys. Lett.* **62**, 693-695 (1993).

381. Romanato, F. *et al*. Strain relaxation in graded composition $InxGa_{1-x}As$/GaAs buffer layers. *J. Appl. Phys.* **86**, 4748-4755 (1999).

382. Bertoli, B., Suarez, E. N., Ayers, J. E. & Jain, F. C. Misfit dislocation density and strain relaxation in graded semiconductor heterostructures with arbitrary composition profiles. *J. Appl. Phys.* **106**, 073519-1-7 (2009).

383. Schubring, N. W., Mantese, J. V., Micheli, A. L., Catalan, A. B. & Lopez, R. J. Charge pumping and pseudopyroelectric effect in active ferroelectric relaxor-type films. *Phys. Rev. Lett.* **68**, 1778-1781 (1992).

384. Bao, D., Yao, X. & Zhang, L. Dielectric enhancement and ferroelectric anomaly of compositionally graded (Pb,Ca)TiO_3 thin films derived by a modified sol–gel technique. *Appl. Phys. Lett.* **76**, 2779-2781 (2000).

385. Pertsev, N. & Zembilgotov, A. Energetics and geometry of 90° domain structures

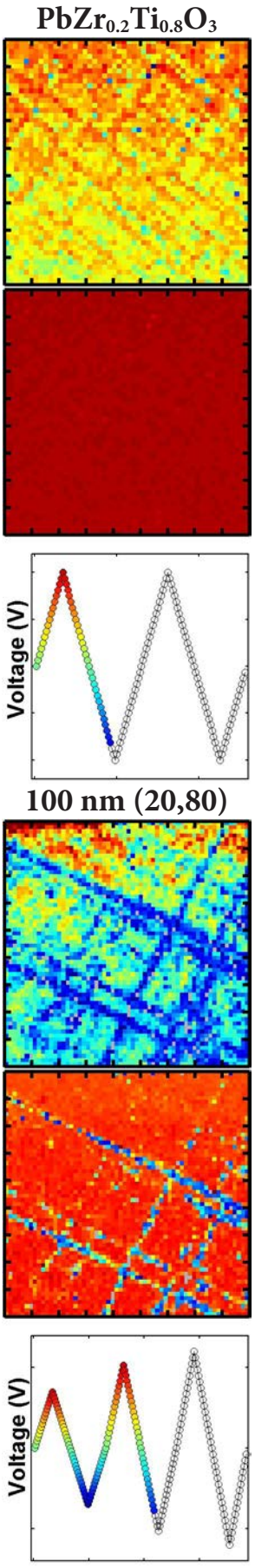

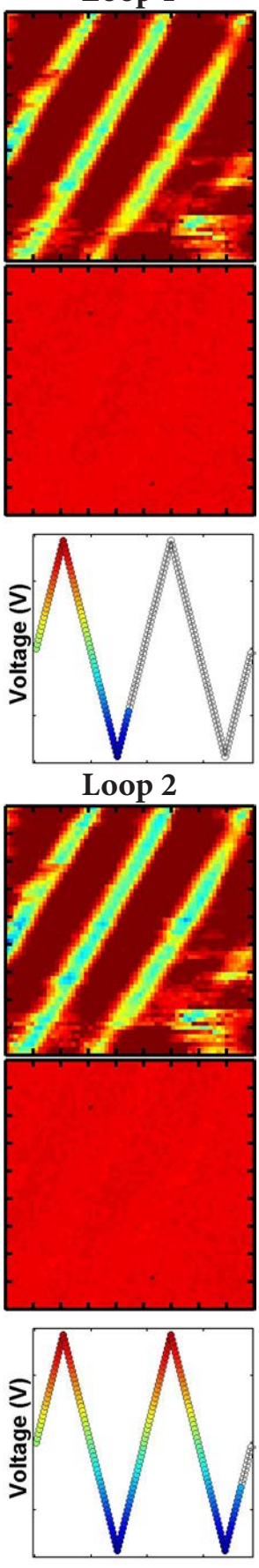

in epitaxial ferroelectric and ferroelastic films. *J. Appl. Phys.* **78**, 6170-6180 (1995).

386. Damjanovic, D. Contributions to the Piezoelectric Effect in Ferroelectric Single Crystals and Ceramics. *J. Am. Chem. Soc.* **88**, 2663-2676 (2005).

387. Warren, W. L. *et al*. Imprint in ferroelectric capacitors. *Jpn. J. Appl. Phys.* **35**, 1521-1524 (1996).

388. Palova, L., Chandra, P. & Rabe, K. Modeling the dependence of properties of ferroelectric thin film on thickness. *Phys. Rev. B* **76**, 014112-1-12 (2007).

389. Haun, M., Furman, E., Jang, S. & Cross, L. Thermodynamic theory of the lead zirconate-titanate solid solution system, part I: phenomenology. *Ferroelectrics* **99**, 13-25 (1989).

390. Lee, J., Choi, C. H., Park, B. H., Noh, T. W. & Lee, J. K. Built-in voltages and asymmetric polarization switching in $Pb(Zr,Ti)O_3$ thin film capacitors. *Appl. Phys. Lett.* **72**, 3380-3382 (1998).

391. Resta, R. Towards a Bulk Theory of Flexoelectricity. *Phys. Rev. Lett.* **105**, 127601-1-5 (2010).

392. Ma, W. A study of flexoelectric coupling associated internal electric field and stress in thin film ferroelectrics. *Phys. Status Solidi* **245**, 761-768 (2008).

393. Ma, W. & Cross, L. E. Strain-gradient-induced electric polarization in lead zirconate titanate ceramics. *Appl. Phys. Lett.* **82**, 3293-3295 (2003).

394. Gao, P. *et al*. Ferroelastic domain switching dynamics under electrical and mechanical excitations. *Nat. Commun.* **5**, 3801-1-8 (2014).

395. Britson, J., Nelson, C., Pan, X. & Chen, L. First-order morphological transition of ferroelastic domains in ferroelectric thin films. *Acta Mater.* **75**, 188-197 (2014).

396. Tagantsev, A. K. Electric polarization in crystals and its response to thermal and elastic perturbations. *Phase Transit.* **35**, 119-203 (1991).

397. Nakamura, K. & Kawamura, Y. Orientation dependence of electromechanical coupling factors in $KNbO_3$. *IEEE Trans. Ultrason. Ferroelect. Freq. Control* **47**, 750-755 (2000).

398. Wang, Q., Du, X., Xu, B. & Eric Cross, L. Electromechanical coupling and output efficiency of piezoelectric bending actuators. *IEEE Trans. Ultrason. Ferroelect. Freq. Control* **46**, 638-646 (1999).

399. Whatmore, R. Pyroelectric devices and materials. *Rep. Prog. Phys.* **49**, 1335-1386 (1986).

400. Shur, D. & Rosenman, G. Figures of merit for ferroelectric electron emission cathodes. *J. Appl. Phys.* **80**, 3445-3450 (1996).

401. Li, D. & Bonnell, D. A. Controlled patterning of ferroelectric domains: fundamental concepts and applications. *Annu. Rev. Mater. Res.* **38**, 351-368 (2008).

402. Chen, L. *et al*. Formation of 90 degrees elastic domains during local 180 degrees switching in epitaxial ferroelectric thin films. *Appl. Phys. Lett.* **84**, 254-256 (2004).

403. Farokhipoor, S. *et al.* Artificial chemical and magnetic structure at the domain walls of an epitaxial oxide. *Nature* **515**, 379-383 (2014).

404. Salje, E. & Zhang, H. Domain boundary engineering. *Phase Transit.* **82**, 452-469 (2009).

405. Vasudevan, R. *et al.* Domain wall geometry controls conduction in ferroelectrics. *Nano Lett.* **12**, 5524-5531 (2012).

406. Guyonnet, J., Gaponenko, I., Gariglio, S. & Paruch, P. Conduction at domain walls in insulating $Pb(Zr_{0.2}Ti_{0.8})O_3$ thin films. *Adv. Mater.* **23**, 5377-5382 (2011).

407. Farokhipoor, S. & Noheda, B. Conduction through 71 degrees domain walls in $BiFeO_3$ thin films. *Phys. Rev. Lett.* **107**, 127601-1-4 (2011).

408. Maksymovych, P. *et al.* Tunable Metallic Conductance in Ferroelectric Nanodomains. *Nano Lett.* **12**, 209-213 (2012).

409. Crassous, A., Sluka, T., Tagantsev, A. K. & Setter, N. Polarization charge as a reconfigurable quasi-dopant in ferroelectric thin films. *Nat. Nanotechnol.* **10**, 614-618 (2015).

410. Parkin, S. S., Hayashi, M. & Thomas, L. Magnetic domain-wall racetrack memory. *Science* **320**, 190-194 (2008).

411. Yamanouchi, M., Chiba, D., Matsukura, F. & Ohno, H. Current-induced domain-wall switching in a ferromagnetic semiconductor structure. *Nature* **428**, 539-542 (2004).

412. McGilly, L. J., Yudin, P., Feigl, L., Tagantsev, A. K. & Setter, N. Controlling domain wall motion in ferroelectric thin films. *Nat. Nanotechnol.* **10**, 145-150 (2015).

413. Su, D. *et al.* Origin of 90° domain wall pinning in $Pb(Zr_{0.2}Ti_{0.8})O_3$ heteroepitaxial thin films. *Appl. Phys. Lett.* **99**, 102902-102904 (2011).

414. Nagarajan, V. *et al.* Dynamics of ferroelastic domains in ferroelectric thin films. *Nat. Mater.* **2**, 43-47 (2003).

415. Roelofs, A. *et al.* Depolarizing-field-mediated 180° switching in ferroelectric thin films with 90° domains. *Appl. Phys. Lett.* **80**, 1424-1426 (2002).

416. Khan, A. I., Marti, X., Serrao, C., Ramesh, R. & Salahuddin, S. Voltage-controlled ferroelastic switching in $Pb(Zr_{0.2}Ti_{0.8})O_3$ thin films. *Nano Lett.* **15**, 2229-2234 (2015).

417. Ganpule, C. S. *et al.* Role of 90° domains in lead zirconate titanate thin films. *Appl. Phys. Lett.* **77**, 292-294 (2000).

418. Lee, K., Choi, J., Lee, J. & Baik, S. Domain formation in epitaxial $Pb(Zr,Ti)O_3$ thin films. *J. Appl. Phys.* **90**, 4095-4102 (2001).

419. Gao, P. *et al.* Atomic-scale mechanisms of ferroelastic domain-wall-mediated ferroelectric switching. *Nat. Commun.* **4**, 1-9 (2013).

420. Damodaran, A. R., Breckenfeld, E., Choquette, A. K. & Martin, L. W. Stabilization of mixed-phase structures in highly strained $BiFeO_3$ thin films via chemical-alloying. *Appl. Phys. Lett.* **100**, 082904-1-4 (2012).

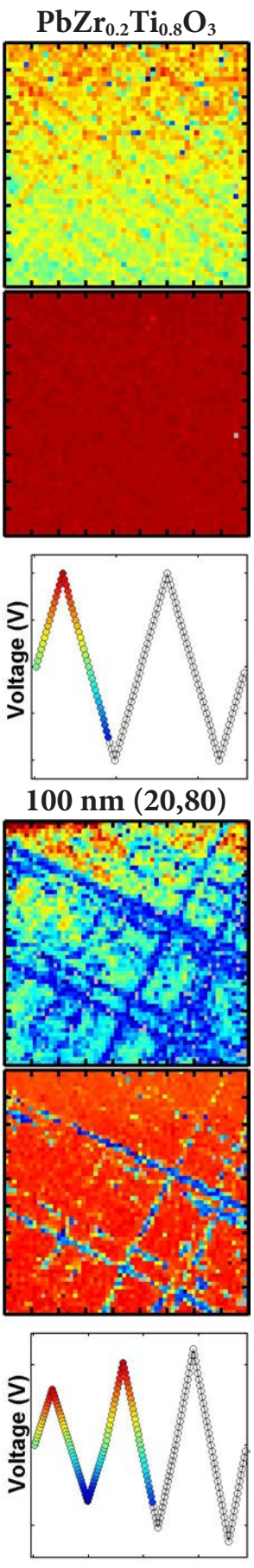

Mixed-Phase PZT

Loop 1

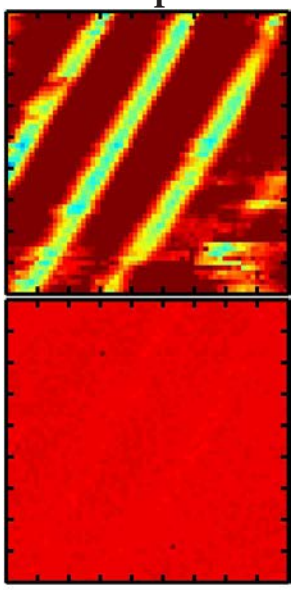

Loop 2

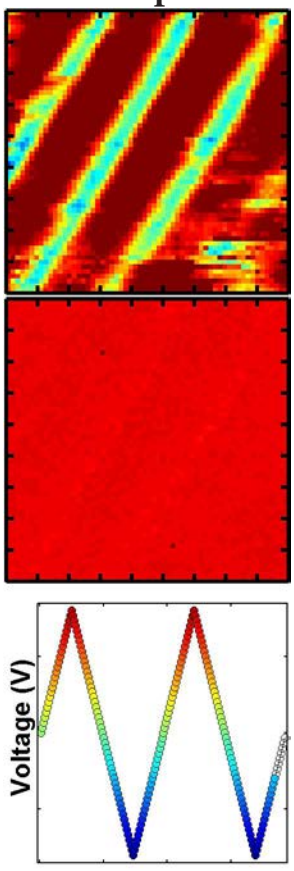

421. Damodaran, A. R., Lee, S., Karthik, J., MacLaren, S. & Martin, L. W. Temperature and thickness evolution and epitaxial breakdown in highly strained $BiFeO_3$ thin films. *Phys. Rev. B* **85**, 024113-1-9 (2012).

422. Dupé, B. *et al.* Competing phases in $BiFeO_3$ thin films under compressive epitaxial strain. *Phys. Rev. B* **81**, 144128-1-5 (2010).

423. Chen, Z. *et al.* Low-Symmetry Monoclinic Phases and Polarization Rotation Path Mediated by Epitaxial Strain in Multiferroic $BiFeO_3$ Thin Films. *Adv. Funct. Mater.* **21**, 133-138 (2011).

424. Scott, J. F. Iso-Structural Phase Transitions in $BiFeO_3$. *Adv Mater* **22**, 2106-2107 (2010).

425. Zhang, J. *et al.* Large field-induced strains in a lead-free piezoelectric material. *Nat. Nanotechnol.* **6**, 98-102 (2011).

426. Vasudevan, R. K. *et al.* Nanoscale control of phase variants in strain-engineered $BiFeO_3$. *Nano Lett.* **11**, 3346-3354 (2011).

427. Qi, X., Dho, J., Tomov, R., Blamire, M. G. & MacManus-Driscoll, J. L. Greatly reduced leakage current and conduction mechanism in aliovalent-ion-doped $BiFeO_3$. *Appl. Phys. Lett.* **86**, 2903-1-3 (2005).

428. Kim, J. K., Kim, S. S., Kim, W., Bhalla, A. S. & Guo, R. Enhanced ferroelectric properties of Cr-doped $BiFeO_3$ thin films grown by chemical solution deposition. *Appl. Phys. Lett.* **88**, 2901-1-3 (2006).

429. Xiao, X. *et al.* Greatly reduced leakage current in $BiFeO_3$ thin film by oxygen ion implantation. *J. Phys. D* **40**, 5775-5777 (2007).

430. Li, Y., Hu, S., Liu, Z. & Chen, L. Effect of substrate constraint on the stability and evolution of ferroelectric domain structures in thin films. *Acta Mater.* **50**, 395-411 (2002).

431. Bdikin, I. K. *et al.* Domain dynamics in piezoresponse force spectroscopy: Quantitative deconvolution and hysteresis loop fine structure. *Appl. Phys. Lett.* **92**, 182909-1-3 (2008).

432. Sethna, J. P. *et al.* Hysteresis and hierarchies: Dynamics of disorder-driven first-order phase transformations. *Phys. Rev. Lett.* **70**, 3347-3350 (1993).

433. Coleman, T. F. & Li, Y. An interior trust region approach for nonlinear minimization subject to bounds. *SIAM J. Optimiz.* **6**, 418-445 (1996).

434. Coleman, T. & Li, Y. On the Convergence of Reflective Newton Methods for Large-scale Nonlinear Minimization Subject to Bounds vol. 67. *Ithaca, NY, USA: Cornell University* (1994).

435. Marquardt, D. W. An algorithm for least-squares estimation of nonlinear parameters. *J. Soc. Ind. App. Math.* **11**, 431-441 (1963).

436. Ugray, Z. *et al.* Scatter search and local NLP solvers: A multistart framework for global optimization. *INFORMS J. Comput* **19**, 328-340 (2007).

437. Dixon, L. & Szegö, G. The global optimization problem: an introduction.

Towards Globe. Optimiz. **2**, 1-15 (1978).

438. Kittel, C. Theory of the structure of ferromagnetic domains in films and small particles. *Physical Review* **70**, 965-971 (1946).

439. Runkler, T. A. in *Data Analytics: Models and Algorithms for Intelligent Data Analysis* (Springer Science & Business Media, 2012).

440. Bonnet, N. Artificial intelligence and pattern recognition techniques in microscope image processing and analysis. *Adv. Imag. Elect. Phys.* **114**, 1-77 (2000).

441. Hastie, T., Tibshirani, R., Friedman, J. & Franklin, J. The elements of statistical learning: data mining, inference and prediction. *Math. Intellig.* **27**, 83-85 (2005).

442. Vasudevan, R. K. *et al*. Multidimensional dynamic piezoresponse measurements: Unraveling local relaxation behavior in relaxor-ferroelectrics via big data. *J. Appl. Phys.* **118**, 072003-1-10 (2015).

443. Kalinin, S. V., Sumpter, B. G. & Archibald, R. K. Big-deep-smart data in imaging for guiding materials design. *Nature materials* **14**, 973-980 (2015).

444. Vasudevan, R. K. *et al*. Big data in reciprocal space: Sliding fast Fourier transforms for determining periodicity. *Appl. Phys. Lett.* **106**, 091601-1-5 (2015).

445. Vasudevan, R. K., Tselev, A., Baddorf, A. P. & Kalinin, S. V. Big-data reflection high energy electron diffraction analysis for understanding epitaxial film growth processes. *ACS nano* **8**, 10899-10908 (2014).

446. Belianinov, A. *et al*. Research Update: Spatially resolved mapping of electronic structure on atomic level by multivariate statistical analysis. *Appl. Phys. Lett. Mater.* **2**, 120701-1-10 (2014).

447. Ievlev, A. & Kalinin, S. V. Data encoding based on the shape of the ferroelectric domains produced by the a scanning probe microscopy tip. *Nanoscale* **7**, 11040-11047 (2015).

448. Belianinov, A., Kalinin, S. V. & Jesse, S. Complete information acquisition in scanning probe microscopy. *Nature Communications* **6**, 1-3 (2015).

449. Agar, J. C. *et al*. Labile Ferroelastic Domain Walls in Compositionally-Graded Ferroelectric Thin Films. *Nat. Mater.* ((Under Consideration)).

450. Prokhorenko, S., Kohlstedt, H. & Pertsev, N. Ferroelectric-ferromagnetic multilayers: A magnetoelectric heterostructure with high output charge signal. *J. Appl. Phys.* **116**, 114107-1-11 (2014).

451. Prokhorenko, S. & Pertsev, N. Free-standing ferroelectric multilayers: Crossover from thin-film to bulk behavior. *J. Appl. Phys.* **110**, 074116-1-8 (2011).

452. Uecker, R. *et al*. Spiral formation during Czochralski growth of rare-earth scandates. *J. Cryst. Growth* **295**, 84-91 (2006).

453. Huang, F. Theory of strain relaxation for epitaxial layers grown on substrate of a finite dimension. *Phys. Rev. Lett.* **85**, 784-787 (2000).

454. Kasper, E. & Lyutovich, K. Strain adjustment with thin virtual substrates. *Sol. -Stat. Electron.* **48**, 1257-1263 (2004).

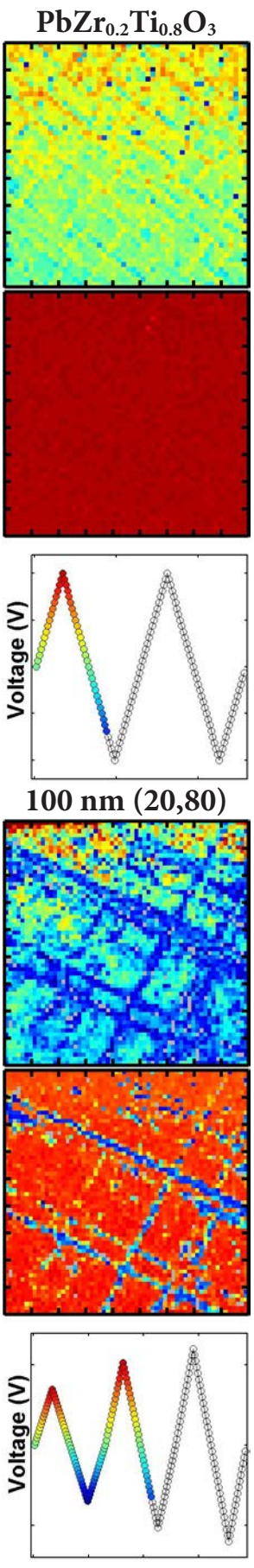

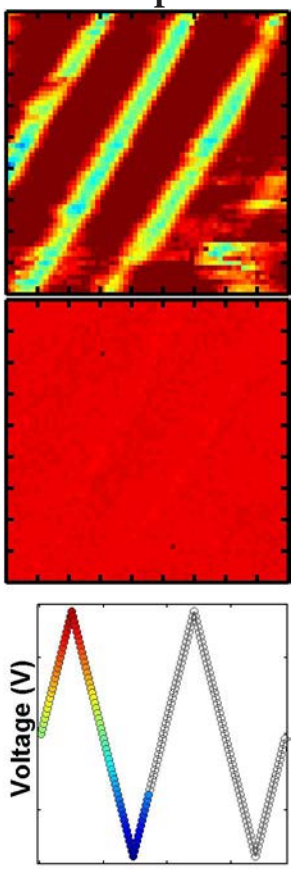

455. Lee, M. L., Leitz, C. W., Cheng, Z., Antoniadis, D. A. & Fitzgerald, E. A. Strained Ge channel p-type metal-oxide-semiconductor field-effect transistors grown on $Si_{1-x}Ge_x$/Si virtual substrates. *Adv. Mater. for Micro. and Nano-Sys.* **1**, 1-5 (2002).

456. Hoshina, Y., Yamada, A. & Konagai, M. Growth and characterization of highly tensile-strained Ge on $In_xGa_{1-x}As$ virtual substrate by solid source molecular beam epitaxy. *Jpn. J. Appl. Phys.* **48**, 111102-1-3 (2009).

457. Christen, H. M. & Eres, G. Recent advances in pulsed-laser deposition of complex oxides. *J. Phys. Condens. Matter.* **20**, 264005-1-27 (2008).

458. Breckenfeld, E. *et al.* Effect of growth induced (non) stoichiometry on the structure, dielectric response, and thermal conductivity of $SrTiO_3$ thin films. *Chem. Mater.* **24**, 331-337 (2012).

459. Dam, B., Rector, J., Johansson, J., Huijbregtse, J. & De Groot, D. Mechanism of incongruent ablation of $SrTiO_3$. *J. Appl. Phys.* **83**, 3386-3389 (1998).

460. Breckenfeld, E. *et al.* Effect of growth induced (non) stoichiometry on interfacial conductance in $LaAlO_3/SrTiO_3$. *Phys. Rev. Lett.* **110**, 196804-1-6 (2013).

461. Ohnishi, T., Shibuya, K., Yamamoto, T. & Lippmaa, M. Defects and transport in complex oxide thin films. *J. Appl. Phys.* **103**, 103703-1-6 (2008).

462. Ohnishi, T., Lippmaa, M., Yamamoto, T., Meguro, S. & Koinuma, H. Improved stoichiometry and misfit control in perovskite thin film formation at a critical fluence by pulsed laser deposition. *Appl. Phys. Lett.* **87**, 241919-1-3 (2005).

463. Suzuki, T., Nishi, Y. & Fujimoto, M. Analysis of misfit relaxation in heteroepitaxial $BaTiO_3$ thin films. *Philos. Mag. A* **79**, 2461-2483 (1999).

464. Hirano, T., Taga, M. & Kobayashi, T. Effect of nonstoichiometry on dielectric properties of strontium titanate thin films grown by ArF excimer laser ablation. *Jpn. J. Appl. Phys.* **32**, 1760-1763 (1993).

465. Lippmaa, M., Nakagawa, N., Kawasaki, M., Ohashi, S. & Koinuma, H. Dielectric Properties of Homoepitaxial SrTiO3SrTiO3SrTiO3 Thin Films Grown in the Step-Flow Mode. *J. Electroceram.* **4**, 365-368 (2000).

466. Ota, H. *et al.* Surface morphology and dielectric properties of stoichiometric and off-stoichiometric $SrTiO_3$ thin films grown by molecular beam epitaxy. *Jpn. J. Appl. Phys.* **38**, 1535-1537 (1999).

467. Oh, D. *et al.* Thermal conductivity as a metric for the crystalline quality of $SrTiO_3$ epitaxial layers. *Appl. Phys. Lett.* **98**, 221904-1-3 (2011).

468. Bai, Y., Zheng, G. & Shi, S. Direct measurement of giant electrocaloric effect in BaTiO3 multilayer thick film structure beyond theoretical prediction. *Appl. Phys. Lett.* **96**, 192902-1-3 (2010).

469. Lichtman, D. & Ready, J. Laser beam induced electron emission. *Phys. Rev. Lett.* **10**, 342-348 (1963).

470. Smith, H. M. & Turner, A. Vacuum deposited thin films using a ruby laser. *Appl. Opt.* **4**, 147-148 (1965).

471. Schwarz, H. & Tourtellotte, H. Vacuum deposition by high-energy laser with emphasis on barium titanate films. *J. Vac. Sci. Technol.* **6**, 373-378 (1969).

472. Bykovskii, Y. A. *et al*. Yield of various ions from a laser-produced plasma. *Sov. J. Plasma Phys.* **4**, 180-184 (1978).

473. Dubowski, J., Williams, D., Sewell, P. & Norman, P. Epitaxial growth of (100) CdTe on (100) GaAs induced by pulsed laser evaporation. *Appl. Phys. Lett.* **46**, 1081-1083 (1985).

474. Cheung, J., Khoshnevisan, M. & Magee, T. Heteroepitaxial growth of CdTe on GaAs by laser assisted deposition. *Appl. Phys. Lett.* **43**, 462-464 (1983).

475. Ashfold, M. N., Claeyssens, F., Fuge, G. M. & Henley, S. J. Pulsed laser ablation and deposition of thin films. *Chem. Soc. Rev.* **33**, 23-31 (2004).

476. Dreyfus, R., Kelly, R. & Walkup, R. Laser-induced fluorescence studies of excimer laser ablation of Al_2O_3. *Appl. Phys. Lett.* **49**, 1478-1480 (1986).

477. Wicklein, S. *et al*. Pulsed laser ablation of complex oxides: The role of congruent ablation and preferential scattering for the film stoichiometry. *Appl. Phys. Lett.* **101**, 131601-1-3 (2012).

478. Floro, J. *et al*. The dynamic competition between stress generation and relaxation mechanisms during coalescence of Volmer–Weber thin films. *J. Appl. Phys.* **89**, 4886-4897 (2001).

479. van der Merwe, Jan H & Jesser, W. The prediction and confirmation of critical epitaxial parameters. *J. Appl. Phys.* **64**, 4968-4974 (1988).

480. Baskaran, A. & Smereka, P. Mechanisms of stranski-krastanov growth. *J. Appl. Phys.* **111**, 044321-1-6 (2012).

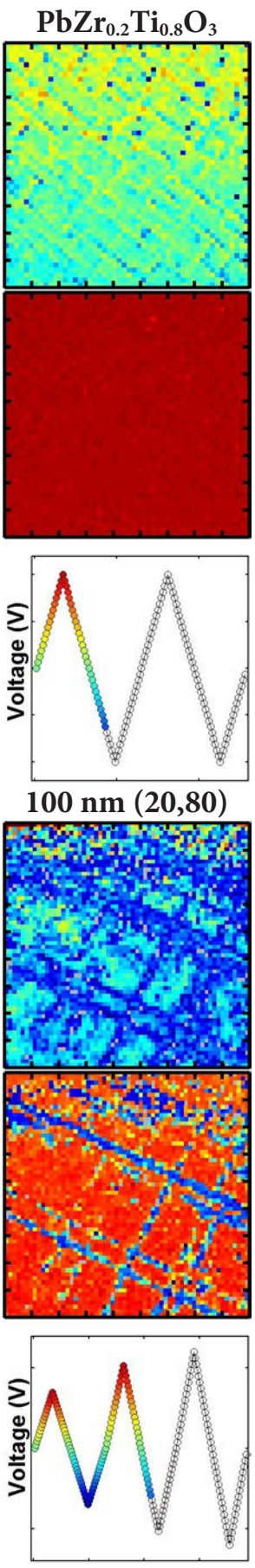

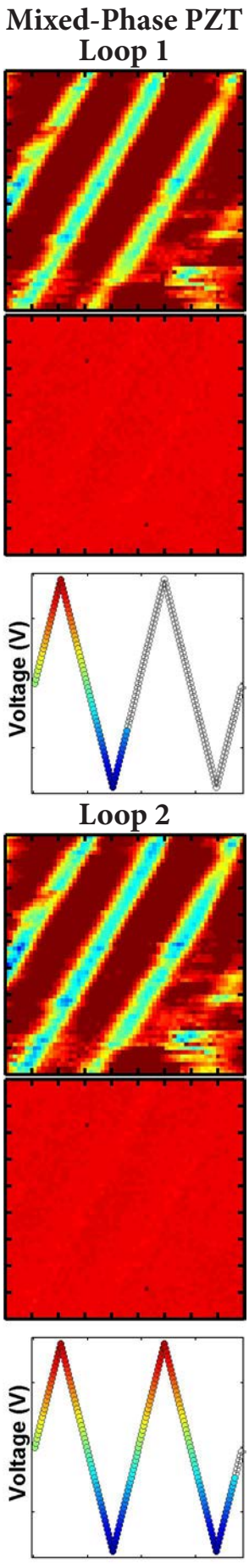
Mixed-Phase PZT
Loop 1
Voltage (V)
Loop 2
Voltage (V)

Contributions

I would like to specifically acknowledge the contributions of others who assisted with certain aspects of this work.

The growth and macroscopic measurements of the single-layer $PbZr_{0.8}TiO_3$ and compositionally-graded heterostructures were conducted in close collaboration with R. V. K. Mangalam. Analysis of the results were completed by J. C. Agar.

Nanobeam electron diffraction and strain mapping were conducted by J. Kacher.

Standard loop fitting algorithm was written by M. B. Okatan.

Scanning probe studies on mixed-phase $PbTiO_3$ and $PbZr_{1-x}Ti_xO_3$ heterostructures was conducted in a close collaboration with A. R. Damodaran and S. Pandya whose contributions were equivalent to J. C. Agar. Preliminary analysis on mixed-phase $PbTiO_3$ and $PbZr_{1-x}Ti_xO_3$ heterostructures included in this thesis was conducted by J. C. Agar.

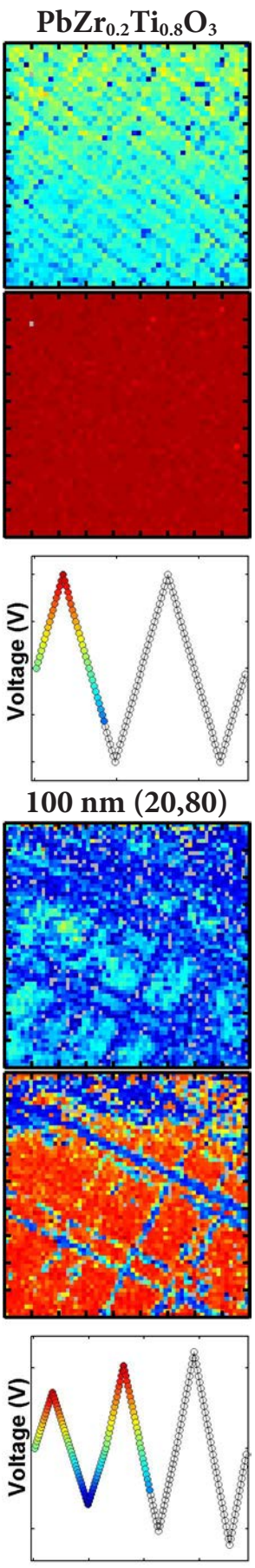

Mixed-Phase PZT
Loop 1

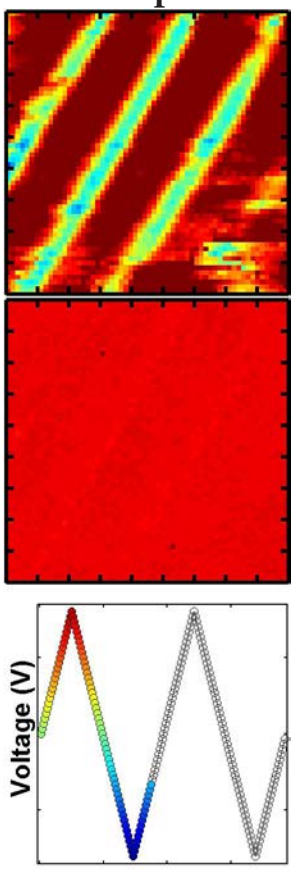

Loop 2

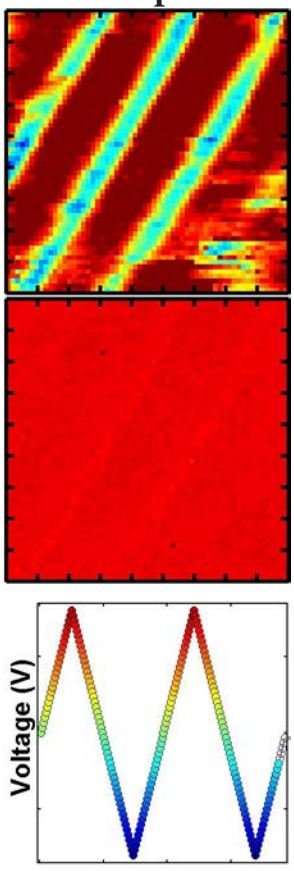

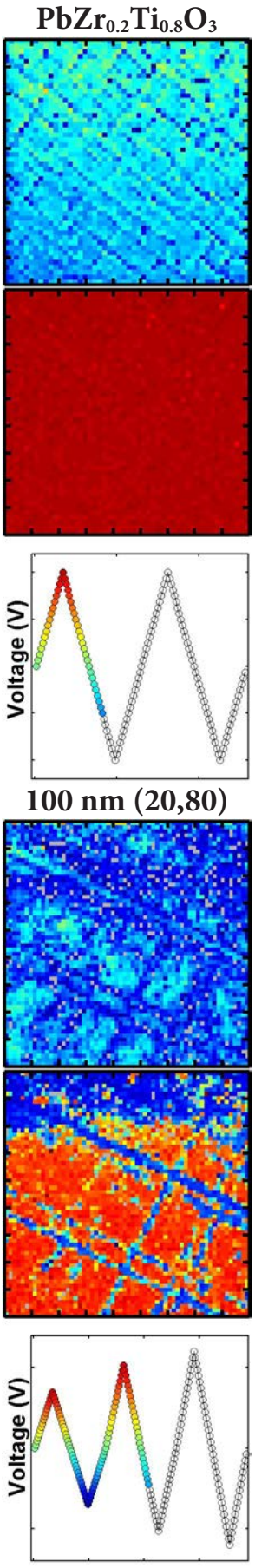
PbZr0.2Ti0.8O3
Voltage (V)
100 nm (20,80)
Voltage (V)

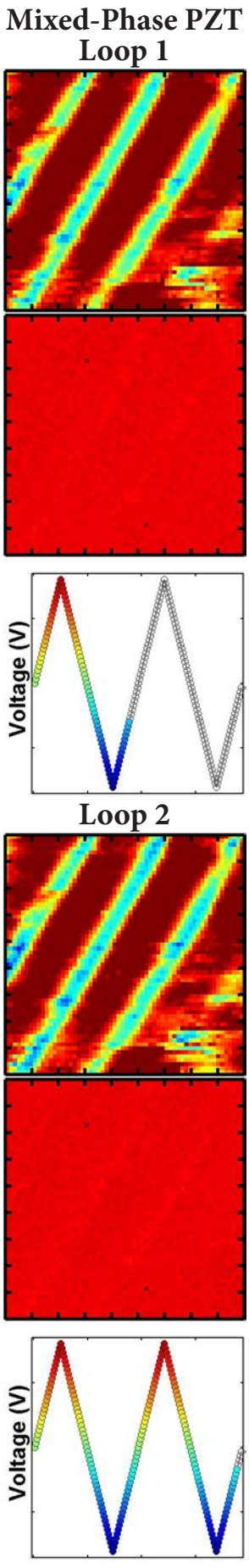
Mixed-Phase PZT
Loop 1
Voltage (V)
Loop 2
Voltage (V)

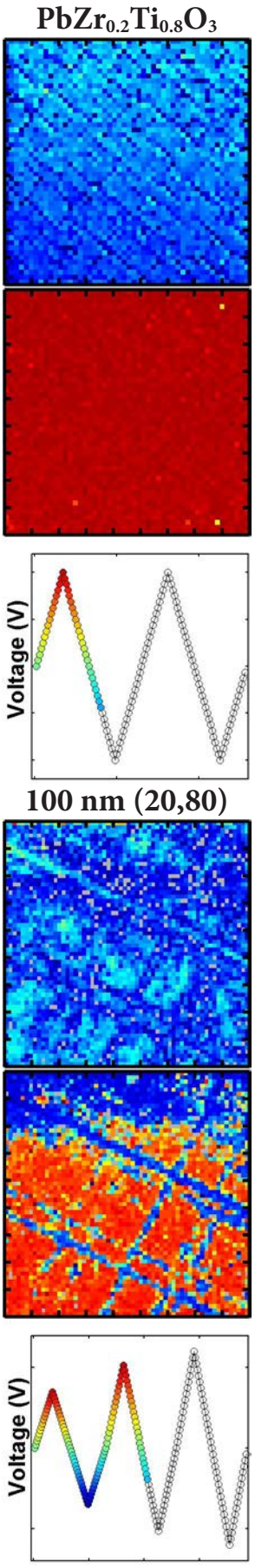
PbZr0.2Ti0.8O3
Voltage (V)
100 nm (20,80)
Voltage (V)

Mixed-Phase PZT
Loop 1

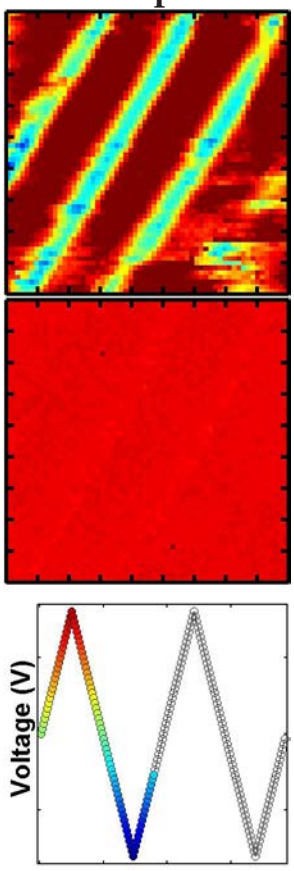

Loop 2

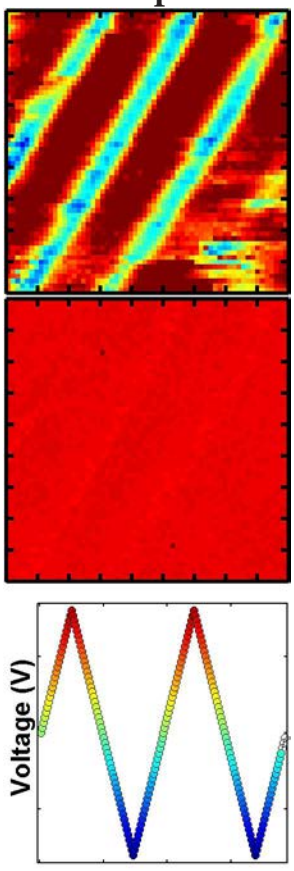

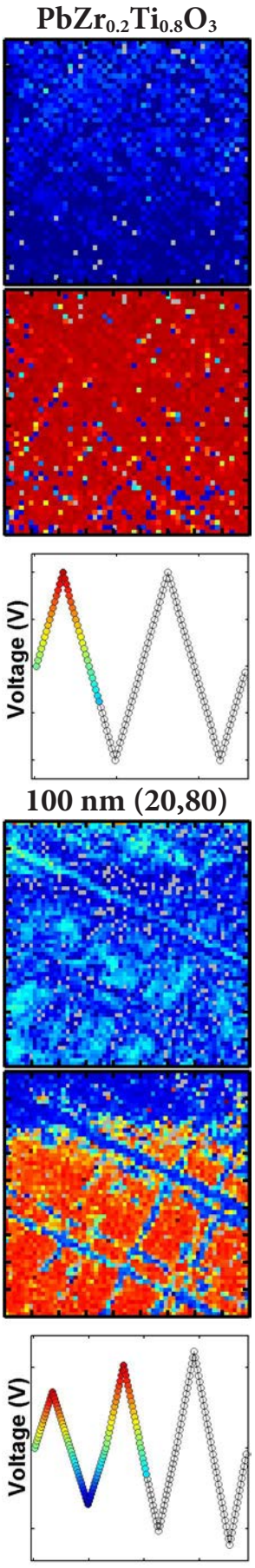
PbZr0.2Ti0.8O3
Voltage (V)
100 nm (20,80)
Voltage (V)

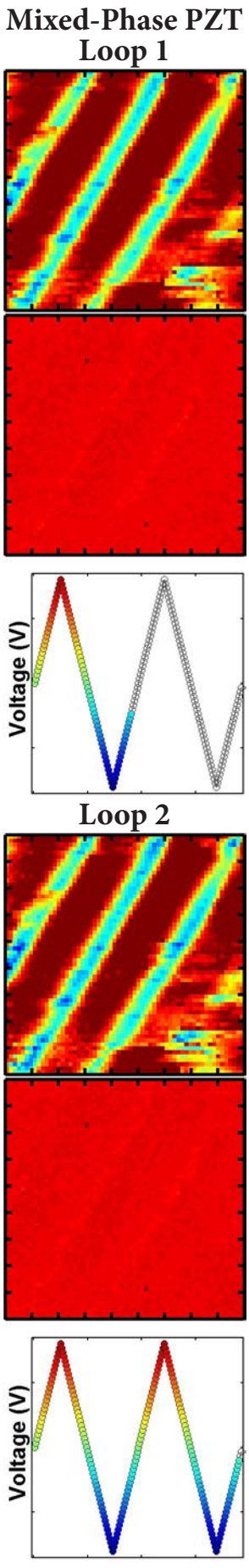
Mixed-Phase PZT
Loop 1
Voltage (V)
Loop 2
Voltage (V)

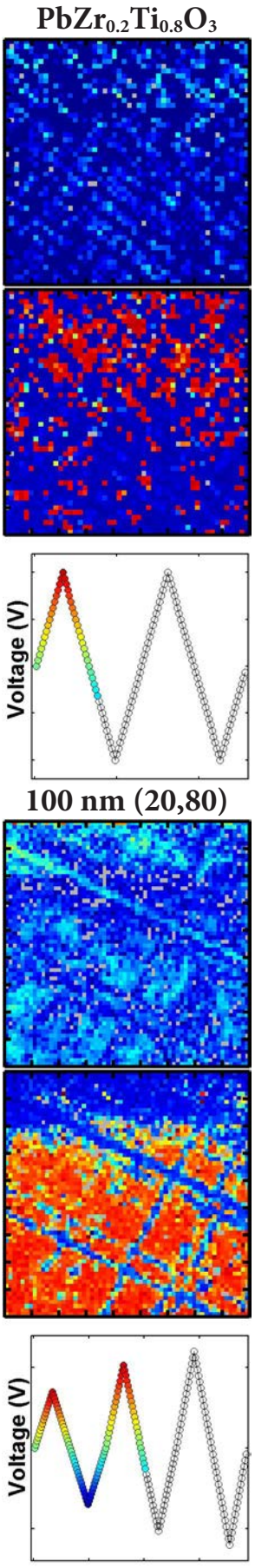
PbZr0.2Ti0.8O3
Voltage (V)
100 nm (20,80)
Voltage (V)

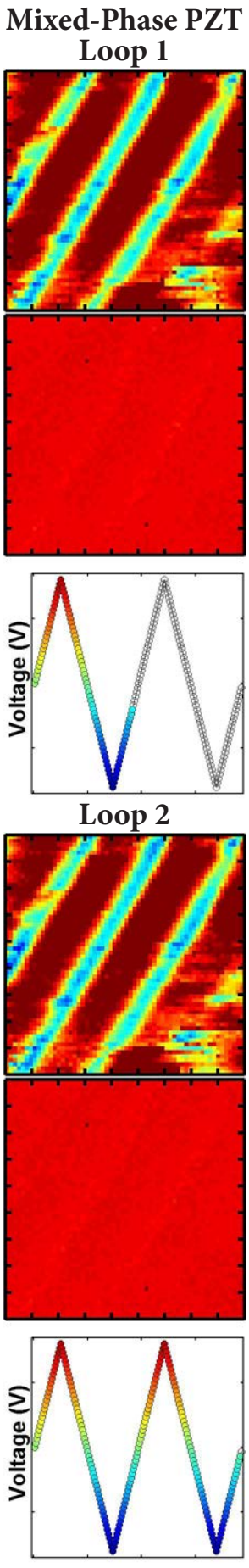
Mixed-Phase PZT
Loop 1
Voltage (V)
Loop 2
Voltage (V)

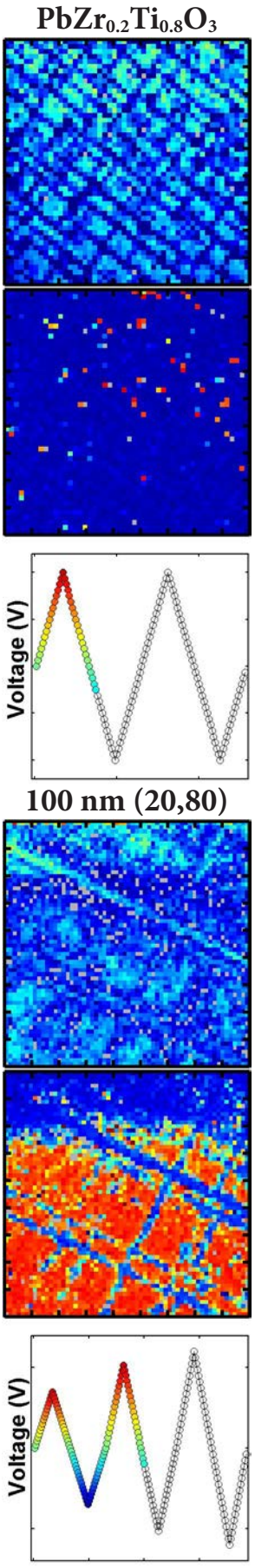
PbZr0.2Ti0.8O3
Voltage (V)
100 nm (20,80)
Voltage (V)

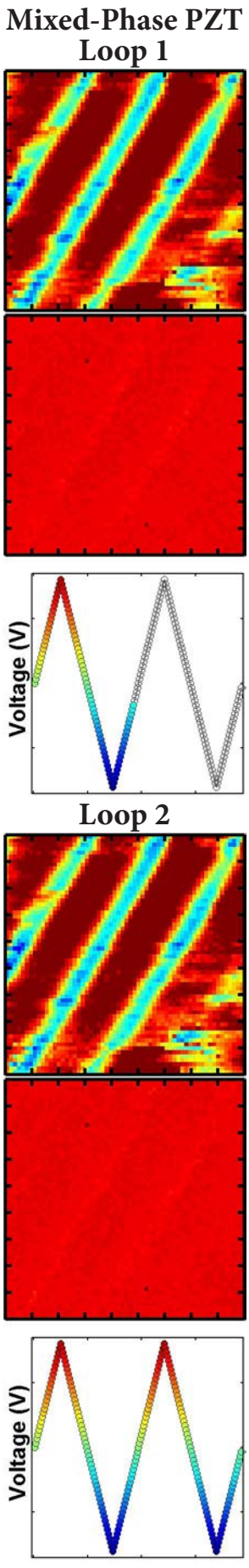
Mixed-Phase PZT
Loop 1
Voltage (V)
Loop 2
Voltage (V)

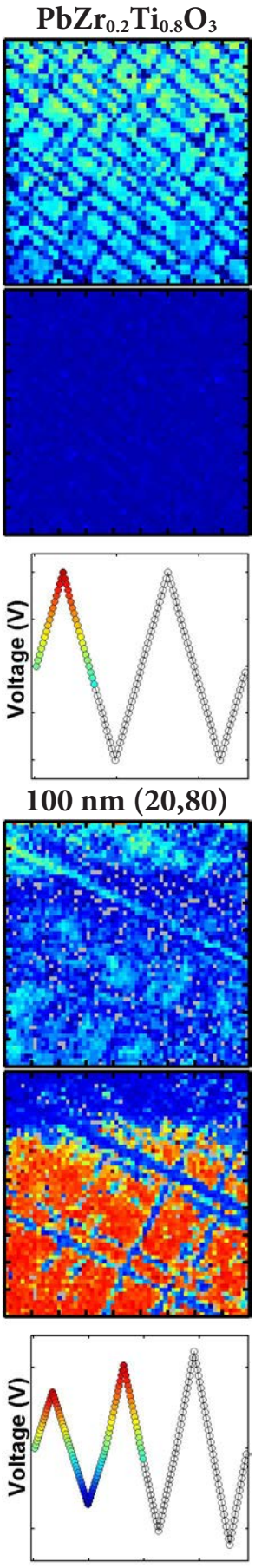
PbZr0.2Ti0.8O3
Voltage (V)
100 nm (20,80)
Voltage (V)